

DTIC

1

# PROCEEDINGS OF THE CONFERENCE ON LOW REYNOLDS NUMBER AIRFOIL AERODYNAMICS

AD-A163 609

Edited by  
Thomas J. Mueller ✓  
UNDAS-CP-77B123  
June 1985

Contract No. N00014-85-G-0123



DTIC  
ELECTE  
JAN 31 1986  
S B D

Sponsored by  
NATIONAL AERONAUTICS AND SPACE ADMINISTRATION  
LANGLEY RESEARCH CENTER  
HAMPTON, VIRGINIA

AND

U.S. NAVY  
OFFICE OF NAVAL RESEARCH  
ARLINGTON, VIRGINIA

AND

THE UNIVERSITY OF NOTRE DAME  
DEPARTMENT OF AEROSPACE AND MECHANICAL ENGINEERING  
NOTRE DAME, INDIANA

DISTRIBUTION STATEMENT A

Approved for public release  
Distribution Unlimited

DTIC FILE COPY

86 1 6 044

The views, opinions, and/or findings contained in this report are those of the author(s) and should not be construed as an official NASA, U.S. Navy or University of Notre Dame position, policy, or decision, unless so designated by other documentation.

# PROCEEDINGS OF THE CONFERENCE ON LOW REYNOLDS NUMBER AIRFOIL AERODYNAMICS

Edited by  
Thomas J. Mueller  
UNDAS-CP-77B123  
June 1985



DTIC  
ELECTE  
JAN 31 1986  
S B D

Sponsored by  
NATIONAL AERONAUTICS AND SPACE ADMINISTRATION  
LANGLEY RESEARCH CENTER  
HAMPTON, VIRGINIA

AND

U.S. NAVY  
OFFICE OF NAVAL RESEARCH  
ARLINGTON, VIRGINIA

AND

THE UNIVERSITY OF NOTRE DAME  
DEPARTMENT OF AEROSPACE AND MECHANICAL ENGINEERING  
NOTRE DAME, INDIANA

DISTRIBUTION STATEMENT A

Approved for public release  
Distribution Unlimited

## PREFACE

Current interest in a variety of low Reynolds number applications has focused attention on the design and evaluation of efficient airfoil sections at chord Reynolds numbers from about 100,000 to about 1,000,000. These applications include remotely piloted vehicles (RPVs) at high altitudes, sailplanes, ultra-light man-carrying/man powered aircraft, mini-RPVs at low altitudes and wind turbines/propellers.

Although the design and evaluation techniques for airfoil sections above chord Reynolds numbers of 500,000 are reasonably well developed, problems related to boundary layer separation and transition have made it difficult to extend these techniques to lower Reynolds numbers. Presently available design and analysis techniques require improved criteria for laminar separation, transition, reattachment and turbulent separation. Mathematical models of these complex phenomena require additional, very careful experimental studies. Because of the sensitivity of the low Reynolds number airfoil boundary layer to freestream and surface-generated disturbances, definitive experiments are very difficult. Therefore, it is important that theoreticians and experimentalists work closely together in order to advance our understanding of these phenomena.

The purpose of this Conference on Low Reynolds Number Airfoil Aerodynamics is to bring together those researchers who have been active in areas closely related to this subject. It is hoped that this occasion will provide the discussion and exchange of ideas necessary to indicate the present status and future direction for research.

This Conference is sponsored by the National Aeronautics and Space Administration, Langley Research Center, Hampton, Virginia, (Purchase Order No. L771778), the U.S. Navy Office of Naval Research, Arlington, Virginia, (Contract No. N00014-85-G-0123) and the Department of Aerospace and Mechanical Engineering, University of Notre Dame, Notre Dame, Indiana. It is a pleasure to thank D.M. Somers and W.D. Harvey (NASA Langley Research Center), R. Whitehead (U.S. Navy, ONR) and R. Foch (U.S. Navy, NRL) for the support and encouragement needed to produce this Conference. The authors should also be commended for preparing their papers in time to have the Proceedings available at the Conference.

Accession For	
WHS	<input checked="" type="checkbox"/>
STIC	<input type="checkbox"/>
Unann	<input type="checkbox"/>
Just	<input type="checkbox"/>
<b>PER LETTER</b>	
By	
Distribution	
Availability Codes	
Avail and/or	
Dist	Special
<b>A-1</b>	

Thomas J. Mueller  
Conference Organizer  
Department of Aerospace and  
Mechanical Engineering  
University of Notre Dame  
Notre Dame, IN 46556  
U.S.A.



## CONTENTS

### AIRFOIL DESIGN

Airfoil Design for Reynolds Numbers Between 50,000 and 500,000	
R. Eppler and D.M. Somers . . . . .	1
Low Reynolds Number Airfoil Design	
M.D. Maughmer and M.S. Selig . . . . .	15
Airfoil Design at Low Reynolds Number with Constrained Pitching Moment	
R.H. Liebeck and P.P. Comacho . . . . .	27
A Viscous-Inviscid Coupling Method for the Design of Low Reynolds Number Airfoil Sections	
A.A. Hassan . . . . .	53

### COMPUTATIONAL STUDIES AND STABILITY

Effect of Pressure Gradients on the Growth of Subharmonic Disturbances in Boundary Layers	
T. Herbert and F.P. Bertolotti . . . . .	65
Computational and Theoretical Studies of Unsteady Viscous Aerodynamics	
J.C. Wu . . . . .	77

### LAMINAR SEPARATION BUBBLE

Research on Laminar Separation Bubbles at Delft University of Technology in Relation to Low Reynolds Number Airfoil Aerodynamics	
J.L. van Ingen and L.M.M. Boermans . . . . .	89
An Analysis of a Separation Bubble Transition Criterion at Low Reynolds Numbers	
G.S. Schmidt, M.M. O'Meara and T.J. Mueller . . . . .	125
Theoretical and Experimental Study of Low Reynolds Number Transitional Separation Bubbles	
C. Gleyzes, J. Cousteix and J.L. Bonnet . . . . .	137
Low Reynolds Number Separation Bubble Research at UTRC	
W.P. Patrick and D.E. Edwards . . . . .	153
Separation Bubble Behavior for a NACA 23009 Airfoil	
S.S. Fisher, J.D. Abbitt and G.W. O'Leary . . . . .	169

## AIRFOIL AND FINITE WING EXPERIMENTS

Aspect Ratio Effects on the Aerodynamics of a Wortmann Airfoil at Low Reynolds Number	
J.F. Marchman, III, A.A. Abtahi and V. Sumantran . . . . .	183
Performance of Finite Wings at Low Reynolds Numbers	
W.G. Bastedo, Jr. and T.J. Mueller . . . . .	195
An Environmental Aerodynamic Test System for Low-Reynolds-Number Applications	
H.-T. Liu, E.W. Geller and M. Cooper . . . . .	207

## ANALYSIS OF FLOW OVER AIRFOILS

Symmetry Breaking and Lift Hysteresis Arising From Massive Laminar Separation: A Study of Multiple Steady-State Solutions	
H.K. Cheng . . . . .	219
Computational Study of Flow Over Miley and Wortmann Airfoils	
A.P. Kothari and J.D. Anderson, Jr. . . . .	235

## UNSTEADY FLOW EXPERIMENTS

Experiments on Unsteady Flows About Wing Sections	
E. Krause, G. Erhardt and B. Schweitzer . . . . .	255
Streamwise and Spanwise Vortical Patterns Visualized over Airfoils in Unsteady Flow	
F. Finaish, P. Freymuth and W. Bank . . . . .	269
Preliminary Experiments in Unsteady Flow on Airfoils at Low Reynolds Numbers	
M. Brendel and T.J. Mueller . . . . .	281

## SURFACE AND FREESTREAM DISTURBANCES

On Effects of Three-Dimensional Roughness on Transition and Receptivity to Disturbances	
T.C. Corke and M.V. Morkovin . . . . .	293
The Effect of Trip Wire Roughness on the Performance of the Wortmann FX 63-137 Airfoil at Low Reynolds Numbers	
A.F. Huber II and T.J. Mueller . . . . .	307

SURFACE AND FREESTREAM DISTURBANCES (cont'd)

Acoustic and Turbulence Influence on Low-Reynolds  
Number Wing Pressure Distributions

V. Sumantran, Z. Sun and J.F. Marchman III . . . . . 323

Propeller Slipstream/Wing Boundary Layer Effects  
at Low Reynolds Numbers

S.J. Miley, R.M. Howard and B.J. Holmes . . . . . 335

# AIRFOIL DESIGN FOR REYNOLDS NUMBERS BETWEEN 50,000 AND 500,000

by

Richard Eppler  
Universität Stuttgart

and

Dan M. Somers  
NASA Langley Research Center, Hampton/VA

## ABSTRACT

The design of airfoils for Reynolds numbers between 50,000 and 500,000 is governed by the problem of laminar separation bubbles. All other problems such as potential-flow design and analysis methods as well as boundary-layer computation can be solved much more reliably and are, therefore, only mentioned briefly. The relevant dimensions and some similarity parameters of the separation bubble are discussed and a simple analogy model is described. This model allows a critical Reynolds number to be defined, above which the additional drag due to the bubble seems to be negligible. Several examples are presented which support the validity of this empirically-founded, critical Reynolds number. No drag penalty due to the bubble can as yet be predicted by the theory, however.

The critical Reynolds number of the upper surface can be different from that of the lower surface. Both critical Reynolds numbers depend on the lift coefficient. For most applications, the Reynolds number depends on the lift coefficient as well. The airfoil should be designed such that the critical Reynolds numbers of both surfaces are lower, for every lift coefficient, than the application Reynolds number. How this objective can be met using a particular airfoil design method in a simple, straightforward manner is described. The limitations of this design method are also discussed. Further improvements can be achieved if better empirical laws for the critical Reynolds number and, eventually, for the drag penalty due to the bubble can be established from recent experiments.

## 1. MATHEMATICAL MODEL

The flow around airfoils can be modelled according to Prandtl's boundary-layer concept, if the Reynolds number is high enough. In this case, the flow outside of a thin boundary layer near the airfoil surface is idealized as inviscid potential flow which yields the boundary conditions for the viscous flow in the boundary layer. In references [1] and [2], a mathematical model and a computer program for computing such flows is described. It contains:

- A conformal-mapping method for the solution of the inviscid airfoil design problem, which requires the computation of the airfoil shape

from given properties of the potential-flow velocity (or pressure) distribution.

- A higher-order panel method for the solution of the inviscid, airfoil analysis problem, which requires the computation of the potential flow for a given airfoil shape.
- An approximative boundary-layer computation method for calculating the boundary-layer flow for a given potential-flow velocity distribution.
- A method for the computation of lift and drag from potential and boundary flows.

Additional details of this mathematical model will be given only as far as is necessary for understanding the present paper.

## 2. AIRFOIL DESIGN METHOD

In the airfoil design method (of references [1] and [2]) the velocity distribution of an airfoil at a certain angle of attack  $\alpha$  cannot be specified directly. Instead, the angle of attack  $\alpha^*$  at which the potential-flow velocity is to be constant, is specified for each segment of the airfoil. In addition, a pressure-recovery function is introduced toward the trailing edge. This method allows the velocity gradient to be accurately controlled and modified. Such modifications normally violate the closure of the airfoil trailing edge. The method contains many options for a so-called trailing-edge iteration, which allow the pressuregradient modifications to be compensated for automatically in order to always achieve a closed airfoil. This feature of the method will not be mentioned in each instance, when a velocity distribution is introduced and modified.

## 3. BOUNDARY LAYER AND SEPARATION BUBBLE

Turbulent boundary layers cause more skin friction than laminar boundary layers, but also withstand much more adverse pressure gradient before separating. Boundary-layer transition should, therefore, be prevented as long as no separation is present, which is the case in a favorable pressure gradient (increasing potential-flow velocity). As soon as a region with adverse pressure gradient is approached, which must occur toward the trailing edge, transition must be promoted in order to prevent laminar separation.

For Reynolds numbers between 50,000 and 500,000, it is much easier to maintain a laminar boundary layer than to achieve a transition far enough forward. Boundary-layer transition is, therefore, a central issue.

Although it is sometimes reasonable to talk about a transition "point", it must be emphasized that boundary-layer transition is not concentrated at a point but occurs, rather, over some distance. First, certain Tollmien-Schlichting waves are amplified, then secondary instabilities occur, and, after additional nonlinear developments, the transition to a completely irregular turbulent motion begins in layers with very high shear velocities like in free shear layers. Obviously, the flow

in such free shear layers is much more unstable than the flow in boundary layers. The first instability, the amplification of the Tollmien-Schlichting waves, depends on two parameters. One parameter is a local Reynolds number based on, for example, the local, potential-flow velocity  $U$  and the local boundary-layer momentum thickness  $\delta_2$

$$R_{\delta_2} = \frac{U\delta_2}{\nu}$$

The other parameter concerns the velocity distribution  $u(y)$  in the boundary layer, the so-called velocity profile, where  $y$  is the axis perpendicular to the surface and  $u$  is the velocity component in the boundary layer parallel to the surface. This component approaches  $U$  as  $y$  approaches  $\delta$ , the boundary-layer thickness. The shape of the velocity profile can be characterized by a shape parameter, for example

$$H_{32} = \frac{\delta_3}{\delta_2}$$

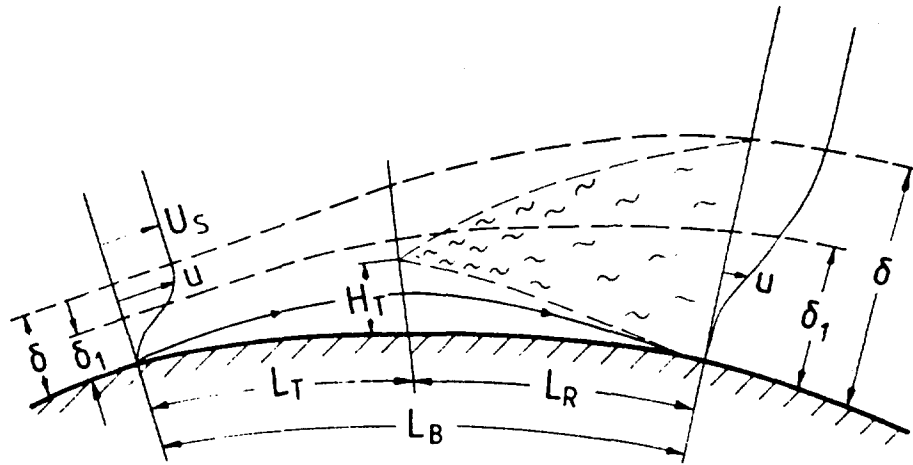
where  $\delta_3$  is the boundary-layer energy thickness. This shape parameter is lower for profiles having an inflection point than for profiles having none. Very strong inflection leads to reversed flow near the surface and, thus, to separation. Given certain additional assumptions, a lower limit for  $H_{32}$  ( $= 1.51509$ ) exists at which separation of the laminar boundary layer occurs. Low values of  $H_{32}$  and, thus, separation are always caused by adverse pressure gradients. The general facts concerning stability can now be stated precisely.

- Increasing Reynolds number yields less stable boundary layers. For any boundary-layer profile, there exists a limit for  $R_{\delta_2}$ , below which the boundary layer is stable.
- Decreasing  $H_{32}$  and adverse pressure gradients promote instability; the stability limit for  $Re_{\delta_2}$  decreases rapidly as  $H_{32}$  decreases.

Although these statements only concern the stability, transition also exhibits a similar trend. It is possible to develop approximative local transition criteria, where transition is assumed if  $R_{\delta_2}$  exceeds a value which depends only on  $H_{32}$  [1]. Such empirical criteria do not model the transition process and must, therefore, be used carefully. They can only detect the end of the laminar boundary layer, whether the laminar separation, or the beginning of the last phases of the transition process. Most experiments for detecting transition determine only the beginning of the fully developed turbulent boundary layer which occurs later than the end of the laminar boundary layer. The general tendency is, however, always true. Transition is promoted by adverse pressure gradients which, simultaneously, increase the separation danger. The question is always: Which will occur first? If the laminar boundary layer separates, a large wake forms which causes high drag. If transition occurs before laminar separation, the drag is much lower.

A more complicated phenomenon often occurs, however. The laminar boundary layer separates and a wake forms in which the pressure is approximately constant. This wake is bounded by a free shear layer which is much more unstable than the corresponding boundary layer. Accordingly, transition occurs in the free shear layer within a short distance of

separation. The resulting turbulence spreads out and may reach the surface. Downstream of this reattachment, a turbulent boundary layer forms. This phenomenon is called a laminar separation bubble and is sketched in figure 1.



Separation Transition Reattachment

Figure 1: Sketch of the separation bubble.

It has been claimed that transition never occurs without a bubble. This seems highly unlikely, although for Reynolds numbers between 50,000 and 500,000, transition by means of a separation bubble will be the most frequent case.

The laminar separation bubble has been the subject of much research since 1942, when F.W. Schmitz [3] first described it. Therefore, only those details which influence the design of airfoils will be discussed.

It is generally accepted that increasing Reynolds number decreases the length  $L_T$  from separation to transition in the free shear layer and, thus, the size of the bubble. For a given airfoil at a certain angle of attack, a transition Reynolds number can be defined as

$$R_T = \frac{U_s L_T}{\nu}$$

which is nearly independent of the chord Reynolds number  $Re$ . It is very unlikely that  $R_T$  is a universal constant as suggested by Ntim [4]. There is much evidence that  $R_T$  depends strongly on the relative thickness  $H_T/L_T$  of the bubble. Moreover, the increase in boundary-layer thickness and, thus, the drag penalty due to the bubble depend on the absolute thickness  $H_T$  of the bubble.

It is crucial that some information about the bubble and its associa-

ted drag penalty be available during the airfoil design procedure. The effect of the bubble can be empirically estimated during the boundary-layer computation. Turbulent boundary layers have, for the same pressure gradient, higher  $H_{32}$  values than laminar boundary layers. For example, the laminar boundary layer on a flat plate yields  $H_{32} = 1.573$ ; the turbulent one,  $H_{32} \approx 1.77$ . If transition is introduced into the computation, an abrupt increase in  $H_{32}$  usually results. There are cases, however, in which  $H_{32}$  increases only slowly near the beginning of the turbulent boundary layer. These cases become more obvious if the laminar boundary layer separates and then the boundary-layer parameters of the separating laminar boundary layer are used as initial conditions for the turbulent boundary layer calculations. The region over which the  $H_{32}$  of the turbulent boundary layer does not reach high values can be considered as an analogy to the separation bubble. Thus, the length  $L_B$  of the bubble analogy can be evaluated. Additional information is required, however, to evaluate the thickness of the bubble and, accordingly, the drag penalty due to the bubble. If, following laminar separation, the potential-flow velocity  $U$  were constant, the flow would not separate from the surface because the resulting free shear layer has the same, constant velocity. Thus, it can be seen that the thickness of the resulting wake depends on the decrease in  $U(x)$  which would occur had there been no separation. Therefore the decrease  $\Delta U_B$  in  $U(x)$  over the length  $L_B$  of the bubble analogy is used as the criterion for the bubble effect. Specifically  $L_B$  is the length from the beginning of the turbulent boundary-layer computation to the point where  $H_{32} = 1.6$  and  $\Delta U_B$  is the velocity decrease over  $L_B$ . Comparisons with many experimental results indicate that essentially no drag penalty is incurred if

$$\frac{\Delta U_B}{U_S} < 0.042 \quad .$$

If  $U_B/U_S$  exceeds 0.042, a warning is given indicating that no drag penalty has been included and that, therefore, the predicted drag coefficients are probably too low.

Comparisons of experimental [5] and theoretical results for airfoil 387 which was designed previously for model aircraft, illustrate the validity of this warning. This airfoil and its potential-flow velocity distributions for three angles of attack are shown in figure 2.

The theoretical and experimental section characteristics for Reynolds numbers of 200,000, 100,000, and 60,000 are shown in figures 3, 4, and 5, respectively. The bubble warning is indicated by triangles at the appropriate points along the  $c_l - c_d$  curves. If the triangle points upward ( $\Delta$ ), a significant (drag-producing) bubble is predicted on the upper surface. If the triangle points downward ( $\nabla$ ), the bubble warning is for the lower surface. Bubble warnings for both surfaces result in a six-pointed star. For  $Re = 200,000$  (figure 3), the agreement between theory and experiment is remarkable, especially considering the empirical nature of the boundary-layer method and the difficulties associated with measuring section characteristics, particularly drag coefficients, at such a low Reynolds number. For  $Re = 100,000$  (fig. 4), bubble warnings appear for almost all lift coefficients and the agreement between theory and experiment is correspondingly poorer.

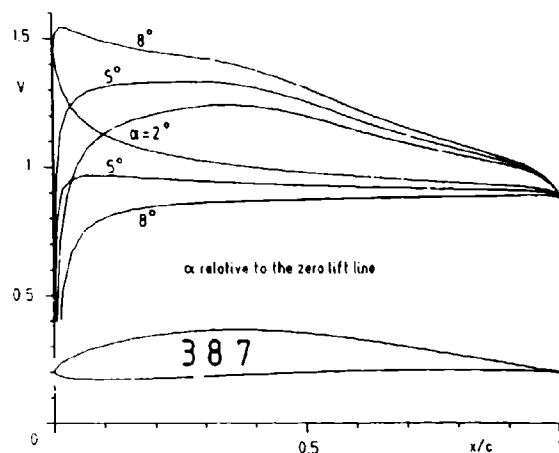


Figure 2:  
Airfoil 387 with  
velocity distribu-  
tions

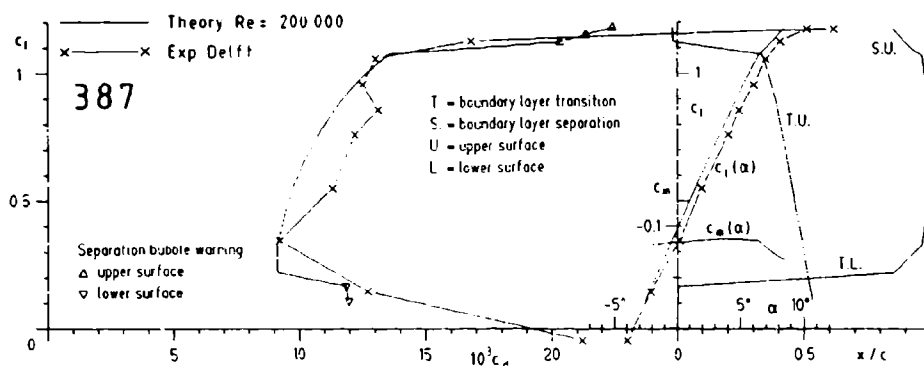


Figure 3: Theoretical and experimental section characteristics  
of airfoil 387,  $Re = 200,000$

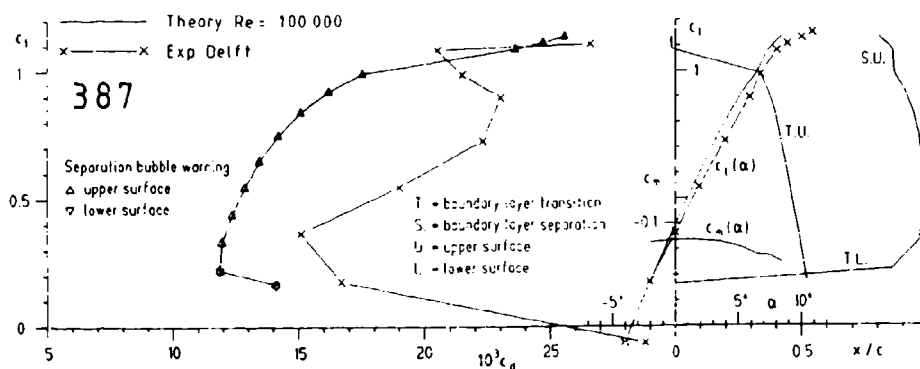


Figure 4: Theoretical and experimental section characteristics  
of airfoil 387,  $Re = 100,000$

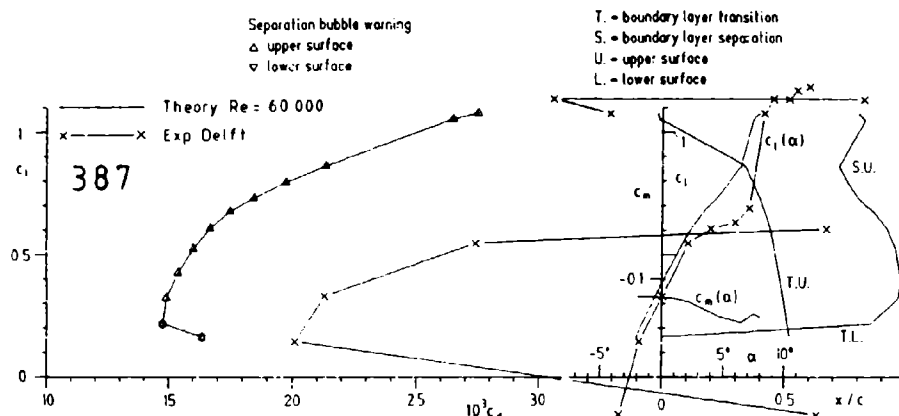


Figure 5: Theoretical and experimental section characteristics of airfoil 387,  $Re = 60,000$

For  $Re = 60,000$  (fig.5), numerous warnings are again present and the agreement is still poorer. It should be noted, however, that the method predicts the laminar "stall" at  $c_l = 0.6$  and the following turbulent reattachment and then turbulent stall at higher angles of attack.

#### 4. AIRFOIL DESIGN

Because most airfoils are applied to aircraft having essentially constant wing loadings, the Reynolds number depends on the lift coefficient. For a given lift coefficient  $c_{l0}$  and Reynolds number  $R_0$ , the Reynolds number  $Re$  for any other lift coefficient  $c_l$  is

$$Re = R_0 \sqrt{\frac{c_{l0}}{c_l}}.$$

Typically, an airfoil designed for low Reynolds numbers might be required to operate over a range of lift coefficients from 0.2 to 1.4. In this case,  $c_{l0}$  might be 1.4 and  $R_0$ , 250,000.

An example of such an airfoil is shown in figure 6. The concave pressure-recovery functions selected should produce little shear stress and, therefore, little friction drag. The section characteristics for five Reynolds numbers from 250,000 to  $1 \times 10^6$  are shown in figure 7. Lots of bubble warnings are present and, therefore, very poor performance must be expected for this airfoil. The source of these bubble warnings is the steep, adverse pressure gradient at the beginning of the pressure recovery. The velocity distribution must be modified to eliminate these warnings.

At one angle of attack  $\alpha$ , the thickness of the bubble on the upper surface can be reduced by introducing a transition ramp as sketched in

figure 6. If laminar separation occurs at the beginning of the ramp, the adverse pressure gradient thereafter is not large and the bubble will be thin. As the angle of attack is reduced, however, the adverse pressure gradient along the ramp is also reduced and, eventually, an

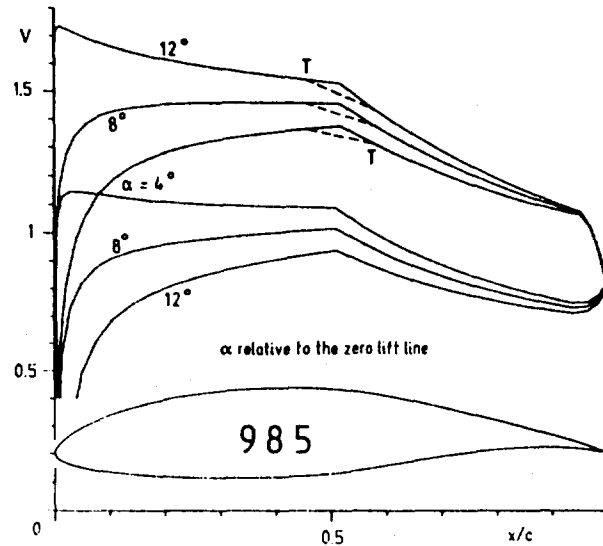


Figure 6: Airfoil 985 with velocity distributions

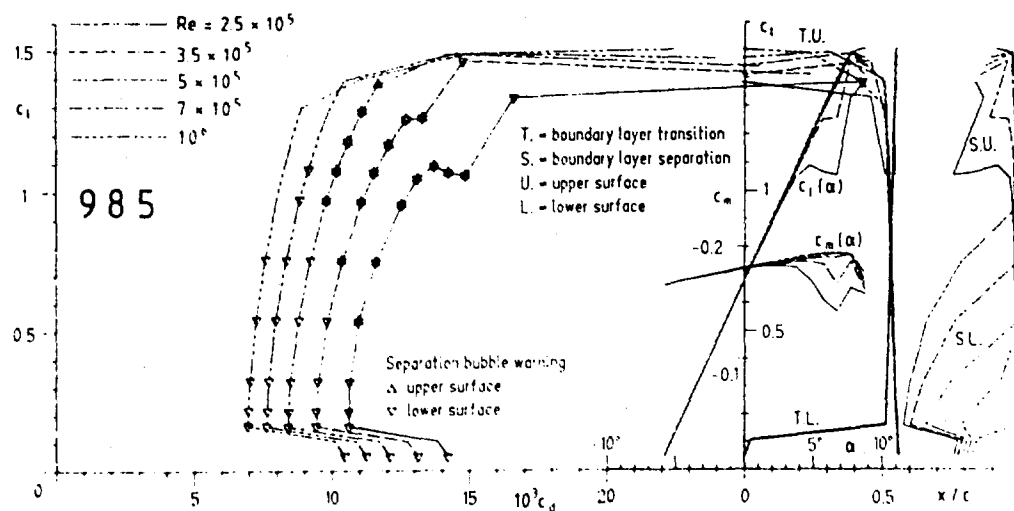


Figure 7: Theoretical section characteristics of airfoil 985

angle of attack will be reached at which laminar separation or transition does not occur on the ramp. At that angle of attack, a thick bubble can again form downstream of the end of the ramp, at the beginning of the main pressure recovery. If, at a certain  $\alpha$ , the adverse pressure gradient on the upper surface aft of laminar separation is small over a long segment, a thin bubble will result. As  $\alpha$  is decreased, however, that small adverse gradient is reduced so much that it no longer causes laminar separation or transition in this segment. Transition/laminar separation jumps from the beginning to the end of this segment within a narrow  $\alpha$ -range. This jump can be seen in figure 7, for example, where transition/laminar separation jumps from the leading edge to the middle of the upper surface near  $c_l = 1.4$ . Above this  $c_l$ , no bubble warnings appear for the upper surface. The reverse is true for the lower surface where transition/laminar separation jumps from the leading edge to midchord near  $c_l = 0.1$ . Thus, these jumps are beneficial over a narrow range of angles of attack but not over a wider range.

To reduce the number of bubble warnings over a wide range of lift coefficients, it is necessary to eliminate any sharp corner in the velocity distribution as shown, for example, in figure 8. Airfoil 987 has velocity distributions very similar to those of airfoil 985 except that the corners near the beginning of the pressure recovery are rounded or smoothed. Transition/laminar separation moves gradually through this region. The adverse pressure gradient is, however, small only for a short distance downstream of transition/laminar separation. The bubble thickness is reduced less than in the case of a jump but it is reduced over a wider range of lift coefficients. The number of bubble warnings has been reduced significantly as shown in figure 9. Also note that the slope of the transition/laminar separation lines T.U.( $c_l$ ) has changed markedly.

There is a general connection between the slope of these lines and the critical Reynolds number  $R_{crit}(c_l)$  above which no bubble warnings appear. Increasing slope means decreasing  $R_{crit}$ . The slope of T.U.( $c_l$ ) can be controlled by a simple, straight-forward technique for selecting the  $\alpha$ -values used in the airfoil design method of [1]. Airfoil 987 does not yet satisfy the design requirements completely. For  $c_l > 0.8$  and  $R \leq 350,000$ , bubble warnings appear for the lower surface. This is not acceptable because the airfoil must perform efficiently under these conditions. On the other hand, the bubble warnings for the upper surface for the same Reynolds numbers and  $c_l < 0.8$  are unimportant because the airfoil operates at higher Reynolds numbers over this  $c_l$  range. For these conditions, the lower surface is even better than necessary as indicated by the lack of warnings. Thus, the airfoil should be modified such that, for the lower Reynolds numbers, the warnings for the lower surface are eliminated for high lift coefficients. Additional warnings for low lift coefficients are, of course, acceptable. This modification requires the slope of T.U.( $c_l$ ) to be increased for high  $c_l$  and to be decreased for low  $c_l$ .

The resulting airfoil 989 is presented in figure 10 and its section characteristics, in figure 11. The shape and the velocity distributions of airfoil 989 are not very different from those of airfoil 987, but

the improvement is significant.

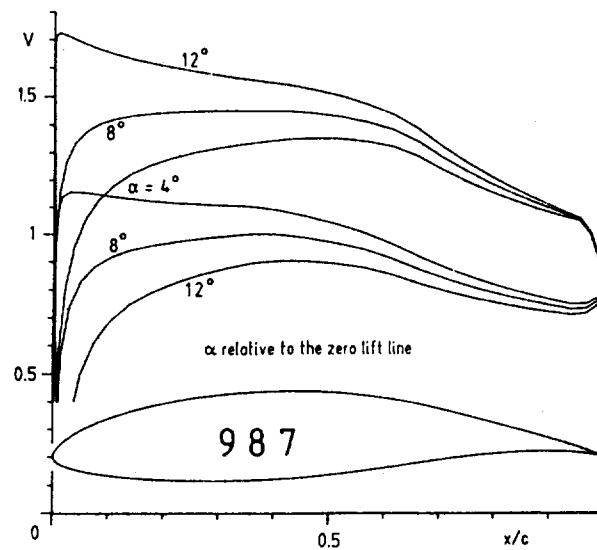


Figure 8: Airfoil 987 with velocity distributions.

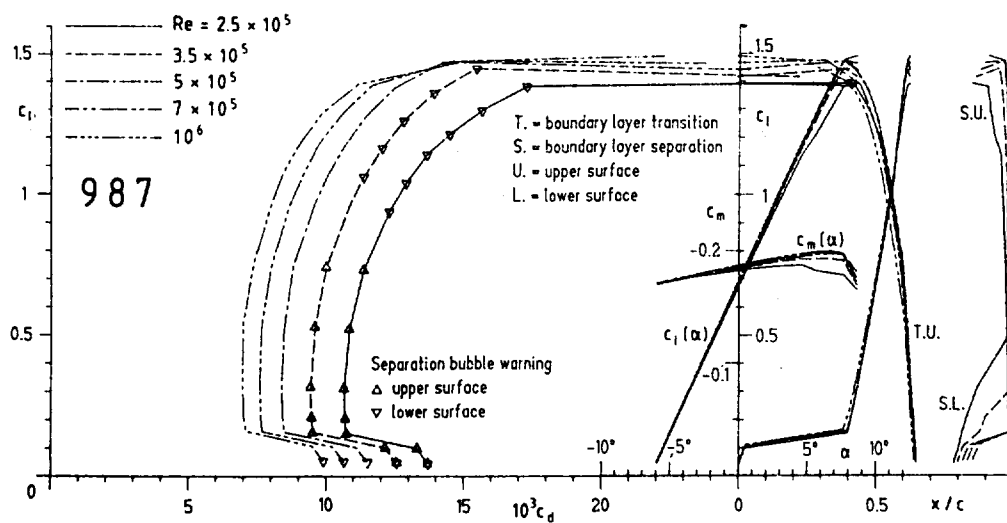


Figure 9: Theoretical section characteristics of airfoil 987

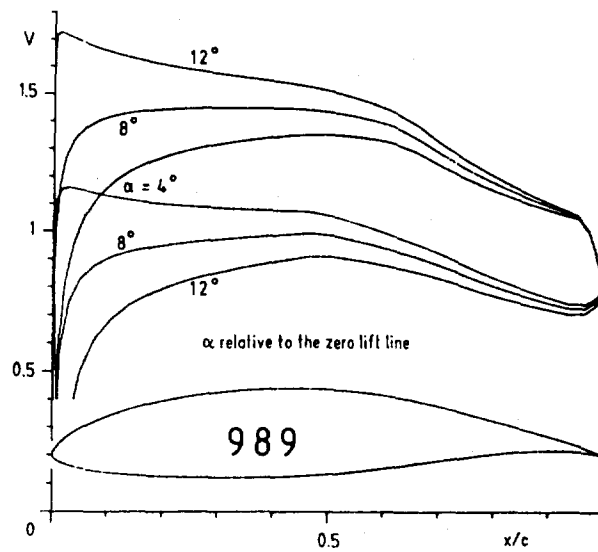


Figure 10: Airfoil 989 with velocity distributions

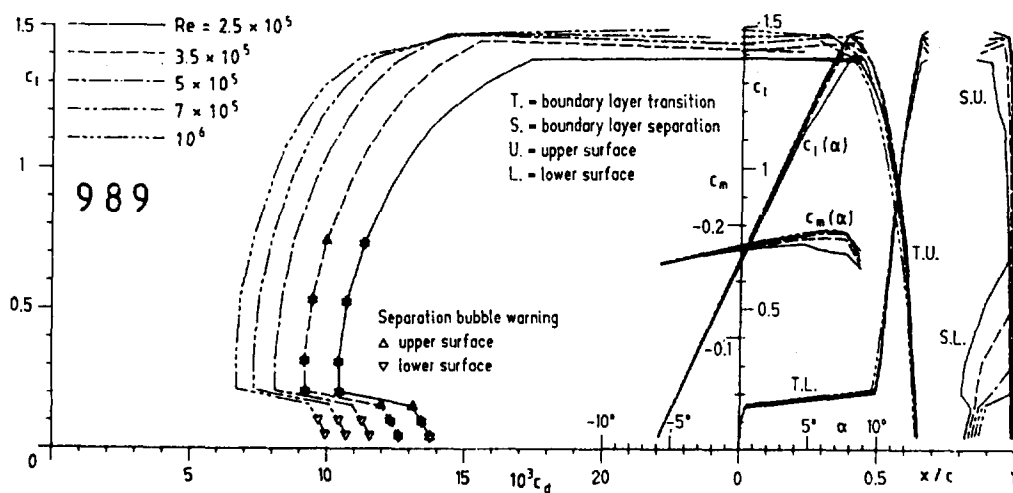


Figure 11: Theoretical section characteristics of airfoil 989

Of course, even lower Reynolds numbers can be accommodated if the transition ramp is made longer. A certain limit is reached, however, when the ramp extends over the entire chord length. An example of an airfoil intended for Reynolds numbers below 100,000 for high  $c_l$  and correspondingly higher  $Re$  for low  $c_l$  is given in figures 12 and 13. Note the slope of T.U. ( $c_l$ ) for the upper surface. It increases with  $c_l$  which reduces  $Re_{crit}$ . For  $Re = 50,000$ , this airfoil still has a narrow  $c_l$  range without bubble warnings.

If airfoils must be designed for even lower  $R$  the  $c_l$  range over which T.U. ( $c_l$ ) changes rapidly must be reduced. The resulting airfoils will accordingly have a narrower  $c_l$  range over which they can be applied.

The absolute limit is a "point" design. If, for a certain  $c_l$ , transition/laminar separation jumps from the leading edge almost to the trailing along the upper surface, then  $Re_{crit}$  cannot be further reduced for that surface. The lower surface is no problem in this case. It can be designed such that no adverse pressure gradient exists for any  $c_l$  higher than a certain  $c_l^*$ .

An example for such a design is airfoil 63, shown in figures 14 and 15. It is extremely thin (4,45 %) and has, for  $R = 50,000$ , a narrow  $c_l$  range without bubble warnings. For  $R = 30,000$ , however, even this airfoil has no  $c_l$  without warning. Obviously it is nearly impossible to achieve transition for that Reynolds number at all. A completely different approach must be taken in this all laminar flow area. This approach should not rely on the boundary-layer approximation. For that reason, this paper does not try to enter the area of  $R < 50,000$ . It could even be said that Reynolds numbers below 50,000 should be prohibited by law.

#### REFERENCES

- [1] R. Eppler, and D. M. Somers: A Computer Program for the Design and Analysis of Low-Speed Airfoils. NASA TM-80210, 1980.
- [2] R. Eppler, and D. M. Somers: Supplement To: A Computer Program for the Design and Analysis of Low-Speed Airfoils. NASA TM-81862, 1980.
- [3] F. W. Schmitz: Aerodynamik des Flugmodells, 4<sup>th</sup> ed., Carl-Lange-Verlag Duisburg, 1957.
- [4] B. A. Ntim: A theoretical and experimental investigation of separation bubbles. Ph. D. Thesis, University of London, 1965.
- [5] D. F. Volkers: Preliminary Results of Windtunnel Measurements on Some Airfoil Sections at Reynolds Numbers Between  $0.6 \times 10^5$  and  $5.0 \times 10^5$ . Memorandum M-276, Delft University of Technology, Department of Aerospace Engineering, The Netherlands, 1977.

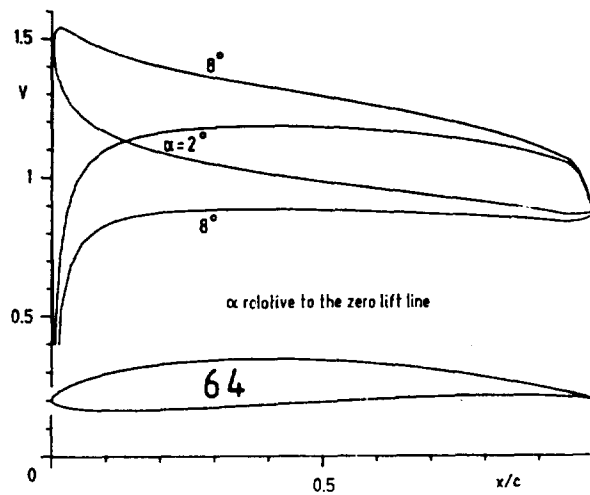


Figure 12: Airfoil 64 with velocity distributions.

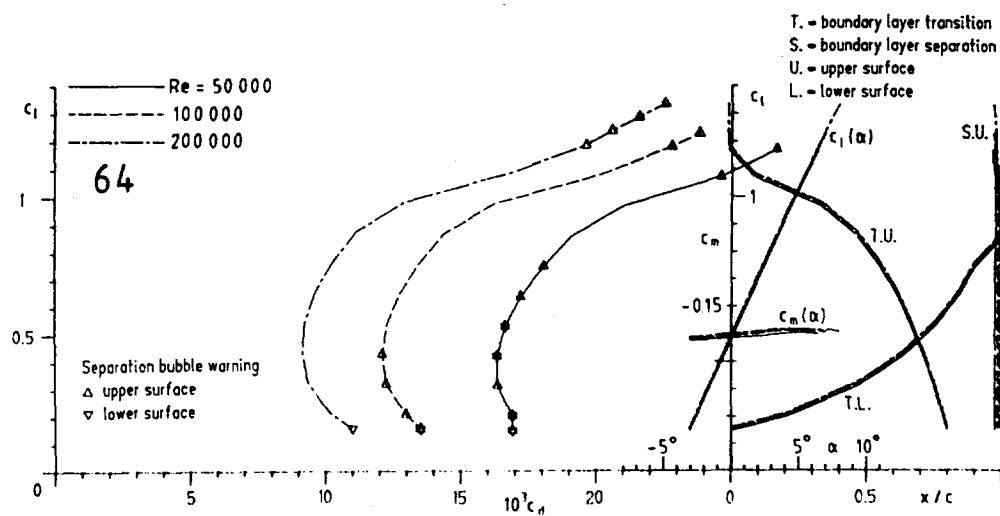


Figure 13: Theoretical section characteristics of airfoil 64

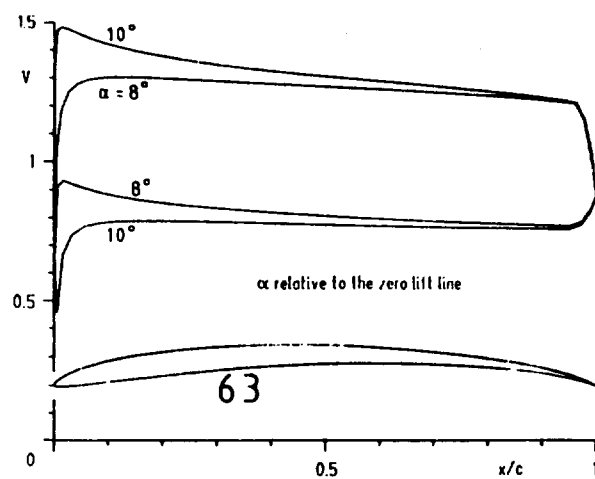


Figure 14: Airfoil 63 with velocity distributions.

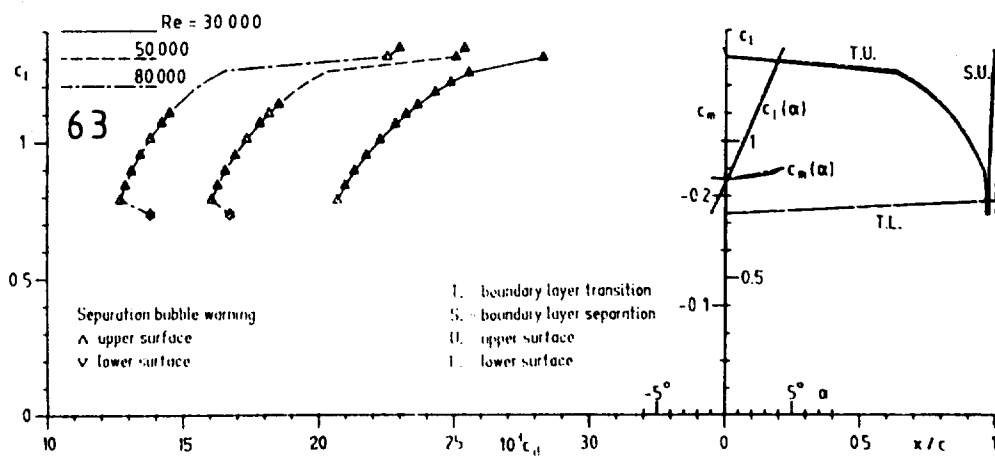


Figure 15: Theoretical section characteristics of airfoil 63.

## LOW REYNOLDS NUMBER AIRFOIL DESIGN

Mark D. Maughmer  
The Pennsylvania State University  
University Park, PA

Michael S. Selig  
Princeton University  
Princeton, New Jersey

### ABSTRACT

Due to the dependency of airfoil performance at low Reynolds numbers on the location of the laminar separation bubble, the design philosophies of such airfoils are considerably different than those employed at higher Reynolds numbers. While a great deal of current research is directed toward furthering the understanding of the flow behavior in the Reynolds number range of 50,000 to 500,000, for the most part, the results of these efforts have yet to be adequately implemented into the design process. To facilitate the design of low Reynolds number airfoils using existing methods, a first step in developing design philosophies has been undertaken by correlating analysis results obtained using the Eppler and Somers computer code with experimental data. From this study, it is found that the velocity distributions of the airfoils for which the method produces reasonable performance predictions can be characterized by particular features. By specifying velocity distributions incorporating these features, a number of new profiles having anticipated performance levels superior to existing sections have been designed. One of the airfoils obtained in this manner is examined. In addition to the velocity distribution features suggested by the correlations of calculated and experimental results, another aspect which appears to benefit low Reynolds number airfoil performance is the implementation of a condition which forces the pressure gradients occurring at the trailing edge, which are generally unbounded, to be finite. The potential benefits of using such a condition are discussed, and an example airfoil designed by an appropriately modified version of the Eppler and Somers code is presented.

### INTRODUCTION

While the design and analysis of airfoils for Reynolds numbers above 500,000 can be accomplished with a high level of confidence that the resulting aerodynamics will be as predicted, this is not the case for airfoils intended to operate at lower Reynolds numbers. As discussed in Refs. [1]-[4], the occurrence of laminar (transitional) separation bubbles can have a dominating influence on the aerodynamic characteristics of an airfoil. At the present time, the capability of satisfactorily accounting for the effects of such bubbles is limited. Thus, the difficulties in achieving reliable performance predictions for airfoils operating at low Reynolds numbers, particularly below about

200,000, are due primarily to the inability of determining the location and behavior of the separation bubble and its effect on the downstream boundary layer development.

Although experimental programs, such as those of Refs. [4]-[5], have resulted in significant progress toward the understanding of laminar separation bubbles, and there are numerous contributions toward the development of analytical prediction methods, including those of Refs. [6]-[9], considerable work remains before adequate engineering methods for the design and analysis of airfoils at low Reynolds numbers result. In fact, it has been demonstrated that the aerodynamics of low Reynolds number flows are so sensitive to external influences not under the control of a designer, such as free-stream turbulence, surface contamination, and so-forth, it may be that improving the analytical prediction capability for particular flow conditions is only of limited value in that an actual design must perform over the wide range of flow environments encountered operationally. Thus, from the standpoint of airfoil design, the most beneficial result of researching the behavior of flows at low Reynolds numbers may prove to be the understanding which facilitates the specification of velocity distributions that minimize the impact of environmental factors on the separation bubble and airfoil performance.

In order to carry out the design of low Reynolds number airfoils between now and the time that reliable predictions are possible, there is a need for design philosophies which, when used in conjunction with existing methods, will result in airfoils having actual characteristics close to those intended. In this regard, it is necessary to define the relationship between the velocity distribution on an airfoil and the development of laminar separation bubbles. As a design goal, it is desired to minimize the impact on the airfoil aerodynamics caused by the sensitivity of the laminar bubble to angle of attack changes and variations in the flowfield environment. The work discussed in this paper represents a first step in determining what features and characteristics of the velocity distribution on an airfoil lead to desirable and predictable low Reynolds number airfoil performance.

#### CORRELATION OF THEORETICAL AND EXPERIMENTAL RESULTS

In order to gain insight into the types of velocity distributions well suited for airfoils operating at low Reynolds numbers, analysis results obtained using the Eppler and Somers computer code [10] have been correlated with wind tunnel results of Althaus [11]. While the details are reported fully in Ref. [12], some of the important observations of this comparison will be briefly recounted here.

Among the airfoils for which wind tunnel test results were considered, in addition to examples having no hysteresis in the lift and drag characteristics, there are sections demonstrating hysteresis at relatively high angles of attack as is normally associated with short bubble or leading edge stall, as well as examples exhibiting hysteresis in the middle angle of attack range with behavior similar to that normally associated with long bubble or thin airfoil stall. In the case

of short bubble hysteresis, as represented in Fig. 1, a short laminar separation bubble is formed near the leading edge of the airfoil. As the angle of attack is increased, a point is reached for which the airfoil stalls either by a bursting of the leading edge bubble, or by a trailing edge stall in which the upper surface turbulent separation point moves sufficiently far upstream to stall the airfoil. As the angle of attack is decreased from that of stall, hysteresis is caused by the short bubble reattaching at an angle less than that which caused stall for increasing angles of attack. From the experimental results examined, this type of hysteresis largely disappears when the Reynolds number is increased to values greater than 200,000.

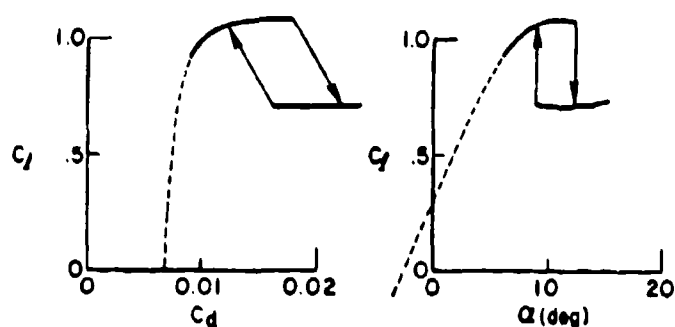


Fig. 1 Typical leading edge (short bubble) stall hysteresis.

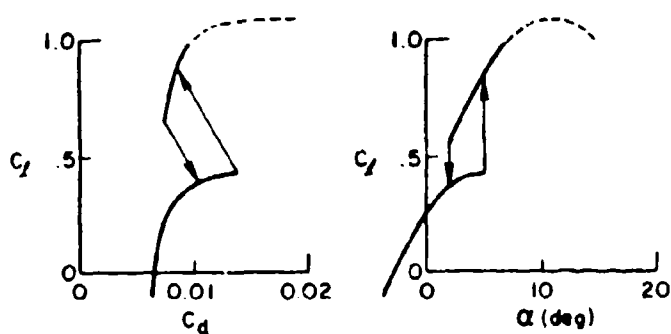


Fig. 2 Typical mid-polar (long bubble) hysteresis.

For the wind tunnel results considered, the long bubble type hysteresis, as depicted in Fig. 2, is confined to Reynolds numbers below 100,000. In this case, a laminar separation bubble is formed near the midchord and grows larger with increasing angles of attack. This causes the lift curve to flatten out and the drag to increase significantly until, at some point, the bubble collapses into a short bubble near the nose of the airfoil. Upon collapse of the bubble, the drag coefficient is decreased markedly and is accompanied by a jump in the lift coefficient. Upon decreasing the angle of attack, the reformation of the long bubble occurs at a lower angle of attack than that at which collapse occurred with increasing angles. Thus, airfoils exhibiting long-bubble type hysteresis tend to have a high drag knee which extends through the middle-range of the drag polar. It should be noted that a number of the airfoils considered display both long and short bubble hysteresis behavior.

To a large extent, the hysteresis effects caused by laminar separation bubbles can be eliminated by the use of artificial turbulation [1], [11]. As expected, however, because of the sensitivity of separation bubble behavior to flowfield variations, the design and placement of turbulators to achieve desired effects is extremely critical and benefits are confined to a relatively narrow range of operating conditions. Consequently, any performance gains achieved at one operating condition are largely offset by the drag increase which accompanies the use of turbulators away from the intended angle of attack and Reynolds number. For these reasons, the concentration of the effort discussed in this paper has been on the design of low Reynolds number airfoils which do not require the use of turbulators.

In attempting to predict the aerodynamic characteristics of airfoils at low Reynolds numbers, in its current form, the Eppler and Somers code is unable to fully account for the effects of laminar separation bubbles. In particular, the program execution is such that if laminar separation is predicted before an empirically developed transition criterion is satisfied, then an immediate transition is assumed and the calculations continue using a turbulent boundary layer model. While such treatment is reasonable for a short separation bubble which generally has little effect on the aerodynamic characteristics of an airfoil, this is not true in the case of a long separation bubble which can extend over most of the airfoil upper surface. This difficulty is addressed briefly by the code in that if a separation bubble is predicted to be longer than three percent of the chordlength, a warning is generated that the predicted sectional characteristics may not be indicative of the actual characteristics. As expected, this warning commonly appears for airfoils analyzed at low Reynolds numbers.

In spite of the limitations of the Eppler and Somers code regarding separation bubbles, through the experience of correlating predicted aerodynamic characteristics to those obtained experimentally, it can still be very useful for the design of low Reynolds number airfoils. Most simply, this usefulness is achieved by specifying velocity distributions which tend to suppress the formation of the long laminar

separation bubbles which are not handled by the code. Because the short bubble type hysteresis generally occurs near the stalling angle of attack, its impact on aircraft flight mechanics can be eliminated simply by restricting the operation of the aircraft to angles of attack less than those for which stall hysteresis occurs. The erratic flight behavior which would be caused by the long bubble type hysteresis near the middle of the operational angle of attack range, as well as the degradation in aerodynamic performance, are both unacceptable. Thus, a primary goal in the design of airfoils for low Reynolds numbers is to prevent the formation of long separation bubbles.

In examining the potential flow velocity distributions of the airfoils considered, it is observed that airfoils demonstrating long bubble hysteresis are characterized by concave upper surface pressure recoveries. Airfoils not exhibiting long bubble hysteresis, on the other hand, are characterized by linear or convex upper surface recoveries. With a concave recovery, the flow separates upon entry into the adverse pressure gradient at the beginning of the recovery and, since the gradient is steep, reattachment is difficult and a long bubble forms. Increasing the angle of attack further aggravates the situation in that the bubble length steadily increases until the bubble eventually collapses. In the case of the convex recovery distribution, the pressure gradients are not as steep as those of the concave recovery and reattachment is not as difficult. As the angle of attack is increased, both the separation and reattachment points move forward toward the leading edge and, as the reattachment point moves forward at a slightly greater rate than does the separation point, the length of the bubble decreases. Thus, the bubble does not collapse in this case and hysteresis does not occur.

An additional observation resulting from the comparison of the computational and experimental results, which has also been noted by other researchers (Refs. [3] and [7]), is that the short bubble type hysteresis appears to be dependent on both the leading edge shape as well as the severity of the adverse pressure gradient on the upper surface following a pressure peak near the leading edge of an airfoil. Further, as has also been concluded by others and is discussed in Ref. [13], the agreement between predicted and experimental results is much better for airfoils in which steep adverse pressure gradients in the vicinity of the trailing edge, as caused by upper surface aft loading, are avoided.

#### Low Reynolds Number Airfoil Design Example

By making use of the observations noted in the preceding section to facilitate the specification of design velocity distributions, it is possible to design airfoils for use at low Reynolds numbers. In so doing, it is hoped that the actual performance of the airfoil is not significantly different from that predicted using the Eppler and Somers code. A number of airfoils designed in this manner, intended for use on radio-controlled model sailplanes, are presented in Refs. [12] and [14].

An example of an airfoil based on the observations noted is the

S2027, presented along with its calculated velocity distributions in Fig. 3. This section, which originally appeared in Ref. [14], is intended for the FAI/F3B model sailplane competition event. Although this event requires tasks in duration, distance, and speed, it is the speed task, along with the structural demands for a large thickness ratio to withstand the loads imposed by winch launching, which dictate the design requirements. Consequently, the design goal of the S2027 is to have low drag in the range of lift coefficients required for high speed, while still maintaining reasonable performance for duration and climb at moderate lift coefficients. The aerodynamic characteristics of this airfoil obtained using the analysis capability of the Eppler and Somers code are shown in Fig. 4. Theoretically, this design demonstrates a number of advantages over other sections commonly used for this event. More significantly, reports from users of the section indicate that its design goals have been met successfully.

#### APPLICATION OF FINITE TRAILING EDGE PRESSURE GRADIENTS

The potential flow velocity distribution for any airfoil having a non-zero trailing edge loading is characterized by the presence of unbounded normal and streamwise pressure gradients at the trailing edge. These singularities give rise to strong viscous-inviscid interactions which lead to the break-down of conventional boundary layer theory in the vicinity of the trailing edge. As fully discussed in Ref. [13], these interactions can cause the velocity distribution on an airfoil in the actual flow to differ significantly from that predicted by the potential flow methods often used in the design process.

By including the effects of normal pressure gradients in the vicinity of the trailing edge, wake thickness, and wake curvature, Melnik, et al. [15] have developed a boundary layer theory able to account for the strong viscous interactions due to the singularities in the inviscid flow solution. This fully self-consistent boundary layer theory has been incorporated into the viscous, compressible airfoil analysis code, GRUMFOIL [16]. As an alternative approach, a method is introduced in Ref. [13] for which the singularities at the trailing edge are eliminated. The resulting designs represent a class of airfoils for which the strong viscous-inviscid interactions in the vicinity of the trailing edge are minimized. For such airfoils, which have finite trailing edge pressure gradients, the potential flow design velocity distribution is in much better agreement with that developed in the real flow than is generally the case. In addition, conventional boundary layer theory is sufficient for predicting the viscous flow behavior of such airfoils. Perhaps of most importance, however, by forcing the trailing edge pressure gradients to be bounded, it is expected that the real flow will be able to pass off the airfoil and into the wake as smoothly as is possible. In so doing, not only are the critical pressure recoveries used in modern airfoil design more likely to be realized without unpredicted flow separations, but the possibility exists for some significant gains in airfoil performance.

As fully reported in Ref. [17], the design of airfoils having finite trailing edge pressure gradients can be accomplished using an

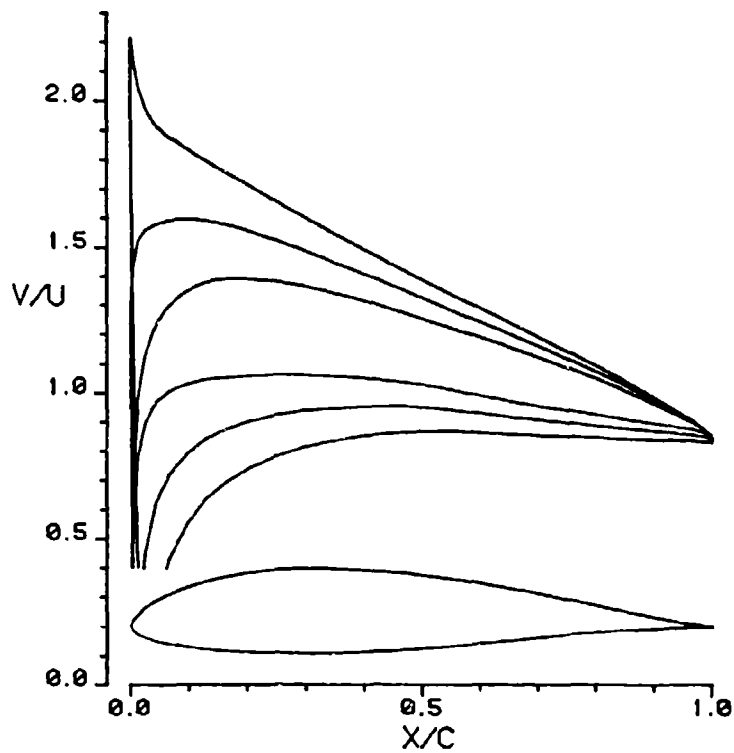


Fig. 3 The S2027 airfoil and calculated velocity distributions. Alpha = 4, 8 and 12 deg. relative to the zero-lift line.

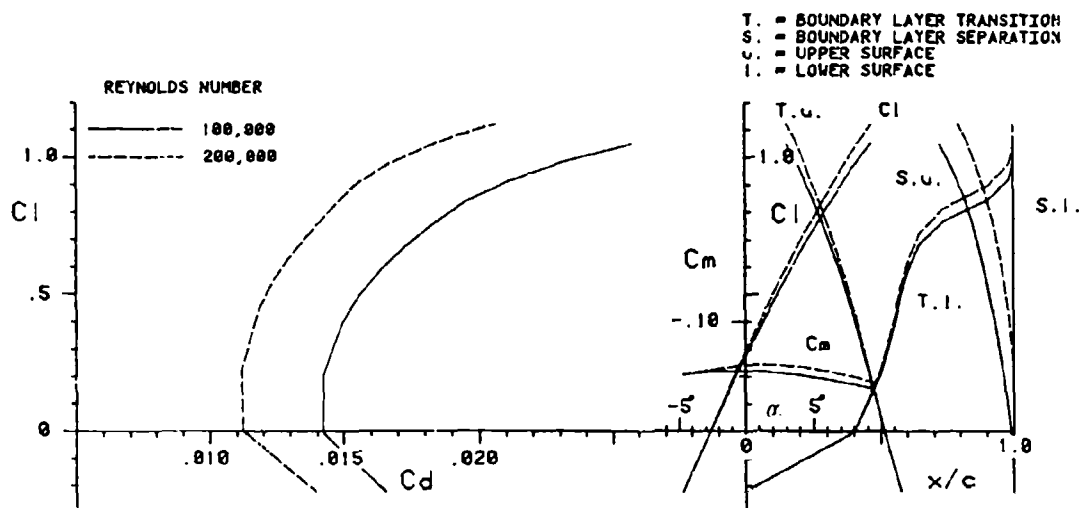


Fig. 4 Theoretical section characteristics for the S2027 airfoil obtained using the Eppler and Somers code.

appropriately modified version of the Eppler and Somers code. One of the conditions which must be met for the generation of such airfoils is manifested in the code as an integral constraint involving the velocity at each point on the airfoil. Admissible velocity distributions must simultaneously satisfy this integral constraint along with that which insures uniformity of the velocity at infinity and the two that guarantee a closed profile. Thus, the condition for finite trailing edge pressure gradients has a global influence and effects not only the flow at the trailing edge, but also the shape of the velocity distribution as the trailing edge is approached.

In order to demonstrate how a profile can be altered by the integral constraint which must be satisfied for finite trailing edge pressure gradients, consider the airfoil obtained using the unmodified Eppler and Somers code, shown in Fig. 5, along with the result, presented in Fig. 6, of using the same input data set in the modified code. Clearly, for the case in which an airfoil is a long way from satisfying the conditions for finite trailing edge pressure gradients, imposing the additional constraint can have a significant influence. In general, however, the geometrical alternations necessary to satisfy the additional constraint are much less dramatic than those demonstrated by this example.

#### Design Example Having Finite Trailing Edge Pressure Gradients

Because the influence of viscous effects on the flow over an airfoil become relatively more important as the Reynolds number is decreased, the use of finite trailing edge pressure gradients should be increasingly beneficial as the Reynolds number at which the airfoil operates is decreased. An example of an airfoil designed for low Reynolds numbers and having finite trailing edge pressure gradients is given in Fig. 7. This section is a redesigned S2027 obtained using the modified version of the Eppler and Somers code. Shown in Fig. 8 are the theoretical section characteristics for this redesigned airfoil. Of greater significance than the performance advantage predicted, the specified design potential flow velocity distribution of the redesigned airfoil is less altered by viscous effects than is that of the original section. Because of this, which has been verified using the GRUMFOIL code, the actual aerodynamic behavior of the redesigned airfoil should be closer to that expected than it is in the case of the original design.

#### CLOSING REMARKS AND RECOMMENDATIONS

Through the correlation of low Reynolds number experimental results with analytical results of the Eppler and Somers code, particular characteristics of the velocity distribution on an airfoil have been identified which lead to acceptable agreement between the actual and predicted aerodynamics. By specifying design velocity distributions which have these characteristics, it is hoped that airfoils for use at low Reynolds numbers can be developed whose actual performance and behavior is close to that anticipated. In addition, given the

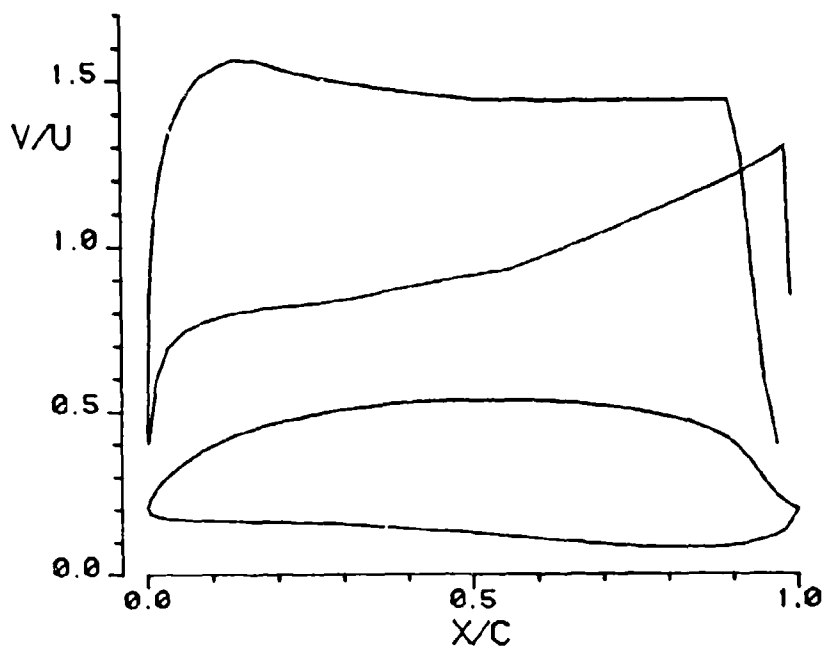


Fig. 5 Airfoil and velocity distribution obtained using the Eppler and Somers code. Alpha = 8 deg. relative to zero-lift line.

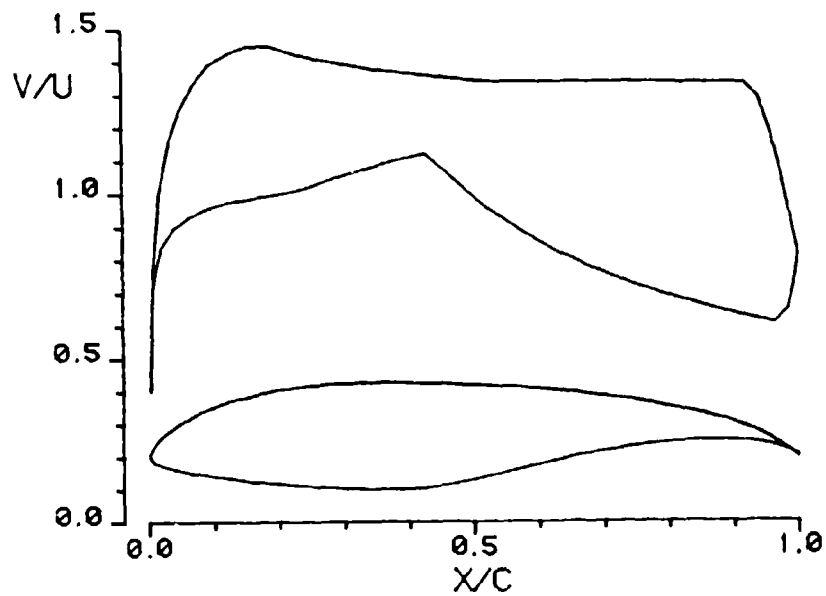


Fig. 6 Airfoil and velocity distribution obtained using the Eppler and Somers code modified to generate airfoils having finite trailing edge pressure gradients. Alpha = 8 deg. relative to the zero-lift line.

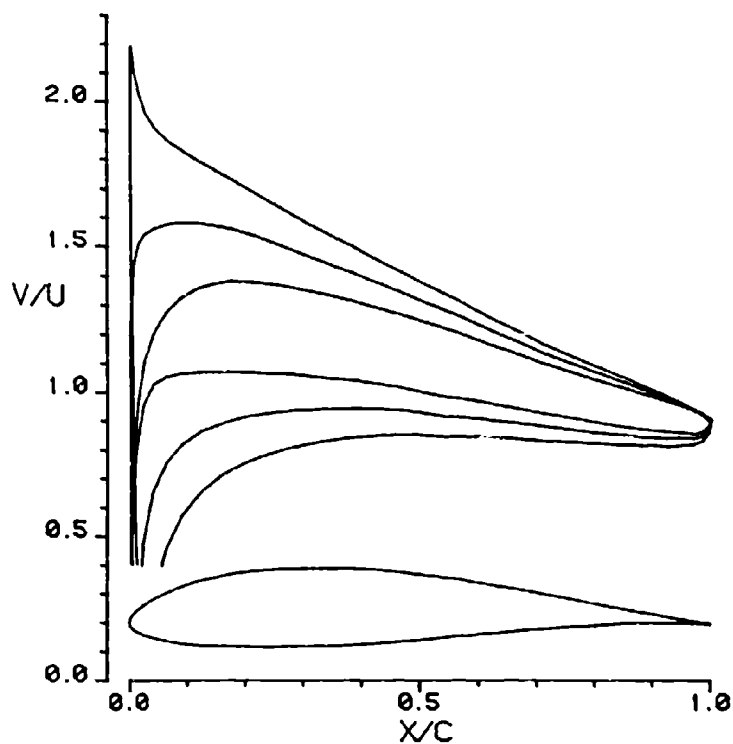


Fig. 7 The redesigned S2027 airfoil and calculated velocity distributions.  $\alpha = 4, 8$  and  $12$  deg. relative to the zero-lift line.

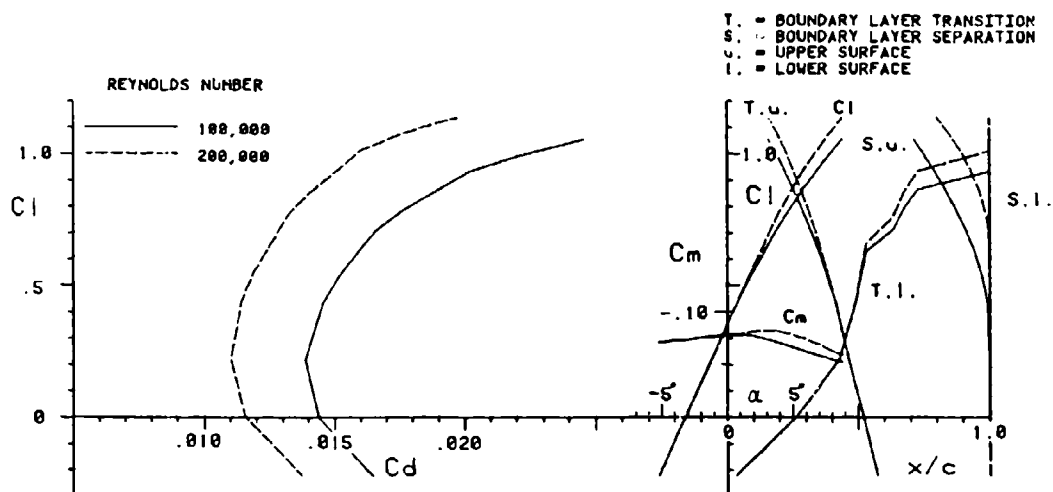


Fig. 8 Theoretical section characteristics for the redesigned S2027 obtained using the Eppler and Somers code.

significant influence of viscous effects on flows at low Reynolds numbers, the use of finite trailing edge pressure gradients can further increase the likelihood of obtaining the predicted aerodynamic behavior by minimizing the strong viscous interactions in the vicinity of the trailing edge. As a consequence, while more research is needed to experimentally verify that the benefits demonstrated computationally are possible, the use of finite trailing edge pressure gradients offers the potential for achieving some significant gains in airfoil performance.

A clear extension of the correlation between experimental and predicted low Reynolds number airfoil data would be the consideration of data from facilities other than that of the Laminar Wind Tunnel at Stuttgart [11]. The number of different airfoils which have been tested by the few facilities which have undertaken low Reynolds number testing is very limited. Consequently, both the empirical and purely analytical approaches to developing methods for predicting the aerodynamics of low Reynolds number airfoils could greatly benefit from additional experimental data. It is important that such results include the details of laminar separation bubble formation such as the locations of laminar separation and turbulent reattachment. In addition, it is important that the flow environment in which these data are taken is fully documented.

Until such a time that the flow over an airfoil at low Reynolds numbers can be adequately treated analytically, the design of airfoils for these flow conditions must be accomplished by means of empirical approaches such as that which has been described. In fact, even after rigorous analytical solutions are available for use in design, it is likely they will be costly and time consuming in terms of computer usage. Consequently, given the iterative nature of the design process, the speed and low cost of empirical approaches will justify their continued development and application for some time. Thus, in considering modifications to the Eppler and Somers code to make it more suitable for the analysis of low Reynolds number airfoils, it is likely that improvements could be gained by including a more detailed separation bubble calculation, such as those developed in Refs. [6]-[7], than is presently employed. Finally, due to the increased relative importance at low Reynolds number of viscous effects, the inclusion of displacement thickness-potential flow iteration might ultimately prove necessary.

#### REFERENCES

1. Carmichael, B. H., "Low Reynolds Number Airfoil Survey, Volume I," NASA CR-165803, Nov. 1981.
2. Lissaman, P.B.S., "Low-Reynolds-Number Airfoils," Annual Review of Fluid Mechanics, Vol. 15, 1983, pp. 223-239.
3. Ward, J. W., "The Behavior and Effects of Laminar Separation Bubbles on Aerofoils in Incompressible Flow," Journal of the Royal Aeronautical Society, Vol. 67, Dec. 1963, pp. 783-790.

4. Mueller, T. J., "The Influence of Laminar Separation and Transition on Low Reynolds Number Airfoil Hysteresis," AIAA Paper No. 84-1617, June 1984.
5. Mueller, T. J., Pohlen, L. J., Conigliaro, P. E. and Jansen, B. J., Jr., "The Influence of Free-Stream Disturbances on Low Reynolds Number Airfoil Experiments," Experiments in Fluids, Vol. 1, pp. 3-14, 1983.
6. Van Ingen, J. L., "On the Calculation of Laminar Separation Bubbles in Two-Dimensional Incompressible Flow," AGARD CP-168, 1975, pp. 1-16.
7. Roberts, W. B., "Calculation of Laminar Separation Bubbles and Their Effect on Airfoil Performance," AIAA Paper No. 79-0285, Jan. 1979.
8. Kothari, A. P. and Anderson, J. D., Jr., "Flows Over Low Reynolds Number Airfoils-Compressible Navier-Stokes Numerical Solutions," AIAA Paper No. 85-0107, Jan. 1985.
9. Cheng, H. K. and Lee, C. J., "Laminar Separation Studied as an Airfoil Problem," Third Symposium on Numerical and Physical Aspects of Aerodynamic Flows, Jan. 1985, pp. 39-61.
10. Eppler, R. and Somers, D. M., "A Computer Program for the Design and Analysis of Low-Speed Airfoils," NASA TM 80210, August 1980.
11. Althaus, D., Profilpolaren für den Modellflug, Neckar-Verlag Vs-Villingen, 1980.
12. Selig, M. S., "The Design of Airfoils at Low Reynolds Numbers," AIAA Paper No. 85-0074, Jan. 1985.
13. Ormsbee, A. I. and Maughmer, M. D., "A Class of Airfoils Having Finite Trailing Edge Pressure Gradients," AIAA Paper No. 85-0206, Jan. 1985.
14. Selig, M. S., "The Design of Airfoils at Low Reynolds Numbers," Soartech 3, July 1984 (available c/o H. A. Stokely, 1504 Horseshoe Circle, Virginia Beach, VA, 23451).
15. Melnik, R. E., Chow, R. R., Mead, H. R. and Jameson, A., "An Improved Viscid/Inviscid Interaction Procedure for Transonic Flow Over Airfoils," Grumman Aerospace Corporation, Report RE-682, March 1984.
16. Mead, H. R. and Melnik, R. E., "GRUMFOIL - A Computer Code for the Viscous Transonic Flow Over Airfoils," Grumman Aerospace Corporation, Report RE-681, March 1984.
17. Ormsbee, A. I. and Maughmer, M. D., "Trailing Edge Flow Conditions as a Factor in Airfoil Design," University of Illinois Technical Report AAE 84-1, UIIU-ENG 84 0501, Jan. 1984.

# AIRFOIL DESIGN AT LOW REYNOLDS NUMBER WITH CONSTRAINED PITCHING MOMENT

R. H. Liebeck and P. P. Camacho  
Douglas Aircraft Company  
Long Beach, CA

## ABSTRACT

A study has been conducted to evaluate the effect of a pitching moment constraint on the performance of low Reynolds number airfoils designed for high lift. Two airfoils have been theoretically designed and experimentally evaluated for a design  $C_l$  of 1.2 at a Reynolds number of  $0.40 \times 10^6$  with a  $C_{lmax}$  of 1.8. Airfoil LNV109A was designed to provide a specified pitching moment -0.05, and has a thickness of 13%. Airfoil LA203A was not constrained, and it has a thickness of 15.7% and a pitching moment of -0.17. Both airfoils use Stratford pressure recoveries; however, airfoil LA203A is distinguished by its aft-loading. The airfoils were tested in the Douglas Long Beach Wind Tunnel over a Reynolds number range from  $0.25 \times 10^6$  to  $0.65 \times 10^6$ , and both met the design goals with the pitching moment constrained airfoil having higher drag at the lower Reynolds numbers.

## INTRODUCTION

The airfoil design problem considered in this study was to develop and compare two airfoils for the basic specification:

$$\begin{aligned}RN &= 0.40 \times 10^6 \\0.5 &< C_l < 1.5 \\C_{lmax} &= 1.8\end{aligned}$$

where the two airfoils were to be distinguished by the requirement that one of them would have a pitching moment on the order of -0.05, while the pitching moment of the other airfoil was left unconstrained. Both airfoils were to be designed to have minimum drag over the design  $C_l$ -range, and a secondary goal was to minimize the performance degradation which would likely be imposed by the pitching moment constraint on the one airfoil. Airfoils designed and theoretically analyzed to meet this specification, were then tested in the Douglas Long Beach Wind Tunnel to verify their performance.

The transition mechanism for the Reynolds number range considered in the present study is typically a laminar separation "bubble". Here the laminar boundary layer in an adverse pressure gradient separates and subsequently reattaches as a turbulent boundary layer. Bubble length varies - increasing with decreasing Reynolds number. A

stable bubble length may be on the order of 2% to as much as 10% of the airfoil chord. Beyond this length, the bubble is likely to "burst", and the flow separates downstream over the entire airfoil. Alternatively, at higher Reynolds numbers, while a bubble may exist, it is so short that transition may be considered as instantaneous. In this study, considerable attention has been directed toward the control of laminar bubbles.

The theory used in the design of the airfoils for this study is described in Reference 1, where the basic approach is to first define an "optimized" airfoil pressure distribution for a given Reynolds number and design lift coefficient. This pressure distribution comes from a family of pressure distributions which have been derived using boundary-layer and potential-flow theories together with the calculus of variations. It is characterized by an upper surface pressure distribution which consists of a rooftop plus a pressure recovery region based on the theory of Stratford [2] which avoids separation by a constant specified margin along its entire length. Next, the Douglas inverse airfoil design program [3] is used to calculate the corresponding airfoil shape. A typical airfoil design is shown in Figure 1. Finally, the Douglas MADAAM airfoil analysis program, which employs the boundary-layer calculation of Reference 4, is used to theoretically predict the aerodynamic performance of the airfoil.

The Stratford imminent separation pressure recovery distribution requires that the boundary layer be established as fully turbulent at the onset of the severe initial pressure rise, and for Reynolds numbers above  $10^6$  this has been accomplished via the transition ramp shown in the pressure distribution of Figure 1. Here laminar boundary layer on the rooftop region has become sufficiently unstable by the time it reaches the transition ramp, and the mild adverse gradient provided by the ramp causes almost instantaneous transition to a turbulent boundary layer, particularly at  $RN > 5 \times 10^6$ .

As mentioned above for the case of lower Reynolds numbers (say,  $10^6$  and below), the transition mechanism is typically a laminar separation bubble which is initiated by an adverse pressure gradient. For airfoils of the class considered in this study, one of the primary factors controlling the behavior of the laminar bubble is the local Reynolds number  $RN_p$  at the rooftop peak (i.e.  $RN$  based on the velocity at the rooftop peak and the length of the rooftop). As a general rule, if  $RN_p$  is less than  $0.10 \times 10^6$ , the laminar bubble is likely to burst; however, there are several other important factors such as the airfoil surface condition and turbulence level in the free-stream onset flow which can have a strong influence on transition.

Given a free-stream Reynolds number, the method of Reference 1 provides an infinite family of optimized pressure distributions for the upper surface of the airfoil as shown in Figure 2, where that

particular member of the family which provides the maximum lift is also identified. As the rooftop length is increased beyond that of the maximum lift value, the rooftop level is reduced; however, the peak Reynolds number increases, as indicated in example in Figure 2. Also, the loss in lift coefficient  $C_{l_u}$  which results from increasing the rooftop length beyond the maximum lift value is rather gradual as can be seen from the values given in Figure 2.  $C_{l_u}$  refers to the lift contribution of the upper surface of the airfoil, and the actual lift of an airfoil is roughly proportional to  $C_{l_u}$  for a family of airfoils of the same thickness.  $C_l$ , the actual lift coefficient of an airfoil, will be less than  $C_{l_u}$ .

Another method of controlling transition involves the use of transition strips, which artificially induce transition when properly sized and located on the airfoil surface. A major difficulty arises from the fact that a strip which has been sized for a Reynolds number of  $0.25 \times 10^6$  will be too high for a Reynolds number of  $0.50 \times 10^6$  by a factor of  $\sqrt{2}$ . While transition strips have been used in some of the testing in this study, it is desirable that an airfoil design should not depend on them.

Specification of the boundary-layer transition region of the pressure distribution represents one of the more difficult areas of airfoil design for low Reynolds numbers. A laminar boundary layer is quite sensitive to an adverse pressure gradient, and the goal is to set the gradient such that it causes instability and subsequent transition without creating a large laminar separation bubble. The magnitude of the transition ramp gradient can be easily specified in the design pressure distribution; however, it will vary as the airfoil is moved off the corresponding design angle of attack. A long rooftop length offers an additional virtue here. As the rooftop length is increased, the transition ramp moves aft on the airfoil chord, where the effect of an angle of attack change on the pressure distribution is reduced. This phenomenon, together with those described above, have had a fundamental effect on the airfoil designs of this study. Unfortunately, the long rooftop can not be utilized in the case of the airfoil which is constrained to have a low pitching moment. The reason for this is described in the next section.

#### AIRFOIL DESIGN RATIONALE

Airfoil LNV109A, shown with its theoretical chordwise pressure distribution in Figure 3, represents the design solution for the constrained pitching moment of -0.05. In order to meet the moment requirement, and achieve a  $C_{l_{max}}$  of 1.8, it was necessary to "front-load" the upper surface which resulted in relatively short rooftop. In this case, there was more concern regarding potential difficulties with laminar bubbles. As discussed earlier, experience at Douglas has shown that a short rooftop is not desirable from a

standpoint of minimizing the size of a laminar bubble. The rooftop was therefore rounded into the Stratford recovery region to the extent that a transition ramp of constant slope no longer existed. The pitching moment constraint could also be accommodated by adding reflex on the airfoil's lower surface near the trailing edge which would also serve to increase the airfoil thickness. Unfortunately, this would result in a decrease in  $C_{lmax}$  since said reflex is in effect unloading the aft portion of the airfoil. Here the conflict between low pitching moment and high  $C_{lmax}$  has become apparent, and it is intensified by the low Reynolds number laminar bubble difficulties.

In order to provide the most dramatic comparison possible, an aft-cambered design was selected for the unconstrained (with respect to pitching moment) airfoil. Figure 4 shows the geometry and design chordwise pressure distribution of airfoil LA203A. This airfoil is distinguished from airfoil LNV109A by being thicker (15.7% versus 13%) and having a larger negative pitching moment (-0.17 versus -0.05). The results from testing various airfoils with a Gurney flap and from testing the aft-loaded Wortmann FX63-137 airfoil suggested that it would be worthwhile to design an airfoil which would combine the Stratford recovery distribution with some mild aft-loading. This would allow specification of a Stratford distribution which was not required to recover to a positive pressure coefficient at the trailing edge which, in principle, implies a significant increase in the load carrying capability of the upper surface pressure distribution. Concern remained as to how successfully the flow could negotiate the steeper pressure rise at the trailing edge after it leaves the Stratford distribution.

The FX63-137 airfoil has an upper surface pressure coefficient on the order of  $C_p = -0.3$  just upstream of the steep pressure rise at the trailing edge. For the design of airfoil LA203A, a more conservative value of  $C_p = -0.1$  was chosen in hope of reducing the potential for separation near the trailing edge. This still provides for substantial aft-loading when it is compared to airfoil LNV109A which has a trailing edge pressure coefficient of  $C_p = +0.18$ . The Stratford distribution is very sensitive to the trailing edge pressure coefficient, and a change in its value at the trailing edge does not simply shift the level of the corresponding rooftop and pressure recover region. Instead, a small change in the trailing edge pressure coefficient results in a relatively significant change in the rooftop level and/or length.

The change from  $C_p = +0.18$  used on airfoil LNV109A to  $C_p = -0.10$  for airfoil LA203A allowed for an increase in the loading of the upper surface pressure distribution. This was utilized by extending the rooftop aft and reducing the rooftop level as compared with airfoil LNV109A. In addition, the design Reynolds number for the Stratford recovery distribution was reduced from  $0.6 \times 10^6$  (which was used on airfoil LNV109A) to  $0.2 \times 10^6$ . Both of these changes should have a positive effect on the performance of airfoil LA203A.

Increasing the rooftop length should tend to reduce the size of the laminar bubble as the previous testing has shown, and the reduction in the design Reynolds number makes the corresponding recovery distribution more conservative. The aft-loading on the upper surface pressure distribution has allowed a similar increase in aft-loading on the lower surface.

Tables of coordinates of airfoils LNV109A and LA203A are given in the Appendix.

#### DESCRIPTION OF WIND TUNNEL AND INSTRUMENTATION

The Douglas Long Beach Low Speed Wind Tunnel is a closed circuit, single return facility with a 38 by 54 inch rectangular cross section 10 feet long. A 100 horsepower motor drives a three bladed propeller and is capable of producing a top speed of 195 miles per hour in a clear test section. Nozzle contraction ratio is 6.5:1, and this together with screens and honeycomb results in a low turbulence level in the test section (turbulence factor on the order of 1.03, percent turbulence 0.5%). The airfoil models were mounted to span the 38 inch dimension of the test section.

The 6 inch chord airfoil models had 48 chordwise surface pressure orifices located at the middle of the 38 inch span. These orifices were staggered at  $15^\circ$  to the chordwise direction in order to prevent interference. In addition, 4 chordwise pressure orifices were located 10 inches from each end of the wing to check on three-dimensional effects. A wake rake with 21 total head tubes and 4 static pressure orifices was located 9 inches ( $1\frac{1}{2}$  chordlengths) behind the model on an externally controlled traversing mechanism which allowed centering of the wake within the rake span. The rake was set at an angle of  $21^\circ$  with respect to the span to maximize the number of tubes within the wake itself.

Pressure orifices on the wing and rake were connected to vertical oil-filled manometer banks which were photographed for data recording. Lift and pitching moment were calculated from the wing surface pressures, and drag was calculated from the wake rake pressures. Effects of forced transition were studied using transition strips of glass beads (.006 inch diameter) on 0.125 inch chordwise width strips. Yarn tufts were used to visualize basic flow phenomena such as separation near the ends of the wings and on the wind tunnel walls.

Existence of laminar separation bubbles was identified by a short constant pressure "plateau" in the pressure recovery region. This real time information was one virtue of using the somewhat archaic system of manometer boards for pressure data.

## RESULTS

Airfoils LNV109A and LA203A were tested at Reynolds numbers of 0.250, 0.375, 0.500, and 0.650  $\times 10^6$ . Past experience has shown that airfoil performance can vary significantly within this Reynolds number range, and consequently the relatively fine "mesh" of said parameter is justified. Both airfoils were tested clean and with 0.006" glass bead transition strips located appropriately on their upper surfaces. While transition strips are regarded as undesirable in a flight vehicle application, testing with same can assist in the assessment of laminar bubble effects.

### Airfoil LNV109A

The performance curves for airfoil LNV109A with free transition are given in Figure 5, and the corresponding chordwise pressure distributions for the four test Reynolds numbers are given in Figures 6, 7, 8, and 9. At a Reynolds number of 0.250  $\times 10^6$ , the lift curve in Figure 5 shows total laminar separation between  $\alpha = 0^\circ$  and  $10^\circ$ , which indicates that the airfoil is unuseable at this Reynolds number without a transition inducing artifice. Otherwise, the performance of airfoil LNV109A is acceptable and meets the design specification. The lift curves of Figure 5 show a reduction of  $C_{lmax}$  with increasing Reynolds number which has been typical for this Reynolds number range - including the NACA4415 airfoil which was tested in a previous study.

Chordwise pressure distribution results in Figures 6 through 9 show the presence of a laminar bubble which increases in length with decreasing Reynolds number and/or lift coefficient. This behavior is typical in this Reynolds number regime and is intensified by the very short rooftop of airfoil LNV109A. It should be noted that, in spite of the laminar bubble, the flow remains attached at the trailing edge ( $C_p > 0$ ) in all cases except at  $RN = 0.250 \times 10^6$ .

The size of the laminar bubble suggested that the performance of airfoil LNV109A might be improved by an appropriately sized transition strip. Consequently, a 1/8 inch wide strip of 0.006 inch glass beads was located at  $x/c = 25\%$ , and the test series was repeated. Figures 10 through 13 give a comparison of the resulting airfoil performance curves with and without the transition strip, and the chordwise pressure distributions shown in Figures 14 through 17 indicate that the transition strip has effectively eliminated the laminar bubble. Figures 10 and 11 show that the strip causes a slight increase in drag at high lift and reduction in  $C_{lmax}$  at  $RN = 0.650$  and  $0.500 \times 10^6$ , while Figure 12 shows that the strip has reduced the drag everywhere at  $RN = 0.375 \times 10^6$ . The set of polars in Figures 10 through 13 demonstrates that a transition strip can only be properly sized for a narrow range of Reynolds numbers. A comparison with the theoretical drag prediction of the method of Reference 4 is given in Figure 18a which clearly defines the drag

penalty of the laminar bubble. Lack of agreement of the theoretical prediction with the transition fixed data suggests that the strip itself causes an increase in drag (in this particular case).

#### Airfoil LA203A

Airfoil LA203A was tested over the same conditions as airfoil LNV109A and the resulting performance curves with free transition are given in Figure 19 with the chordwise pressure distributions in Figures 20 through 23. Overall, the performance of airfoil LA203A shown in Figure 19 is regarded as very good. The low drag range is relatively broad and performance at  $RN = 0.250 \times 10^6$  is acceptable. Maximum lift is slightly lower than desired, and the typical trend of increase in  $C_{lmax}$  with decrease in Reynolds number prevails. Evidence of a laminar bubble appears to be significant only at  $RN = 0.250 \times 10^6$  (Figure 23), and the pressure distributions of Figures 20 and 21 indicate that the bubble is almost nonexistent at  $RN = 0.650$  and  $0.500 \times 10^6$ . The pressure distributions also indicate that the flow is attached at the trailing edge ( $C_p > 0$ ) in all cases prior to stall.

Addition of a transition strip of 0.006" glass beads at  $x/c = 47\%$  had no effect on the performance of airfoil LA203A at  $RN = 0.650$  and  $0.500 \times 10^6$ , and it increased the drag at  $RN = 0.375$  and  $0.250 \times 10^6$ . This suggests the strip was improperly located, and  $x/c = 40\%$  would have been better. However, since airfoil LA203A performed well in the clean configuration, additional testing with transition strips was not considered. Figure 18b offers a comparison of the experimental drag polar at  $RN = 0.375 \times 10^6$  with the theoretical prediction of Reference 4. The close agreement here confirms that there is no apparent drag penalty due to the laminar bubble.

#### Comparison of Airfoils LNV109A and LA203A

The performance of the test airfoils is compared in Figures 24 through 27 where the results used are transition free except for airfoil LNV109A at  $RN = 0.250 \times 10^6$ . Airfoil LA203A has lower drag than LNV109A below  $C_l = 1.5$  at all the test Reynolds numbers, and the difference in drag increases with decreasing Reynolds number. Airfoil LNV109A has a higher  $C_{lmax}$  at all Reynolds numbers and its drag performance is close to that of LA203A at  $RN = 0.650 \times 10^6$ .

A comparison of airfoil LA203A with the Wortmann FX63-137 airfoil at  $RN = 0.500 \times 10^6$  is given in Figure 28. The data for the FX63-137 was obtained from testing in the Douglas Long Beach Wind Tunnel in an earlier study. Airfoil LA203A has a higher  $C_{lmax}$ , lower drag above  $C_l = 1.0$ , a slightly lower pitching moment, and is 15 percent thicker (.02 in  $t/c$ ).

## CONCLUSIONS

Both airfoils have achieved the design goals in principle. Airfoil LNV109A has met all the specified requirements including the additional pitching moment constraint. However, it suffers a drag penalty at the lower Reynolds numbers due to the laminar bubble and requires that transition be artificially induced at  $Re = 0.250 \times 10^6$ . Airfoil LA203A, with no constraint on its pitching moment performed very well at all of the test Reynolds numbers with transition free, and its only shortcoming was a  $C_{lmax}$  on the order of 1.7 instead of the desired 1.8.

As discussed in the Introduction, the difficulty with transition and consequent laminar bubble is due to the relatively short rooftop of airfoil LNV109A. Specifying a high  $C_{lmax}$  and low pitching moment appears to require this. Relaxing either of these requirements allows the design of an airfoil with a longer rooftop and a more tractable laminar bubble. Elimination of the pitching moment constraint permits the aerodynamicist to retreat to his favorite "free lunch"; namely, aft-camber. From an airplane design point of view, where trim drag must be considered, it is likely that a more optimum airfoil lies somewhere between LNV109A and LA203A.

Finally, it is interesting to note that aft-loading appears to help drag-rise due to the laminar bubble just as it helps drag-rise due to compressibility. As is the case for the recompression shock, the laminar bubble is always there, and the question at low Reynolds numbers is how to deal with it efficiently.

## REFERENCES

1. Liebeck, R. H.: "A Class of Airfoils Designed for High Lift Without Separation in Incompressible Flow," Douglas Report No. MDC-1097/01, December 1971. (Restricted Distribution).
2. Stratford, B. S.: "The Prediction of Separation of the Turbulent Boundary Layer," Journal of Fluid Mechanics, Vol. 5, 1959.
3. James, R. M.: "A New Look at Two-Dimensional Incompressible Airfoil Theory," Douglas Report No. MDC J0918/01, May 1971 (Restricted Distribution).
4. Cebeci, T., et al: "A Two-Point Finite-Difference Boundary-Layer Methods for Incompressible and Compressible Two-Dimensional and Axisymmetric Laminar and Turbulent Flows Including Infinite-Swept Wings," Douglas Report No. MDC J7986, September 1978.

# HIGH-LIFT AIRFOIL AND PRESSURE DISTRIBUTION

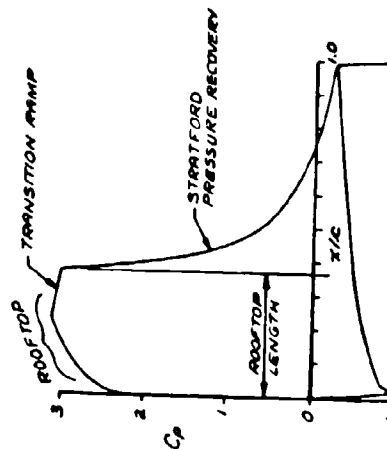


FIGURE 1

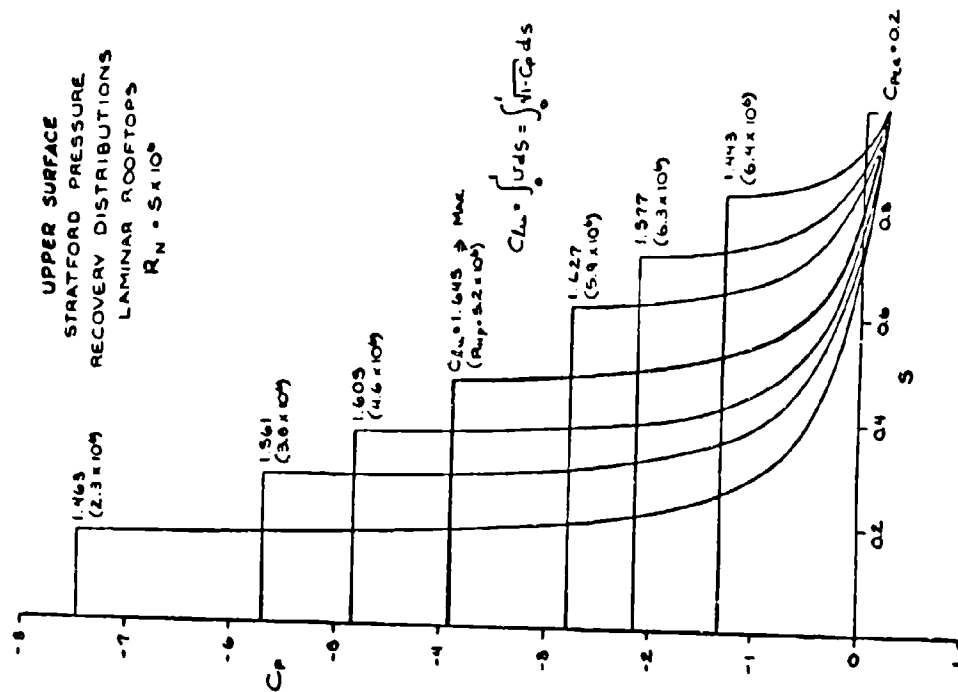


FIGURE 2

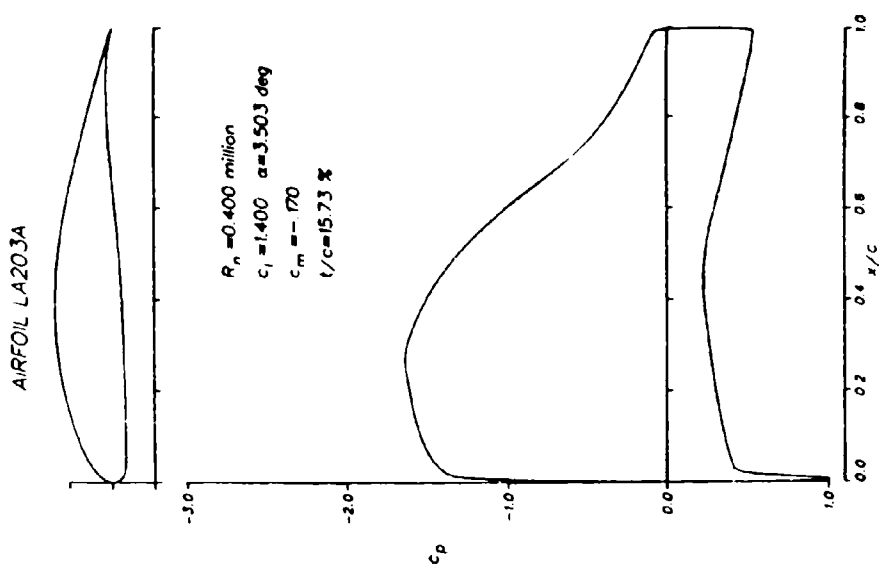


FIGURE 4

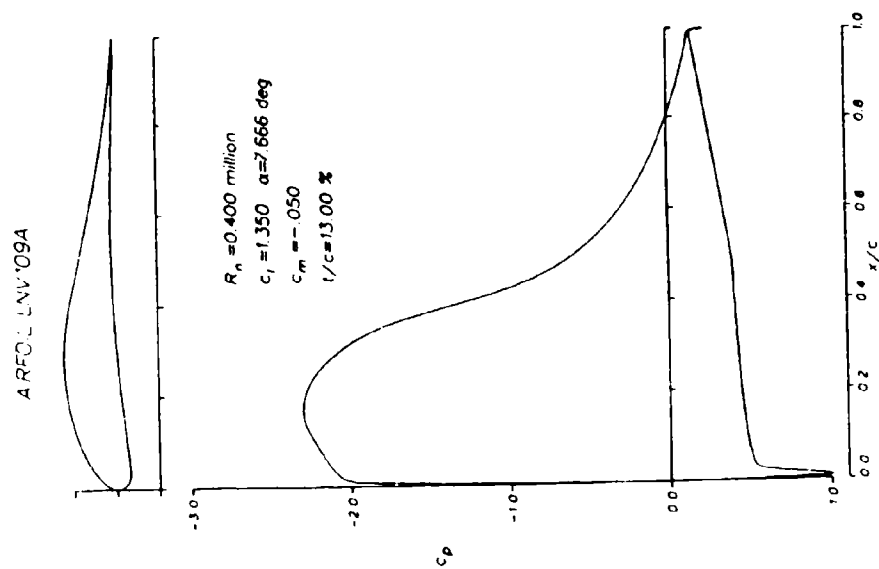


FIGURE 3

# AIRFOIL PERFORMANCE CURVE(S)

Sym	Airfoil	$R_N(10^6)$	Transition
□	LNV109A	0.650	Free
○	LNV109A	0.500	Free
△	LNV109A	0.375	Free
◇	LNV109A	0.250	Free

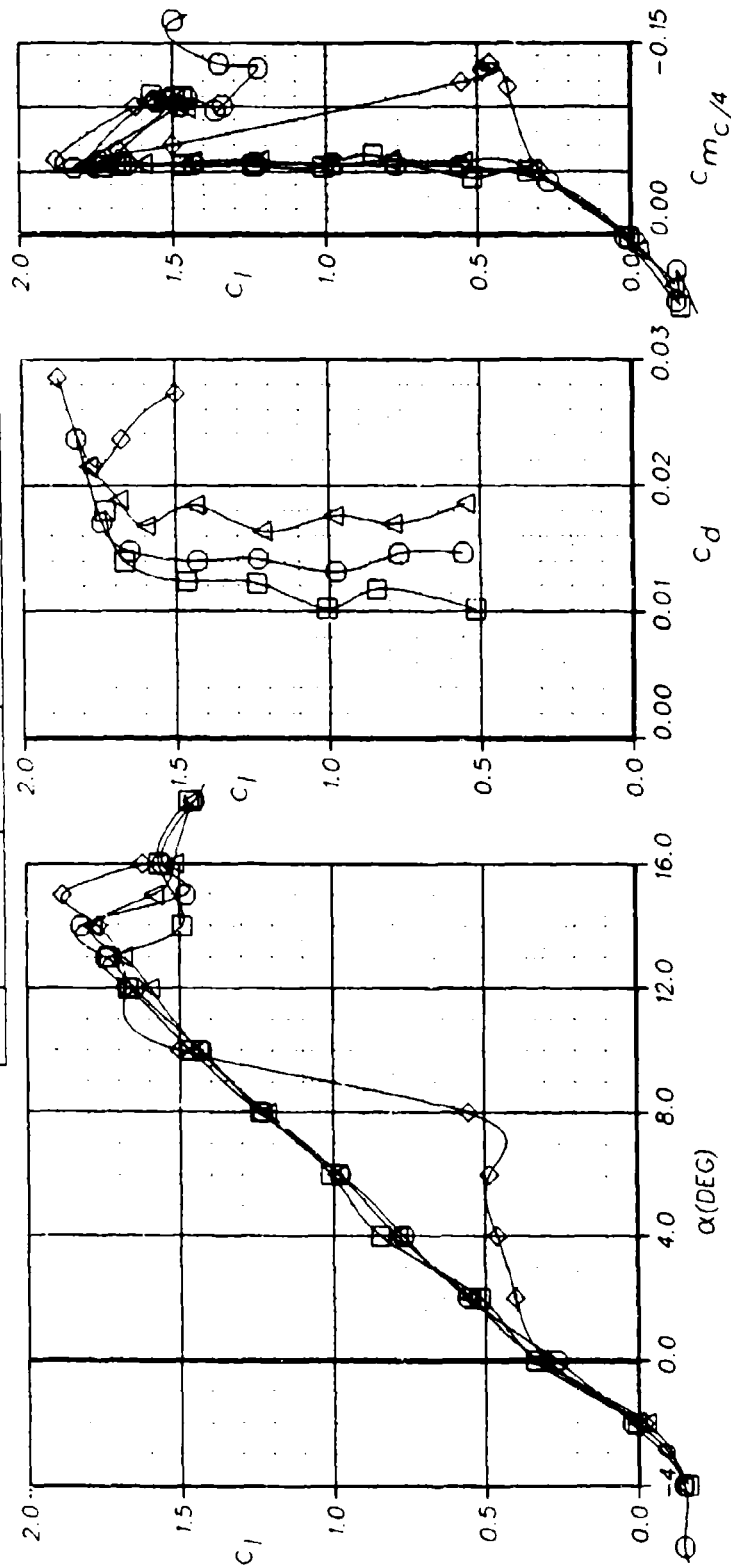


FIGURE 5

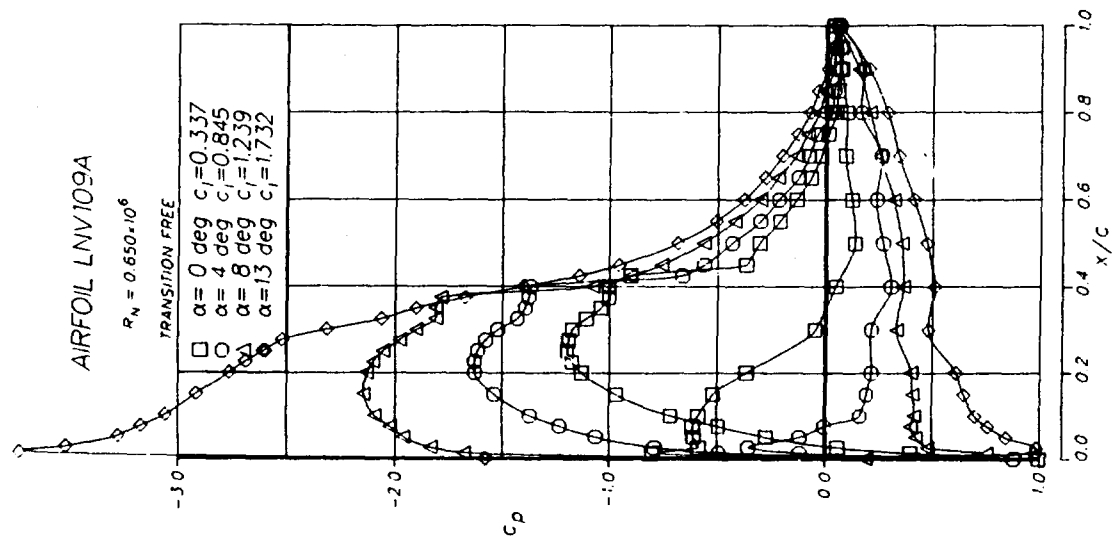


FIGURE 6

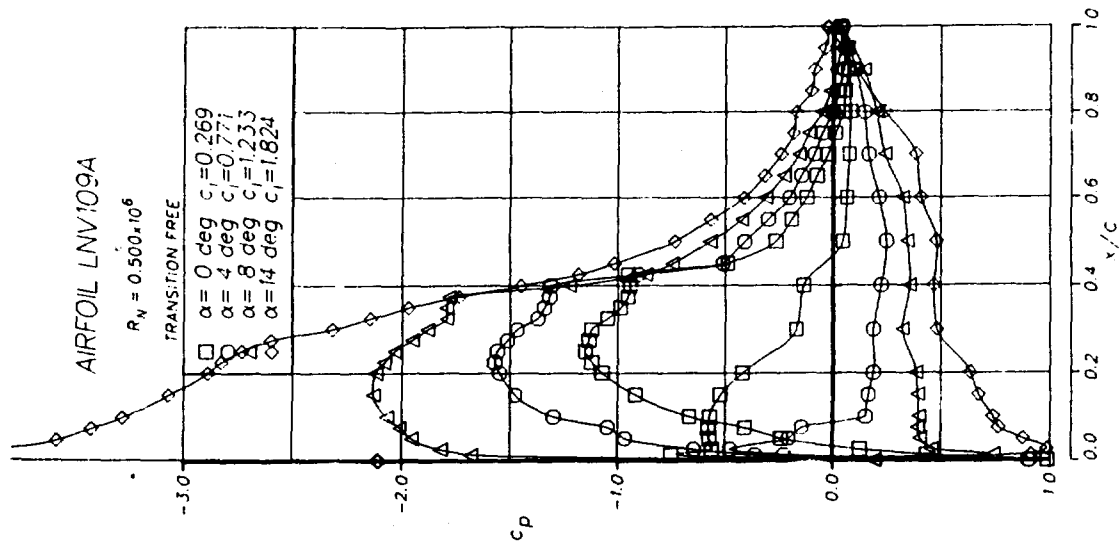


FIGURE 7

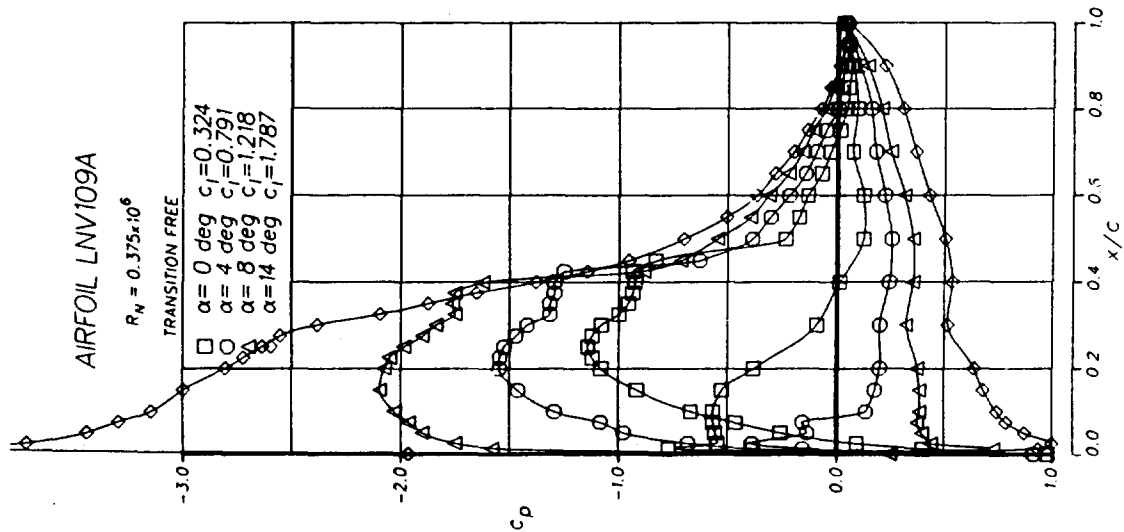


FIGURE 8

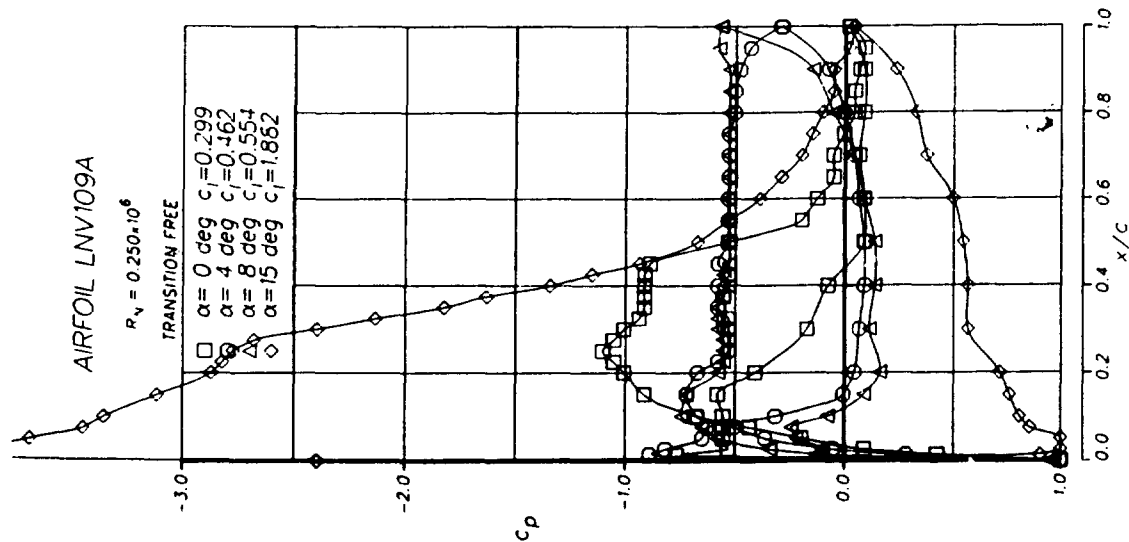


FIGURE 9

# AIRFOIL PERFORMANCE CURVE(S)

Sym	Airfoil	$R_N(10^6)$	Transition
□	LNVI09A	0.650	Free
○	LNVI09A	0.650	.006 in $x/c = 25\%$

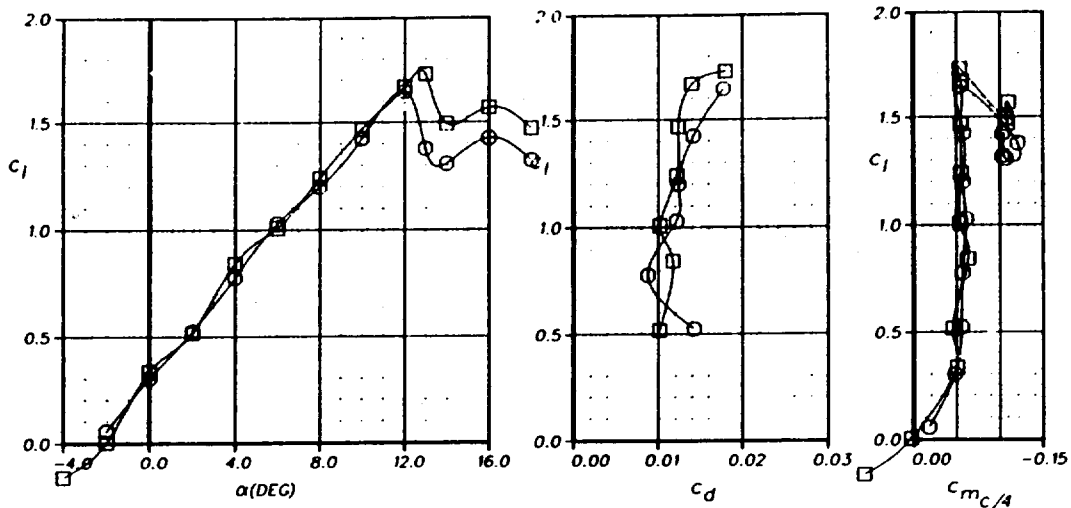


FIGURE 10

# AIRFOIL PERFORMANCE CURVE(S)

Sym	Airfoil	$R_N(10^6)$	Transition
□	LNVI09A	0.500	Free
○	LNVI09A	0.500	.006 in $x/c = 25\%$

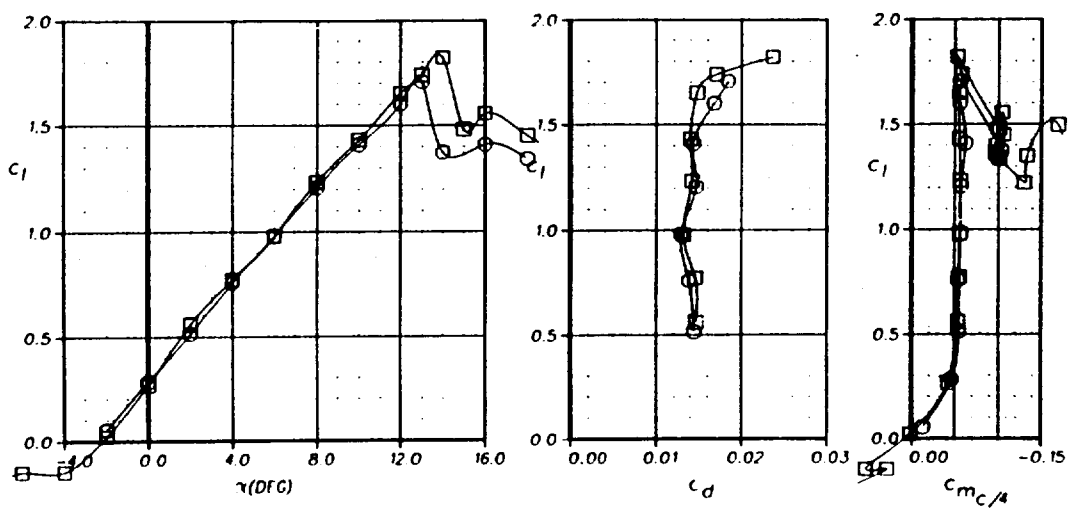


FIGURE 11

AIRFOIL PERFORMANCE CURVE (5)

Sym	Airfoil	$R_N(10^6)$	Transition
□	LNVI09A	0.375	free
○	LNVI09A	0.375	006 in s/c - 25%

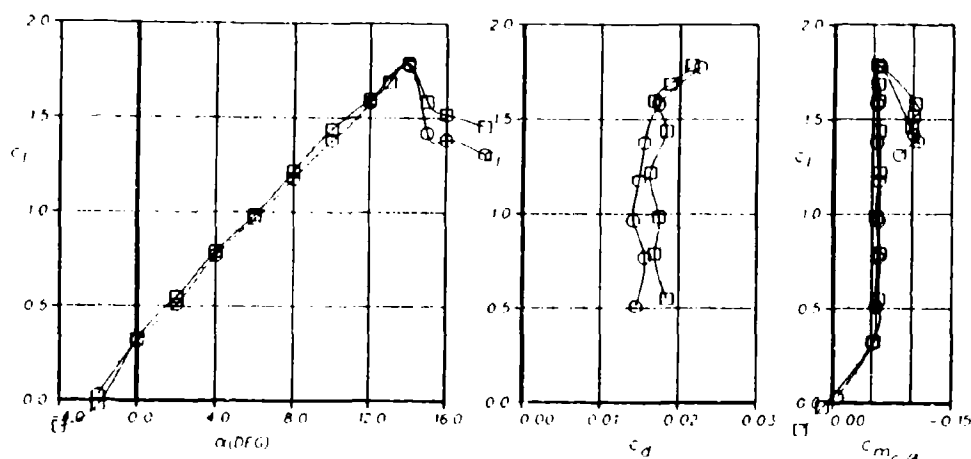


FIGURE 12

AIRFOIL PERFORMANCE CURVE (6)

Sym	Airfoil	$R_N(10^6)$	Transition
□	LNVI09A	0.250	free
○	LNVI09A	0.250	006 in s/c - 25%

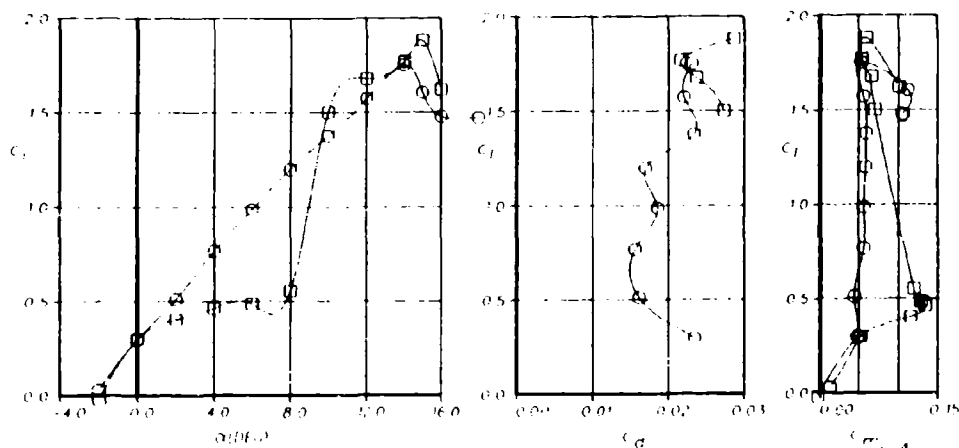


FIGURE 13

# AIRFOIL LNV109A

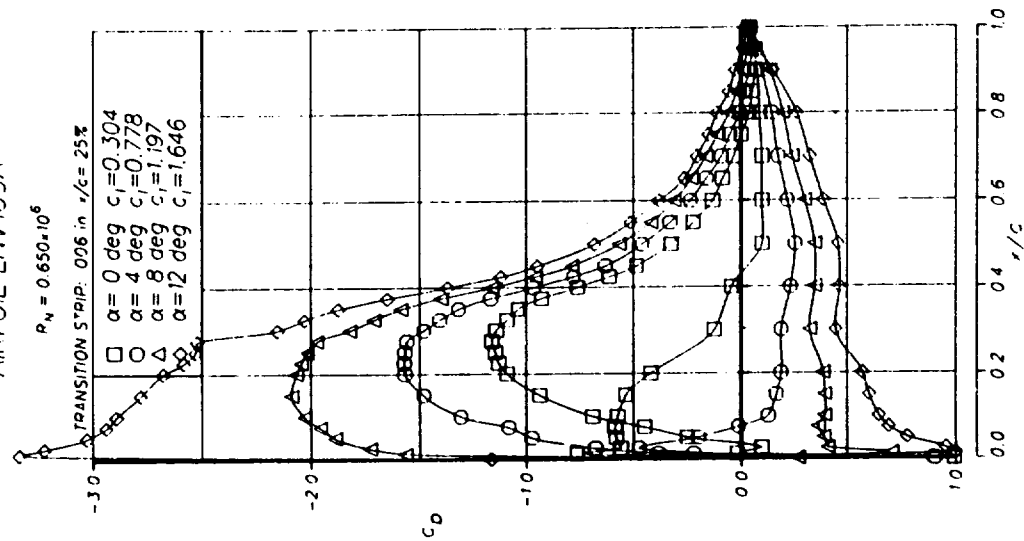


FIGURE 4

# AIRFOIL LNV109A

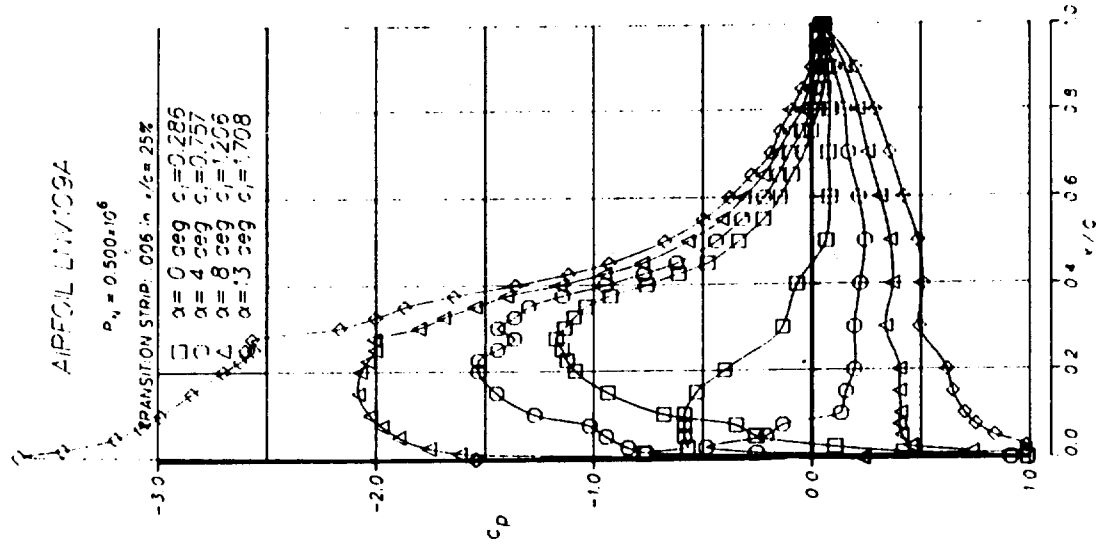


FIGURE 5

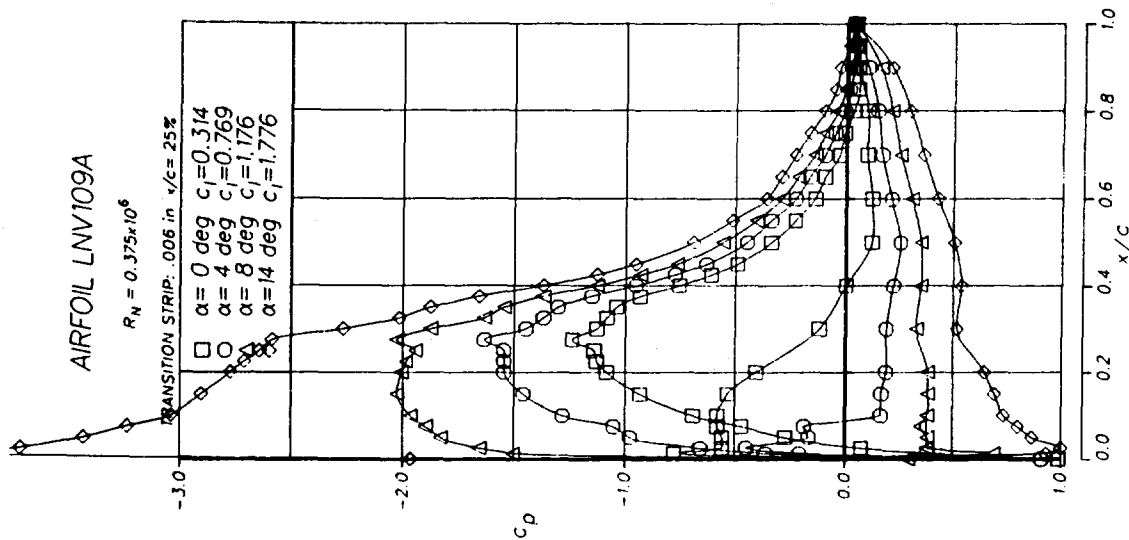


FIGURE 16

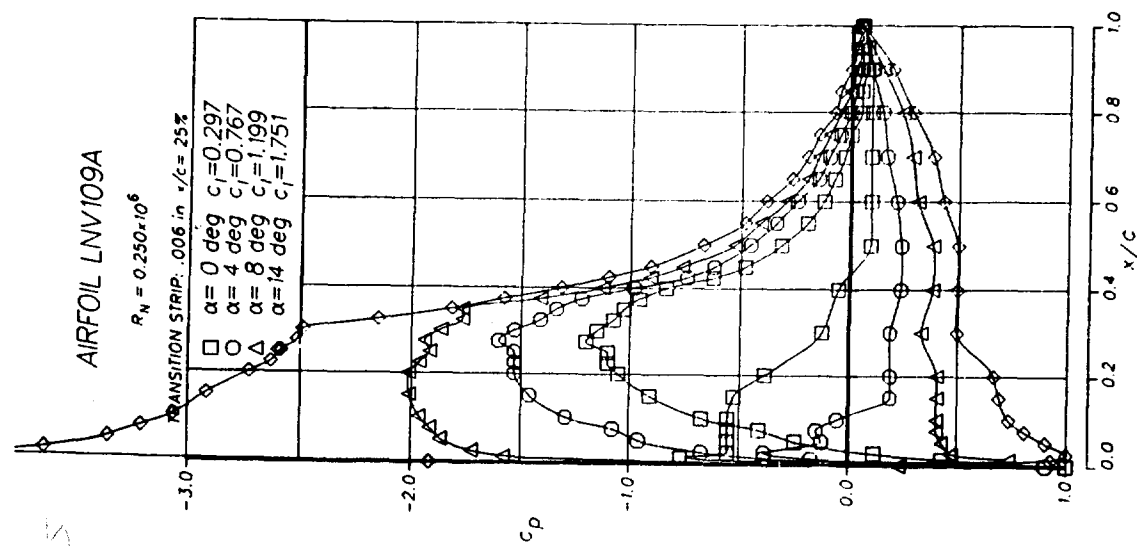


FIGURE 17

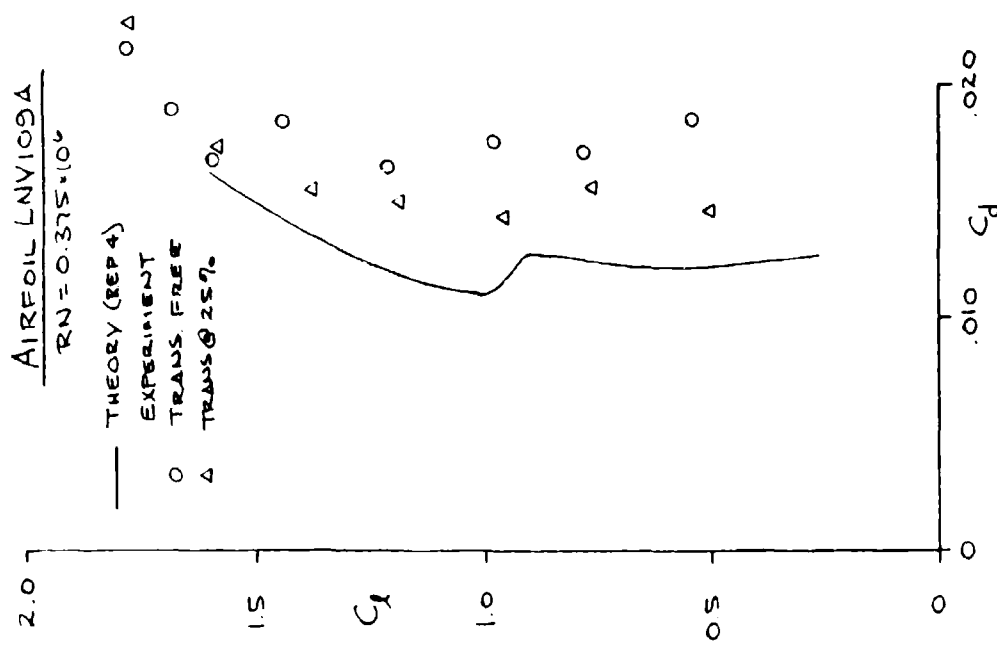


FIGURE 18A

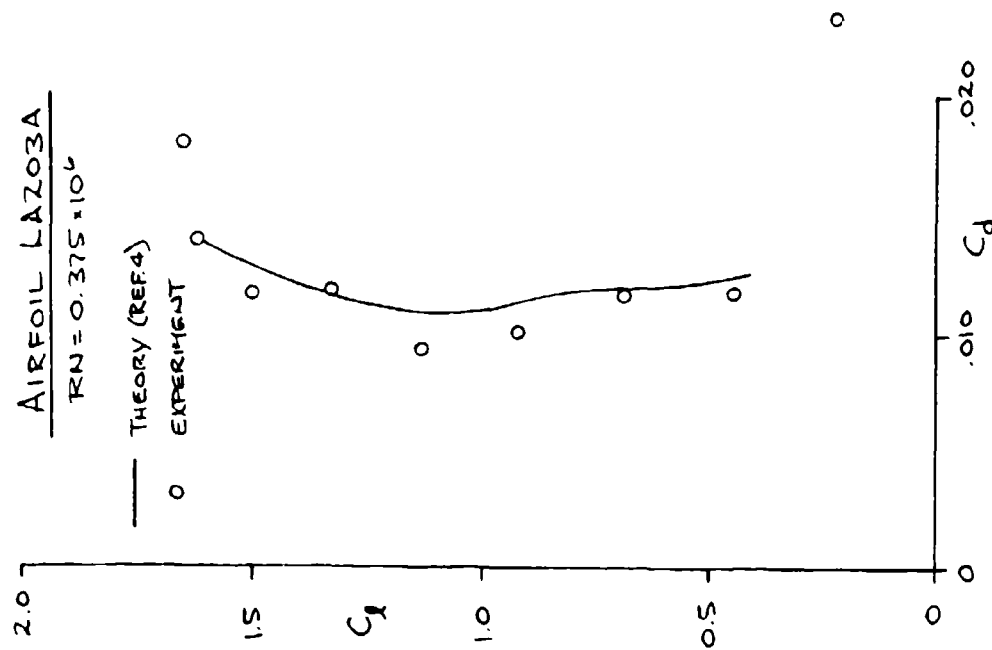


FIGURE 18B

# AIRFOIL PERFORMANCE CURVE(S)

$S_c, m$	Airfoil	$R_N (10^6)$	Transition
□	LA20.3A	0.650	Free
○	LA20.3A	0.500	Free
△	LA20.3A	0.375	Free
◇	LA20.3A	0.250	Free

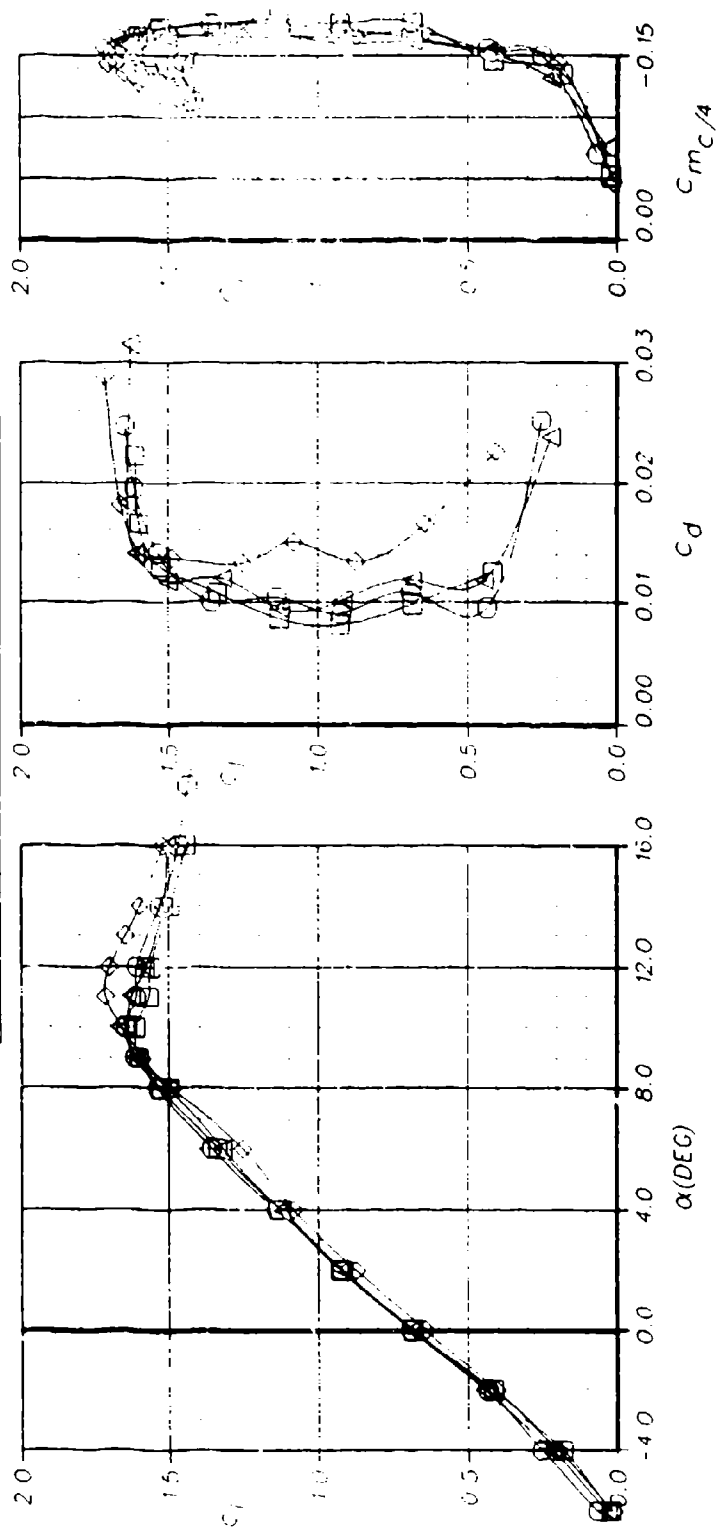


FIGURE 19

# AIRFOIL LA203A

$R_N = 0.650 \times 10^6$

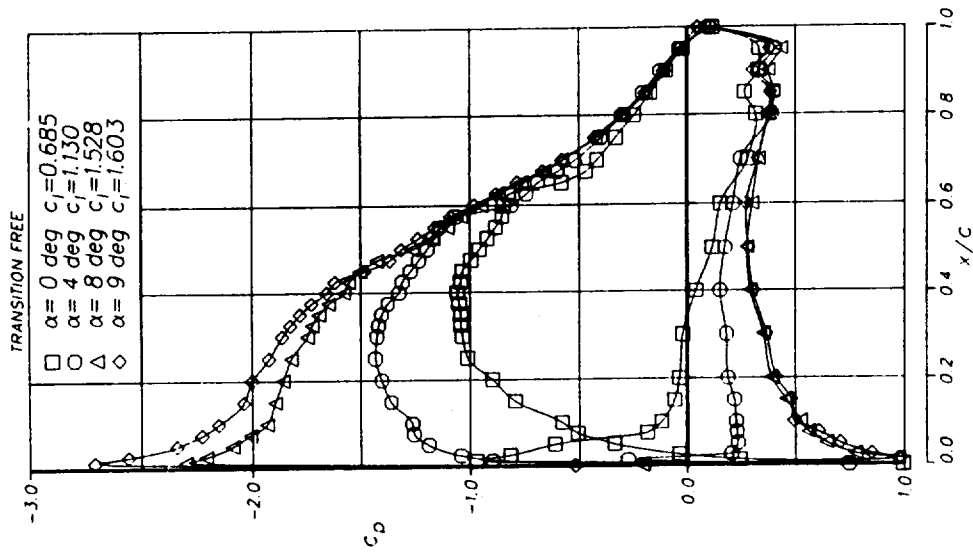


FIGURE 20

# AIRFOIL LA203A

$R_N = 0.500 \times 10^6$

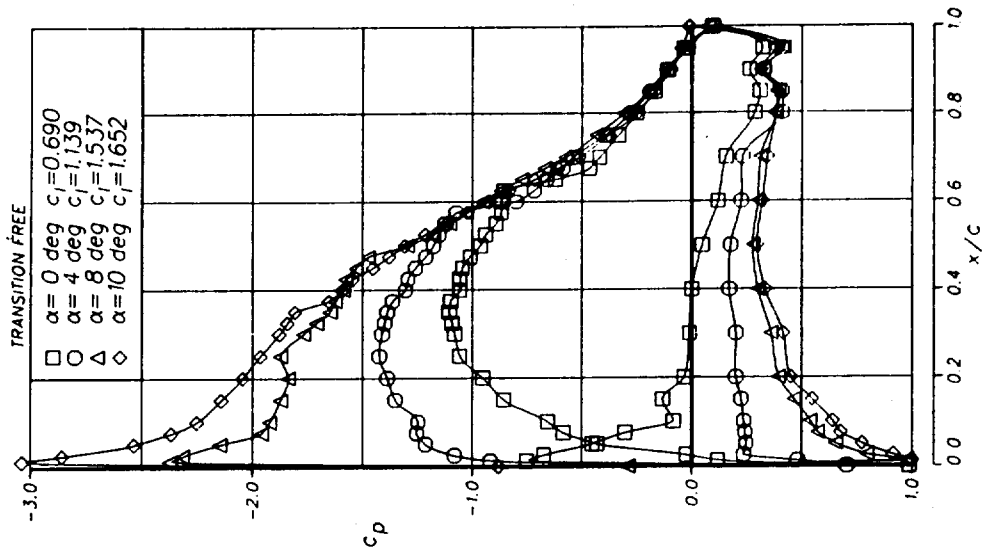


FIGURE 21

# AIRFOIL LA203A

$R_N = 0.375 \times 10^6$

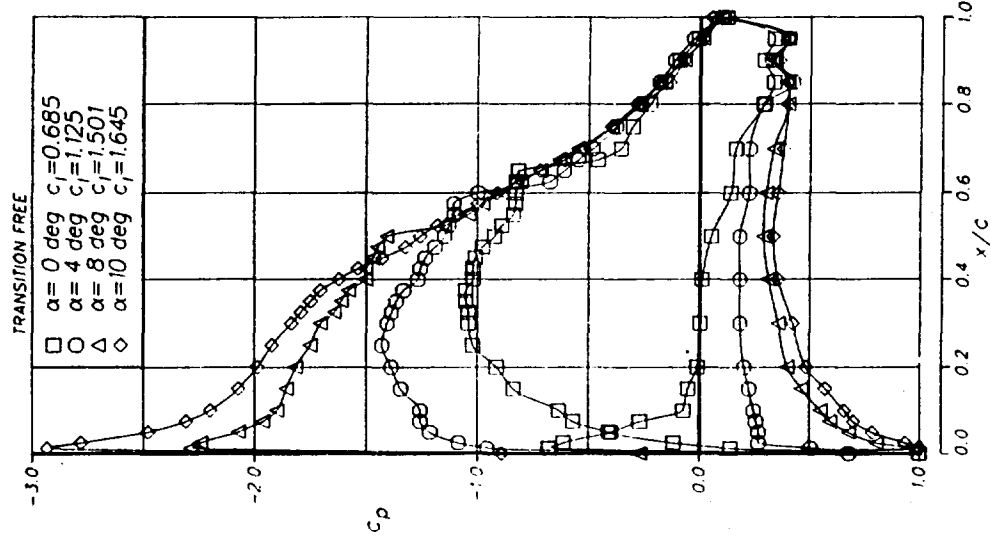


FIGURE 22

# AIRFOIL LA203A

$R_N = 0.250 \times 10^6$

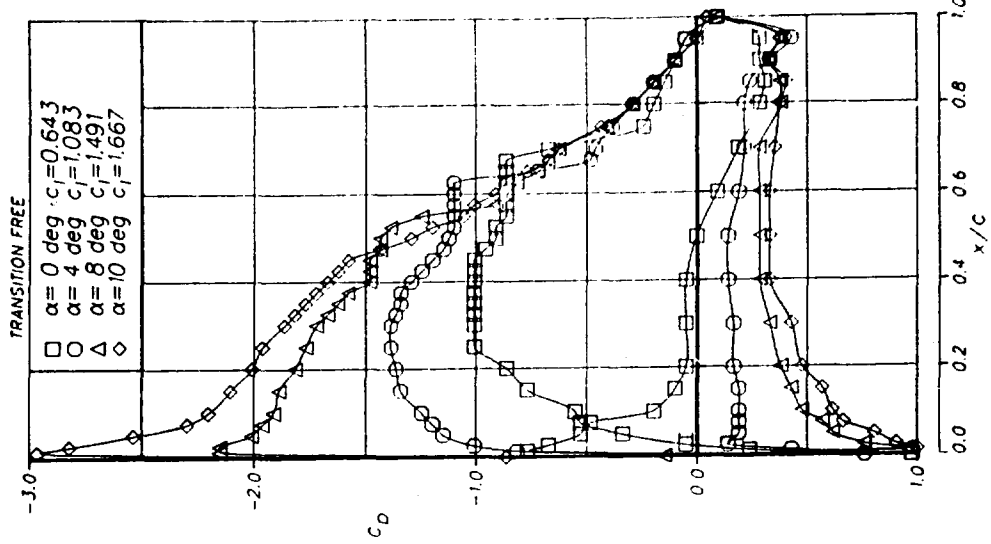


FIGURE 23

# AIRFOIL PERFORMANCE CURVE(S)

Sym	Airfoil	$R_N(10^6)$	Transition
□	LNV109A	0.650	Free
○	LA20.3A	0.650	Free

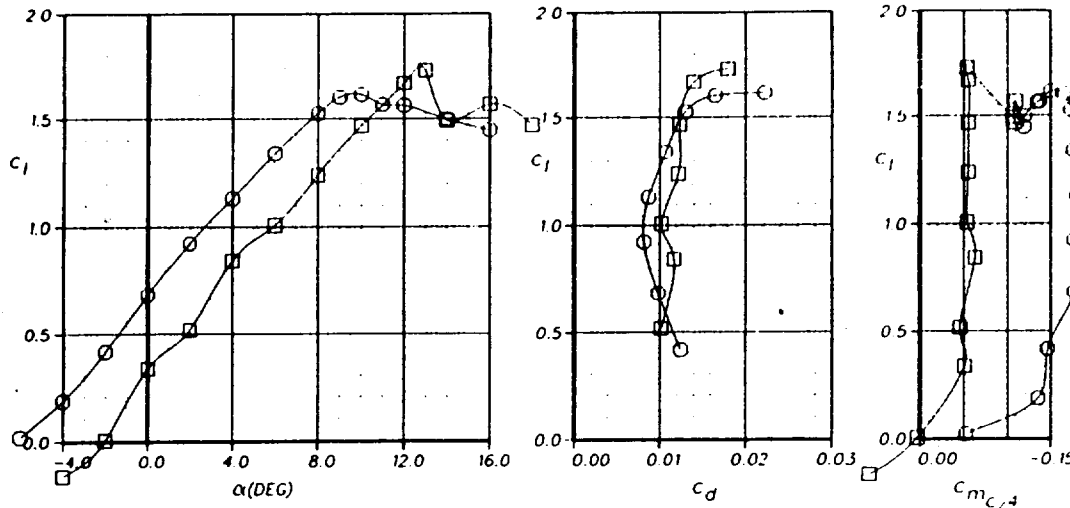


Figure 24

# AIRFOIL PERFORMANCE CURVE(S)

Sym	Airfoil	$R_N(10^6)$	Transition
□	LNV109A	0.500	Free
○	LA20.3A	0.500	Free

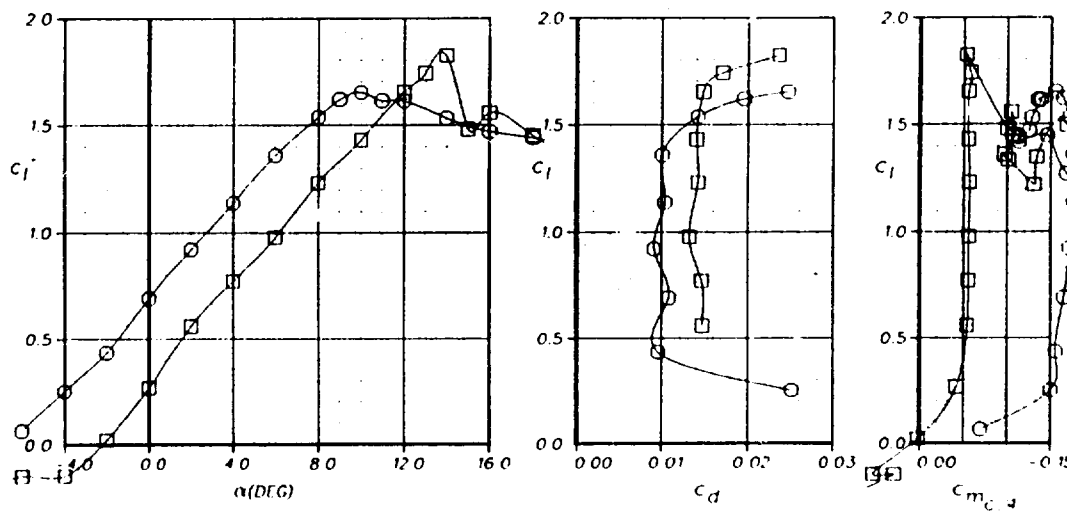


Figure 25

# AIRFOIL PERFORMANCE CURVE (%)

Sym	Airfoil	$R_N(10^6)$	Transition
□	LNV109A	0.375	Free
○	LA20.3A	0.375	Free

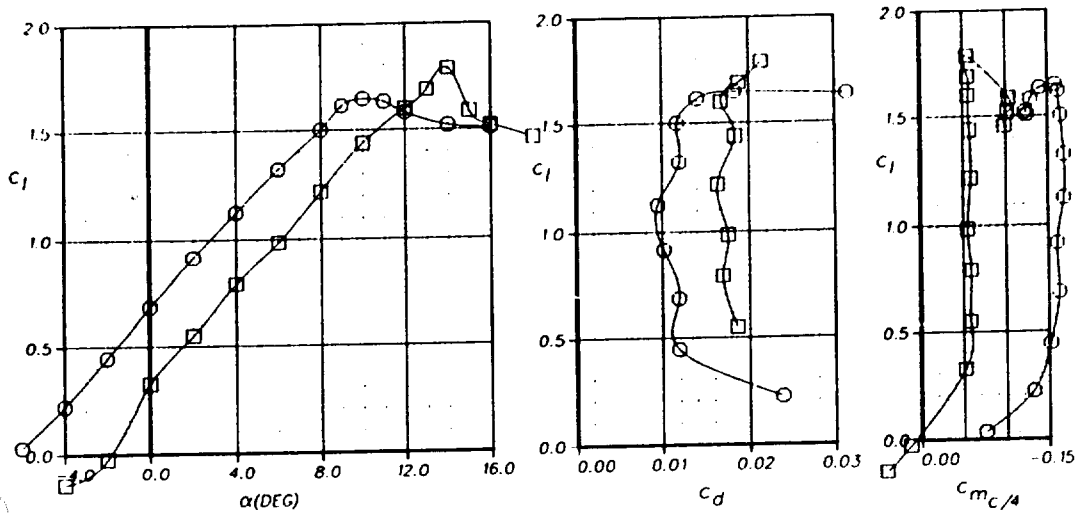


Figure 26

# AIRFOIL PERFORMANCE CURVE (S)

Sym	Airfoil	$R_N(10^6)$	Transition
□	LNV109A	0.250	006 in $s/c = 25\%$
○	LA20.3A	0.250	Free

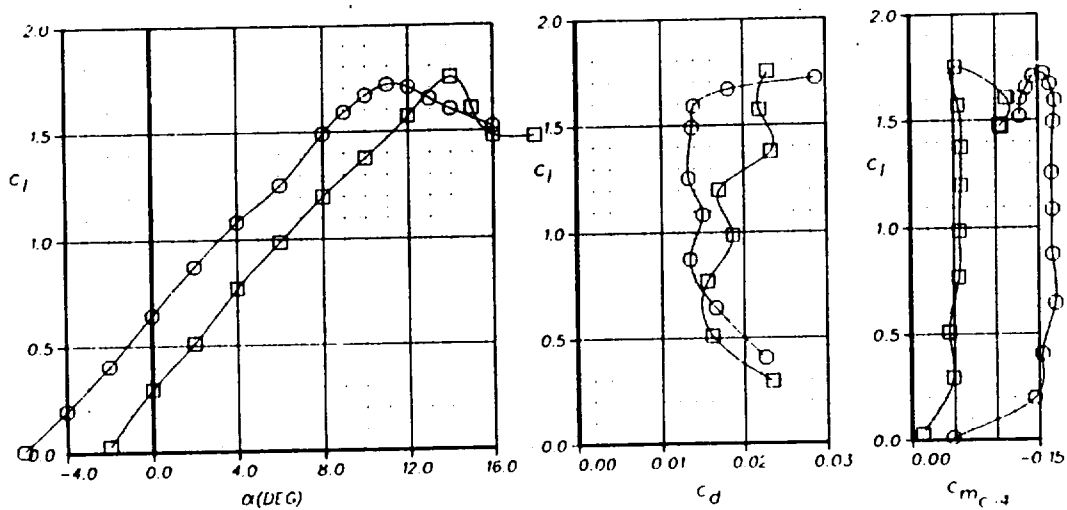


Figure 27

# AIRFOIL PERFORMANCE CURVE(S)

Sym	Airfoil	$P_N (10^6)$	Transition
□	LA203A	0.500	Free
○	FX63-137	0.500	Free

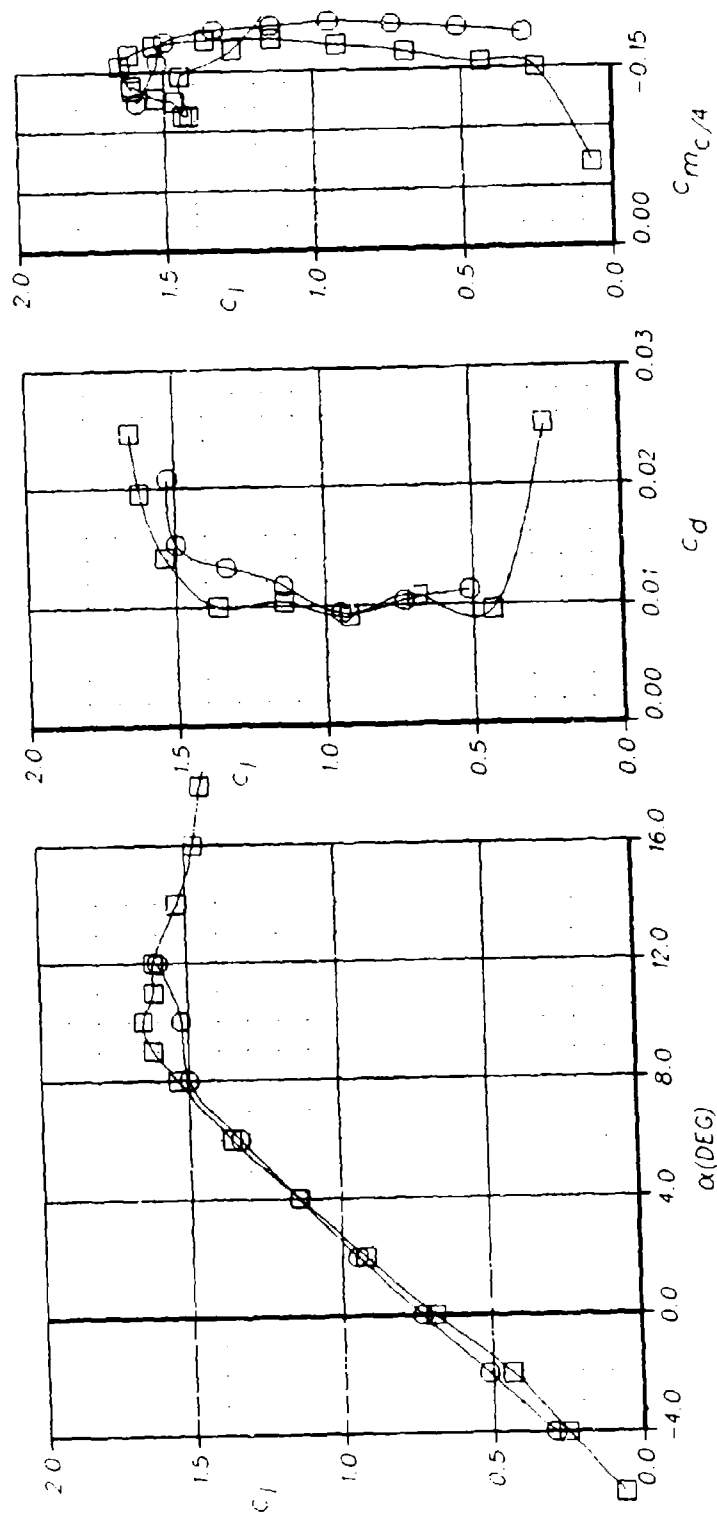


Figure 28

# APPENDIX

AIRFOIL LNW 109A  
CHORD = 1.000000  
THICKNESS = 0.129873

I	X	ZU	ZL	ZC	ZT	I	X	ZU	ZL	ZC	ZT
1	1.000000	0.000001	-0.000001	-0.000000	0.000001	1	1.000000	-0.000000	-0.000000	-0.000000	0.000000
2	0.993938	0.000343	0.000097	0.000223	0.000320	2	0.993938	0.003044	0.002384	-0.000000	0.000000
3	0.986151	0.001101	-0.000030	0.000532	0.000570	3	0.986151	0.005883	0.004425	0.002384	0.000330
4	0.976665	0.001787	0.000093	0.000940	0.000847	4	0.976665	0.008985	0.006392	0.004425	0.000729
5	0.965516	0.002657	0.000273	0.001465	0.001192	5	0.965516	0.012408	0.008211	0.006392	0.001297
6	0.952740	0.003750	0.000505	0.002121	0.001616	6	0.952740	0.016162	0.009838	0.008211	0.002098
7	0.938365	0.005056	0.000789	0.002923	0.002134	7	0.938365	0.020258	0.011218	0.009838	0.003162
8	0.922500	0.006639	0.001124	0.003882	0.002754	8	0.922500	0.024700	0.013056	0.011218	0.004520
9	0.904134	0.008509	0.001515	0.005012	0.003497	9	0.904134	0.029490	0.014940	0.013056	0.006199
10	0.884369	0.010690	0.001955	0.006322	0.004368	10	0.884369	0.034630	0.016848	0.014940	0.008217
11	0.862500	0.013204	0.002443	0.007823	0.005381	11	0.862500	0.040113	0.018744	0.016848	0.010591
12	0.838856	0.016064	0.002973	0.009521	0.006548	12	0.838856	0.045936	0.020644	0.018744	0.013325
13	0.812261	0.019300	0.003538	0.011419	0.007881	13	0.812261	0.052086	0.022613	0.020644	0.016244
14	0.785551	0.022912	0.004130	0.013521	0.009391	14	0.785551	0.058495	0.024759	0.022613	0.019287
15	0.757971	0.026914	0.004735	0.015824	0.011089	15	0.757971	0.065291	0.026996	0.024759	0.022300
16	0.729807	0.031312	0.005340	0.018326	0.012986	16	0.729807	0.072424	0.029344	0.026996	0.025788
17	0.701524	0.036110	0.005927	0.021018	0.015091	17	0.701524	0.079895	0.031812	0.029344	0.029448
18	0.674154	0.041303	0.006477	0.023890	0.017413	18	0.674154	0.087697	0.034448	0.031812	0.033303
19	0.646886	0.046886	0.006968	0.026927	0.020199	19	0.646886	0.096463	0.037176	0.034448	0.037024
20	0.619613	0.052846	0.007376	0.030111	0.022735	20	0.619613	0.106063	0.040014	0.037176	0.040960
21	0.592579	0.059164	0.007672	0.033418	0.025746	21	0.592579	0.117640	0.042822	0.040014	0.045195
22	0.574167	0.065913	0.007824	0.036820	0.028994	22	0.574167	0.131219	0.045617	0.042822	0.049681
23	0.549490	0.072756	0.007802	0.040279	0.032477	23	0.549490	0.146836	0.048336	0.045617	0.054405
24	0.519653	0.079234	0.007552	0.043743	0.036191	24	0.519653	0.164490	0.050917	0.048336	0.059336
25	0.489759	0.087493	0.006997	0.047137	0.040139	25	0.489759	0.184176	0.053336	0.050917	0.064405
26	0.459916	0.097011	0.006064	0.050383	0.044318	26	0.459916	0.205916	0.055696	0.053336	0.069681
27	0.430226	0.107216	0.004793	0.053454	0.048661	27	0.430226	0.230740	0.057024	0.055696	0.075024
28	0.400796	0.118249	0.003265	0.056257	0.053292	28	0.400796	0.258696	0.058259	0.057024	0.080497
29	0.371724	0.130425	0.001516	0.058806	0.058640	29	0.371724	0.289819	0.059419	0.058259	0.086033
30	0.343127	0.143790	0.000425	0.061074	0.064236	30	0.343127	0.324142	0.060424	0.059419	0.091769
31	0.315090	0.158232	-0.000232	0.062970	0.069783	31	0.315090	0.361559	0.061225	0.060424	0.097639
32	0.287718	0.173718	-0.004782	0.064501	0.075317	32	0.287718	0.402024	0.061824	0.061225	0.103696
33	0.261106	0.190106	-0.009608	0.065732	0.080895	33	0.261106	0.445644	0.062224	0.061824	0.109977
34	0.235350	0.207434	-0.014644	0.066644	0.086644	34	0.235350	0.492424	0.062524	0.062224	0.116479
35	0.210538	0.225350	-0.019338	0.067156	0.092512	35	0.210538	0.542424	0.062724	0.062524	0.123139
36	0.186758	0.243758	-0.023645	0.067338	0.098645	36	0.186758	0.595644	0.062824	0.062724	0.129977
37	0.164095	0.262644	-0.027244	0.067338	0.104970	37	0.164095	0.652024	0.062824	0.062824	0.136977
38	0.142628	0.282024	-0.030112	0.067156	0.111338	38	0.142628	0.711559	0.062524	0.062824	0.144095
39	0.122185	0.295430	-0.032211	0.066644	0.117755	39	0.122185	0.773424	0.062024	0.062524	0.151339
40	0.102624	0.308824	-0.033610	0.065820	0.123878	40	0.102624	0.838644	0.061336	0.062024	0.158758
41	0.084095	0.322224	-0.034224	0.064644	0.129724	41	0.084095	0.907024	0.060424	0.061336	0.166296
42	0.067156	0.336666	-0.034066	0.063089	0.135244	42	0.067156	0.978424	0.059419	0.060424	0.173977
43	0.051744	0.352024	-0.033132	0.061090	0.140424	43	0.051744	0.105244	0.058259	0.059419	0.181769
44	0.037155	0.368330	-0.031262	0.058695	0.145244	44	0.037155	0.112424	0.056996	0.058259	0.189639
45	0.023594	0.385318	-0.028424	0.055936	0.149644	45	0.023594	0.120024	0.055696	0.056996	0.197639
46	0.011544	0.403044	-0.024755	0.052512	0.153644	46	0.011544	0.128024	0.054424	0.055696	0.205758
47	0.001427	0.421222	-0.020224	0.048444	0.157244	47	0.001427	0.136424	0.053136	0.054424	0.213977
48	0.007465	0.439824	-0.015138	0.043755	0.160424	48	0.007465	0.145244	0.051824	0.053136	0.222296
49	0.003544	0.458824	-0.009644	0.038424	0.163244	49	0.003544	0.154424	0.050424	0.051824	0.230758
50	0.000887	0.478139	-0.003081	0.032644	0.165644	50	0.000887	0.164024	0.049024	0.050424	0.239377
51	0.000000	-0.000000	-0.000000	-0.000000	0.0	51	0.000000	-0.000000	-0.000000	-0.000000	0.0

AIRFOIL LA 203A  
CHORD = 1.000000  
THICKNESS = 0.157306

I	X	ZU	ZL	ZC	ZT
1	1.000000	-0.000000	-0.000000	-0.000000	0.000000
2	0.993938	0.003044	0.002384	-0.000000	0.000330
3	0.986151	0.005883	0.004425	0.002384	0.000729
4	0.976665	0.008985	0.006392	0.004425	0.001297
5	0.965516	0.012408	0.008211	0.006392	0.002098
6	0.952740	0.016162	0.009838	0.008211	0.003162
7	0.938365	0.020258	0.011218	0.009838	0.004520
8	0.922500	0.024700	0.013056	0.011218	0.006199
9	0.904134	0.029490	0.014940	0.013056	0.008217
10	0.884369	0.034630	0.016848	0.014940	0.010591
11	0.862500	0.040113	0.018744	0.016848	0.013325
12	0.838856	0.045936	0.020644	0.018744	0.016244
13	0.812261	0.052086	0.022613	0.020644	0.019287
14	0.785551	0.058495	0.024759	0.022613	0.022300
15	0.757971	0.065291	0.026996	0.024759	0.025788
16	0.729807	0.072424	0.029344	0.026996	0.029448
17	0.701524	0.079895	0.031812	0.029344	0.033303
18	0.674154	0.087697	0.034448	0.031812	0.037024
19	0.646886	0.096463	0.037176	0.034448	0.040960
20	0.619613	0.106063	0.040014	0.037176	0.045195
21	0.592579	0.117640	0.042822	0.040014	0.049681
22	0.574167	0.131219	0.045617	0.042822	0.054405
23	0.549490	0.146836	0.048336	0.045617	0.059336
24	0.519653	0.164490	0.050917	0.048336	0.064405
25	0.489759	0.184176	0.053336	0.050917	0.069681
26	0.459916	0.205916	0.055696	0.053336	0.075024
27	0.430226	0.230740	0.057024	0.055696	0.080497
28	0.400796	0.258696	0.058259	0.057024	0.086033
29	0.371724	0.289819	0.059419	0.058259	0.091769
30	0.343127	0.324142	0.060424	0.059419	0.097639
31	0.315090	0.361559	0.061225	0.060424	0.103696
32	0.287718	0.402024	0.061824	0.061225	0.109977
33	0.261106	0.445644	0.062224	0.061824	0.116479
34	0.235350	0.492424	0.062524	0.062224	0.123139
35	0.210538	0.542424	0.062724	0.062524	0.129977
36	0.186758	0.595644	0.062824	0.062724	0.136977
37	0.164095	0.652024	0.062824	0.062824	0.144095
38	0.142628	0.711559	0.062524	0.062824	0.151339
39	0.122185	0.773424	0.062024	0.062524	0.158758
40	0.102624	0.838644	0.061336	0.062024	0.166296
41	0.084095	0.907024	0.060424	0.061336	0.173977
42	0.067156	0.978424	0.059419	0.060424	0.181769
43	0.051744	1.052024	0.058259	0.059419	0.189639
44	0.037155	1.124424	0.056996	0.058259	0.197639
45	0.023594	1.199644	0.055696	0.056996	0.205758
46	0.011544	1.277824	0.054424	0.055696	0.213977
47	0.001427	1.358824	0.053136	0.054424	0.222296
48	0.007465	1.442644	0.051824	0.053136	0.230758
49	0.003544	1.529244	0.050424	0.051824	0.239377
50	0.000887	1.619644	0.049024	0.050424	0.248096
51	0.000000	-0.000000	-0.000000	-0.000000	0.0

# A VISCOUS-INVISCID COUPLING METHOD FOR THE DESIGN OF LOW REYNOLDS NUMBER AIRFOIL SECTIONS

Ahmed A. Hassan  
Assistant Professor  
Department of Mechanical and Aerospace Engineering  
Arizona State University  
Tempe, Arizona 85287

## ABSTRACT

An interactive numerical coupling procedure has been developed for the design of airfoil sections with an allowance for viscous effects, provided that the boundary layer is fully attached over the airfoil. Special emphasis is given to the design of Natural Laminar Flow (NLF) Airfoils. The method described combines, in an iterative process, an inviscid hodograph-based inverse-design algorithm (IDA) developed by the author, the inviscid-analysis algorithm (FLO6) by Jameson, and the boundary layer algorithm (LTBLCEQL) by Miner, Anderson and Lewis. In the physical plane, the inviscid computational results define an airfoil configuration (or displacement surface) having a preset trailing edge gap. Viscous effects are then incorporated in the design procedure via the displacement surface concept. As expected, the numerical results suggest that airfoils having long runs of NLF are easily obtained, provided that the proper choice of the gradients of the prescribed input pressure distribution is made.

## INTRODUCTION

In recent years, great strides have been made in the development of fast, more efficient numerical procedures for the computation of the flow past given airfoil shapes (direct or analysis problem) [1-2] and conversely, for finding the airfoil configuration that would yield a specified input pressure distribution (inverse or design problem) [3-5]. The ability to control specific aerodynamic characteristics using a direct method is absent, and usually can be classified as a "trial and error" approach. However, the main advantage of such a method is its rapid convergence and of course, its firm control of the airfoil configuration since it is specified. On the other hand, in inverse methods, since the pressure distribution is specified, usually a better control of the aerodynamic characteristics is possible. The prime advantage of these methods lies in the ease of ensuring a certain type of favorable flow behavior in regions known to be crucial to the overall flow quality. Most frequently, an objective is to guarantee a favorable pressure gradient over most if not all of the airfoil's surface to eliminate

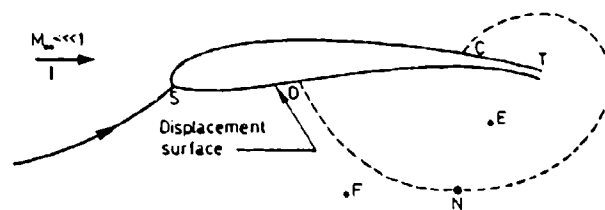
laminar and/or turbulent separation [6], shock-induced separation [7] and postpone laminar-turbulent transition [8-10]. Moreover, with the current interest in more efficient air transports and hence less drag-producing airfoil sections, it is apparent that Natural Laminar Flow (NLF) Airfoils are prime candidates for these design methods.

Unfortunately, as in most design procedures, the lack of control of the airfoil closure and geometrical regularity represents a minor draw back of such methods [3]. Therefore, it is obvious that for many practical applications, structural or aerodynamic, the most desirable design procedure is one that combines the advantages from a direct computational method with those of an inverse method. Thus, the shortcomings of each are overcome by the strengths of the other. Such methods, commonly termed "hybrid methods" have been successfully used in the design of supercritical cascades [11] and airfoils [12]. In this paper, a similar hybrid method is briefly described and utilized for the design of NLF airfoil sections. It is noteworthy that the work reported here arose in conjunction with a numerical parametric study on the effect of varying the input pressure distribution (utilized by the inverse-design algorithm IDA) at selected points (support points) on the geometry and the closure of the resulting airfoil. Of special interest to the present study is the rates at which the flow accelerates and decelerates on the suction and pressure sides of the airfoil and their consequent effect on the preservation of NLF. Though the examples shown are for low Reynolds numbers, the method has proved to be successful in the design of shock-free supercritical airfoils [7] at considerably higher Reynolds numbers.

#### INVISCID AIRFOIL DESIGN

The present inverse procedure represents an application of a numerical method which was developed earlier by the author (originally suggested by Sobieczky) for the design of shock-free transonic airfoils [5]. The inverse-design algorithm (IDA) is based on a conformal transformation of the semi-infinite, two-sheeted Riemann hodograph free-surface representation of the airfoil, Fig.(1), into the unit circle. The input to the design procedure includes a prescription of a target pressure distribution (or equivalently a Mach number distribution) and the free-stream conditions. The input Mach number distributions for three airfoils A, B and C are shown in Fig.(2) in comparison with a reference distribution which is similar to that utilized in the numerical parametric study. The reference distribution resembles that utilized by Hassan et al. [3,5] in their design method for subcritical and shock-free supercritical airfoils. In Fig.(2) the rates at which the flow accelerates from the front stagnation point and then decelerates are varied and their effect on the preservation of laminar flow is later discussed.

Utilizing the input Mach number distribution  $M_i$  and realizing that the stream function has a value of zero on the unit circle, we



Sketch of incompressible flow past a lifting airfoil in the physical plane.

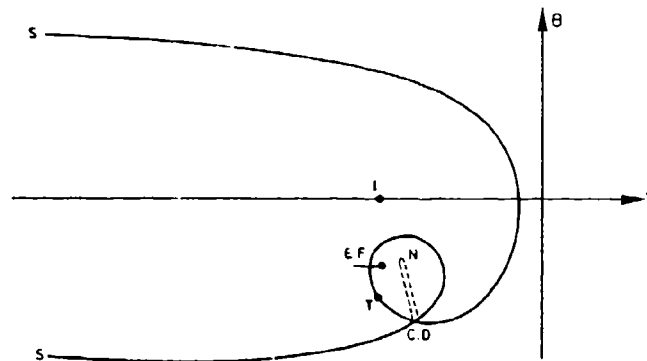


Fig. (1) Hodograph representation ( $v$ : Prandtl-Meyer function,  $\theta$ : flow deflection angle) of the inviscid flow field sketched above. stagnation point S, trailing edge T, far-field I, branch point N.  $q_E = q_F$ ,  $\theta_E = \theta_F$ .

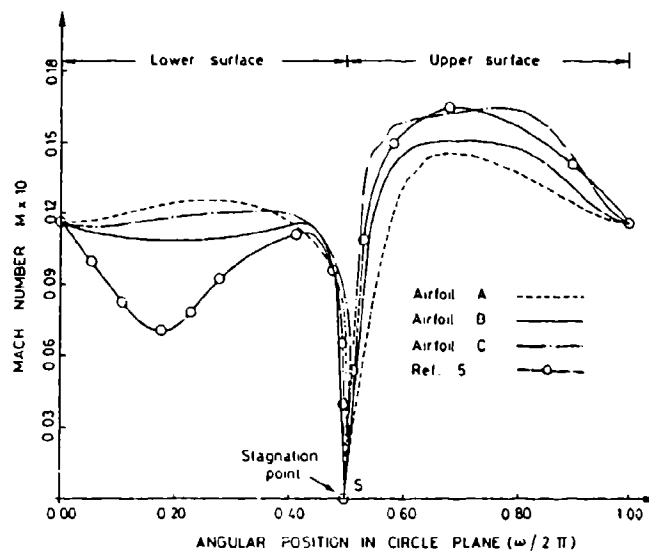


Fig. (2) Input Mach number distributions for airfoils A, B, and C with cusped trailing edges. The trailing edge position is determined as part of the solution.

proceed to solve the full stream function equation (subject to Dirichlet boundary conditions) using a second-order accurate direct solver. In the present procedure the stagnation streamline leaves the contour of the airfoil at a cusped trailing edge. In direct analysis, this defines the amount of circulation around the airfoil and the location of the stagnation point near the leading edge. For an indirect method such as the present one, the situation is exactly the reverse: since the mapped stagnation point location is arbitrary chosen [5], we have to vary the far-field circulation until the stagnation streamline reaches the surface perpendicular to the airfoil at the stagnation point  $S$ . The results obtained for the normal derivative of the stream function along the unit circle are then utilized in finding the inviscid airfoil coordinates in the physical plane. The airfoil configuration (or displacement surface) which usually has a preset trailing edge gap is then analyzed utilizing the inviscid direct procedure explained below prior to the next step where viscous effects are to be incorporated.

### INVISCID AIRFOIL ANALYSIS

The analysis of the airfoil configuration which results from the inviscid design procedure at design and off-design conditions is carried out using Jameson's [2] full potential algorithm FL06. This direct procedure utilizes a finite-difference method to solve for a reduced potential function which is introduced to circumvent the numerical singularities introduced by conformally mapping the airfoil into the unit circle. The tangency condition on the airfoil's surface is numerically implemented through a Neumann boundary condition which is prescribed on the unit circle. The direct computation of the flow results in a pressure distribution or equivalently a Mach number distribution  $M_A$  which is in turn manually compared with the desired input target Mach number distribution  $M_I$ . If the agreement is unsatisfactory, the above inverse-design procedure is repeated with a slightly modified target pressure. The inviscid inverse/direct iterative procedure is repeated until satisfactory agreement between the two pressure distributions is achieved. At this stage, the inviscid flow computations are terminated and the target pressure distribution with its corresponding airfoil configuration (or displacement surface) are utilized as input to the numerical procedure described below for calculating the development of the boundary layer.

### CORRECTION FOR BOUNDARY LAYER EFFECTS

To account for viscous effects, the basic approach is to calculate a boundary layer displacement thickness  $\delta^*$  and to use it to correct the location of the displacement surface, Fig.(3). That is, vector subtraction of the displacement thickness (derived from the solution of the boundary layer equations) from the inviscid displacement surface produces the effective airfoil configuration, viz.,

(airfoil effective ordinate + $\delta^*$ ) -	$\{\delta^*\}$	=	$n_e$
displacement surface from inviscid flow calculation	displacement thickness from boundary layer flow calculation		airfoil effective normal ordinate

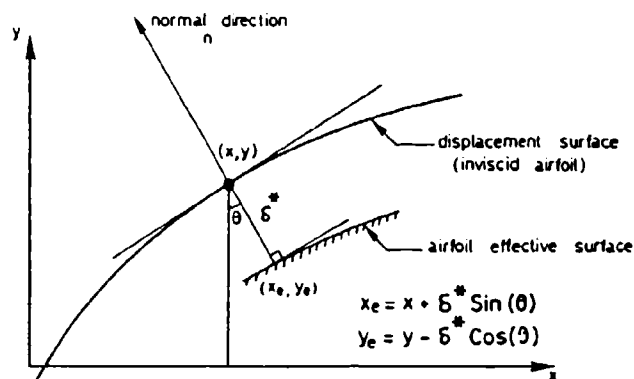


Fig. (3) Sketch illustrating the relative positions of the displacement surface and the resulting effective airfoil surface.

In the above equation, the boundary-layer-type flow computations are performed using the LTBLCEQL (Laminar and/or Turbulent Boundary Layers in Chemical Equilibrium) algorithm of Miner, Anderson and Lewis [13]. In their solution method, the laminar and turbulent boundary layer equations are expressed in Levy-Lees variables [14]. The governing equations are then cast into a general parabolic form and then solved using a Crank-Nicolson type implicit finite-difference scheme, originally employed by Blottner and Lenard [15].

At the end of execution of the potential codes IDA and FL06, transfer of pressure distribution data and geometrical data to LTBLCEQL takes place. Since the computational grids of IDA and FL06 (100 circumferential  $\times$  64 radial) are not identical to that used in LTBLCEQL (250 streamwise  $\times$  100 normal), this transfer usually requires interpolation for the pressure distribution and the geometrical data. The computations proceed by assuming laminar flow to commence from the front stagnation point where a local analytic solution is utilized. As the computations proceed, the flow is allowed to develop and change from laminar to turbulent once a local criterion based on the vorticity Reynolds number is satisfied [14]. The utilized transition model allows for a gradual laminar to turbulent transition which takes place over a finite length of the airfoil's surface. The length of the transition region is based on the criteria given by Owen [16]. If a point of laminar or turbulent separation is detected during the computations, the entire design procedure is terminated. Though for all such cases the effective airfoil was never generated, information relating to the effect of changing the Mach number distribution at selected points on the separation point location was very useful. In the absence of

separation, the displacement thickness is computed at every stream-wise station and then subtracted from the normal coordinates of the displacement surface to yield the effective airfoil coordinates  $x_e$  and  $y_e$ , Fig.(3). A manual check is then carried out to search for airfoil contour crossings (i.e., whether the resulting airfoil has a fishtail or not). Should these occur, usually in the trailing edge region, the entire inviscid-viscous design procedure is repeated with a slightly modified target pressure distribution at and near the trailing edge. This modification usually results in a larger inviscid trailing edge gap hence correcting the crossings problem when viscous effects are subsequently incorporated.

## RESULTS AND DISCUSSION

The interactive inviscid-viscous design procedure is shown in the flow chart of Fig.(4) with the location of the manual operator

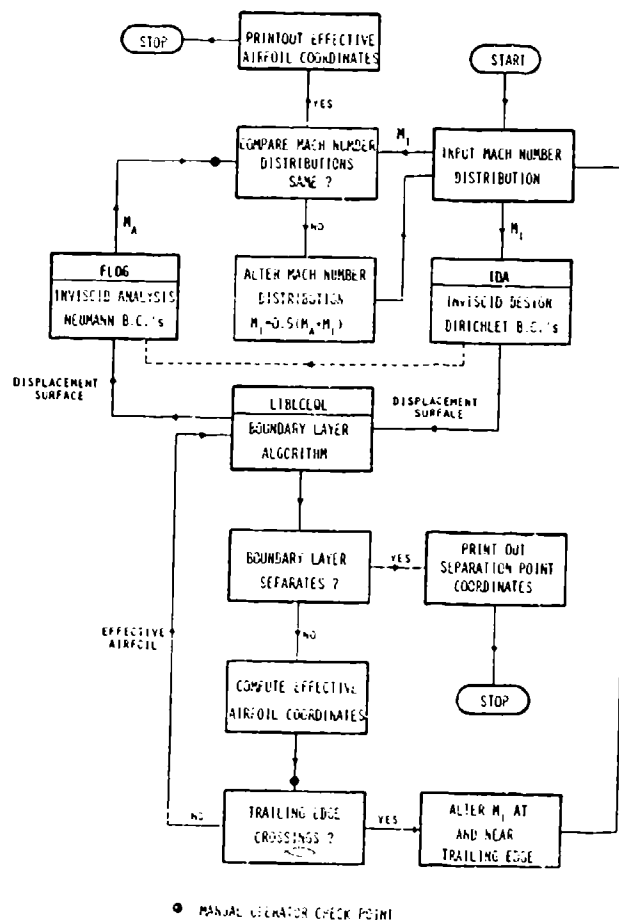


Fig. (4) Flow chart illustrating the numerical inviscid-viscous coupling procedure. The dotted line signifies inviscid iteration.

interrupt check points. The results depicted in Figs. (5,6) and (7) are intended only to demonstrate the capabilities of the present inviscid-viscous coupling procedure in the design of Natural Laminar Flow (NLF) Airfoils.

The first example (airfoil A) was an attempt to study the effect of gradually accelerating the flow on the lower surface (up to  $\omega/2\pi = 0.25$ ) Fig.(2), which then is followed by a smooth deceleration up to the trailing edge. On the upper surface, the flow is accelerated rapidly to a maximum at  $\omega/2\pi = 0.63$  and then decelerated through a shallow convex pressure distribution (notice that the distribution of Ref.[5] in Fig.(2) is slightly concave). In Fig.(5)

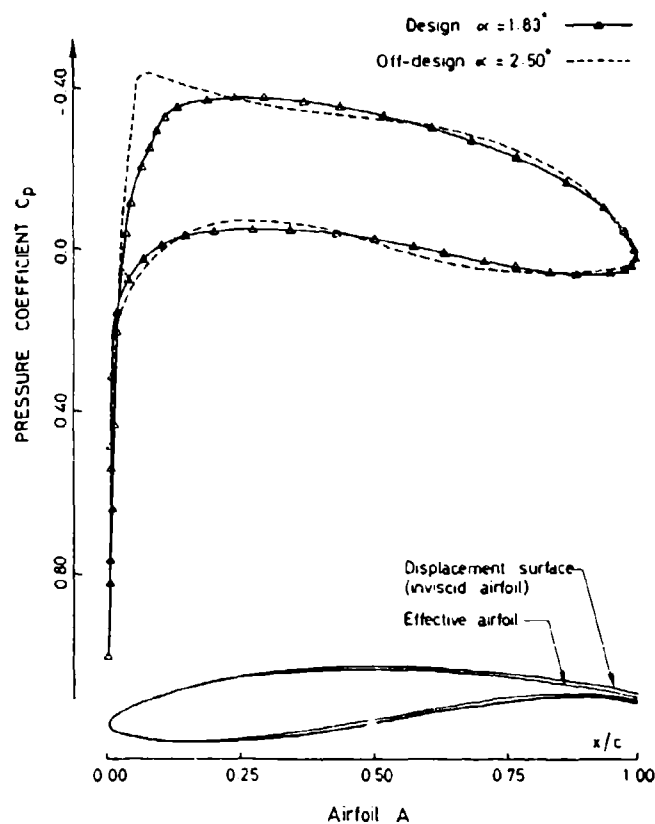


Fig. (5) Pressure distributions at design and off-design conditions and the computed inviscid and effective airfoil configurations ( $M_\infty=0.012$ ,  $Re = 2.78 \times 10^5$ ,  $C_L=0.5925$ ,  $C_D=0.0038$ ,  $x_{max}/c=0.1194$ )

the inviscid and effective airfoil configurations are shown. Analysis of the design pressure distribution indicated NLF up to  $0.39 x/c$  on the pressure side and up to  $0.25 x/c$  on the suction side. At off-design conditions ( $\alpha = 2.50^\circ$ ), these numbers are reduced to  $0.12$ , and  $0.35 x/c$  respectively.

The second example (airfoil B) corresponded to reversing the trend of the input Mach number distribution for airfoil A. That is,

on the pressure side the flow rapidly accelerates to a point of maximum Mach number at  $\omega/2\pi = 0.44$  which is followed by a shallow deceleration to a minimum Mach number at  $\omega/2\pi = 0.23$ , then accelerates again as it reaches the trailing edge. On the suction side, the rate of acceleration of the flow is higher than that for airfoil A. This acceleration portion is followed by a constant Mach number ramp which in turn is followed by a convex deceleration distribution. At design conditions, NLF is maintained up to  $0.12 x/c$  and  $0.56 x/c$  on the suction and pressure sides respectively. At off-design conditions ( $\alpha = 3.00^\circ$ ) these numbers are reduced to  $0.07 x/c$  and  $0.39 x/c$  respectively. The inviscid and effective airfoil configurations for airfoil B and the corresponding pressure distributions at design and off-design conditions are illustrated in Fig.(6)

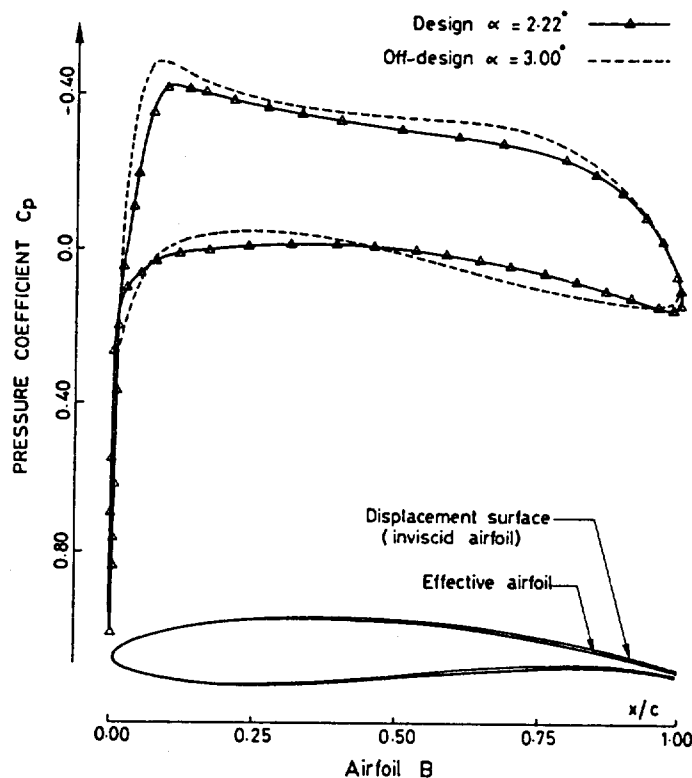


Fig. (6) Pressure distributions at design and off-design conditions and the computed inviscid and effective airfoil configurations ( $M_\infty=0.0127$ ,  $Re = 2.94 \times 10^5$ ,  $C_L=0.6811$ ,  $C_D=0.0043$ ,  $t_{max}/c = 0.1120$ )

In the light of the results obtained from analyzing airfoils A and B regarding the extent of NLF on the pressure and suction surfaces, we prescribed the Mach number distribution shown in Fig. (2) for airfoil C. Here on the lower surface, the flow is allowed to accelerate from the front stagnation point to a maximum Mach number at  $\omega/2\pi = 0.38$  where it gradually decelerates almost to the trailing edge. On the upper surface, the flow is allowed to accelerate over most of the surface until it reaches a maximum Mach number at  $\omega/2\pi = 0.8$  where this is followed by a relatively steep convex distribution. For this case, NLF was maintained up to  $0.32 x/c$  and  $0.45 x/c$

on the suction and pressure sides respectively. At off-design conditions ( $\alpha = 2.00^\circ$ ), these numbers were reduced to 0.22  $x/c$  and 0.31  $x/c$  respectively. The pressure distributions at design and off-design conditions as well as the inviscid and effective airfoil configurations for airfoil C are given in Fig. (7).

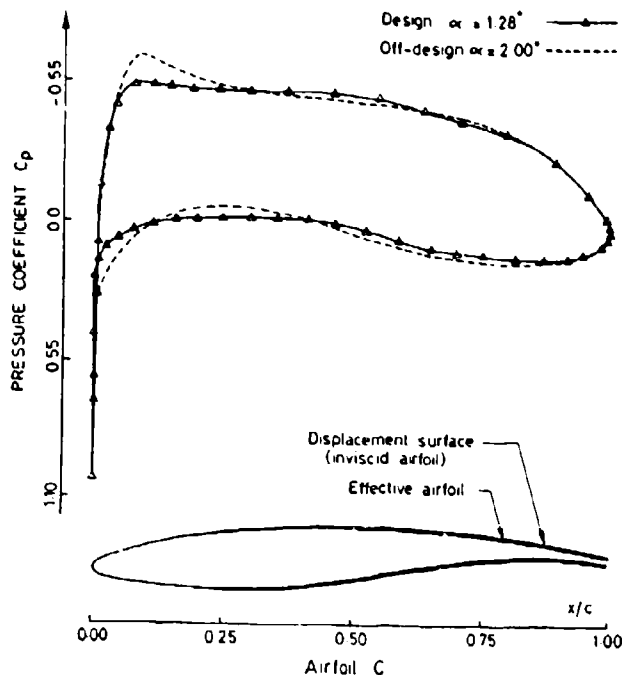


Fig. (7) Pressure distributions at design and off-design conditions and the computed inviscid and effective airfoil configurations ( $M_\infty = 0.0135$ ,  $Re = 3.13 \times 10^5$ ,  $C_L = 0.7620$ ,  $C_D = 0.0058$ ,  $c_{max}/c = 0.1044$ )

In consideration of the above results, it seems that the ideal input Mach number distribution would be one where the flow accelerates very rapidly on the lower surface and then gradually decelerates towards the trailing edge. On the upper surface, the reverse is true. Here the flow is left to accelerate over most of the upper surface and then decelerates towards the trailing edge. The implications of the hypothesized Mach number distribution are two-fold: on the one hand, at design conditions, longer runs of NLF are obtained, and on the other hand rapid acceleration from the front stagnation point usually results in an airfoil having a small leading edge radius of curvature. At off-design conditions, the analysis of such an airfoil usually indicates the presence of leading edge separation. Also on the upper surface the steeper the deceleration portion becomes, the higher is the tendency for turbulent separation to occur. It is thus apparent here that we should try to optimize the prescribed input pressure distribution

for the purpose of drag minimization through the maximization of NLF. It is hoped that the results of this study have cast more light on the nature of what constitutes a practical input Mach number distribution in the computational plane.

## CONCLUSION

An interactive viscous-inviscid numerical coupling procedure has been developed for the design of three Natural Laminar Flow (NLF) airfoils. Although it has not been possible through this study to produce a fully automated iterative coupling procedure, more work on this avenue could produce a considerable savings in computing time. The present procedure could definitely be enhanced by the addition of an optimization module with an overall design objective of viscous drag reduction and with constraints imposed on the gradients of the prescribed input pressure distribution. Moreover, the method in its present form has some limitations, most notably in its applicability to flows with boundary-layer separation. For severe flow situations, such as massive boundary layer separation which occurs at high angles of attack, a Navier-Stokes approach to model viscous effects within the numerical calculations would undoubtedly be required.

## ACKNOWLEDGEMENT

The author is indebted to Dr. Bruce J. Holmes of NASA Langley for the introduction to the field of Laminar Flow Control. The author would also like to thank Dr. F.C. Anderson of NASA Langley and Professor C.H. Lewis of the Virginia Polytechnic and State University for useful discussions on the use of the LTBCEQL Code.

## REFERENCES

1. Murman, E.M. and Cole, J.D., "Calculation of Plane Steady Transonic Flows," AIAA Journal, Vol.9, No.1, pp.114-121, 1971.
2. Jameson, A., "Iterative Solution of Transonic Flows Over Airfoils and Wings, Including Flows at Mach 1," Communications on Pure Applied Mathematics, Vol.27, pp.283-304, 1974.
3. Hassan, A.A., Seebass, A.R., and Sobieczky, H., "Transonic Airfoils With A Given Pressure Distribution," AIAA 14th Fluid and Plasma Dynamics Conference, Palo Alto, CA, AIAA Paper 81-1235, 1981.
4. Volpe, G. and Melnik, R.F., "The Role of Constraints in The Inverse Design Problem for Transonic Airfoils," AIAA 14th Fluid and Plasma Dynamics Conference, Palo Alto, CA, AIAA Paper 81-1233, 1981.
5. Hassan, A.A., Seebass, A.R., and Sobieczky, H., "Subsonic Airfoils With A Given Pressure Distribution," AIAA Journal, Vol.22, No.9, pp.1185-1191, 1984.

6. Stratford, R.S., "The Prediction of Separation of The Turbulent Boundary Layer," Journal of Fluid Mechanics, Vol.9, pp.1-16, 1959.
7. Hassan, A.A., "The Design of Shock-Free Supercritical Airfoils Including Viscous Effects," Proceedings of the International Conference on Inverse Design Concepts in Engineering Sciences (ICIDES), Austin, Texas, pp.175-191, 1984.
8. Somers, D.M., "Design and Experimental Results for A Natural - Laminar - Flow Airfoil for General Aviation Applications," NASA TP-1861, 1981.
9. Holmes, B.J., and Obara, C.J., "Observations and Implications of Natural Laminar Flow on Practical Airplane Surfaces," Journal of Aircraft, Vol.20, No.12, pp.993-1006, 1983.
10. Holmes, B.J., Obara, C.J., Gregorek, G.M., Hoffman, M.J., and Freuhler, R.J., "Flight Investigation of Natural Laminar Flow on The Bellanca Skyrocket II," SAE paper 830717, 1983.
11. Ives, D.C., "Inverse and Hybrid Compressor Cascade Design Methods," Proceedings of the International conference on Inverse Design Concepts in Engineering Sciences (ICIDES), Austin, Texas, pp. 555-572, 1984.
12. Tranen, T.L., "A Rapid Computer Aided Transonic Airfoil Design Method," AIAA Paper 74-501, 1974.
13. Miner, E.W., Anderson, E.C., and Lewis, C.H., "A Computer Program for Two-Dimensional and Axisymmetric Nonreacting Perfect Gas and Equilibrium Chemically Reacting Laminar, Transitional and/or Turbulent Boundary Layer Flows," Virginia Polytechnic Institute and State University, College of Engineering Report VPI-E 71-8, 1971.
14. Anderson, E.C. and Lewis, C.H., "Laminar or Turbulent Boundary-Layer Flows of Perfect Gases or Reacting Gas Mixtures in Chemical Equilibrium," NASA CR-1893, 1971.
15. Blottner, F.G. and Lenard, M., "Finite Rate Plasma Generation in the Laminar Air Boundary Layer of Slender Reentry bodies," Transactions of the 8th Symposium on Ballistic Missile and Space Technology, San Diego, CA, pp.3-33, 1963.
16. Owen, F.K., "Transition Experiments On A Flat Plate at Subsonic And Supersonic Speeds," AIAA Journal, Vol.8, No.3, 1970.

# EFFECT OF PRESSURE GRADIENTS ON THE GROWTH OF SUBHARMONIC DISTURBANCES IN BOUNDARY LAYERS

*Thorwald Herbert*

*Fabio P. Bertolotti*

Department of Engineering Science and Mechanics  
Virginia Polytechnic Institute and State University  
Blacksburg, Virginia 24061

## ABSTRACT

The control of the complex interaction between transition and separation in boundary layers with strong adverse pressure gradients is key to the successful design of high-performance airfoils for the range of low Reynolds numbers. We try to gain some understanding for this complex interaction by studying the cascade of primary (TS wave) and secondary instability of these flows. The analysis predicts that subharmonic modes are the most dangerous disturbances in low-noise environments. These modes can be two-dimensional and lead to vortex pairing as in free shear layers. Under different conditions, the modes can be three-dimensional with a spanwise wavelength of the order of the TS wavelength and lead to breakdown near the wall. The theoretical predictions of growth rates and disturbance velocities are verified by comparison with experimental results for the Blasius flow. The effect of pressure gradients is studied using the Falkner-Skan family of profiles. The issue of spatial vs. temporal growth in a streamwise varying flow is discussed. The conditions for occurrence of the two-dimensional or three-dimensional form of subharmonic disturbances are outlined, and related to results for the free shear layer. Finally, we discuss criteria for the take-over of subharmonic disturbances and the application of the theory to the flow over an airfoil.

## INTRODUCTION

In high-Reynolds-number aerodynamics, the effect of transition is mainly a quantitative change in drag. At low Reynolds number, however, and in combination with the separating shear layers in strong adverse pressure gradients, the occurrence, location, and nature of transition are crucial for the performance of the airfoil and may jeopardize successful operation of an RPV.

From an initially attached flow over a wing at a high angle of attack, at least three phenomena may develop:

- The flow undergoes transition early enough to allow the turbulent boundary layer, with its greater momentum near the wall, to remain attached through most of the region of adverse pressure gradient.

- If transition is delayed, the flow separates in a laminar state and develops a free shear layer. Further downstream, transition occurs and the turbulent flow reattaches to the surface, enclosing a separation bubble.
- If transition in the separating free shear layer occurs too far downstream and too far away from the wall, the flow permanently leaves the surface, causing violent stall over the wing.

An analysis of the primary (TS wave) instability, in conjunction with some  $e^n$  criterion is insufficient to predict occurrence and structure of the transitional flow. Such an analysis cannot account for the peculiarities of the disturbance background, nor can it decide whether instability of the separating shear layer will occur in the form of basically two-dimensional waves with subsequent two-dimensional pairing, or will lead to three-dimensional phenomena that activate strong vortex stretching and cause breakdown into wall-bound turbulence. In the later stages of transition, the structure of the boundary layer flow is governed by secondary and higher instabilities. Therefore, understanding the nature of the instabilities after the TS waves reach finite amplitude seems to be key to understanding the separation bubble.

The analysis of secondary instability rests on Floquet systems of linear stability equations. The periodic coefficients in these equations are provided by finite-amplitude TS waves. Primary and principal parametric resonance yield fundamental (peak-valley splitting) and subharmonic disturbances, respectively, with the latter disturbances being "most dangerous" in low-noise environments. The theory has been developed for nonlinear equilibrium states in plane Poiseuille flow [1] and extended to other flows by use of simplifying assumptions. Results of the simplified theory for the Blasius boundary layer are in good agreement with experimental data [2-4]. Disturbance velocities as well as the local growth rates are correctly predicted. Since secondary disturbances grow on a fast convective time scale, their occurrence is closely related to breakdown and transition. It seems possible, therefore, to design a new class of methods for predicting the location and type of transition in a given disturbance environment. Our efforts are directed towards the development of such methods.

The theory of secondary instability [1-4] uses the temporal growth concept. Application to boundary-layer flows other than the Blasius profile is primarily a matter of proper numerical treatment, and of finding orientation in the multidimensional parameter space. For this purpose, we have chosen the Falkner-Skan family of profiles, which can be easily replaced by the local velocity distributions over an airfoil. From the analysis of primary instability, it is known that the concept of spatial growth is more natural to be used with streamwise varying flows. We have, therefore, implemented the spatial growth concept into the analysis of secondary instability. In the following, we describe the development of this theory, a first set of results for boundary layers in adverse pressure gradients, and some hurdles still to be overcome on the way to a more sophisticated transition prediction.

### GOVERNING EQUATIONS FOR SECONDARY INSTABILITY

The following derivation is confined to steady, incompressible, constant temperature shear-layer flows having a weak variation in the streamwise coordinate. The analysis is divided into two parts: the construction of the periodic basic flow and the investigation of superposed secondary disturbances with amplitudes sufficiently small for linearization.

### Construction of the Periodic Basic Flow

We consider the flow over a semi-infinite plate at an angle  $P\pi/2$  to the free stream. Let  $X$  denote the distance from the leading edge along the plate,  $Y$  the distance normal to the plate, and  $Z = z$  the spanwise direction,  $U_*$  the inviscid flow velocity at the surface, and  $X_0$  the location at which the stability analysis is performed. The undisturbed boundary layer stream function is given by

$$\Psi_{FS}(X, Y, t) = U_* f(y) \delta, \quad \delta = \left[ (2-P) \frac{\nu x}{U_*} \right]^{\frac{1}{2}}, \quad y = \frac{Y}{\delta} \quad (1)$$

where  $f(y)$  satisfies the Falkner-Skan equation

$$f''' + ff'' + P(1-f'^2) = 0 \quad (2)$$

$$f(0) = f'(0) = 0, \quad f'(y \rightarrow \infty) = 1 \quad (3)$$

Due to the weak variation of the Falkner-Skan profile with  $X$ , we apply the parallel-flow approximation and assume the profile to be locally one-dimensional,  $V_o(y, X_0)$ . We use  $\delta$  and  $U_*$  as characteristic quantities for nondimensionalization, and define the Reynolds number by  $R = U_* \delta / \nu$ . At sufficiently high  $R$ , primary disturbances appear in the form of TS waves with the stream function given by

$$\psi_1 = A(X) [\phi(y) e^{i\alpha_r(X-ct)} + \phi^\dagger(y) e^{-i\alpha_r(X-ct)}] \quad (4)$$

The  $\dagger$  denotes the complex conjugate,  $\alpha = \alpha_r + i\alpha_i$  and  $\phi(y)$  are solutions to the Orr-Sommerfeld eigenvalue problem,  $\alpha_r$  is the streamwise wavenumber,  $\alpha_i$  is the growth rate, and  $c$  is the phase velocity. The variation of the amplitude is given by

$$A(X) = A_{in} \exp\left(-\int_{X_{in}}^X \alpha_i dX\right) \quad (5)$$

where  $A_{in}$  is the TS amplitude at an initial location  $X_{in}$ . In presence of a TS wave of finite amplitude, the two-dimensional flow has the form

$$\mathbf{v}_2(X, y, t) = \mathbf{V}_o(y) + A(X) \mathbf{v}_1(X-ct, y) \quad (6)$$

The eigenfunction  $\phi(y)$  in (4) is normalized such that  $A$  measures the streamwise rms fluctuation of the disturbance. We neglect the nonlinear distortion of the wave under the shape assumption [3], and also neglect the weak variation of the TS amplitude in comparison with the explosive growth of secondary disturbances, thus considering locally  $A_0 = A(X_0)$ . These approximations have been justified by numerical experiments and physical arguments. The time dependence is eliminated by changing from a fixed coordinate system to a coordinate system moving with the phase velocity of the TS wave,  $x = X - ct$ , and the flow becomes periodic in the moving streamwise coordinate  $x$ ,

$$\tilde{\mathbf{v}}_2(x, y) = \mathbf{V}_o(y) + A_0 \tilde{\mathbf{v}}_1(x, y) \quad (7)$$

Here, and elsewhere, the  $\sim$  symbolizes the periodicity of the function.

Fig. 1 illustrates the above steps. In a neighborhood of  $X_0$  both the Falkner-Skan profile and the TS wave amplitude are assumed constant, thus extending the periodic flow from  $-\infty$  to  $\infty$ . A detailed study of temporally and spatially growing TS waves for Falkner-Skan profiles has been presented by Wazzan et al. [5]. The

periodic basic flow (7) can be considered as known from any standard procedure for analysis of TS waves.

### Secondary Disturbances. Linear model.

We study the evolution of secondary disturbances through a linear stability analysis of the periodic basic flow (7). A small secondary disturbance  $\mathbf{v}_3 = (u_3, v_3, w_3)$  is superimposed on the basic flow,

$$\mathbf{v}(x, y, z, t) = \tilde{\mathbf{v}}_2(x, y) + \epsilon \mathbf{v}_3(x, y, z, t), \quad \epsilon \ll 1 \quad (8)$$

and the compound flow is inserted into the Navier-Stokes equations. The nonlinear convective term  $\epsilon^2 (\mathbf{v}_3 \cdot \nabla) \mathbf{v}_3$  is dropped in view of the small disturbance amplitude, yielding linear equations for  $\mathbf{v}_3$ ,

$$\frac{\partial}{\partial t} \mathbf{v}_3 + (\tilde{\mathbf{v}}_2 \cdot \nabla) \mathbf{v}_3 + (\mathbf{v}_3 \cdot \nabla) \tilde{\mathbf{v}}_2 = -\nabla p_3 + \frac{1}{R} \nabla^2 \mathbf{v}_3 \quad (9a)$$

$$\nabla \cdot \mathbf{v}_3 = 0 \quad (9b)$$

subject to the boundary conditions  $\mathbf{v}_3(x, 0, z, t) = 0$ ,  $\mathbf{v}_3(x, y \rightarrow \infty, z, t) = 0$ . The linear secondary stability problem, hence, is an eigenvalue problem. Taking the curl of (9a) for eliminating the pressure, introducing  $\zeta_1 = -\nabla^2 \psi_1$  and the disturbance vorticity  $\omega_3 = (\xi_3, \eta_3, \zeta_3)$ , and using continuity to eliminate the  $z$ -component of velocity  $w_3$ , we obtain a system of linear differential equations for  $u_3$  and  $v_3$ ,

$$\begin{aligned} & \left( \frac{1}{R} \nabla^2 - (U_0 - c) \frac{\partial}{\partial x} - \frac{\partial}{\partial t} \right) \nabla^2 v_3 + \frac{d^2 U_0}{dy^2} \frac{\partial v_3}{\partial x} + \\ & A \left[ \left( \frac{\partial \psi_1}{\partial x} \frac{\partial}{\partial y} - \frac{\partial \psi_1}{\partial y} \frac{\partial}{\partial x} \right) \nabla^2 v_3 + \frac{\partial^2 \psi_1}{\partial x^2} \left( \frac{\partial \zeta_3}{\partial y} + \frac{\partial \eta_3}{\partial z} \right) - \frac{\partial^2 \psi_1}{\partial x \partial y} \left( \frac{\partial \zeta_3}{\partial x} + \frac{\partial \xi_3}{\partial z} \right) - \right. \\ & \left. \frac{\partial \zeta_1}{\partial x} \left( 2 \frac{\partial u_3}{\partial x} + \frac{\partial v_3}{\partial y} \right) - \frac{\partial \zeta_1}{\partial y} \frac{\partial v_3}{\partial x} - \left( u_3 \frac{\partial}{\partial x} + v_3 \frac{\partial}{\partial y} \right) \frac{\partial \zeta_1}{\partial x} \right] = 0 \quad (10a) \end{aligned}$$

$$\begin{aligned} & \left( \frac{1}{R} \nabla^2 - (U_0 - c) \frac{\partial}{\partial x} - \frac{\partial}{\partial t} \right) \frac{\partial \eta_3}{\partial z} - \frac{dU_0}{dy} \frac{\partial^2 v_3}{\partial z^2} + A \left[ - \frac{\partial^2 \psi_1}{\partial y^2} \frac{\partial^2 v_3}{\partial z^2} + \right. \\ & \left. \left( \frac{\partial \psi_1}{\partial x} \frac{\partial}{\partial y} - \frac{\partial \psi_1}{\partial y} \frac{\partial}{\partial x} - \frac{\partial^2 \psi_1}{\partial x \partial y} \right) \frac{\partial \eta_3}{\partial z} + \frac{\partial^2 \psi_1}{\partial x^2} \left( \frac{\partial^2 u_3}{\partial x \partial y} + \frac{\partial^2 v_3}{\partial y^2} \right) \right] = 0 \quad (10b) \end{aligned}$$

Note that  $\partial \eta_3 / \partial z$  and  $\partial \xi_3 / \partial z$  are expressible in terms of  $u_3$  and  $v_3$ . These equations have three important features: linearity, coefficients independent of time and spanwise coordinate  $z$ , and coefficients periodic in  $x$  due to the presence of  $\tilde{\mathbf{v}}_1$ . The first two allow the use of normal modes in  $t$  and  $z$ ,

$$\mathbf{v}_3(x, y, z, t) = e^{i\beta z} e^{\sigma t} \hat{\mathbf{v}}_3(x, y) \quad (11)$$

where the spanwise wavenumber  $\beta$  is real, and  $\sigma$  is in general complex. The third feature provides the form of the solution according to Floquet theory. Apart from the  $y$  dependence, the secondary disturbance equations are essentially of Hill type

in  $x$ , and can be written in a form with real coefficients. Letting  $\gamma$  denote the characteristic exponent, and  $\lambda_x = 2\pi/\alpha$ , the TS wavelength, we find two classes of solutions  $\hat{v}_3$  in the form

$$\hat{v}_3(x, y) = e^{\gamma x} \tilde{v}_f(x, y) \quad \tilde{v}_f(x + \lambda_x, y) = \tilde{v}_f(x, y) \quad (12a)$$

$$\hat{v}_3(x, y) = e^{\gamma x} \tilde{v}_s(x, y) \quad \tilde{v}_s(x + 2\lambda_x, y) = \tilde{v}_s(x, y) \quad (12b)$$

where we denote  $\tilde{v}_f(x, y)$  as the "fundamental" mode, and  $\tilde{v}_s(x, y)$  as the "subharmonic" mode. Being periodic, we represent  $\tilde{v}_f$  and  $\tilde{v}_s$  by Fourier series,

$$\tilde{v}_f(x, y) = \sum_{n=-\infty}^{\infty} \bar{v}_{2n}(y) e^{i2n\hat{\alpha}x} \quad \hat{\alpha} = \alpha/2 \quad (13a)$$

$$\tilde{v}_s(x, y) = \sum_{n=-\infty}^{\infty} \bar{v}_{2n+1}(y) e^{i(2n+1)\hat{\alpha}x} \quad (13b)$$

and combine the series to obtain the final form of the secondary disturbances

$$v_3(x, y, z, t) = e^{i\beta z} e^{\sigma t} e^{\gamma x} \sum_{n=-\infty}^{\infty} \bar{v}_n(y) e^{in\hat{\alpha}x} \quad (14)$$

These solutions reproduce the experimentally observed behavior of three-dimensional disturbances [1,3]. The fundamental mode produces the  $\lambda_x$ -periodic "in-line" or peak-valley splitting pattern as observed by Saric & Thomas [6, Fig. 1]. The aperiodic term  $\bar{v}_0(y)$  in the series (13a) gives rise to both a mean flow distortion and a spanwise periodic longitudinal vortex structure. The subharmonic mode produces the  $2\lambda_x$ -periodic staggered structure [6, Fig. 2, 3] and has no aperiodic term in the series (13b). Both the fundamental and subharmonic modes can undergo exponential growth in time or space, consistent with experience from numerical simulations and experiments.

The basic flow (7) and secondary disturbance (14) are introduced into the equations (10) and the terms multiplied by exponentials of like index are collected and set equal to zero. Two uncoupled infinite sets of equations result for the fundamental components  $\bar{v}_{2n}(y)$  and subharmonic components  $\bar{v}_{2n+1}(y)$ .

### SPATIAL AND TEMPORAL GROWTH IN A MOVING FRAME

Owing to the occurrence of two generally complex quantities  $\sigma$  and  $\gamma$  in eq. (14), we are faced with a similar ambiguity as known from the Orr-Sommerfeld problem: we can choose between the concepts of temporal or spatial growth. Temporal growth analysis is simpler and requires less computational effort since  $\sigma$  appears linearly in the equations, while  $\gamma$  appears up to fourth power. Moreover, a relation exists between the two types of growth, and can be utilized to approximately transform temporal into spatial growth rates.

For primary disturbances, spatial growth is measured with respect to the laboratory frame of coordinates. In order to arrive at a consistent formulation of temporal and spatial amplification for secondary modes, we express the velocity field (14) in laboratory coordinates,

$$v_3(X, y, z, t) = e^{i\beta z} e^{(\sigma - \gamma c)t} e^{\gamma X} \sum_{n=-\infty}^{\infty} \bar{v}_n(y) e^{in\hat{\alpha}(X - ct)} \quad (15)$$

To restrict the disturbance exclusively to temporal amplification we set the "spatial" exponent  $\gamma$  to zero and solve for the "temporal" exponent  $\sigma$  as an eigenvalue. The real part of  $\sigma$  dictates growth and decay in both coordinate systems, hence the moving and the laboratory fixed observer witness the same temporal growth. For purely real  $\sigma$ , the mode is fixed in the  $(x, y, z, t)$  frame and, hence, tuned with the TS wave. For complex  $\sigma$ , the mode propagates upstream or downstream in the moving coordinate system, and thus travels with a phase speed different from that of the TS wave. Calculations have shown that at realistic amplitudes the dominant, i. e. most unstable, mode is associated with a real eigenvalue.

A spatially amplified disturbance in the moving coordinate system can be computed by setting  $\sigma$  equal to zero and solving for  $\gamma$  as an eigenvalue. To a laboratory fixed observer, however, this disturbance mode exhibits mixed spatial-temporal amplification, since in (15) both  $\sigma$  and  $\gamma$  are multiplied by time.

The two cases of most interest are those of either temporal or spatial amplification in laboratory coordinates. Indeed, experimental observation shows that in boundary layers the growth of primary and secondary disturbances is only spatial.

In order to obtain disturbance modes with purely spatial amplification in the laboratory frame, we note from (15) that the time-dependent factor  $e^{(\sigma - \gamma c)t}$  can be suppressed by choosing  $\sigma = \gamma c$ . In the moving frame, we therefore search for solutions of the form

$$\mathbf{v}_3(x, y, z, t) = e^{i\beta z} e^{\gamma ct} e^{\gamma x} \sum_{n=-\infty}^{\infty} \bar{\mathbf{v}}_n(y) e^{in\alpha x} \quad (16)$$

and solve for  $\gamma$  as the eigenvalue. (Recall that computations must be carried out in the moving coordinate system for only there is the Floquet theory applicable.) All information on spatially growing modes in this report is calculated using this approach.

## RESULTS AND COMPARISON WITH EXPERIMENTS

We have studied fundamental and subharmonic modes using both the temporal and spatial growth concept. The lowest Fourier truncation [3] has been used, and a spectral collocation method applied for numerical solution. While fundamental instability (peak-valley splitting) is a typical threshold phenomenon that occurs only above a certain level of the TS amplitude, subharmonic instability can appear at arbitrarily small amplitudes due to Craik resonance. Therefore, subharmonic instability is likely to be the preferred route to transition in low-disturbance environments such as in free flight. In the following, we consequently focus our attention on subharmonic modes.

Previous results for the Blasius profile [2-4] were obtained with the temporal growth concept and converted to spatial growth rates by using the transformation  $\gamma_r = \sigma_r/c$ . While justified at sufficiently small  $\sigma_r$ , this transformation may be questionable at the large growth rates of the dominant secondary mode. In Fig. 2 we compare results for spatial growth rates obtained from both concepts. The transformation of temporal data provides a surprisingly good approximation, and slightly overpredicts the spatial growth rates. The parameter  $b = 10^3 \beta/R$  describes a wave of fixed physical spanwise wavenumber as it travels downstream.

Fig. 3 juxtaposes experimental [7] and theoretical results for the spatial amplitude growth of TS wave and subharmonic mode for the Blasius profile. The initial TS amplitude is  $A_{in} = 0.44\%$  at branch I, ( $R_I = 535$ ) and grows to  $1.23\%$  at branch II ( $R_{II} = 855$ ). A virtual leading-edge correction of 20 cm has been applied to the experimental data in order to bring the experimental  $R_{II} = 840$  into agreement with the theoretical value, 855.

The initial subharmonic amplitude was chosen at  $B_{in} = 0.00126\%$  in order to match the experimental value of  $B$  at  $R_{II}$ . For data points at  $R > 700$  the computed growth rate closely follows the observed slope, confirming the parametric nature of subharmonic instability in the initial stages of growth. The measurements at  $R < 700$  were taken shortly downstream of the vibrating ribbon ( $R = 575$ ) where neither the TS wave nor the subharmonic mode are fully established. Fig. 4 shows the selectivity of the subharmonic instability mechanism with respect to  $b$  at  $R = 700$  and 853. Based on the maximum spatial growth rate, the theory predicts  $b = 0.27$  at  $R = 700$  and  $b = 0.29$  at  $R = 855$ . However, natural selection of  $b$  in experiments also depends on the spectral content of the background noise. The observed value of  $b = 0.33$  is close to maximum amplification throughout the range of measurement.

The destabilizing effect of an adverse pressure gradient on the dominant subharmonic mode is shown in Fig. 5. A decrease in the pressure coefficient increases the growth rate as well as the range of unstable spanwise wavenumbers. A likely consequence of this effect is the amplification of a relatively narrow band of spanwise wavenumbers in regions of favorable pressure gradients, which sets the stage for the downstream development. Most surprising in Fig. 5 is the sharp cutoff at  $\beta \approx 0.05$  for the inflectional profiles, indicating strong damping of the vortex pairing mode at a TS amplitude of  $1\%$ . Detuned modes ( $\sigma$  complex) are less amplified than the dominant mode in all profiles and at all values of TS amplitude we have investigated.

While the adverse pressure gradient enhances the growth rates of both the TS wave and the subharmonic disturbance, there is only a moderate effect on qualitative features. Dramatic changes occur, however, in the eigenfunctions, i. e. in the disturbance velocity profiles. A comparison of mean and streamwise rms profiles is given in Fig. 6 for the Blasius profile,  $P = 0$ , and in Fig. 7 for the Falkner-Skan profile near separation,  $P = -0.18$ . Fig. 6 shows the agreement of the spatial result for the subharmonic mode with the experimental data [7]. Comparison with [2, Fig. 14] also indicates that spatial and temporal results for the velocity profiles are hardly distinguishable. The position of the maxima with respect to the critical layer at  $y_c$  (for the TS wave below, and for the subharmonic mode above  $y_c$ ) is qualitatively unaffected by the pressure gradient. However,  $y_c$  in Fig. 7 is further away from the wall. A second maximum develops in the TS profile owing to the gradual changeover from viscous to vortical (inviscid inflectional) instability. Experimental data on disturbance velocities are scarce. At the present, we can only say that our results are not inconsistent with measurements [8, Fig. 14] in the separating flow over an airfoil.

#### COMPARISON OF WALL-BOUND AND FREE SHEAR LAYERS

Boundary layer profiles near the point of separation exhibit high inflectionality and maximum shear stress far from the wall, thus bearing resemblance to a free

shear layer. This observation leads one to enquire under which conditions the two types of flow share stability characteristics. In the light of separation and reattachment we place particular attention on the preferred spanwise wavelength of subharmonic modes, in other words, on the two-dimensional or three-dimensional nature of secondary disturbances.

The inviscid stability of a spatially periodic free-shear layer has been studied numerically by Pierrehumbert & Widnall [9]. They found the layer to be most unstable with respect to a two-dimensional ( $\beta = 0$ ) subharmonic mode, and the growth rate monotonically decreasing with increasing  $\beta$  [9, Fig. 5]. The disturbances undergo pure exponential growth, and are tuned ( $\sigma$  real).

Growth rates for the pairing mode and a three-dimensional subharmonic mode in the Falkner-Skan profile at separation are shown in Fig. 8 as a function of the TS amplitude. Under these conditions, three-dimensional secondary instability is dominant up to TS amplitudes of 18%. At low amplitudes, the vorticity concentrations generated by the TS wave are too feeble to overcome the damping effect of the wall on the pairing mode. Vortex pairing takes the lead at very large amplitudes of the primary disturbance, but still competes with three-dimensional phenomena. This is more clearly shown by the growth rates as a function of the spanwise wavenumber  $b$  in Fig. 9. Note the similarity of the curve for  $A = 30\%$  with the result in [9, Fig. 5] for amplitudes in the same range.

Our results show that the damping presence of the wall can be overcome by increasing the TS amplitude and, hence, the vorticity concentration near the critical layer. This process is accompanied by a changeover to a basically inviscid vortical mechanism. The large amplitudes required for the pairing mode to dominate can hardly be reached by viscous growth. Moreover, strong three-dimensional instability would appear below these levels. Amplitudes in the range of 20% have been observed, however, in the shear layer separating from an airfoil [8].

### DISCUSSION AND CONCLUSIONS

The development of the theory for spatially growing disturbances and the application to highly inflectional boundary-layer profiles has extended the scope of the secondary stability analysis. By use of different transformations, the spectral collocation method has been adapted to a wide class of profiles that covers the flow over an airfoil. Comparison of spatial and temporal results for growth rates and velocity distributions justifies the use of either one of these concepts. While the temporal analysis is computationally more efficient, the spatial analysis is clearly superior for generating results at given frequency, e.g for comparison with experiments.

Growth rates for subharmonic and fundamental modes of secondary instability have been studied in a wide range of the parameters  $R$ ,  $\alpha$ ,  $A$ ,  $\beta$ , and  $P$ . Detailed results will be reported elsewhere. These results emphasize the dominant role of subharmonic modes at low TS amplitudes. Preliminary results also indicate that the evolution of the unstable flow in a favorable, but decreasing pressure gradient selects a relatively narrow band of spanwise wavenumbers for secondary instability. Whenever TS instability occurs sufficiently far upstream in order to provide significant amplitudes ( $>1\%$ , say) at the point of separation, strongly amplified three-dimensional disturbances are likely to cause breakdown into wall-bound turbulence, and reattachment of the flow. This conclusion is consistent with

experiments [8]. A stronger statement requires not only the stability analysis of profiles downstream from separation, but also criteria for the onset of self-sustained growth of secondary disturbances. Two-dimensional vortex pairing is found to require very large TS amplitudes. These amplitudes can only develop from strong inviscid growth and in absence of competing three-dimensional disturbances. These conditions can only be met in a separating shear layer sufficiently far from the wall.

In order to develop a more detailed map of dangerous modes and improved criteria for the occurrence of three-dimensional secondary modes, we currently attempt the stability analysis of the flow over an FX-63-137 airfoil. The two-dimensional steady flow over the airfoil is computed using the code NSE-2D kindly provided by N. L. Sankar. Although the results on global characteristics such as  $C_L$  and  $C_D$  are correctly calculated, the local velocity profiles do not meet the requirements of the stability analysis. The high resolution for the boundary-layer flow will be achieved by a new version of the code using double precision (64 bit) arithmetic.

Another field of activity is the development of theoretical criteria for the onset of self-sustained growth of secondary disturbances. Secondary instability does not necessarily lead to transition, as shown by Kachanov & Levchenko [7, Fig. 2]. Once the secondary mode reaches sufficiently large amplitude, however, the nonlinear interaction with the TS wave and the distortion of the mean flow lead to continuous growth disregarding the parametric origin of the secondary disturbance. Calculation of the critical amplitude level is outside the scope of the present theory. Empirical data are unavailable. Therefore, we aim at extending the theory for the analysis of nonlinear interactions between primary and secondary disturbances. This analysis will also reveal the mechanism of self-sustained growth.

#### ACKNOWLEDGEMENT

This work is supported by the Office of Naval Research under Contract N0014-84-K-0093

#### REFERENCES

- [1] Herbert, Th., "Modes of secondary instability in plane Poiseuille flow," in: Tatsumi, T. (ed.) *Turbulence and Chaotic Phenomena in Fluids*, Amsterdam: North-Holland, pp. 53-58 (1984).
- [2] Herbert, Th., "Analysis of the subharmonic route to transition in boundary layers," AIAA Paper No. 84-0009, 1984.
- [3] Herbert, Th., "Secondary instability of plane shear flows - theory and application," in: Kozlov, V. V. (ed.) *Laminar-Turbulent Transition*, Berlin: Springer-Verlag, to appear (1985).
- [4] Herbert, Th., "Three-dimensional phenomena in the transitional flat-plate boundary layer," AIAA Paper No. 85-0489, 1985.
- [5] Wazzan, A. R., Okamura, T. T. & Smith, A. M. O., "Spatial and temporal stability charts for the Falkner-Skan boundary layer profiles," Douglas Aircraft Co., Report No. DAC-67086, 1968.

- [6] Saric, W. S. & Thomas, A. S. W. "Experiments on the subharmonic route to transition in boundary layers," in: Tatsumi, T. (ed.) *Turbulence and Chaotic Phenomena in Fluids*, North-Holland, Amsterdam, pp. 117-122 (1984)
- [7] Kachanov, Yu. S. & Levchenko, V. Ya., "The resonant interaction of disturbances at laminar-turbulent transition in a boundary layer," *J. Fluid Mech.*, **138**, pp. 209-247, 1984.
- [8] Kozlov, V. V., "The interconnection of flow separation and stability," in: Kozlov, V. V. (ed.) *Laminar-Turbulent Transition*, Berlin: Springer-Verlag, to appear (1985).
- [9] Pierrehumbert, R. T. & Widnall, S. E., "The two- and three-dimensional instabilities of a spatially periodic shear layer," *J. Fluid Mech.*, **114**, pp. 59-82, 1982.

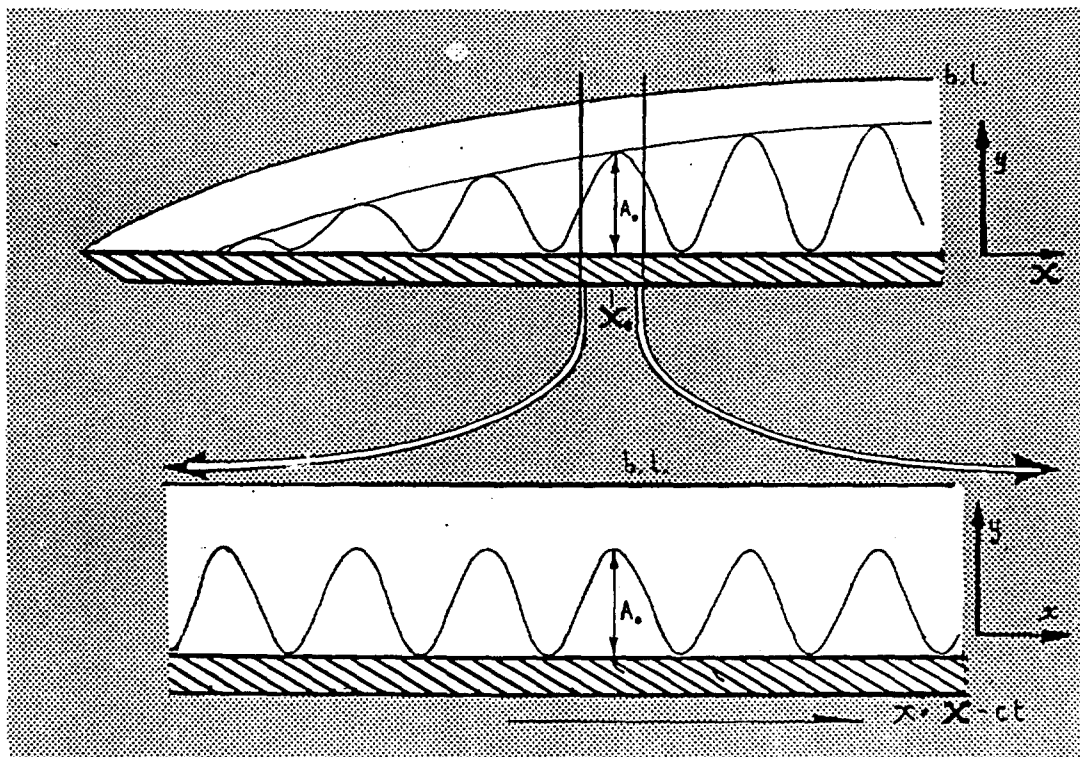


Figure 1. Construction of the periodic basic flow. The weak streamwise variation of boundary-layer thickness and TS wave amplitude are neglected. The local conditions at  $X_0$  are extended into a periodic flow.

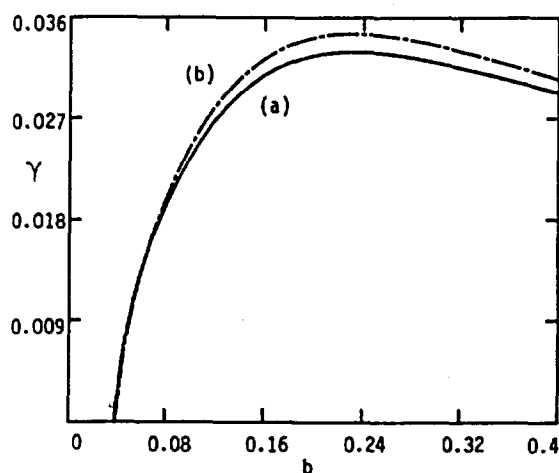


Figure 2. Spatial growth rate  $\gamma$  versus spanwise wavenumber  $b$  obtained (a) by direct calculation and (b) by transformation of temporal growth rates.  $R = 1168$ ,  $F = 83$ ,  $A = 1\%$ ,  $P = 0$ . ( $F = 10^6 \alpha_{r,c}/R$ ).

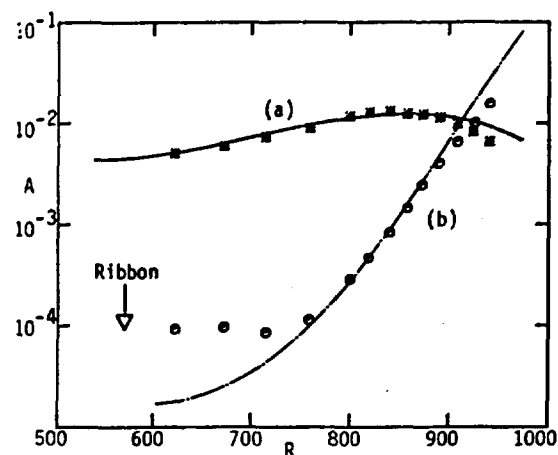


Figure 3. Theoretical and experimental [7] amplitude variation with  $R$  for (a) the TS wave ( $A_{in} = 0.44\%$ ) and (b) the subharmonic mode ( $B_{in} = 0.00126\%$ ).  $F = 124$ ,  $b = 0.33$ ,  $P = 0$ .

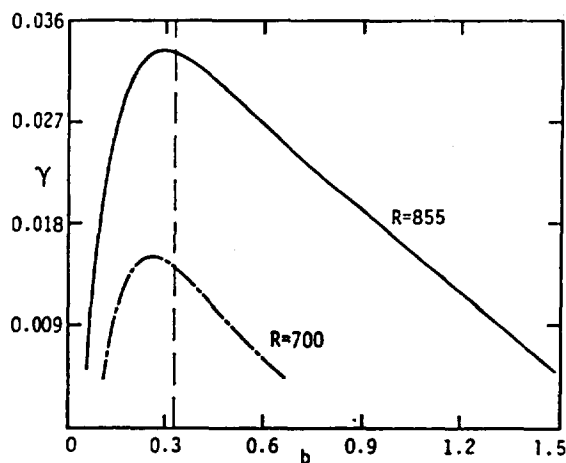


Figure 4. Spatial growth rate  $\gamma$  versus spanwise wavenumber  $b$  for the conditions of Fig. 3. The TS amplitudes are  $A = 0.74\%$  at  $R = 700$ ,  $A = 1.23\%$  at  $R = 855$ . The vertical line marks the observed wavenumber  $b = 0.33$ .

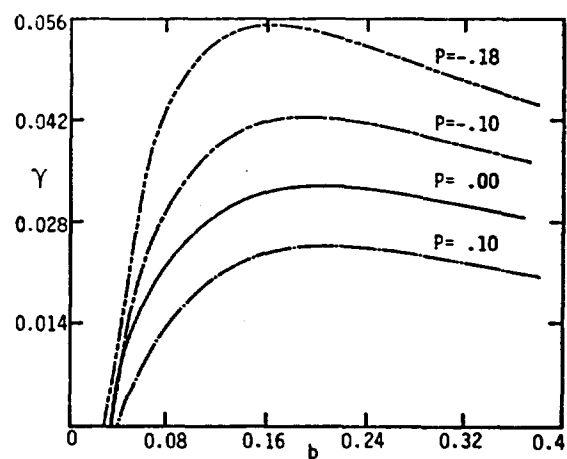


Figure 5. Spatial growth rate  $\gamma$  versus spanwise wavenumber  $b$  for various values of the pressure coefficient  $P$ .  $R = 1168$ ,  $F = 83$ ,  $A = 1\%$ .

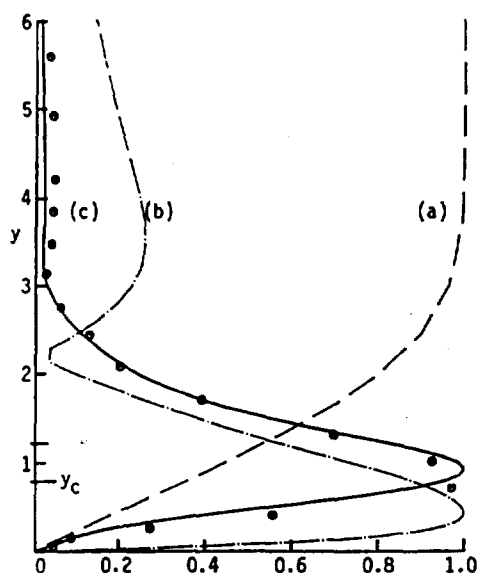


Figure 6. Blasius profile (a), and streamwise rms fluctuations for the TS wave (b) and the subharmonic mode (c) for  $R = 873$ ,  $b = 0.33$ ,  $F = 124$ ,  $A = 1.22\%$ . Experimental points from [7, Fig 21].

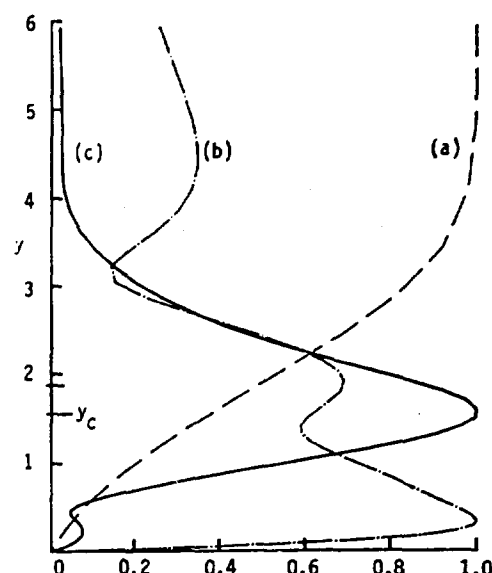


Figure 7. Falkner-Skan profile near separation (a), and streamwise rms fluctuations for the TS wave (b) and the subharmonic mode (c) for  $P = -0.18$ ,  $R = 873$ ,  $b = 0.33$ ,  $F = 124$ ,  $A = 1.22\%$ .

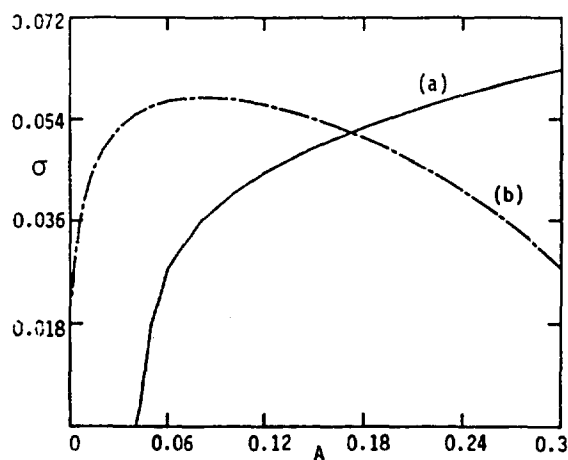


Figure 8. Temporal growth rate  $\sigma$  versus TS amplitude  $A$  for tuned modes with  $b = 0$  (a) and  $b = 0.36$  (b).  $P = -.198$ ,  $R = 1000$ ,  $\alpha = 0.5$ ,  $F = 245$ .

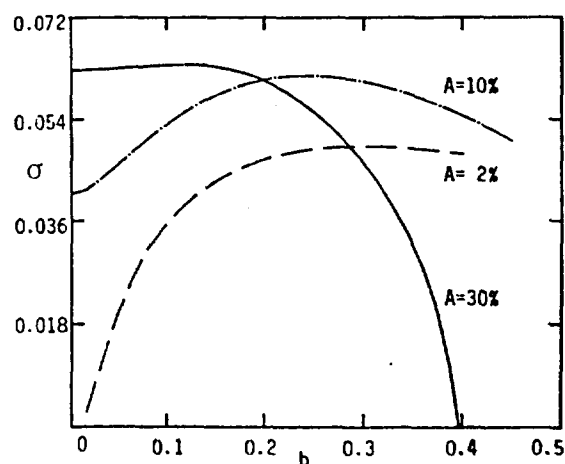


Figure 9. Temporal growth rate  $\sigma$  versus spanwise wavenumber  $b$  for various TS amplitudes  $A$  in a profile at separation.  $P = -.198$ ,  $R = 1000$ ,  $\alpha = 0.5$ ,  $F = 245$ .

# COMPUTATIONAL AND THEORETICAL STUDIES OF UNSTEADY VISCOUS AERODYNAMICS

J. C. Wu  
School of Aerospace Engineering  
Georgia Institute of Technology  
Atlanta, Georgia 30342

## ABSTRACT

A coordinated theoretical and computational approach for analyzing unsteady aerodynamics of viscous fluids is reviewed. This approach permits aerodynamic computations to be confined to the viscous region of the flow and aerodynamic analyses to be carried out with a knowledge of the viscous region of the flow only. The approach also permits the individual flow zones contribution to unsteady aerodynamic load to be identified and their relative importance evaluated. This approach is based on viscous flow equations. For aerodynamic flows in the absence of appreciable recirculating regions, the approach produces classical theories of aerodynamics and panel-vortex lattice computation procedures. The approach is ideally-suited for aerodynamic analyses of unsteady flows containing massive separated regions.

## INTRODUCTION

Near the beginning of this century, when the Wright Brothers experimented with powered flight, theoretical aerodynamics existed as a very young and uncertain discipline. Earlier theories of aerodynamics were based on the assumption of an inviscid fluid and were counter-productive since they predicted zero lift. Almost concurrent with the historic flight of the Wright Brothers in 1903, however, the relation between the circulation around an airfoil and the lift force acting on the airfoil was recognized. This relation formed the basis for an amazing and rapid development of theoretical aerodynamics in the first quarter of this century. Theories formulated during this period of time retained the assumption of an inviscid fluid. The incorporation of the concept of circulation into theoretical aerodynamics, however, permitted accurate predictions of aerodynamic forces under circumstances of great practical importance. Theories of aerodynamics based on the concept of circulation are referred to as classical aerodynamic theories. These theories have contributed immeasurably to advances in aeronautics. Even today, with computational aerodynamics occupying the center stage of aerodynamic research, classical theories are continuing to play a central role in aeronautical engineering. The prevailing opinion of aerodynamic researchers, however, appears to be that, with the complexity and the performance envelop of modern aircraft broadened substantially beyond the scope of classical theories, the development of computational procedures for modern aerodynamic problems is a more rewarding undertaking than the development of new theoretical, non-computational, approaches.

Theoretical research and computational research of course need not be mutually exclusive. Historically, theoretical aerodynamics and experimental aerodynamics have supplemented and reinforced each other. Presumably, interactions between the theoretical branch and the more modern computational branch of aerodynamics can be similarly beneficial. In this paper, recent

research of the present author in unsteady viscous aerodynamics aimed at promoting such interactions is reviewed. In particular, a combined theoretical and computation approach well-suited for analyzing unsteady aerodynamics of viscous fluids is described. This present approach offers valuable physical insights to the problem of unsteady aerodynamics as well as suggestions for improving and generalizing existing inviscid theories and computation procedures. The most important attributes of this approach are: (1) unsteady aerodynamic analyses can be performed with a knowledge of only the viscous region of the flowfield and (2) individual flow elements contributing to the unsteady aerodynamic load can be identified and their relative importance evaluated accurately. These attributes are available for flows containing massive recirculating regions as well as for those containing no appreciable recirculating regions.

Various aspects of this theoretical and computational approach have been reported previously by the present author and his colleagues for various types of flows, including compressible flows and steady flows. At the present, however, the development of this approach has reached a reasonable stage of completion only for unsteady incompressible flows. The present paper gives an overall description of the approach for unsteady incompressible flows. Additional information about various detailed aspects of the present approach, about extensions of the approach to steady flows and compressible flows together with results obtained are available in references cited.

## AERODYNAMIC FLOW

To focus attention, a solid body immersed in and moving relative to a viscous fluid occupying an infinite space is considered in this paper. The fluid is at rest infinitely far from the solid. Aerodynamic forces and moments acting on the solid body are to be predicted and explained. A most remarkable feature of classical theories of aerodynamics is that they predict and explain aerodynamic loads with only minimal information about the flowfields involved. It is well-known, however, that classical theories of aerodynamics has a restricted scope of application. This restricted scope is usually attributed to the inviscid fluid assumption used in the mathematical derivation of these theories. As it turns out, however, it is possible to predict aerodynamic loads accurately with only a partial knowledge about the flowfield without relying upon the inviscid fluid assumption.

A theorem of fluid dynamics which has existed for some time [1] states that, for an incompressible flow,

The motion of a fluid occupying a limited simply-connected region is determinate when the value of vorticity at every point of the region and the value of the normal velocity at every point of the boundary are known. In the case of an  $n$ -ply connected region, the values of the circulation in the several independent circuits of the region must also be known.

Obviously, if the motion of a fluid is determinate, then the aerodynamic load acting on a solid body immersed in the fluid is determinate. According to the theorem stated earlier, then, aerodynamic analyses require a knowledge of only the vorticity distribution in the fluid. It is well-known that, in

incompressible aerodynamic flows, viscous forces exist only in the region of non-zero vorticity. In consequence, in predicting aerodynamic load, it is in principle necessary to know only the viscous part of the overall flow. To put this principle into practice, the aerodynamic load acting on a solid body needs to be expressed in terms of the vorticity environment of the solid. Furthermore, in computational efforts, special procedures are needed to confine the solution field to the viscous region. These topics are reviewed in this paper.

For brevity, the term "viscous region" is used in this paper to describe a region of non-zero vorticity. The viscous region in an aerodynamic flow is generally composed of distinct zones. For flows where no massive recirculating regions are present, the viscous region adjacent to the solid body is restricted to thin boundary layers. The thickness of a boundary layer, compared to the length of the solid body, is of the order  $Re^{-1/2}$  where  $Re$  is the flow Reynolds number based on the solid body length and the translational velocity of the solid. The boundary layers feed into a wake flow which, by virtue of its vorticity content, is viscous. The wake is divisible into several components. In the case of a lifting body set into motion suddenly, a concentrated dose of vorticity is left behind by the lifting body after the onset of the motion. This "starting vortex" becomes diffused with increasing time. As the motion of the lifting body continues, the vorticity in the boundary layers around the body continues to feed into the wake, and a vortical region extending between the body and the starting vortex comes into existence. In addition, "tip vortices" present in three-dimensional flows are also continuations of boundary layers. In general, near wakes, i.e., vorticity that are recently "shed" from the vicinity of the solid body as continuations of boundary layers are thin in problems of interest in aeronautics. The thinness of the vorticity layers permits simplifications of theoretical and computational procedures.

For flows where massive recirculating regions are present, the viscous region contains, in addition, recirculating zones whose characteristic length is comparable to the length of the solid body. The wakes in such flows are not thin. Procedures for analyzing these flows are substantially more difficult than those for analyzing flows containing no massive separated region.

## VISCOUS THEORY OF AERODYNAMICS

The word "theory" is used in this paper in its familiar context to designate a systematic statement of principles. The following three equations state mathematically the principle that aerodynamic force and moment acting on a solid body is directly related to the viscous environment of the solid.

$$\int_{R_f} \vec{\omega} dR + \int_{R_s} \vec{\omega} dR = 0 \quad (1)$$

$$F = -\frac{\rho}{n-1} \frac{d}{dt} \int_{R_f} \vec{r} \times \vec{\omega} dR - \frac{\rho}{n-1} \frac{d}{dt} \int_{R_s} \vec{r} \times \vec{\omega} dR + \rho \frac{d}{dt} \int_{R_s} \vec{v} dR \quad (2)$$

where  $\vec{v}$  is the velocity field;  $\vec{\omega}$  is the vorticity field, defined as the curl of the velocity field;  $R_s$  is the region occupied by a solid immersed in and moving relative to a fluid;  $R_f$  is the region occupied by the fluid;  $\vec{r}$  is a position vector,  $\rho$

is the density of the fluid;  $n$  is the dimensionality of the problem and is equal to 2 or 3 depending on whether the aerodynamic flow is two-dimensional or three-dimensional and  $\vec{F}$  is the aerodynamic force acting on the solid.

Equations (1) and (2) are derived rigorously from the familiar Navier-Stokes equations without using any simplifying assumptions not already contained in the Navier-Stokes Equations. Equation (1) states that the total vorticity in the infinite unlimited region jointly occupied by the fluid and the solid is zero.

Equation (2) states that the aerodynamic force acting on a solid body is composed of contributions from the solid motion and the fluid motion. The contribution from the fluid, represented by the first integral in Eq. (2), is proportional to the time rate of change of the total, integrated, first moment of vorticity,  $\vec{r} \times \vec{\omega}$ , in the fluid. An equation similar to Eq. (2) has been presented [2] for the moment of aerodynamic force.

Equations (1) and (2) form a viscous theory of aerodynamics valid for various types of flows, including those containing massive recirculating regions. Since the integrands in these equations vanish in the viscous region where the vorticity is not zero, this theory obviously permits the prediction of aerodynamic load with a knowledge only of the viscous part of the overall flowfield.

The present viscous theory relates the aerodynamic load to distributed vorticity that exists in the viscous part of the flow. For flows containing no recirculating regions, the distributed vorticity in the flow exists only in thin boundary layers and wakes and are reasonably approximated by vortex sheets and vortex filaments. With such approximations, the viscous theory described here yields results that are identical to well-known classical theories of aerodynamics [2]. The re-derivation of classical theories without relying upon an inviscid fluid assumption is highly significant. It not only removes conceptual difficulties associated with classical theories, but also permits physical insights to be gained and the range of applications of classical theories to be extended with certainty.

Equation (2) can be re-expressed as

$$\vec{F} = - \sum_{k=1}^K \left( \frac{\rho}{n-1} \frac{d}{dt} \int_{R_k} \vec{r} \times \vec{\omega} dR \right) + \vec{S} \quad (3)$$

where  $R_k$  is a fluid region occupied by a viscous zone, and  $\vec{S}$  represents the contributions of the solid motion to the aerodynamic force, i.e., the last two terms of Eq. (2). Each term in the sum of Eq. (3) represents the contribution of an individual zone to the aerodynamic force. The zone are boundary layers, wakes, recirculating flows, etc. Obviously, if the vorticity distribution in a viscous zone is known, then the contribution of that zone to the aerodynamic force can be evaluated individually and the relative importance of this zone can be readily assessed. The present viscous theory of aerodynamics therefore offers an unprecedented opportunity to gain physical insight to the process of generation of aerodynamic load.

## COMPUTATION OF VISCOUS AERODYNAMIC FLOWS

It has been shown [3] that the following mathematical formulation is

completely equivalent to the familiar Navier-Stokes and continuity equations describing the time-dependent incompressible motion of a viscous fluid:

$$\vec{v}(\vec{r}) = - \int_{R_f} \vec{\omega}_o \times \nabla_o P dR_o - \int_{R_s} \vec{\omega}_o \times \nabla_o P dR_o \quad (4)$$

and

$$\frac{\partial \vec{\omega}}{\partial t} = - (\vec{v} \cdot \nabla) \vec{\omega} + (\vec{\omega} \cdot \nabla) \vec{v} + \nu \nabla^2 \vec{\omega} \quad (5)$$

where the subscript "o" indicates that a variable, a differentiation, or an integration is evaluated in the  $\vec{r}_o$  space, and P is the fundamental solution of the elliptic differential equation given by

$$P(\vec{r}, \vec{r}_o) = \begin{cases} - \frac{1}{4\pi |\vec{r}_o - \vec{r}|} & \text{in three-dimensional problems} \\ - \frac{1}{2\pi} \ln \frac{r}{|\vec{r}_o - \vec{r}|} & \text{in two-dimensional problems} \end{cases} \quad (6)$$

Equation (4) is valid in a reference frame at rest relative to the fluid at infinity. In Eq. (4), the first integral represents the Biot-Savart velocity field associated with the vorticity in the fluid region, the second integral represents the Biot-Savart velocity field associated with the vorticity in the solid region. If the solid is not rotating, then the second integral vanishes. Equation (4) is a kinematic relation between the velocity and vorticity fields at the same instant of time.

$$\vec{v}(\vec{r}) = - \sum_{k=1}^K \left( \int_{R_k} \vec{\omega}_o \times \nabla_o P dR_o \right) - \int_{R_s} \vec{\omega}_o \times \nabla_o P dR_o \quad (7)$$

With Eq. (7), the Biot-Savart velocity field associated with each viscous zone  $R_k$  can be evaluated individually. The simple addition of the Biot-Savart velocity fields of the individual viscous zones and the solid contribution gives the total velocity field.

Equation (5) describes the kinetic aspect of the flow. That is, it describes the change of the vorticity field due to kinetic processes. This equation is known as the vorticity transport equation. The three terms on the right-hand side of Eq. (5) represents respectively the convection of vorticity with the fluid, the amplification and rotation of vorticity by the strain rate, and the diffusion of vorticity through viscous action.

#### Confinement of Solution to Viscous Region

A numerical procedure can be established on the basis of Eqs. (4) and (5), together with appropriate boundary conditions, to compute the development of the vorticity field with time. This procedure advances the vorticity solution from an old time level to a subsequent new time level through a computation loop consisting of a kinematic part and a kinetic part.

In the kinetic part, known vorticity and velocity values at the old time level are used in Eq. (5) to determine new vorticity values in the interior of the fluid domain at the subsequent time level. Since each term in Eq. (5) is non-zero

only in the viscous region, the kinetic part of computation can be confined to the viscous region of the flow.

The kinematic part of the computation takes on an auxiliary role in the computation loop. With new vorticity values computed kinematically, this part produces new velocity values at the subsequent time level. These new velocity values are needed for subsequent computations advancing the solution further. Also, in the physical problem, velocity boundary conditions, and not the vorticity boundary condition, is specified. The kinematic part of the computation loop also produces the needed vorticity boundary values for the subsequent time level [4]. It is important to note here that, with Eq. (4), the computation of velocity values can be carried out explicitly, one point at a time. The computation of velocity values can therefore be confined to any arbitrary region of interest. In particular, computation of velocity values can be confined to the viscous region of the flow. Since the kinetic part of the computation can be also confined to the viscous region, the entire solution can be confined to the viscous region.

It is noted that the ability to confine the solution field to the viscous region in the kinematic part of the computation is not available to familiar finite-difference and finite-element methods for solving viscous flow problems. This ability is unique to integral formulations such as Eqs. (4) and (7) obtained using the concept of principal solutions [3]. In the current literature, there exist a number of "inviscid" computation methods in which the Biot-Savart velocity fields associated with vortex panels, source-sink panels or vortex lattices are incorporated into the computation procedure. These methods, in reality, need not be constructed on the basis of an inviscid fluid assumption.

#### Vortex Lattice and Panel Methods

In a flow containing no appreciable recirculating regions, viscous zones present are the boundary layers, the near wake and the far wake. If these viscous zones are represented by vortex sheets, then Eqs. (4) and (5) lead to computational procedures familiarly known as panel or vortex lattice method. In this section, such a procedure is outlined using the flow past non-rotating airfoil as a reference problem. This airfoil problem possesses the essential features of interest and serves to bring into focus the most important features associated with the procedure. Using the concepts presented here, panel-vortex lattice methods can be constructed also for aerodynamic flows associated with other types of lifting bodies, including rotating bodies in three-dimensional flows.

Vortex Sheet Approximation. As discussed earlier, Eqs. (4) and (5) represent respectively the kinematic and the kinetic aspects of a flow problem. For the flow under consideration, Eq. (5) gives, in a reference frame attached to the airfoil,

$$\vec{v}(\vec{r}) = - \int_{S^+} \vec{\gamma}_0 \times \nabla_0 P ds_0 - \int_W \vec{\gamma}_0 \times \nabla_0 P ds_0 + \vec{v}_\infty \quad (8)$$

where  $\vec{v}_\infty$  is the freestream velocity  $S^+$  and  $W$  are respectively the locations of the vortex sheet representing the boundary layers and the wake, and  $\vec{\gamma}$  is the strength of the vortex sheets defined by

$$\vec{\gamma} = \int \vec{\omega} \, dn \quad (9)$$

where the integration is performed across a boundary layer or a wake layer.

If the strength and location of the vortex sheets representing the boundary layers and the wake are known at a given time level, the following procedure can be used to determine new location and strength of these vortex sheets at a subsequent time level. The different zones of the flow, i.e., the boundary layers, the near wake, and the far wake are computed differently so that the computation can take advantage of the different physical characteristics of the different zones.

Near Wake. In the near wake, if the flow Reynolds number is not exceedingly small, then the effective diffusion rate is much smaller than the convection rate. Equation (5) can be justifiably approximated by omitting viscous diffusion, i.e., the last term in Eq. (5). This approximation, like the representation of the wake layer by a sheet, does not imply the fluid is inviscid. It merely acknowledges and exploits the fact that in the near wake the viscous diffusion term is negligibly small compared to the other terms in Eq. (5). In the immediate neighborhood of the airfoil's trailing edge, vorticity gradients across the wake are large and viscous diffusion is important. This neighborhood contains "nascent" wake vorticity, i.e., vorticity which has only recently left the boundary layer zone. An inviscid analysis to determine the strength and location of a nascent vortex segment representing this part of the near wake is inappropriate and it leads to controversies in unsteady flows. Indeed, the approximation of the nascent wake vorticity by a single vortex segment introduces substantial errors whenever flow unsteadiness is large. In general, approximations of nascent vorticity should be guided by viscous analyses. In reality, flows on opposite sides of the airfoil merge at the trailing edge. Thus the nascent wake is more reasonably approximated by two adjacent vortex sheets with different strengths and moving at different speeds in cases of large flow unsteadiness. Within a layer of vorticity, boundary layer approximations are valid and the vorticity is related to the velocity component  $u$  tangential to the layer by  $\omega = -\partial u / \partial n$ . Integrating this expression across the boundary layer and using Eq. (9), one concludes then the velocity at the boundary layer's outer edge is equal in magnitude to the strength of the vortex sheet representing the boundary layer. The magnitude of the flux of vorticity crossing any streamwise station of the boundary layer is one half the square of the vortex strength, as can be easily shown by multiplying the above expression for  $\omega$  by  $u$  and integrating the result across a boundary layer. The above conclusions can be used to calculate the total vorticity in the nascent vortex segments.

With the diffusion term omitted, Eq. (5) can be re-expressed [5] as

$$\frac{d}{dt} \int_S \vec{\omega} \cdot \vec{n} \, ds = 0 \quad (10)$$

where  $S$  is any open material surface lying in and moving with the fluid.

Equation (10) is a statement of Kelvin's circulation theorem for distributed vorticity, derived usually in the context of an inviscid fluid. It is, however, more revealing to view Eq. (10) in the context of a viscous fluid. That is, in the flow of

a viscous fluid, the flux of vorticity across an open material surface is approximately invariant with respect to time in zones where viscous diffusion is slow compared to convection. This fact suggests the use of a Lagrangian reference frame, rather than a Euler reference frame, in the kinetic computation of the near wake. In most vortex lattice and panel methods available today, the strength and geometry of the near wake are computed using a "force-free" condition. This force-free condition in essence permits the near wake vortex panels or lattices to convect computationally with the fluid, but not to diffuse. In actual computations, if the vortex sheet that approximates the near wake is discretized into finite elements, then a vortex panel method is produced for the near wake. If the vortex panels are further approximated by vortex filaments, then a vortex lattice method is produced. The strength of the new vortex filaments or vortex panels are required to be such that the integrated vortex strength of each panel or each segment of vortex filament remains invariant. This requirement is a consequence of Kelvin's circulation theory. Vortex layers in the interior of a fluid are kinetically unstable and tend to roll-up. This roll-up process is a consequence of the convective process and can be simulated computationally [6].

Far Wake. For a far wake located at a large distance from the airfoil, the Biot-Savart velocity field associated with the far wake is small in the vicinity of the airfoil. The circulation, i.e., the total integrated vorticity, of the far wake, however, needs to be known in order to ensure that the total vorticity of the flow is conserved computationally. In computing aerodynamic flows, it is often permissible to truncate the computation field and thus eliminating detailed far wake computations. The circulation of the far wake can be determined by keeping an accurate record of the flux of vorticity leaving the boundary of the truncated computation field. Since the far wake is expected to move at nearly the freestream velocity, a knowledge of the circulation only is sufficient for calculating the contribution of the far wake to aerodynamic load using Eqs. (2)

Boundary Layers. Let  $S^+$  be a surface surrounding the solid surface  $S$  and at an infinitesimal distance from  $S$ . With prescribed solid velocity, the location of  $S^+$  is known.

Applying Eq. (8) to points  $r_s$  located on the solid surface  $S$ , one has

$$\vec{v}_s = - \int_{S^+} \vec{\gamma}_o \times \nabla_o P_s ds_o - \int_W \vec{\gamma}_o \times \nabla_o P_s ds_o + \vec{v}_\infty \quad (11)$$

where  $\vec{v}_s$  is the prescribed solid velocity, zero for the problem under consideration, and  $P_s$  is given by Eq. (6) with  $\vec{r}$  replaced by  $\vec{r}_s$ .

With known strength and location of the wake vortex, the last integral in Eq. (11) can be computed for each point on  $\vec{r}_s$ . Equation (11) can then be written in the form

$$\int_{S^+} \vec{\gamma}_o \times \nabla_o P_s dS_o = \vec{f}(\vec{r}_s) \quad (12)$$

where  $\vec{f}(\vec{r}_s)$  is a known function of  $\vec{r}_s$ .

Equation (12) is a Fredholm integral equation containing  $\vec{\gamma}$  as the unknown function. Equation (12), subject to a constraint, uniquely determines  $\vec{\gamma}$ . The constraint is the principle of total vorticity conservation, Eq. (1), which gives

$$\int_{S^+} \vec{\gamma} \, ds = - \int_W \vec{\gamma} \, ds \quad (13)$$

The computation of the vortex sheet strength representing the boundary layers as described above, involves only the kinematic aspect of the flow problem. This is a consequence of two facts. First, the location of the boundary layer vortex sheet is known and need not be computed kinetically. Second, on the solid surface, vorticity is not conserved but is being generated continuously [3] through the kinematic no-slip condition in a viscous flow.

General Features. The procedures outlined above for the near wake, the far wake and the boundary layer, when combined, form a computation loop which advances the solution in time. There exists many options for each part of this computation loop. For example, in computing the convection of the near wake, velocity values on the vortex system can either be calculated at the old time level, or the new time level, or a combination of these two. The latter two options involve iterative procedures.

Many existing panel methods utilizes source-sink distributions in place of vortex sheets. Sources and sinks do not exist physically in the interior of incompressible flowfields. In consequence, source-sink methods do not readily lend themselves to physical interpretations and they give rise to conceptual difficulties. Several researchers, e.g. Kim and Mook [7], developed panel/lattice methods using vortex element. In these methods, the concept of an inviscid fluid is still employed. In consequence, several difficult issues remain. It needs to be emphasized, even at the risk of appearing repetitive, that although the present procedure closely resembles existing panel-lattice procedures conceived on the basis of an inviscid fluid idealization, the present procedure is based on the approximation of a viscous flow. In consequence, the present procedure leads readily to physical insights which permits conceptual and computational difficulties to be understood and resolved. Furthermore, improvements and refinements of the panel-lattice methods can be devised on the basis of these physical insight.

### Viscous Corrections

The general solution procedure just described provides information about time-dependent distributions of vorticity in the flow approximately. This information yields, through Eq. (2), aerodynamic force and moment acting on the airfoil approximately. Errors introduced by the vortex-sheet approximation are relatively small as long as the flow Reynolds number is not exceedingly small and hence the vorticity layers present in the flow are not thick. These errors can be corrected after the geometry and the strength of the vortex sheets present in the flow are computed.

As discussed earlier, the velocity at the outer edge of a boundary layer is equal in magnitude to the strength of the vortex sheet representing the boundary layer. Thus the strength of the vortex sheet, once computed, provides the

needed boundary information (or equivalent the tangential pressure gradient through Bernoulli's equation) for a boundary layer computation. This boundary layer computation starts at the forward stagnation point and marches downstream along the airfoil surface. The boundary layer solution produces the detailed distribution of vorticity across the boundary layer which can be used in conjunction with Eq. (2) in aerodynamic analyses. A procedure similar to the one just outlined for boundary layer computations can be used to determine the detailed distribution of vorticity in the wake layer. It is obvious that this wake computation needs to be carried out only for the near wake.

### Flows Containing Massive Recirculating Regions

A flow containing massive recirculating regions can be treated using a procedure similar to the one just described for flows containing no appreciable recirculating region. The near wake and the recirculating zones in such a flow contain distributed vorticity. In the kinetic part of computation of these zones, it is appropriate to use the full vorticity transport equation, Eq. (5), rather than simplified panel or lattice methods. For computing the far wake and the boundary layer zones, the procedures outlined for flows containing no appreciable recirculating zone are directly applicable.

At a given time level, with known strength of the vortex sheet representing the boundary layers, known circulation of the far wake and known distribution of vorticity in the near wake and the recirculating zones, Eq. (7) is used to compute velocity values in the near wake. In this computation, the vorticity in the boundary layers may be approximated by a vortex sheet. The velocity values are then used in Eq. (5) to compute a new vorticity distribution at a subsequent time level.

If the wake extends beyond the truncated computation field, then an accurate record of the vortex flux leaving the boundary of the computation field is kept. This record is used to evaluate the circulation of the far wake, i.e., the wake outside the computation domain.

Procedures for computing the vortex strength  $\vec{\gamma}$  representing the boundary layer is identical to those outlined earlier in connection with the vortex panel-lattice procedure and is based on Eqs. (12) and (13). For the present problem, however, the Biot-Savart velocity associated with the wake and the recirculating zones is computed using Eq. (7), rather than the approximate Equation (8). Also in Eq. (13), the right hand side in the present problem is an integral of the distributed vorticity in the wake and the recirculating zones.

The solution procedure just outlined is identical to the panel-vortex lattice procedure outlined earlier, except that the wake vorticity and the recirculating vorticity are not approximated by vortex sheets. Two unique attributes of this procedure have been established. First, with the present procedure, the computation field can be confined to the viscous region of the flow only. Second, within the viscous zone, boundary layer zones can be computed separately from the wake and the recirculating zones. By confining the solution field to the viscous region, the present procedure offers drastic reductions in computational efforts in simulating aerodynamic flows. By treating boundary layer zones separately from other viscous zones, the present procedure permits computational grids and numerical methods to be tailored to the special length

scales and flow characteristics existing in the different zones. This leads to highly accurate and highly efficient numerical procedures [5, 8]. The vorticity distributions in each of the viscous zones can be used in Eqs. (2) and (3) to evaluate the contribution of that zone to the aerodynamic load.

### CONCLUDING REMARKS

A coordinated theoretical and computational approach has been established for analyzing unsteady aerodynamics of viscous fluids. This approach permits aerodynamic computations to be confined to the viscous region of the flow and aerodynamic analyses to be carried out with a knowledge of the viscous region of the flow only. Furthermore, this approach permits the identification of individual flow zones contributing to unsteady aerodynamic load and the evaluation of the relative importance of each zone.

For aerodynamic flows in the absence of appreciable recirculating regions, the boundary and wake layers are justifiably approximated by vortex sheets. The present procedure then yield theories and computational procedures similar to classical theories and panel-vortex methods. The present approach, however, is not based on the concept of an inviscid fluid. Rather, the exact location of vorticity in thin boundary and wake layers are approximated. In consequence, the present procedure leads readily to physical insights which permit conceptual and computational difficulties to be understood and resolved. The present approach is ideally-suited for aerodynamic analyses of flows containing massive separated regions. For such flows, the ability to confine the analyses to viscous zones and to separately treat these zones are of crucial importance.

A large number of aerodynamic problems have been studied using the theoretical and/or computational procedures outlined in this paper. These problems include laminar and turbulent flows past non-rotating airfoils at high angles of attack [8, 9, 10, 11]. In these studies, it was found that periodic shedding of vorticity from the recirculating zone occurs and the flow is unsteady even though the airfoil moves at a constant speed. Problems of flows past oscillating airfoils [12], of flows past three-dimensional bodies of relatively simple shape [13] of vortex-airfoil interaction [14, 15], of apparent mass properties of two- and three-dimensional aerodynamic bodies [14] and of aerodynamic performance of Weis-Fogh wings [15, 16] have also been studied. These studies conclusively demonstrated the attributes of the theoretical and computational procedures described in this paper.

### ACKNOWLEDGEMENTS

This work is supported by AFOSR under Grant No. AFOSR-82-0108 and by ARO under Contract No. DAAG-29-82-K-0094.

### REFERENCES

1. Lamb, H., Hydrodynamics, Dover, New York, Chapter VII, pp. 203-204, 1945.
2. Wu, J.C., "Aerodynamic Force and Moment in Steady and Time-Dependent Viscous Flows," AIAA J. 19:4, pp. 432-441, 1981.

3. Wu, J.C. "Problems of General Viscous Flows," Chapter 4 of Developments in Boundary Element Methods - 2, Applied Science Publishers, London, pp. 69-109, 1982.
4. Wu, J.C., "Numerical Boundary Conditions for Viscous Flow Problems," AIAA J. 14:8, pp. 1042-1049, 1976.
5. Batchelor, G.K., Fluid Dynamics, Cambridge University Press, Cambridge, England, pp. 273-274, 1967.
6. Wu, J.C. and Gulcat, U., "Separate Treatment of Attached and Detached Flow Regions in General Viscous Flows," AIAA J., 19:1, pp. 20-27, 1981.
7. Kim, M.J. and Mook, D.T., "Application of Continuous Vortex Panels to General Unsteady Two-Dimensional Lifting Flows," AIAA Paper No. 85-0282, 1985.
8. Wu, J.C., Wang, C.M. and Gulcat, U., "Zonal Solution of Unsteady Viscous Flow Problems," AIAA Paper 84-1637, 1984.
9. Sugavanam, A. and Wu, J.C., "Numerical Study of Separated Turbulent Flow Over Airfoils," AIAA J., Vol. 20, pp. 464-470, 1982.
10. El Refaee, M.M., Wu, J.C. and Lekoudis, S., "Solutions of Unsteady Two-Dimensional Compressible Navier-Stokes Equations Using Integral Representation Method," AIAA J., Vol. 20, pp. 356-362, 1982.
11. Wu, J.C., Rizk, Y. and Sankar, N.L., "Some Non-Linear Time Dependent Problems of Viscous Flows," Developments in Boundary Element Methods - 3, Applied Science Publishers, London, pp. 137-170, 1983.
12. Sankar, N.L., "Numerical Study of Laminar Unsteady Flow Over Airfoils," Georgia Institute of Technology, Ph.D. Thesis, 1977.
13. Thompson, J.F., Shanks, S.P. and Wu, J.C., "Numerical Solution of Three-Dimensional Navier-Stokes Equations Showing Trailing Tip Vortices," AIAA J., 12:6, pp. 787-794, 1974.
14. Wu, J.C., Sankar, N.L. and Hsu, T.M., "Unsteady Aerodynamics of an Airfoil Encountering a Passing Vortex," AIAA Paper No. 85-0203, January 1985.
15. Wu, J.C., Sankar, N. L. and Hsu, T.M., "Some Applications of a Generalized Aerodynamic Forces and Moments Theory," AIAA Paper No. 83-0543, 1983.
16. Wu, J.C. and Hu-Chen, H., "Unsteady Aerodynamics of Articulate Lifting Bodies," AIAA Paper No. 84-2184, 1984.

RESEARCH ON LAMINAR SEPARATION BUBBLES AT  
DELFT UNIVERSITY OF TECHNOLOGY IN RELATION  
TO LOW REYNOLDS NUMBER AIRFOIL AERODYNAMICS

J.L. van Ingen and  
L.M.M. Boermans  
Department of Aerospace Engineering  
Delft University of Technology  
Kluyverweg 1, 2629 HS Delft, The Netherlands

ABSTRACT

This paper gives an overview of research on laminar separation bubbles at Delft University of Technology in relation to low Reynolds number airfoil aerodynamics. Results of flow visualisation studies are used to define an empirical relation for the angle, at which the separation streamline leaves the wall. The  $e^n$  transition prediction method is extended to separated flows. It is shown that a simple bursting criterion is provided by Stratford's limiting pressure distribution for a zero skin friction turbulent boundary layer. A universal description of the laminar part of the bubble is proposed, resulting in a simple bubble prediction method. The effect of tripping devices to decrease the adverse effect of the bubble on drag is discussed. Finally some results of low Reynolds number airfoil tests are reported.

1. INTRODUCTION

At the low Speed Laboratory (LSL) of the Department of Aerospace Engineering of the Delft University of Technology a long term research program has been going on concerning the analysis and design of airfoil sections for low speed flow. The program was started in 1966 by the first author while spending a sabbatical year at the Lockheed Georgia Research Laboratories. First results of a computer program, which used computer graphics as a novelty, have been published in [1,2,3].

This prototype program used some -at that time - readily available methods for the calculation of: the potential flow pressure distribution (conformal transformation due to Timman [4]); the laminar boundary layer (Thwaites [5]); transition ( $e^n$  method due to Smith and Gamberoni [6] and Van Ingen [7]); the turbulent boundary layer (Heads entrainment method [8]).

Very soon it became apparent that also accurate methods to calculate laminar separation bubbles were required for predicting the characteristics of airfoils at low Reynolds numbers. Research at Delft then was concentrated for some time on the laminar separation bubble [9,10,11].

A schematic description of the flowfield and the pressure distribution in the bubble region is given in fig. 1. It contains the definition of some bubble related parameters.

The present paper will focus attention on the separation region (around S); the laminar part of the bubble (S-T); transition (T) and reattachment (R). As in most engineering calculation methods we will treat the pressure distribution in the bubble as a local perturbation only of the pressure distribution curve SR which would occur for a turbulent

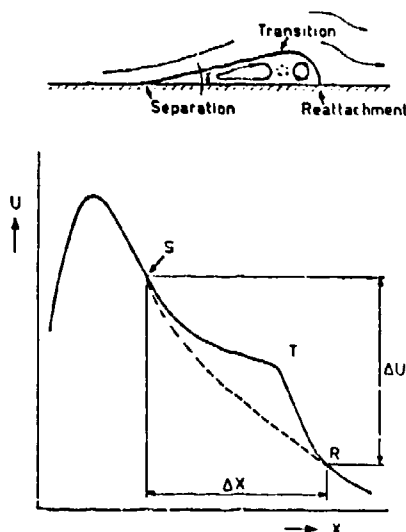


Fig. 1: Schematic diagram of flow field and pressure distribution in a laminar separation bubble.

$$\text{Crabtree: } \sigma = 1 - \left(\frac{U_R}{U_S}\right)^2$$

$$\text{Crabtree (mod.): } \sigma_{cr} = 1 - \left(\frac{U_R}{U_T}\right)^2$$

$$\text{Gaster: } P = - \frac{\theta_S^2}{\nu} \frac{\Delta U}{\Delta x}$$

boundary layer. Hence the laminar separation point S and the reattachment point R are thought to be on the turbulent curve. In reality a slight undershoot is often noticed, both upstream of S and downstream of R. When the flow downstream of the separation point fails to reattach, a large adverse effect on the drag and/or stalling behaviour of the airfoil is noticed. Hence an accurate prediction of this 'bursting process' is necessary.

The present status of the LSL airfoil analysis and design program may be found in [12,13]. It is being used extensively for sailplane applications [14,15,16,17].

It has been found that the effect of the laminar separation bubble on the airfoil characteristics is also due to its influence on the downstream development of the turbulent boundary layer. This effect may be noticed at chord Reynolds numbers as high as  $5 \times 10^6$ .

In recent years attention has been given to means to provoke earlier transition in the bubble, such that its detrimental effects are reduced. Besides conventional tripping devices, the so-called pneumatic turbulators, first used by Pfenninger [18] and rediscovered by Horstmann and Quast [19], were studied extensively in close cooperation between LSL and DFVLR Braunschweig [20].

In the present paper we will review this research at LSL related to laminar separation bubbles and its effects on airfoil characteristics at low Reynolds numbers. To keep the size of the paper within reasonable limits, the reader will have to be referred to the original papers for detailed information.

## 2. SOME USEFUL RELATIONS FOR SEPARATING LAMINAR FLOW

In a small neighbourhood of the separation point, where the inertial forces may be neglected, the Navier-Stokes equations admit a simple analytical solution (see [21,22,23]). Important results are:

The separation streamline leaves the wall at an angle  $\gamma$  (fig. 1) which is determined by:

$$\tan(\gamma) = -3 \frac{d\tau_0}{dx} / \frac{\partial p}{\partial x} \quad (1)$$

where all quantities in (1) are evaluated at the separation point.  
The equation for the streamlines ( $\psi = \text{constant}$ ) reads:

$$y^2(x \tan \gamma - y) = \text{constant} \quad (2)$$

where  $x$  is the distance downstream of separation.  
The shear stress is zero at  $y = y_1$  for which:

$$y_1 = \frac{1}{3} x \tan \gamma \quad (3)$$

The velocity component  $u$  equals zero at  $y_2$  for which:

$$y_2 = \frac{2}{3} x \tan \gamma$$

Hence (when  $y_3$  denotes the distance to the wall of the separation streamline):

$$y_1 : y_2 : y_3 = 1 : 2 : 3 \quad (3)$$

The pressure gradient is at an angle  $1/3 \gamma$  with the wall and hence for thin bubbles, where  $\gamma$  is small, the pressure gradient normal to the wall is small so that the boundary layer equations might still give a reasonable result.

If we start from the boundary layer equations and assume small values of  $u$  and  $v$  we can also arrive at the previous results. Here it is assumed a priori that  $\partial p / \partial x$  is independent of  $y$ . The result (3) also follows from the expression for the velocity profile in the form:

$$\frac{u}{U} = \lambda \frac{y}{\theta} + \frac{1}{2} m \left(\frac{y}{\theta}\right)^2 \quad (4)$$

which is valid for a sufficiently small neighbourhood of the wall, not necessarily near the separation point only. From (4) it follows that the stream function  $\psi$  is given by:

$$\frac{\psi}{U\theta} = \frac{1}{2} \lambda \left(\frac{y}{\theta}\right)^2 + \frac{1}{6} m \left(\frac{y}{\theta}\right)^3 \quad (5)$$

From (5) we find that  $\psi = 0$  for  $y = 0$  and for:

$$y_3/\theta = -3\lambda/m \quad (6)$$

furthermore:

$$y_2/\theta = -2\lambda/m \quad (7)$$

$$y_1/\theta = -\lambda/m \quad (8)$$

Hence eq. (4) reproduces (3). In what follows we will sometimes use  $g = y_3/\theta$  as shape factor for the velocity profiles with reversed flow. An analogous behaviour is shown for solutions with reversed flow of the Falkner-Skan equation:

$$F''' + FF'' + \beta(1-F'^2) = 0 \quad (9)$$

This equation describes the similar solutions corresponding to the pressure distribution:

$$U = u_1 x^{m_1} \quad (10)$$

where  $u_1$  and  $m_1$  are constants ( $x$  is here measured from the origin of the flow.

In (9)  $F$  is the non-dimensional streamfunction, primes denote differentiation w.r.t. non-dimensional  $y$ ;  $\beta$  is the pressure gradient parameter related to  $m_1$  by

$$\beta = \frac{2 m_1}{(m_1 + 1)} \quad (11)$$

For  $\beta > 0$  equation (9) only allows solutions with positive skin friction; for  $0 < \beta < -.198838$  solutions with positive and negative skin friction are possible;  $\beta = -.198838$  represents the separation solution. Extensive tables of solutions with positive skin friction may be found in [24]. Some of the reversed flow solutions have been calculated first by Stewartson [25]. Table 1 gives some improved results obtained at LSL. It follows from the table that with a good approximation  $y_2/y_3 = 2/3$  and  $g = y_3/\theta = -3\lambda/m$  as for the velocity profile (4). It should be noted that at the end of the table, corresponding to velocity profiles which

$\beta$	$\lambda$	$m$	$H$	$L$	$\frac{y_2}{y_3}$	$g = \frac{y_3}{\theta}$	$-\frac{3\lambda}{m}$
-.198838	0	.06815	4.029	.8218	.667	0	0
-.18	-.0545	.05601	5.529	.7343	.667	2.917	2.920
-.10	-.0545	.01503	12.62	.3308	.678	10.665	10.000
-.05	-.0258	.00283	28.096	.1190	.698	25.748	27.350
-.025	-.0106	.00051	59.821	.0418	.721	56.478	62.353

Table 1: Some results for reversed flow solutions of eq. (9).

are found far downstream in a separation bubble, extremely large values of the shape factor  $H$  occur. This is due to the strong increase in  $\delta^*$  which in turn follows from the thick region with reversed flow. Because the velocities in the separated region remain very small it may be expected that eq. (2) remains valid within a separation bubble at appreciable distances downstream of separation. This is illustrated by fig. 2 in which measured streamlines from a smoke picture of a separation bubble [10] are compared to results of a calculation using eq. (2). It should be noted that the streamlines can only be calculated when  $\gamma$  is known. In this case the value of  $\gamma$  was taken from the smoke picture.

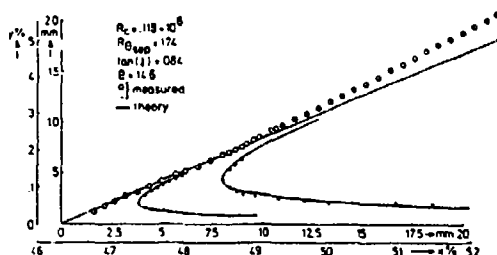


Fig. 2: Streamlines from smoke picture and comparison with equation (2).

### 3. RESULTS OF FLOW VISUALIZATION STUDIES OF LAMINAR SEPARATION BUBBLES

When a boundary layer calculation is performed for a prescribed pressure distribution, generally a singularity will occur at separation for which the wall shear stress  $\tau_0$  tends to zero like the square root of the distance to separation (Goldstein, [26]). In this case eq. (1) would predict a separation angle  $\gamma$  of 90 degrees, which is obviously in contradiction with experimental evidence. Usual ways to proceed with the calculation through the separation point, are to use the Navier-Stokes equations or at least a strong interaction model coupled with the boundary layer equations.

An alternative way was followed at LSL, in order to develop an engineering method for the calculation of separation bubbles. An extensive series of flow visualization studies was made in the hope that a sufficiently general empirical relation might be found from which the separation angle  $\gamma$  can be determined as a function of the boundary layer characteristics upstream of separation. Once  $\gamma$  is known the separated flow might be calculated using simple methods.

A first series of results has been reported in [9]. Measurements were performed on seven different model configurations in three different low speed windtunnels. The flow was made visible by means of tobacco smoke introduced into the separation bubble. The shape of the front part of the bubble was determined photographically, from which the separation angle  $\gamma$  could be measured.

The results are shown in fig. 3, where measured values of  $\tan(\gamma)$  are plotted vs. the corresponding value of  $R_0$  at separation. It follows that a reasonably unique relation exists between  $\gamma$  and  $(R_0)_{\text{sep}}$  which can be approximated by

$$\tan(\gamma) = B/(R_0)_{\text{sep}} \quad (12)$$

with a value for the 'constant'  $B$  of about 15 to 20.

Later [10], similar experiments have been performed on a Wortmann FX 66-S-196V1 airfoil (series 1 in chapter 7); results are given in fig. 4. For these experiments the chord Reynolds number was reduced to such low values that bursting of the bubble occurred. It follows from fig. 4 that even after bursting relation (12) remains valid. In the LSL airfoil computer program, equation (12) is used with a constant mean value for  $B$  equal to 17.5.

When the separation streamline for a curved wall is plotted in boundary layer coordinates, where distances are measured along and normal to the

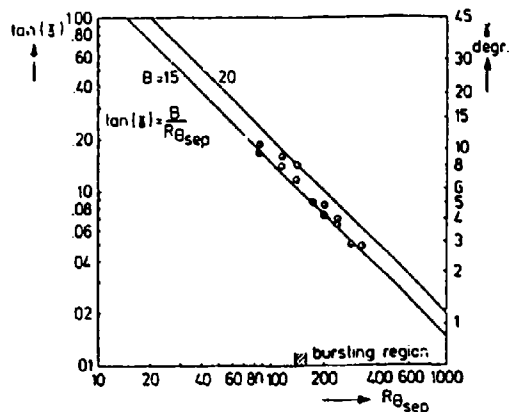
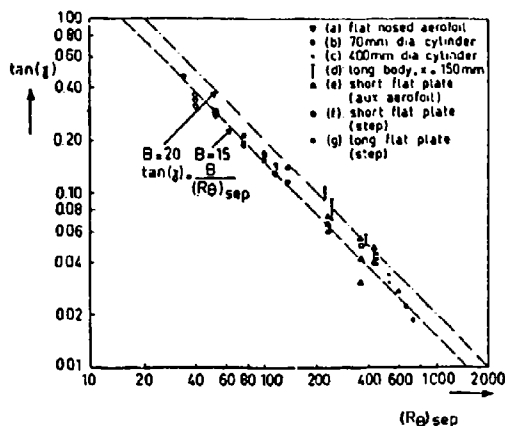


Fig. 3: Separation angles from [9]. Fig. 4: Separation angles from [10].

wall, respectively, the dividing streamline in the laminar part of the bubble is reasonably straight or slightly curved upwards (fig. 2). This finding has been used [9,10,11] to develop a simple calculation procedure for the separated laminar flow. This method employs the Von Karman momentum integral relation and the first 'compatibility condition' of the boundary layer equations. This condition relates the curvature of the velocity profile at the wall to the streamwise pressure gradient. The following additional assumptions are made.

- The angle  $\gamma$  can be determined from  $(Re)_{sep}$  by an empirical relation such as (12) with  $B = 17.5$ .
- The 'separation streamline' has a prescribed shape in the laminar part of the bubble.
- The reversed flow velocity profiles can be represented by the Stewartson second branch solutions of the Falkner-Skan equation.

It should be observed that the pressure distribution in the separated region is not given a priori but it follows from the calculations. In other words: the pressure distribution is determined such that the assumed shape of the separation streamline is compatible with the other assumptions and with the equations used. Initial conditions which are required to start the calculation at the separation point are  $\theta$  and  $U$ . These conditions follow from the boundary layer calculation upstream of the separation point.

The above mentioned method has been used for some time in the LSL airfoil computer program. The resulting pressure distributions were always found to be very similar, showing the characteristic flattening in the laminar part of the bubble (fig. 1). At a later stage, the pressure distributions have been directly derived from a universal relation which is based on a combination of experimental evidence and calculations (see chapter 4).

#### 4. A POSTULATED UNIVERSAL DESCRIPTION OF THE LAMINAR PART OF THE BUBBLE

In order to arrive at a universal model of the laminar part of the bubble we start from the boundary layer equation:

$$u \frac{\partial u}{\partial x} + v \frac{\partial u}{\partial y} = -\frac{1}{\rho} \frac{dp}{dx} + \nu \frac{\partial^2 u}{\partial y^2} \quad (13)$$

and the continuity equation:

$$\frac{\partial u}{\partial x} + \frac{\partial v}{\partial y} = 0 \quad (14)$$

It seems reasonable to assume the validity of (13) even within the separated region if only we refrain from prescribing the pressure distribution. The pressure gradient term in (13) can be related to the velocity  $U$  at the edge of the boundary layer using the Bernoulli equation.

We now make (13) and (14) non-dimensional by using  $\theta_{sep}$  as a characteristic length and  $U_{sep}$  as a characteristic velocity. Taking again  $x$  as the distance downstream of separation we now define:

$$(R_\theta)_{sep} = (U_{sep} \theta_{sep} / \nu)$$

$$\bar{y} = y / \theta_{sep} \quad \bar{u} = u / U_{sep} \quad \bar{v} = v / U_{sep} \quad (15)$$

$$\bar{x} = x / (\theta_{sep} (R_\theta)_{sep}) \quad \bar{v} = (v (R_\theta)_{sep}) / U_{sep}$$

Note that in non-dimensionalizing  $x$  and  $v$  a factor  $(R_\theta)_{sep}$  has been used. This is to obtain values of  $\bar{x}$  and  $\bar{v}$  with a reasonable order of magnitude and moreover to arrive at the following equations which do not contain the Reynolds number explicitly:

$$\bar{u} \frac{\partial \bar{u}}{\partial \bar{x}} + \bar{v} \frac{\partial \bar{u}}{\partial \bar{y}} = 0 \frac{d\bar{u}}{d\bar{x}} + \frac{\partial^2 \bar{u}}{\partial \bar{y}^2} \quad (16)$$

$$\frac{\partial \bar{u}}{\partial \bar{x}} + \frac{\partial \bar{v}}{\partial \bar{y}} = 0 \quad (17)$$

If now we make the following assumptions:

- $\bar{u} = U/U_{sep}$  is a universal function of  $\bar{x}$  downstream of separation.
- All velocity profiles at separation are the same when plotted as  $u/U_{sep}$  vs  $y/\theta_{sep}$ .

Then equations (16) and (17) and the corresponding boundary conditions are always the same leading to a universal solution. From this it would follow that

$$\bar{u} = U/U_{sep}, \quad \bar{\theta} = \theta/\theta_{sep}, \quad y_3/\theta_{sep} \quad \text{and} \quad g = y_3/\theta$$

are universal functions of  $\bar{x}$ . It should be stressed that the available experimental evidence to support assumption (a) is scarce and scattered. Moreover the assumption (b) may be questioned, because the various

separation profiles certainly show a variation of the shape factor  $H$  [10,27]. Nevertheless we will proceed on this line because it will lead us to a useful frame of reference to present further experimental results.

If  $g = y_3/\theta$  is a universal function of  $\xi$ , then we find (note that  $g = 0$  at separation):

$$\tan \gamma = \left( \frac{dy_3}{dx} \right)_{x=0} = \left( \frac{dy_3}{d\xi} \frac{d\xi}{dx} \right)_{x=0} = \frac{\left( \frac{dg}{d\xi} \right)_{\xi=0}}{(R/\theta)_{\text{sep}}} \quad (18)$$

With  $\left( \frac{dg}{d\xi} \right)_{\xi=0}$  equal to a universal constant, say  $B$ , we retrieve our experimental relation (12).

From a limited number of experiments we derived the following relation for  $\bar{U}$  as a function of  $\xi$ :

$$\bar{U} = U/U_{\text{sep}} = 0.978 + 0.022 e^{-4.545 \xi - 2.5 \xi^2} \quad 0 < \xi < 1.3333 \quad (19)$$

$$\bar{U} = 0.978 \quad \xi > 1.3333$$

Using the momentum integral relation and some relations between characteristic parameters for the Stewartson boundary layers, we derived the following relation for  $\bar{\theta}$  in the bubble:

$$\bar{\theta} = \theta/\theta_{\text{sep}} = [1 + 1.52 (1 - (1 - 0.75 \xi)^4)]^{1.25} \quad 0 < \xi < 1.3333 \quad (20)$$

$$\bar{\theta} = 1.1935 \quad \xi > 1.3333$$

Both equations (19) and (20) are at present used as a standard in the LSL airfoil analysis and design program. Because these relations are not based on sound theoretical or experimental evidence, it is planned to investigate the subject of the present chapter in more detail in the future.

## 5. THE $e^n$ METHOD FOR TRANSITION PREDICTION

The  $e^n$  method for transition prediction for attached flows was developed in 1956 independently by Smith and Gamberoni [6] and Van Ingen [7]. The method was extended by Van Ingen to the case of suction [28] and separated flows [10,11].

The method employs linear stability theory to calculate the amplification factor  $\sigma$  for unstable disturbances in the laminar boundary layer ( $\sigma$  is defined as the natural logarithm of the ratio between the amplitude of a disturbance at a given position to the amplitude at neutral stability). It is found that at the experimentally determined transition position the calculated amplification factor for the critical disturbances attains nearly the same value (about 9) in many different cases for flows with low free stream turbulence levels. To include the effects of higher free stream turbulence levels, the critical amplification factor was made dependent on the turbulence level by Mack [29] and Van

Ingen [10,11].

To obtain the critical disturbance, calculations are made for many different disturbance frequencies; the envelope  $\sigma_a$  of the  $\sigma$ - $x$  curves for these different frequencies is used as the critical amplification factor controlling transition. Denoting the value of  $\sigma_a$  at transition by  $n$ , it follows that the calculated ratio of the amplitude  $a$  of the unstable disturbances to the neutral amplitude  $a_0$  is given by:

$$a/a_0 = e^n \quad (21)$$

This of course explains the name of this semi-empirical method. It is customary at LSL to use  $\sigma_a$  instead of  $n$ .

In linear stability theory a given two-dimensional laminar main flow is subjected to sinusoidal disturbances with a disturbance stream function:

$$\psi = \phi(y) e^{i(\alpha x - \omega t)} \quad (22)$$

For the spatial mode  $\omega$  is real and  $\alpha$  is complex  $\alpha = \alpha_r + i \alpha_i$ . This leads to a factor  $e^{-\alpha_i x}$  in the disturbance amplitude and  $\sigma$  follows from:

$$\sigma = \int_{x_0}^x -\alpha_i dx \quad (23)$$

where  $x_0$  is the streamwise position where the disturbance with frequency  $\omega$  is neutrally stable.

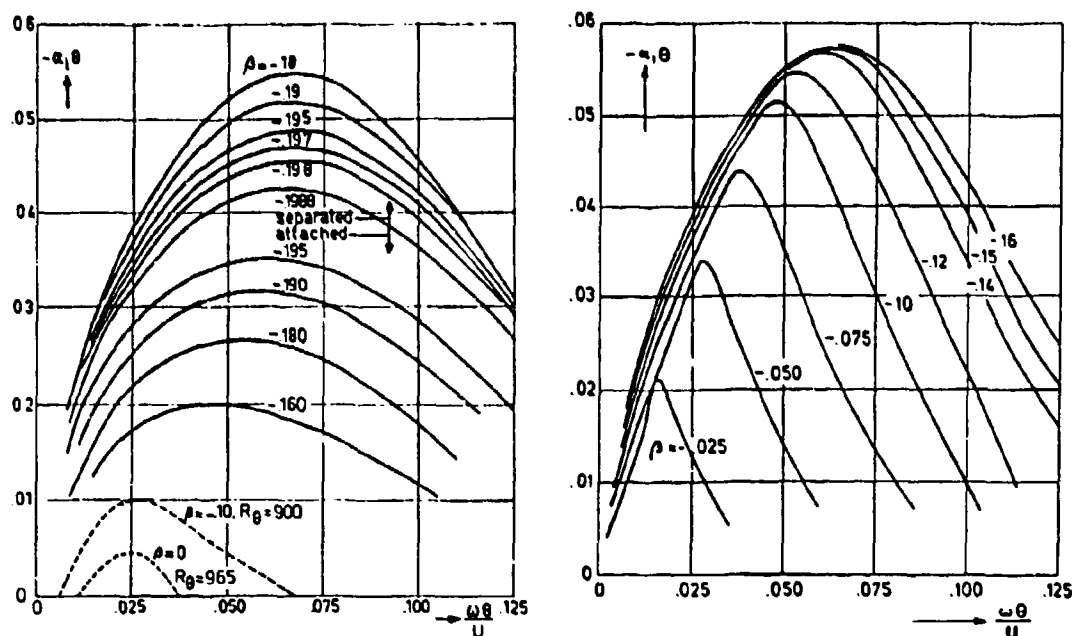
All stability data obtained from [30,31,32] and some additional inviscid stability calculations at LSL [10] (fig. 5), have been reduced to a table containing about 300 numbers.

Using this table, the amplification rate  $-\alpha_i$  can easily be obtained for any velocity profile, as soon as the critical Reynolds number is known. At LSL a boundary layer calculation method is used [10] which for attached flow is similar to Thwaites' method. It contains an extra parameter however, which makes the prediction of the separation position as accurate as for Stratford's two-layer method [33]. In separated flows an integral method is used in which the shape of the separation streamline is prescribed. Both for attached and separated flow the primary profile shape parameter is  $m/m_{sep}$ . The critical Reynolds number is a function of  $m/m_{sep}$ ; this function is assumed to be equal to that obtained for the Falkner-Skan solutions.

It is clear that  $\sigma$  is a function of  $x$  and  $\omega$  for a given boundary layer;  $\sigma$  can be calculated as soon as stability diagrams are available for the velocity profiles for successive streamwise positions  $x$ .

Since transition occurs in a region rather than in a point, Van Ingen introduced two values of  $\sigma_a$  namely  $\sigma_1$  and  $\sigma_2$  [10] corresponding to beginning and end of the transition region. The values of  $\sigma_1$  and  $\sigma_2$  depend on the free stream turbulence characteristics.

Although it is clear that the initial disturbances cannot be sufficiently characterised by the r.m.s. value of free stream turbulence alone, it



a) Attached and separated flow. b) Separated flow.

Fig. 5: Inviscid instability for Hartree's and Stewartson's velocity profiles. For attached flow  $-\alpha_1\theta \rightarrow 0$  for  $\beta \rightarrow 0$ , for comparison the viscous instability is shown for  $\beta = 0$  and  $-0.10$  when  $R_0$  is about 1000.

may be attempted to find a relation between  $\sigma_1$ ,  $\sigma_2$  and the r.m.s. free stream turbulence  $Tu$  (in %).

In many different papers relations between  $Tu$ ,  $R_0$  or  $R_x$  at transition have been given for the flat plate. The measured transition positions may be converted to  $\sigma_a$ -values. Then  $\sigma_a$  will decrease when  $Tu$  increases; fig. 6 shows a collection of these data; for  $Tu > 0.1\%$  the relation used by Mack in fig. 3 of [29] can be approximated by:

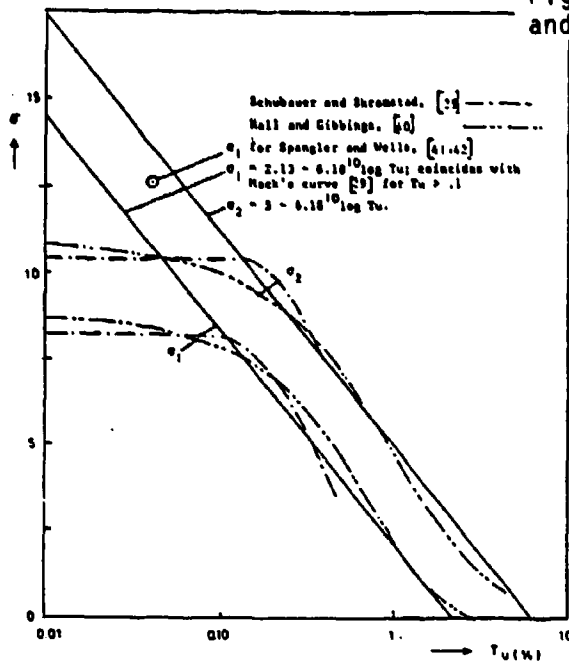
$$\sigma_1 = 2.13 - 6.18^{10} \log Tu \quad (24)$$

while for  $\sigma_2$  a reasonable approximation is:

$$\sigma_2 = 5 - 6.18^{10} \log Tu \quad (25)$$

For values of  $Tu < 0.1\%$  there is much more scatter because in this region sound disturbances may become the factor controlling transition rather than turbulence. We may also use the relations (24) and (25) for  $Tu < 0.1\%$ ; but then we should define an 'effective' value for  $Tu$ . Of course this does not solve the problem because we can only define an 'effective  $Tu$ ' for a wind tunnel after transition experiments have been made in that same tunnel.

Fig. 6: Relations between  $\sigma_1$ ,  $\sigma_2$  and  $Tu$  for the flat plate.



In the LSL airfoil program we use the mean value of  $\sigma_1$  and  $\sigma_2$  which is called  $\sigma_{turb}$  to predict a 'transition point' where the turbulent boundary layer calculation is started.

The value for  $Tu$  which is used, is based on calibration calculations using available transition experiments in different wind tunnels and in free flight of gliders.

At present we use values according to table 2 [12].

Facility	$Tu$ (%)	$\sigma_{turb}$
NACA LTT and similar tunnels	0.10	9.75
Advanced low turbulence tunnels such as at LSL	0.06	11.2
Free flight of gliders	0.014	15.0

Table 2:  $Tu$  used for different facilities.

Application of the  $e^n$  method requires the evaluation of eq. (23) for a range of reduced frequencies  $\omega v/U_\infty^2$ ; this is done on a routine basis in the LSL airfoil program. For separation bubbles a short-cut method was developed [10,11] which is thought to provide a reasonably accurate first estimate of the transition position in the separated flow at rather low values of the Reynolds number, where no appreciable amplification occurs prior to separation. This short-cut method will be described in the remainder of the present chapter.

Starting from (23) and using the non-dimensional coordinate  $\xi$  we can write:

$$\sigma = \int -\alpha_i dx = (R_\theta)_{\text{sep}} \int \frac{-\alpha_i \theta}{\theta/\theta_{\text{sep}}} d\xi \quad (26)$$

The non-dimensional frequency  $\omega\theta/U$  may be written as:

$$\omega\theta/U = (\omega \theta_{\text{sep}}/U_{\text{sep}})(\theta/\theta_{\text{sep}})(U/U_{\text{sep}})^{-1} \quad (27)$$

Then, using the results of chapter 4 that  $U/U_{\text{sep}}$ ,  $\theta/\theta_{\text{sep}}$  and the shape factor may be taken as universal functions of  $\xi$ , it follows that for each frequency the integral in (26) is a universal function of  $\xi$ . Then, also the envelope of the integrals for the different frequencies is a universal function of  $\xi$ . Hence we can write:

$$\sigma_a = (R_\theta)_{\text{sep}} F(\xi) \quad (28)$$

where  $F(\xi)$  is a universal function of  $\xi$  which may be determined from the known relations between  $\xi$ ,  $g$ ,  $\beta$  and the various stability data. A simplified calculation can be made when it is assumed that in first approximation in the laminar part of the bubble  $\theta$ ,  $U$  and  $R_\theta$  are constant and equal to their values at separation. Then constant values of  $\omega\theta/U^2$  also mean constant values of  $\omega\theta/U$ . Furthermore it may be assumed that downstream of separation  $g$  is proportional to  $\xi$  according to

$$g = B \xi \quad (29)$$

Hence (26) can be written as

$$\sigma = \frac{(R_\theta)_{\text{sep}}}{B} \int (-\alpha_i \theta) dg \quad (30)$$

In [10] a different parameter  $z$  was used according to

$$z = g * m_{\text{sep}} \quad (31)$$

so that (30) leads to:

$$\sigma = 10^{-4} \frac{(R_\theta)_{\text{sep}}}{B m_{\text{sep}}} [10^4 \int (-\alpha_i \theta) dz] \quad (32)$$

The powers of 10 have been introduced to obtain values for the integral of a suitable order of magnitude. Similarly we can over a short interval upstream of separation, assuming  $\lambda$  to be proportional to  $x_{\text{sep}} - x$ , perform the integration w.r.t.  $\lambda$  instead of  $x$ .

Now we make the further assumption that the Reynolds number is so high that the stability characteristics are given with sufficient accuracy by the limiting values determined from the inviscid stability equation. Then  $-\alpha_i \theta$  only depends on the value of  $\omega\theta/U$  and the profile parameter  $\beta$  or  $z$ . Hence the integration w.r.t.  $z$  in eq. (32) can be performed once

for all independently of  $(R_\theta)_{sep}$  or the pressure distribution for different values of  $\omega/U$ . A similar result holds for the integration w.r.t.  $z$  upstream of separation. The inviscid instability for different values of  $\beta$  is shown in figs. 5a and 5b. Values of  $10^4 \int (-\alpha_i \theta) dz$  are shown in fig. 7 for different values of  $\omega/U$  together with the envelope giving the maximum value  $I$  of the integral as a function of  $z$ . Hence the maximum amplification factor  $\sigma_a$  follows from (32) in the form:

$$\sigma_a = 10^{-4} \frac{(R_\theta)_{sep}}{B \cdot m_{sep}} I \quad (33)$$

Values of  $z$  and  $I$  for reversed flows may be found in table 3. According to previous experience with the transition prediction method it may be expected that transition will occur in practice as soon as the calculated value of  $\sigma_a$  exceeds a critical value which is of the order of 9, but will depend on  $Tu$ . Assuming a critical value of  $\sigma_a$  the transition position may be found as follows. From the known values of  $(R_\theta)_{sep}$ ,  $m_{sep}$ ,  $B$  and the critical value of  $\sigma_a$  we find from eq. (33) the value of  $I$  at which transition will occur. Then table 3 gives the corresponding

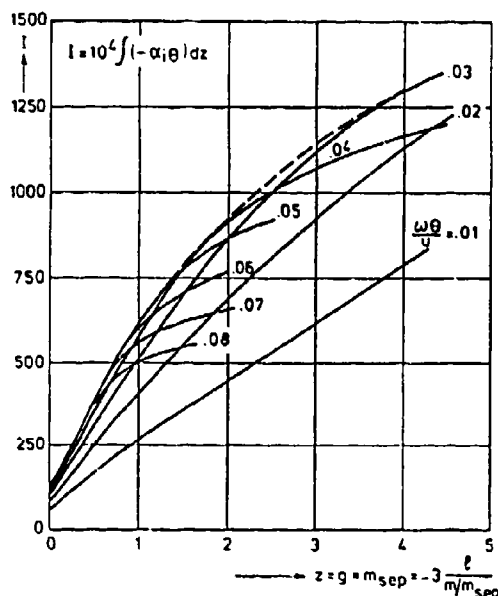


Fig. 7: Amplification integral.

$\beta$	$z = g \cdot m_{sep}$	$I$
-.198838	0	127
-.198	.042	145
-.197	.061	154
-.195	.088	167
-.190	.134	190
-.180	.199	225
-.160	.307	285
-.150	.360	315
-.140	.420	348
-.120	.556	422
-.100	.682	483
-.075	1.107	659
-.050	1.864	883
-.025	4.249	1331

Table 3:  $z$  and  $I$  as a function of the Hartree shape parameter  $\beta$  for reversed flows.

value of  $z = g * m_{sep}$ ; then eq. (29) and (31) determine the distance between the separation and transition points.

At LSL we use this short-cut method to obtain a first estimate of the transition position only. Subsequently we always perform the full amplification calculation where also the upstream influence is taken into account. This may lead to a shorter bubble than follows from the short-cut method.

Comparing (28) and (33) it follows that the function  $F(\xi)$  is related to  $I$  according to:

$$10^4 F(\xi) = I / (B * m_{sep}) \quad (34)$$

Plots for  $I$  and  $10^4 F(\xi)$  are shown in figs. 8 and 9. For small values of  $\xi$  and  $z$  we may use as a good approximation:

$$10^4 F(\xi) = 70 + 530 \xi \quad (35)$$

$$I = 122.5 + 530 z$$

For large values of  $z$  and  $\xi$  we may use:

$$I = 650 \sqrt{z} \quad (36)$$

$$10^4 F(\xi) = 491 \sqrt{\xi}$$

The linear approximation (35) will be used in chapter 7 as a frame of reference for some further experimental results.

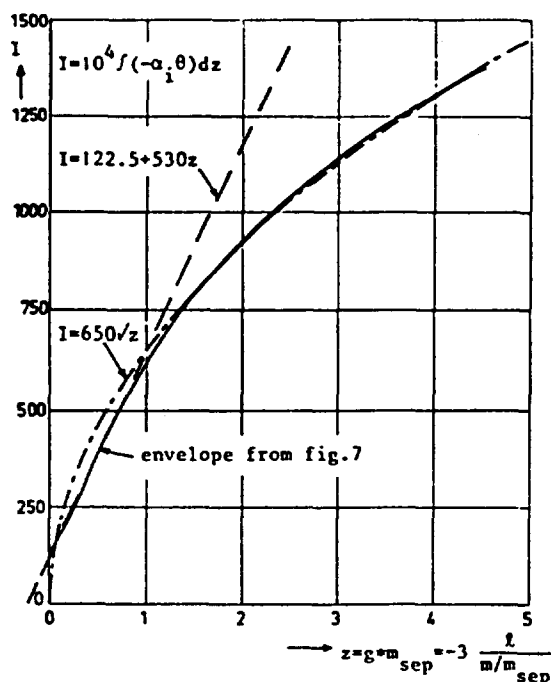


Fig. 8: The integral  $I$  and approximations (35) and (36).

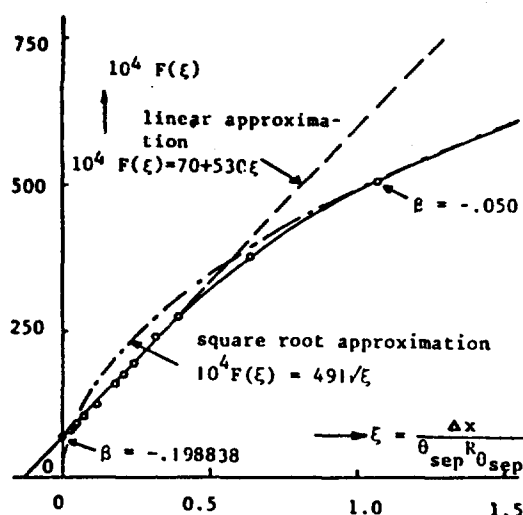


Fig. 9: The function  $F(\xi)$  and approximations (35) and (36).

The square root approximation may be brought in a familiar form, which has been used by previous writers to present their experimental results. It should be noted that (36) completely neglects the amplification upstream of separation but is rather accurate for large values of  $z$ . Combining eqs. (33), (36) and (29) it follows that the position of transition  $x_{tr}$  follows from (take  $x_{sep} = 0$ ):

$$\frac{x_{tr}}{\theta_{sep}} = \frac{\sigma_a^2 10^8 B m_{sep}}{650^2 (R_\theta)_{sep}} = \frac{237 \sigma_a^2 B m_{sep}}{(R_\theta)_{sep}} \quad (37)$$

Using as mean values  $B = 17.5$  and  $m_{sep} = 0.10$  we find:

$$\frac{x_{tr}}{\theta_{sep}} = \frac{415 \sigma_a^2}{R_{\theta_{sep}}} = .0415 \sigma_a^2 \frac{10^4}{R_{\theta_{sep}}} \quad (38)$$

Horton [35] used the following relation

$$\frac{x_{tr}}{\theta_{sep}} = C \frac{10^4}{(R_\theta)_{sep}} \quad (39)$$

with values of  $C$  ranging from 3 to 5. This range of  $C$  values corresponds to  $\sigma_a$  values between 8.5 and 11. It should be noted that (36) and hence (39) can only be used when transition occurs rather far downstream in the bubble; that means it is a very low Reynolds number approximation. It would lead to the unrealistic result that, with increasing Reynolds number the bubble would only disappear at infinite Reynolds numbers. At the higher Reynolds numbers it should be expected that (35) is a better approximation.

It should be stressed again however that all approximations discussed in this chapter are based on the assumption that no appreciable amplification occurs upstream of separation. Only the full amplification calculation which we use in the LSL airfoil program will give a proper prediction of transition.

## 6. POSSIBLE METHODS TO PREDICT BURSTING OF THE BUBBLE

A number of methods may be used to predict whether reattachment of the shear layer will occur downstream of transition. A few of these methods will be briefly described in this chapter; some experimental checks will be given in chapter 7.

In [47] Crahtree observed that there seems to be a maximum limit to the pressure rise which a reattaching turbulent shear layer may overcome. From a number of experiments he deduced that the pressure coefficient

$$\sigma = 1 - \left( \frac{U_R}{U_S} \right)^2 \quad (40)$$

is nearly constant for short bubbles about to burst; the constant value he suggested was 0.35. Since it seems better to correlate different experimental results on the pressure rise between transition and reattachment we will use a slightly different coefficient  $\sigma_{cr}$  defined by:

$$\sigma_{cr} = 1 - \left( \frac{U_R}{U_T} \right)^2 \quad (41)$$

If eq. (40) or (41) is to be used to predict whether reattachment will occur, the value of  $U_R$  at the possible reattachment point has to be known. In a first approximation this may be taken from the pressure distribution which would occur without the bubble being present, at the position  $x_{tr}$  (the 'inviscid pressure distribution').

In [35] Horton gave a method to predict whether and where reattachment may occur. This method is based on the simple criterion that  $\left( \frac{\theta}{U} \frac{dU}{dx} \right)_r = \text{constant} = -.0082$  for all turbulent shear layers.

Gaster [36] defined a bursting limit for the maximum value of the mean pressure gradient over the bubble  $-\frac{\theta_{sep}^2}{\nu} \frac{\Delta U}{\Delta x}$  as a function of  $R_{\theta_{sep}}$  (see fig. 1 and also chapter 8).

A simple criterion for bursting was found at LSL to be provided by Stratford's zero skin friction limiting pressure distribution [34]. This is the adverse pressure distribution which a turbulent boundary layer can just negotiate without separation. This limiting pressure distribution curve, starting at the measured transition point T (fig. 1) can at low Reynolds number fail to cross the 'inviscid pressure distribution curve'. This means that the requested pressure rise is more than the Stratford pressure recovery can provide and hence bursting occurs. For our experimental results on a Wortmann airfoil (chapter 7) this gave a very good prediction of the bursting Reynolds number.

In the airfoil design and analysis program at LSL we use at present the Stratford curve in a standard method to predict bursting.

## 7. SOME FURTHER EXPERIMENTAL RESULTS

Some further experimental results were obtained on a few different configurations [11]. In what follows these will be referred to as:

- Series 1: Wortmann airfoil FX66-S-196 V1,  $\alpha = 1$  degr in a small noisy tunnel.
- Series 2: The same Wortmann airfoil but now on a larger scale in the large low turbulence tunnel at LSL.
- Series 3: A circular cylinder with a wedge-shaped tail in the large tunnel (one of the configurations of [9]).
- Series 4: Same as series 3 but noise from the small tunnel recorded on tape and replayed in the test section of the large low turbulence tunnel.

Fig. 10 shows pressure distributions for series 1 for various chord Reynolds numbers. Below  $R_c = .118 \cdot 10^6$  bursting is seen to occur. Separation angles  $\gamma$  for this case were shown in fig. 4 already. Fig. 11

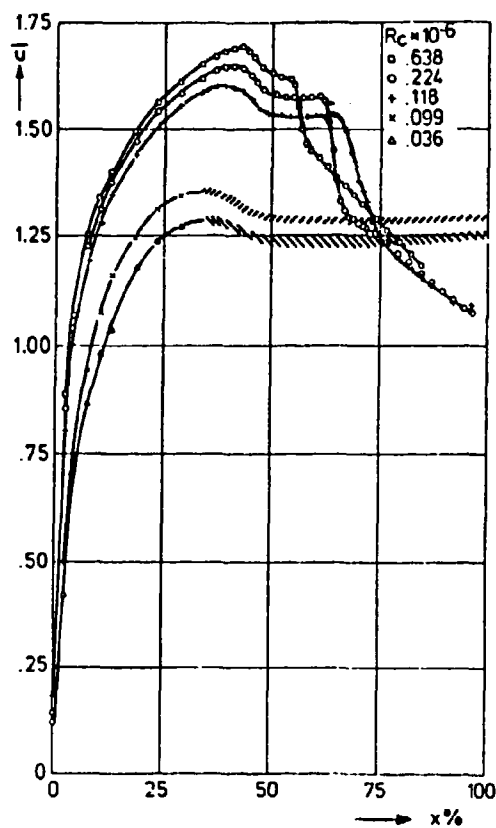


Fig. 10: Pressure distributions for series 1.

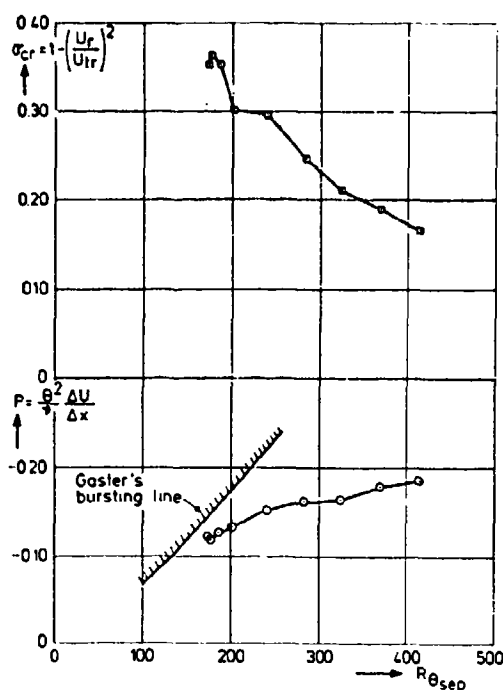


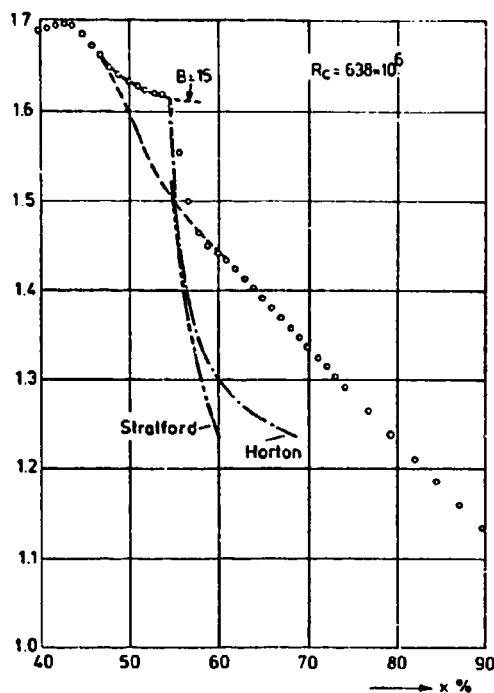
Fig. 11: Bursting parameters for series 1.

gives results for series 1, plotted in the way of Crabtree and Gaster; the figures indicate that a reasonable prediction of bursting would have resulted from both methods. Figs. 12a and 12b show the pressure distribution for the highest  $R_c$  and for the lowest Reynolds number

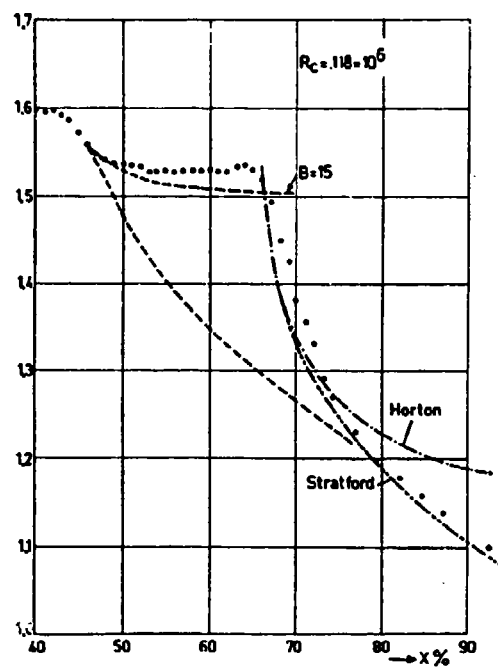
before bursting occurs. Indicated are predictions with the method referred to in chapter 3 for  $B = 15$  (note that at present we use  $B = 17.5$ ). Furthermore the critical curves according to Horton and Stratford are indicated. Bursting occurs as soon as the critical curves do no longer cross the 'inviscid pressure distribution'. It follows that at  $R_c = .118 \cdot 10^6$  bursting is nearly reached.

The length of the laminar part of the bubble (the distance between S and T in fig. 1) is shown for all series in fig. 13, plotted in a conventional way. There is a large scatter which is partly due to experimental error but certainly also due to the different 'effective turbulence levels'  $Tu$  in the various experiments. The grid, shown in fig. 13 is based on equations (28), (35) and (25); it should represent the effect of  $Tu$ .

A better idea of the experimental scatter follows from fig. 14 where only the results for series 2 are shown. The vertical bars indicate errors in  $\Delta x$  of  $\pm 0.5\%$  chord; hence the total length of the bar corre-



(a)  $R_C = .638 * 10^6$ .



(b)  $R_C = .118 * 10^6$ .

Fig. 12: Pressure distributions and critical curves for bursting for two cases; series 1.

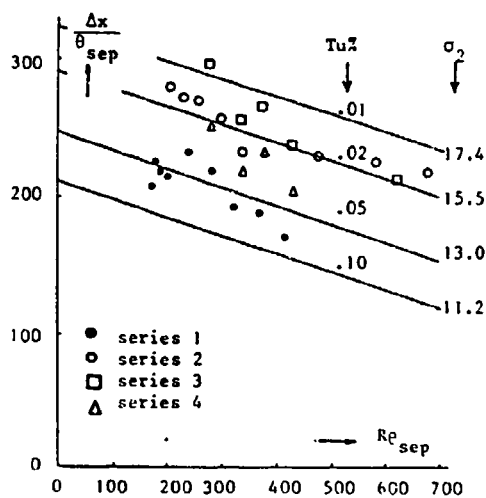


Fig. 13: Length of laminar part of the bubble; all series.

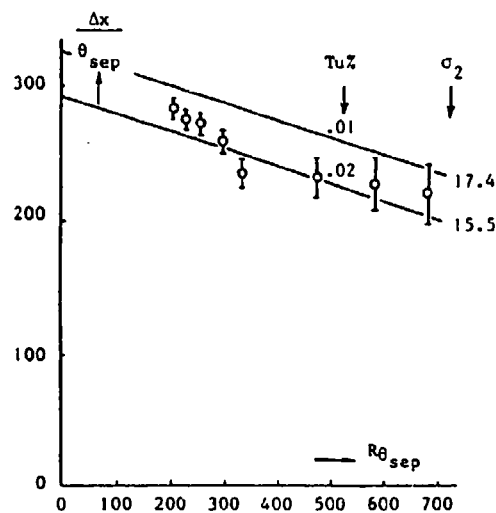


Fig. 14: Length of laminar part of the bubble; series 2.

sponds to 1% chord). With increasing  $R_{\theta_{sep}}$  the scatter band widens. A

better way of plotting is suggested by the linear approximation, discussed in chapter 5. As an example fig. 15 shows a replot of fig. 14 but now in the variables of chapter 5. The scatter band now has a more constant width; moreover the trend appears to be linear in accordance with the linear approximation in fig. 9 and equation (35). In fact this approximation was developed after the results of fig. 15 had been obtained. A compilation of the results for all series in the improved plot is given in fig. 16. Note that, although there remains some scatter, the experimental points seem to follow the linear trend for constant  $Tu$  (and hence constant  $\sigma_2$ ) as indicated by equation (35).

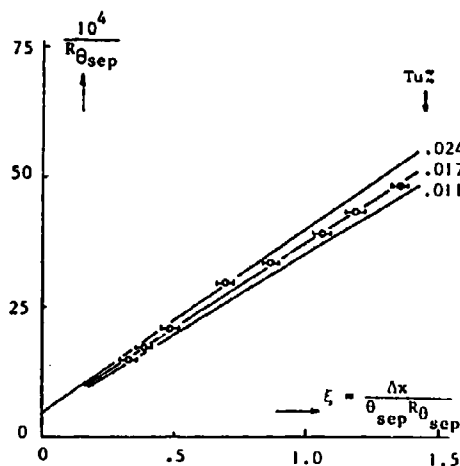


Fig. 15: Results for series 2; improved plot.

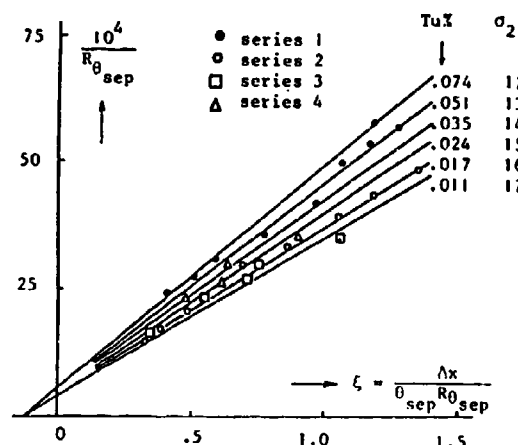


Fig. 16: Results for all series; improved plot.

## 8. SOME CONSEQUENCES FROM THE SIMPLE BUBBLE CALCULATION PROCEDURE

In previous chapters we derived a number of elements for a simple short-cut bubble calculation procedure using the reduced streamwise coordinate  $\xi$ . The non-dimensional edge velocity  $\bar{U}$  and momentum loss thickness  $\bar{\theta}$  follow from equations (19) and (20). For a given effective turbulence level  $Tu$ , the critical amplification factor follows from  $\sigma_2$  using equation (25). Then the value of  $\xi$  at transition follows from (28) and (35) for a known value of  $(R_{\theta})_{sep}$ . The Stratford limiting curve starting at T is uniquely determined by  $R_{\theta}$  at T which follows from  $\bar{U}$  and  $\bar{\theta}$  at T.

As an example fig. 17 shows results for  $Tu = 0.1\%$ . If a linear  $\bar{U}(\xi)$  distribution is assumed for the inviscid pressure distribution between S and R, possible bursting conditions follow from tangents to the Stratford curves going through S. From the points of tangency values for Crabtree's and Gasters parameters can be obtained. Note that Gasters

parameter  $P = -\frac{\theta_s^2}{v} \frac{\Delta U}{\Delta x}$  is equal to  $\frac{d\bar{U}}{d\xi}$  for the linear distribution.

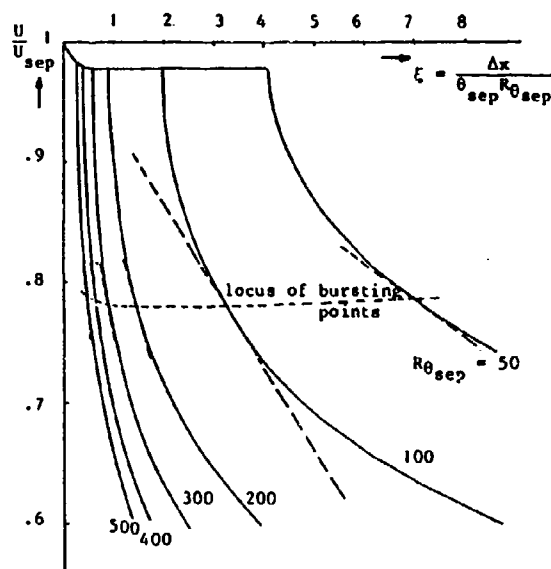


Fig. 17: Results of simple bubble calculation procedure;  $Tu = 0.1\%$ .

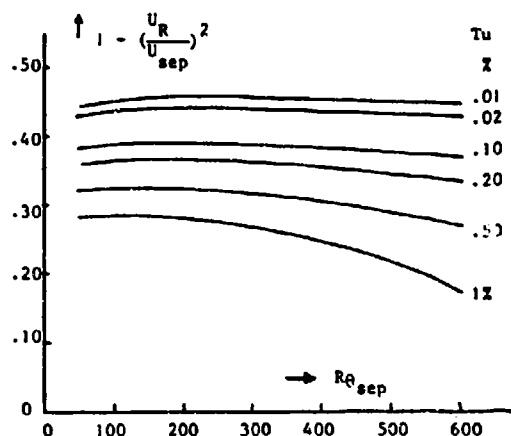


Fig. 18: Modified Crabtree parameter, eq. (41) according to the simple procedure.

Repeating this procedure for various values of  $Tu$  produced the results indicated in figs. 18 and 19. Fig. 18 gives the modified Crabtree parameter, equation (41), as a function of  $(R_\theta)_{sep}$  for various  $Tu$ . It follows that indeed the pressure recovery coefficient is very nearly constant for a given value of  $Tu$ , except at the very high turbulence levels.

Fig. 19 gives Gasters parameter for various  $Tu$  as a function of  $(R_\theta)_{sep}$ :

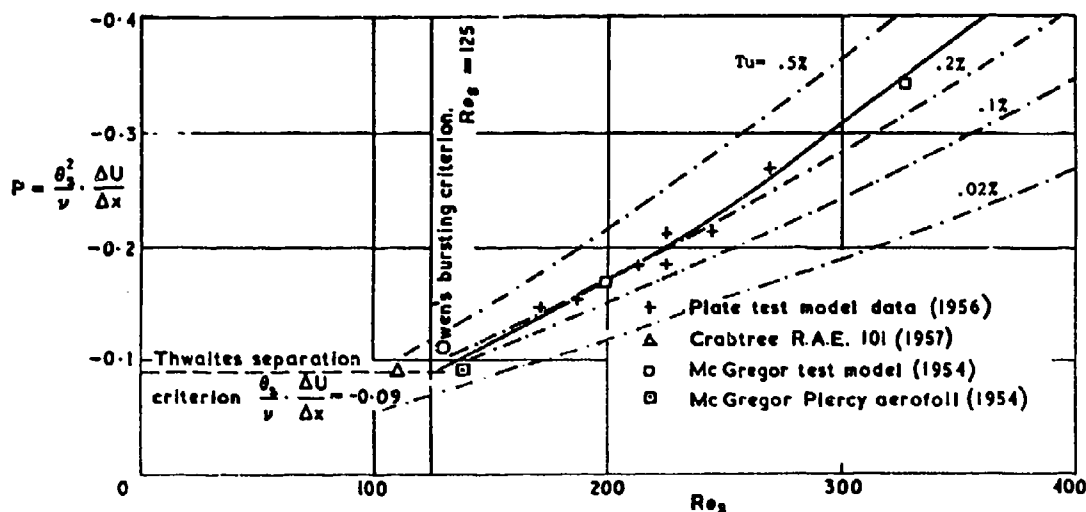


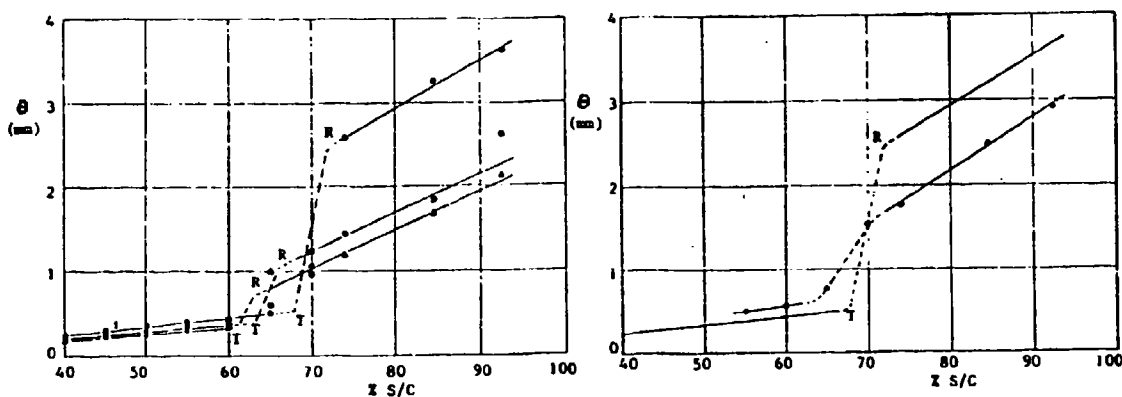
Fig. 19: Gasters bursting parameter according to the simple procedure; -- present results for various  $Tu$ .

the limiting curve given by Gaster in [36] is indicated in the figure. It follows that the present method reproduces Gaster's curve for  $Tu$  about equal to 0.2%.

## 9. MORE DETAILED INVESTIGATIONS OF THE BUBBLE FLOW

In applications of the LSL airfoil program it was found that at low Reynolds numbers the program underestimates the airfoil drag. This is due to using improper starting conditions for the turbulent boundary layer calculation downstream of reattachment. Therefore a more detailed investigation of the flow in separation bubbles was started. Lack of space does not permit to discuss this in detail.

Some results of boundary layer measurements with a traversing total head tube for the Wortmann airfoil (series 1) are shown in fig. 20 [27]. It is seen that a strong increase of  $\theta$  between T and R occurs. It also follows that early tripping of the boundary layer may reduce the downstream value of  $\theta$  and hence also the drag.



(a)  $\theta(x)$  for three values of  $R_c$ ;  $0.154 \cdot 10^6$ ;  $0.218 \cdot 10^6$ ;  $C$  (b) The effect of tripping on  $\theta(x)$  at  $R_c = 0.154 \cdot 10^6$ .

Fig. 20: Results of boundary layer measurements for the Wortmann airfoil (series 1).

Similar results for the HQ 17/14.38 airfoil, now obtained using a single hot-wire, and including turbulence intensity are shown in fig. 21a and 21b. A detailed discussion of these results may be found in [20]. Wall shear stress distributions were also obtained using Preston tubes. Measurements with cross-wires in a boundary layer channel have shown [38] that the turbulent shear stress downstream of reattachment is much larger than would be predicted by the usual mixing length models. A research program on the development of turbulence through separation, transition and reattachment is being started at LSL.

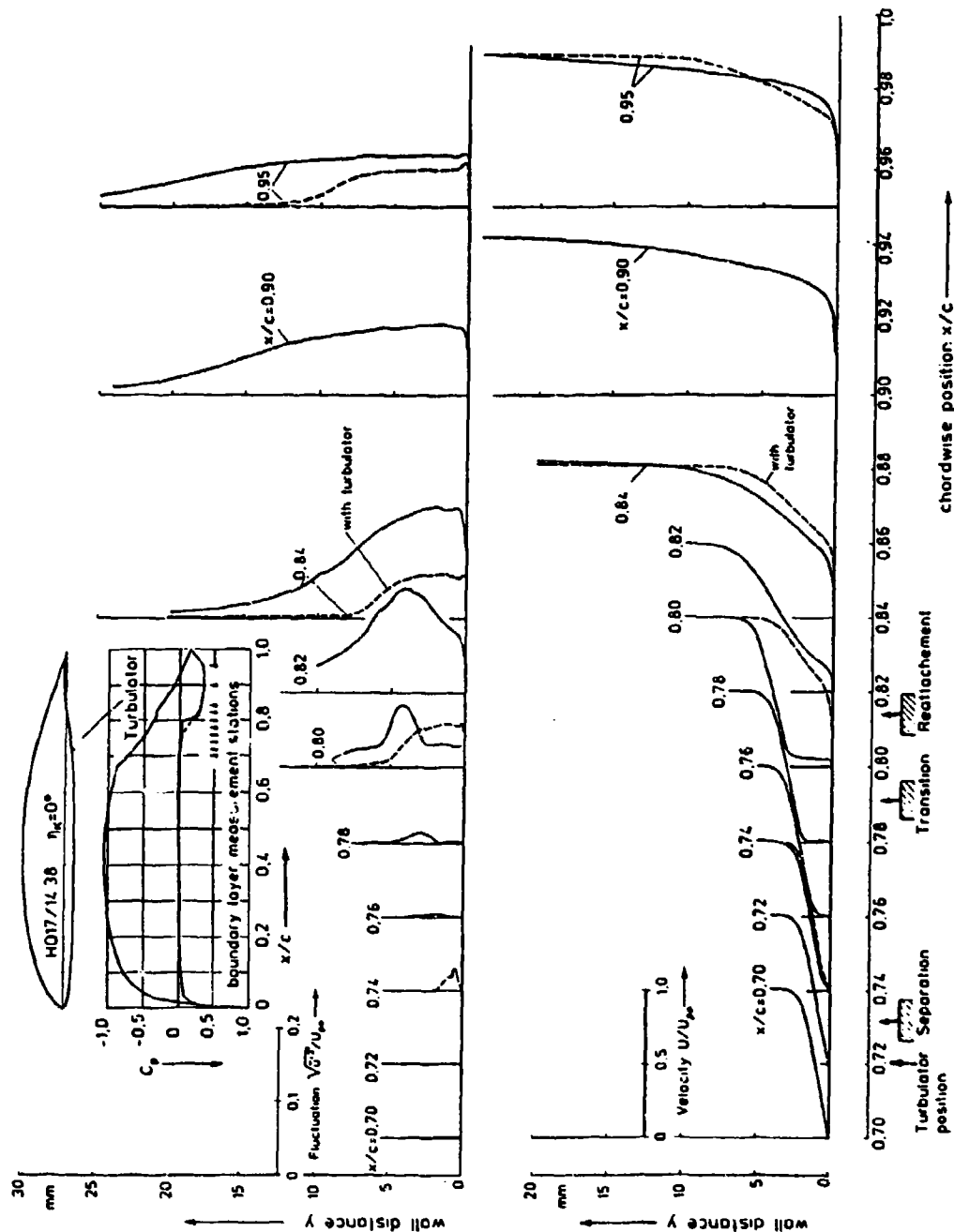


Figure 21a. Boundary layer velocity  $U/U_\infty$  and fluctuation  $\sqrt{u'^2}/U_\infty$  profiles for lower surface of airfoil HQ 17/14.38 with and without laminar separation bubble,  $Re = 2 \cdot 10^6$

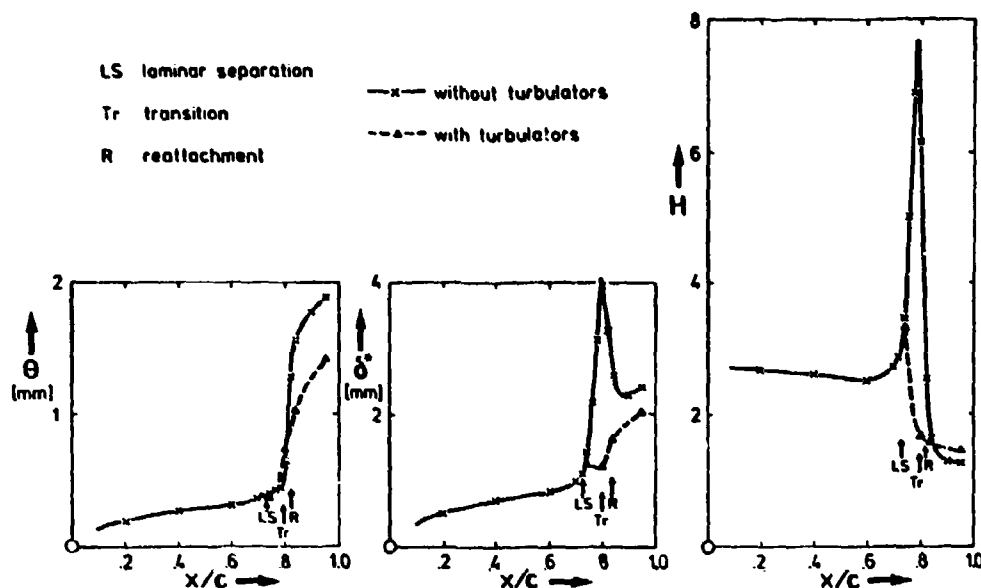


Fig. 21b: Integral boundary layer parameters for the HQ 17/14.38 airfoil; derived from fig. 21a.

#### 10. SOME TYPICAL RESULTS OF LOW REYNOLDS NUMBER AIRFOIL TESTS

In this chapter some typical examples of experimental results are described in which laminar separation bubbles, and the elimination of them, play an important role with respect to airfoil characteristics. All measurements, ranging from  $Re_c = .5 \cdot 10^5$  to  $2.5 \cdot 10^6$ , were performed in the Low-Speed Low Turbulence Wind tunnel of LSL.

Fig. 22 shows the measured characteristics of a well-known airfoil designed by Eppler for model airplane application, E 205. The measuring technique is briefly described in [43]; a model with span 0.75 m and chord 0.15 m was suspended between two reflexion plates at the tips and with one tip connected to the wind tunnel balance system. The lift was measured with the balance system, the drag was measured with a wake rake connected to a sensitive Mensor Quartz manometer.

Oil flow patterns and stethoscope measurements show that the flow on the lower surface is laminar at angles of attack higher than about -2 degr. At lower angles of attack transition moves forward rapidly and a laminar separation bubble appears near the nose of the airfoil. Large laminar separation bubbles are present on the upper surface of the airfoil. For instance at  $\alpha = 5$  degr. and  $Re_c = 1 \cdot 10^5$  laminar separation occurs at 25% c, transition at 62% c and reattachment at 70% c. At  $Re_c = .6 \cdot 10^5$

the separated boundary layer fails to reattach on the airfoil surface between  $\alpha = 2$  degr and roughly 8 degr (hysteresis). At higher angles of attack there is a laminar separation bubble on the forward part of the airfoil and turbulent separation on the rearward part at all Re-numbers. The flow behaviour and characteristics of this airfoil are very similar to E 387 [43] which was also measured with a 0.6 mm trip wire positioned 10% c in front of the airfoil and 2.7% c below the chord line. This

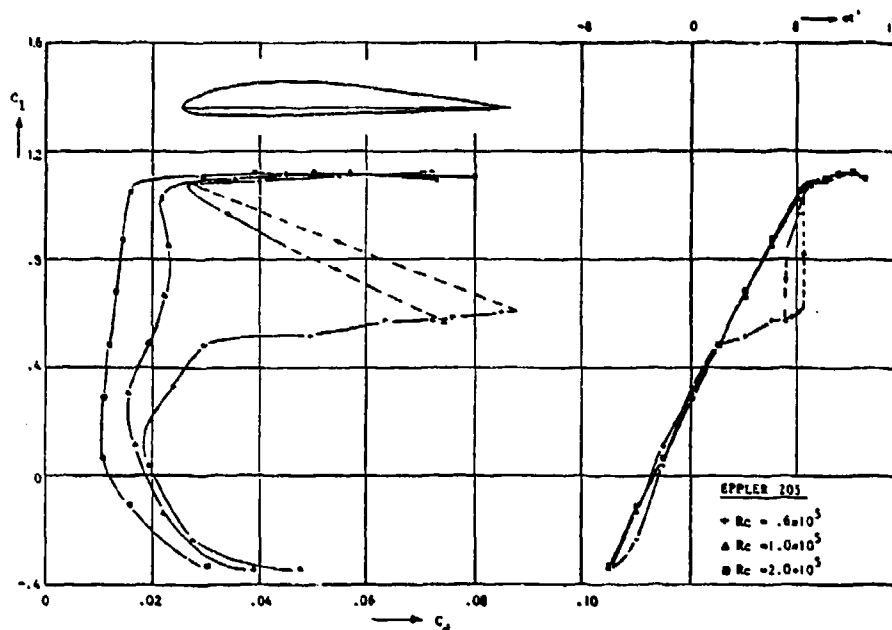


Fig. 22: Measured aerodynamic characteristics of airfoil E205.

position of the wire, which guarantees attached flow at  $R_c = .6 \times 10^5$ , was obtained by translating the wire in front of the airfoil at several angles of attack. Similar results may be expected with a trip wire in front of airfoil E 205.

Fig. 23 shows some measured characteristics of another low Reynolds number airfoil, E 61, measured in the same way [44]. Again, the flow on the lower surface is laminar at angles of attack higher than 1 degr. At decreasing angles of attack transition moves forward rapidly and a laminar separation bubble appears on the first 20% c at 0 degr and -1 degr. At -1.5 degr angle of attack a long bubble extending to about 60% c is present. On the upper surface reattachment fails at angles of attack below about 6 degr. At 6.5 degr a laminar separation bubble is present between 50% c and 85% c while turbulent separation occurs at 95% c. At increasing angles of attack the bubble decreases in length and moves forward, as does the turbulent separation position.

To provoke transition, single frequency sound was radiated perpendicular to the upper wing surface; the sound pressure level (SPL) at the wing surface was measured at the actual wind speed. At 4.8 degr angle of attack the sound pressure level and frequency (estimated from boundary layer instability calculations first) were varied systematically. The most effective sound frequency was 300 Hz at  $R_c = .8 \times 10^5$  (and 145 Hz at  $R_c = .5 \times 10^5$ ). Fig. 23 shows the effect of both frequencies and SPL 104 dB on the characteristics. Fig. 24 shows an example of the effect of the sound pressure level on the lift and drag, indicating the sensitivity of the flow and hence the measured airfoil characteristics for sound disturbances in the tunnel flow.

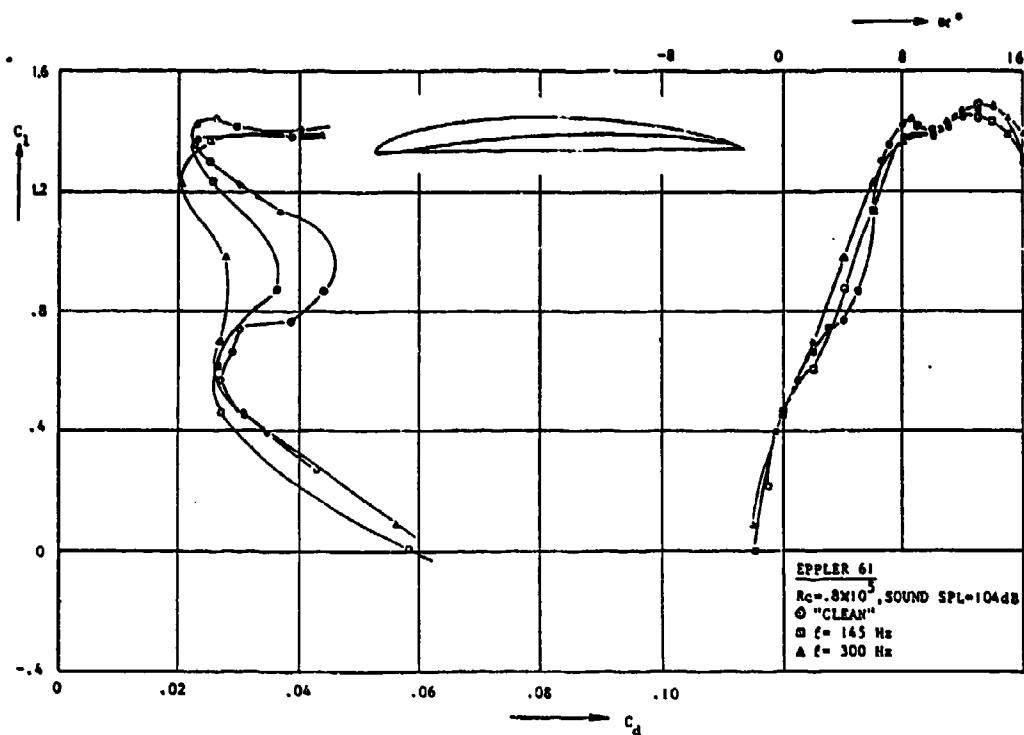


Fig. 23: Measured aerodynamic characteristics of airfoil E61 and the effect of single frequency sound disturbances.

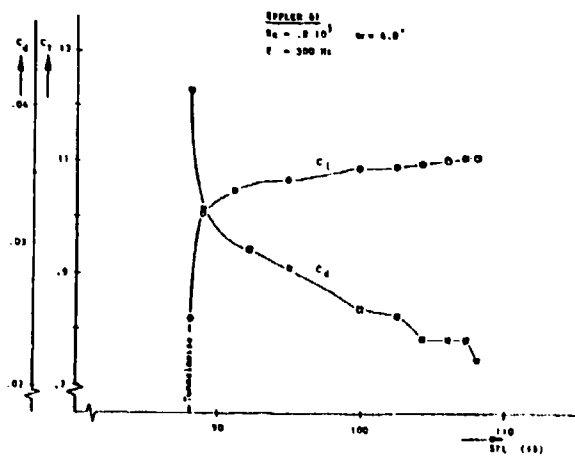


Fig. 24: Effect of sound pressure level on lift and drag coefficient of E61.

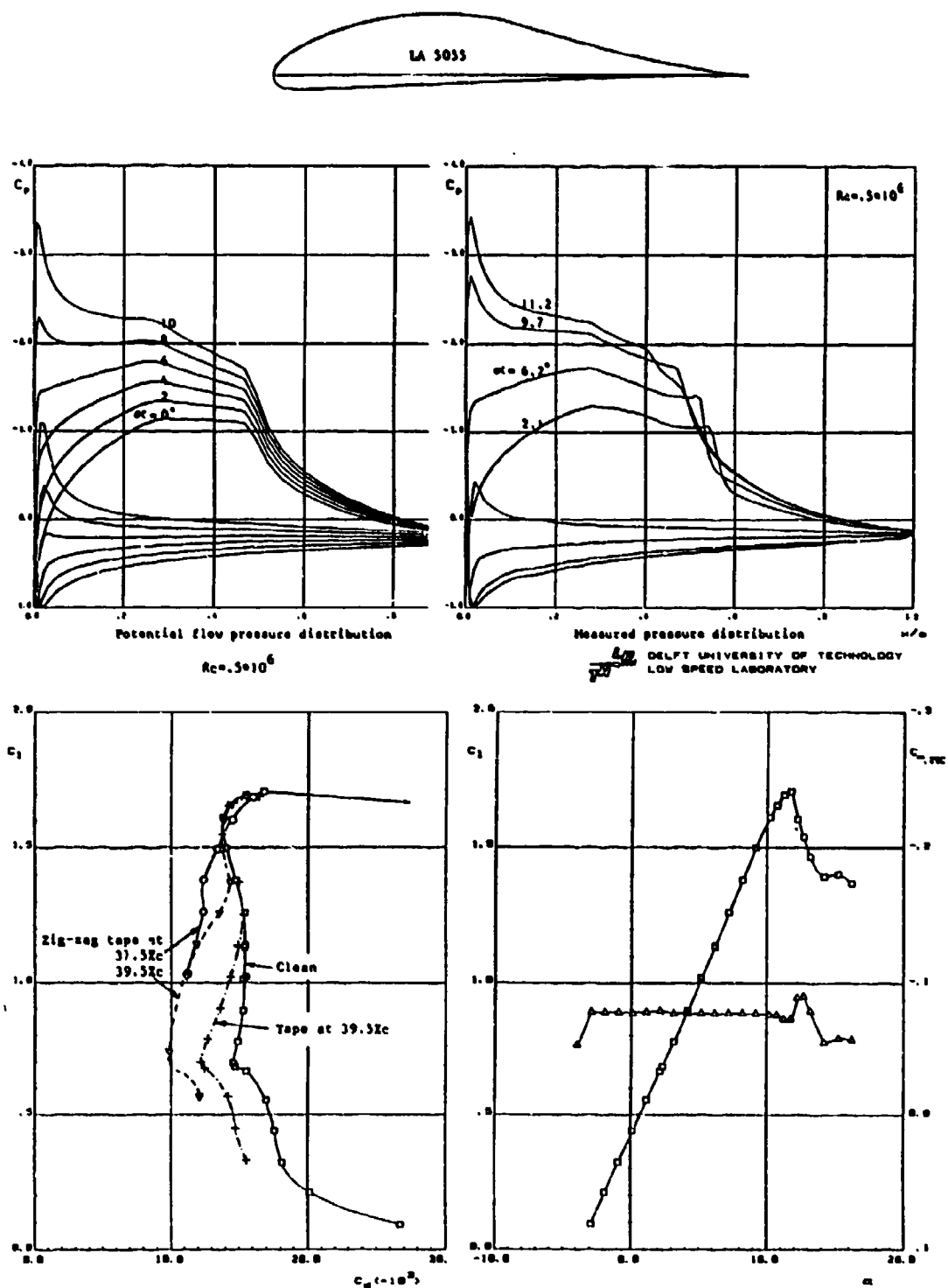


Fig. 25: Aerodynamic characteristics and pressure distributions of airfoil LA5055; effect of straight tape and zig-zag tape.

In the next examples the results were obtained by pressure measurements with models spanning the height of the wind tunnel test section (height 1.25 m, width 1.80 m).

Fig. 25 shows some results of the Liebeck LA 5055 airfoil [45]. To prevent early separation near the tunnel walls, suction was applied in a small region on the walls along the upper surface. The airfoil, designed for  $C_L = 1.04$  at  $\alpha = 4.82$  degr and  $R_c = 0.6 \cdot 10^6$ , has a distinct instability region between 27% c and 47% c upper surface, as shown in the potential flow pressure distributions. However, (detrimental) laminar separation bubbles are present at  $R_c = 0.5 \cdot 10^6$  (and  $R_c = 1 \cdot 10^6$ , not shown here) as shown in the measured pressure distributions. The flow on the lower surface is laminar at angles of attack higher than 2 degr. A strip of tape, height 0.25 mm and width 11 mm, positioned at 39.5% c, shows improvement at lift coefficients below 1.25. A zig-zag form, cut from the same tape (the idea was to strengthen the tendency of the Tollmien-Schlichting waves to become three-dimensional by matching the zig-zags to the expected spanwise wave length) shows a remarkable improvement, positioned at 39.5% c and 37.5% c. Similar results were obtained at  $R_c = 1 \cdot 10^6$ . In fact, no better results could be obtained with tape with digged-in bumps every 5 mm span of height 0.65 mm or 1 mm, positioned between 39% c and 47% c. Finally, it is mentioned that the maximum lift coefficient of 1.61 at  $R_c = 1 \cdot 10^6$  could be raised to 2.27 with semi triangular vortex generators [46] positioned at 20% c, despite of the very steep Stratford type pressure distribution on the rearward part of the airfoil.

Fig. 26 shows results of measurements on the DU 80-176 airfoil, designed at our institute for sailplane application [14]. Oil flow patterns indicated the absence of a laminar separation bubble on the upper surface at practical combinations of lift coefficient and Reynolds number,

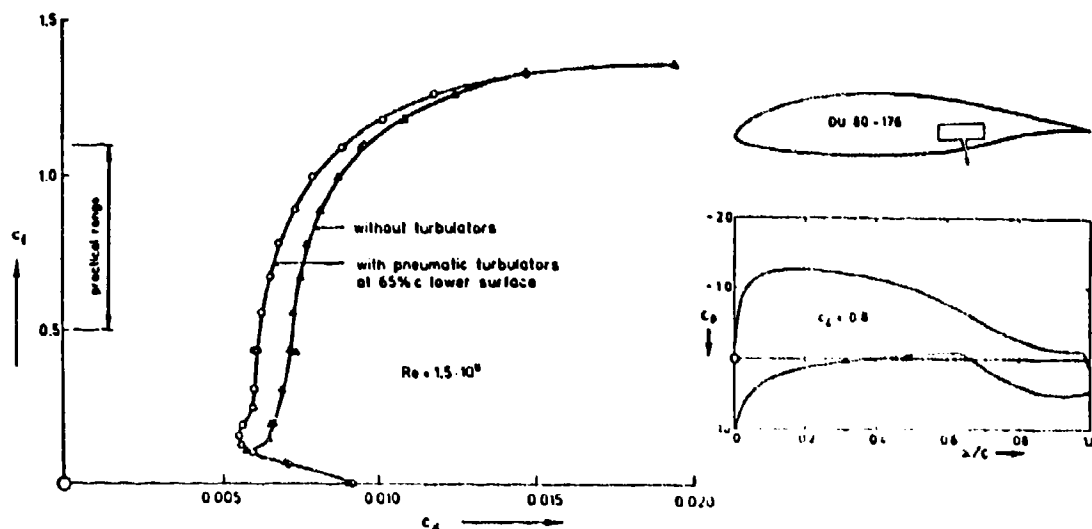


Fig. 26: Drag polars and potential flow pressure distribution of airfoil DU 80-176; effect of pneumatic turbulators.

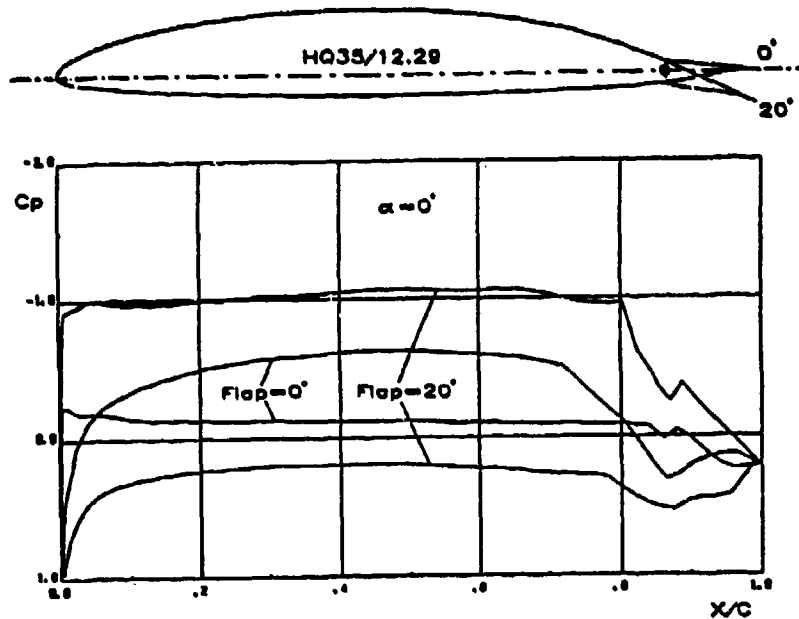


Fig. 27: Measured pressure distribution of airfoil HQ 35/12.29 (flap = 0 degr,  $R_c = 2 \times 10^6$ ; flap = 20 degr,  $R_c = 1 \times 10^6$ ).

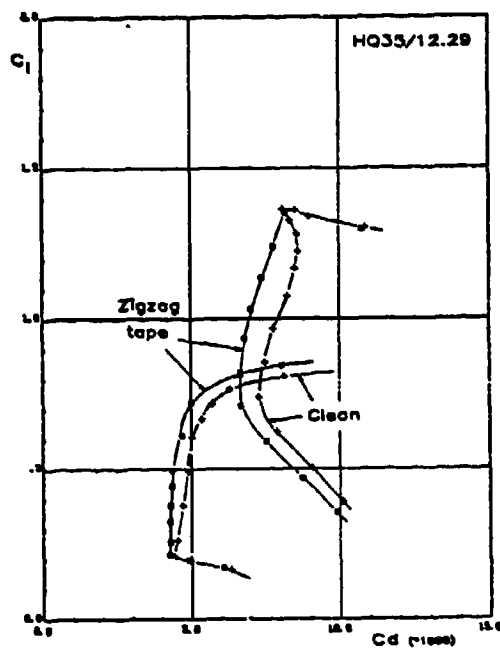


Fig. 28: Effect of zig-zag tape at 69% c upper surface and 83% c lower surface.

and the existence of a pronounced laminar separation bubble on the lower surface downstream of the pressure rise at 65% c, as intended. This bubble was eliminated and the drag reduced, fig. 26, by using pneumatic turbulators at 65% c, i.e. blowing a small amount of air through orifices periodically spaced in spanwise direction [20]. They function like roughness with adjustable height [16].

A slightly more cambered version of this airfoil was applied in modifying the wing of an existing high performance sailplane just by adding material to the surface. An air intake nozzle for each wing half with a diameter of only 6.5 mm was needed for the 870 pneumatic turbulators to do their job. Flight performance measurements before and after the wing modification showed an improvement of about 5% in glide ratio over the entire flight speed range.

Several types of high performance sailplanes are provided with pneumatic turbulators nowadays.

Another airfoil for sailplane application, HQ 35/12.29, designed by K.H. Horstmann and A. Quast of DFVLR Braunschweig (West-Germany), is shown in fig. 27. This 12.29% c thin airfoil has a camber changing flap of 13.5% chord length. In actual practice this flap extends along the whole span of the sailplane wing. Very long laminar flow regions are present on both the upper and lower surface as shown in the measured pressure distributions. Due to the stability of the laminar boundary layer and the pressure rise on the rear of the airfoil, laminar separation bubbles are present again. Fig. 28 shows the drag decrease obtained with zig-zag

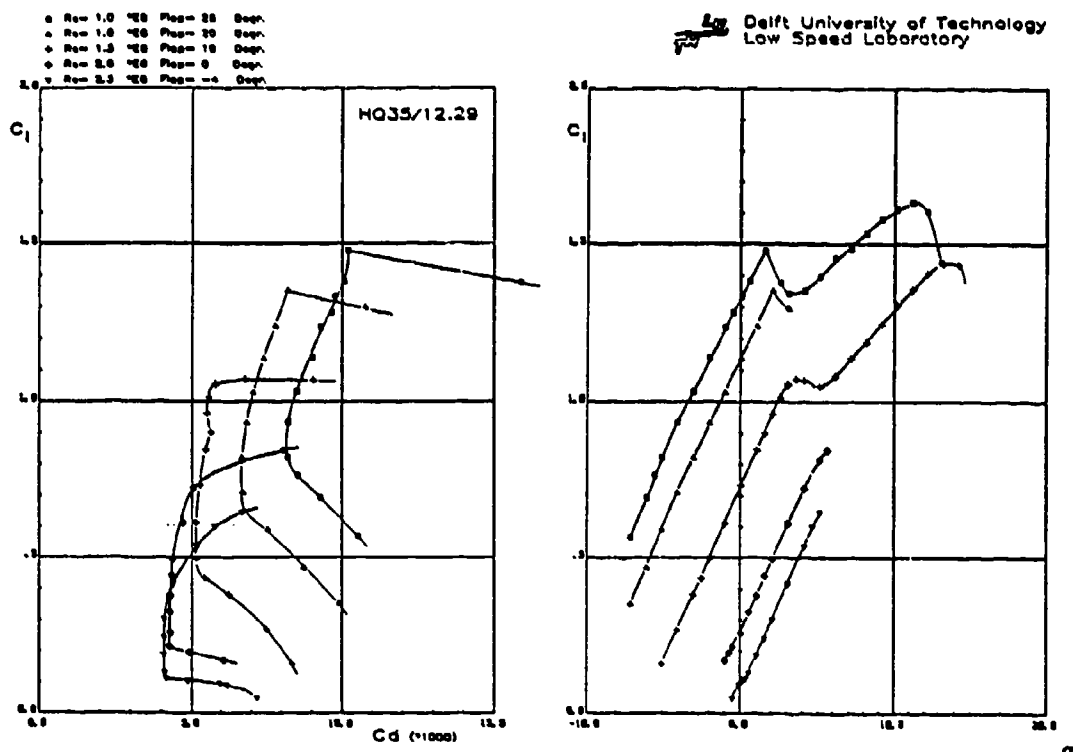


Fig. 29: Measured aerodynamic characteristics of airfoil HQ 35/12.29 with zig-zag tape at 69% c upper surface and 83% lower surface.

tape, mentioned before, at 69% c on the upper surface and 83% c on the lower surface, and fig. 29 presents the airfoil characteristics with these triggering devices at several practical combinations of Reynolds number and flap deflection.

The concave corner in the upper and/or lower surface contour at the flap hinge leads to local separation of the turbulent boundary layer. Systematically filling and rounding of this corner did not result in a drag reduction. More research is needed to exploit this phenomenon.

## 11. NOMENCLATURE

The symbols used are the conventional ones. Only a few are mentioned specifically below. Because the material of this paper is taken from various existing papers, some symbols have more than one meaning.

B	constant, eq. ( )
c	chord length
F	$F(\xi)$ , eq. (28) and (34)
g	$y_3/\theta$ ; shape parameter
H	$\delta^*/\theta$
I	envelope of $10^4 \int (-\alpha_i \theta) dz$
$\ell$	$\tau_0 \theta(uU)$
m	$-\frac{\theta^2}{v} \frac{dU}{dx}$
P	$-\frac{\theta^2}{v} \frac{\Delta U}{\Delta x}$ , Gasters parameter, fig. 1
$R_c$	$U_\infty c/v$
$R_\theta$	$U\theta/v$
s	distance along wall
Tu	turbulence level; %
U	edge velocity
$U_{po}$	hypothetical inviscid flow velocity at the surface
$U_\infty$	free stream speed
$\bar{U}$	$U/U_\infty$ in figs. 10 and 12; $U/U_{sep}$ elsewhere
$\Delta U$	see fig. 1
x	distance along wall, in general measured from separation point
x/c	non-dimensional distance along chord
$\Delta x$	sometimes ST in fig. 1
$\Delta x$	sometimes SR in fig. 1
y	distance from wall
$y_1$	y for $\tau = 0$
$y_2$	y for $u = 0$
$y_3$	y for separation streamline
z	$g * m_{sep}$
$\alpha$	$\alpha_r + i\alpha_i$
$-\alpha_i$	spatial amplification rate

$R_c$	$U_\infty c/\nu$
$R_\theta$	$U\theta/\nu$
$s$	distance along wall
$Tu$	turbulence level; %
$U$	edge velocity
$U_{po}$	hypothetical inviscid flow velocity at the surface
$U_\infty$	free stream speed
$\bar{U}$	$U/U_\infty$ in figs. 10 and 12; $U/U_{sep}$ elsewhere
$\Delta U$	see fig. 1
$x$	distance along wall, in general measured from separation point
$x/c$	non-dimensional distance along chord
$\Delta x$	sometimes ST in fig. 1
$\Delta x$	sometimes SR in fig. 1
$y$	distance from wall
$y_1$	$y$ for $\tau = 0$
$y_2$	$y$ for $u = 0$
$y_3$	$y$ for separation streamline
$z$	$g * m_{sep}$
$\alpha$	$\alpha_r + i\alpha_i$
$-\alpha_i$	spatial amplification rate
$\beta$	Falkner-Skan parameter
$\gamma$	separation angle (fig. 1)
$\delta^*$	displacement thickness
$\theta$	momentum loss thickness
$\bar{\theta}$	$\theta/\theta_{sep}$
$\sigma$	amplification factor; eq. (23)
$\sigma_a$	envelope of $\sigma$ -x
$\sigma_1$	$\sigma$ at beginning of transition
$\sigma_2$	$\sigma$ at end of transition
$\sigma_{turb}$	$0.5(\sigma_1 + \sigma_2)$
$\sigma$	Crabtree parameter, fig. 1
$\sigma_{cr}$	modified Crabtree, fig. 1
$\omega_{cr}$	disturbance frequency
$\xi$	$\frac{x}{\theta_{sep}(R_\theta)_{sep}}$

#### Subscripts:

$S, s, sep$	separation
$T, tr$	transition
$R, r$	reattachment

$\beta$	Falkner-Skan parameter
$\gamma$	separation angle (fig. 1)
$\delta^*$	displacement thickness
$\theta$	momentum loss thickness
$\bar{\theta}$	$\theta/\theta_{\text{sep}}$
$\sigma$	amplification factor; eq. (23)
$\sigma_a$	envelope of $\sigma$ -x
$\sigma_1$	$\sigma$ at beginning of transition
$\sigma_2$	$\sigma$ at end of transition
$\sigma_{\text{turb}}$	$0.5(\sigma_1 + \sigma_2)$
$\sigma$	Crabtree parameter, fig. 1
$\sigma_{\text{cr}}$	modified Crabtree, fig. 1
$\omega$	disturbance frequency
$\xi$	$\frac{x}{\theta_{\text{sep}} (R)_{\theta_{\text{sep}}}}$

#### Subscripts:

S, s, sep	separation
T, tr	transition
R, r	reattachment

## 12. ACKNOWLEDGEMENTS

The authors are indebted to their colleagues of the scientific, technical and administrative staff at the Department of Aerospace Engineering for their continuing support during the execution of the research program described in this paper.

They also wish to express their appreciation to DFVLR, Institut für Entwurfsaerodynamik, Braunschweig, for permission to publish the HQ 35/12.29 results which were obtained at LSL under contract with DFVLR.

## 13. REFERENCES

1. Cornish, J.J., 'Airfoil analysis and synthesis utilizing computer graphics', SAE Paper 670845, 1967.
2. Haas, M.E. and Ingen, J.L. van, 'Computer graphics techniques applied to airfoil design', Software Age, Vol. 1, nr 1, September 1967, pp. 34-42.
3. Ingen, J.L. van, 'Advanced computer technology in aerodynamics': a program for airfoil section design utilizing computer graphics. Lecture notes for Von Karman Institute of Fluid Dynamics (1969), AGARD lecture series no. 37 'High Reynolds-number subsonic aerodynamics', pp. 8.1-8.33, 1970.

4. Timman, R., 'The direct and inverse problem of aerofoil theory'. A method to obtain numerical solutions. National Aerospace Laboratory NLR, Amsterdam, report NLL-F16, 1951.
5. Thwaites, B., 'Approximate calculation of the laminar boundary layer'. Aeron. Quart., 1, pp. 245-280, 1949.
6. Smith, A.M.O., Gamberoni, N., 'Transition, pressure gradient, and stability theory', Douglas Aircraft Co., report ES 26388, 1956.
7. Ingen, J.L. van, 'A suggested semi-empirical method for the calculation of the boundary layer transition region'. Delft University of Technology, Dept. of Aerospace Engineering, report VTH-74, 1956.
8. Head, M.R., 'Entrainment in the turbulent boundary layer', R and M 3152, 1958.
9. Dobbinga, E., Ingen, J.L. van, Kooi, J.W., 'Some research on two-dimensional laminar separation bubbles', AGARD CP-102, paper nr. 2, Lisbon, 1972.
10. Ingen, J.L. van, 'On the calculation of laminar separation bubbles in two-dimensional incompressible flow'. In AGARD CP-168: 'Flow Separation', Göttingen, 1975.
11. Ingen, J.L. van, 'Transition, pressure gradient, suction, separation and stability theory'. In AGARD CP-224: Laminar-Turbulent Transition, Copenhagen, 1977.
12. Ingen, J.L. van, Boermans, L.M.M. and Blom, J.J.H., 'Low speed airfoil section research at Delft University of Technology. ICAS-80-10.1, Munich, 1980.
13. Ingen, J.L. van, 'On the analysis and design of low speed airfoils using potential flow methods and boundary layer theory'. Report LR-365, Department of Aerospace Engineering, Delft University of Technology, 1982.
14. Boermans, L.M.M. and Selen, H.J.W., 'Design and tests of airfoils for sailplanes with an application to the ASW-19B'. ICAS paper 82-5.5.2, 1982.
15. Boermans, L.L.M., Selen, H.J.W. and Wijnheijmer, M.L., 'Wind tunnel tests on two wing segments of the ASW-19 sailplane'. Memorandum M-379, Delft University of Technology, Dept. of Aerospace Engineering, 1980.
16. Boermans, L.M.M. and Oolbekkink, B., 'Wind tunnel tests on an outer wing segment of the ASW-19X sailplane'. Report LR-369, Delft University of Technology, Department of Aerospace Engineering, 1983.

17. Boermans, L.M.M. and Blom, J.J.H., 'Low-speed aerodynamic characteristics of an 18% thick airfoil section designed for the all-flying tailplane of the M-300 sailplane'. Delft University of Technology, Dept. of Aerospace Engineering, report LR-226, 1976.
18. Pfenninger, W., 'Untersuchungen über Reibungsverminderungen an Tragflügeln, insbesondere mit Hilfe von Grenzschichtabsaugung'. Mitt. a.d. Inst. f. Aerodynamik, ETH Zürich Nr. 13, Verlag Gebr. Leeman & Co., Zürich, 1946.
19. Horstmann, K.H. and Quast, A., 'Widerstandsverminderung durch Blästurbulatoren'. DFVLR-FB 81-33, 1981.
20. Horstmann, K.H., Quast, A. and Boermans, L.M.M., 'Pneumatic turbulators - a device for drag reduction at Reynolds numbers below  $5 \times 10^6$ '. Paper no. 20 in AGARD CP-365, Brussels, 1984.
21. Legendre, R., 'Décollement laminaire régulier'. Comptes Rendus 241, pp. 732-734, 1955.
22. Oswatitsch, K., 'Die Ablosungsbedingung von Grenzschichten'. In: Grenzschichtforschung/Boundary layer research. IUTAM Symposium, Freiburg/Br. 1957, Springer Verlag, pp. 357-367, 1958.
23. Batchelor, G.K., 'An introduction to fluid dynamics', Cambridge Univ. Press, 1970.
24. Smith, A.M.O., 'Improved solutions on the Falkner-Skan boundary layer equation'. Sherman M. Fairchild Fund Paper FF-10, Inst. Aero. Sci. 1954.
25. Stewartson, K., 'Further solutions of the Falkner-Skan equation'. Proc. Cambr. Soc, 50, pp. 454-465, 1954.
26. Goldstein, S., 'On laminar boundary layer flow near a position of separation'. Quart. J. Mech. Appl. Math. Vol. 1, pp. 43-69, 1948.
27. Liu, C.Y. and Sandborn, V.A., 'Evaluation of the separation properties of laminar boundary layers', the Aeron. Quarterly, Vol. XIX, Aug. 1968, part 3, pp. 235-242.
28. Ingen, J.L. van, 'Theoretical and experimental investigations of incompressible laminar boundary layers with and without suction'. Report VTH-124, Delft University of Technology, Dept. of Aerospace Engineering, 1965.
29. Mack, L.M., 'A numerical method for the prediction of high-speed boundary-layer transition using linear theory'. Paper nr. 4 in Aerodynamic analysis requiring advanced computers; NASA SP-347, 1975.
30. Wazzan, A.R., Okamura, T.T. and Smith, A.M.O., 'Spatial and temporal stability charts for the Falkner-Skan boundary layer profiles'. DAC 67086, Sept. 1968, McDonnell Douglas Corp.

31. Kummerer, H., 'Numerische Untersuchungen zur Stabilität ebener laminarer Grenzschichtströmungen'. Dissertation Technische Hochschule, Stuttgart, 1973.
32. Taghavi, H. and Wazzan, A.R., 'Spatial stability of some Falkner-Skan profiles with reversed flow'. Physics of Fluids, Vol. 17, no. 12, Dec. 1974, pp. 2181-2183.
33. Stratford, B.S., 'Flow in the laminar boundary layer near separation'. R and M 3002, 1957.
34. Stratford, B.S., 'The prediction of separation of the turbulent boundary layer'. Journal of Fluid Mechanics, Vol. 5, pt. 1, January 1959, pp. 1-16.
35. Horton, H.P., 'A semi-empirical theory for the growth of laminar separation bubbles. A.R.C.-CP 1073, 1967.
36. Gaster, M., 'The structure and behaviour of laminar separation bubbles'. In: AGARD CP4, Separated Flows, 1966, part 2, pp. 813-854.
37. Vogelaar, H., 'An experimental investigation of the laminar separation bubble on a Wortmann FX 66 S 196V1 wing section with and without a trip wire'. Engineering Thesis. Delft, September 1981.
38. Oudheusden, B. van, 'Experimental investigation of transition and the development of turbulence in boundary layer flow in an adverse pressure gradient'. Engineering Thesis, Delft, March 1985 (limited distribution).
39. Schubauer, G.B. and Skramstad, H.K., 'Laminar boundary layer oscillations and transition on a flat plate'. NACA Report 909, 1948.
40. Hall, D.J. and Gibbings, J.C., 'Influence of stream boundary layer transition'. Journal Mechanical Engineering Science, Vol. 14, no. 2, pp. 134-146 (1972).
41. Wells, C.S., 'Effects of free stream turbulence on boundary layer transition'. AIAA Journal, Vol. 5, No. 1, January 1967, pp. 172-174.
42. Spangler, J.G. and Wells, C.S., 'Effects of free stream disturbances on boundary-layer transition'. AIAA Journal, Vol. 6, No. 3, March 1968, pp. 543-545.
43. Volkers, D.F., 'Preliminary results of wind tunnel measurements on some airfoil sections at Reynolds numbers between  $0.6 \cdot 10^5$  and  $5.0 \cdot 10^5$ . Memorandum M-276, Department of Aerospace Engineering, Delft University of Technology, 1977.
44. Boermans, L.M.M., Vries, J. de and Hegen, G.H., 'Preliminary results of wind tunnel measurements at low Reynolds numbers on airfoil section E 61'. Intern Rapport LSW 80-5, LSL, Department of Aerospace Engineering, Delft University of Technology, 1980.

45. Timmer, W.A., 'Experimental low speed aerodynamic characteristics of the Liebeck LA 5055 airfoil'. To be published as a Report by Department of Aerospace Engineering en Institute for Windenergy, Delft University of Technology.
46. Wentz, W.H. and Seetharam, H.C., 'Development of a fowler flap system for a high performance general aviation airfoil'. NASA CR-2443, 1974.
47. Crabtree, L.F., 'The formation of regions of separated flow on wing surfaces'. R and M 3122, 1959.

# AN ANALYSIS OF A SEPARATION BUBBLE TRANSITION CRITERION AT LOW REYNOLDS NUMBERS

Gordon S. Schmidt  
Matthew M. O'Meara  
Thomas J. Mueller

Aerospace and Mechanical Engineering  
University of Notre Dame  
Notre Dame, Indiana 46556

## ABSTRACT

An investigation of a simple criterion governing the length of a separation bubble's laminar portion was conducted. This criterion stated that transition occurs in a separation bubble when a critical value of the Reynolds number based on the external velocity at separation and the distance from the point of laminar separation was exceeded. The focus of the present study was to determine the factors influencing this criterion within the context of separation bubbles formed on low Reynolds number airfoils. Using measurements of the flow about a NACA 663-018 airfoil obtained at chord Reynolds numbers ranging from 50,000 to 200,000, it was found that several factors affect this criterion. These included the chord Reynolds number, the angle of attack, and the free stream disturbance environment. Finally, it was found that, for the turbulence levels considered ( $< 0.2\%$ ), turbulence intensity did not significantly affect the transition Reynolds number.

## INTRODUCTION

A separation bubble (Figure 1) significantly influences the performance of subsonic airfoils operating at Reynolds numbers on the order of 100,000. These conditions are nearly critical for attached boundary layers. Thus, transition is unlikely to take place, and laminar separation usually occurs. The highly unstable free shear layer which forms downstream of separation provides a means by which transition can occur, and the turbulent mixing which follows causes reattachment through a momentum exchange across the viscous layer. The separation bubble that appears as a result of the above processes is therefore an almost essential phenomenon with regard to the development of attached turbulent boundary layers on low Reynolds number airfoils. However, the increase in momentum thickness over the length of the separation bubble is usually much greater than that which would have occurred had the boundary layer remained attached. Hence, a proportional increase in drag is associated with the formation of a separation bubble. Furthermore, the increase in boundary layer thickness due to a separation bubble may lead to premature turbulent separation (Figure 2) and the accompanying deterioration in airfoil performance usually associated with stalling.

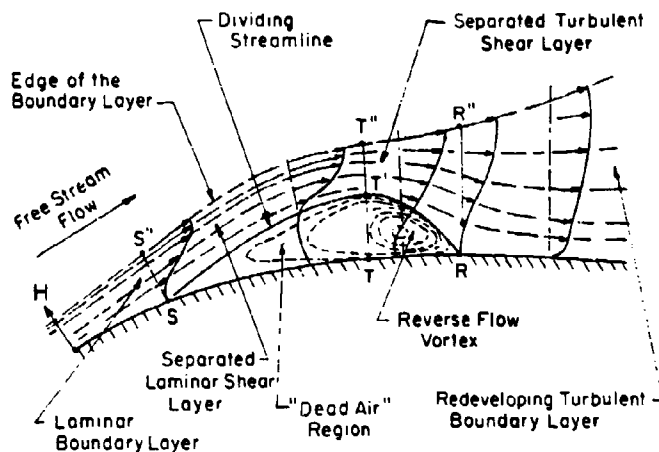


Figure 1. Flow in the Vicinity of a Separation Bubble [8].

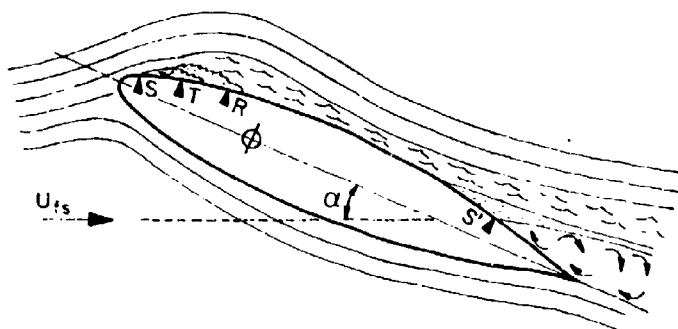


Figure 2. Sketch of the Flow Around an Airfoil at Low Reynolds Numbers Showing the Separation Bubble and Turbulent Separation Near the Trailing Edge.

Obviously, it is desirable to have the ability to predict the effect of separation bubbles on airfoil performance. Several numerical schemes have recently been developed which are capable of doing this [1,2]. These methods involve an inverse formulation of the boundary layer equation. The nature of this equation depends, of course, on whether the flow being computed is laminar or turbulent. Empirical relationships are incorporated into the programs for determining the extent of the laminar portion of the bubble; i.e., the location where the boundary layer equation must change from a laminar form to a turbulent one. Since these empiricisms have been based on separation bubble data obtained at high Reynolds numbers, there is some doubt as to their applicability at low Reynolds numbers. In

addition, these correlations do not take into account changes in the free stream disturbance environment.

During the past year, the separation bubble formed on an NACA 663-018 airfoil at chord Reynolds numbers ranging from 50,000 to 200,000 was investigated using hot-wire anemometry and surface pressure measurements. Data obtained under a variety of testing conditions was used in this paper to examine the characteristics at low Reynolds numbers of a frequently used transition model.

### APPARATUS AND PROCEDURE

The indraft, low speed tunnel used in this investigation is shown schematically in Figure 3. In order to achieve certain testing conditions, this basic tunnel configuration was slightly altered through the introduction of flow restricting devices.

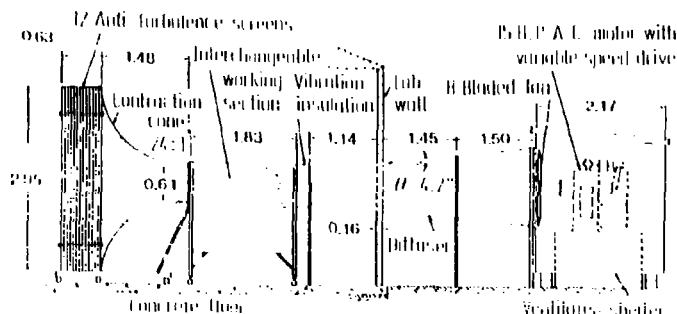


Figure 3. Low Speed, Low Turbulence Wind Tunnel.

These devices consisted of a wooden frame packed with plastic drinking straws. The flow restrictors, when used, were clamped securely between the test section and the diffuser. The effect of introducing one or two flow restrictors was to decrease the freestream velocity and to increase the level of freestream turbulence. Part of this increase in turbulence intensity has been associated with an increase in the sound pressure level inside the tunnel [3]. The freestream turbulence intensities associated with the three tunnel configurations used throughout this study are shown in Figure 4 [4].

All experiments were performed using two NACA 663-018 airfoil models. Both of these models had a chord of 250 mm and a span of 410 mm. The first model was made of smooth gray epoxy and was used for all hot-wire anemometry tests. The second model was equipped with 93 static pressure taps and was used to obtain airfoil pressure distributions. This model was constructed with 46 upper surface and 46 lower surface taps with the remaining tap located at the leading edge. The airfoil models were mounted horizontally between large side plates in order to simulate two-dimensional flow conditions.

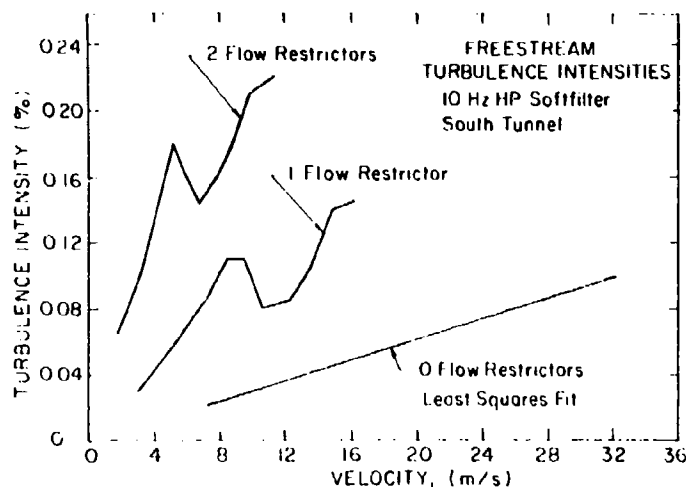


Figure 4. Turbulence Intensity versus Test Section Velocity for Various Tunnel Configurations [4].

Static pressure distributions were obtained using the pressure tap model and a series of pressure transducers and switching mechanisms. The airfoil pressure taps were connected through tubing to two Scanivalve main body devices. These devices were designed to transmit the pressures to electronic manometers and to sequentially switch pressure passage from tap to tap. The analog-to-digital and digital-to-analog capabilities of an appropriately configured Digital Equipment Corporation PDP 11/23 minicomputer were used to sample the analog output of the manometers and to automatically step through a complete circuit of pressure taps. Free stream dynamic pressures were measured through a standard pitot-static tube placed upstream of the model.

The boundary layer over the airfoil was surveyed in a two step process using a Thermal Systems, Inc. hot-wire anemometry system. The anemometer unit (Model 1050) was operated in the constant temperature mode with a DISA type 55P15 single-wire boundary layer probe. The probe was calibrated using a computer code (PDP 11/23) which calculated a best-fit polynomial to represent the calibration data. The first phase of hot-wire anemometry testing involved measuring the mean and fluctuating velocity components of the boundary layer at 20 to 24 stations along the airfoil upper surface. The locations of these stations varied depending on the size and position of the separation bubble. Data acquisition software was again used to sample the various analog outputs and to automate probe traversing. Once velocity and turbulence intensity properties were acquired, energy spectral data was obtained in the free shear layer downstream of separation. Data was acquired at the points of maximum turbulence intensity of each profile (points of inflection in corresponding velocity profiles) at a sampling rate of 5000 Hz. This data was ensemble averaged which produced a single time history from which

energy spectral densities were calculated [4].

### EXPERIMENTAL RESULTS

During the data acquisition phase of this investigation, the separation bubble flow field over the airfoil was surveyed for twelve different conditions. These conditions were chosen in such a way that the effects of chord Reynolds number, angle of attack, and disturbance environment were isolated. In documenting the flow field, static pressure distributions over the airfoil were obtained, and velocity and turbulence intensity profiles were acquired at selected stations along the airfoil upper surface. In addition, energy spectral data was obtained in the region of the separation bubble in order to explore the stability of the laminar free shear layer. Collectively, this data was used to analyze the entire separation bubble flow field [5]. The present discussion, however, is focused solely on a detailed analysis of a single transition model. Only the experimental data pertaining to this specific topic will be addressed in this paper.

Because pressure data was available at close intervals along the airfoil upper surface, it was extremely useful in pinpointing the locations of the separation bubbles. As is evident in the representative distribution shown in Figure 5, the bubbles formed on the NACA 663-018 airfoil produced well-defined pressure "plateaus."

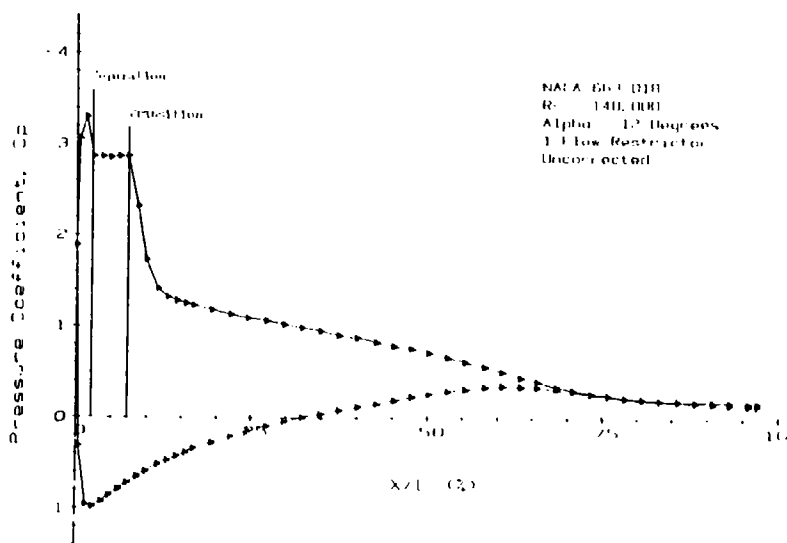


Figure 5. Representative Pressure Distribution About the NACA 663-018 Airfoil Showing the Location of Laminar Separation and Transition.

For each testing condition, the point of flow separation was determined after a close examination of both the pressure and hot-wire anemometry data. The external velocities at separation which were used in calculating various parameters were obtained from the pressure

data. The point of free shear layer transition was taken as the downstream edge of the constant pressure region. This location was confirmed by the corresponding hot-wire anemometry data which indicated a large jump in the maximum turbulence intensity and a broadband energy spectrum downstream of this station [5]. Thus, the data provided a consistent indication of the laminar length of the separation bubble which enabled a detailed analysis of an existing separation bubble transition model.

## DISCUSSION OF RESULTS

A recurring hypothesis concerning the transition from laminar to turbulent flow in a separation bubble is that there exists a constant Reynolds number,  $R_\delta$ , based on the external velocity at separation,  $(U_e)_s$ , and the length of the laminar portion of the bubble,  $\ell$ . This concept was first proposed by von Doenhoff more than forty years ago [6]. He suggested that  $R_\delta = 50,000$  on the basis of experimental measurements. In 1959, Dryden presented a review of the research involving this transition length Reynolds number [7]. He reported that experimentally determined values of  $R_\delta$  ranged from 2000 to as much as 380,000. Factors appearing to contribute to this large variation were body shape (pressure distribution), free stream turbulence, and the chord Reynolds number. Despite these observations, the notion of an invariant  $R_\delta$  has persisted. Horton used the concept in his model of separation bubble growth and bursting [8]. He defended the idea by questioning the accuracy of some of the data discussed by Dryden, stressing the importance of using airfoil models with closely spaced pressure taps if  $R_\delta$  was to be inferred from pressure data. Using more recent data taken by several researchers from Queen Mary College, University of London, he found that  $R_\delta$  varied from 30,000 to 50,000 and suggested that a mean value of 40,000 be used. He speculated that the experimental variation in this data was mainly due to the level of fluctuations present in the boundary layer at separation. Young supported this argument in his survey of separation bubble research [9]. On the basis of additional experiments, he stated that as the free stream turbulence was increased from a low level to about 0.35%, a relatively small reduction in the laminar part of a separation bubble occurred, but with an increase above this level a more marked effect was noticed. In addition, he speculated that changes in the frequency content of the turbulence may have affected the results.

The transition models currently used in programs capable of computing the flow in the vicinity of separation bubbles continue to employ the notion of a relatively invariant transition Reynolds number. Kwon and Pletcher [1] incorporated the following model into their computational scheme:

$$(R_\delta)_T = 1.0607(R_\delta)_S + 33,185$$

where  $R_\delta$  was based on the distance along the airfoil surface from the stagnation point. The experimental sources for this model are listed in [10]. Since  $(R_\delta)_T = (R_\delta)_S + R_\delta$ , the above correlation can be rearranged into the following form:

$$R_L = 0.0607(R_S)_S + 33,185$$

Thus,  $R_L$  is seen to be weakly dependent on  $(R_S)_S$ . For a given pressure distribution, the location of separation is fixed and a linear relationship exists between  $R_L$  and the chord Reynolds number.

Crimi and Reeves [11] based a separation bubble transition model on an analogy to roughness-induced transition. They hypothesized that transition would occur when a critical local Reynolds number was exceeded which in turn depended on the height of the free shear layer from the airfoil surface. Based on measurements corresponding to chord Reynolds numbers ranging from  $1.5 \times 10^6$  to  $6 \times 10^6$ , the following transition model was developed:

$$a_T \delta_T / (\delta_1)_S = 10^6 / (R_{\delta_1})_S^2$$

where  $a_T \delta_T$  was the height within the bubble at which the tangential velocity was zero,  $(\delta_1)_S$  was the boundary layer displacement thickness at separation, and  $(R_{\delta_1})_S$  was the Reynolds number based on  $(\delta_1)_S$  and the external velocity at separation. This relationship was also used by Cebeci and Clark in their separated flow code [2]. Venkatesworlu and Marsden [12] devised a similar criterion which involved the height of the separation bubble at transition,  $h_T$ :

$$h_T / (\delta_1)_S = 4.8 \times 10^6 / (R_{\delta_1})_S^2$$

This correlation was also based on high Reynolds number data. The difference between the constants can be partially explained by the fact that  $h_T > a_T \delta_T$  (see Figure 1).

These height-related transition criteria can be used to argue that  $R_L$  is constant if the following assumptions are made:

1. The bubble height at transition is proportional to the product of  $z$  and  $\tan \gamma$ , where  $\gamma$  is the angle formed between the dividing streamline and the airfoil surface.
2.  $\tan \gamma = B / (R_{\delta_2})_S$   
This correlation was proposed by Dobbinga, et al [13] with  $B$  ranging from 15 to 20.
3. There exists a unique value for  $(H_{12})_S$ , the boundary layer shape factor at separation.

Given the above assumptions,  $R_L$  is related to the constant proposed by Venkatesworlu and Marsden in the following manner:

$$R_L = (4.8 \times 10^6) / (B \times H_{12})_S$$

For the Hartree separation velocity profile [14],  $(H_{12})_S = 4.02922$ . Assuming that  $B = 20$ ,  $R_L$  is found to equal  $5.9 \times 10^4$  which is consistent with actual measurements. Of course,  $(H_{12})_S$  does vary somewhat, depending on the pressure distribution [15]. The separation angle parameter  $B$  also is a function of the pressure distribution

[13]. Thus, the height-based criterion would lead one to expect that  $R_\ell$  depends at least weakly on the pressure distribution.

The present data was used to determine the effect on  $R_\ell$  of such variables as chord Reynolds number, angle of attack, and the free stream disturbance environment. Figure 6 shows  $R_\ell$  plotted against the chord Reynolds number  $R_C$ . The data is seen to divide into three groups, each group corresponding to a particular wind tunnel configuration. This suggests that free stream disturbances significantly affect the value of  $R_\ell$ . Also, each group exhibits a linear variation with  $R_C$ . This trend was predicted by the Kwon and Pletcher transition model. However, the intercepts of all three groups are much less than the value 33,185 which resulted from the high Reynolds number correlation. Thus, use of the Kwon and Pletcher model would result for these cases in overestimating the length of the separation bubbles.

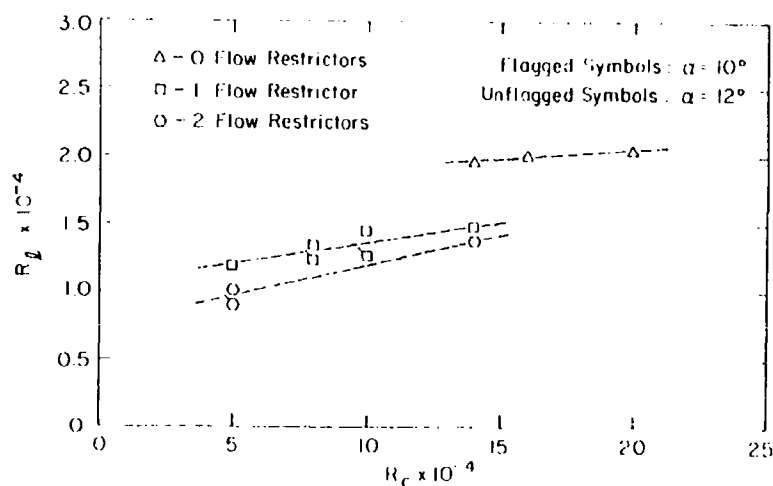


Figure 6. Transition Reynolds Number versus Chord Reynolds Number for Various Tunnel Configurations [5].

Also evident in the data is an apparent angle of attack influence on  $R_\ell$ . As the flow incidence increases from 10 to 12 degrees, a small growth in  $R_\ell$  occurs. Sensitivity to the pressure distribution, and hence the angle of attack, was anticipated by both the model of Kwon and Pletcher as well as by the height-related criteria. However, no particular trend in  $R_\ell$  versus angle of attack was predicted.

In an effort to sort out the effects of free stream turbulence on the laminar length of a separation bubble,  $R_\ell$  was plotted versus the free stream turbulence intensity (Figure 7). This graph possesses two striking features. First,  $R_\ell$  is seen to increase linearly with the turbulence intensity. This appears to directly contradict the observation that  $R_\ell$  decreases as the free stream turbulence intensity increases [16]. Apparently, the increase in chord Reynolds number which accompanies the growth in turbulence intensity has an

overpowering effect on  $R_L$ . This is not surprising if one recalls Young's observation concerning the effect of turbulence intensity on  $R_L$ . Thus, the trend noticed here might reverse for turbulence magnitudes above some critical value.

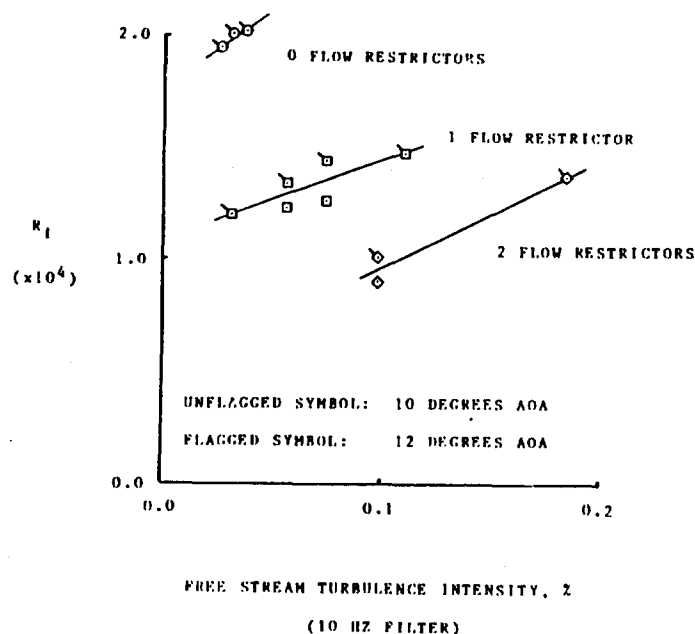


Figure 7. Transition Reynolds Number Versus Turbulence Intensity for Various Tunnel Configurations.

The second important feature of Figure 7 is that for a given value of turbulence intensity, multiple values of  $R_L$  can occur depending on the wind tunnel configuration. This seems to imply that some characteristic of the free stream other than the turbulence intensity has a substantial effect on  $R_L$ . In fact, the impact of this unknown characteristic outweighs the effects of chord Reynolds number and turbulence intensity for the conditions investigated. Factors which might be influencing  $R_L$  are the frequency content of the free stream turbulence as suggested by Young or the turbulence length scale [16]. Also, the test section acoustic environment may be responsible. An analysis of the energy spectral data may provide some clues as to the identity of the unknown factor.

#### CONCLUSIONS AND RECOMMENDATIONS

A study has been conducted of a simple transition criterion often used to predict the extent of laminar flow in a separation bubble. This investigation was based on measurements of the separation bubbles formed on an NACA 663-018 airfoil at low Reynolds numbers. The transition criterion suggested that transition would occur when a critical value of the Reynolds number based on the external velocity at separation and the distance along the airfoil surface from the point of laminar separation was exceeded. Based on the results of the present investigation, it was found that the value of this critical Reynolds number depended on the chord Reynolds number, the airfoil's

angle of attack, and the free stream disturbance environment. This confirmed the observation of researchers who studied the separation bubbles formed at Reynolds numbers an order of magnitude higher. It was also found that for the range of turbulence intensities considered (0.026 to 0.184 %) the magnitude of the free stream turbulence did not significantly affect the value of the critical Reynolds number. Although the test section environment clearly influenced the magnitude of the critical Reynolds number, no single characteristic of the flow was isolated. Possible candidates are the frequency content or the length scale of the free stream turbulence; or perhaps the acoustic environment. Further study of the free stream turbulence characteristics is needed.

In summary, the concept of a critical Reynolds number appears to be useful for both high and low Reynolds number flows. However, the influence of such factors as the chord Reynolds number, pressure distribution and turbulence environment must be investigated further before the characteristics of separation bubbles can be confidently predicted.

#### NOMENCLATURE

a	fraction of boundary layer thickness corresponding to the height at which tangential velocity is zero
B	constant used in separation angle correlation
C	airfoil chord
$C_p$	pressure coefficient, $C_p = (P_i - P_{fs})/Q_{fs}$
h	height of the separation bubble
$H_{12}$	$\delta_1/\delta_2$
$\ell$	$S_T - S_S$
P	static pressure
Q	dynamic pressure
$R_c$	$U_{fs}C/\nu$
$R_\ell$	$(U_e)S_\ell/\nu$
$R_S$	$(U_e)S_S/\nu$
$R\delta_1$	$U_e\delta_1/\nu$
$R\delta_2$	$U_e\delta_2/\nu$
S	distance along airfoil surface measured from the stagnation point
U	velocity
X	distance along airfoil chord

#### Greek Symbols

$\gamma$	separation angle formed between the dividing streamline and the airfoil surface
$\delta$	boundary layer thickness
$\delta_1$	boundary layer displacement thickness
$\delta_2$	boundary layer momentum thickness
$\nu$	kinematic viscosity

#### Subscripts

e	edge of boundary layer
fs	free stream
i	refers to pressure tap i
S	separation
T	transition

## ACKNOWLEDGEMENTS

This research was sponsored by the NASA Langley Research Center under Grant NSG-1419 and the University of Notre Dame Department of Aerospace and Mechanical Engineering.

## REFERENCES

1. Kwon, O.K., and Pletcher, R.H., "Prediction of Subsonic Separation Bubbles on Airfoils by Viscous-Inviscid Interaction," Second Symposium on Numerical and Physical Aspects of Aerodynamic Flows, Jan. 17-20, 1983, California State University, Long Beach, CA.
2. Cebeci, T., and Clark, R.W., "An Iterative Approach to Subsonic Flows with Separation," Second Symposium on Numerical and Physical Aspects of Aerodynamic Flows, Jan 17-20, 1983, California State University, Long Beach, CA.
3. Mueller, T.J., Pohlen, L.J., Conigliaro, P.E., and Jansen, B.J., Jr., "The Influence of Free-Stream Disturbances on Low Reynolds Number Airfoil Experiments," Experiments in Fluids, Vol. 1, pp. 3-14, Springer-Verlag, 1983.
4. Brendel, M. and Huber, II, A.F., "An Experimental Investigation of Flow Quality in an Indraft Subsonic Wind Tunnel Using a Single Hot Wire Anemometer," an internal Aerospace Laboratory report, University of Notre Dame, November 1984.
5. O'Meara, M.M., "An Experimental Investigation of the Separation Bubble Flow Field Over an Airfoil at Low Reynolds Numbers," M.S. Thesis, University of Notre Dame, 1985.
6. Ward, J.W., "The Behaviour and Effects of Laminar Separation Bubbles on Aerofoils in Incompressible Flow," Journal of the Royal Aeronautical Society, 67, December 1963, pp. 783-790.
7. Dryden, H.L., "Transition from Laminar to Turbulent Flow," Turbulent Flows and Heat Transfer, Princeton University Press, Princeton, NJ, pp. 25-26, 1959.
8. Horton, H.P., "Laminar Separation Bubbles in Two and Three Dimensional Incompressible Flow," Ph.D. Thesis, University of London, 1968.
9. Young, A.D., "Some Special Boundary Layer Problems," Zeitschrift für Flugwissenschaften und Weltraumforschung, 1:6, Nov/Dec 1977, pp. 401-414.
10. Kwon, O.K., and Pletcher, R.H., "Prediction of Incompressible Separated Boundary Layers Including Viscous-Inviscid Interaction," Trans. of the ASME, 101, 1979, pp. 466-472.

11. Crimi, P., and Reeves, B.L., "Analysis of Leading-Edge Separation Bubbles on Airfoils," AIAA J., 14:11, Nov 1976, pp. 1548-1555.
12. Carmichael, B.H., "Low Reynolds Number Airfoil Survey," Volume I, NASA Contractor Report 165803, November 1981.
13. Dobbinga, E., Ingen, J.L. van, Kooi, J.W., "Some Research on Two-Dimensional Laminar Separation Bubbles," AGARD CP-102, Paper No. 2, Lisbon, 1972.
14. Eppler, R., and Somers, D.M., "A Computer Program for the Design and Analysis of Low-Speed Airfoils," NASA Technical Memorandum 80210, August 1980.
15. Liu, C.Y., and Sandborn, V.A., "Evaluation of the Separation Properties of Laminar Boundary Layers," The Aeronautical Quarterly, August 1968, pp. 235-242.
16. Roberts, W.B., "A Study of the Effect of Reynolds Number and Laminar Separation Bubbles on the Flow Through Axial Compressor Cascades," D.Sc. Thesis, U. Libre de Bruxelles and VKI, 1973.

# THEORETICAL AND EXPERIMENTAL STUDY OF LOW REYNOLDS NUMBER TRANSITIONAL SEPARATION BUBBLES

C. Gleyzes - J. Cousteix - J.L. Bonnet

ONERA/CERT  
Department of Aerothermodynamics  
2 avenue Edouard Belin  
31055 TOULOUSE Cedex - FRANCE

## ABSTRACT

This paper presents a review of our work on transitional separation bubbles. An experimental study in two-dimensional flows provided first information about the effects of separation bubbles on the flow on the upper surface of an airfoil, at low Reynolds number. A detailed study of the transition mechanisms was also performed, and was very helpful in the understanding of the phenomenon, while boundary layer surveys allowed us validation of the calculation method.

This method is based on an inverse boundary layer calculation, associated with a local viscous-inviscid interaction. Transition being a critical problem, an adequate criterion had to be developed. Extension to three-dimensional infinite swept wing configuration is in progress.

## 1 - INTRODUCTION

The positive pressure gradient, downstream of the suction peak at the leading edge of an airfoil at incidence, may, under some conditions, induce large perturbations on the general pattern of the flow.

If Reynolds number (here  $Re_c = U_\infty c / \nu$  where  $c$  is the chord of the airfoil) is large, the boundary layer becomes quickly turbulent and is not much affected by the gradient ; if  $Re_c$  is low enough, the boundary layer remains laminar and separation may occur, generally inducing a transitional separation bubble.

Previous studies have already shown that the effect of this bubble upon the downstream turbulent boundary layer is important and has to be taken into account, in the determination of lift and drag characteristics of the airfoil.

For that, we have carried out our study in two parallel directions :

- an experimental study of the separation bubbles, with a special care on transition mechanisms ;
- a theoretical and numerical approach, in order to design a calculation method able to predict the evolution of the boundary layer across a short separation bubble.

## 2 - EXPERIMENTAL STUDY

### 2.1. Experimental Apparatus

This study was performed in a 300 x 400 mm<sup>2</sup> subsonic wind tunnel. Two types of models were used :

- A 200 mm chord peaky profile (ONERA LC 100 D) which provided global results about the effects of leading edge bubble and also some detailed results about the transition process in long bubbles.

- A special model, called Enlarged Leading Edge (ELE). This model corresponds to the leading edge of a 2 500 mm airfoil and is fitted with a blown flap. Previous studies (Réf. /1/) have shown that the flow in the vicinity of the leading edge is defined by the position of stagnation point, which was fixed here for each Reynolds number, by a combination of model incidence ( $\alpha$ ), flap angle ( $\beta$ ) and blow rate. Because of the scale of the model, a detailed study of short separation bubbles and of the corresponding transition process could be carried out.

### 2.2. Global Results

These experiments have been performed for a wide range of Reynolds numbers ( $8 \cdot 10^4 < Re_c < 10^6$ ) and incidence ( $3 < \alpha < 9^\circ$ ) (/2/).

An example of the velocity distribution deduced from wall pressure measurements is presented in figure 1 :

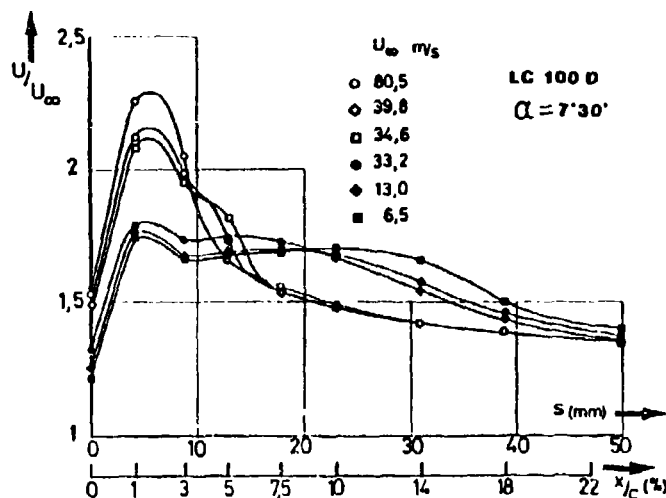


Figure 1

Velocity distributions in the leading edge region

For this incidence, the two types of bubbles exist, depending on Reynolds number. For short bubbles ( $Re_c > 0.45 \cdot 10^6$ ), the velocity distribution is close to the high Reynolds number one, except in a small domain around the bubble, where the difference is however small. When decreasing tunnel speed, a change in the velocity distribution occurs for a given Reynolds number (here  $Re_c \approx 0.45 \cdot 10^6$ ). There is a sudden increase in the disturbed region, associated with a drop of the suction peak. This corresponds to the classical bursting of a short bubble in a long bubble.

An important remark about the bursting phenomenon caused by a Reynolds number decrease, is that no discontinuity in the size of the separation region seems to exist /3/. This is confirmed in figure 2, where momentum thickness at 75 % of the chord has been plotted, versus tunnel speed. For the bursting point, there is a change in the slope of the curve, but continuity in the evolution.

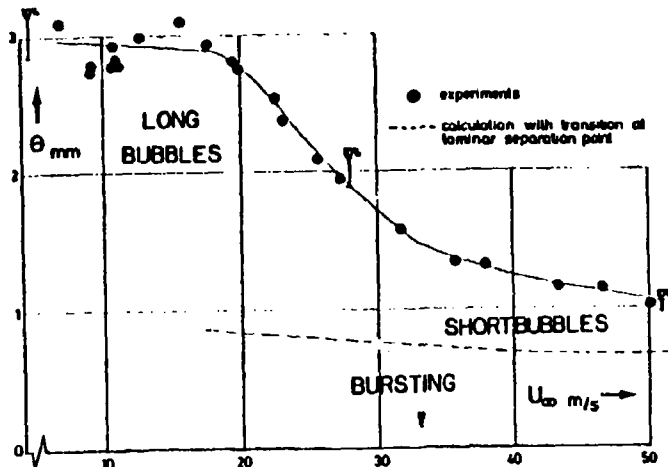


Figure 2  
Momentum thickness  
at  $x/c = 75\%$   
(LC 100 D)

The increase in momentum thickness is also shown, compared with a calculation assuming a transition at separation, with continuity in momentum thickness. This increase is very large for long bubbles and is far from negligible for short bubbles.

From our experiments, as well as from other studies of separation bubbles (/3/, /5/), we have tried to give a global view of the evolution of these separation bubbles.

In figure 3, we have schematically plotted the evolution of a characteristic length  $L/c$  of the separated region for different incidences, as a function of Reynolds number.

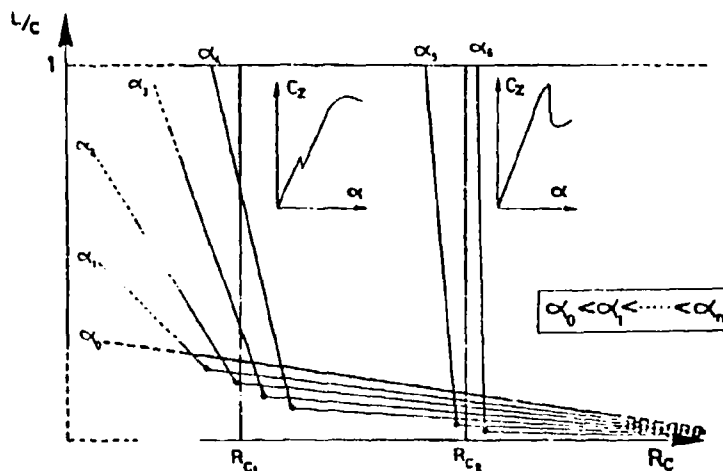


Figure 3 Schematic evolution of separated region

Beyond a given incidence (here  $\alpha_0$ ), no separation occurs and the boundary layer remains laminar, up to natural transition. For a moderate incidence  $\alpha_2$ , (between 5 and 10°, depending upon the airfoil), the evolution of  $L/c$  when decreasing  $Re_c$ , is characterized by a continuous increase, with a much higher rate below bursting Reynolds number, leading to a complete separation. When increasing incidence, bursting Reynolds number increases.

If we look now at the evolution of  $L/c$  for a given Reynolds number, two major schemes exist :

. If  $Re_c$  is low ( $Re_{c1}$  for instance), increasing angle of attack induces first a decrease in the size of the short bubble, up to  $\alpha = \alpha_2$ . With a further increase in incidence, bubble bursts and the size of the separated region may, in this case, strongly increase. The size of the long bubble goes then increasing with incidence, up to complete stalling. The lift coefficient curve may or not present a break at bursting point, according to the type of airfoil.

. If  $Re_c$  is higher ( $Re_{c2}$  for instance), the evolution with incidence is similar, up to the bursting point which corresponds to a higher incidence ; but due to the higher adverse pressure gradient, an increase in incidence causes boundary layer complete separation and stalling is then sudden.

### 2.3. Detailed results about short bubbles

These results have been obtained on ELE model. A first series of experiments has been performed with the natural turbulence of the tunnel (around .4 %) while a turbulence generating grid has been added in a second series, to investigate the influence of turbulence level. Reynolds number based on a 2 500 mm chord was between  $8 \cdot 10^5$  and  $8 \cdot 10^6$  and the position of stagnation point was adjusted to the same place, for each configuration.

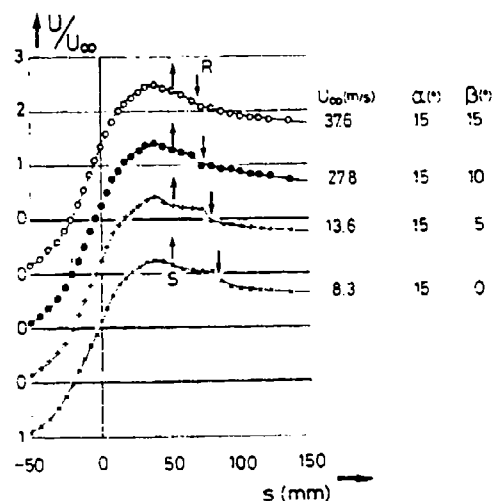


Figure 4  
Velocity distributions in the  
leading edge region (E.L.E.)

2.3.1. Low Turbulence Configuration. Velocity distributions deduced from wall pressure measurements are presented in figure 4.

Position of separation and reattachment indicated by oil surface visualizations have also been reported and confirm the reduction of the size of the bubble when increasing Reynolds number.

Hot wire measurements provided boundary layer mean velocity profiles in the bubble, as well upstream and downstream of it. An example of these results is plotted in figure 5 for  $Re_C = 2.2 \cdot 10^6$ .

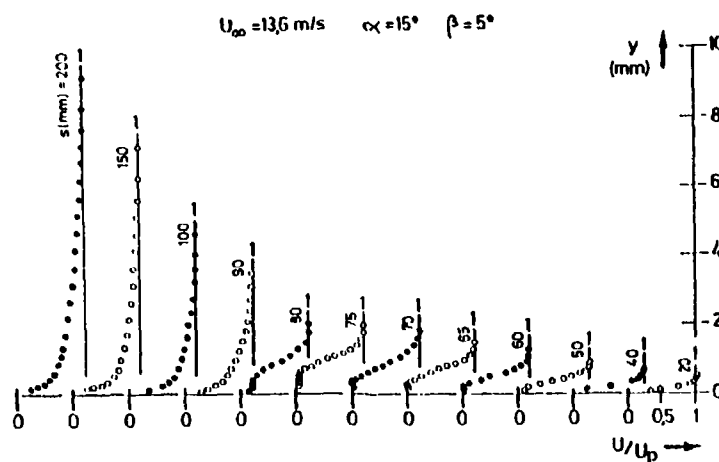


Figure 5  
Mean velocity  
profiles  
(Hot wire)

The use of BRAGG cells for the LDA measurements allowed us to get the negative values of the velocity in the bubble. A comparison between hot wire and LDA measurements is presented in figure 6, for the same configuration. Agreement is good, except of course in the vicinity of the reverse flow region, where hot wire is in default.

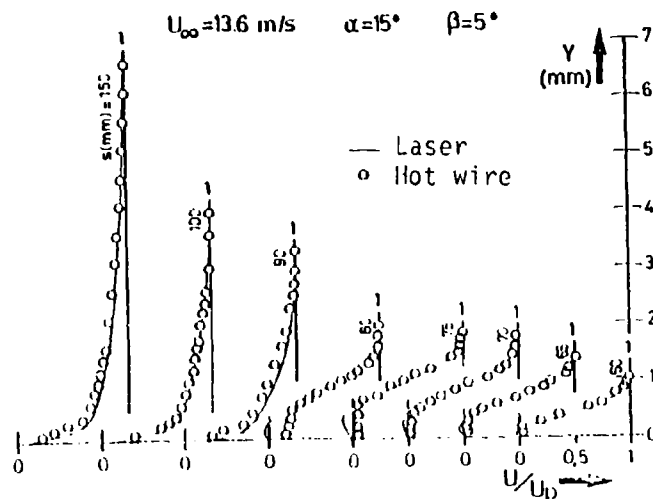


Figure 6  
Mean velocity  
profiles  
Comparison LDA -  
Hot wire

Concerning the fluctuating velocity measurements, LDA results were not significant, due to the size of the measurement volume, compared with the boundary layer thickness. Figure 7 gives, for  $Re_c = 2.2 \cdot 10^6$ , the evolution of RMS longitudinal velocity fluctuation ( $\sqrt{u'^2}/U_p$ ) measured with hot wire.

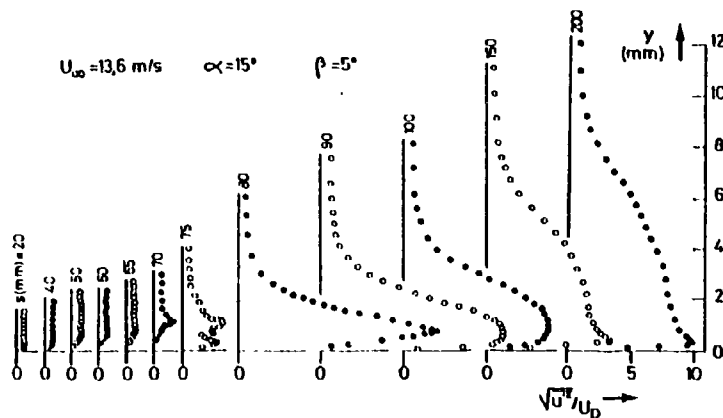


Figure 7  
Velocity  
fluctuation  
profiles  
(Hot wire)

If we look at this set of results, we can see, for stations at  $s = 20$  and  $50$  mm, a laminar boundary layer going to separation, which occurs between  $50$  and  $60$  mm.

Between  $60$  and  $75$  mm, a reverse flow region develops near the wall, under a strong shear layer. The intensity of the shear layer increases downstream, as can be seen on the turbulence profiles. Between  $75$  and  $80$  mm, a sudden change in the shape of mean velocity profiles occurs, in the near wall part of the boundary layer, while the outer part is not affected. This change is associated with a rapid increase in the turbulence level. The phenomenon is characteristic of a very quick transition which occurs between these two stations.

**2.3.2. High Turbulence Configuration.** For this case, wall pressure and hot wire measurements have been performed. The first ones gave similar results as in the previous configuration with, however, a significant reduction of the perturbation. This reduction, caused by an increase in turbulence level, is confirmed by the hot wire measurements.

#### 2.4. Study of the Transition Process

For long and short bubbles, the study of the transition mechanisms has been done through smoke visualizations /6/ associated with a spectral analysis of the hot wire signal.

**2.4.1. Long Bubble Case.** This study has been performed on the  $200$  mm model, for  $Re = 1.8 \cdot 10^5$ . In this configuration, the quality of the visualizations is fairly poor and figure 8 gives an example for a lower Reynolds number. The phenomenon is qualitatively identical but the lower convection velocity allows a better understanding.

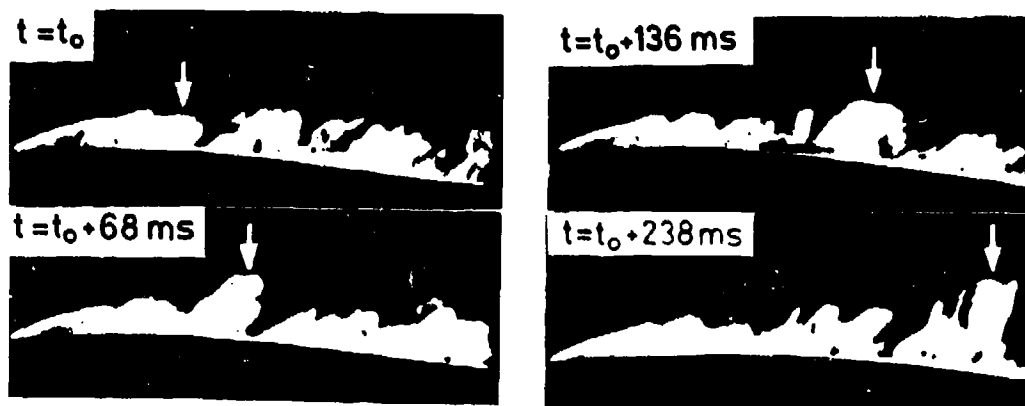
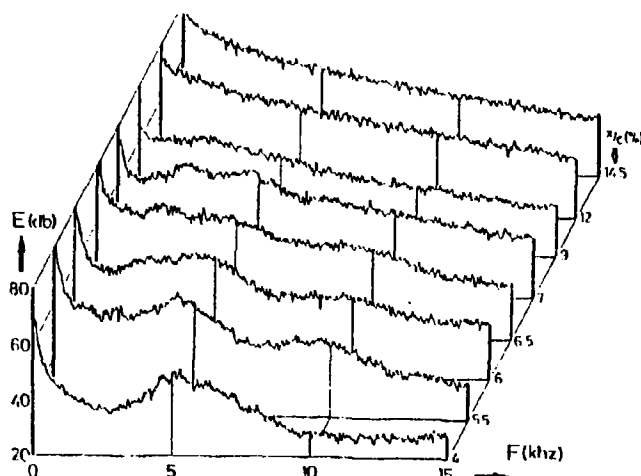


Figure 8 Visualization of leading edge bubble

On the other hand, figure 9 reports the evolution with  $x/c$  of the spectral power of the velocity fluctuation, in the vicinity of the maximum of this fluctuation.

Figure 9  
Spectral analysis  
of Hot wire signal  
(Long bubble)



The study of this set of results gives a good idea of the transition process.

For  $x/c = 4\%$ , spectral analysis indicates a maximum around 5 kHz, while visualizations show regular oscillations of the shear layer. When going downstream ( $x/c = 5.5$  and  $6\%$ ), the amplitude of these oscillations grows and visualizations show the oscillations give finally birth to regularly spaced vortices, at a frequency of about 4.7 kHz. On the hot wire signal, the convection of these vortices can be associated with the 10 kHz harmonic. Note that, up to this point, the flow seems to remain fairly two-dimensional (/6/, /7/). Let us now follow, on figure 8, the evolution with time of the vortex pointed by an arrow: we can see that a pairing with the adjacent vortex occurs, giving birth to a new structure, which can be related to the 2.5 kHz subharmonic at  $x/c = 6.5$  and  $7\%$ . Downstream, the structure is convected and progressively disintegrated. Note that downstream of vortex pairing, flow visualizations indicate that the flow becomes rapidly three-dimensional.

2.4.2. Short Bubble Case. This detailed study was performed on ELE model, for  $Re_c = 2.2 \cdot 10^6$  and  $1.4 \cdot 10^6$ . The main result we obtained from flow visualizations and spectral analysis, is that the mechanism leading to transition is the same that for long bubbles.

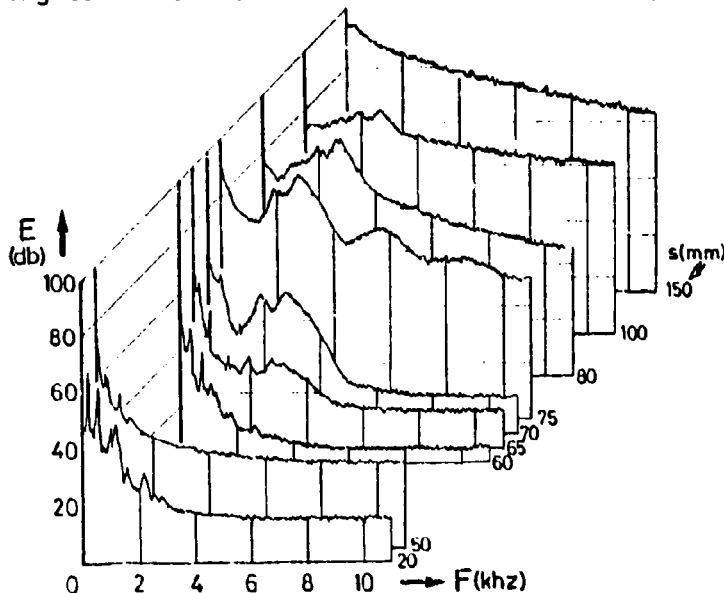


Figure 10  
Spectral analysis  
of Hot wire signal  
(Short bubble)

Figure 10, giving spectral power of the hot wire PMS fluctuation, is very similar to figure 9.

2.4.3. Conclusions. The important point is that no difference seems to exist in the transition mechanisms in short or long bubbles. In both cases, laminar instability waves grow and this growth is fairly rapid, because of the strong instability of boundary layer velocity profiles in an adverse pressure gradient. The difference with the well known transition in zero pressure gradient is that the beginning of transition is not associated with the development of three-dimensional spots /8/, followed by an intermittency region. Here, the amplification of TOLLMIEN-SCHLICHTING waves generate two-dimensional vortices, the desagregation of which leads more or less rapidly to turbulence.

### 3 - THEORETICAL STUDY

#### 3.1. Preliminary Remarks

For the calculation of separation bubbles, classical direct boundary layer calculations lead to a singularity in the vicinity of the zero skin friction point /9/, even if the experimental pressure distribution is used /10/. This singularity leads to the inverse formulation of the problem /11/, /12/.

If we want to predict the evolution of the boundary layer across a separated region, an inviscid calculation must be associated, through a viscous-inviscid interaction /13/, /14/. The inviscid calculation can be done in direct or inverse mode. In the present method, the second solution has been used.

This method gives very good results, but the stability of the successive iterations between inverse boundary layer and inverse inviscid calculations needs a strong under-relaxation. Another possibility would be the quasi simultaneous method of VELDMAN /15/. The introduction of this technique in our method provided fairly good results for purely laminar separation bubbles /16/.

Our method has first been developed and widely tested for two-dimensional subsonic compressible bubbles. Details about it have been given in /17/. We are now trying to extend this method to the case of infinite swept wing conditions. In this aim, we will present it here in the three-dimensional formulation, the two-dimensional one being only a particular case.

### 3.2. Boundary Layer Calculation

Because it is fast and satisfactorily accurate, an integral method has been chosen. The equations are the classical momentum equations, written in the coordinate system related to the external velocity (see figure 11).

For the auxiliary equation, the same equation is taken all along the calculation domain : the entrainment equation.

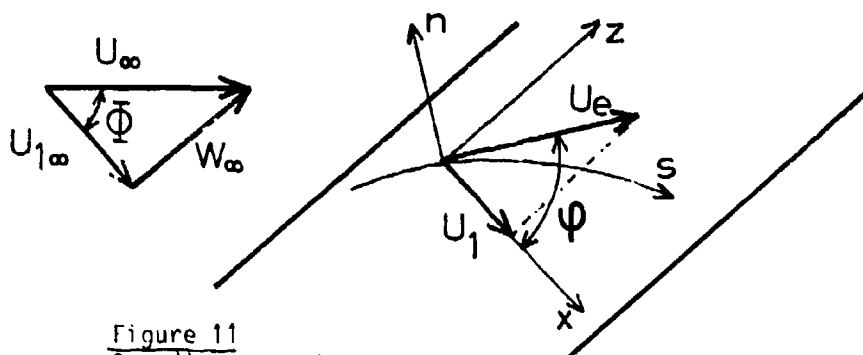


Figure 11  
Coordinate system

In the external streamlines coordinate system, the equations are given in /18/ for the general three-dimensional case. In our particular case, by introducing the parameter  $K = \tan \phi$  (see figure 11), these equations can be written, for an incompressible flow, as :

- momentum :

$$\frac{C_{fs}}{2} = \frac{d\theta_{11}}{ds} + \theta_{11} \left( \frac{H + 2 + K^2}{U_e} \right) \frac{dU_e}{ds} - K \frac{d\theta_{12}}{ds} - \frac{K}{U_e} \theta_{22} \frac{dU_e}{ds} \quad (3.1)$$

$$\frac{C_{fs}}{2} \tan \beta_0 = \frac{d\theta_{21}}{ds} + \theta_{21} \left( \frac{2 + 2K^2}{U_e} \right) \frac{dU_e}{ds} - K \frac{d\theta_{22}}{ds} - \frac{K}{U_e} (\theta_{22} + \theta_{11} + \delta_1) \frac{dU_e}{ds} \quad (3.2)$$

- entrainment :

$$C_E = \frac{d}{ds} (\delta - \delta_1) + \frac{1 + K^2}{U_e} (\delta - \delta_1) \frac{dU_e}{ds} + K \frac{d\delta_2}{ds} \quad (3.3)$$

Note that  $K = 0$  corresponds to the two-dimensional case.

The use of an integral method makes necessary the use of closure relationships. They can be found in /18/, /19/. Note that the use of entrainment equation in laminar needed the development of particular relationships, deduced from the FALKNER-SKAN self-similarity solutions /20/.

### 3.3. Viscous-Inviscid Interaction - Inviscid Calculation

LE BALLEUR /21/ has shown that the interaction relationship could be written in terms of vertical velocity at a given distance of wall. If it is written at  $y = 0$ , boundary layer is equivalent to a transpiration at wall, which is given, in our case, by :

$$w = \left( \frac{v}{U_e} \right)_0 = \frac{1}{\rho_e U_e} \frac{d}{ds} (\rho_0 U_e \delta_1) - \frac{K}{\rho_e U_e} \frac{d}{ds} (\rho_e U_e \delta_2) + \frac{K}{U_e} \frac{dU_e}{ds} (K\delta_1 + \delta_2) \quad (3.4)$$

For the inviscid calculation, our experimental results show we can assume that the bubble induces only a small perturbation around the potential velocity distribution. For the infinite swept wing configuration if  $U_{1FP}$  is the undisturbed velocity distribution normal to the leading edge and  $U_1$  the corresponding one given by the inverse boundary layer calculation, the perturbation velocity  $U_i(x) = U_1(x) - U_{1FP}(x)$  corresponds to a vertical transpiration velocity at wall given by :

$$v_0(x) = \frac{1}{\pi} \int_{-\infty}^{+\infty} \frac{U_i(\xi)}{(\xi - x)} d\xi \quad (3.5)$$

where the integration is taken in the direction normal to the leading edge.

### 3.4. Transition

The problem of transition (practically the determination of the onset and the extent of transition) is one of the main point of the method. A delayed transition would cause the bubble not to reattach ; a too early transition would underestimate the thickness of the downstream turbulent boundary layer.

Physically, transition is initiated by the amplification of laminar instability waves, similar to the TOLLMIE-SCHLICHTING waves observed on a flat plate. This amplification proceeds from a critical point, which is generally upstream of separation. For attached flows, experimental and numerical studies /22/ have shown that two types of instabilities could lead to transition :

. Longitudinal instability, which corresponds to the amplification of these waves in the streamwise direction and which is similar to the two-dimensional case.

. Transversal instability, which corresponds to the amplification in a direction close to the normal to the external streamlines. This type of instabilities only occurs at the lower surface of the airfoil, in a favourable pressure gradient.

For our problem, in fact, only longitudinal instability is involved

3.4.1. Stability Calculations. ARNAL et al. /23/ have studied the stability of attached laminar self-similar velocity profiles. We have extended this study to the separated profiles given in /20/.

These calculations provide for each profile (i.e. for each value of shape parameter  $H$ ), the amplification coefficients  $\alpha_i = (1/A)(dA/ds)$  of a sinusoidal disturbance of amplitude  $A$ , parametrised in frequency and Reynolds number  $R\delta_1$ . A sweep in frequency provides the classical stability diagrams. Figure 12 gives, for the different profiles, neutral curves (i.e. the limit between amplified and damped perturbations). Critical Reynolds number  $R\delta_{1cr}$  corresponds to the value of  $R\delta_1$  below which no perturbation can be amplified. Flat plate neutral curve has been added and we can notice the great instability of separated profiles, linked to low critical Reynolds number and large aperture of neutral curves.

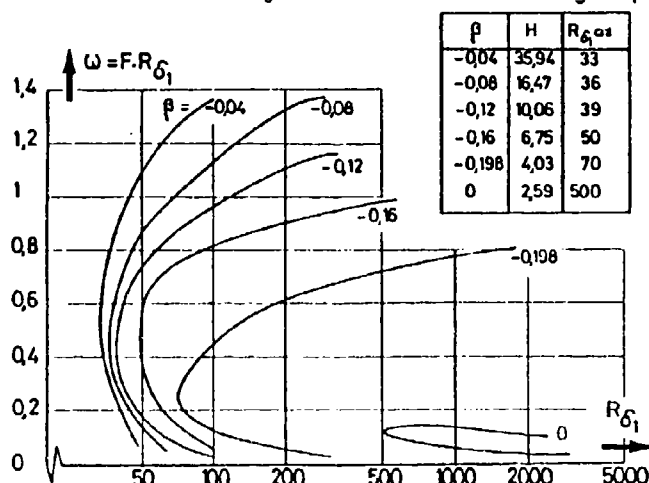


Figure 12  
Neutral curves

3.4.2. Determination Of The Onset Of Transition. For self-similar flows, the study of the evolution with  $R\delta_1$  of the amplitude of any sinusoidal disturbance can be determined from stability diagrams. In this diagram ( $FR\delta_1$  versus  $R\delta_1$ ), perturbations are damped up to the point where they cross the neutral curve. They are then amplified, up to their possible second crossing with the neutral curve. Figure 13 gives an example of the evolution with  $R\delta_1$  of  $\log(A/A_0)$  where  $A_0$  is the amplitude of a given perturbation when entering the amplification domain.

The envelope of these curves then provides, for any value  $R\delta_1$  greater than  $R\delta_{1cr}$ , the total amplification  $n(R\delta_1)$  of the most unstable frequency. Introducing momentum thickness  $\theta_{11}$ , the shape of these curves leads to a simple analytical representation :

$$n(H, R\theta_{11}) = \lambda(H) (R\theta_{11} - R\theta_{11cr} + \sigma) \quad (3.6)$$

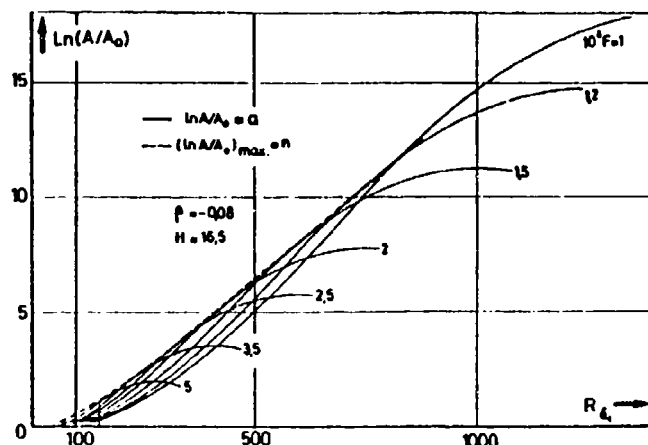


Figure 13

Example of  
amplification  
curves

For practical use, we have first to determine the critical point, where  $n = 0$ . This is done by assuming critical point is obtained when local momentum Reynolds number  $R\theta_{11}$  reaches a critical value  $R\theta_{11cr}$ , given by the critical Reynolds number of the self-similar solution corresponding to the local shape parameter  $H$ .

Determination of total amplification  $n$  at a position  $s$  is obtained by :

$$n(s) = \int_{R\theta_{11cr}}^{R\theta_{11}} \frac{dn}{dR\theta_{11}} dR\theta_{11}$$

where : -  $R\theta_{11}$  is the momentum Reynolds number at station  $s$  ;

-  $\frac{dn}{dR\theta_{11}}$  is deduced from relation (3.6), for the value of local shape parameter  $H$  at station  $s$ .

The onset of transition finally occurs when  $n$  reaches a critical value  $n_T$ , function of turbulence level  $Tu_e$ , through a relation proposed by MACK/24/ :

$$n_T = - 8.43 - 2.4 \text{ Ln}(Tu_e)$$

**3.4.3. Treatment of Transition Region.** The solution of equations at a station  $x_n$  provides, at station  $x_{n+1}$ , the value of the quantity  $\delta_1/\delta$ . From this quantity, closure relationships provide, for purely laminar or turbulent flows, the data necessary to the integration of equations at station  $x_{n+1}$ . In the transition region, the same procedure provides characteristic quantities of two fictitious boundary layers (laminar and turbulent) ; these quantities are then weighted through an intermittency function  $\epsilon$ , to provide the transitional boundary layer characteristics. For two-dimensional attached flows, ARNAL et al. /25/ found that intermittency function was fairly well correlated by the quantity  $\theta_{11}/\theta_{11T}$  (where subscript T corresponds to the beginning of transition). The following formulation was then taken :

$$\epsilon = 1 - \exp(- 2.5 (\theta_{11}/\theta_{11T} - 1))$$

### 3.5. Results

3.5.1. Comparison with our experiments. In figure 14, are presented two sets of results obtained for  $Re_c = 2.2 \cdot 10^6$ , for a local turbulence level of 0.4 and 2.5 %. The agreement between calculation and experiments is quite satisfactory. In particular, the validity of the transition criterion seems good, owing to the correct prediction of either the size of the pressure plateau or the evolution of the shape parameter in the vicinity of reattachment. The influence of turbulence level on the position of transition and, consequently, on the size of the bubble, is also well predicted. Compared with a calculation assuming transition at separation (see dotted line), the increase in momentum thickness is well predicted.

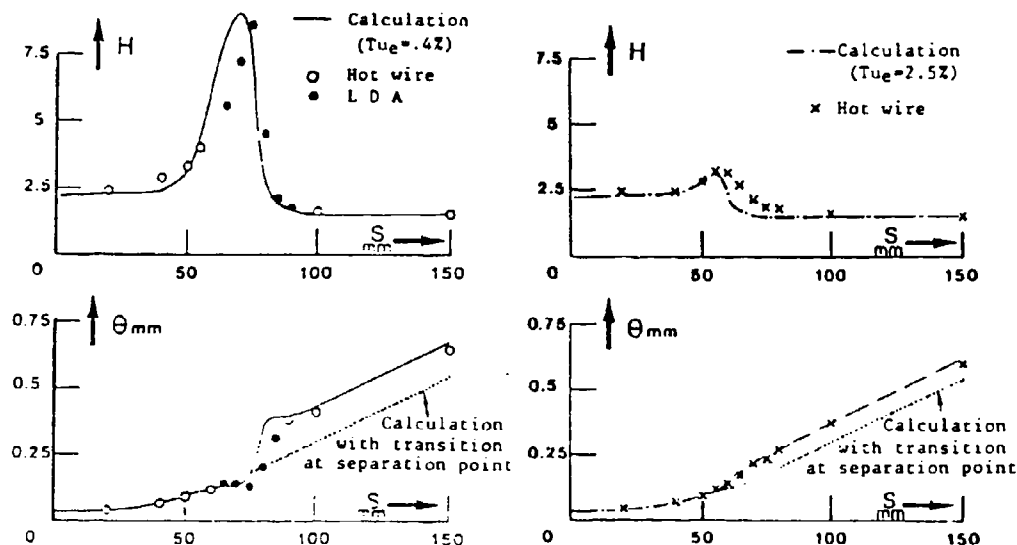


Figure 14 Comparison with our experiments  
(low and high turbulence level)

3.5.2. Infinite Swept Wing Configuration. This study is being developed to provide some help in the experimental study carried out at ONERA /26/. Experimental results concerning pressure distributions at various spanwise positions showed that the infinite swept wing flow configuration was not much affected by a short bubble. Smoothing one of these pressure distributions provided the undisturbed velocity distribution  $U_{1FP}$ . In fact, experimental results about boundary layer are not yet available and the calculation we present is rather academic and mainly consists of a test of the validity of the method and of the numerical procedure.

The evolutions of some computed boundary layer characteristic parameters are plotted in figure 15, compared with a calculation assuming transition at separation /27/. Effects of the bubble are similar to those observed in two-dimensional flows.

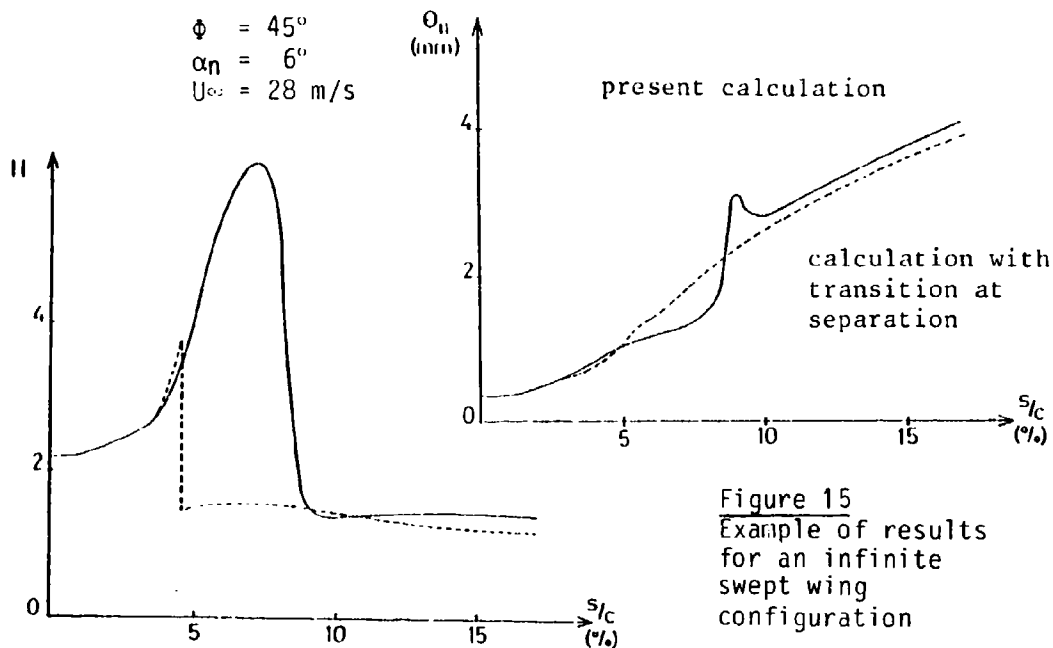


Figure 15  
Example of results  
for an infinite  
swept wing  
configuration

## CONCLUSIONS

The experimental study we have performed provided useful information about transition processes involved in separation bubbles. This study was also very helpful in the choice of the assumptions we have introduced in the calculation method, as well as in the design of the transition criterion. Boundary layer surveys also provided enough data for the validation of the calculation results in two-dimensional flows.

The method is now being extended to the case of infinite swept wing for subsonic compressible flows. Experimental data are needed now to achieve its validation.

## REFERENCES

1. ERLICH E. "Contribution expérimentale à la recherche de la portance maximale des profils en subsonique", Internal Report, ONERA, 1970.
2. GLEYZES C., COUSTEIX J., BONNET J.L. "Bulbe de décollement laminaire avec transition (théorie et expérience)", L'Aéronautique et l'Astronautique, N° 80, Jan. 1980, pp. 41-57.
3. GASTER M. "The structure and behaviour of laminar separation bubbles AGARD CP 4, 1969.
4. OWEN P.R., KLENFER L. "On the laminar boundary layer separation from the leading edge of a thin surface", RAE Report N° Aero 2508, 1983.
5. TANI I. "Low speed flows involving bubble separations", Progress in Aero. Sci., Pergamon Press, Vol. 5, p. 70, 1964.
6. GLEYZES C., COUSTEIX J., BONNET J.L. "Flow visualization of laminar leading edge separation bubbles (long bubble)", International Symposium on Flow Visualization, BOCHUM (RFA), 9-12 sept. 1980.

7. MUELLER T.J., BATILL S.M. "Visualization of the laminar turbulent transition in the flow over an airfoil using the smoke wire technique" AIAA Paper 80-1440, July 1980.
8. ARNAL D., JUILLEN J.C., MICHEL R. "Analyse expérimentale et calcul de l'apparition et du développement de la transition de la couche limite", AGARD CP 224, 1977.
9. GOLDSTEIN S. "On laminar boundary layer flow near a position of separation" - Quart. J. of Mech. and Appl. Math., 1-43, 1948.
10. COUSTEIX J. "Integral method and turbulence models applied to three-dimensional boundary layers", Three-dimensional turbulent boundary layers, Springer Verlag, 1982.
11. CARTER J. "Solution for laminar boundary layer with separation and reattachment", AIAA Paper 74-583, 1974.
12. KLINEBERG J.M., STEGER J.L. "On laminar boundary layer separation", AIAA Paper 74-94, 1974.
13. BRILEY W.R., McDONALD H. "Numerical prediction of incompressible separation bubble", JFM, 69, Part 4, 1975.
14. CEBECI T., STEWARTSON K., WILLIAMS P.G. "Separation and reattachment near the leading edge of a thin airfoil at incidence", AGARD CP 291 1980.
15. VELDMAN A.E.P. "New quasi simultaneous method to calculate interacting boundary layers", AIAA J., 19, pp. 79-85, 1981.
16. COUSTEIX J., GLEYZES C. "Calcul de bulbes de décollement", Internal Report N° 10/5014 DN, Dec. 1983.
17. GLEYZES C., COUSTEIX J., BONNET J.L. "A calculation method of leading edge separation bubbles", Numerical and Physical Aspects of Aerodynamic Flows II, Springer Verlag, 1983.
18. COUSTEIX J. "Analyse théorique et moyens de prévision de la couche limite turbulente tridimensionnelle", ONERA Publication N° 157, 1974.
19. GLEYZES C. "Calcul des bulbes de bord d'attaque de type court sur des aubes de turbomachines en écoulement subsonique compressible", Internal Report, Juillet 1982.
20. CHRISTIAN J.W., HANKEY W.L. "Similar solutions of the attached and separated compressible boundary layer with heat transfer and pressure gradient", ARL 70-0023, 1970.
21. LE BALLEUR J.C. "Couplage visqueux-non visqueux : analyse de problèmes incluant décollements et ondes de choc", La Recherche Aéronautique 1977-6
22. ARNAL D., HABIBALLAH M., COUSTOLS E. "Théorie de l'instabilité laminaire et critères de transition en écoulements bi- et tridimensionnels", La Recherche Aéronautique 1984-2.
23. ARNAL D., HABIBALLAH M. "Résolution numérique des équations de stabilité de la couche limite. Comparaison aux résultats expérimentaux obtenus", Internal Report, 1979.

24. HACK L.M. "Transition and laminar instability", Jet Prob. Lab., Publication 77-15, 1977
25. ARNAL D., HABIBALLAH M., DELCOURT V. "Synthèse sur les méthodes de calcul de la transition développées au DERAT", Internal Report, 1980.
26. SCHMITT V., MANIE F. "Ecoulement subsonique et transsonique sur une aile à flèche variable", La Recherche Aérospatiale, 1979-4.
27. AUPOIX B., COUSTEIX J. "Méthode intégrale de calcul de couche limite tridimensionnelle", Internal Report N° 8/3327 EY, 1980.

## LOW REYNOLDS NUMBER SEPARATION BUBBLE RESEARCH AT UTRC

William P. Patrick and David E. Edwards  
United Technologies Research Center  
East Hartford, CT 06108

### ABSTRACT

A coordinated experimental and analytical program is currently underway at the United Technologies Research Center to study low Reynolds number laminar separation bubbles. The objective of this program is to provide a high quality set of reference data for use in assessing and improving computational methods for predicting laminar boundary layer separation with turbulent reattachment in steady two-dimensional flow. Nonintrusive laser velocimeter measurements of velocity, turbulence, and Reynolds stress profiles will be obtained throughout the flowfield. Additional data will be obtained with flow visualization, surface static pressure measurements, and total pressure and hot-film traverses. Particular attention will be focused on defining the size and location of the separation bubble, determining the location of transition in the separated shear layer, and defining the laminar boundary layer and the development of the recovering reattached turbulent boundary layer. Sensitivity studies will be conducted to determine the effects of Reynolds number and adverse pressure gradient variations on the measured parameters. Additional tests to study the effects of variations of surface roughness, turbulence level, turbulence scale, and surface curvature are also planned.

### INTRODUCTION

Accurate prediction of boundary layer growth on compressor blade surfaces is currently hindered by the lack of a validated computational procedure for treating laminar separation bubble formation. Although present boundary layer procedures are capable of predicting the occurrence of laminar separation, the downstream bubble region must currently be treated in a semi-empirical manner using data correlations derived from various experiments. Although the chordwise extent of short, transitional separation bubbles is not large, a significant problem exists in predicting boundary layer behavior downstream of the bubble reattachment point. In particular, uncertainty exists in the definition of suitable initial boundary conditions to start a turbulent boundary layer calculation at the aft end of the bubble.

A number of laminar bubble investigations have been conducted since Jones [1] first pointed out the presence and behavior of laminar separation bubbles more than 50 years ago. Review articles have been written by Tanl [2] and Ward [3] and less exhaustive but more recent reviews are contained in the papers of Roberts [4] and Mueller and Batill [5]. Several studies using large scale airfoils have documented bubble size and location but in all of these studies the effect of curvature could not be separated from Reynolds number and pressure gradient effects.

At least three experimental studies have been conducted on flat plate test surfaces. They are the studies of McGregor [6], Gaster [7], and Ojha [8]. Gaster used an inverted airfoil to impose a suction peak followed by an adverse pressure gradient on the test surface. By correlating his results with those of Crabtree [9], Woodward [10], and McGregor, he produced the two-parameter bursting criteria. Ojha also studied the bursting phenomena.

Although these studies are useful in defining overall bubble characteristics, detailed measurements suitable for use in assessing the accuracy and assisting the further development of computational procedures for predicting bubble characteristics are lacking. The lack of reference bubble data is due, in part, to the difficulty of the experimental problem. Not only are such bubbles small and very thin, they are also extremely sensitive to flow disturbances produced by intrusive sensors. Design of suitable experiments has also been hindered in the past by the lack of analytical tools to assist the experimentalist in screening candidate test conditions and configurations.

Recognizing the lack of sufficient experimental data on separation phenomena affecting the compressor, fan and turbine blade design process, and with the recent development of codes designed to predict bubble characteristics and Laser Velocimetry techniques capable of studying reversed flow in a nonintrusive manner, the United Technologies Research Center initiated a major thrust in separated flow research approximately six years ago. Experimental studies of compressor and turbine blade trailing edge separated flows [11] and turbulent boundary layer separation with reattachment on a flat plate [12-13] have been completed. An investigation of shock-induced turbulent boundary layer separation with reattachment is currently in progress. Simultaneously, a multi-faceted analytical program was underway to develop numerical procedures for the prediction of strongly interacting viscous and inviscid flows with emphasis on separated flows [14-23]. Werle has presented a comprehensive overview of the UTRC program [24].

#### LAMINAR SEPARATION BUBBLE STUDIES

A coordinated experimental and analytical program is currently underway to study low Reynolds number laminar separation bubble formation in steady two-dimensional flow. This program will build on the experience gained in a previous effort [12, 13] which was directed at turbulent boundary layer separation and reattachment on a flat plate. The objective of the low Reynolds number program is to use non-intrusive Laser Velocimetry to provide a high quality set of reference data for use in assessing and improving computational methods for predicting compressor blade laminar boundary layer separation with turbulent reattachment. The overall program consists of five Phases as outlined in Table I. In Phase I, Exploratory Studies, the capability of producing a two-dimensional laminar separation bubble on flat plate in the UTRC Boundary Layer Wind Tunnel will be demonstrated. The objective is to generate a "short bubble" of sufficient size to permit adequate resolution of velocity profiles within the incident laminar

and reattached turbulent boundary layers as well as within the bubble. In Phase II, Detailed Studies of Baseline Case, a comprehensive set of high quality reference data for the baseline case will be obtained with a Laser Velocimeter to obtain mean velocity, turbulence, and Reynolds stress profiles throughout the flow field, in addition to flow visualization, surface static pressure measurements, and hot-film and total pressure traverses. Particular attention will be focused on defining the size and location of the separation bubble, determining the location of transition in the separated shear layer, and defining the laminar boundary layer and the development of the reattached turbulent boundary layer. In Phase III, Sensitivity Studies, the sensitivity of the laminar separation bubble to changes in incident Reynolds number, pressure gradient, turbulence intensity, and turbulence scale will be assessed. In Phase IV, Additional Sensitivity Studies, other factors which could influence the inception and behavior of laminar separation bubbles in compressor-like flows will be studied. Surface curvature and roughness are two parameters to be studied in this phase of the program. Other possibly relevant effects include the incident laminar boundary layer pressure gradient history and sound waves (intensity and frequency variations).

#### Experimental Facility

The experimental program will be conducted in the UTRC Boundary Layer Wind Tunnel which is shown schematically in Fig. 1. It is of a recirculating design and consists of a blower, a settling chamber/plenum, a contraction nozzle, the test section, a temperature control heat exchanger, and a return duct. This tunnel was designed to produce large scale two-dimensional boundary layers with Reynolds numbers, freestream turbulence levels, and pressure coefficient distributions typical of turbomachinery blades. A thorough calibration of the flow characteristics of the tunnel [25] has shown the flow to be highly two-dimensional and steady. The tunnel combines the abilities to vary test section turbulence, Reynolds number, and pressure gradient while maintaining a highly two-dimensional flow. The tunnel velocity can be set between 10 ft/sec and 100 ft/sec. The freestream turbulence level can be varied between 0.25 percent and 10 percent with the addition of turbulence generating grids. The longitudinal macroscale of the turbulence has been documented and ranges from nearly negligible levels for screen-generated turbulence to between 1 cm and 7 cm for grid turbulence.

A new test section designed for separation bubble studies is shown in Fig. 2. The upper wall test surface consists of a leading edge boundary layer scoop, a boundary layer development section, and a test plate fabricated from an 0.5 in-thick cast aluminum tool plate. The lower wall of the test section is fabricated from a single piece of 61 in x 34 in x 0.75 in polypropylene. The flexible lower wall has been designed with a series of spanwise slots and a movable support structure to permit a wide variation in the location, extent, and strength of the adverse pressure gradient region within the test section. Corner bleed slots along the length of the test plate are available to enhance flow two-dimensionality. One of the test section side walls is

made from select quality float glass to facilitate backscatter LV measurements. A 72 in. long constant area section will provide sufficient length downstream of the test section to probe the reattached turbulent boundary layer as it develops an equilibrium velocity profile.

## ANALYTICAL SCREENING

### Satisfaction of Gaster Criteria

The two-parameter bursting criteria of Gaster [7] was used as a guide in the preliminary selection of the test section dimensions to ensure that "short" transitional separation bubbles would be produced in the test section. The Gaster criteria delineate the boundary between short and long separation bubble formation in a plane defined by a deceleration parameter,  $(\theta_s^2/\nu)(\Delta U/\Delta x)$ , and the Reynolds number based on momentum thickness at separation,  $Re_{\theta_s}$ . Figs. 3(a) and 3(b) show the laminar separation bubble characteristics defined by the Gaster criteria for the test section having an 8.25 in inlet height when operated at 30 ft/sec and 15 ft/sec respectively with divergence angle as a parameter. For example, as shown in Fig. 3 when the divergence angle is two degrees or less the boundary layer will not separate at either flow speed. At 30 ft/sec, a divergence angle of 15 deg will produce a short separation bubble when  $Re_{\theta_s} > 220$ . At 15 ft/sec, however, the same 15 deg divergence angle will produce a long bubble when  $Re_{\theta_s} > 240$ .

### Numerical Computations

Based upon the the Gaster plots several candidate tunnel configurations and test conditions were identified which satisfied the Gaster criteria for short laminar separation bubbles. An analytical screening of these proposed test cases was conducted using the IVAN (Inviscid-Viscous Analysis) code to determine whether or not a laminar separation bubble would occur and to provide preliminary estimates of the bubble height and length. The IVAN code, which is based on Interacting Boundary Layer Theory, uses a stream function representation for the inviscid flow field and an inverse boundary layer analysis to represent the viscous flow field with displacement thickness coupling between the two solutions. The finite difference form of the inviscid and viscous flow equations are locally solved together with a quasi-simultaneous update procedure [23]. The modeling of transition (onset as well as the length) and turbulence plays a crucial role in the analysis of laminar separation bubbles as has been demonstrated by Carter and Vatsa [16] and Davis and Carter [21]. For this initial study, Roberts' transition model for separated flows [26] and Cebeci and Smith's turbulence model [27] are employed. In Roberts' model transition is assumed to have occurred when the following relation is satisfied:

$$\frac{U_{\infty}}{\nu} > 25,000 \log [ \coth (TF \times 10) ] \quad (1)$$

$$TF = T(u) \left( \frac{c}{A} \right)^{1/5} \quad (2)$$

In accordance with Roberts' suggestion [26] the assumption that  $TF = T(u)$  was used in the following calculations.

The matrix of tunnel configurations and test conditions (eight cases) that were analyzed in this study are shown in Table 2 and are plotted on Fig. 3. The configuration variations included inlet and exit tunnel height, diffuser angle, and location of the diffuser throat from the leading edge of the test section. In addition, the effect of inlet flow velocity on the separation bubble was evaluated. Five tunnel configurations designated as T1-T5 were used in this study and the inviscid computational grids used to represent them in the analysis are shown in Fig. 4. The test conditions corresponded to conditions anticipated for the baseline case. The inlet turbulence level was assumed to be 0.25 percent. To facilitate the experimental measurements a large separation bubble was desired for the baseline case, since Roberts' criterion indicate that the size of the bubble would be reduced when  $T(u)$  was increased during Phase III Sensitivity Studies.

In all cases analyzed in this study the inviscid analysis used a grid consisting of 101 uniformly spaced points in the x-direction and 21 points distributed in the y-direction such that the smallest step occurred at the lower wall. The boundary layer on the upper surface (contoured wall) was assumed to be turbulent (a trip strip will be used in the experiment to guarantee that the upper wall boundary layer is turbulent) with weak interaction with the inviscid flow field and hence could be neglected in this analytical screening. The boundary layer analysis on the lower surface used the same x-grid as the inviscid analysis with 100 grid points across the boundary layer. Additional calculations using finer computational grids in the separated flow region were made to insure that the results were not grid dependent. All calculations were converged to the precision level of the 32-bit Apollo DN 460 computer.

Results of this series of flow cases are shown in Table III. The Reynolds number, based on momentum thickness at separation,  $Re_{\theta_s}$ , the streamwise length of the separation bubble, and the height of the backflow region for each of the flow cases are shown in this table. In addition, velocity contours are plotted in Fig. 5 for all cases except those cases which had open separation. Several observations can be made from Table III and Fig. 5. First, for all of the cases with an inlet velocity of 30 ft/sec, the length of the separation bubble does not differ significantly (approximately 3 inches) even though the diffuser angle and the distance from the leading edge to the diffuser throat varies in each of these cases. This behavior was anticipated since the length of the separation bubble is dependent upon the distance from separation to transition and, as stated before, Roberts' transition criteria is a function of velocity, viscosity, and turbulence level and is not a function of approach length. However, it is noted that while increasing the diffuser angle does not increase the length of the separation bubble, it does increase the height of the backflow region ( $U < 0$ ) and the height of the recirculation region as can be observed when comparing cases 1 and 4 or cases 2 and 5. The height of the recirculation region as predicted by the analysis should be

considered a conservative estimate since in some recent work by Davis and Carter [21], an analysis using transition and turbulence models similar to those applied in the present study significantly underpredicted the height of a laminar separation bubble while correctly predicting the length of the bubble.

The effect of the Reynolds number on the laminar separation bubble was also evaluated in this study by varying the tunnel velocity while holding all other parameters fixed. However, reduction of the inlet velocity to 15 ft/sec for tunnel configurations T1 and T3 (cases 3 and 6) produced flows with open separation. Specifically, these flows had laminar separation and transition in the separated shear layer but there was insufficient energy in the turbulent shear layer to result in flow reattachment.

The T5 configuration was then introduced in this study. This configuration was designed based upon the results of the first 6 cases. In the previous cases when the inlet velocity was reduced flow had open separation. Thus, it was conjectured that a possible way to prevent open separation was to decrease the length of the adverse pressure gradient region (from 13 inches to 9 inches). The flow through the T5 configuration was analyzed at inlet velocities of 30 ft/sec and 15 ft/sec (cases 7 and 8) and the results of these with analyses are shown in Table III and Figs. 5(e) and 5(f). By comparing cases 4 and 7, it is observed that a reduction in the length of the adverse pressure gradient region only changes the results slightly for the flow with an inlet velocity of 30 ft/sec. However, when the inlet velocity is reduced to 15 ft/sec the flow in this configuration produced a separation bubble that was 7.2 inches in length with a backflow height of .097 inches whereas previously (case 6) the flow had open separation. Note in Fig. 3(b) that both cases 6 and 8 are essentially on the bursting boundary as defined by the Gaster criteria. Although numerical calculations indicated that case 6 would produce a long bubble whereas case 8, having a shorter adverse pressure gradient, would produce a short bubble, in practice case 8 might be unsteady (i.e. oscillating between short and long bubble regimes). The displacement thickness for cases 7 and 8 is shown in Fig. 6. The effect of reducing the inlet velocity from 30 ft/sec to 15 ft/sec caused the displacement thickness to approximately double in the separated flow region. Finally, the surface pressure for cases 7 and 8 is shown in Fig. 7. From this figure, it is observed that case 8 has a longer pressure plateau than case 7 which is consistent with the greater extent of separated flow found in this case.

Based upon the results of this study the T5 tunnel configuration has been chosen as the baseline configuration for Phase I Experimental Screening. An inlet flow velocity between 15 and 30 ft/sec should produce the desired large, steady, two-dimensional, "short" transitional separation bubble desired for the baseline case.

#### PROGRESS SUMMARY

The four-phase program outlined above is being conducted under the

sponsorship of NASA Lewis Research Center (Contract NAS3-23693) and availability of a summary report is anticipated in 1987. Interim publications regarding this specified program and other elements of the UTRC research program in the area of low Reynolds number separation are anticipated.

#### NOMENCLATURE

c	chord length
h	height of test section
l	length from separation to transition
TF	turbulence factor
T(u)	turbulence intensity
U	axial velocity
x	axial distance
$\theta$	momentum thickness
$\Lambda$	turbulence macroscale
$\nu$	kinematic viscosity

#### Subscripts:

o	inlet condition
s	at separation
$\infty$	freestream

#### REFERENCES

1. Jones, B. M., "An Experimental Study of the Stalling of Wings," ARC R&M 1588, Dec. 1933.
2. Tanl, I., "Low Speed Flows Involving Bubble Separations," Progress in Aeronautical Sciences, 5, 1964, pp. 70-103.
3. Ward, J. W., "The Behavior and Effects of Laminar Separation Bubbles on Aerofolls in Incompressible Flow," J. of the Royal Aeronautical Society, 67, pp. 783-790.
4. Roberts, W. B., "The Effect of Reynolds Number and Laminar Separation on Axial Cascade Performance," ASME J. of Engineering for Power, April 1975, pp. 261-274.
5. Mueller, T. J. and S. M. Batill, "Experimental Studies of Separation on a Two-Dimensional Airfoil at Low Reynolds Number," AIAA J., 20:4, Apr. 1982, pp. 457-463.
6. McGregor, I., "Regions of Localized Boundary Layer Separation and their Role in the Nose Stalling of Aerofolls," Ph.D. Thesis, Queen Mary College, University of London, 1954.
7. Gaster, M., "The Structure and Behavior of Laminar Separation Bubbles," ARC R&M 3595, 1969.

8. Ojha, S. K., "An Experimental Study of Laminar Separation Bubbles," J. of the Aeronautical Society of India, 21:3, Aug. 1969, pp. 275-303.
9. Crabtree, L. F., "The Formation of Regions of Separated Flow on Wing Surfaces, Part II. Laminar Separation Bubbles and the Mechanism of Leading Edge Stall," ARC R&M 3122, 1959.
10. Woodward, D. S., "An Investigation of the Parameters Controlling the Behavior of Laminar Separation Bubbles," RAE Tech. Memo Aero. 1003, F.M. 3888, 1967.
11. Paterson, R. W., and H. D. Weingold, "Experimental Investigation of a Simulated Compressor Trailing Edge Flowfield," AIAA Paper 84-0101, Jan. 1984.
12. Patrick, W. P., "Mean Flowfield Measurements In a Separated and Reattached Flat Plate Turbulent Boundary Layer," AIAA Paper 85-1568, to be presented at the AIAA 18th Fluid Dynamics, Plasma Dynamics, and Laser Conference to be held in Cincinnati, Ohio, July 16-18, 1985.
13. Patrick, W. P., "Flowfield Measurements In a Separated and Reattached Flat Plate Turbulent Boundary Layer," Final Report for Contract NAS3-22770, In preparation.
14. Carter, J. E., "Viscous-Inviscid Interaction Analysis of Transonic Turbulent Separated Flow," AIAA Paper 81-1241, June 1981.
15. Vatsa, V. N., M. J. Werle, and J. M. Verdon, "Viscid/Inviscid Interaction at Laminar and Turbulent Symmetric Trailing Edges," AIAA Paper 82-0165, Jan. 1982.
16. Carter, J. E. and V. N. Vatsa, "Analysis of Airfoil Leading Edge Separation Bubbles," NASA Contractor Report 168935, May 1982.
17. Vatsa, V. N. and J. E. Carter, "Analysis of Airfoil Leading-Edge Separation Bubbles," AIAA J., 22:12, Dec. 1984, pp. 1697-1704.
18. Davis, R. T., and M. J. Werle, "Progress on Interacting Boundary-Layer Computation at High Reynolds Number," appearing in Numerical and Physical Aspects of Aerodynamic Flows, pp. 187-210, Springer-Verlag, New York, 1982.
19. Vatsa, V. N. and J. M. Verdon, "Viscid/Inviscid Interaction Analysis of Separated Trailing-Edge Flows," AIAA J., 23:4, Apr. 1985, pp. 481-489.
20. Edwards, D. ., and W. P. Patrick, "An Experimental/Theoretical Investigation of Turbulent Separating and Reattaching Flows," presented at Open-Forum Session, AIAA 6th Computational Fluid Dynamics Conference, Danvers, MA, July 13-15, 1983.

21. Davis, R. L., and J. E. Carter, "Analysis of Airfoil Transitional Separation Bubbles," NASA Contractor Report 3791, April 1984.
22. Edwards, D. E., J. E. Carter, and M. M. Hafez, "Viscous/Inviscid Interaction Analysis of Transonic Shock Induced Separated Flow Including Normal Pressure Gradients," AIAA Paper 85-0371, Jan. 1985.
23. Edwards, D. E., and J. E. Carter, "A Quasi-Simultaneous Finite Difference Approach for Strongly Interacting Flow," presented at the Third Symposium on Numerical and Physical Aspects of Aerodynamic Flows, Long Beach, CA, Jan. 1985.
24. Werle, M. J., "Compressor and Turbine Blade Boundary Layer Separation," presented at the AGARD Propulsion and Energetics Panel 61st Specialists Meeting on Viscous Effects in Turbomachines, Copenhagen, Denmark, June 1983.
25. Blair, M. F., D. A. Bailey, and R. H. Schlinker, "Development of a Large-Scale Wind Tunnel for Simulation of Turbomachinery Airfoil Boundary Layers," Trans. of the ASME, J. of Engineering for Power, 103, Oct. 1981, pp. 678-687.
26. Roberts, W. B., "Calculation of Laminar Separation Bubbles and Their Effect on Airfoil Performance," AIAA J., 18: 1, 1980, pp. 25-31.
27. Cebeci, T. and A. O. Smith: Analysis of Turbulent Boundary Layers, Academic Press, 1974.

**Table I Experimental/Analytical Research Program for Low Reynolds Separation Bubbles**

<b>Phase I: Exploratory Studies</b> <ul style="list-style-type: none"> <li>● Definition of Flow Conditions</li> <li>● Analytical Screening</li> <li>● Experimental Screening</li> <li>● Experimental Definition of Baseline Case</li> </ul>	<b>Phase II: Detailed Studies of Baseline Case</b> <ul style="list-style-type: none"> <li>● Measurements</li> <li>● Data Analysis</li> <li>● Code Assessment</li> </ul>
<b>Phase III: Sensitivity Studies</b> <ul style="list-style-type: none"> <li>● Reynolds Number Variations</li> <li>● Pressure Gradient Variations</li> <li>● Turbulence Intensity Variations</li> <li>● Turbulence Scale Variations</li> <li>● Code Assessments</li> <li>● Other Effects</li> </ul>	<b>Phase IV: Additional Sensitivity Studies</b> <ul style="list-style-type: none"> <li>● Surface Curvature</li> <li>● Surface Roughness</li> <li>● Code Assessment</li> </ul>

**Table II Matrix of Tunnel Configurations and Test Conditions**

TEST CASE	DIFFUSER ANGLE (DEGREES)	LEADING EDGE FROM DIFFUSER THROAT (INCHES)	INLET TUNNEL HEIGHT (INCHES)	EXIT TUNNEL HEIGHT (INCHES)	INLET VELOCITY (FT/SEC)	GEOMETRY	INLET TURBULENCE %
1.	10.	12.	0.25	12.	30.	11	.25
2.	10.	6.	0.25	12.	30.	12	.25
3.	10.	12.	0.25	12.	15.	11	.25
4.	15.	12.	0.25	12.	30.	13	.25
5.	15.	6.	0.25	12.	30.	14	.25
6.	15.	12.	0.25	12.	15.	13	.25
7.	15.	12.	0.25	10.0	30.	15	.25
8.	15.	12.	0.25	10.0	15.	15	.25

**Table III Results of Test Cases**

TEST CASE	INLET VELOCITY (FT/SEC)	Re <sub>s</sub> Separation	STREAMWISE LENGTH OF LAMINAR SEPARATION BUBBLE (INCHES)	BACKFLOW HEIGHT (INCHES)
1.	30.	365.	3.0	.018
2.	30.	323.	2.2	.006
3.	15.	----- OPEN SEPARATION -----		
4.	30.	336.	3.4	.030
5.	30.	285.	2.9	.023
6.	15.	----- OPEN SEPARATION -----		
7.	30.	356.	3.1	.019
8.	15.	229.	7.2	.097

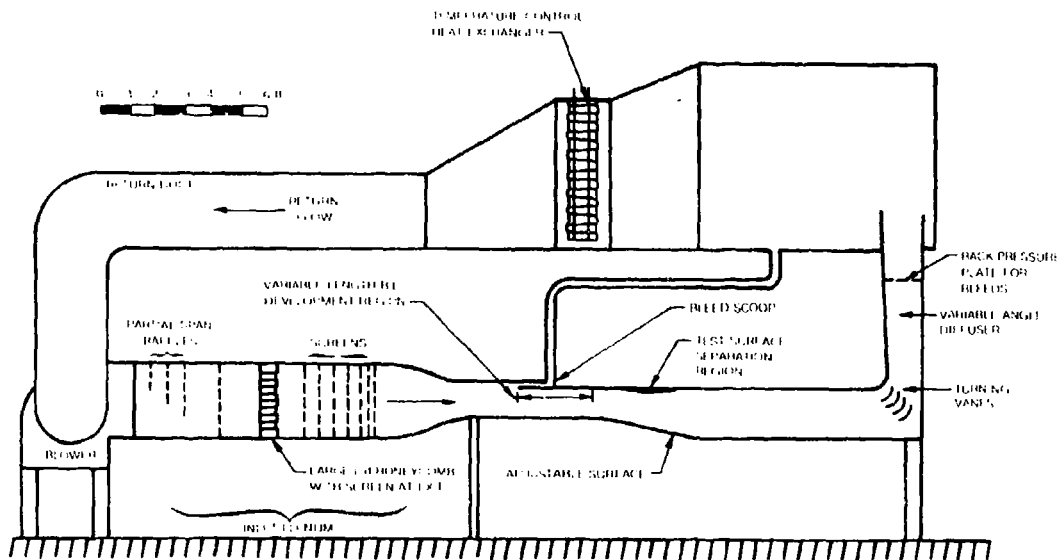


**Fig. 1 UTRC Boundary Layer Wind Tunnel**

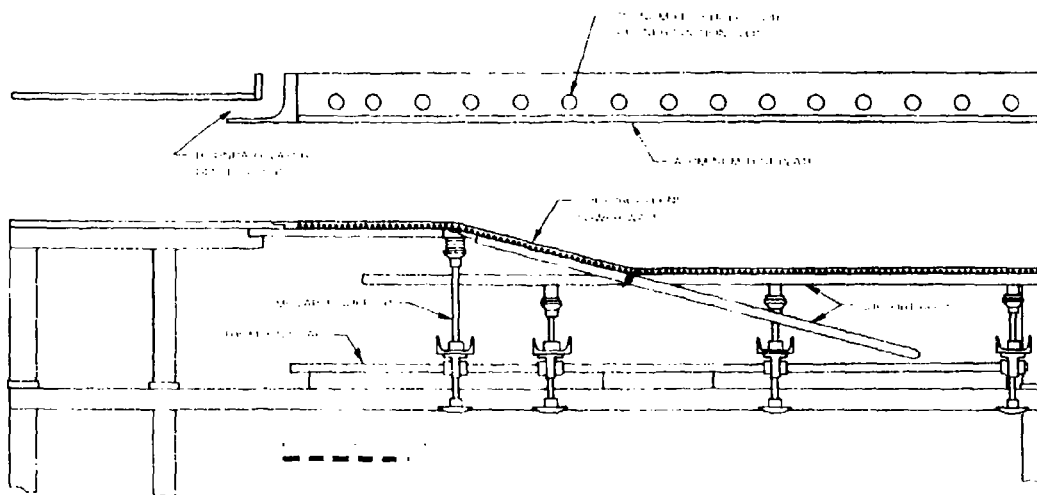
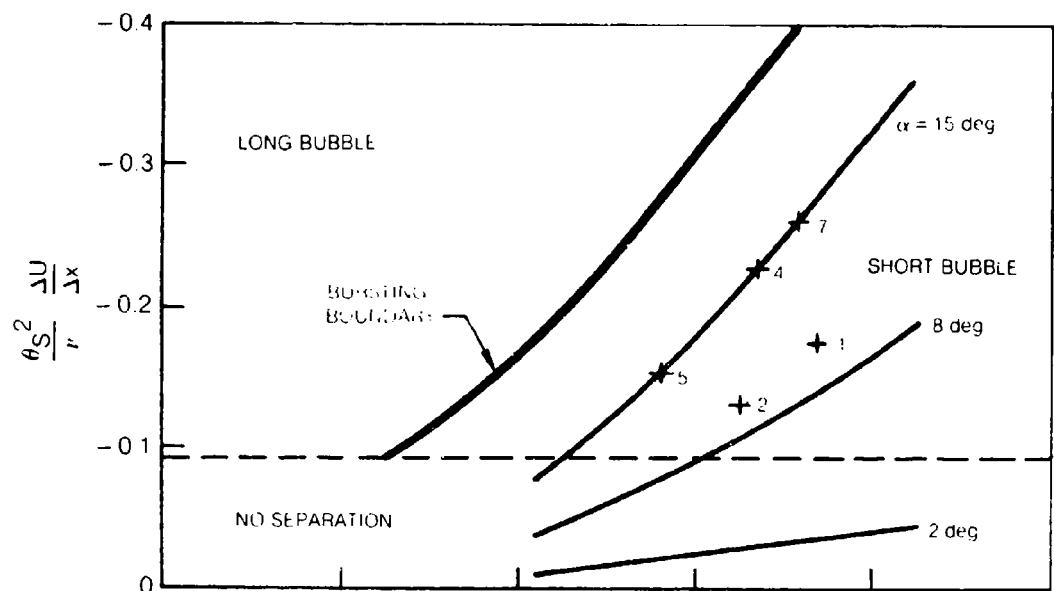
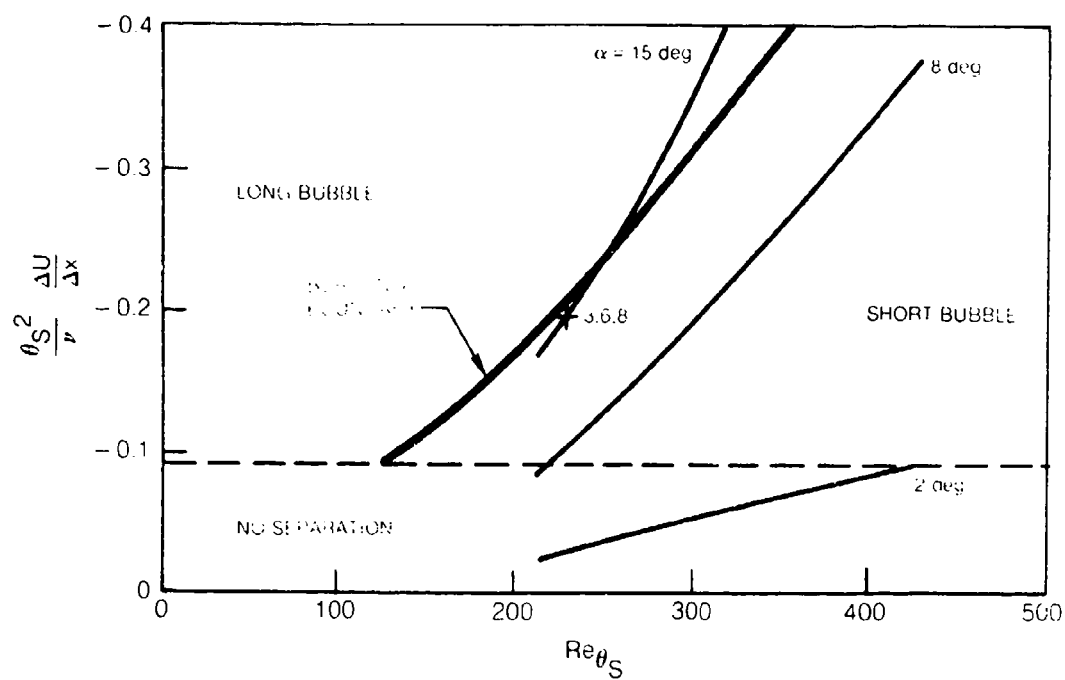


**Fig. 2 Test Section for Laminar Separation Bubble Studies**



a)  $U_\infty = 30$  ft/sec



b)  $U_\infty = 15$  ft/sec

**Fig. 3 Wind Tunnel Capabilities vs Gaster Separation Criteria ( $h_0 = 8.25$  in.)  
Pluses Represent Test Cases Studies in Analytical Screening**

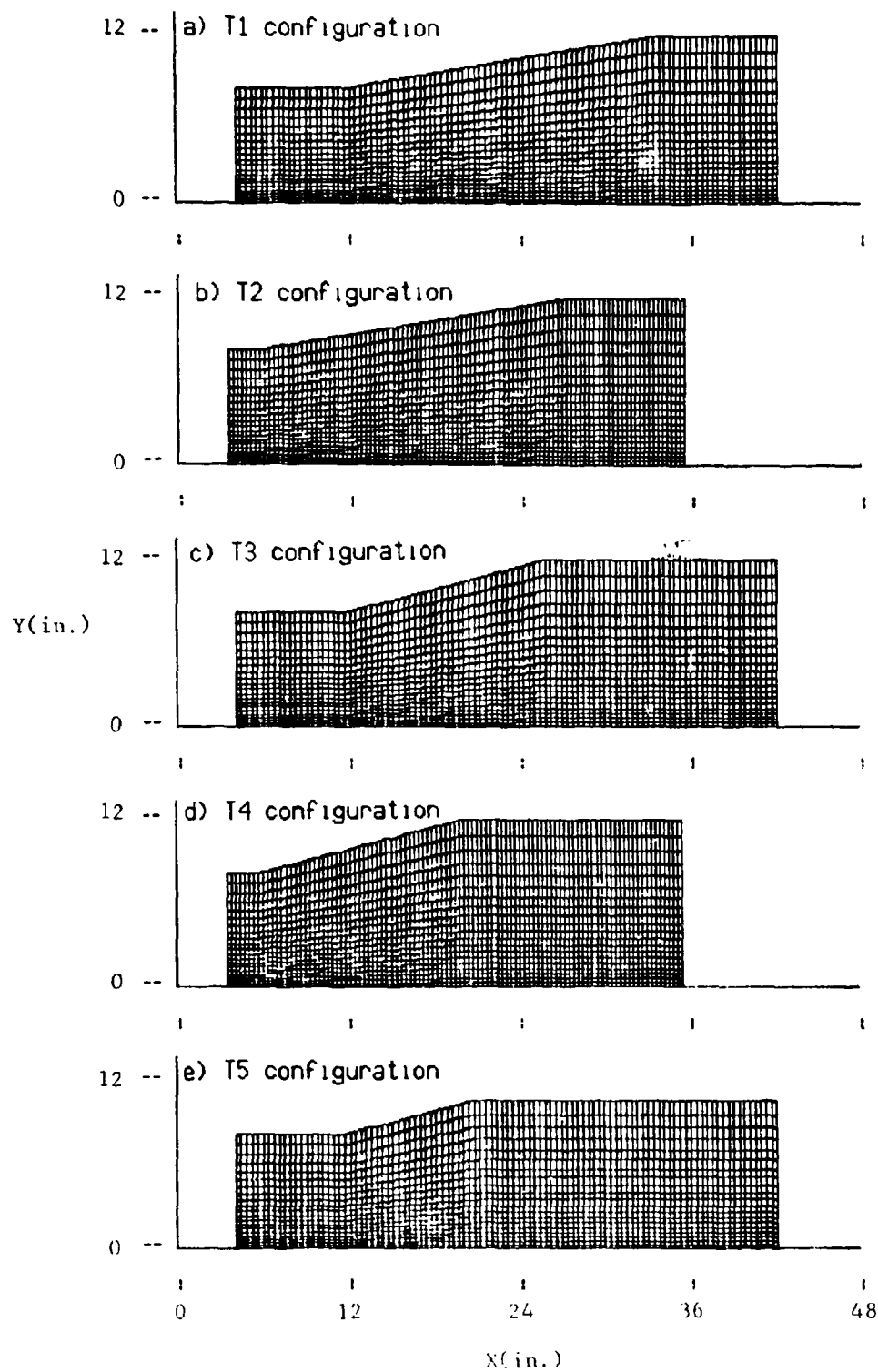
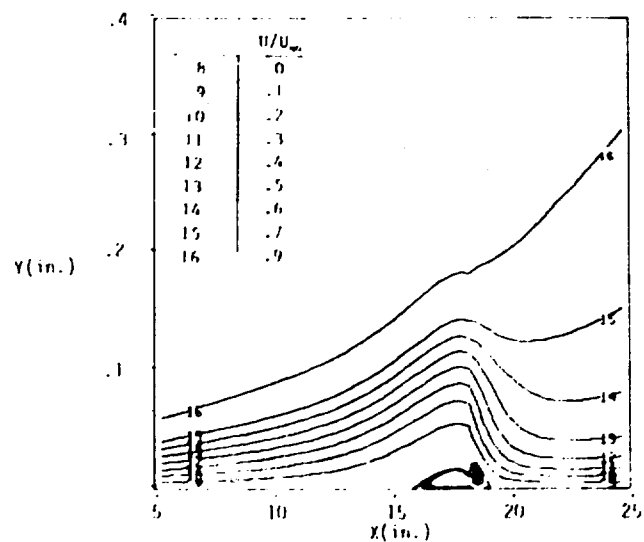
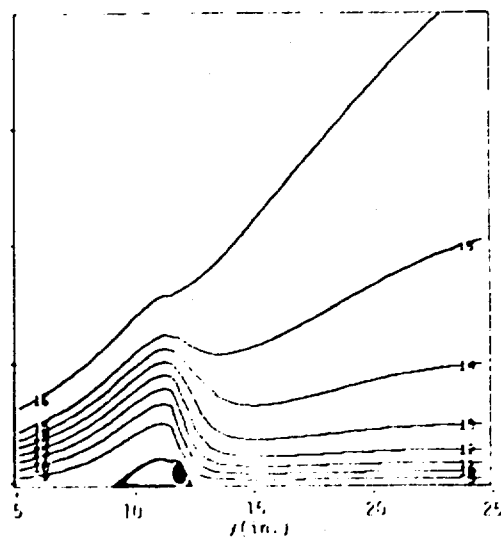


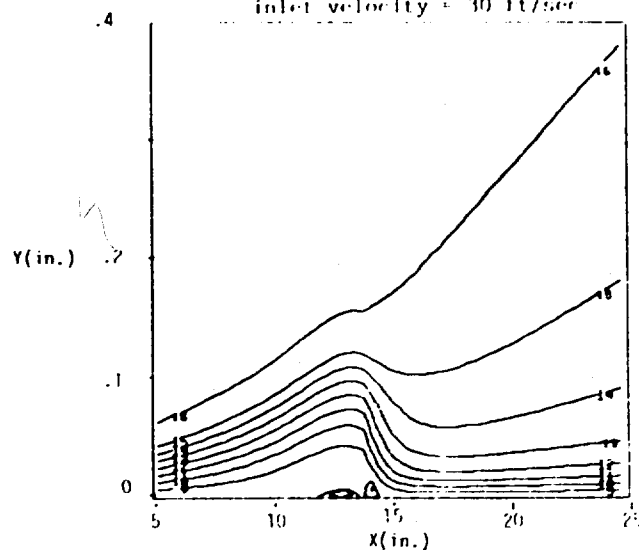
Fig. 4 Tunnel Configurations and Computational Mesh



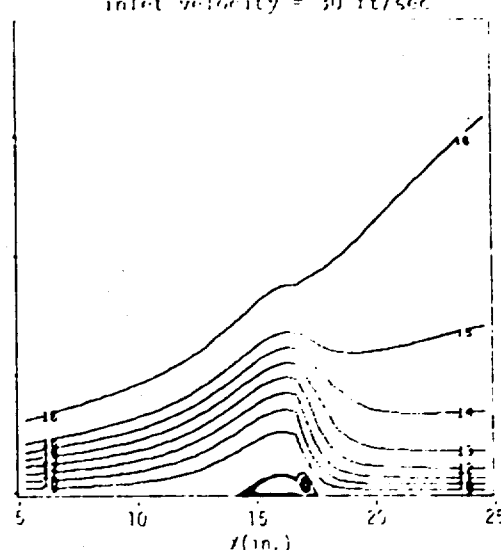
a) Case 1, T1 configuration,  
inlet velocity = 30 ft/sec



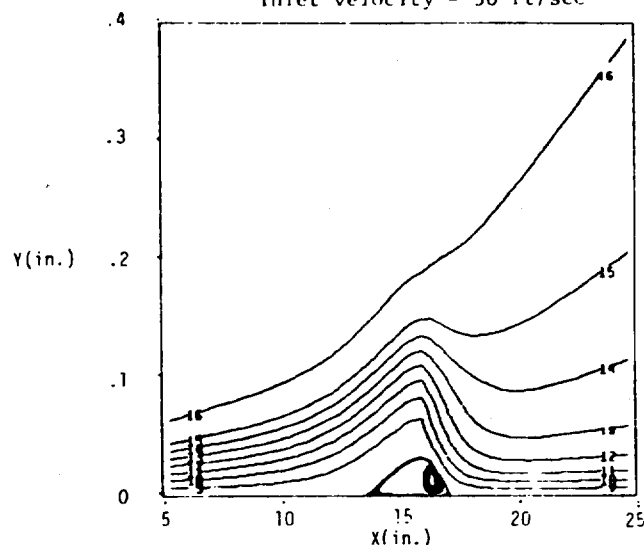
d) Case 5, T4 configuration,  
inlet velocity = 30 ft/sec



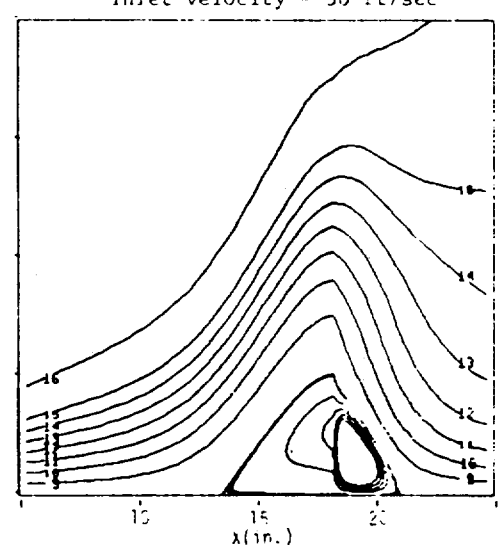
b) Case 2, T2 configuration,  
inlet velocity = 30 ft/sec



e) Case 7, T5 configuration,  
inlet velocity = 30 ft/sec



c) Case 4, T3 configuration,  
inlet velocity = 30 ft/sec



f) Case 8, T5 configuration,  
inlet velocity = 15 ft/sec

Fig. 5 Velocity Contours

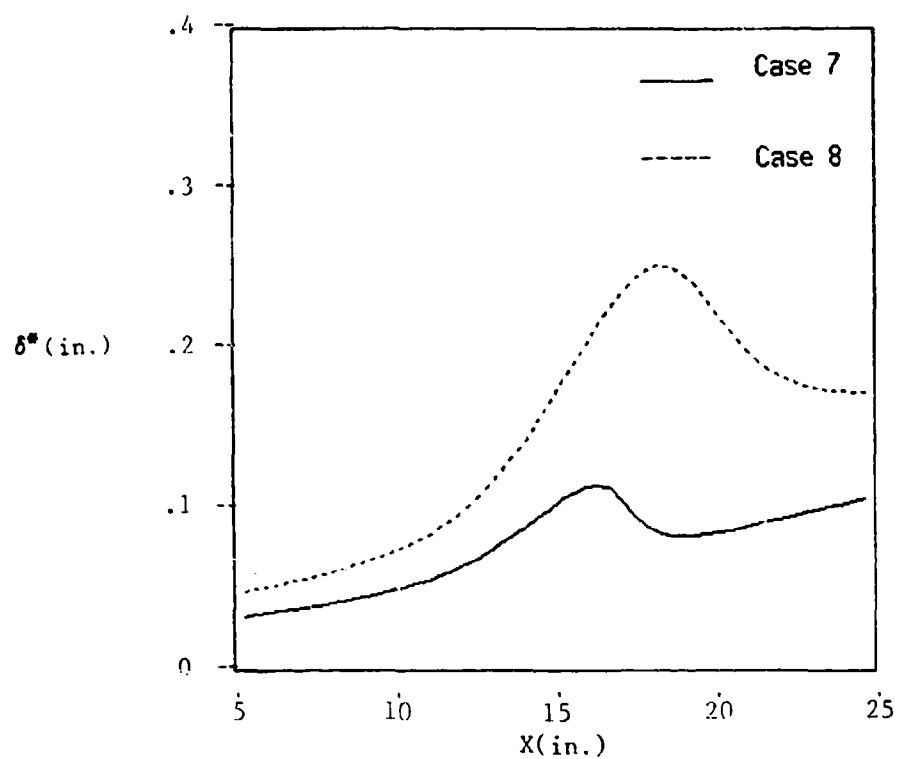


Fig. 6 Displacement Thickness Distributions

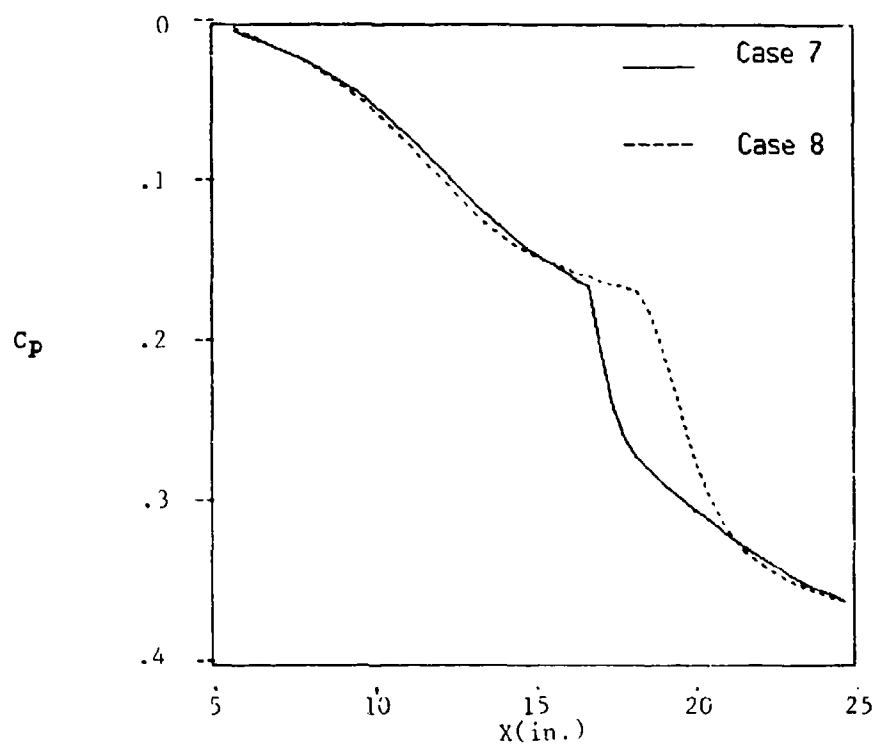


Fig. 7 Wall Pressure Distributions

SEPARATION BUBBLE BEHAVIOR  
FOR A NACA 23009 AIRFOIL

S. S. Fisher,\* J. D. Abbitt,\*\* and G. W. O'Leary\*\*  
Department of Mechanical and Aerospace Engineering  
University of Virginia  
Charlottesville, Virginia 22901

ABSTRACT

The smoke wire flow visualization technique has been employed to obtain photographic records of streaming patterns over a smooth-surface NACA 23009 airfoil at chord Reynolds numbers low enough to result in the formation of a suction-side separation bubble. Test angles of attack range from zero to beyond that for full stall. Chord Reynolds numbers range from 15,000 to 133,000. A high aspect ratio model is employed and observations are restricted to a narrow mid-span section. The tests are carried out in a wind tunnel for which free stream turbulence and fan-induced noise are very low. These photographs reveal, in various combinations and to a high degree of detail, the following processes: laminar boundary layer separation, vortex roll-up and turbulence breakdown within the separated layer, turbulent entrainment of the separated layer and flow reattachment to the airfoil surface, thereby resulting in a separation bubble, and turbulent boundary layer separation. Surface pressure data support and expand the flow interpretations which may be drawn from the photographs. The important features of these patterns are in keeping with previous observations for other airfoils and with physical expectations.

INTRODUCTION

The results presented in this paper constitute a first attempt by the authors to characterize and understand the separation and reattachment events which occur in flows over airfoils at values for the chord Reynolds number  $Re$  low enough for a separation bubble to form. Such a bubble forms when  $Re$  is small enough for the flow to first separate at a point where the boundary layer is still laminar, and when  $Re$  is still large enough for transition to turbulence to take place within the separated layer in such a manner that turbulent mixing can entrain the separated fluid sufficient to allow the external flow to reattach itself to the surface.

The objective of this work is to contribute to the state of knowledge and understandings regarding these bubbles. Understandings which might lead to a reduction in the bubble size or to reduction in its detrimental effects upon airfoil aerodynamics are of primary interest. A long-term objective of this work is to contribute to the development of of airfoils and wings which exhibit improved aerodynamic behavior when operated in the  $Re$  range where these bubbles tend to form.

---

\* Professor

\*\* Graduate Student

Two procedural objectives which were adopted for this work were (a) to investigate flows which were as two-dimensional as practical and (b) to investigate flows which were as free from extraneous perturbation as practical. Two-dimensionality was approached by employing a high aspect ratio wing model and by setting its span equal to that of the wind tunnel. Extraneous perturbations were kept small by employing a low-turbulence, low-noise tunnel.

The NACA 23009 airfoil section is not a particularly strong candidate for aerodynamic application at values of  $Re$  where separation bubbles tend to form. This section was chosen instead because a high quality wing model which incorporated this profile shape was available in the laboratory. As it turns out, the general physical characteristics of separation bubbles are not highly airfoil-specific.

No attempt will be made in this paper to review the state of understandings of flows over airfoils at lower Reynolds numbers or of related aerodynamic behaviors. For the reader who wishes to become better informed in these matters, Refs. 1 and 2 represent excellent starting points. Review of Refs. 3-9 is also recommended.

## APPARATUS

### Wind Tunnel

A schematic diagram of the wind tunnel employed for these tests is presented in Fig. 1. This tunnel is of the open-return type and is housed within a large, closed room. Its test section lateral dimensions are 0.61 m by 0.61 m. It is driven by a 12.5 hp DC electric motor

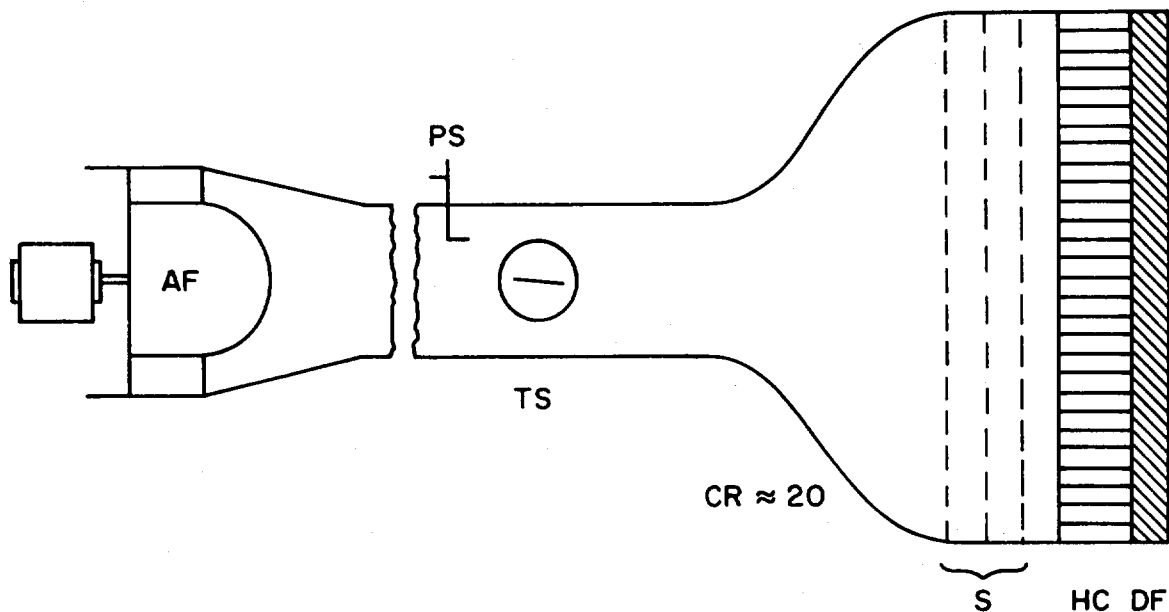


Figure 1. Wind tunnel schematic diagram, side view.  
 AF = axi-vane fan, CR = contraction ratio (area), DF = dust filter, HS = honeycomb (flow straightener), PS = pitot-static probe, S = screens (3, 1 mm mesh).

connected to a commercial axial-vane fan. The range of available free stream flow speeds is from approximately 1 m/s to 32 m/s. Speed constancy at any given setting is excellent.

Two important features of the design of this tunnel are its carefully constructed, high-contraction-ratio entrance section and its large separation distance between test section and fan (5 m). These features result in, respectively, a very low test section turbulence level (typically 0.1% or less) and very low fan-related test section noise.

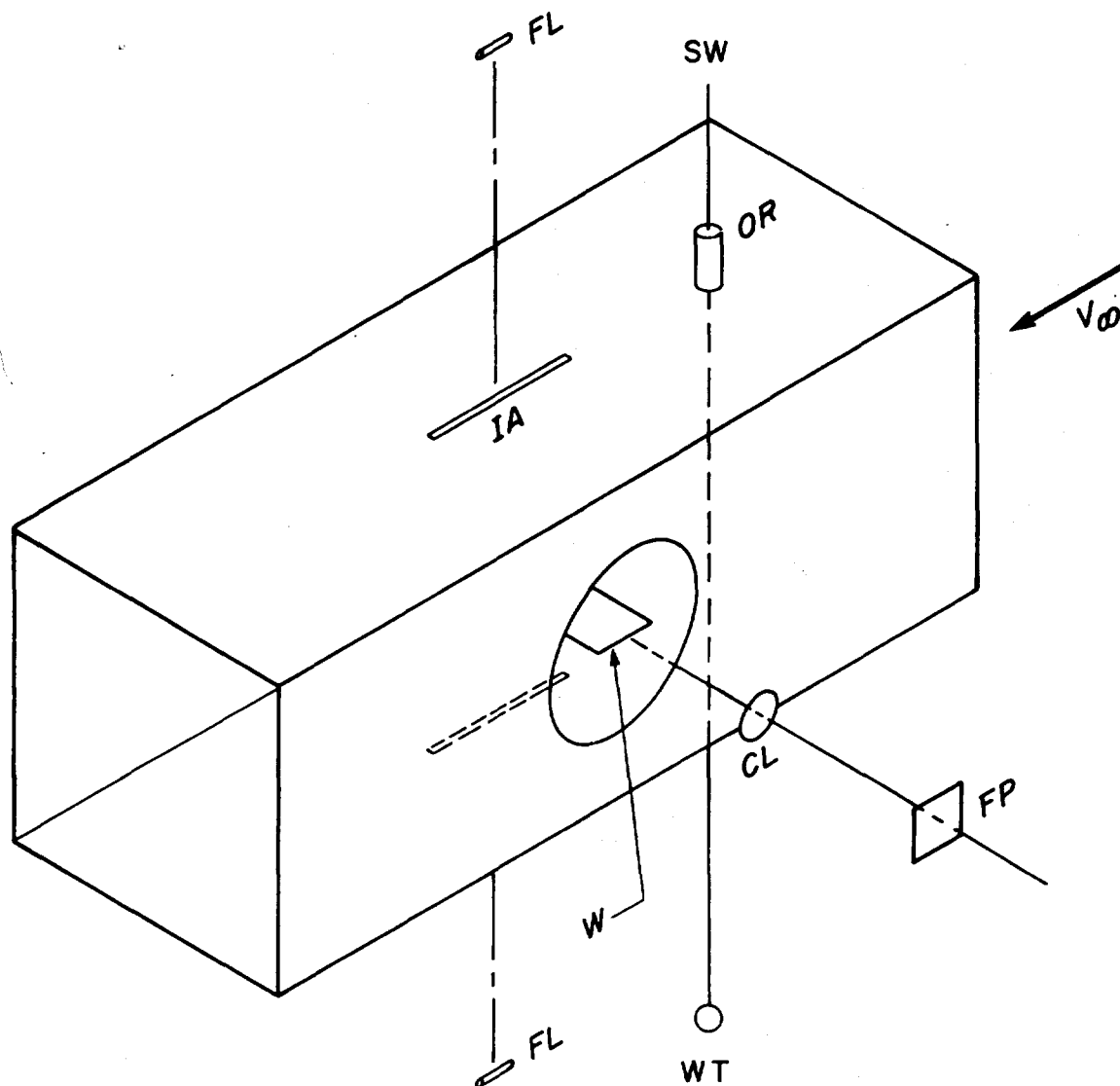


Figure 2. Smoke wire apparatus.  
CL = camera lens, FL = flashlamp, FP = film plate, IA = illumination aperture, OR = oil reservoir, SW = smoke wire  
W = wing, WT = weight.

## Smoke Wire

A diagram of the smoke wire apparatus, approximately to scale, is shown in Fig. 2. This apparatus was constructed following the description of Batill and Mueller [10]. In the wind tunnel, the wing was centered vertically with its span axis horizontal. Its suction side was turned down. The smoke wire was stretched vertically across the tunnel at mid-span 0.5 m upstream of wing center.

The process of forming "smoke" filaments by means of this wire is as follows. First, a mineral-type oil is distributed along the wire. This oil distributes itself, naturally, in the form of small, closely spaced, approximately equal diameter beads. The wire is then heated by passing an electrical current through it. This heating causes each bead to evaporate, and the resulting vapor is carried downstream in the form of a narrow filament, provided that the wire Reynolds numbers is not too high. Within a few wire diameters, the oil vapor condenses into a very small droplet fog. This fog filament is then used to follow stream or streak lines for the flow.

In these experiments, as the sheet of smoke filaments passed over the wing, it was flash-illuminated by a thin vertical sheet of light. This light was produced by two matched xenon flashlamps positioned symmetrically above and below the test section. Each lamp was housed inside an opaque conduit which is not shown in the figure. This conduit was needed to reduce the amount of stray light which could reach the photographic plate.

The smoke filament pattern was photographed through a 55 mm diameter "zoom"-type camera lens. The focal length adjustment for this lens was from 80 to 200 mm. It was installed in a large Polaroid bellows-type camera (Model MP-3) together with an 0.10 m by 0.13 m film plate. The depth of field resolved by this photographic arrangement was such that only a narrow mid-span section of the wind tunnel was brought into focus. All test section windows were transparent acrylic.

The photographic system was light-limited. The lens aperture was opened full ( $f4$ ) and each flashlamp was operated at maximum output ( $\sim 20$  J per lamp per flash). Type 57 Polaroid film, ASA 3000, was employed. During film exposure, room lights were switched off.

A special two-channel timer was employed to control the interval over which electrical current was passed through the wire, and to trigger the flashlamps following a proper delay.

The wire was 0.08 mm (0.0031 in.) diameter nichrome. The oil was a commercial fluid intended for use in toy locomotives. This oil was applied to the wire by raising and lowering it through a standard hypodermic syringe and needle located at the top of the tunnel. See "oil reservoir" in Fig. 2.

## Wing Model

The wing model was made of aluminum, had a chord length of 0.127 m, and a span length of 0.61 m. Nine pressure taps were included along its suction surface, ranging in position from the 5% to the 80% chord station. Seven taps were included along its pressure surface, ranging in position from the 10% to the 75% chord station. These taps were 0.5 mm in diameter and were separated 2.5 mm in span one from the next. Their mean spanwise location was 0.13 m from the tunnel wall. The test section wall boundary layer thickness never exceeded 0.10 m. Prior to installation in the tunnel, the wing was sprayed with a thin layer of flat black paint and sanded smooth with No. 240 sandpaper. Wing angle of attack was adjusted externally by rotating the wing about its mid-chord line. Each angle was set by increasing from a lower value.

## Pressure Measurements

All pressures were measured by means of a 10 Torr variable-capacitance diaphragm-type pressure transducer. Wind tunnel dynamic pressure was sensed by a pitot-static probe positioned as shown in Fig. 1.

## RESULTS

### Preliminary Remarks

In each photograph, the flow will be from left to right. On all photographs, shadow lines will be seen to extend across the flow beginning at the airfoil leading edge and trailing edge. These lines are the product of the two-sided illumination. Additional striations normal to the flow will be seen in several of the photographs. These striations are caused by drops of oil which have spilled onto the lower illumination window. Photograph-to-photograph differences in the size and spacing of the smoke filaments will also appear. These differences arise mainly due to variations in the elapsed time between oiling and heating of the wire. With increase in this time, the smaller oil beads which initially form along the wire coalesce into larger beads.

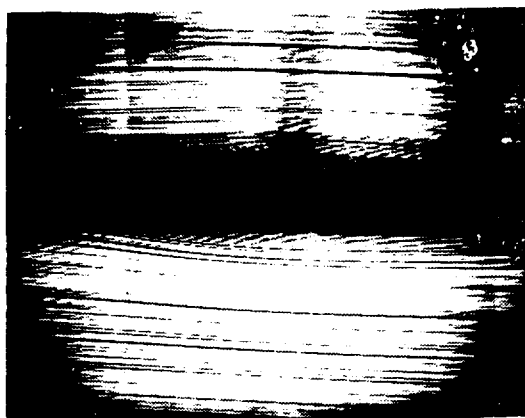
In each photograph, an image of all but the leading edge part of the airfoil profile appears. This image is produced by illumination light scattered from the airfoil surface into the camera. Near the leading edge, this light cannot be "seen" by the camera.

Optical distortion of the photographic images is negligible. Also, because the smoke wire was located some 6000 wire diameters upstream of wing center, distortion of the wing free stream flow by this wire was always quite small. The most important effect of the wire upon this flow was a buoyant one caused by wire heating. This effect was most important at the lowest flow speed. There it reduced the wing angle of attack by as much as  $1^\circ$ .

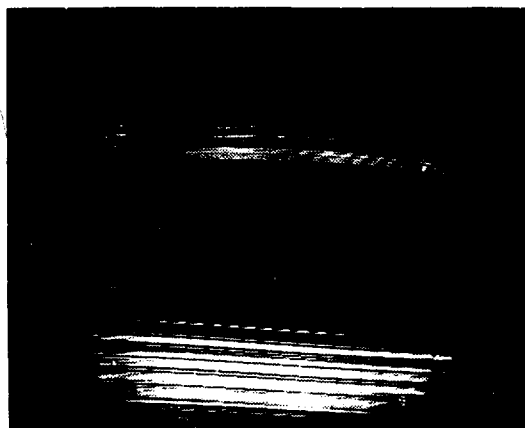
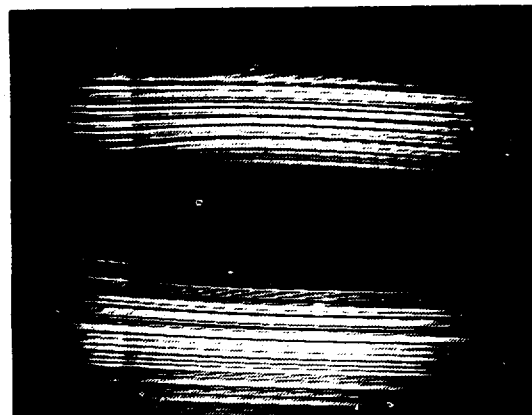
Angle of attack values which will be stated for these results may be in systematic error by up to  $1^\circ$ . Beyond this fact, the  $1\sigma$  uncertainty in these values is of order  $0.1^\circ$ .

Photographs for  $Re = 15,000$ : Figure 3a

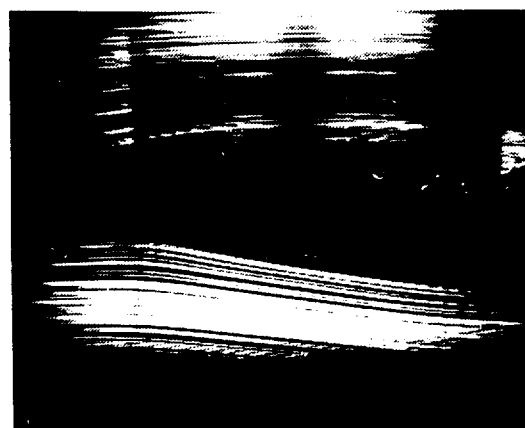
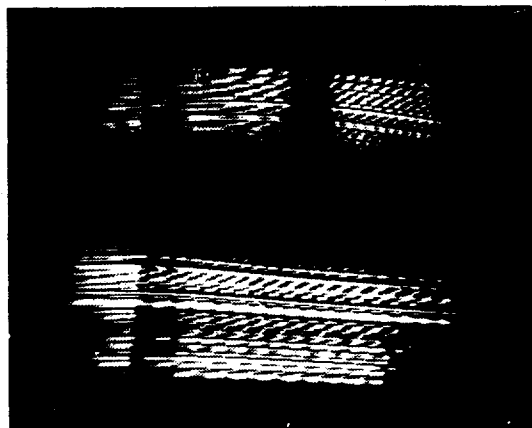
$\alpha = 0^\circ$  For this photograph, the free stream flow speed is very low (1.8 m/s). Careful inspection of the flow pattern in the immediate vicinity of the airfoil reveals that the suction-side laminar boundary layer separates ahead of mid-chord and does not reattach. No indication



$0^\circ$



$5^\circ$



$10^\circ$



(a)  $Re = 15,000$

(b)  $Re = 33,000$

Figure 3. Smoke wire photographs.

of any unstable flow behavior appears within the separated region. The entire flow field displayed within the photograph is laminar.

$\alpha = 5^\circ$  At this angle, the suction-side laminar boundary layer separates just downstream of the leading edge. The separated layer then exhibits a rolled-up vortex near the trailing edge. This vortex represents an instability which can eventually lead to turbulence breakdown. The less stable behavior of this separated flow compared to the one above may be understood in terms of the stronger suction-side adverse pressure gradient and the increased axial length of the separated region.

$\alpha = 10^\circ$  At this angle of attack, as would be expected, the thickness of the separated region increases and breakdown toward turbulence proceeds to an even greater extent.

Photographs for  $Re = 33,000$ : Figure 3b

$\alpha = 0^\circ$  The flow pattern exhibited in this photograph is similar to that in its counterpart in Fig. 3a. However, in this case, note that the pressure-side flow has also separated, beginning near the mid-chord station.

$\alpha = 5^\circ$  For this photograph, compared to its counterpart in Fig. 3a, the thickness of the separated region is reduced and turbulence breakdown within this region develops to an increased extent. Unfortunately, due to the faintness of the filaments within the separated region near the trailing edge, the increased mixing there is not resolved in this reproduced version of the original photograph.

$\alpha = 10^\circ$  This pattern is in all major respects identical with its counterpart in Fig. 3a.

Photographs for  $Re = 66,000$ : Figure 4

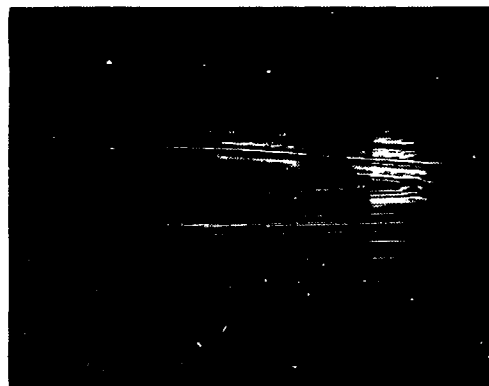
$\alpha = 0^\circ$  Under this flow condition, the suction-side laminar boundary layer separates near the mid-chord station. Unstable flow behavior in the separated region then begins downstream of the trailing edge. Through this unstable behavior, the suction-side flow is able to reattach itself to the pressure-side flow.

$\alpha = 3^\circ$  At this angle, the suction-side boundary layer separates near the leading edge. Also, through unstable flow behavior, the suction-side and pressure-side flows are able to rejoin downstream of the trailing edge.

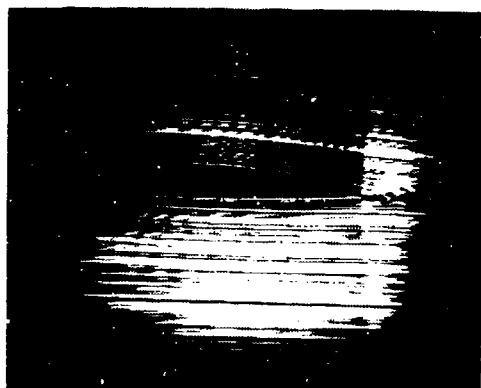
$\alpha = 4^\circ$  At this angle, the separated external flow is able to reattach itself upstream of the trailing edge, at approximately 80% of chord. In this photograph, we see the first example of an airfoil separation bubble.

$\alpha = 5^\circ$  At this angle, the external flow reattachment point has moved forward to approximately the 40% chord station. The size of the separation bubble is correspondingly reduced, in width as well as in length.

$\alpha = 10^\circ$  At this angle, the slope at which the external flow moves away from the surface becomes so large that subsequent turbulence breakdown within the high shear portion of the separated layer cannot produce entrainment sufficient to enable this flow to reattach within the extent of the photograph.



$0^\circ$



$3^\circ$



$5^\circ$



$4^\circ$



$10^\circ$

$Re = 66,000$

Figure 9. Smoke wire photographs

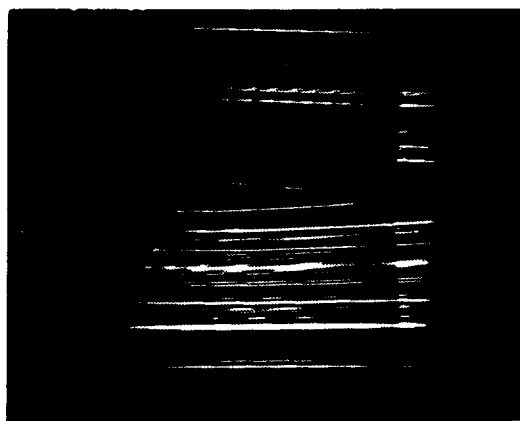
Photographs for  $Re = 100,000$ : Figure 5

$\alpha = 0^\circ$  Here the displayed flow field is almost entirely laminar. Also, separation of the suction-side boundary layer is confined to the vicinity of the trailing edge.

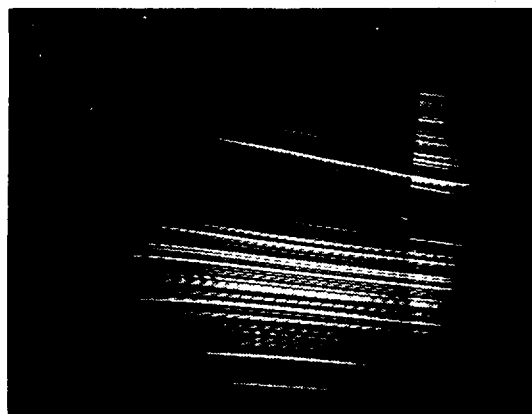
$\alpha = 5^\circ$  At this angle, a separation bubble is formed beginning near the leading edge and ending near mid-chord.

$\alpha = 10^\circ$  At this angle, a separation bubble no doubt forms, but it cannot be resolved in the photograph. However, it is fairly clear that the reattached, turbulent boundary layer separates upstream of the trailing edge.

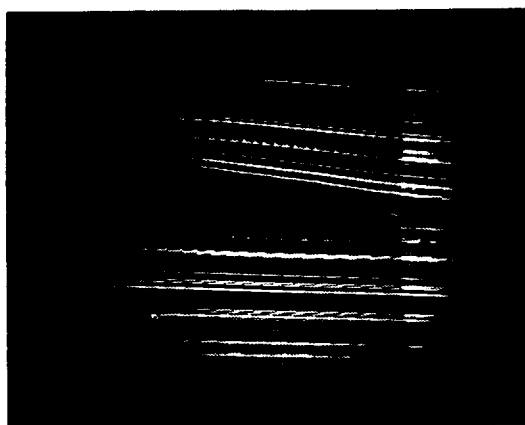
$\alpha = 15^\circ$  For this Reynolds number as for the previous, lesser ones, at this angle of attack the suction-side flow separates and does not reattach within the field of view.



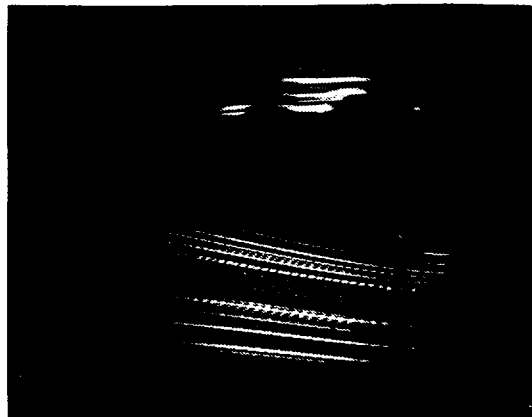
$0^\circ$



$10^\circ$



$5^\circ$



$15^\circ$

$Re = 100,000$

Figure 5. Smoke wire photographs.

In the last three photographs in this figure, note that the pressure-side laminar boundary layer also separates, near the leading edge. Note also that resulting separated region exhibits no unstable behavior. This increased stability, compared to that exhibited by the suction-side region, is directly attributable to the favorable streamwise pressure gradient which exists over the pressure side all the way from just downstream of the leading edge to the trailing edge. The existence of this gradient is indicated by the reduction in smoke filament spacing in the streamwise direction along this side.

Photographs for  $Re = 133,000$ : Figure 6

For this test condition, the Reynolds number based on wire diameter has increased to 85 and, at this high value, strongly increased mixing in the wake region immediately behind the wire produces significant smoke-filament spreading. Although this mixing almost totally dies out by the time the filament reaches the airfoil, each filament remains broadened and flow field resolution is correspondingly degraded.

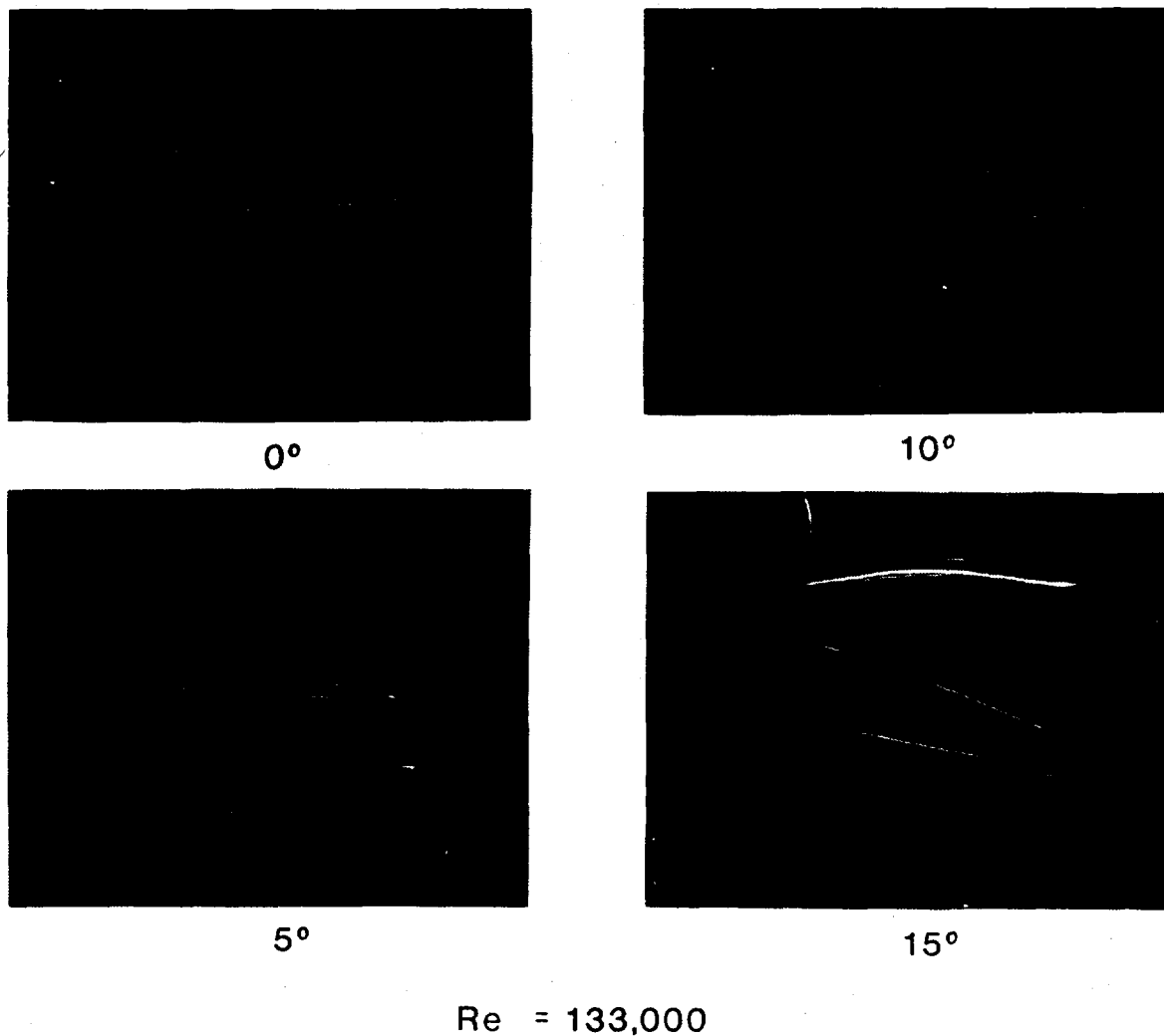


Figure 6. Smoke wire photographs.

$\alpha = 0^\circ$  At this angle, based on earlier photographs, the flow is expected to remain fully laminar and fully attached. The observed smoke pattern is consistent with this expectation.

$\alpha = 5^\circ$  At this angle, based on previous photographs, formation of a separation bubble is expected ahead of the mid-chord station. Due to filament spreading, no clear evidence for this bubble may be seen in the photograph. Its existence is confirmed, however, by corresponding surface pressure data. These pressure data will not be presented here.

$\alpha = 10^\circ$  Again in this photograph, it is impossible to resolve the presence of a separation bubble, although it is easy to reason that a small one forms. From the general sweep of the suction-side filaments downstream of mid-chord, it would appear that, as expected on the basis of earlier photographs, the turbulent boundary layer separates upstream of the trailing edge.

$\alpha = 15^\circ$  Again at this  $Re$ , at this high angle of attack, the suction-side flow separates and does not reattach within the field of view.

#### COMPARISON WITH PREVIOUS RESULTS

Smoke wire photographs similar to the ones displayed here have been presented by Batill and Mueller [10,11] for a NACA 66<sub>3</sub>-018 airfoil for several different angles of attack and for chord Reynolds numbers of 40,000 and 50,000. Similar photographs have also been presented by Mueller and Burns [12] for an Eppler 61 airfoil, again for several different angles of attack, for chord Reynolds numbers of 46,000 and 87,000. These investigators used a wind tunnel which is very similar to the one used for the present tests. The chord length for their wing model was approximately twice that employed here. The diameter of their smoke wire was equal to that employed here.

Although the above investigators employed airfoil shapes which differed considerably from that of the NACA 23009, the qualitative, and even the semi-qualitative, features of the streaming patterns which they observe are quite similar to those which are found here. This concurrence is expected. The basic physical processes which come into play are for the most part independent of the detailed shape of the airfoil.

An improved aspect of the present photographs compared to these previous ones is that the flow region immediately next to the airfoil is resolved. Evidently because these other investigators used thicker wings and a smaller diameter camera lens, the region immediately next to each of their airfoil sections, including the section profile, was not resolved.

#### CONCLUDING REMARKS

The present results provide a significant added demonstration of the great power of the smoke wire technique for revealing the detailed features of aerodynamic flows. With this technique, the investigator can

obtain an essentially complete, and for all practical purposes interference-free, representation of such a flow. Moreover, very little effort or expense is required.

The several flow behaviors which have been delineated in this paper do not constitute very much of a mystery. Each would be readily familiar to by anyone having extensive experience with aerodynamic flows and boundary layer theory. In fact, it is probably an accurate statement that a great fraction of the individual flow features which have been mentioned could, with reasonable amounts of effort, be reproduced analytically. Surely boundary layer theory is capable of, given the imposed external-flow pressure/velocity field and a sufficiently sophisticated computational approach, accurate modeling of laminar boundary layer separation. Also, again given the external-flow pressure/velocity field, existing full-Navier-Stokes computer codes would be expected to be capable of predicting the observed developments of the laminar part of the separated layer, perhaps even to the extent of predicting initial instability roll-up features. It is also presumably practical, still again given the external pressure/velocity field and using quasi-analytical methods, to predict the major aspects of the transition-to-turbulence and wall-attachment processes for the separated flow, and to predict any downstream separation of the reattached turbulent boundary layer. Furthermore, given these individual modeling capabilities, it could well be within the present state of the art to couple these models together with a suitable model for the external flow and iterate the entire package to some self-consistent convergence.

Of course, the big problem with any analytical/computational approach of the above type is that it would, when developed to a sufficient level of accuracy, be very, very expensive. For this reason, for any research program aimed primarily at arriving at airfoil designs which exhibit improved aerodynamic performance at lower Reynolds number, particularly in view of the relative ease with which reliable experimental data, of the present and other types, may be obtained, it would seem highly advisable to give strong weight to approaches which center upon experimentation. Furthermore, because streaming patterns tend to be much more revealing of the important underlying physical processes than direct aerodynamic force and moment measurements, major emphasis on investigations of this type is warranted.

#### ACKNOWLEDGEMENTS

We wish to thank Professor G. B. Matthews of our department for his assistance with this work. We also wish to thank Mr. W. D. Harvey of the NASA Langley Research Center for his financial support of this effort. We are also grateful for technical assistance provided by S. Mangalam, P. Stack, and L. Weinstein of NASA LRC.

## REFERENCES

1. Mueller, T. J., "Low Reynolds Number Vehicles," AGARDograph No. 288, Feb. 1985.
2. Carmichael, B. H., "Low Reynolds Number Airfoil Survey," Vol. I, NASA CR 165803, Nov. 1981.
3. Chang, P. K., Separation of Flow, Pergamon Press, 1970, pp. 323-331.
4. Chang, P. K., Control of Flow Separation, McGraw-Hill, 1976, pp. 21-23, 167-170, 189-196, 212-228.
5. Schlichting, H., and E. Truckenbrodt, Aerodynamics of the Airplane, translation by H. J. Ramm, McGraw-Hill, 1979, pp. 81-94.
6. Simons, M., Model Airplane Aerodynamics, Argus Books Ltd., Herts, England, 1978, Ch. 8.
7. Lissaman, P. B. S., "Low-Reynolds-Number Airfoils," Ann. Rev. Fluid Mech. 15, 1983, pp. 223-239.
8. Schmitz, F. W., "Aerodynamics of the Model Airplane. Part I. Airfoil Measurements," NASA-TN-X-60976, Nov. 1967 (originally published in Germany, 1941).
9. Gaster, M., "The Structure and Behavior of Separation Bubbles," British ARC R&M 3595, March 1967.
10. Batill, S. M., and T. J. Mueller, "Visualization of Transition in the Flow over an Airfoil Using the Smoke-Wire Technique," AIAA J. 19:3, March 1981, pp. 340-345.
11. Mueller, T. J., and S. M. Batill, "Experimental Studies of Separation on a Two-Dimensional Airfoil at Low Reynolds Numbers," AIAA J. 20:4, April 1982, pp. 457-463.
12. Mueller, T. J., and T. F. Burns, "Experimental Studies of the Eppler 61 Airfoil at Low Reynolds Numbers," AIAA Paper 82-0345.

ASPECT RATIO EFFECTS  
ON THE AERODYNAMICS OF A WORTMANN AIRFOIL AT LOW REYNOLDS NUMBER

J. F. Marchman, III, A. A. Abtahi and V. Sumantran  
Department of Aerospace and Ocean Engineering  
Virginia Polytechnic Institute and State University  
Blacksburg, Virginia 24060

ABSTRACT

Wind tunnel tests were conducted on a series of wings employing the Wortmann FX-63-137-ESM airfoil to determine the influence of wing aspect ratio on the aerodynamic behavior of that section at low Reynolds numbers. Tests were performed in the six by six foot test section of the Virginia Tech Stability Wind Tunnel at a free stream turbulence level of two one-hundredths of a percent. Tests were conducted at Reynolds numbers between 50,000 and 500,000 with model wing aspect ratios of 4, 6, 8 and 10. Test results showed that aspect ratio influences the size of the low Reynolds number stall hysteresis loop and the range of Reynolds number over which the hysteresis loop exists as well as having the usual effects on the slope of the lift curve and the magnitude of the maximum lift coefficient. Flow visualization tests showed no three dimensional flow patterns at low Reynolds numbers other than the expected wing tip flows.

INTRODUCTION

Past research on low Reynolds number aerodynamics has concentrated on two dimensional airfoil aerodynamic characteristics. The reasons for this concentration have been primarily twofold. Three dimensional aerodynamic research requires a well equipped wind tunnel with an excellent force balance system; however, most balance systems are not very accurate at the low force levels encountered in low Reynolds number flows. The lack of funding for serious research restricted some past efforts to a very simple level of testing; ie, testing which can be accomplished with simple pressure manometers and pressure tapped models, a technique which is essentially limited to two dimensional data collection. Much of this past data have come from research by model airplane or sailplane enthusiasts. The earliest such work was that of Schmitz(1) for model airplane wings. Schmitz was the first to report the stall hysteresis effect. Althaus(2) also studied a selection of model airplane airfoil designs as did others at Delft(3). All of this research examined only two dimensional behavior and omitted any mention of pitching moment data. Most recent work has also concentrated on 2-D data.

Much of the past low Reynolds number airfoil research has relied on pressure measurement data collection techniques, either pressure integration around the airfoil surface to get lift and drag or pressure measurement in the airfoil's wake to obtain drag via momentum deficit analysis. Both of these techniques are subject to well known flaws as well as being only two dimensional techniques. Chordwise pressure

integration can obtain two dimensional lift, drag and pitching moment but it cannot include any skin friction effects in the data reduction. Pressure taps must also be very carefully constructed so as to avoid any alteration of the boundary layer due to pressure tap roughness effects. The momentum deficit method is easy to use but largely depends on the assumption of linear momentum losses in the airfoil wake, limiting its applicability to low and moderate angles of attack.

Many of the past investigations of low Reynolds number aerodynamics have also been conducted in less than optimum wind tunnel test conditions. It is well known that wind tunnel turbulence levels have a strong influence on data at low Reynolds number and that excessive turbulence can reduce or even eliminate the stall hysteresis loop which is perhaps the most significant aerodynamic effect seen at low Reynolds numbers(4), yet much of past research has been in tunnels with rather large free stream turbulence levels. Much of the research has also been done in tunnels where model size to test section area ratios have been too large. It is usually assumed that when wind tunnel blockage exceeds ten percent test results will be, at best, questionable, yet some researchers continue to conduct tests with model/support arrangements that exceed ten percent blockage over a significant range of angle of attack. Usually the worst blockage problems will be at high angle of attack, the very area where the critical stall hysteresis loop occurs.

One result of the past use of a wide range of test conditions is a large degree of uncertainty with respect to published data. As an example, tests conducted at Stuttgart in two different wind tunnels with the exact same two dimensional model of the Wortmann airfoil appear to show two different values of zero lift angle of attack for a Reynolds number of 280,000.(5) The two tunnels, Stuttgart No.1 and Stuttgart No.2 are known to have different turbulence levels, however it is unlikely that turbulence can account for a zero lift shift, and one must assume that the researchers were equally careful in conducting and reducing the data from both series of tests.

Low free stream turbulence levels are essential if meaningful aerodynamic data is to be obtained at low Reynolds numbers. The Virginia Tech Stability Wind Tunnel has documented turbulence levels of less than two hundredths of a percent as measured by Saric(6) and as frequently verified by use of hot wire surveys of the test section during the present low Reynolds number testing. Tests at Virginia Tech have shown that if this turbulence level is increased even a small amount there can be significant alteration of the stall hysteresis loop(4). Reference 4 also shows that tunnel acoustic effects can influence the loop. In facilities where turbulence levels are high and where fan noise is not isolated from the test section these two effects can combine for very significant alteration of the test data.

Another requirement for three dimensional testing at low Reynolds numbers is an accurate strain gauge balance system with the ability to remotely control the model's angle of attack. The Virginia Tech wind tunnel uses a very sensitive six component strain gauge balance designed and built at NASA-Langley. This strut balance was fitted with a motor driven, computer controlled extension which mounted on the strut's

moment balance to allow remote operation of the model angle of attack through a range from minus ten to plus thirty degrees.

The present study was prompted by the need to obtain three dimensional aerodynamic data for wings at low Reynolds number conditions. The airfoil section chosen was the Wortmann FX-63-137-ESM airfoil and testing was to be done at aspect ratios of four through ten and over a Reynolds number range from 50,000 to 500,000. Lift, drag and pitching moment data were to be collected throughout these ranges.

### EXPERIMENTAL PROCEDURES

The airfoil section chosen for these tests was the Eppler modified Wortmann FX-63-137-ESM, shown in Figure 1. Models were tested with aspect ratios of four, six, eight and ten. This aspect ratio range dictated a model chord of five inches, giving a span of from twenty to fifty inches. This allowed ample clearance between the model wing tips and the wind tunnel test section walls in the six-by-six foot test section. The test section of the Virginia Tech Stability Wind Tunnel (Figure 2) is 6x6x28 feet, part of a closed circuit tunnel with a fourteen foot diameter fan powered by a 600hp motor. The tunnel's seven sets of fine mesh stainless steel anti-turbulence screens and the presence of a large air exchange section between the fan and the test section combine to give the very low turbulence levels mentioned earlier.



FIGURE 1: WORTMANN FX-63-137-ESM

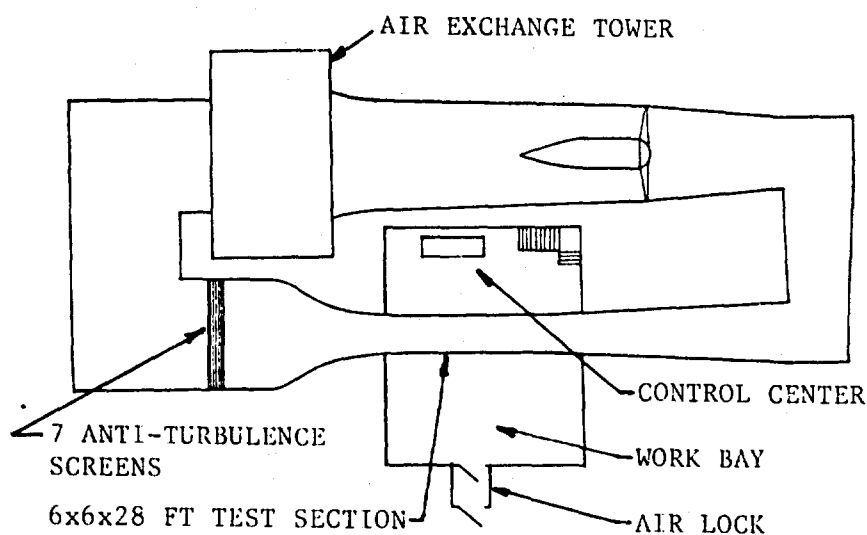


FIGURE 2: VIRGINIA TECH STABILITY WIND TUNNEL

The model was machined in sections from a solid aluminum block in order to allow combinations of the sections to form the desired aspect ratios of four, six, eight and ten. Sections were milled to the necessary tolerances and the assembled models hand finished and painted to assure a smooth surface. The test models were bolted to the modified strut balance described earlier for testing. Model angle of attack was remotely controlled through the wind tunnel's Hewlett Packard 9836 computer via relays and a model actuator control as shown schematically in Figure 3. Angle of attack indication was obtained from a precision electronic inclinometer incorporated into the angle of attack actuation device.

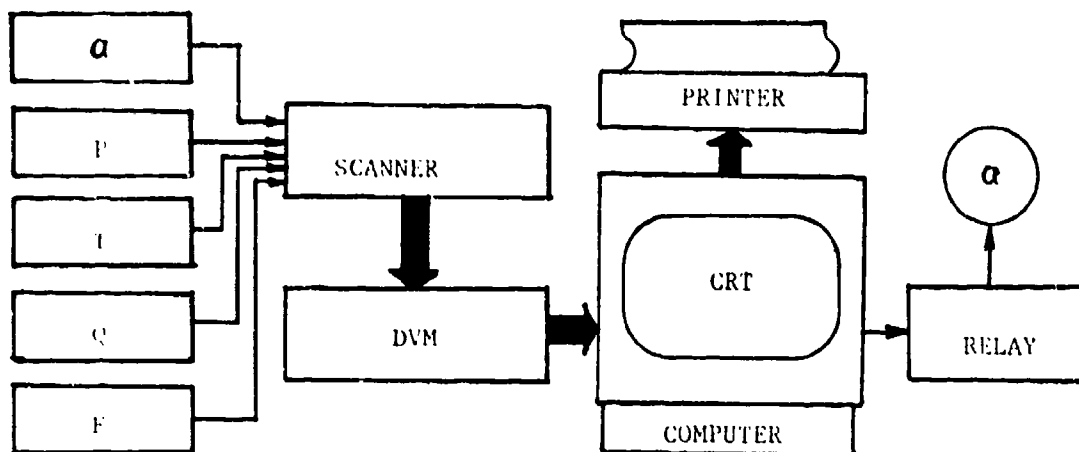


FIGURE 3: SCHEMATIC OF DATA ACQUISITION SYSTEM

The balance strut was shrouded to prevent forces on the strut itself. Because of the relative size of the shrouded strut and the models tests were also run to evaluate the influence of the strut on flow angularity seen by the model, specifically, the effect of the strut on the wing's zero lift angle of attack. Tests were conducted using the aspect ratio eight wing model as well as an aspect ratio 8, five inch chord flat plate (where the zero lift angle must be zero degrees). Wing model tests were conducted using inverted models and image struts. From these tests zero lift angle shifts were evaluated and applied as corrections to all collected data. The angle of attack electric inclinometer was recalibrated prior to each series of tests.

The complete test procedure was programed into the HP 9836 computer. After the desired range of angle of attack and angle increments were entered into the system along with model geometry data, balance system tare readings were taken and the wind tunnel was brought up to the speed needed for the desired test Reynolds number. The computer then ran the model through the preset angle of attack program while the tunnel operator kept the tunnel at the desired speed. At each angle of attack the data acquisition system (Figure 3) scanned all the strain gauge balances and the tunnel temperature, dynamic pressure and static pressure 50 times, averaged the data, subtracted tare data and made any other preprogramed corrections, then printed out all the corrected force, moment, pressure, temperature and Reynolds number data

along with calculated force and moment coefficients. During this time the computer CRT displayed real time plots of lift and drag coefficient versus angle of attack along with current angle of attack information.

Each test was repeated at least twice to assure accuracy and repeatability. Repeatability was found to be excellent except at the lowest Reynolds numbers tested, around 70,000. Even at this lowest Reynolds number the lift data were quite reliable, however the drag data exhibited significant scatter. To gain added confidence in the data, tests were also run measuring momentum deficits behind the wing and by measuring pressures chordwise around the wing and comparing these two dimensional measurements with the measured force data corrected to infinite aspect ratio. These comparisons were usually quite good, giving considerable confidence in the force balance data. Greater accuracy in the drag data for the lowest Reynolds number case would have been desirable, however, since a Re of 70,000 number represent speeds lower than would be encountered by even a small RPV, further efforts to improve accuracy at that speed did not appear worthwhile. It must be kept in mind that at this lowest Reynolds number the wing is seen to behave as a "thin airfoil" or flat plate with leading edge separation over most of the range of angle of attack and thus of little interest in this study.

#### DATA ANALYSIS

Because of the large quantity of data collected in these tests it is possible only to present a small portion in this report. Before examining the effect of aspect ratio it will be useful to first take a look at the effects of Reynolds number on the results for at least one aspect ratio. Figure 4 presents the lift coefficient data for the aspect ratio 10 model for four of the test values of Reynolds number. It is seen that, except for the Re = 70,000 case, the linear portions of each curve are coincident, having a slope of 4.3 per radian. At a Reynolds number of 100,000 the wing experiences an abrupt stall at an angle of attack of fourteen degrees, indicating a rather sudden bursting of the laminar bubble before any turbulent separation can proceed far upstream from the trailing edge. At the higher Reynolds numbers it appears that the turbulent boundary layer behind the laminar bubble separates over the rear of the wing and that separation point moves forward substantially before the laminar bubble bursts and leads to full upper surface separation. It is also seen that as Reynolds number increases, the hysteresis loop moves to the right. At the 70,000 Reynolds number the wing exhibits "thin airfoil" or "flat plate" behavior with upper surface separation at zero degrees and a linear behavior only between minus four and zero degrees.

The Reynolds number effects seen in Figure 4 were typical of those seen at all aspect ratios. At a given aspect ratio it appears that as Reynolds number increases, turbulent separation can move further toward the wing's leading edge before the laminar bubble "bursts" and total upper surface separation occurs. If Reynolds number continues to increase there will be some value of Reynolds number where a normal separation can progress across the wing's upper surface without bursting. At this point the hysteresis loop will cease to exist. This

point appears to be a function of both Reynolds number and aspect ratio. For the aspect ratio eight model the hysteresis loop had disappeared at the 300,000 Reynolds number case. Large lift forces at large angle of attack for the aspect ratio ten case at a Reynolds number of 300,000 prevented complete testing in that case.

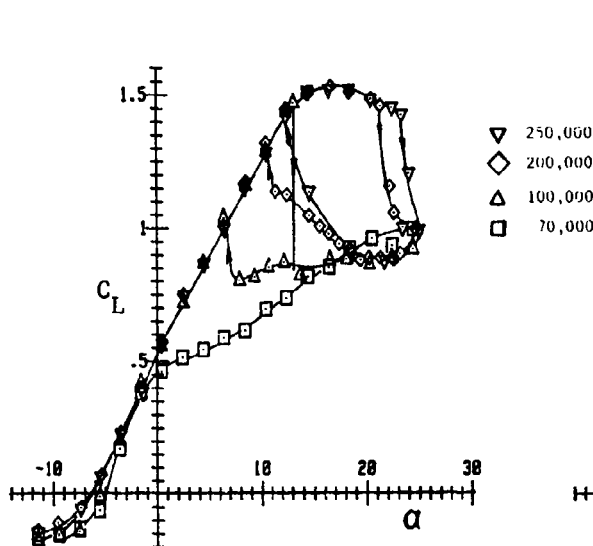


FIGURE 4: EFFECTS OF  $Re$  ON  $C_L$   
AT ASPECT RATIO  $10^L$

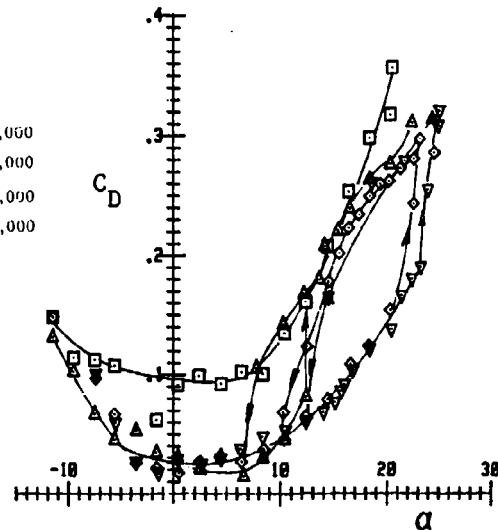


FIGURE 5: EFFECTS OF  $Re$  ON  $C_D$   
AT ASPECT RATIO  $10^D$

The drag coefficient data for aspect ratio ten are shown in Figure 5 for the same Reynolds numbers as before. It is seen that at Reynolds numbers of 100,000 and above the data seems to follow the same curve. The data for  $Re = 70,000$  give higher values of drag coefficient since there is a significant amount of flow separation in this case. The drag hysteresis loops are also shown and, as expected, show large increases in drag when the wing is in the stalled portion of the loop. More scatter is seen in the drag data than was seen in the lift data as expected due to the lower magnitudes of the drag forces. The data however are seen to be quite consistent, easily accommodating curves through the data points, and were found to be very repeatable in subsequent tests run at several different times throughout the course of a year.

The quarter chord pitching moment data for this same case are seen in Figure 6. It appears that the wing exhibits increasingly stable behavior as Reynolds number increases with unstable behavior in the stall region in all cases. The wing is generally unstable anywhere in the hysteresis loop.

The primary purpose of this research was to examine aspect ratio effects on the low Reynolds number aerodynamics of the Wortmann airfoil. This will be done in Figures 7 - 15. Since lift coefficient is usually considered of primary importance, aspect ratio effects on the lift

coefficient data will be examined in more detail than the effects on the other coefficients. Figure 7 shows the effects of aspect ratio on the lift coefficient data for a Reynolds number of 200,000. It is seen that as aspect ratio increases from four to ten the slope of the lift curve increases from 3.15 to 4.3. The value of maximum lift coefficient increases from 1.45 to 1.55. The angle of attack range of the hysteresis loop appears to be unaffected by aspect ratio; however, the size or area of the loop is seen to decrease as aspect ratio increases. This result indicated that in addition to the previously known aerodynamic advantages of high aspect ratio may be added the advantage of less pronounced hysteresis losses in stall at low Reynolds numbers.

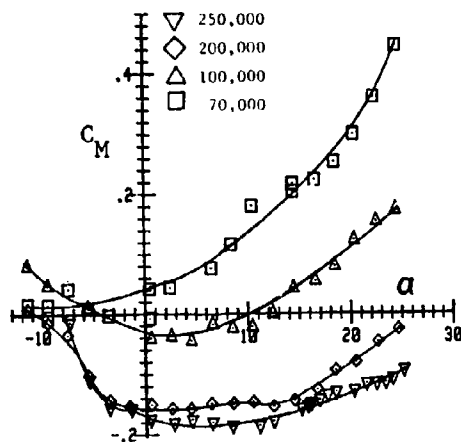


FIGURE 6: EFFECTS OF  $Re$  ON  $C_M$  AT ASPECT RATIO 10.

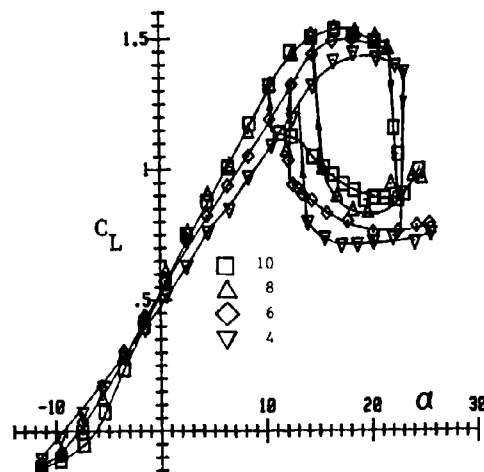


FIGURE 7: EFFECTS OF ASPECT RATIO ON  $C_L$  FOR  $Re=200,000$

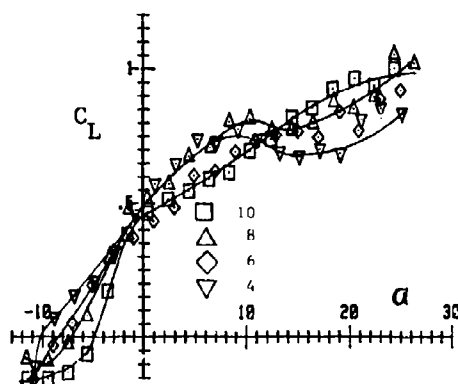


FIGURE 8: EFFECTS OF ASPECT RATIO ON  $C_L$  FOR  $Re=70,000$

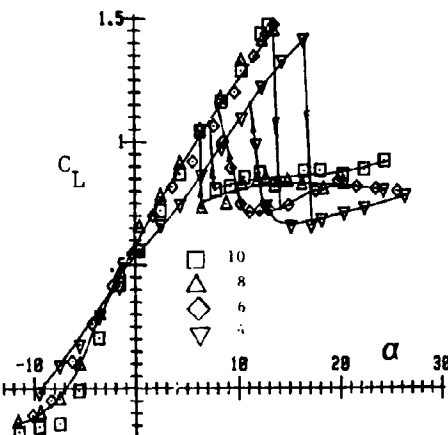


FIGURE 9: EFFECTS OF ASPECT RATIO ON  $C_L$  FOR  $Re=100,000$

Figures 8 - 10 show similar effects for Reynolds numbers of 70,000, 100,000 and 300,000 respectively. As seen earlier, at lower Reynolds numbers stall occurs more abruptly. The same effects of aspect ratio mentioned above apply to these data with the possible exception of the 70,000 case where "thin airfoil" behavior exists and the curves are more erratic. It appears that in the 70,000 Reynolds number case the slope of the linear portion of the lift curve does not necessarily increase with aspect ratio; however, the post stall lifting ability of the wing does seem to increase with aspect ratio.

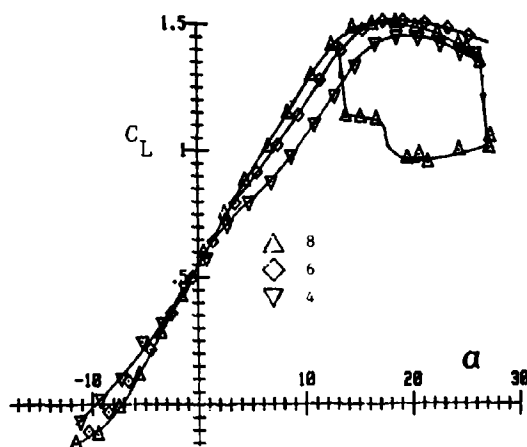


FIGURE 10: EFFECTS OF ASPECT RATIO ON  $C_L$  FOR  $Re=300,000$

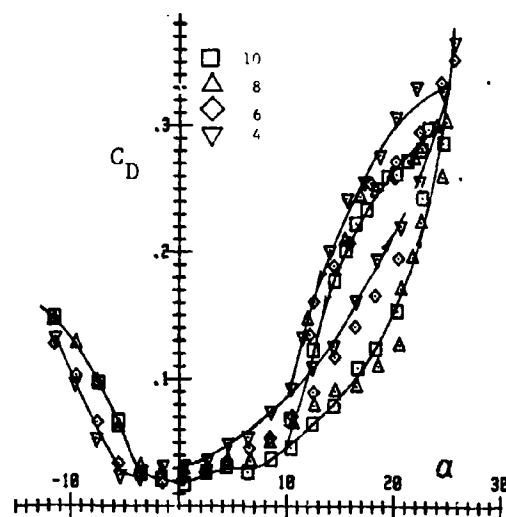


FIGURE 11: EFFECTS OF ASPECT RATIO ON  $C_D$  FOR  $Re=200,000$

An example of the drag coefficient data is seen in Figure 11 for a Reynolds number of 200,000. These data are similar to those at other Reynolds numbers and show the generally expected decrease in drag over most of the range of angle of attack as aspect ratio is increased. Figure 12 shows the quarter chord pitching moment data for the same cases. The most obvious feature of this figure is the unstable behavior exhibited in the stall hysteresis loop with marginal stability at angles of attack above zero degrees.

The previous data showed that all of the models tested exhibited "thin airfoil" or "flat plate" behavior in lift at a Reynolds number of 70,000. This is in agreement with data found in past studies of several different airfoils at low Reynolds number which show that as Reynolds number decreases below 100,000 the basic behavior of the wing changes. It was therefore of interest to try to find the approximate Reynolds number where this change occurred for the test wings and to examine the effects of aspect ratio on that change. Tests were therefore conducted for each aspect ratio wing and the results are shown in Figures 13 - 15 for aspect ratios of four, six and ten, respectively. These figures show that aspect ratio has a pronounced effect on this transition in

aerodynamic behavior. At an aspect ratio of four the change takes place at an approximate Reynolds number of 74,000. This increases to 83,000 at an aspect ratio of six and to over 92,000 for the aspect ratio ten case.

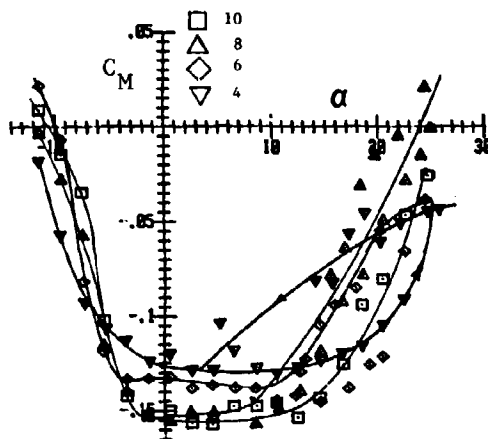


FIGURE 12: EFFECTS OF ASPECT RATIO ON  $C_L$  FOR  $Re=200,000$

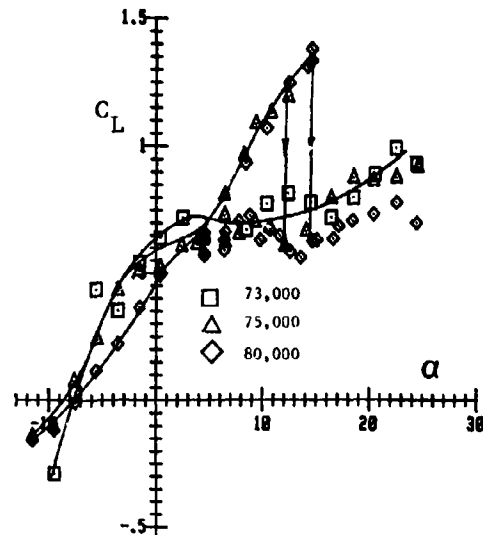


FIGURE 13: ASPECT RATIO 4 CHANGE TO "THIN AIRFOIL" BEHAVIOR

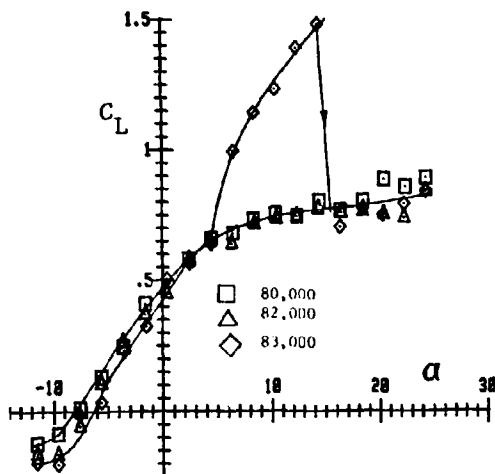


FIGURE 14: ASPECT RATIO 6 CHANGE TO "THIN AIRFOIL BEHAVIOR

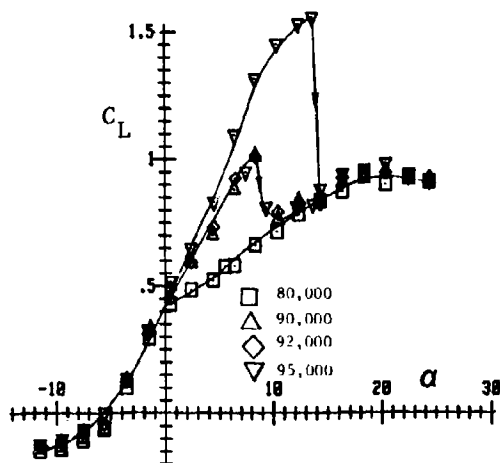


FIGURE 15: ASPECT RATIO 10 CHANGE TO "THIN AIRFOIL" BEHAVIOR



FIGURE 16: SAMPLE FLOW VISUALIZATION  
PHOTOGRAPH AT  $Re=200,000$ ,  $AR=4$

Flow visualization tests were also conducted to examine the three dimensional nature of the flow and stall patterns on the test wings. The technique used was the well known naphthalene/trichlorethane thin film evaporation method. The results of these tests are discussed in more detail in Reference 4; however, the result most relevant to this paper is that the nature of the flow over the wings was found to be essentially two dimensional except at the wing tips where the usual three dimensional wing tip flow effects were observed. A typical result is seen in Figure 16. No evidence was seen of any three dimensional stall cells or other effects which do not normally occur on wings.

#### CONCLUSIONS

The principal results of this research can be summarized as follows:

1. As is the case at higher Reynolds numbers the slope of the lift coefficient versus angle of attack curve increases as aspect ratio increases.
2. As aspect ratio increases there is a slight increase in the maximum lift coefficient for a given Reynolds number.
3. While aspect ratio does not appear to influence the angle of attack range of the hysteresis loop for a given Reynolds number, increasing the aspect ratio does appear to reduce the area within the hysteresis loop.

4. As is the case at higher Reynolds numbers, increasing the aspect ratio reduces the drag coefficient of the wing.

5. The Reynolds number at which the wing changes from a normal low Reynolds number aerodynamic behavior to a "thin airfoil" behavior was shown to increase as aspect ratio increases. This is the only result from these tests which may indicate that any benefits may accrue from using a lower aspect ratio wing under certain conditions.

6. No unusual three dimensional flow patterns were observed during flow visualization tests; ie, flow separation and laminar bubble behavior appeared quite two dimensional except near the wing tips.

#### ACKNOWLEDGEMENTS

The authors would like to acknowledge the financial support of the Office of Naval Research under contract number N00014-84-0093 as well as that of the Virginia Tech Department of Aerospace and Ocean Engineering, without which this research would have been impossible.

#### REFERENCES

1. Schmitz, F. W., "Aerodynamics of the Model Airplane", Ludwig Prandtl Prize for 1941, Translation by Redstone Scientific Information Center.
2. Althaus, D., "Profilpolaren fur den Modellflug", N.V. Neekar Verlag Villingen-Schwenningen, 1980.
3. Volkers, D. F., "Preliminary Results of Wind Tunnel Measurements on some Airfoil Sections at Reynolds Numbers Between 60,000 and 500,000", Delft University of Technology, Memo M-276, June 1979.
4. Sumantran, V, Sun, Z, and Marchman, J. F., "Acoustic and Turbulence Influence on Low Reynolds Number Wing Pressure Distributions", Proceedings of the Conference on Low Reynolds Number Airfoil Aerodynamics, University of Notre Dame, June 1985.
5. Carmichael, B.H., "Low Reynolds Number Airfoil Survey", NASA CR-165873, November 1981.
6. Saric, W. S. and Yates, L. G., "Generation of Crossflow Vortices in a Three Dimensional Flat Plate Flow", Proceedings from the Second IUTAM Symposium on Laminar Turbulent Transition, Novosibirsk, USSR, July, 1984

# PERFORMANCE OF FINITE WINGS AT LOW REYNOLDS NUMBERS

William G. Bastedo, Jr.  
and  
Thomas J. Mueller

Aerospace and Mechanical Engineering  
University of Notre Dame  
Notre Dame, Indiana 46556

## ABSTRACT

The performance of three rectangular wings of aspect ratios equal to 5.4, 4.0 and 3.0 were studied at chord Reynolds numbers ranging from 80,000 to 200,000. Each wing utilized the Wortmann FX 63-137 airfoil section, and two-dimensional data for this profile was also obtained. Examination of the data revealed that increasing chord Reynolds number increased performance of the wings and the airfoil, while reducing aspect ratio decreased the lift curve slope and overall performance. This data supported the applicability of simple techniques for predicting wing performance from airfoil data.

## INTRODUCTION

Because the concept of flight implies that sufficient lift be generated to offset the force of gravity, the aerodynamics of lifting surfaces has been of great concern. Mathematicians have developed methods to predict the pressure distributions about airfoils moving through an ideal fluid. Because engineers have not developed the technology to build aircraft with infinite aspect ratio lifting surfaces, nor have they found an ideal medium in which to fly, airfoil section information of this type was not of much use to the pragmatic engineers. The Wright brothers recognized this deficiency and developed wind tunnel and force measuring capabilities to test airfoil designs [2]. Armed with accurate airfoil data, wing aerodynamicists have studied and modelled three-dimensional lifting surfaces with great success for many years [3]. This work, however, dealt with the "practical" flight Reynolds numbers of the times, (chord Reynolds numbers greater than 1,000,000) where boundary layers often undergo natural transition from laminar to turbulent flow slightly downstream of the leading edge; regions of separated flow are small, lift curves are usually linear, and airfoil and wing performance is predicted with great success. These models (e.g., lifting line, vortex-lattice and panelling methods) are based upon potential flow theory and do not account for separated flow phenomena, such as laminar separation bubbles. Therefore, their applicability to the low Reynolds number flight regime needs to be rigorously examined.

Experimental low Reynolds number aerodynamic research is a necessary, but inherently problematic, predecessor to analytic modelling. The resulting data is necessary to provide basic information for and to verify predictions by such models. Good experimental data is quite difficult to obtain however [1,4,5].

Laminar separation bubbles having a dominant effect on airfoil and wing performance have been found to be sensitive to free stream turbulence levels [6], surface smoothness [7] and testing method [1,4-9]. Therefore, extreme care must be exercised when analyzing and comparing low Reynolds number experimental data.

This paper discusses the performance of three rectangular planform wings with aspect ratios of 5.4, 4.0 and 3.0, and compares these results to two-dimensional data for the Wortmann FX 63-137 airfoil section (the profile used for the wings).

### EXPERIMENTAL PROCEDURE

All experiments were performed in one of the subsonic wind tunnels of the Notre Dame Aerospace Laboratory. Air flow velocities ranged from 7.5 m/s ( $Re = 80,000$ ) to 19 m/s ( $Re = 200,000$ ) for the 152.4 mm (6 in.) chord models used. Test models were rectangular wings cast in the same mold and trimmed to the different spans in order to generate appropriate aspect ratios. Each model was cast using a metal reinforced epoxy and sanded to minimize surface roughness. The wings were semi-span models, used in conjunction with a reflection plate to simulate full-span conditions. The infinite aspect ratio case (airfoil model) was simply the largest aspect ratio wing model with a second end-plate used at the free end. Wing aspect ratio was defined to be twice the ratio of the actual span to the chord length for the rectangular wings. A detailed description of both the facilities and the models can be obtained in Reference 4.

Measurements of the lift and drag forces generated by the models was accomplished with an externally mounted, two-component strain-gauge balance and an Apple IIe based data acquisition system. This is shown in Figure 1. A data acquisition and reduction algorithm

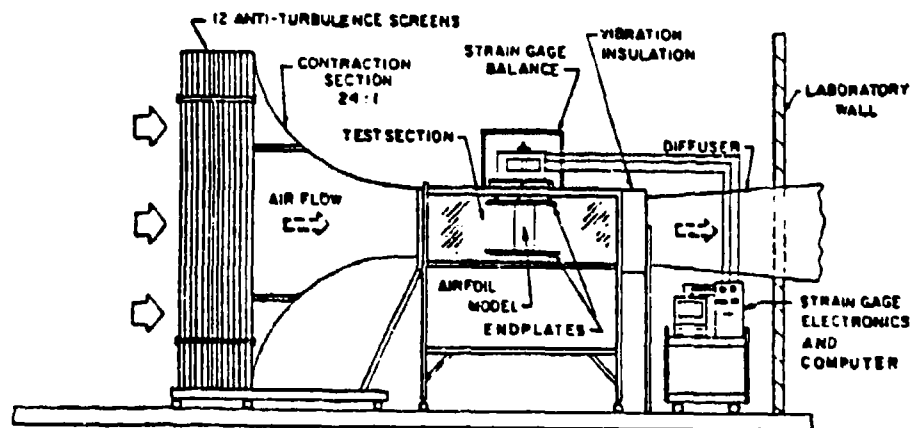


Figure 1. Experimental Apparatus for Force Balance Testing.

allowed sampling of the lift, drag and a reference pressure port (which was calibrated to give free-stream dynamic pressure readings) at a rate of 37 Hz on each channel. These readings were obtained over an eight second time period and averaged to insure accurate measurement. Reference 4 lists the accuracy of the equipment and uncertainty estimates associated with these measurements. In no case was the uncertainty estimated to be greater than  $\pm 7\%$ . Each test was performed several times to insure the accuracy of the tests. Standard wind tunnel corrections were not applied to the data.

## EXPERIMENTAL RESULTS

Trends in wing and airfoil performance were studied with respect to aspect ratio and Reynolds number. It was found that increasing the chord Reynolds number increased performance. As expected, increasing wing aspect ratio increased lift curve slope and the magnitude of the maximum lift coefficient. For reference, Figures 2 and 3 show the

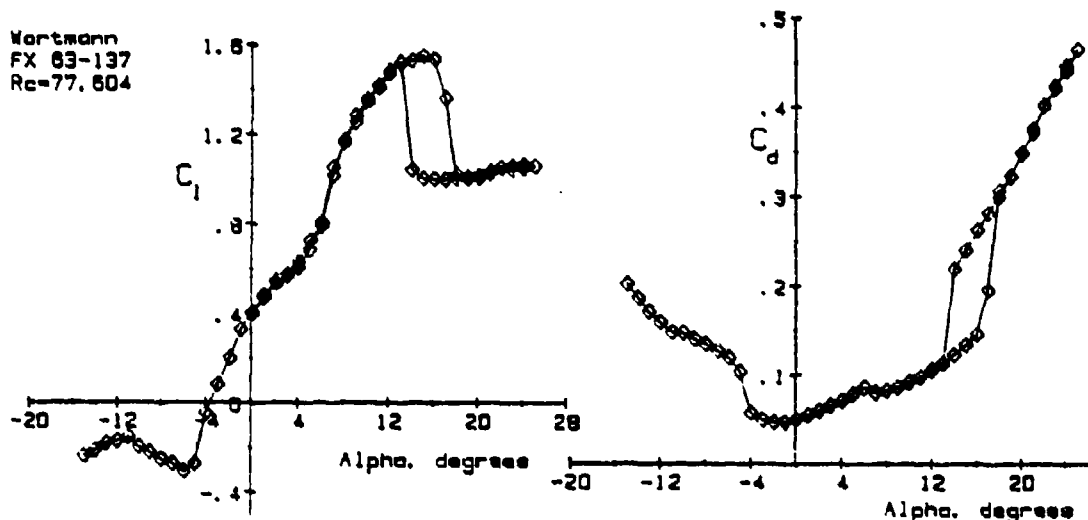


Figure 2. Two-Dimensional Lift and Drag Coefficients versus Angle of Attack,  $R_c = 80,000$ .

two-dimensional performance at  $R_c = 80,000$  and  $200,000$ . All cases tested showed post-stall hysteresis loops that have been shown to be associated with "short" separation bubble formation and their abrupt bursting. This two-dimensional data was compared to similar data obtained from Reference 10. The lift data compared reasonably well, but drag measurements varied greatly as shown in Figure 4. This is attributed to differences in the testing methods [1,4].

### Performance with Respect to Reynolds Number

Tables 1-2 present summaries of the maximum lift coefficient and minimum drag coefficient for all of the cases tested. As can be seen,

the two-dimensional  $C_{l_{max}}$  was not greatly affected by increasing Reynolds number, but the minimum drag coefficient was decreased by 40%. This effect was not quite as pronounced for the finite wings.

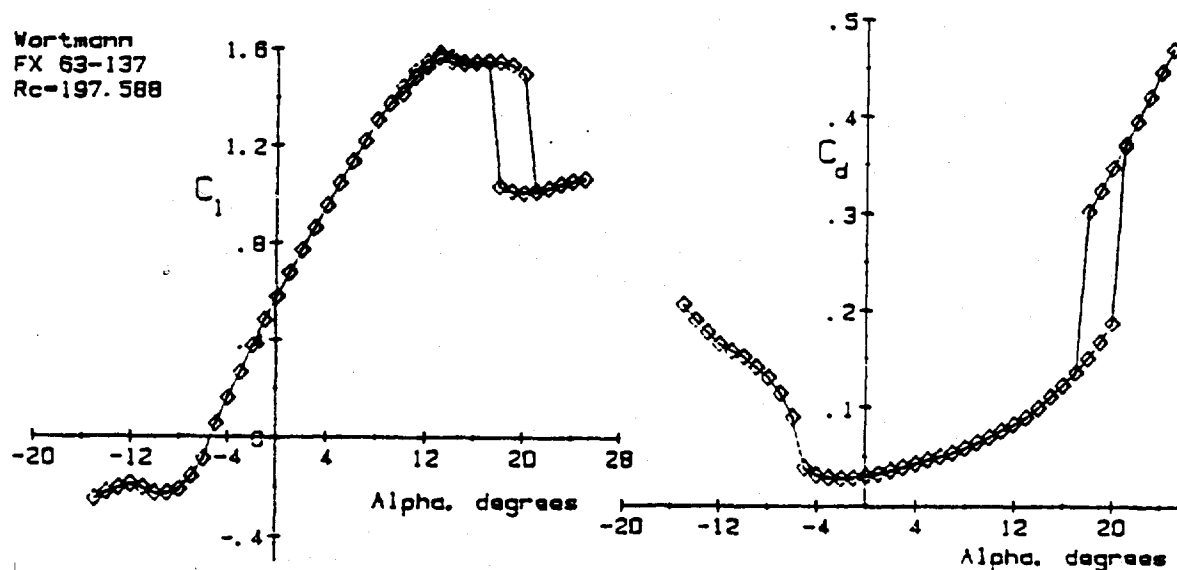


Figure 3. Two-Dimensional Lift and Drag Coefficients versus Angle of Attack,  $R_c = 200,000$ .

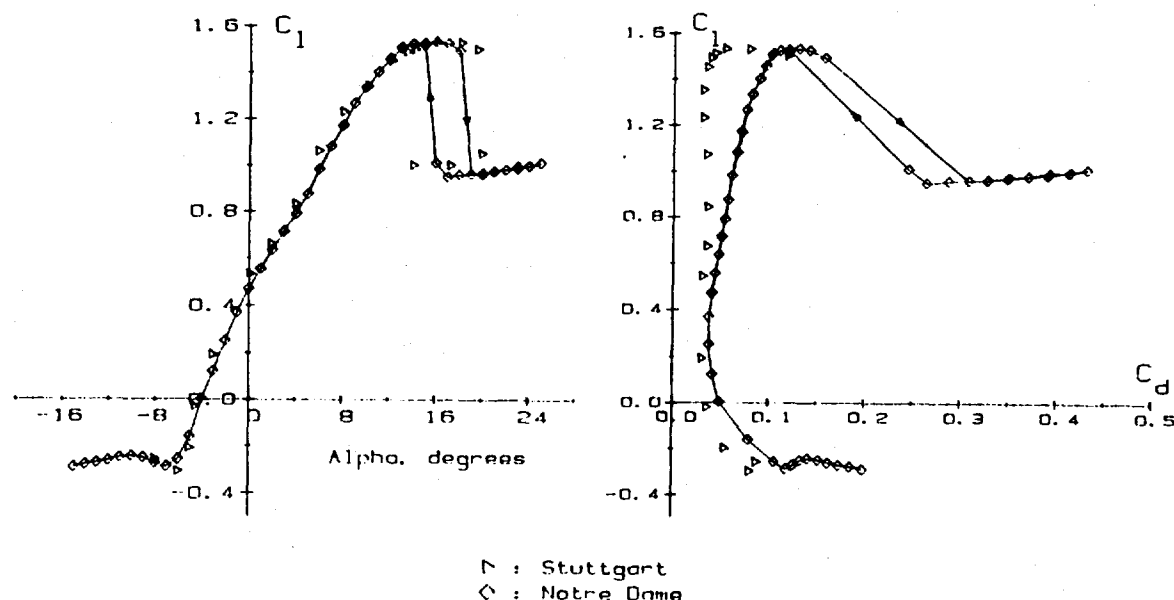


Figure 4. Comparison of Lift and Drag Coefficients for the FX 63-137 Airfoil at  $R_c = 100,000$  from Two Wind Facilities Using Different Measurement Techniques for Drag.

TABLE 1

Summary of  $C_{L\max}$  for Various Reynolds Numbers and Aspect Ratios.

ANGLE OF OCCURRENCE \ $C_{L\max}$	$A = \infty$	5.4	4.0	3.0
$R_c = 80,000$	1.62 15°	1.43 17°	1.27 18°	- -
$= 100,000$	1.66 16°	1.44 18°	1.36 20°	1.25 21°
$= 150,000$	1.65 13°	1.50 20°	1.45 21°	1.33 23°
$= 200,000$	1.64 13°	1.49 20°	1.46 21°	1.36 24°

TABLE 2

Summary of  $C_{D\min}$  for Various Reynolds Numbers and Aspect Ratios.

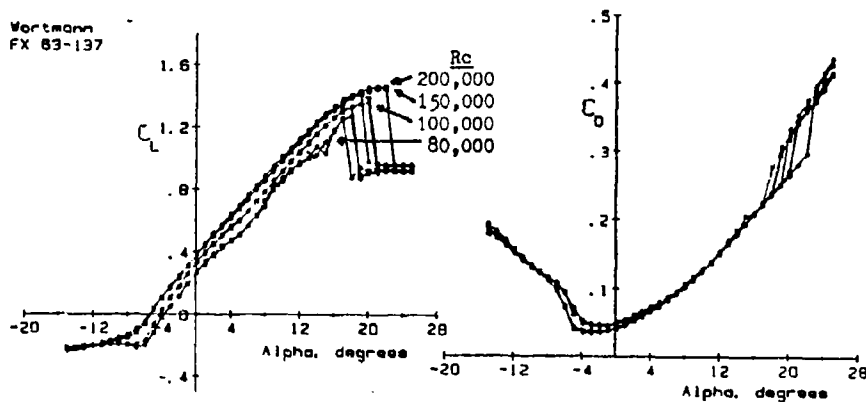
ANGLE OF OCCURRENCE \ $C_{D\min}$	$A = \infty$	5.4	4.0	3.0
$R_c = 80,000$	0.047 -2°	0.051 -2°	0.046 -1°	- -
$= 100,000$	0.042 -2°	0.042 -2°	0.044 -2°	0.046 -2°
$= 150,000$	0.030 -2°	0.035 -2°	0.037 -2°	0.041 -2°
$= 200,000$	0.028 -2°	0.032 -2°	0.035 -2°	0.039 -3°

TABLE 3

Summary of  $(L/D)_{\max}$  for Various Reynolds Numbers and Aspect Ratios.

$L/D)_{\max}$ ANGLE OF OCCURRENCE	$A = \infty$	5.4	4.0	3.0
$R_c = 80,000$	14.6 $10^\circ$	8.0 $8^\circ$	6.5 $7^\circ$	- -
$=100,000$	16.8 $8^\circ$	9.1 $7^\circ$	7.7 $4^\circ$	6.4 $4^\circ$
$=150,000$	20.4 $6^\circ$	11.1 $2^\circ$	9.4 $3^\circ$	6.9 $3^\circ$
$=200,000$	22.6 $7^\circ$	12.3 $2^\circ$	9.8 $2^\circ$	7.3 $3^\circ$

Figure 5 shows the lift and drag coefficients versus angle of attack for the  $A = 4.0$  wing at the four different Reynolds numbers. The slope of the lift curve did not change drastically, but the zero lift angle shifted and the maximum lift coefficient varied significantly. Aerodynamic efficiency improved slightly with increases in Reynolds number also, as shown in Figure 6. Increasing Reynolds number had the effect of lessening the extent of the hysteresis loop.

Figure 5. The Effect of Reynolds Number on Lift and Drag on the Finite Wing,  $A = 4.0$

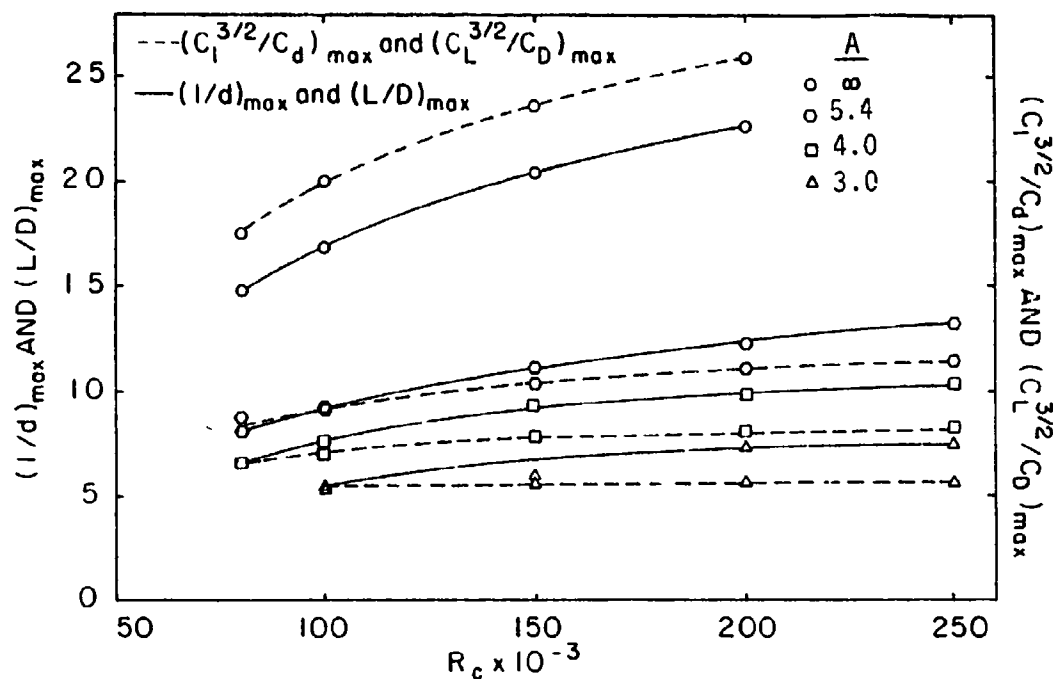


Figure 6. The Effect of Reynolds Number and Aspect Ratio Upon the Maximum Values of the Performance Ratios.

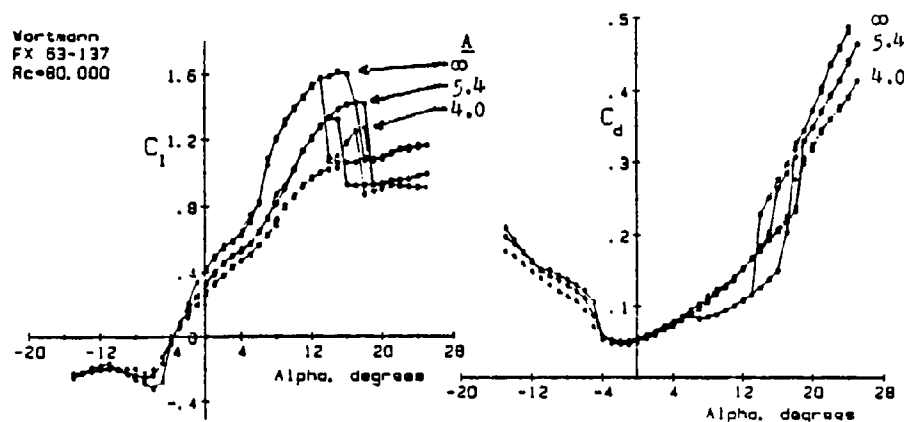


Figure 7. The Effect of Aspect Ratio Upon Lift and Drag at  $R_c = 80,000$ .

#### Performance with Respect to Aspect Ratio

The performance of wings with regard to aspect ratio is of great concern to designers of low Reynolds number vehicles. As was expected, lift curve slopes decreased with decreasing aspect ratio with no change in the zero-lift angle. Figures 7 and 8 illustrate

this at  $Re = 80,000$  and  $200,000$ . Also, Tables 1-3 show that as aspect ratio was reduced, the maximum value of the lift coefficient as well as the lift-to-drag ratio decreased, while the magnitude of the minimum drag coefficient increased, due to the velocity field induced by the tip vortex. This field was observed with flow visualization techniques and its effect upon separation bubble formation and its variation along the span is documented in great detail for the  $A = 4.0$  wing in Reference 4.

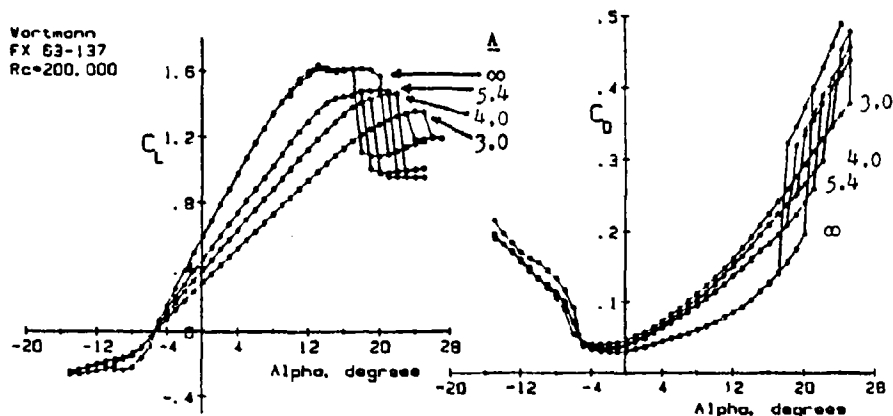


Figure 8. The Effect of Aspect Ratio upon Lift and Drag at  $Re = 200,000$ .

The tip vortex that formed was found to decrease the effective angle of attack along the span, as occurs at higher Reynolds numbers, through measurements of chordwise static pressure distributions along the span of the  $A = 4.0$  wing. Pressure distributions on the inboard 80% of the wing were found to be identical to two-dimensional distributions at the equivalent angle of attack for that spanwise station. This is documented in more detail in Reference 4. Flows at the most outboard 20% of the wing were found to be highly three-dimensional and thus could not be adequately modelled by a two-dimensional pressure distribution.

The results of these experiments were encouraging because of the similarity with those that occur at higher Reynolds numbers. The slopes of the lift curves in Figure 8 can be predicted with the following simple equation from Reference 11:

$$C_{L_{\alpha}} = C_{l_{\alpha}} \frac{A}{(C_{l_{\alpha}}/\pi) + \sqrt{(C_{l_{\alpha}}/\pi)^2 + A^2}} \quad (1)$$

It should be noted however, that this only holds true when the lift curves can be approximated with a straight line; thus it would be of no use at  $Rc = 80,000$ . Also, since lift curves are never truly linear at low Reynolds number conditions, this relationship should be exercised with a great deal of care. Lastly, it was found that a simple lifting line analysis predicted spanwise load distributions on the  $A = 4.0$  wing reasonably well [4], but only when the lift curve was approximately linear. This is shown in Figure 9.

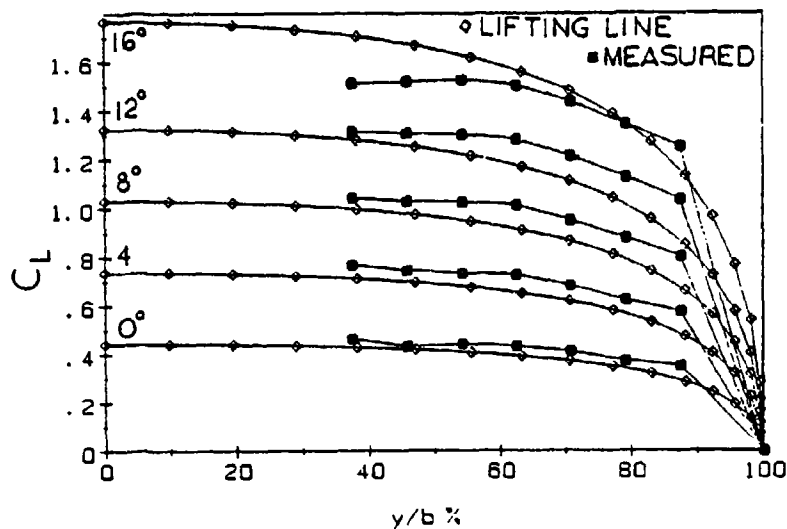


Figure 9. Comparison of Lifting Line Predictions with Spanwise Lift Distributions Obtained from Integrated Pressure Distributions for  $Rc = 200,000$  and  $A = 4.0$ .

#### CONCLUSIONS

The performance of the three finite wings were found to be functions of the chord Reynolds number and wing aspect ratio. The performance of the wings was found to be closely related to the two-dimensional airfoil performance. The wing data was found to be somewhat predictable from the airfoil data, especially when the lift curves approached a linear shape ( $Rc = 200,000$ ). Decreasing the Reynolds number decreased wing performance, and decreasing aspect ratio had a similar effect. Overall, it is believed that careful use of carefully obtained airfoil data will allow prediction of wing performance at low Reynolds number conditions. Further research into this area is deemed to be fruitful and quite necessary.

## NOMENCLATURE

- A traditional aspect ratio, based upon the distance from wing tip to image wing tip,  $b'$ ,  $A = b'^2/S$
- b semi-span length, distance from model root to tip, cm
- $b'$  span length, distance from model tip to image tip, cm
- c chord length of wing or airfoil model, cm
- $C_d$  airfoil section drag coefficient
- $C_D$  wing drag coefficient
- $C_l$  airfoil section lift coefficient
- $C_{l_\alpha}$  airfoil section lift coefficient slope
- $C_L$  wing lift coefficient
- $C_{L_\alpha}$  wing lift coefficient slope
- D wing drag force, N
- d airfoil section drag force, N
- L wing lift force, N
- l airfoil section lift force, N
- Re Reynolds number based upon airfoil or wing chord length  $U_\infty c/\nu$
- S airfoil or wing planform area,  $S = b \cdot c$  for all cases
- $U_\infty$  freestream velocity in the streamwise direction
- y distance measured from semi-span model root

### Greek Symbols

- $\alpha$  angle of attack, degrees
- $\nu$  kinematic viscosity of air,  $m^2/s$

### Subscripts

- max refers to the maximum value of a variable, usually with respect to angle of attack
- min refers to the minimum value of a variable, usually with respect to angle of attack

## ACKNOWLEDGEMENT

This work is supported by the Office of Naval Research under contract No. N00014-83-K-0239.

## REFERENCES

1. Mueller, T.J., "Low Reynolds Number Vehicles," AGARDograph 288, February 1985.
2. Anderson, J.A., Introduction to Flight, New York: McGraw Hill, Inc. 1978.
3. Abbott, I.H., and Von Doenhoff, A.E., Theory of Wing Sections, New York: Dover Publications, Inc., 1984.

4. Bastedo, W.G., "Performance of an Airfoil and Three Finite Wings at Low Reynolds Numbers," M.S. Thesis, University of Notre Dame, December 1984.
5. Mueller, T.J. and Batill, S.M., "Experimental Studies of the Laminar Separation Bubble on a Two-Dimensional Airfoil at Low Reynolds Numbers," AIAA Paper 80-1440, 1980.
6. Mueller, T.J., et al., "The Influence of Free Stream Disturbances on Low Reynolds Number Airfoil Experiments," Experiments in Fluids, Springer-Verlag, 1983.
7. Huber, A.F., "The Effects of Roughness on a Low Reynolds Number Airfoil," M.S. Thesis, University of Notre Dame, May 1985.
8. O'Meara, M.M., "An Experimental Investigation of the Separation Bubble Flow Field Over an Airfoil at Low Reynolds Numbers," M.S. Thesis, University of Notre Dame, May 1985.
9. Mueller, T.J., "The Influence of Laminar Separation and Transition on Low Reynolds Number Hysteresis," AIAA Paper 84-1617, June 1984.
10. Althaus, D., Profilpolaren fur den Modellflug, Neckar-Verlag, 1982.
11. McCormick, B.W., Aerodynamics, Aeronautics, and Flight Mechanics, New York: John Wiley & Sons, Inc., 1979.

# AN ENVIRONMENTAL AERODYNAMIC TEST SYSTEM FOR LOW-REYNOLDS-NUMBER APPLICATIONS

H.-T. Liu, E. W. Geller and M. Cooper  
Flow Industries, Inc.,  
Research and Technology Division  
Kent, WA 98032

## ABSTRACT

An environmental aerodynamic test system (EATS) and a test model, consisting of an instrumented truck with a full-scale Wortman FX 63-137 wing (0.61 m x 3.66 m) mounted on a boom, were designed and assembled. One of the main functions of the EATS is to investigate the effects of atmospheric gusts and turbulence on the performance of candidate wings and overall configurations for remotely piloted vehicles (RPVs). A six-component balance for force/moment measurements is mounted inside the wing. Other on-board instruments and equipment include a sting-mounted cup and vane anemometer, an accelerometer, a pitch/yaw gear, a portable generator, an electric winch, a signal conditioner and an APPLE II computer. The wing is about 5.8 m above the ground and sufficiently above and upstream of the truck to make vehicle flow interference negligible. The EATS is essentially field ready, and experiments are soon to be conducted along a 1.2-km straight racing track.

## INTRODUCTION

Until now, applications of low-Reynolds-number (LRN) aerodynamics have been mainly confined to those of a civilian nature, including radio-controlled model airplanes, sailplanes, wind turbines, ultralight man-carrying, and man-powered aircraft. The recent awareness of the potential importance of high-altitude or low-speed remotely piloted vehicles (RPVs) for military and scientific applications has rekindled the interest in LRN aerodynamics. In the Reynolds number range of interest here, from  $10^5$  to  $10^6$ , the aerodynamics can be reviewed in several broad categories: an unperturbed atmosphere or a real atmosphere; two- or three-dimensional flows; and lift coefficients less than roughly 1.7 or those significantly higher.

To date, essentially all the research data have been obtained in what was hoped to be unperturbed flow. Unfortunately, the data are contaminated to some degree by disturbances inherent in the test procedure using either wind tunnels (Carmichael [1]; Mueller and Jansen [2]) or free-flight testings (Lissaman [3]). For example, test results for the Eppler 61 airfoil from two wind tunnels, one employing integration of wake measurements and the other actual force measurements, differed by a factor of 2 in the value of  $(C_L/C_D)_{\max}$  (Carmichael [1]; Mueller and Burns [4]). Using design techniques that have been experimentally verified for a limited number of cases (Carmichael [1]; Liebeck [5]), airfoils are obtainable with maximum lift coefficients up to roughly 1.7 in unperturbed flow, at least for the higher portion of the LRN range. For the lower range of Reynolds numbers of interest, to quote Lissaman [3], "... the design of LRN airfoil, particularly at Reynolds numbers below

300,000, is still a black art." A qualitative picture of the flow at high lift coefficients in this range of Reynolds numbers exists; yet detailed quantitative information on the upper surface bubble structure, its role in the transition process and the transition process itself is lacking (Mueller [6]).

The major uncertainty of the performance of low-speed, low-altitude RPVs is the impact of environmental effects. While such effects are known to be significant in many instances,\* no meaningful method of assessment exists. Even if the atmospheric turbulence and related parameters were known in detail (which they certainly are not), their impact on the aerodynamic performance could be estimated only in the crudest fashion.

To fill the serious gap in our knowledge of environmental and other aerodynamic effects, an environmental aerodynamic test system (EATS) was designed and assembled. The EATS is an instrumented truck equipped with a six-component aerodynamic balance for force/moment measurements of boom-mounted full-scale wings or RPVs. Our main objective is to determine the magnitudes of changes in the forces and moments on full-scale wings caused by environmental disturbances such as gusts, turbulence and possibly rain. It may also be used as a preflight qualification test bed for flight test vehicles. In this paper, we describe the EATS and some of its performance characteristics. At this time, the EATS is essentially field ready. Test results will be available in the near future.

#### DESCRIPTION OF THE EATS

The EATS is an improved version of an aerodynamic test system designed for hang glider testing (Pregler et al. [7]). It consists of an instrumented pickup truck with a boom furnishing a moving platform on which to mount full-scale LRN wings. Figure 1 is a picture of the EATS. We describe in this section the essential components of the EATS and the first LRN wing to be tested on it.

##### LRN Wing and Mount

The first full-scale LRN wing to be tested has a Wortman FX 63-137 profile corrected by Eppler (referred to as the Wortman wing hereafter). Figure 2 shows a cross-sectional view of the Wortman wing. It has an aspect ratio of 6, with a span of 3.66 m and a chord of 0.61 m. The wing is constructed from high-density foam with a fiberglass-epoxy outer skin painted with polyurethane. An interior aluminum box spar forms the main structural element for bending and torsion. A cavity at midspan (see Figure 2) is reserved for the six-component balance (described below). One of the most critical elements of the wing is the trailing edge, which is highly cambered and very thin. In order to hold its shape and be sufficiently strong and rugged for field deployment, the

\*Paul McCready reported in an LRN Workshop held at ONR (1983) that his man-powered airplane experienced increase in drag when it encountered turbulence during its historic flight across the English Channel.



**Figure 1. Environmental Aerodynamic Test System**

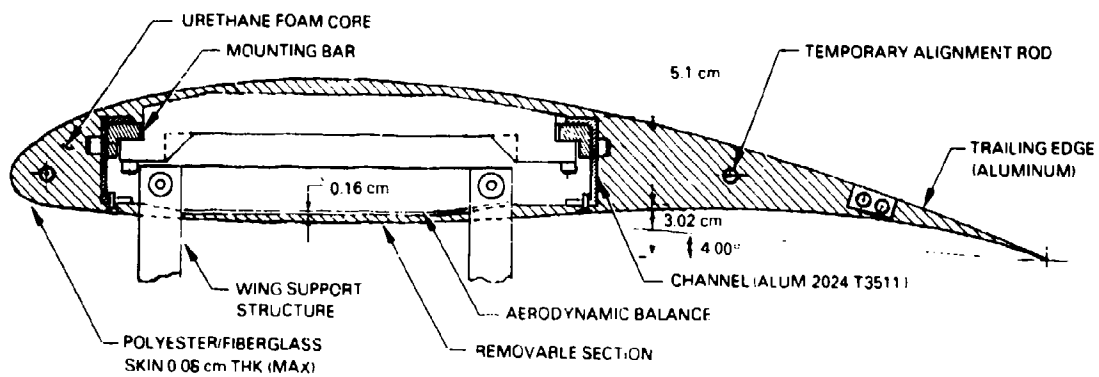


**Figure 2. Cross-Section View of Wortman Wing**

last 8.9 cm of the trailing edge is made of aluminum and accurately machined.

For practical reasons, the Wortman profile was modified to eliminate the zero-thickness trailing edge. A trailing edge thickness of 0.076 cm was obtained by changing the thickness form but not the camber line; 0.038 cm was added to both the upper surface and the lower surface of the wing. This results in an increase in the thickness ratio of one-tenth of one percent, and the aerodynamic perturbation due to this modification is insignificant.

The box spar is constructed by riveting top and bottom aluminum skins to 5.1-cm aluminum channels. In addition to the bending moment, the box carries torsional loads into the balance. The top plate of the balance serves as the structural member at the center section, where there is a cavity in the box spar. The top and bottom skins of the box spar are not carried through the center section, and the loads are transferred from the box spar to the balance.

Aluminum ribs 0.32 cm thick are riveted to the box spar, and the trailing edge is riveted to the ribs. Urethane foam blocks, with a density of  $96.0 \text{ kg/m}^3$ , were glued between the ribs and sanded down to the proper airfoil shape with a straight sanding block using the ribs as templates. The next step was to apply a thin layer of filler in any nicks or undercuts in the foam. The surface was then covered with two layers of light fiberglass cloth ( $102 \text{ gr/m}^2$ ) impregnated with epoxy resin. Finally, the surface was sprayed with one layer of primer and one layer of polyurethane paint.

The wing support consists of two thin U-shaped struts, 0.05 cm thick and 22.2 cm wide, fastened to the bottom balance plate at four points (Figure 3). The struts penetrate the lower wing surface through

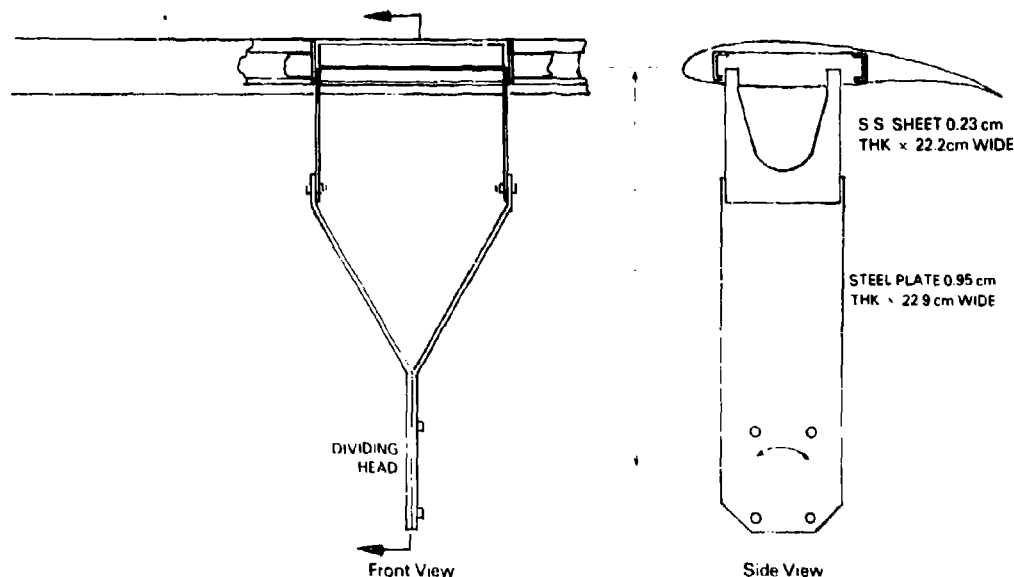


Figure 3. Supporting Struts for the FX 137 Wortman Wing

small slots without touching the wing. This design strategy, with the balance inside the wing, eliminates "tare" corrections for the drag of the struts. The lower ends of the struts are bolted to a Y-shaped support, which is in turn mounted on a dividing head controlling the incidence angle of the wing.

#### Moving Platform and Supporting Framework

The moving platform is a 1979 1-ton pickup truck (F350 Custom). Several modifications were made to minimize the transmission to the wing of vehicle- and road-induced vibrations. In addition to the weight of the EATS equipment, 1000-lb sandbags are loaded on the truck during test runs. The suspension system can be softened by removing one leaf from each of the leaf springs. A pair of air shocks was added to the rear suspension for fine level adjustment, and a set of steel-belted radial tires was installed to facilitate a smooth ride. Prior to test runs, the tire pressure is lowered to about 20 psi to absorb most of the road-induced vibration.

The supporting framework consists of a steel frame rigidly attached to the main beams of the truck, a 3.4-m-long steel boom (15.2 cm square tube) equipped with a motorized winch system, a yaw/pitch table that includes a motorized dividing head (for pitch angles) and a manual adjustment for yaw at increments of 2 degrees up to maximum angles of  $\pm 20$  degrees. The wing is first mounted on the dividing head with the boom in its lowered position flat on the framework. The boom is then raised to the test position (45 degrees to the horizontal) and is braced securely with two steel tubes (5.1 cm square). The dividing head is driven by a Dayton 1/15-hp AC gear motor. A potentiometer is installed on the dividing head for monitoring the incidence angle of the wing. A camper-type enclosure is used to protect the operator and the on-board instruments.

#### Instrumentation

A set of instruments was designed and assembled to measure aerodynamic and atmospheric parameters, particularly the forces and moments exerted on the wing. The aerodynamic parameters are measured with several on-board instruments. These include a six-component balance, a Swoffer cup anemometer and a vane anemometer, which are driven by a preamplifier and a controller, and a single-axis accelerometer, which monitors the vibrational motion of the wing due to engine vibration and road roughness. The atmospheric parameters are measured with sensors mounted on the EATS or on one or more mini-meteorological stations along the side of the test track.

Six-Component Balance. The heart of the EATS is a six-component balance that consists of six miniature load cells each mounted on a flexure designed to minimize the interference between the mutually perpendicular force measurements. The balance (Figure 4) is capable of measuring the drag, lift and side forces and the rolling, pitching and yawing moments. To eliminate strut "tare", the balance is completely enclosed in the full-scale wing (Figure 2).

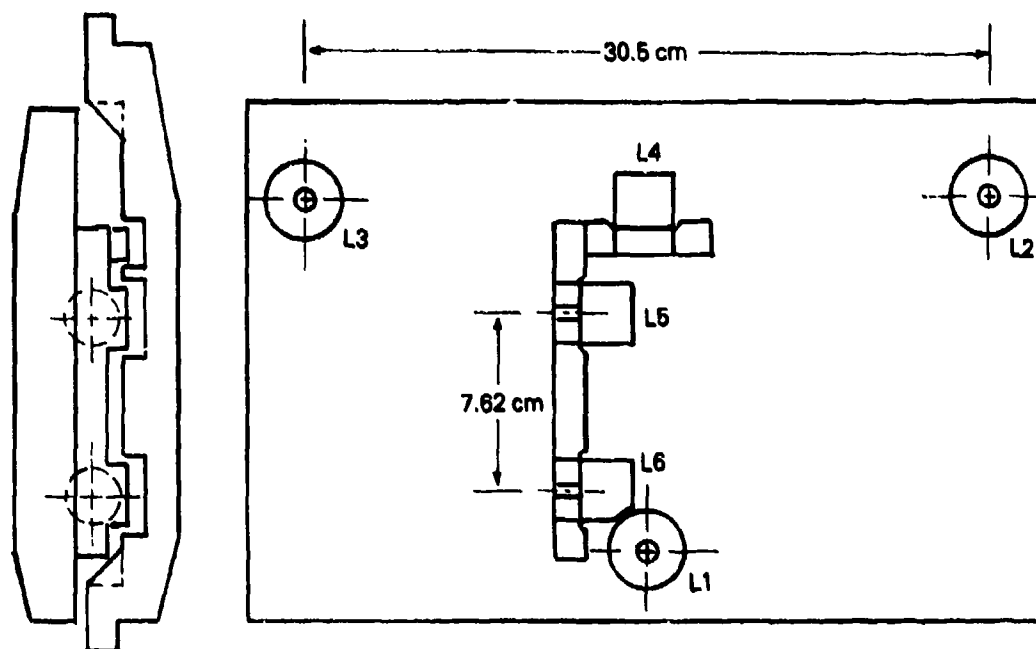


**Figure 4. Layout of the Load Cells in the Six-Component Balance**

The miniature load cells (Sensotec, Model 31 series) were specially ordered with built-in mechanical stops that are capable of providing an overload protection of 5 times the maximum load. They are interchangeable to accommodate different wings and loading ranges. As shown in Figure 4, the load cells are arranged to measure the nominal lift ( $L_1$ ,  $L_2$  and  $L_3$ ), drag ( $L_4$ ) and side force ( $L_5$  and  $L_6$ ). They are rigidly mounted on a bottom steel plate and connected to the top plate via individual flexures. The flexures are made of berillium copper with a thin straight section 2.54 cm long and 0.24 cm in diameter.

The top plate of the balance is bolted to the wing, and the lower plate is mounted onto a pair of U-shaped thin struts that penetrate a removable section of the lower wing surface through four narrow slots (Figure 2). There is no contact between the struts and the wing. Air passage through the slots is blocked by sealing the gaps with thin cellophane sheets, which minimize force transmission from the wing to the struts. There are three 0.3-cm-diameter signal cables taped on each strut along the leading edges. These cables connect the load cells in the wing to the preamplifier mounted below the wing. The thin struts are mounted on a Y-shaped strut (Figure 3) whose lower end is bolted to the dividing head.

**Speed and Direction Sensors.** A Swoffer cup anemometer and a vane anemometer are mounted on a horizontal sting about 2 m below the wing. They measure the relative wind speed and direction (in the horizontal plane) experienced by the wing.

Preamplifier and Controller. A preamplifier is mounted on the top of the boom to amplify the signals of the load cells, of the cup anemometer and the vane anemometer, and of the incidence angle potentiometer to sufficiently high levels for transmission through the long cables to the on-board controller. The controller provides the functions of driving the various sensors and preamplifier, filtering, nulling, amplifying and displaying the signals, and interfacing with the on-board APPLE II computer for data acquisition and analysis. At present, single-pole low-pass filters are set at 36 Hz for all load cell channels. The nulling capability is an important feature that allows removal of the dead loads and, if desired, the steady aerodynamic forces so that the dynamic forces can be greatly amplified. As a result, we can use an 8-bit analog-to-digital converter and still achieve sufficiently high resolution and accuracy.

Accelerometer. A Bruel & Kjaer accelerometer (Type 4384), which has a sensitivity of 9.76 pC/g, is used to measure the vibrational motion of the wing induced by engine vibration and road roughness. The accelerometer may be oriented to measure any component of the vibration. It is mounted on the strut supporting the wing and is driven by a charge amplifier (Kistler Instrument Company, Model 504E).

Mini-Meteorological Stations. To monitor and record the atmospheric conditions during the test runs, mini-meteorological stations equipped with velocity, pressure, temperature and humidity sensors are used. The velocity sensors are Gill UVW anemometers manufactured by R. M. Young Company (Model 27005 with 19-cm-diameter x 30-cm-pitch propellers). The anemometers are mounted on a portable mast. The distance constant (63-percent recovery) and the threshold of the polystyrene propellers are 0.8 m and 0.3 m/s, respectively. The anemometers are driven by a power supply indicator-translator (Model 27503R), which is a combination of a power supply, with complete controls and signal outputs, and panel meters for the three components of the wind speed. A compact weather station, including a thermometer, a barometer and a humidity gauge, is used to provide the readings of air temperature, atmospheric pressure and relative humidity. Preferably, the wind sensors will be mounted on the EATS so that cross-correlations of the performance of the wing with the gusts measured next to the wing may be made. Alternatively, two to three stations could be used along the test track to determine both the spatial and temporal variations of the atmospheric conditions to assess their effects on the performance of LRN wings.

Miscellaneous Apparatus. To supply power to the on-board instruments and equipment, the EATS has two power sources. A 1600-W portable generator (Honda, Model EM 1600X) is used to drive all the on-board instruments. The generator has both AC (115 volts) and DC (12 volts at 8 amp) power. To operate the winch, a DC motor is connected to the 12-volt truck battery.

#### On-Board Computer System

The EATS is equipped with an on-board 64k APPLE IIe computer, with dual 13.3-cm floppy disk drives, for data acquisition and analysis. The computer has an extend 80-column card on which 64k of auxiliary RAM

(random access memory) is available for fast data recording. To facilitate large data storage and high-speed data transfer, a 294k RAM card or solid-state disk emulator manufactured by Synetix (Model 2202) was added to one of the expansion slots of the computer. The RAM card has the capacity of two standard 13.3-cm floppy disk drives while improving the disk I/O speed by a factor from 100 to 500 percent.

The I/O interface card (Interactive Structures, Inc., Model AI-02) has a 16-channel analog-to-digital converter with an 8-bit accuracy. It accepts information in the form of an analog voltage level in the range from 0 to 5 volts.

Two data acquisition programs have been developed. The first, which is written in BASIC, was designed and developed to conduct calibration and measurements of mean values of all the parameters. The results in physical units are immediately displayed on the screen for review after each run. The second program, which is written in a hybrid of assembly language and BASIC, was designed for sampling at high data rates. At present, the highest sampling rate is 12k samples per second, which matches the full capacity of the A/D card. The data are stored in the main memory (up to 34k) and subsequently transferred to the RAM card and finally onto the floppy disks for future analysis. A set of programs is available for statistical analysis of the data.

#### PERFORMANCE CHARACTERISTICS

A series of calibrations and tests was made to determine the performance characteristics of the sensors for measuring the physical variables of interest. In general, calibration includes component and system calibration. For example, both the individual load cells and the balance as a whole are calibrated. According to the manufacturer, the load cells have linearity and hysteresis within  $\pm 0.15$ -percent F.S. (full scale). The repeatability is  $\pm 0.05$ -percent F.S. They are temperature-compensated (15.6 to 71°C) to within  $\pm 0.003$ -percent F.S./°C. After two stages of amplification through the preamplifier and the controller, calibration of individual load cells shows that an accuracy of better than  $\pm 0.3$  percent is maintained.

To calibrate the balance as a whole, we designed a special mechanical device (Figure 5) that is capable of applying known forces independently in two orthogonal directions. For applying a horizontal load to the balance, an L-shaped bell crank with a pair of low-friction bearings installed at the pivotal point is used. By hanging known weights onto the horizontal arm of the bell crank, we transfer vertical gravitational loads into horizontal forces (drag or side force) on the balance with insignificant losses due to static friction in the bearings. The long moment arms of the ball crank assure small force losses due to friction. The balance is mounted on a dividing head that can be rotated in the horizontal plane. To independently apply a vertical load to the balance, weights are placed on top of the balance.

By applying known forces in the drag/side-force direction, we may first determine the first-order correction for the drag/side-force to compensate for the cross coupling that results from using the flexures.

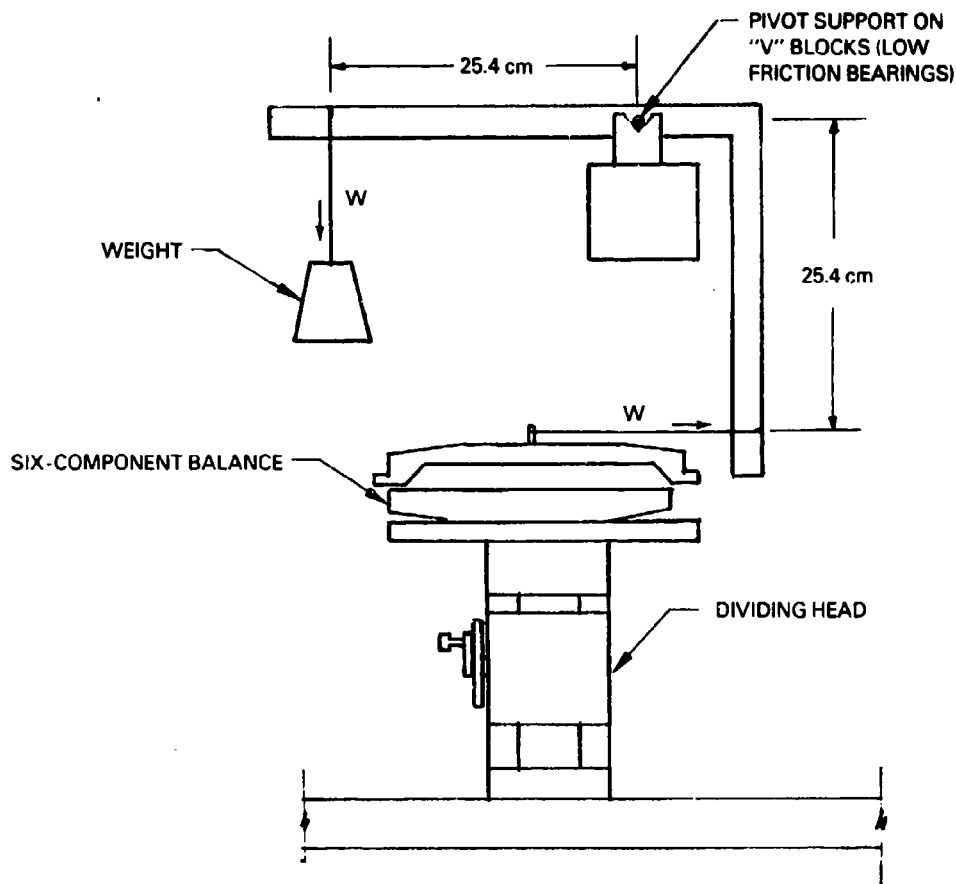


**Figure 5. A Mechanical Device for System Calibration of the Six-Component Balance**

A second-order correction may then be determined by measuring the differences in the readouts of the drag/side-force while applying forces in the other two orthogonal directions. It turns out that the cross coupling between the drag and side-force cells is less than 0.5 percent within the range of expected loads in the two directions. Therefore, no correction is made.

Empirical calibration formulae are derived from a series of static calibrations. For a particular normal force, there are three correction terms. The first is a constant (the first-order correction) multiplying the uncorrected force component in question. The second is also a constant (the second-order correction) multiplying one of the orthogonal force components. And the third is another constant (the second-order correction) multiplying the other orthogonal force component.

Figure 6 shows a typical static calibration of the balance for a range of pitch and yaw angles. The reference used for the calibration is the weight of the top plate (17.37 kg). The normal forces measured at different angles of attack of the balance are plotted in the figure. The results of the static calibration show that the system errors of the balance for the lift, drag and side force are within  $\pm 2$  percent,  $\pm 3$  percent and  $\pm 5$  percent, respectively.

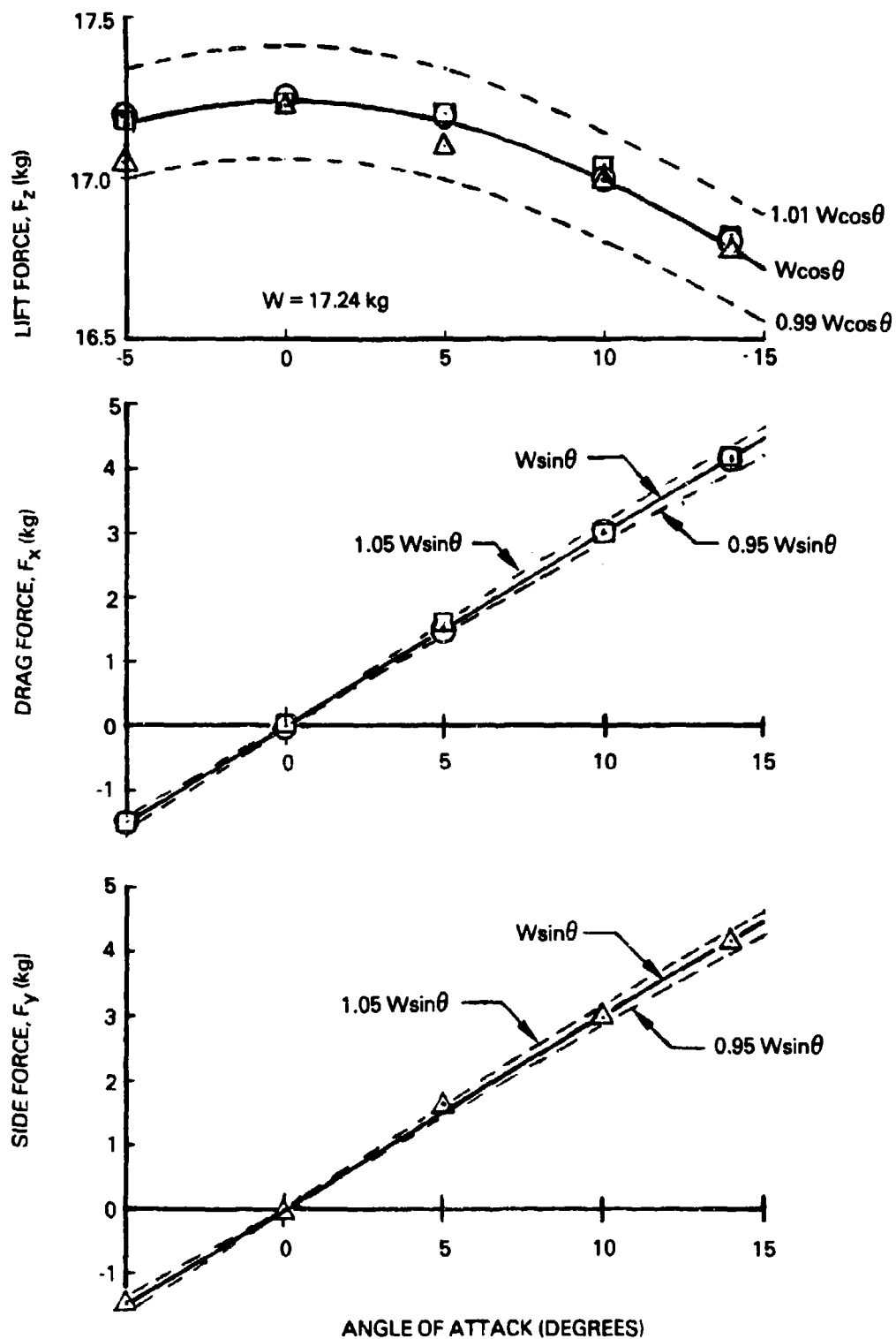


Figure 6. Static Calibration of the Six-Component Balance

The EATS was designed to operate in the range of 3 to 20 m/s. There are two major vibrational sources, the engine vibration and the road roughness. Both induce vibration at the wing via the supporting structure. As a result, the signal-to-noise ratio for the force/moment measurements deteriorates. Typically, for a lift of 400 N and a drag of 40 N, static calibration shows that the ratios of the root-mean-square (rms) lift and drag to the corresponding mean values are within 0.01 percent. With the truck engine running at medium speed, the above ratios increase to 0.2 and 1.7 percent, respectively.

A preliminary test was conducted on a side road to measure the effect of road roughness on the stability of the EATS as a whole. During that exercise, we replaced the load cells and flexures with dummies. With the truck moving at 4.5 to 6.7 m/s, no appreciable swing or sway was visually observed, even with the tires operating at normal pressures. The thin-strut wing mounts appear to function reasonably well in damping part of the vibration transmitted via the supporting structure. From the readouts of the accelerometer, mounted in a vertical orientation on top of the Y-shaped strut, the maximum vertical rms acceleration is about 0.01 g with the truck operating in idling mode and 0.04 g with it moving at about 4.5 m/s. Actual measurements of the rms normal forces with the balance will be conducted soon. Our goal will be to minimize the vertical acceleration to within 0.02 g by implementing a combination of measures described in a previous section.

#### SUMMARY

This paper describes an environmental aerodynamic test system for testing full-scale low-Reynolds-number wings or flight-ready RPVs. The EATS was designed to study environmental effects on the performance of candidate LRN wings and other aerodynamic effects that are difficult or impossible to investigate otherwise. One of its main functions is to determine the changes in the forces and moments on LRN wings caused by environmental disturbances such as gusts, turbulence and rain. We believe that its availability will help fill the LRN knowledge gap and will complement conventional wind tunnel and radio-controlled flight testing and, thus, help in the development of well-behaved LRN wings.

Several special features of the EATS are summarized below.

- o It is capable of testing full-scale RPV wings and RPVs for a range of Reynolds numbers from 150,000 to 1,000,000.
- o It is equipped with a six-component aerodynamic balance and pertinent instruments together with an on-board APPLE computer for force/moment measurements.
- o It is a mobile facility that brings the experiments to the environmental situations of interest.

The EATS is now field ready, and experiments will be conducted in the near future using a nearby racing track. The initial field experiments will be conducted to fine tune the EATS and determine its overall capabilities. Subsequently, force/moment measurements will be conducted

under calm atmospheric conditions to establish a set of baseline data for our first model, the Wortman wing. Finally, experiments under a range of gusty conditions typical of RPV deployment will be conducted. Based on these measurements, the effects of the gusts on the performance of the Wortman wing will be determined.

#### NOMENCLATURE

$C_D$	Drag coefficient
$C_L$	Lift coefficient
$F_x, F_y, F_z$	Force components in the direction of the nominal drag, side force and lift
$W$	Weight
$\theta$	Angle of attack with respect to the balance coordinates

#### ACKNOWLEDGEMENTS

This project is supported by the Office of Naval Research under Contract No. N00014-83-C-0764. The authors would like to thank Messrs. Mike Giles, Paul Tacheron and Ken Theimer for their important contributions during the design and construction of the EATS. In particular, Mr. Giles, who built one of the first aerodynamic test systems for hang glider testing, has been extremely helpful in sharing his invaluable experience with us.

#### REFERENCES

1. Carmichael, B. H., "Low Reynolds Number Airfoil Survey," Vol. 1, NASA CR165803, 1981.
2. Mueller, T. J., and B. J. Jansen, Jr., "Aerodynamic Measurements at Low Reynolds Numbers," AIAA Paper 82-0598, 1982.
3. Lissaman, P. B. S., "Low-Reynolds-Number Airfoils," Ann. Rev. Fl. Mech., 15, 1983, pp. 223-39.
4. Mueller, T. J., and T. R. Burns, "Experimental Studies of the Eppler 61 Airfoil at Low Reynolds Numbers," AIAA Paper 82-0345, 1982.
5. Liebeck, R. H., "Design of Subsonic Airfoils for High Lift," J. Aircr., 15, 1978, pp. 541-61.
6. Mueller, T. J., "Low Reynolds Number Vehicles," AGARDograph No. 288, 1985.
7. Pregler, W., T. Guignard, and M. Giles, "Aerodynamic Test System," Hang Gliding, March 1981.

SYMMETRY BREAKING AND LIFT HYSTERESIS  
ARISING FROM MASSIVE LAMINAR SEPARATION:  
A STUDY OF MULTIPLE STEADY-STATE SOLUTIONS

H.K. Cheng  
Department of Aerospace Engineering  
University of Southern California  
Los Angeles, California 90089-0192

ABSTRACT

The inviscid-viscous interaction of the body-scale flow involving massive laminar separation can be studied as a modified airfoil problem through a triple-deck and other compatible structures modelling steady-state Navier-Stokes solutions at high Reynolds number [1-4]. This paper summarizes a recent development of this approach applied to wing sections [5-7]. The theory admits open and closed wakes, as well as laminar reattachment on wing. Mainly the steady-state solutions pertaining to open-wake models will be studied in detail. Examples of solution bifurcation signifying symmetry breaking, hysteresis and other lift anomalies of the low Reynolds number flows are discussed.

1. INTRODUCTION

Recent interest in remote-controlled and miniature aircrafts, hang gliders, wind mills [8] as well as animal swimming and flying [9,10,11] has drawn attention to the scarcity of aerodynamic data and knowledge at  $Re < 10^6$ . One major obstacle to the flow analysis of this regime is the global interaction of different parts of the separated flow, which is further compounded by the flow instability and turbulence transition. Effective, time-accurate algorithms for solving Navier-Stokes equations on super, as well as moderate-scaled, computers are now available (see, for example [12,13]); which, along with increased research efforts in wind- and water-tunnel experiments [6,14,15] will undoubtedly advance much of our understanding in the near future.

The works discussed below follow an alternative route which treats the massive laminar separation as a modified airfoil problem. A key element which link the unseparated and/or reattached boundary layers to the separated flows is the triple deck of [1-4]. The approach thus finds its root in the asymptotic theory, and, as such, the accuracy is not expected to be high, but its analytical simplicity allows the unveiling of certain behavior of these low-Re flows, which could not be readily recognized in an otherwise more detailed specific, large-scaled computation.

As a thin obstacle, an airfoil may support a variety of steady-state flow structures not envisaged in Sychev's original analysis of the laminar separation from a circular cylinder [2]. In particular, the open-wake with the Kirchhoff free streamlines stipulated therein may breakdown for the thickness ratio less than a certain critical value;

the shear layers may then reattach to form a closed wake behind, or an eddy over the wing. More important is the bifurcation of the steady-state solution, rendering possible lift hysteresis, as well as symmetry breaking of an otherwise symmetrical flow pattern. These have been the aspects considered in [16-18] which address the laminar separation problem beyond trailing-edge stall. Refs. [17,18], where many important examples of multiple solutions and symmetry breaking were given, have limited distribution. This paper will summarize their principal results and clarify a few ambiguities; additional examples, the NACA 663018 section in particular, are analyzed. It must be pointed out that most examples considered stipulate a Kirchhoff-type open wake. The full potential and significance of the model with laminar eddy reattaching on wing or a closed wake are currently being studied.

The assumption of the steady-state laminar model seems to be too idealistic to be useful for airfoils at  $Re > 10^5$ . It is essential to recognize however, that, even at an  $Re$  in the half-million range, separation bubbles (of sizes comparable to the boundary layer or greater) usually occur near the leading edges [19], of which the shear layer is laminar, at least initially. The present study may thus shed light to research on leading-edge bubbles. For  $Re$  well below  $10^5$ , this model can become quite realistic, as evidenced from the many streamline patterns about wing sections and inclined flat plates photographed by Werlé [20] which have been made popular in Van Dyke's Album [21]. Werlé's study also indicates that the shear layer can reattach to the wall while still laminar. Whereas, the important aspect of transition to turbulence is lacking from the study, the laminar model at hand should play an essential role in providing the initial (steady) state, about which questions on hydrodynamic instability (of this non-parallel flow) can be addressed. In this regard, the many multiple steady states brought out by the model should present an interesting aspect of the instability analysis for flows with massive separation. Indeed, Goldstein [22] and Atassi [23] have recently analyzed wave amplification on the Kirchhoff streamline leaving a laminar break-away point, and determined the "receptivity" to disturbances [24]. Their studies have been restricted thus far to a symmetric open wake (assuming also a pair of symmetrical wave trains).

For many airfoils, the lift may have multiple values near stall at  $Re = O(10^5)$ , forming hysteresis loops in the  $C_L$  vs.  $\alpha$  curve. Mueller [15] amplifies the fact that the hysteresis loop has a definite sense (clockwise or anticlockwise) determined by the airfoil geometry. Certain symmetric airfoils exhibit a loss or reversal of aerodynamic damping ( $dC_L/d\alpha \leq 0$ ) as well as symmetry breaking ( $C_L \neq 0$  at  $\alpha = 0$ ) at  $Re$  slightly below  $10^5$ . These features are most clearly shown in the wind-tunnel measurements by Althaus [6] for the symmetric NACA0012 and NACA0033. The damping or control reversal is also seen from data for the NACA663018 profile at  $Re = 1.3 \times 10^5$  in [14]. These steady-lift records based on long-time averaged data signify that the large-scale structures of these flows must be stable. This is especially significant with reference to the state of the symmetry-breaking flows, which may very well be referred to as a "bi-stable state". It is interesting to note that the notion of bi-stable state has long been used in works

on transition experiments with circular cylinders in critical and supercritical  $Re$  ranges, where non-zero  $|C_L|$  can be found [25-28]. This notion seems to be more appropriate, however, for the results in aerodynamics. It is commonly believed [25-28] that the symmetry breaking requires a successful turbulence transition on one side of the obstacle and a laminar break-away on the other side. Our analyses indicate on the other hand that it may also occur with flows on both sides being laminar; symmetry breaking may thus be expected to occur at  $Re$  well below the critical range. In either event, the laminar break-away remains an essential local description which determines finally the body-scale flow.

These anomalous aerodynamic features of symmetrical profiles are by no means irrelevant for wing design at  $Re \lesssim 3 \times 10^5$ , since the chord Reynolds number of the stabilizer surfaces may very well be  $10^5$  and lower, and the tail or canard sections are most likely symmetrical. It is also quite well known that these anomalies can be controlled and averted with the use of turbulators of various types. Experimental and theoretical studies will identify the domains where a turbulator is needed or if the proper functioning of such a measure should fail.

## 2. THE GLOBAL INTERACTION PROBLEM

### Assumptions and Key Elements in the Analysis

We consider an incompressible flow about an airfoil in a uniform free stream and shall be concerned mainly with the determination of the steady-state structure of the body-scale flow. In arriving at the flow model which may represent asymptotically a solution to the Navier-Stokes equations, and consistently with observational data [5,20], we stipulate that the recirculating fluid motion interior of the open or closed wake, or in a laminar bubble, is so weak that the pressure therein can be taken to be uniform. For an open wake, this pressure is assumed to be that in the free stream as in Kirchhoff's free-streamline theory [29-31]. Implicit also is that the flow speed does not far exceed the free-stream velocity.

Not inconsistent with available photo records for flow reattachment and wake closure at  $Re = 10^2$ - $10^4$ , a cusp-ended reattachment is chosen to represent the wake or eddy closure. Its correctness is substantiated by the conclusion from Cheng & Smith [16] where a wake closure with a (parabolic) blunt end is shown to give a non-zero drag for symmetric profiles.

The principal result of the works of Sychev [2] and Smith [3] is the determination of a criterion for the local self-induced pressure rise for the laminar break-away to occur in the "triple deck". Let the streamwise location of the break-away point (on the body scale) be taken as  $x = s$ , the required behavior for the pressure-rise is

$$p - p_c \sim -k \sqrt{s-z} \quad (2.1)$$

where  $k$  is the constant determined from the theory

$$k \equiv \beta(\lambda)^{9/8} \sqrt{\epsilon} \quad (2.2a)$$

with

$$\epsilon \equiv Re^{-1/8} = (\mu/\rho U_{\infty} c)^{1/8} \quad (2.2b)$$

and  $\lambda$  is the local wall shear  $(\mu \partial u / \partial y)_w$  normalized by  $\mu_{\infty} U_{\infty} / \epsilon^4 c$ . The constant  $\beta$  in most applications has been taken as 0.44, determined originally by Smith [3], differing slightly from 0.42 in [32] and 0.41 in [33]. This is the key equation through which the body-scale flow will depend critically and nonlinearly on the break-away location  $x$ , noting that  $p-p_c$  is generally a complicated function of  $s$ . There is also a rather weak Reynolds-number dependence through the  $\sqrt{\epsilon}$ . Though unsuspected in the earlier works, the nonlinearity mentioned enable the solution to bifurcate, leading to multiple steady states which may signify lift hysteresis and symmetry breaking.

$$\text{Domain of Interest: } Re^{1/16} \tau = O(1)$$

Unlike the break-away locations for the circular cylinder in [1,2], the corresponding points on a wing-like section with thickness ratio  $\tau = O(\sqrt{\epsilon})$  may lie anywhere on the entire surface as  $\tau$  varies. For airfoils generated from the family

$$y_w^{\pm} = \tau f^{\pm}(x), \quad 0 < x < 1 \quad (2.3)$$

where the superscripts + and - refer to the upper and the lower surfaces, the body-scale flow is governed by the reduced thickness ratio [16-18]

$$\tilde{\tau} \equiv \tau / \sqrt{\epsilon} = Re^{1/16} \tau \quad (2.4)$$

A similar parameter  $\tilde{\alpha} \equiv Re^{1/16} \alpha$  has appeared in the problem of a flat plate at incidence  $\alpha$ , which model a trailing-edge stall, [34,35] to which the Kirchhoff open wake is however not applicable. The transition to the trailing-edge stall from an open-wake (body-scale) flow is not straightforward. It is seen from [16] that such a transition (if possible) must first reach a stage corresponding to a critical value of  $\tilde{\tau}$ , beyond which the Kirchhoff open wake ceases to exist in the far field and wake closure must be considered in a steady-state model. Before one reaches the limit of a flat plate, the possibility for the (shear-layer) reattachment on the wing surface and various forms of bifurcation noted earlier must be considered. A great deal indeed happens in  $\tilde{\tau}$  of the unit-order range.

Since the thickness ratio  $\tau$  in the domain of interest belongs to the order  $\sqrt{\epsilon}$ , the leading-order perturbation of the body-scale flow may therefore be analyzed first as a linearized problem for a small  $\epsilon$  with a set of fixed but unspecified break-away locations. The essential difference from the classical thin, hydrofoil theory for cavity flow [31] lies in the use of the triple-deck criterion (2.1) at each break-away point instead of the Brillouin-Villat condition [31,36] in the hydrofoil theory.

## The Boundary-Value Problem

As indicated earlier, the flow of interest is first solved as a linearized problem for a set of fixed break-away points; the number in the set depends on the wake or eddy configuration considered. (In this paper, the term "eddy" refers to a recirculation region with the reattachment occurring on the wing surface.) Figure 1 illustrates different portions of the inner boundary for the case involving an open wake, where  $s_1$  and  $s_2$  locate the break-away points on the upper and the lower surface, respectively. (The separation point where the local wall shear vanishes occurs at a distance  $O(\epsilon^3)$  downstream of the  $(s_i's)$ .) On the upper and lower wing surfaces upstream of  $x = s_i$ , the impermeability condition will be applied; along the free streamlines, a constant speed is imposed, which should be the free-stream velocity for the case illustrated.

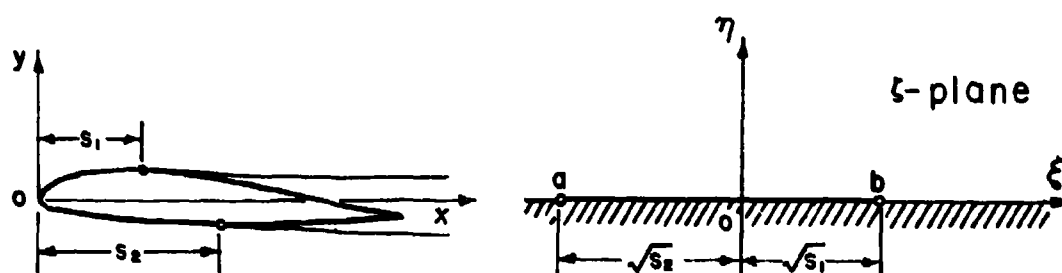


Fig. 1. Coordinates and break-away locations in the physical and transformed planes.

The linearization simplifies the inner boundary conditions to a prescription of the streamwise and transverse perturbation velocities on the upper and lower portions of the  $x$ -axis; the problem can be further reduced to one of finding an analytic function in the upper half  $\zeta$ -plane with data prescribed along the real axis (cf. Fig. 1). A complex velocity potential ( $u-iv$ ) fulfilling this and other requirements indicated earlier can be obtained as a functional of  $f^\pm(x)$ , explicit in  $s_1$ ,  $s_2$ ,  $\tilde{\tau}$  and  $x$ .

Essential to the global problem is the proper flow behavior in the far field. For the open-wake construction at hand, this is given by the asymptotic behavior of the Kirchhoff wake:

$$u-iv \sim -ik_\infty z^{-\frac{1}{2}} \quad (2.5a)$$

where  $z = x+iy$ , and  $k_\infty$  is a known constant depending on  $\tilde{\tau}$ ,  $s_1$  and  $s_2$ . The latter constant must be real and positive. The critical value of the reduced thickness ratio  $\tilde{\tau}_{crit}$ , at which  $k$  vanishes, delimits the domain for the open wake. (Other wake and eddy configurations, including the unseparated flow still remain as the steady-state alternative for  $\tilde{\tau} < \tilde{\tau}_{crit}$ .)

The pressure rise behavior near the break-away may now be described. Its substitution into the triple-deck criterion (2.1) at both break-away locations should provide two simultaneous equations for determining  $s_1$  and  $s_2$ . A helpful simplification is gained by the

linearization, which allows the wall shear  $\lambda$  in (2.1) to be evaluated from the Blasius result  $(0.332)s_1^{-1/2}$ , if one assumes that a fully attached laminar boundary layer lies upstream of the break-away. If separation and reattachment have occurred upstream, this value of  $\lambda$  must accordingly be modified, apart from a modification of inner boundary condition in such a case. Formulations similar to that illustrated above can be made for various combinations of the open and closed wakes, as well as (laminar) eddies. Limiting to at most four break-away points, four prototypes are illustrated in Figs. 2a,b,c,d. Particular cases of (c) involving laminar eddies have been studied in [17,18]. It is essential to point out in this connection that, in the absence of an open wake, (2.5a) is to be replaced by a doublet behavior in the far field

$$u-iv \sim \frac{i\Gamma}{2\pi} \frac{1}{z} + O(z^{-2}) \quad (2.5b)$$

where  $\Gamma$  is a circulation and must be real. The influence of this requirement is so strong that the eddy pressure in the steady-state solution can be uniquely determined in such cases [16-18].

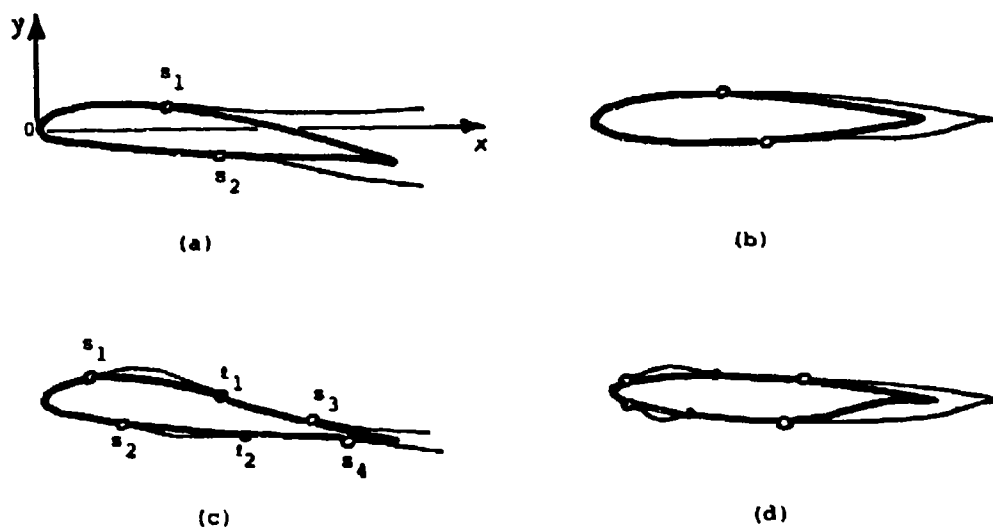


Fig. 2. Illustration of four types of body-scale flows.

A formal solution for (b) explicit in the  $s_i$ 's has been given in [17]. The formal solution for type (d) is similar, except for the additional singularities arising from  $s_1$  and  $s_2$  and the reattachment  $l_1$  and  $l_2$  (cf. Fig. 2d). Concrete examples of the types (b) and (d) have not been thoroughly analyzed, except for symmetrical sections [17].

As noted earlier, the solution to the type (c) flow involving both an open wake and laminar eddy cannot be fully determined for lack of knowledge on the eddy pressure. It is uncertain whether its determination requires knowledge on a detailed structure of the reattachment

and/or the eddy interior. An alternative answer to this question will be discussed at the end of Section 3.

#### Ad Hoc Open-Wake Models

To help explain lift anomalies unaccounted by the foregoing steady-state laminar models, we introduce an open-wake model with the flow breaking away on one side of the leading edge region as sketched in Fig. 3(a). This flow situation may not be recoverable as a special case of the type (a) flow on account of the nonuniformity of the linearized solution at the leading edge [37].

Another ad hoc model serving a similar purpose is sketched in Fig. 3(b) which has an open wake but with a fully attached flow on one side. These models describe a successful early transition and a fully attached (turbulent) boundary layer on one side and a laminar break-away on the other.



Fig. 3. Ad hoc flow models: (a) one-sided leading edge separation, (b) fully attached boundary layer on one side.

### 3. EXAMPLES AND DISCUSSION

Examples of massive laminar separation from symmetric airfoils illustrating break-down of the open wake ( $k_\infty = 0$ ) and multiplicity of open- and closed-wake solutions have been shown in [16]. Laminar break-away from airfoils at incidence and with camber, including reattachment on the wing surface, are studied in [17,18] where symmetry breaking as alternative steady states for a symmetric airfoil are demonstrated. The symmetric profiles considered in [17,18] fall into three families: (i) NACA64A015 (rescaled), (ii) NACA four digit series and (iii) a model Joukowski section. In addition, flows about circular-arc sections of zero thickness (the single-surface airfoil) and inclined flat plates have also been analyzed. The following will review some essential results of this development and discuss a recent study with the symmetric NACA663018 section, for which results from a wind-tunnel study at  $Re$  down to  $4 \times 10^4$  are available [14]. Several aspects of zero-thickness airfoils are omitted to conserve space.

#### The Rescaled NACA64A015

Our study with this family was motivated by the very distinct steady laminar flow pattern recorded by Werlé [20] at  $Re = 7,000$  for NACA64A015. The open-wake solution for this family (generated by the normalized ordinates of this section) provides the first example of symmetry breaking for the study [17]. The results for the break-away

location obtained for the zero incidence are presented as a function of the reduced thickness  $\tilde{\tau} \equiv Re^{1/16} \tau$  in Fig. 4 where the symmetric solution (with  $s_1 = s_2 = s$ ) is shown as a single thin solid curve and the asymmetric solution (with  $s_1 \neq s_2$ ) as two (relatively short) thick solid curves. Three steady states for the open-wake configurations are seen admissible in Fig. 4 over  $0.075 < \tilde{\tau} < 0.095$ . Namely, a symmetric solution with  $s_1 = s_2 = s$ , an asymmetric solution with  $s_1 \neq s_2$  and another with the  $s_1$  and  $s_2$  interchanged between the thick solid curves. Here, the bifurcation of the steady-state solution is seen to take the form of symmetry breaking. The symmetric and asymmetric solutions are cut-off at  $\tilde{\tau} \approx 0.07$  and  $\tilde{\tau} \approx 0.075$ , respectively owing to the open-wake break down of  $k_\infty = 0$ , interestingly, the asymmetrical solution terminated on the right at  $\tilde{\tau} \approx 0.095$ , also for the same reason.<sup>†</sup> These curves may be continued beyond the cut-off through the closed-wake solutions but will not be carried out in this paper (cf. [17], Fig. 12 therein).

Although the open-wake result (in thin solid curve) appears to be the only solution for  $\tilde{\tau} > 0.095$  in Fig. 4, other alternatives with a closed wake or an eddy, as well as a fully attached flow remain possible. Note that, for a given normalized wing shape  $f^\pm(x)$ , the separation of the classical boundary layer is completely determined by the thickness ratio  $\tau/\tilde{\tau}$ .

#### The Model Joukowski Sections

The  $\tilde{\tau}$  range in Fig. 4 over which symmetry breaking was demonstrated, is unsatisfactorily small and it is uncertain if symmetry breaking may be an exception to the rule. For this reason, a study with a model symmetric Joukowski section

$$y_w/C = \pm \tau \sqrt{x}(1-x)^2, \quad 0 < x < 1 \quad (3.1)$$

is undertaken; the relative simplicity of the profile shape allows several critical integrals analytically evaluated, thereby the symmetry-breaking domain will be much more firmly identified. The results are presented in Fig. 5a where the symmetric and asymmetric solutions are again shown as the thin and the thick solid curves, respectively. Unlike the results in the preceding example, symmetric and asymmetric solutions are admitted simultaneously over a much wider domain, namely,  $\tilde{\tau} > 0.16$ . Open-wake solutions do not exist, however, for  $\tilde{\tau}$  less than 0.13, and the symmetric open-wake solution terminates at  $\tilde{\tau} = 0.156$  where the break-away location occurs at  $s = 0.475$  (marked by a full dot). At  $\tilde{\tau} = 0.133$ ,  $s = 0.360$  (marked by an open circle), the symmetric and asymmetric solution branches intersect and branch switching (smoothly) is permissible, including exchanging  $s_1$  and  $s_2$ . Note that, within

<sup>†</sup>The range of  $\tilde{\tau}$  where asymmetrical solutions exist is considerably smaller than the results reported in an earlier version of [17], which proves to be inaccurate.

the limited range  $0.130 < \tilde{\tau} < 0.156$ , four open-wake solutions are admissible, with two being the symmetric and the remainders asymmetric.

The results discussed above concern the zero incidence. Introduction of an incidence  $\alpha \neq 0$  adds considerably more branches to the admissible solutions. Figure 5b shows a typical result for a  $\alpha/\tau = 0.10$ . Features suggesting lift hysteresis are apparent, although considerably richer in its multiplicity. The solutions for the break-away locations in Fig. 5b are paired as  $(s_1, s_2)$ ,  $(s_1', s_2')$  and  $(s_1'', s_2'')$  with the subscripts 1 and 2 referring to the upper and lower wing surfaces, respectively. We observe in Fig. 5b that  $s_1 < s_2$  and  $s_1' < s_2'$ , would lead to a reversal in the lift response, similar to that for a convexed airfoil at small incidence in a Kirchhoff model.

The symmetry breaking and other lift anomalies resulting from the massive laminar separation are brought out more directly in Fig. 5c, where the scaled lift coefficient vs. the incidence, i.e.  $C_L/\tau$  vs.  $\alpha/\tau$ , is illustrated for  $\tilde{\tau} = 0.25$ . The curve giving the positive lift is computed from the solution  $(s_1'', s_2'')$  of Fig. 5b. The near-zero negative lift is produced by the branch  $(s_1, s_2)$ . Note that  $s_1$  and  $s_2$  in Fig. 5b are both very close to the leading edge ( $x=0$ ); this may explain the loss of lift response symptomatic of a few symmetric airfoils of moderate thickness at  $Re \sim 10^4$ - $10^5$ . The positive slopes on the other two lift curves appear to be surprisingly straight, in spite of the nonlinear dependence of the  $C_L$ ,  $s_1$  and  $s_2$  on the  $\alpha/\tau$ . It should be pointed out once again that the results shown correspond to only the open-wake solutions. The limited extent of the upper lift curve is a result of the early breakdown of the open wake. In fact, for  $\alpha/\tau > 0.31$ , the upper curve vanishes with the branch  $(s_1', s_2')$  all together.

#### Symmetric NACA Four-Digit Series

Airfoils belonging to this family is of interest by virtue of their lift anomalies noted earlier. Unlike the two preceding examples, symmetry breaking with open wakes cannot be found among this family. (This may be good news to the recent disturbance-receptivity study [23] which employs this airfoil family and stipulates a symmetric open wake.) The symmetric result is presented in Fig. 6. To help ascertain the types of body-scale flows associated with the observed anomalies, we examine in this case the two ad hoc open-wake models discussed at the end of Section 2 (cf. Fig. 3). Application of the first version of this ad hoc model (Fig. 3a) indicates that the laminar break-away point is rather close to the leading edge for the four-digit family, unless the airfoil is extremely thin, and the lift at zero incidence, if any, will not be significant. Figure 7a presents the results of  $C_L$  vs.  $\alpha$  for the 0012 at  $Re = 80,000$ . The slightly positive lift and the negative lift-curve slope near zero incidence is comparable to Althaus' corresponding wind-tunnel result [6].

The corresponding results obtained from the model of Fig. 3b, which stipulates a fully attached (turbulent) boundary layer on one side, is shown in Fig. 7b for an 0033 section at  $Re \sim 80,000$ . Anomalous high lift,  $C_L \approx 3.4$  is found at zero incidence, suggesting that an early

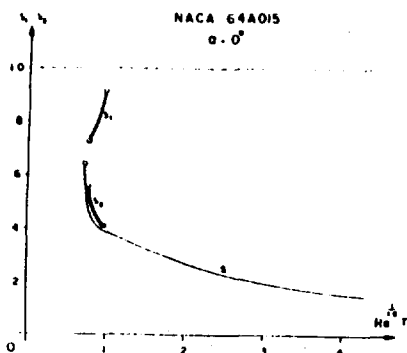


Fig. 4. Break-away locations on a rescaled NACA64A015 at  $\alpha = 0$ .

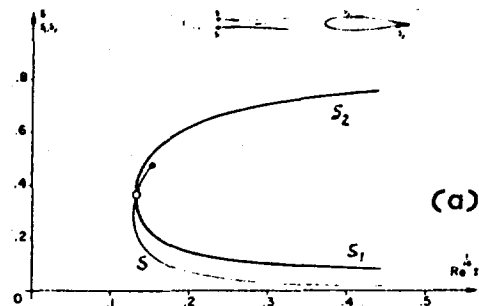


Fig. 5. Solution for Joukowski airfoil: (a)  $\alpha = 0$ .

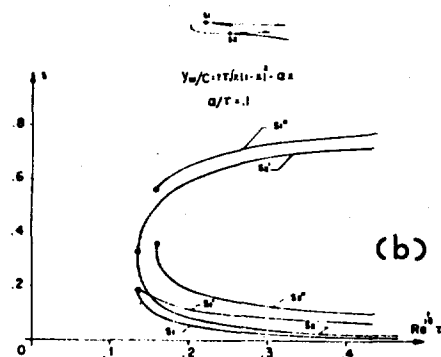


Fig. 5. (b)  $\alpha = \pi/10$

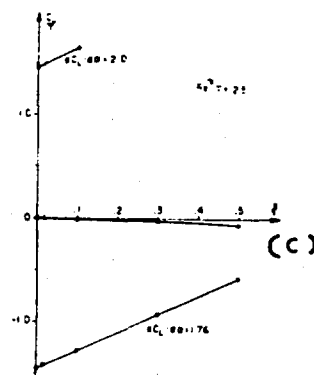


Fig. 5. (c) Three branches of steady lift.

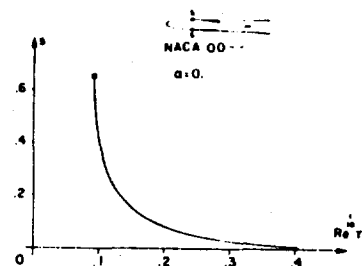


Fig. 6. Results for symmetric NACA four-digit profiles.

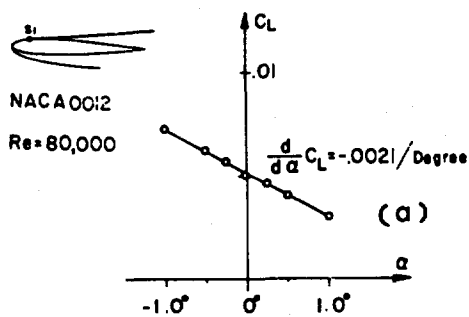
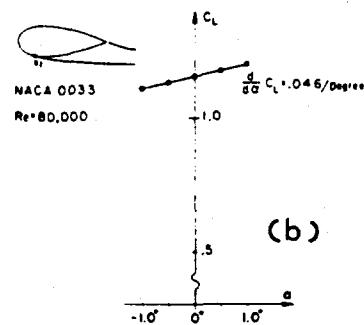


Fig. 7. Lift coeff. vs. incidence at  $Re = 80,000$ : (a) model of Fig. 3a applied to NACA0012, (b) model of Fig. 3b applied to NACA0033.



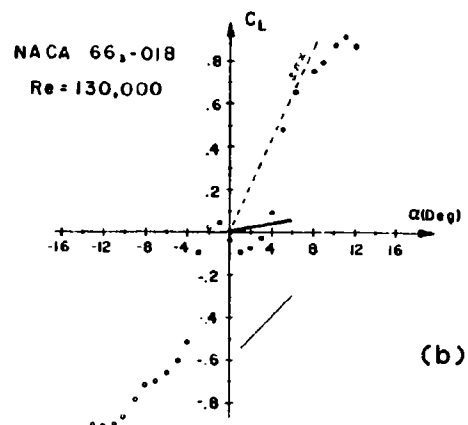
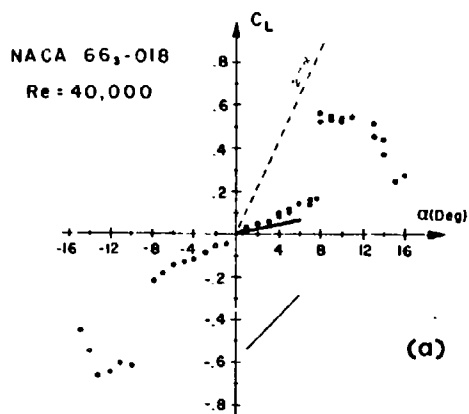


Fig. 8. Lift coeff. vs. incidence of NACA663018: (a) Re = 40,000, (b) Re = 130,000.

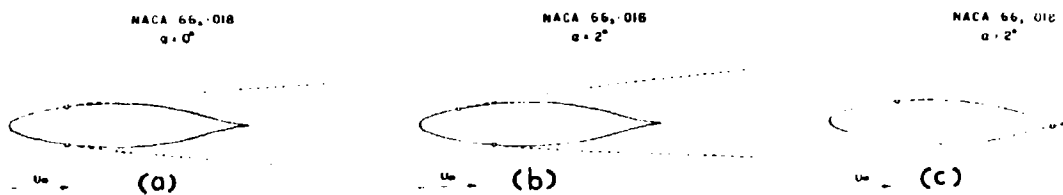


Fig. 9. Free streamlines breaking away from a NACA663018 at Re = 40,000: (a)  $\alpha = 0$ ; (b) and (c) are both solutions to  $\alpha = 2^\circ$ .

transition on one side may explain the pronounced symmetry breaking for the 0033 section reported in Althaus [6]. The slope  $dC_L/d\alpha$  of the model is 0.046 per degree, being about 75% Althaus' value. The magnitude of  $C_L \approx 1.16$  at zero incidence is about 40% higher than Althaus' value (0.68).

#### Study of the Symmetric NACA663018

This symmetric profile is of interest by virtue of the significant loss of aerodynamic damping and other lift anomalies at low incidences observed at low Re. The measured  $C_L$  vs.  $\alpha$  for the smooth model at  $Re \sim 40,000$  and  $130,000$  are reproduced from [14] as open circles in Fig. 8a and Fig. 8b, respectively. Unlike the symmetric NACA four-digit series, symmetry breaking is not apparent or hardly noticeable from the measured data. The  $dC_L/d\alpha$  is very low in (a) and is negative in (b) in the  $|\alpha| < 6^\circ$  range. The latter behavior is reminiscent of the NACA0012 below  $Re \sim 80,000$  [6] but is more pronounced.

The theory assuming an open-wake laminar separation gives results (shown as a thick solid-line segment) in qualitative agreement with experiment at  $|\alpha| < 6^\circ$  for  $Re = 40,000$ . The noticeable difference between theory and experiment in  $dC_L/d\alpha$  may be attributed partly to the uncertainty in the inaccuracy of the force balance due to the low force magnitude for this Re range (see [14]). Such uncertainty is more pronounced in Fig. 8b for the higher Re run, where the noticeable lack of skew symmetry revealed in the test data would suggest a 5% error in the  $C_L$  measured.

An interesting theoretical feature is the absence of laminar open-wake solution for  $|\alpha| > 6^\circ$ . Thus, the abrupt lift increase in the experimental data beyond  $|\alpha| = 8^\circ$ , corresponding to a solution-branch switching, should not be surprising.

Even though symmetry breaking is absent (i.e.  $C_L = 0$  at  $\alpha = 0$ ), large negative lift coefficient can be found from the laminar open-wake model for  $\alpha > 0$ . (To be sure,  $C_L < 0$  at  $\alpha > 0$  and  $C_L > 0$  at  $\alpha < 0$ .) The results are shown as thin solid-line segments in Figs. 8a,b, and have no counterparts in the data reported in [14]. Figs. 9a,b,c illustrate theoretical patterns of the free streamlines at  $\alpha = 0$  and  $2^\circ$ , including a case with large negative lift. The return to a normal lift behavior for  $|\alpha| > 8^\circ$ , together with the corresponding smoke-pattern photo records in [14], suggests a successful turbulence transition has taken place at least on the upper surface. In this instance, the ad hoc model which allows a determination of the laminar break-away on the lower surface may describe well the  $C_L$  characteristic beyond  $6^\circ$  as well as the missing portion of the hysteresis loop in Fig. 8a. This possibility remains to be examined in subsequent works.

#### 4. CONCLUDING REMARKS

This paper has examined several noteworthy features in recent studies on massive laminar separation based on the triple-deck theory. Whereas, the work precludes turbulence transition, and the study addresses mainly steady flows with open wakes, the analyses do bring

to light features relevant to the understanding of hysteresis and other lift anomalies in the regime  $Re < 10^5$ . Fundamental is the multitude of steady states found to be admissible to the large-scale interacting flows. Of interest is a special form of the steady-state bifurcation, namely, symmetry breaking of an otherwise regular flow about a symmetric airfoil at zero incidence, giving rise to steady lifts. The availability of these multitudes of steady states may call for a new strategy of stability analysis of the large-scale flow; the extent to which these richly bifurcating states may influence the transitional flow behavior should be of great interest.

Many basic problems remain to be solved, even within the context of a steady-flow model. A complete asymptotic theory describing the reattachment and the eddy interior, which is compatible with the body-scale flow and will remove the eddy-pressure indeterminacy, is yet to be developed. The stall characteristics of an inclined flat plate at  $Re < 10^5$  represents another interesting issue on laminar (vs. turbulent) separation anterior to the trailing edge. The many features brought out and questions raised from this study may serve as interesting focii for future CFD simulation and wind-tunnel studies.

#### ACKNOWLEDGEMENT

This work is based on research sponsored by the Office of Naval Research, Fluid Dynamics Program Contract N00014-82-K-0315. Helpful assistance from C. Holguin and C.J. Lee is acknowledged.

#### REFERENCES

1. Stewartson, K., SIAM Review 23, 308- , 1981.
2. Sychev, V.V., Izv. Akad. Nauk SSSR Mechan. Zhidkosti gaza. 3, 47-59, 1921.
3. Smith, F.T., Proc. Roy. Soc. London, A, 356, 433-463, 1977.
4. Smith, F.T., IMA J. Appl. Math. 28, 207-281, 1982.
5. Schmitz, F.W., Aerodynamik des Flugmodells, Tragflügelmessungen I, C.J.E. Volckmann Nachf. E. Wette, Berlin-Charlottenburg 2, 1942.
6. Althaus, D., Profilpolaren für den Modellflug: Windkanalmessungen an Profilen im kritischen Reynoldszahlbereich, Nechar-Verlag vs-Villingen, 1983.
7. Carmichael, B.H., NACA-CR 165803, 1981.
8. Mueller, T.J., Low Reynolds Number Vehicles, AGARDograph No. 288, (undated).
9. Lighthill, M.J., Mathematical Biofluidynamics, 1975.
10. Wu, T.Y.T., Brokaw, C.J. & Brennen, C., Swimming and Flying in

Nature, Plenum Press, Vol. I & II, 1974.

11. Cheng, H.K. & Murillo, L.E., J. Fluid Mech., 143, 327-350, 1984.
12. Kuruwila, G. & Anderson, J.D., Jr., AIAA Paper 85-0301, 1985.
13. McCormack, R.W. AIAA Paper 69-354, 1969.
14. Mueller, T.J. & Batill, S.M., AIAA J. 20, No. 4, 457-463, 1982.
15. Mueller, T.J., AIAA Paper 84-1617, Snowmass, Co., 1982,
16. Cheng, H.K. & Smith, F.T., J. Appl. Math. Physics (ZAMP) 33, No. 21, 151-180, 1982.
17. Cheng, H.K., USCAE Report 139, superceding AIAA Paper 84-1612.1985.
18. Cheng, H.K. & Lee, C.J., Proc. 3rd Symp. Numerical and Physical Aspects of Aerodynamic Flows, Springer-Verlag, 1985, (to appear).
19. Tani, I., Progr. Aero. Sci. 5, 70- , 1964.
20. Werle, H., ONERA Pub. No. 156, 1974.
21. Van Dyke, M.D., An Album of Fluid Motion, The Parabolic Press, 19, 25, 26, 1982.
22. Goldstein, M., "Generation of Instability Waves in Flow Separating From Smooth Surfaces", 1985 (to appear in J. Fluid Mech.).
23. Atassi, H.M., AIAA Paper 84-2297, AIAA NASA 9th Aeroacoustic Conf., Oct. 15-17, 1984, Williamsburg, Va.
24. Morkovin, M. & Paranjape, S.V., Z. Flugwiss., 9, 328-335, 1971.
25. Kraemer, K., MITT. MPI f., Strömungsforschung und AVA, Göttingen No. 32, 1964.
26. Bearman, P.W., J. Fluid Mech. 37, 577- , 1969.
27. Kamiya, N., Suzuki, S. & Nishi, R., AIAA Paper 79-1475, Williams Williamsburg, 1979.
28. Schewe, G., J. Fluid Mech. 133, 265-285, 1983.
29. Kirchhoff, G., J. reine angew. Math. 70, 289- , 1869.
30. Dirkhoff, G. & Zarantonello, E.H., Jet, Wakes & Cavities, Acad. Press, 1957.
31. Wu, T.Y.T., Annual Review of Fluid Mech. 4, 243-284, 1972.
32. Korolev, G.L., Sci. J. TSAG, XI, No. 2, 27-36, 1980.

33. Van Domelen, L.L. & Shen, S.F., Proc. 2nd. Symp. Numerical & Physical Aspects Aerodynamic Flows, Sec. 2, Calif. State Univ., Long Beach, Ca., 1983.
34. Brown, S.N. & Stewartson, K., J. Fluid Mech. 42, 561-581, 1970.
35. Melnik, R.E. & Chow, R., Grumman Res. Report RE-510J, 1975,
36. Tulin, M.P., J. Ship Research, 7, No. 3, 16-37, 1964.
37. Van Dyke, M.D., Perturbation Methods in Fluid Mechanics, Academic Press; annotated 1975 edition pub., The Parabolic Press, 1964.

COMPUTATIONAL STUDY OF FLOW OVER  
MILEY AND WORTMANN AIRFOILS

by

Ajay P. Kothari\* and John D. Anderson, Jr.\*\*

Department of Aerospace Engineering  
University of Maryland  
College Park, Maryland 20742

ABSTRACT

A computational tool has been developed that calculates viscous 2-D flowfields about airfoils of interest. The program uses a finite difference implicit technique to solve the compressible Navier-Stokes equations. Both purely laminar as well as transitional turbulent flows are treated. The technique is a time dependent technique and hence it is possible to also compute the transient flowfields.

Flowfields for a Reynolds number range of 500 to 300,000 have been calculated for both the Miley Airfoil (M06-13-128) and the Wortmann Airfoil (FX-63-137). Only the purely laminar results are obtained for the Miley Airfoil whereas for the Wortmann Airfoil both the laminar and turbulent calculations are made and compared with each other. For both these airfoils, the computational results tend to confirm the experimental results of Mueller at Notre Dame.

It was observed that in general all largely separated flows, mostly occurring at large angles of attack, were unsteady whether it was laminar or turbulent. Non-separated (attached) flow results, on the other hand, were observed to be steady.

I. INTRODUCTION

A rising interest in RPV's and the flight regime they fly in have indicated a need for establishing a data base for airfoil properties at low Reynolds number (in the range from 100,000 to 300,000, based on chord length). By far, the vast majority of airfoil data obtained since the Wright Brothers' experiments in 1901 - 1902 have pushed towards the highest possible Reynolds numbers -- quite natural for practical full-scale airplane applications. However, recent interest in remotely-piloted vehicles (RPV's) has created the need for an extensive data base for airfoil properties at low Reynolds numbers. Today, the RPV designer has only fragmentary information on airfoil properties at  $Re = 100,000$  to 300,000. Moreover, the very question as to the optimum basic airfoil shapes for low Reynolds number flight is completely unanswered. The pur-

\* Research Engineer

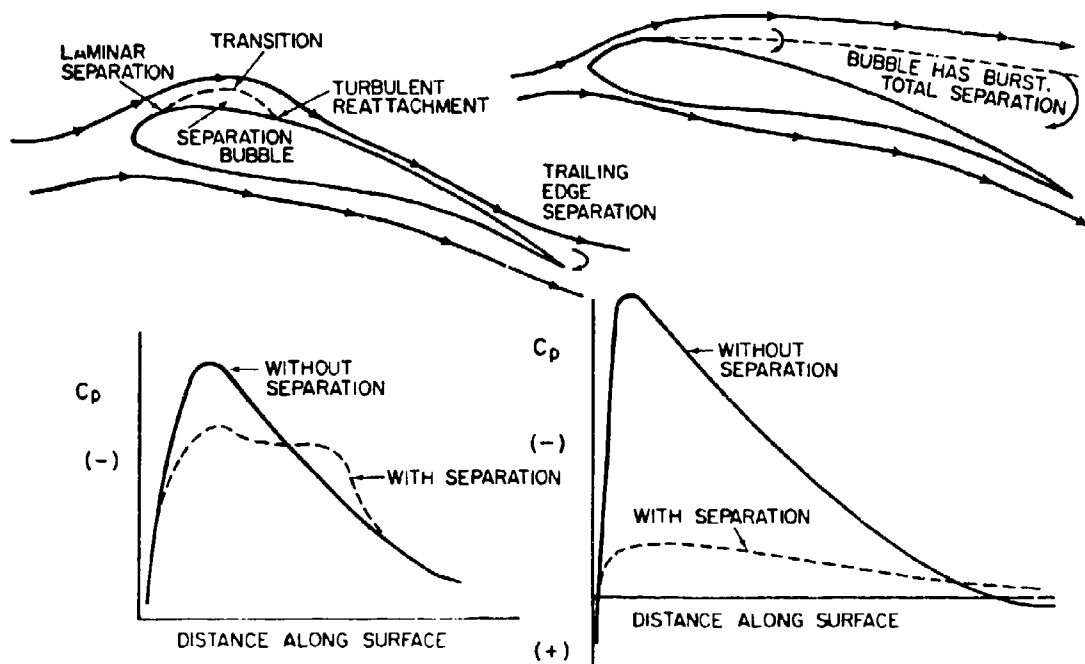
\*\* Professor

pose of the present work is: (1) to establish a computational tool which will allow the accurate calculation of airfoil properties at low Reynolds number, and (2) to use this tool to add to the airfoil data base.

First, some background. Over the past five years, a definitive series of experiments on low Reynolds number flows over airfoils has been carried out by Dr. Thomas Mueller at the University of Notre Dame 1-4. Using a unique low Reynolds number wind tunnel along with smoke-flow techniques, Mueller has provided by far the majority of modern experimental data for low Reynolds number flows over airfoils. This work has not only produced lift and drag coefficient data, but has also underscored the special physics which influences low Reynolds number flows over airfoils. For example, Mueller has highlighted the role of the laminar separation bubble near the leading edge, the highly unstable shear layer created by this bubble, and the tendency to transit to turbulent flow downstream of the bubble. If transition does occur, then reattachment is likely downstream of the bubble as illustrated in Figure 1; on the other hand, if transition does not occur, the laminar separation bubble will "burst", creating a massively separated flow over the top surface of the airfoil, as illustrated in Figure 2.

FIGURE 1

FIGURE 2



In any event, in the Reynolds number range of 100,000 - 300,000, airfoil flows are dominated by such transitional and flow separation phenomena which complicate the generation of definitive airfoil properties. Experimental measurements of aerodynamic forces are further complicated by the low magnitudes of the forces themselves at low Reynolds numbers, hence creating the potential for large experimental error.

In light of the above, there is an important need to parallel the low Reynolds number experiments with independent numerical computations. This is the purpose of the present work. In particular, the present paper is designed to be a direct numerical complement to the experimental work of Mueller reported in Reference 4, which treated an airfoil designed specifically for low Reynolds number applications -- the Miley Airfoil. In the present work, we present numerical results for the low Reynolds number flow over a Miley airfoil, and compare them with the experimental data of Reference 4. Moreover, we also present numerical results for another airfoil designed for low Reynolds number applications -- the Wortmann airfoil -- and compare with experimental data given in References 5 and 6. To the authors' knowledge, the present results are the first direct application of a detailed Navier-Stokes solution to the flow over the two airfoils mentioned above.

The numerical solutions presented in the present paper were obtained from the full, compressible, two-dimensional Navier-Stokes equations. The solution technique utilizes a time-dependent, implicit finite-difference procedure patterned after the new implicit MacCormack algorithm first introduced in 1981 (see Reference 7). One of our goals in the present work has been to develop reasonably practical Navier-Stokes solutions for low Reynolds number airfoils -- solutions that do not require the use of a super computer. We typically solve these airfoil flows on a relatively old UNIVAC 1180 in running times of two to three hours -- reasonably practical for Navier-Stokes solutions. Moreover, we have modified MacCormack's implicit technique given in Reference 7 to handle the curvilinear, boundary-fitted coordinate system which must be wrapped around the airfoil. In the above sense, the computational tool described here is a contribution by itself, along with the numerical results produced by the tool.

## II. FORMULATION OF THE PROBLEM

Again examining Figures 1 and 2, the physics of the low Reynolds number flow over an airfoil is governed by transitional and separated flow phenomena. Since one purpose of the present work is to study these physical effects, the only proper recourse is to solve the complete Navier-Stokes equations instead of a simpler but approximate boundary layer/inviscid interaction problem. We want the equations to contain all the requisite physics -- hence the use of the full, compressible Navier-Stokes equations. These equations, in nondimensional, strong conservation form, are given as

$$\frac{\partial \bar{U}}{\partial \bar{t}} + \frac{\partial \bar{F}}{\partial \bar{x}} + \frac{\partial \bar{G}}{\partial \bar{y}} = 0 \quad (1)$$

where

$$\bar{U} = \begin{Bmatrix} \rho \\ \rho u \\ \rho v \\ \rho E \end{Bmatrix} \quad (2) \quad \bar{F} = \begin{Bmatrix} \rho u \\ \rho u^2 + p + 2/3 \mu \left( \frac{\partial u}{\partial x} + \frac{\partial v}{\partial y} \right) / R_e - 2 \mu \left( \frac{\partial u}{\partial x} \right) / R_e \\ \rho u v - \mu \left( \frac{\partial u}{\partial y} + \frac{\partial v}{\partial x} \right) / R_e \\ \rho u H - P_{\text{ring}} k \frac{\partial T}{\partial x} + \frac{u}{R_e} \left[ 2/3 \mu \left( \frac{\partial u}{\partial x} + \frac{\partial v}{\partial y} \right) - 2 \mu \frac{\partial u}{\partial x} \right] \\ + \frac{v}{R_e} \left[ - \mu \left( \frac{\partial v}{\partial x} + \frac{\partial u}{\partial y} \right) \right] \end{Bmatrix} \quad (3)$$

$$\bar{G} = \begin{Bmatrix} \rho v \\ \rho u v - \mu \left( \frac{\partial v}{\partial x} + \frac{\partial u}{\partial y} \right) / R_e \\ \rho v^2 + p + 2/3 \mu \left( \frac{\partial u}{\partial x} + \frac{\partial v}{\partial y} \right) / R_e - 2 \mu \left( \frac{\partial v}{\partial y} \right) / R_e \\ \rho v H - P_{\text{ring}} k \frac{\partial T}{\partial y} + \frac{v}{R_e} \left[ - \mu \left( \frac{\partial v}{\partial x} + \frac{\partial u}{\partial y} \right) \right] \\ + \frac{v}{R_e} \left[ 2/3 \mu \left( \frac{\partial u}{\partial x} + \frac{\partial v}{\partial y} \right) - 2 \mu \frac{\partial v}{\partial y} \right] \end{Bmatrix} \quad (4)$$

Both laminar and turbulent flows are calculated. For the laminar flows, the molecular viscosity coefficient  $\mu$  is given by Sutherland's law:

$$\frac{\mu}{\mu_{\text{ref}}} = \left( \frac{T}{T_{\text{ref}}} \right)^{3/2} \frac{T_{\text{ref}} + 110}{T + 110} \quad (5)$$

The Prandtl number is assumed to be constant:

$$Pr = \frac{\mu C_p}{k} = 1.0$$

For the turbulent flows, the popular Baldwin-Lomax turbulence model<sup>8</sup> is used. This model is designed specifically for separated flows; it is a two-layer eddy viscosity model which uses local vorticity rather than boundary layer thickness to obtain the turbulent viscosity coefficient,  $\mu_T$ . The details of the model as applied to the present work are described in Ref. 14.

For the turbulent flow calculations, wherever  $\mu$  appears in Eqs. 1-4, it is replaced by the sum ( $\mu_L + \mu$ ). Similarly, wherever  $k$  appears in Eqs. 1-4, it is replaced by ( $k_T + k$ ), where  $k_T$  is the turbulent thermal conductivity defined from the turbulent Prandtl number,

$$Pr_T = \frac{\mu_T C_p}{k_T} = 1.0.$$

As suggested in Reference 8, transition to turbulent flow is assumed to take place when  $\mu_T > 14\mu$ . Hence, the model does allow a prediction of the transition point. From the present results, the transition point always occurs in a region of rapidly increasing vorticity, which clearly identifies the transition region. We make no claims as to the accuracy of transition predicted by this model.

### III. NUMERICAL SOLUTION TECHNIQUE

The above equations are first transformed into curvilinear coordinates appropriate to a boundary-fitted coordinate system wrapped around the airfoil. The grid is generated by Thompson's elliptic approach, described in Reference 9. A typical C-type grid used in the present calculations is illustrated in Figures 3 and 4; Figure 3 shows the full extent of the grid both upstream and downstream of the airfoil, and Figure 4 is a detail showing only the portion of the grid near the airfoil. Note the concentration of grid points near the surface in order to help define the viscous phenomena.

The Navier-Stokes equations in curvilinear coordinates are then solved numerically using the new implicit finite-difference procedure presented by MacCormack<sup>7</sup> in 1981. In earlier investigation, Wright<sup>10</sup> at the University of Maryland solved the Navier-Stokes equations by means of MacCormack's older explicit technique; the solutions were carried out at an unrealistically low Reynolds number of 15,000, and required an inordinate amount of computer time (more than a day on a VAX computer). The present work, using MacCormack's new implicit technique, is an order-of-magnitude improvement over Reference 10, and covers a Reynolds number range from 500 to  $10^6$ . Typical running times for the present cases are 2 to 3 hours on a UNIVAC 1180 -- constituting a somewhat practical tool by today's standards.

Details of the present numerical solutions can be found in Reference 11. Please note that the solution procedure is time-dependent, with the desired steady-state results obtained asymptotically at large times.

For the boundary fitted (curvilinear) coordinate system required

for the calculation of flow around airfoils, the procedure for implicitly solving the equations is considerably modified from that given in Reference 7.

ENTIRE VIEW OF THE GRID  
FOR  $Re = 100,000$   $M = 0.5$

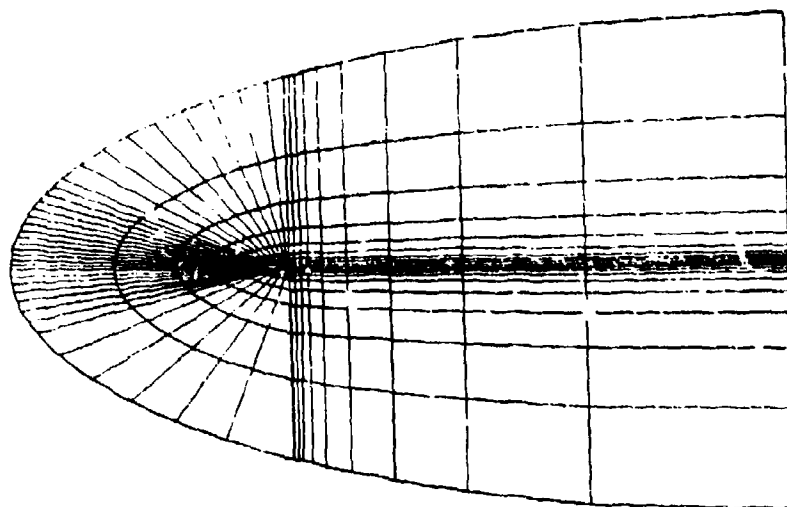
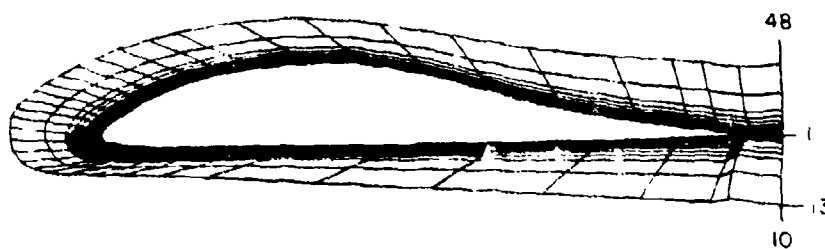


FIGURE 3



VIEW NEAR THE FOIL  
FOR  $Re = 100,000$   $M = 0.5$

FIGURE 4

The Navier-Stokes equation for curvilinear coordinate systems in conservation form are

$$\frac{\partial U'}{\partial \xi} + \frac{\partial F'}{\partial \eta} + \frac{\partial G'}{\partial \zeta} = 0 \quad (6)$$

where

$$U' = J'U$$

$$F' = y_{\eta} F - x_{\eta} G \quad (7)$$

and

$$G' = -y_{\xi} F + x_{\xi} G$$

The implicit difference equation for equation (6) is

$$(1 + \Delta t \frac{\partial A'}{\partial \zeta} + \Delta t \frac{\partial B'}{\partial \eta}) \frac{\partial U^{n+1}}{\partial t} = \frac{\partial U^n}{\partial t} \quad (8)$$

$$\begin{aligned} \text{where } A' &= y_{\eta} A - x_{\eta} B \\ B' &= -y_{\zeta} A + x_{\zeta} B \end{aligned} \quad (9)$$

and A & B are the Jacobians

$$A = \frac{\partial F}{\partial U} \quad \text{and} \quad B = \frac{\partial G}{\partial U}$$

Approximate factorization of equation (8) yields

$$(1 + \Delta t \frac{\partial A'}{\partial \zeta})(1 + \Delta t \frac{\partial B'}{\partial \eta}) \frac{\partial U^{n+1}}{\partial t} = \frac{\partial U^n}{\partial t} \quad (10)$$

#### IV RESULTS AND DISCUSSION

Two different airfoils are treated in the present work, the Miley M06-13-128 and the Wortmann FX63-137. Both of these airfoils were designed for relatively low Reynolds number applications. Both airfoils have been examined experimentally by Mueller<sup>4,6</sup>; the results given here are a direct numerical complement to these experimental results.

The numerical results are obtained from a solution of the compressible Navier-Stokes equations; this is done intentionally to allow future applications to high subsonic and transonic cases. However, such compressible Navier-Stokes solutions frequently encounter instabilities when applied to low Mach number cases ( $M \leq 0.1$ ), and when stable, the convergence times are inordinately large. The present calculations are no exception. Therefore, all the computed results presented herein were made for a freestream Mach number of 0.5, whereas the experimental results were obtained at very low speeds ( $M_{\infty} \approx 0.03$ ). Although this may at first thought seem like an "apples-and-oranges" comparison, in reality it is not. The low Reynolds number flows treated herein are dominated by viscous effects, which are relatively Mach number independent. Indeed, a numerical experiment was run to examine this effect; the same case was run at  $M_{\infty} = 0.5, 0.3$  and  $0.2$ , and  $C_L$  as well as the basic flow phenomena remained relatively the same. At no time did the computed local Mach number even get close to unity; the flow at  $M_{\infty} = 0.5$  exhibits no super-critical effects at all. On this basis, we feel that for these highly viscous-dominated flows, the computed results with  $M_{\infty} = 0.5$  are reasonably accurate reflections of the phenomena at low speeds, and therefore the following comparisons with low-speed experimental data are valid.

## A. Miley M06-13-128 Airfoil

Lift and drag coefficient data are shown in Figures 5 and 6 respectively for  $Re = 100,000$ .

FIGURE 5: Lift coefficient versus the angle of attack for Miley Airfoil at  $Re=100,000$

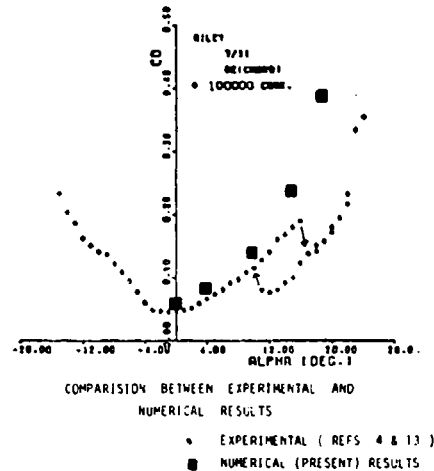
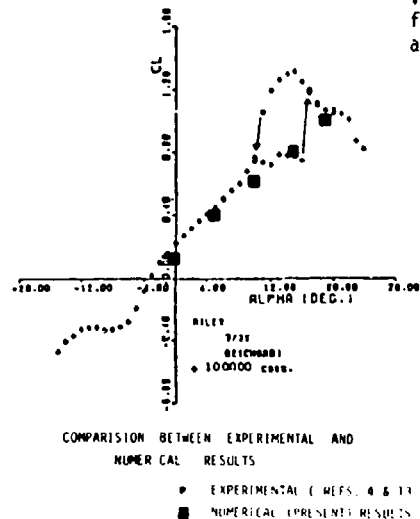


FIGURE 6: Drag coefficient versus the angle of attack for Miley Airfoil at  $Re=100,000$

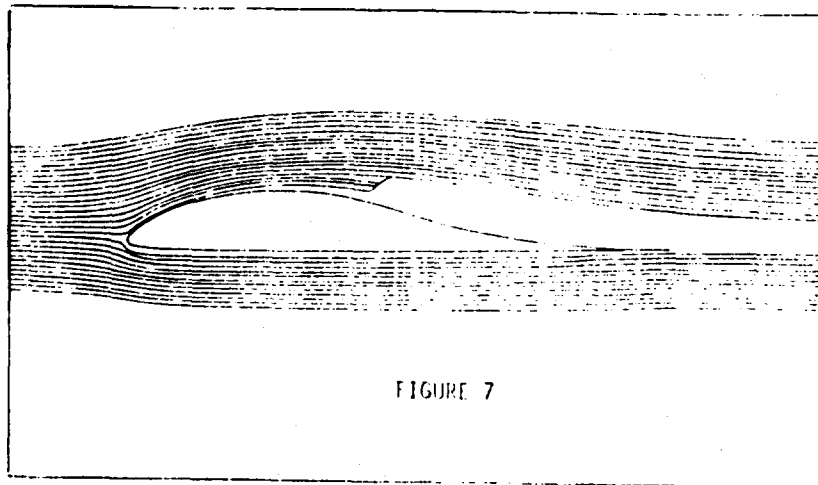
The small diamonds are experimental data from Mueller<sup>4</sup>, and the large squares are calculated results from the present Navier-Stokes solutions. The calculated results in Figures 5 and 6 are for totally laminar flow. The experimentally measured lift slope below about  $10^\circ$  angle of attack is relatively small -- a well known characteristic of low Reynolds number effects on airfoils.<sup>12</sup> The present Navier-Stokes calculations of the lift slope in this angle of attack range agree well with Mueller's experimental data as seen in Fig. 5. At higher angle of attack, the experimental data exhibit an interesting hysteresis phenomena, with lower  $C_L$  for increasing  $\alpha$ , and higher  $C_L$  for decreasing  $\alpha$ . This is the exact opposite of the hysteresis phenomena sometimes exhibited by more conventional airfoils; this peculiar behavior for the Miley airfoil is explained by Mueller<sup>4</sup> as caused by "the location of separation and/or transition in the airfoil boundary layer." Since the calculated results shown in Figures 5 and 6 are for laminar flow only, the experimentally observed hysteresis loop is not simulated numerically; the proper physics for such a simulation is not modeled in the calculations shown for this case. Examining the drag coefficient results shown in Figure 6, the calculations agree fairly well with experiment for low angles of attack. However, at high  $\alpha$  the laminar flow calculations exhibit massive flow separation on the top surface of

the airfoil, and hence the calculated drag is much higher than the measured values at high  $\alpha$ . This is because of the very large pressure drag due to flow separation (form drag) predicted for the laminar flow case, in comparison to that for the experimental case which exhibits transition and hence a larger region of attached flow.

There are two important observations to be made from the comparisons between calculation and experiment in Figures 5 and 6.

- (1) The calculated results tend to verify the measurements of Mueller at low angle of attack. This is important, because one of the major problems associated with low Reynolds number testing is the low magnitude of the forces involved. This creates the possibility of large experimental error in the force measurements<sup>6</sup>, particularly in the case of drag, which is usually an order-of-magnitude smaller than the lift. The present calculations seem to support the accuracy of Mueller's measurements.
- (2) The calculations allow a comparison between skin friction drag coefficient,  $C_{Df}$  and pressure drag coefficient  $C_{Dp}$  (form drag). It is interesting to note that the present calculations indicate that drag at low  $\alpha$  is almost totally pressure drag (contrary to conventional airfoil experience). For example, at  $\alpha = 0^\circ$ , the calculated values of  $C_{Df}$  and  $C_{Dp}$  are .00472 and .0586 respectively. Such a comparison is explained by Figure 7, which shows a large region of laminar separation over the top surface at  $\alpha = 0^\circ$ .

FIGURE 7. LAMINAR FLOW OVER AN AIRFOIL AT  $\alpha = 0^\circ$   
 $Re = 100,000$   
 $M = 0.5$



Separation is predicted by the calculations to occur at  $x/c = .45$ , where  $x$  is the distance along the chord, and  $c$  is the chord length. The calculated streamline pattern shown in Figure 7 is very similar to the smoke flow photograph for the same case obtained by Mueller<sup>6</sup>, and shown in Figure 8.

SMOKE FLOW PICTURE FOR FLOW OVER  
MILEY AIRFOIL  
 $Re = 100,000$  Angle of attack =  $0.0$  degree.

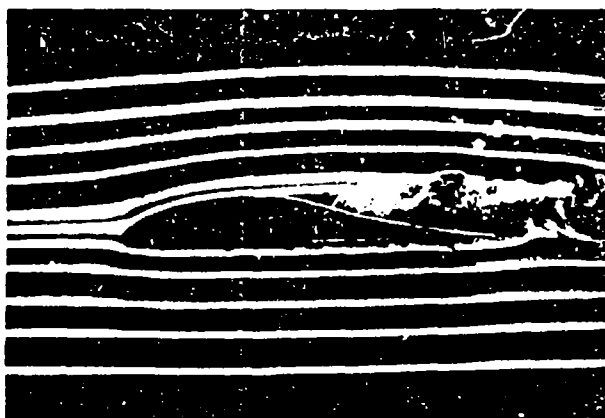


FIGURE 8

This photograph also shows that a large region of separated flow exists over the Miley airfoil at  $\alpha = 0^\circ$ .

The present Navier-Stokes calculations reveal other interesting aspects of the flowfield around the Miley airfoil as follows. A detailed velocity vector diagram in the nose region of the airfoil at  $\alpha = 0^\circ$  is shown in Figure 9.

DETAILS OF THE FLOWFIELD NEAR  
THE LEADING EDGE  
Steady state  $Re = 100,000$

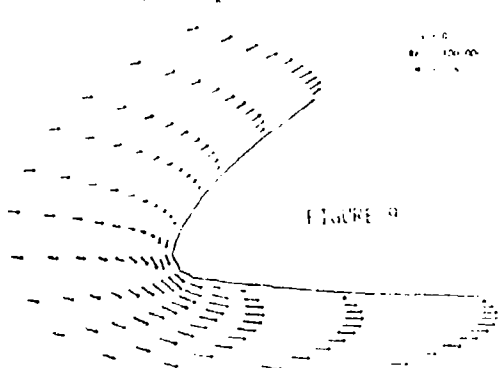


FIGURE 9

VELOCITY VECTOR DIAGRAM FOR  
FLOWFIELD NEAR THE LEADING EDGE

$\alpha = 19^\circ$   
 $Re = 100,000$   
 $M = 0.5$

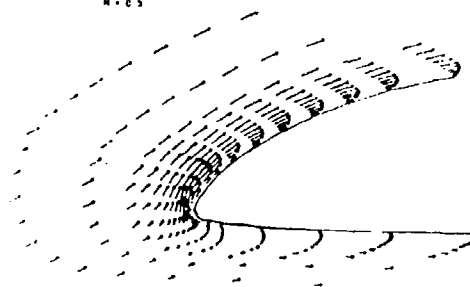


FIGURE 10

It is interesting to note from this diagram that at  $\alpha = 0^\circ$  the stagnation point falls on the top surface of the airfoil, just slightly downstream of the nose (conventional airfoils at conventional Reynolds numbers usually exhibit the stagnation point on the bottom surface when lift is produced). The behavior shown in Figure 9 is supported by closely examining the smoke flow photograph in Figure 8, which also shows the stagnation point occurring above the leading edge. On the other hand, examining Figure 10, the computed velocity vector diagram in the nose region at  $\alpha = 19^\circ$  shows the stagnation point well below the leading

edge, as expected. Details of the computed pressure field around the airfoil at  $\alpha = 0^\circ$  are illustrated by Figures 11-13. In Figure 11, the computed surface pressure distribution on the top and bottom surfaces is shown.

In order to plot the entire pressure field around the airfoil, Fig. 12 serves to establish a coordinate system, with the airfoil in the x-y plane as shown, and with the flowfield variable (say static pressure,  $p$ ) plotted on the z axis. With the coordinate system in mind, examine Figure 13. This shows a "carpet plot" of the static pressure distribution;  $p$  is shown as a function of x and y, and hence a three-dimensional pressure surface as generated which is drawn above the x-y plane.

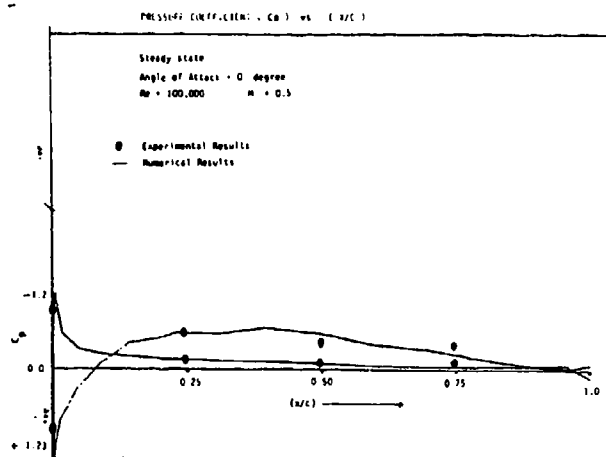


FIGURE 11

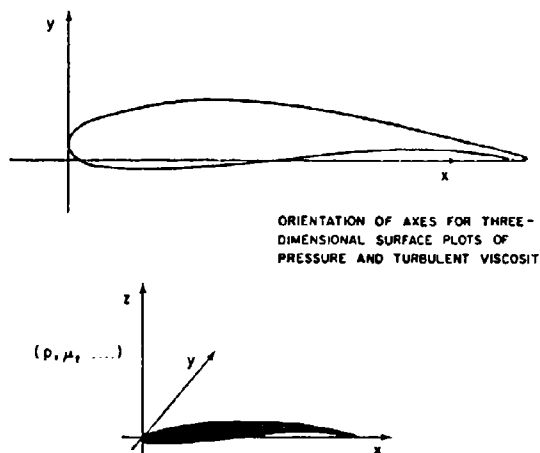


FIGURE 12

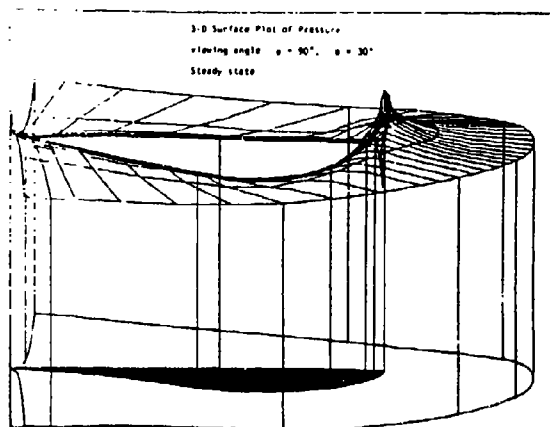


FIGURE 13

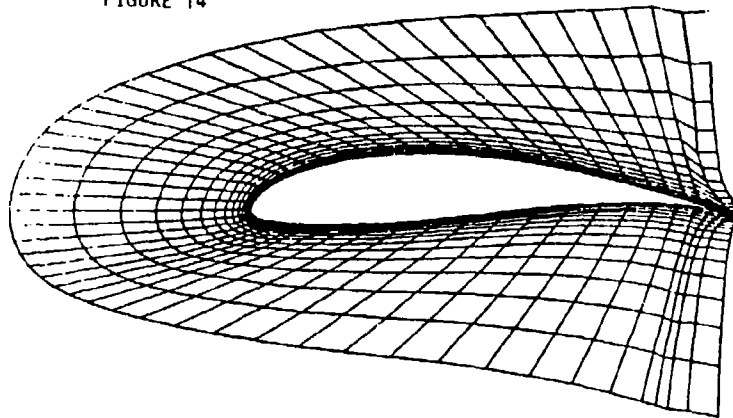
The entire diagram is slightly rotated in Figure 13 to allow a three-dimensional perspective. Note that the gradual compression in the nose region is clearly illustrated in Fig. 13.

#### B. Wortmann FX63-137 Airfoil

The shape of the Wortmann FX63-137 airfoil, and the portion of the numerical grid in the near vicinity of the airfoil, are shown in Figure 14.

WORTMANN AIRFOIL ( FX63-137 )  
GRID NEAR THE AIRFOIL

FIGURE 14



For this airfoil,  
both laminar and  
turbulent cases  
were computed.

B.1 Re=100,000

Figures 15 and 16 show the lift and drag coefficients respectively for Re=100,000.

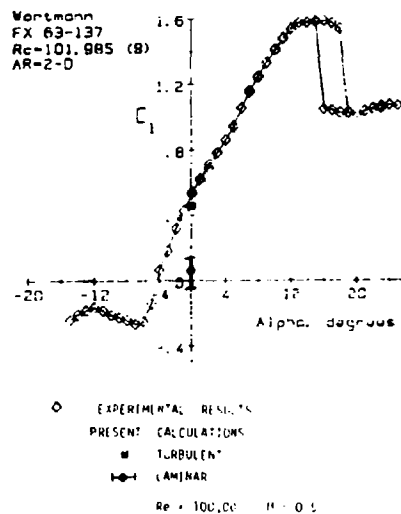
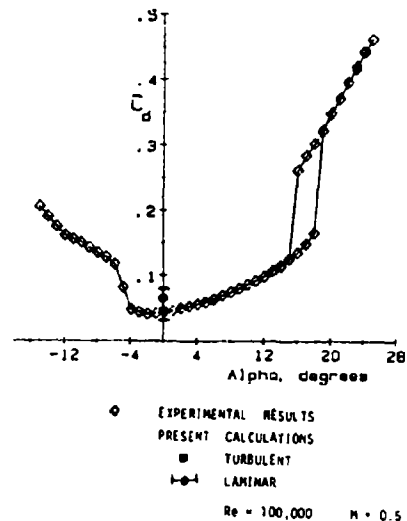


FIGURE 15: Lift coefficient versus the angle of attack for Wortmann Airfoil at Re=100,000

FIGURE 16: Drag coefficient versus the angle of attack for Wortmann Airfoil at Re=100,000



The open diamonds are experimental data from Mueller<sup>6</sup>. The solid symbols are results at  $\alpha=0^\circ$  from the present calculations; the solid squares denote turbulent flow results, and the solid circles with the range bar denote totally laminar flow results. Here it was observed that the purely laminar flow results were quite unsteady with the major flow features repeating themselves at intervals of about 1.5 non-dimensional time.

These repetitive results are shown in Figures 17(a), (b) and (c) at non-dimensional times of  $T_n = 6.27$ ,  $7.04$  and  $7.73$  respectively. These results express the formulation of a vortex on the upper surface near the trailing edge and the shedding there of. The value of  $C_L$  also varies for these three times from  $C_L = .0915$  to  $C_L = -.045$  to  $C_L = .1161$  corresponding to states in Figures 17(a), (b) and (c) respectively. The reason for the consistently low value of the lift and high value of the drag coefficients in the laminar flow in comparison to the turbulent flow becomes obvious when we look at the streamline patterns for the laminar and turbulent flows in Figures 18 and 19 respectively. Figure 18 is plotted at a particular value of non-dimensional time of  $T_n = 7.04$ .

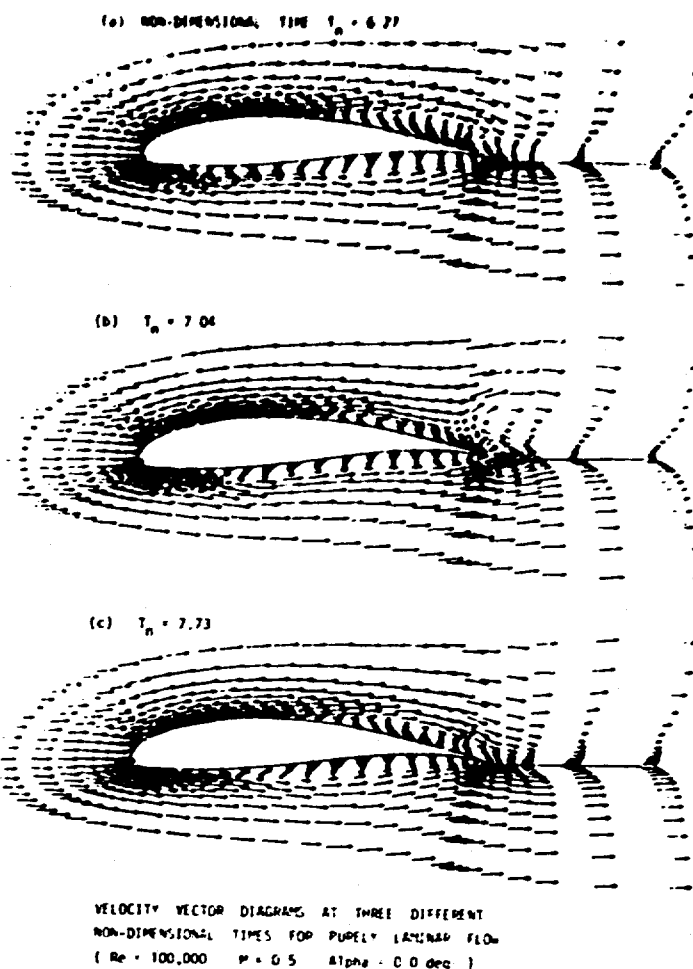
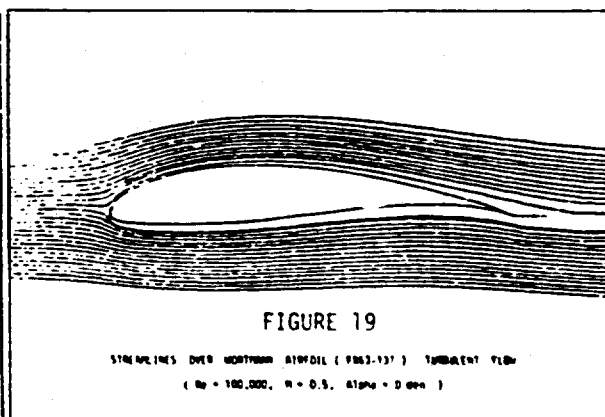
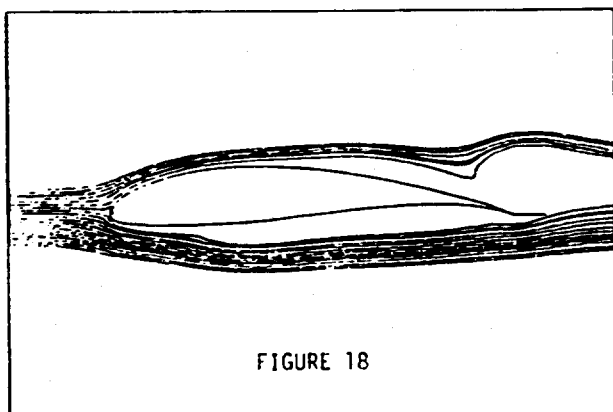


FIGURE 17

STREAMLINES OVER WORTHEN AIRFOIL ( FIG. 13 ) - LAMINAR FLOW (UPSTREAM RESULTS)  
(  $Re = 100,000$ ,  $M = 0.5$ ,  $\alpha = 0.0$  deg )  
NON-DIMENSIONAL TIME  $T_n = 7.04$

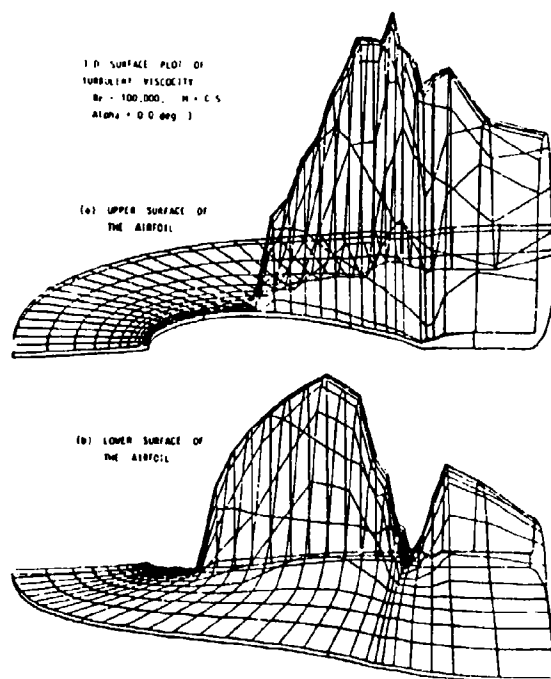


Massive flow separation on both the upper and lower surfaces is seen. Because of this separation, the laminar flow calculations consistently yield considerably lower  $C_L$ 's and higher  $C_D$ 's. The turbulent flow

results, on the other hand, yield excellent agreement with the experimental data of Mueller, as seen in Figures 15 and 16. The reason for this agreement is that the turbulent flow is completely attached, as shown in Figure 19. Using the Baldwin-Lomax turbulence model the transition on the upper surface is predicted at about 40% chord from the leading edge, and transition on the lower surface is predicted at about 20% chord. This completely attaches the flow on both the upper and lower surfaces of the airfoil, hence increasing lift and decreasing drag.

The calculated locations of the transition points and the magnitude of the turbulent viscosity are shown in Figure 20(a) and (b) for the upper and lower surfaces of the airfoil respectively.

FIGURE 20



This figure again is a "carpet plot" of  $\mu_t$  where the physical grid is in x-y plane and the magnitude of  $\mu_t$  is plotted in z direction. (Refer again to Figure 12 for the orientation of the axes.) The 3-D surface representing  $\mu_t$  is then rotated about the x-axis and Fig. 20 is the perspective as seen from this viewing angle. On the lower surface near the trailing edge the presence of a favorable pressure gradient causes a considerable reduction in the vorticity and hence the turbulent viscosity. Reflecting back on Figures 15 and 16, the computed results seem to indicate that the real flow at  $Re=100,000$  is probably more turbulent than laminar. Again, we interpret the comparison shown in Figures 15 and 16 as a numerical confirmation of the relative accuracy of the low Reynolds number measurements of Mueller<sup>6</sup>.

In Figure 16, at  $\alpha=0^\circ$ , the computed skin friction and pressure drag coefficients are  $C_{Df} = .0016 \pm .0004$  and  $C_{Dp} = .057 \pm .025$

respectively for the laminar case, and  $C_{Df} = .0074$  and  $C_{Dp} = .039$  for the turbulent case.

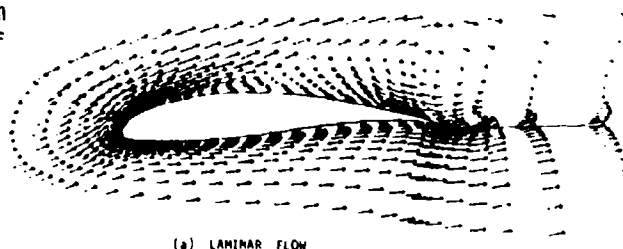
## B.2 Re = 60,000

Both the purely laminar and the turbulent cases are calculated for

this low Reynolds number for the angle of attack of 14 degrees. Such a low Reynolds number was selected because the flow is expected to be at most transitional at  $Re = 60,000$ . This was evident from the calculated distribution of turbulent viscosity where the highest  $\mu_t$  observed was equal to 30. Figure 21(a) and (b) are velocity vector diagrams for both the laminar and turbulent cases at the same non-dimensional time of  $T_n = 2.48$ . There is very little effect on the major flow field structure due to turbulence. The calculated values of  $C_L$  for laminar case was 1.0735 and for the turbulent case was 1.0886. However both the cases were observed to be unsteady.

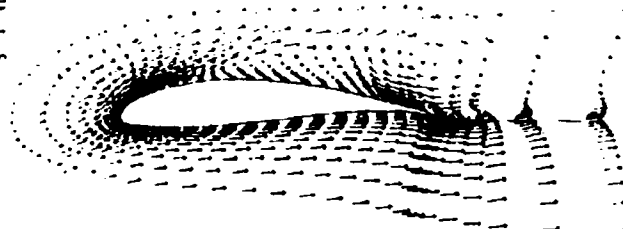
VELOCITY VECTOR DIAGRAMS AT THE SAME NON-DIMENSIONAL TIME FOR BOTH LAMINAR AND TURBULENT FLOWS  
(  $Re = 60,000$   $M = 0.5$   $\alpha = 14.0$  deg. )

NON-DIMENSIONAL TIME  $T_n = 2.48$



(a) LAMINAR FLOW

FIGURE 21



(b) TURBULENT FLOW WITH  
BALDWIN-LOMAX TURBULENCE MODEL

### B.3 $Re = 300,000$

For this case of higher Reynolds number, both laminar and turbulent calculations were made. Both were observed to be unsteady at high angle-of-attack due to the presence of a large separated region. Both  $C_L$  and  $C_D$  were observed to be time varying. The calculated value of highest turbulent viscosity  $\mu_t$  was about 70 to 100.

INSTANTANEOUS STREAMLINE PLOT FOR TURBULENT CASE  
(  $Re = 300,000$   $M = 0.5$   $\alpha = 14.0$  deg )

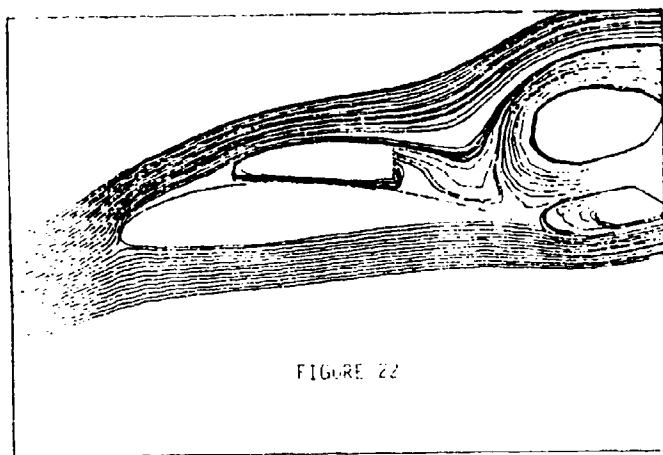


FIGURE 22

Turbulent flow results are presented in Figures 22, 23 and 24. Figure 22 is an instantaneous streamline plot at a particular time instant corresponding to nondimensional time  $T_n = 3.993$ .

Presence of large vortices is clearly seen on the upper surface. The unsteadiness in the flow is evidenced by Figure 23 where velocity vector plots are shown at nondimensional times  $T_n = 3.993, 4.687, 5.45$  and  $6.145$  in Fig. 23 (a), (b), (c) and (d) respectively.

The formation and movement of the vortices is seen. Clearly the flow is unsteady. The flow near the leading edge is, however, less unsteady. Figure 24(a) and (b) are velocity vector plots at  $T_n = 5.381$  and  $T_n = 6.145$ .

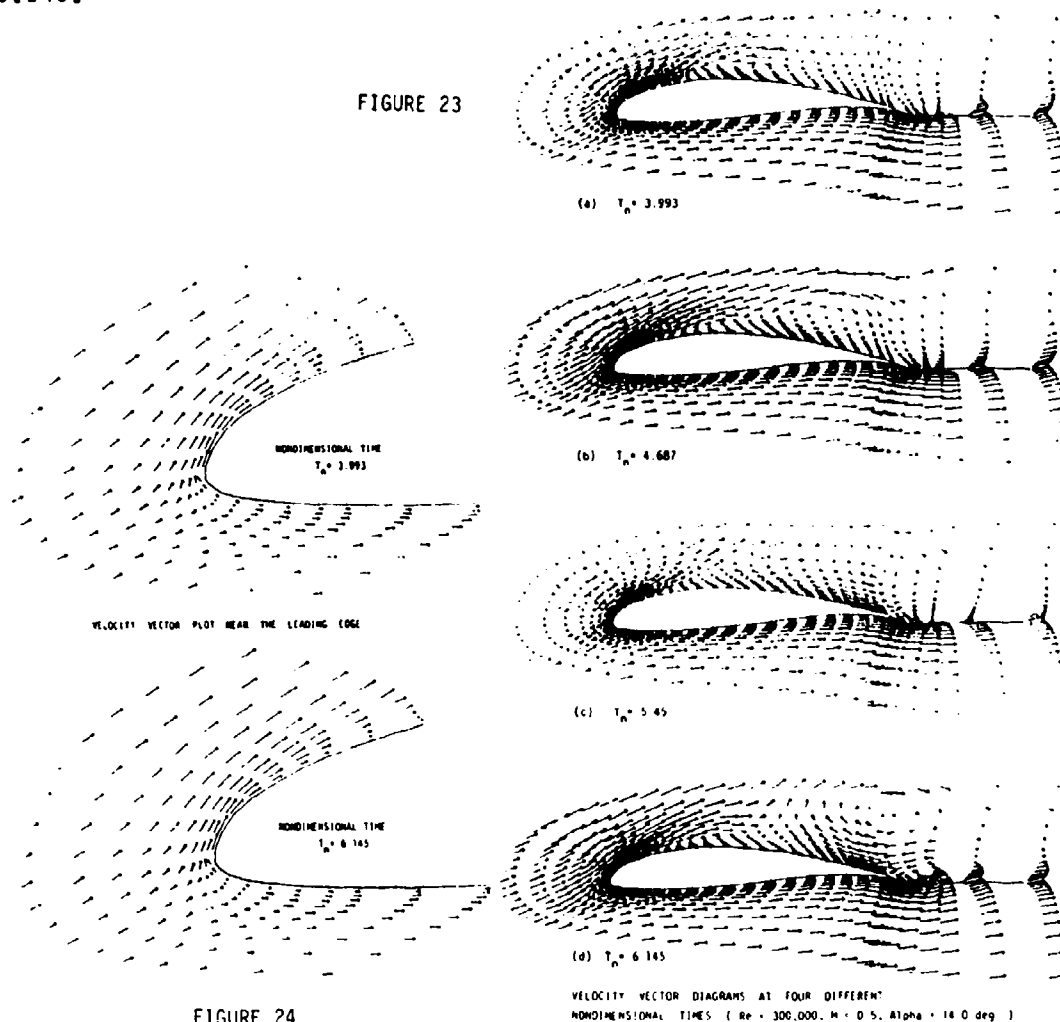


FIGURE 24

They are almost identical. The value of  $C_L$  however was calculated to change by  $\pm 13.5\%$  and that of  $C_D$  by  $\pm 15.0\%$ .

It is interesting to note that the flow did not attach for the turbulent case; it was the same as the laminar case at the same angle of attack and Reynolds number. The separation point was almost at the same  $x/c \approx .2$  for both these cases, although it too moved somewhat with time. The turbulent case was started with the initial conditions which were final conditions of an already largely separated laminar case. The turbulence then generated was not adequate to transfer energy from external regions through the shear layer to into the boundary layer, thus not attaching the flow. Thus a history of the flow is brought into the

solution making it non-unique. Whether this phenomenon can be responsible for the "hysteresis" in the lift and drag curves will be the subject of further research.

## V CONCLUSIONS

The following general conclusions are made:

- (1) With this computer simulation program it is possible to calculate the entire (2-D) flowfields around an airfoil and calculate  $C_p$ ,  $C_L$  and  $C_D$ .
- (2) It is also possible to study the physics of the flowfield, e.g. vortex formulation, shedding and reformulation etc. for the unsteady flows. All large separated regions were observed to be unsteady.
- (3) It is also possible to predict the transition point and also the level of turbulence in the flowfield. Comparison between purely laminar and turbulent cases can be made enabling us to separate out the effect of turbulence on the flow, a definite advantage of computational research.
- (4) The calculated lift and drag coefficients at low and moderate angles of attack agree very well with the experimental data of Mueller. In light of the tenuous nature and various uncertainties of low Reynolds number force measurements, particularly drag, we feel that the present calculations tend to confirm the accuracy of Mueller's measurements.
- (5) Contrary to conventional airfoil experience obtained at high Reynolds numbers wherein the airfoil drag at low angle of attack is mainly skin friction drag, the present calculations at low Reynolds number (300,000 and below) show that approximately 80% of the total drag is pressure drag, even when the flow is attached at low angles of attack. This may be due to the large region of highly viscous flow surrounding the airfoil and trailing downstream in the wake, causing the airfoil to act effectively as a large almost semi-infinite body. The fact that pressure drag dominates skin friction drag should have a major impact on the design philosophy for low Reynolds number airfoils.

Pertaining to the airfoils treated in the present work, the following specific conclusions are also made.

(a) Miley Airfoil

- a.1 Laminar calculation prediction of  $C_L$  and  $C_D$  up to angle of attack of  $10^\circ$  agreed quite well with experiments by Thomas Mueller at Notre Dame for  $Re=100,000$  indicating the flow to be more laminar than transitional. At higher angles, more disagreement was evident.
- a.2 For low Reynolds numbers like  $Re=100,000$ , the leading edge stagnation point was observed to be on the upper surface as seen in the experiments.

(b) Wortmann Airfoil

- b.1 Both laminar and turbulent cases were calculated for  $Re = 60,000, 100,000$  and  $300,000$ . Purely laminar calculation was observed to be unsteady with vortex forming and shedding on the upper surface separation region.
- b.2 Consider a Wortmann airfoil at zero angle of attack at  $Re = 100,000$ . Purely laminar flow calculations for this case show separated flow over both the top and bottom surfaces of the airfoil. Moreover, this flow is unsteady, and results in a band of lift and drag coefficients which do not agree with Mueller's measurements. On the other hand, a turbulent flow calculation (using the popular Baldwin-Lomax turbulence model) indicates transition at about 40% chord, and yields completely attached flow. This flow is steady, and results in lift and drag coefficients that agree excellently with Mueller's measurements. In this vein, the current numerical experiments help to interpret the experimental results, and indicate that even at the low Reynolds number of  $100,000$ , such flows are truly transitional and turbulent in nature.
- b.3 For  $Re=100,000$  and  $\alpha=0$  case, no separation was observed on either upper or lower sides, for the turbulent calculation.
- b.4 All cases that yielded large separation zones (at  $\alpha=14^\circ$ ) were observed to be unsteady. This was true of laminar cases but was also true of turbulent cases. Both the  $C_L$ 's and  $C_D$ 's for such cases were a function of time. However the time interval is quite small - the observed Strouhal number based on chord length is of the order .2 to .5. This corresponds to time scale of 1-10 milliseconds for most cases.
- b.5 For the unsteady case, the magnitude of  $C_{p_{max}}$  and  $C_{p_{min}}$  was also observed to change.

### ACKNOWLEDGEMENT

This work was initiated by the Naval Research Laboratory under contract NRL N000-81-K-2037, with Mr. Richard Foch as contract monitor. The work is presently sponsored by the Office of Naval Research under ONR contract N00014-84-K-0181 with Dr. R. Whitehead as program manager. The authors thank both Dr. Whitehead and Mr. Foch for their interest and many helpful discussions. Appreciation also goes to the Computer Science Center at the University of Maryland for contributing a major portion of the computer time.

### REFERENCES

1. Mueller, T.J. and Batill, S.M., "Experimental Studies of the Laminar Separation Bubble on a Two-Dimensional Airfoil at Low Reynolds Numbers", AIAA Paper 80-1440, July 1980.
2. Arena, A.V. and Mueller, T.J., "Laminar Separation, Transition, and Turbulent Reattachment near the Leading Edge of Airfoils", AIAA Journal, Vol. 18, No. 7, pp. 747-753, July 1980.
3. Mueller, T.J. and Burns, T.F., "Experimental Studies of the Eppler 51 Airfoil at Low Reynolds Numbers", AIAA Paper No. 82-0345, 1982.
4. Pohlen, L.J. and Mueller, T.J., "Boundary Layer Characteristics of the Miley Airfoil at Low Reynolds Numbers", Journal of Aircraft, Vol. 21, No. 9, pp. 658-664, Sept. 1984.
5. Althaus, Dieter "Profilpolaren fur den modellflug", Neckar-Verlag vs-Villingen W. Germany, 1980.
6. Mueller, T.J., Private Communication. Unpublished data from University of Notre Dame, Oct. 1984.
7. McCormack, R.W., "A Numerical Method for Solving the Equations of Compressible Flow", AIAA Paper No. 81-0110, 1981.
8. Baldwin, B.S. and Lomax, H., "Thin Layer Approximation and Algebraic Model for Separated Turbulent Flows", AIAA Paper No. 78-257, January 1978.
9. Thompson, J.F., Thames, F.C., and Mastin, C.W., "Automatic Numerical Generation of Body-Fitted Curvilinear Coordinate Systems for Fields Containing Any Number of Arbitrary Two-Dimensional Bodies", Journal of Computational Physics, Vol. 15, No. 3, 1974.
10. Wright, A.F., "A Numerical Investigation of Low-Reynolds Number Flow Over an Airfoil", M.S. Thesis, Dept. of Aerospace Engineering, University of Maryland, 1983.
11. Kothari, Ajay P., Anderson, John D., Jr. and Rayhavan, V., "The

Aerodynamics of Airfoils at Low Reynolds Number (Computational Aspects)". Report to the Naval Research Laboratory under NRL Contract No. N00014-81-k-2037, Department of Aerospace Engineering, University of Maryland, May 1984. (Also Aerospace Engineering TR-84-10).

12. Abbott, J.H. and von Doenhoff, A.E., Theory of Wing Sections, Dover, New York, 1959.
13. Pohlen, L.J. and Mueller T.J., "Experimental Studies of the Effect of Boundary Layer Transition on the Performance of the Miley Airfoil at Low Reynolds Numbers". Final report to the Naval Research Laboratory. Report Number UNDAS-2036-FR-5, University of Notre Dame, February 1983.
14. Kothari, A.P. and Anderson, J.D., Jr., "Flows Over Low Reynolds Number Airfoils - Compressible Navier Stokes Solutions," AIAA Paper No. 85-0107, Presented at the AIAA 23rd Aerospace Sciences Meeting, January, 1985.

## EXPERIMENTS ON UNSTEADY FLOWS ABOUT WING SECTIONS

E. Krause, G. Ehrhardt, B. Schweitzer  
Aerodynamisches Institut der RWTH Aachen  
Aachen, West Germany

### ABSTRACT

Vortex shedding on wing sections due to time dependent variation of the free stream velocity is presently being studied experimentally at the Aerodynamisches Institut of the RWTH Aachen. The aim of the investigation is to obtain information about the details of the flow structure, in particular in the vicinity of the trailing edge, to determine shedding frequencies, range of stability of the vortex street, extent of the separated region, and to measure the time-dependent surface pressure distribution as a function of freestream Strouhal number and Reynolds number for accelerated and decelerated flows. The angle of attack is held constant in the experiments. So far, results were obtained on a water table, and in the water tunnel of the Aerodynamisches Institut. Presently experiments are being set up in an Eiffel tunnel.

### INTRODUCTION

Unsteady flows about wings, rotor and turbine blades have attracted increased interest in recent years. Motivation for investigations of unsteady flow phenomena is mainly stimulated by the desire to improve design conditions on one hand, and to be able to cope with time dependent perturbations of otherwise steady flows in a more effective way. Such disturbances may be of particular interest for aerodynamic applications, which are characterized by a relatively low Reynolds number.

In the case of rotor blades, the angle of attack and the local freestream velocity vary periodically during the flight. The influence of the variation of the angle of attack on the flow was already investigated in a number of experiments with oscillating wing models [1]. Experiments, in which the freestream velocity was varied as a function of time, either periodically, or aperiodically, and in which the angle of attack was held constant, are either rare or have not been done at all. Such a flow is of particular interest for studying the local flow behaviour in the vicinity of the trailing edge with the specific objectives to analyse the variation of the extent of the separated region, to find out, under what conditions vortex shedding occurs, and, whether the Kutta condition is violated. For the reasons just mentioned an experimental investigation was initiated in the special collaborative research programme 25 "Vortical Flows in Aerodynamics", sponsored by the Deutsche Forschungsgemeinschaft at the Rheinisch-Westfälische Technische Hochschule Aachen. It is aimed at clarifying some of the questions, relevant to time dependent freestream variations.

Because of difficulties, encountered in unsteady high-speed flows, the investigation was initiated in low-speed flows. So far, experiments were carried out on

a water table, and in a water tunnel. The Reynolds numbers obtained varied between  $Re = 1.5 \cdot 10^3$ , and  $Re = 2 \cdot 10^4$ , and the Strouhal numbers between  $Sr = 0.07$  and  $Sr = 0.29$ . The experiments on the water table will be described first. The section that then follows contains a discussion of the flow studies in the water tunnel. In the last section, a short description of a new experimental facility is given, which uses an Eiffel type wind tunnel for future investigations of flows with time dependent freestream velocities. The maximum Reynolds numbers of this facility is about  $2.5 \cdot 10^5$ . Similar investigations are described in [2] and [3].

## DESCRIPTION OF EXPERIMENTS

### Flow Visualization Studies on a Water Table

First investigations were carried out on a water table, which is schematically depicted in Fig 1. The water is set in motion through two sets of disks (1), which push the water into two long open channels (2). At the end of channel the flow is turned by 180 degrees by guiding vanes and is then led into the test channel (3). A screen (4) in the inlet cross section damps out flow non-uniformities, and in the middle of the test channel the flow has almost constant velocity. In order to be able to let the freestream velocity vary with time, a sluice-like device (5) was built into the water table at the end of the test channel. The gate is driven by a motor through which three modes, opening and closing alone, and in combination could be operated. Because of the influence of surface waves, periodic variation could not be verified in the experiments. But, as will be seen, the variation of the flow structure, in particular in the vicinity of the trailing edge, in the wake and in the separated region can clearly be recognized for the three modes mentioned, that is to say for acceleration and deceleration alone, and for a decelerated and accelerated freestream. Fig. 2 shows two free stream velocity profiles for Reynolds numbers  $Re = 1500$  and  $Re = 3000$  as a function of time. The deformation of the velocity profile during the acceleration phase through wave motion is evident.

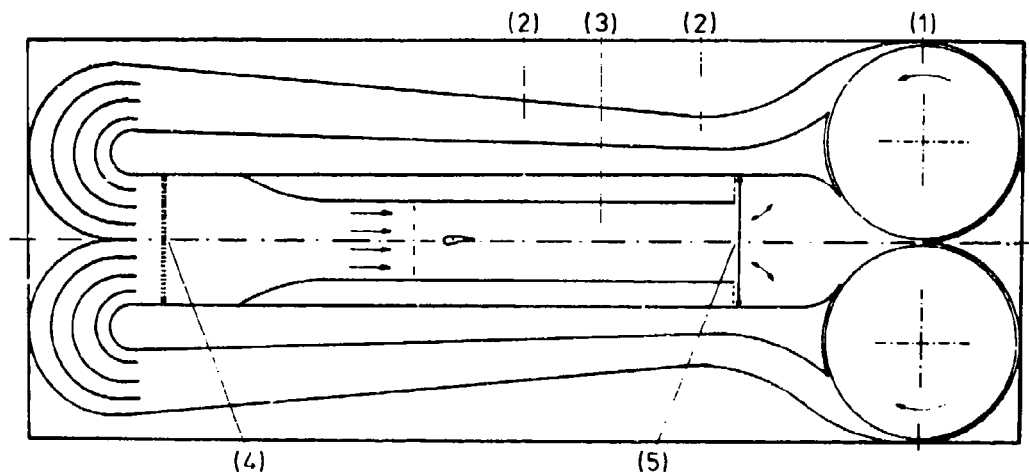


Fig. 1 Schematic of the water table of the Aerodynamisches Institut.  
(1) rotating disks, (2) channels, test channel (3), screen (4), sluice gate (5)

The shape of the velocity profiles verified in the experiments depended on several parameters. The influence on the Reynolds number is indicated in Fig. 2. Note that the Reynolds number is based on the freestream velocity for steady flow conditions. For  $Re = 1500$  the freestream velocity is  $u_{\infty} = 2.15$  cm/s, and for  $Re = 3000$  it is  $u_{\infty} = 4.3$  cm/s. The other parameters to be mentioned are the shape of the profile, the angle of attack, and the duration of the acceleration and deceleration. In the experiments carried out so far, the profiles NACA 4412 and NACA 4424 were used. Comparison experiments showed that the shape of the profile had little or no influence on the freestream

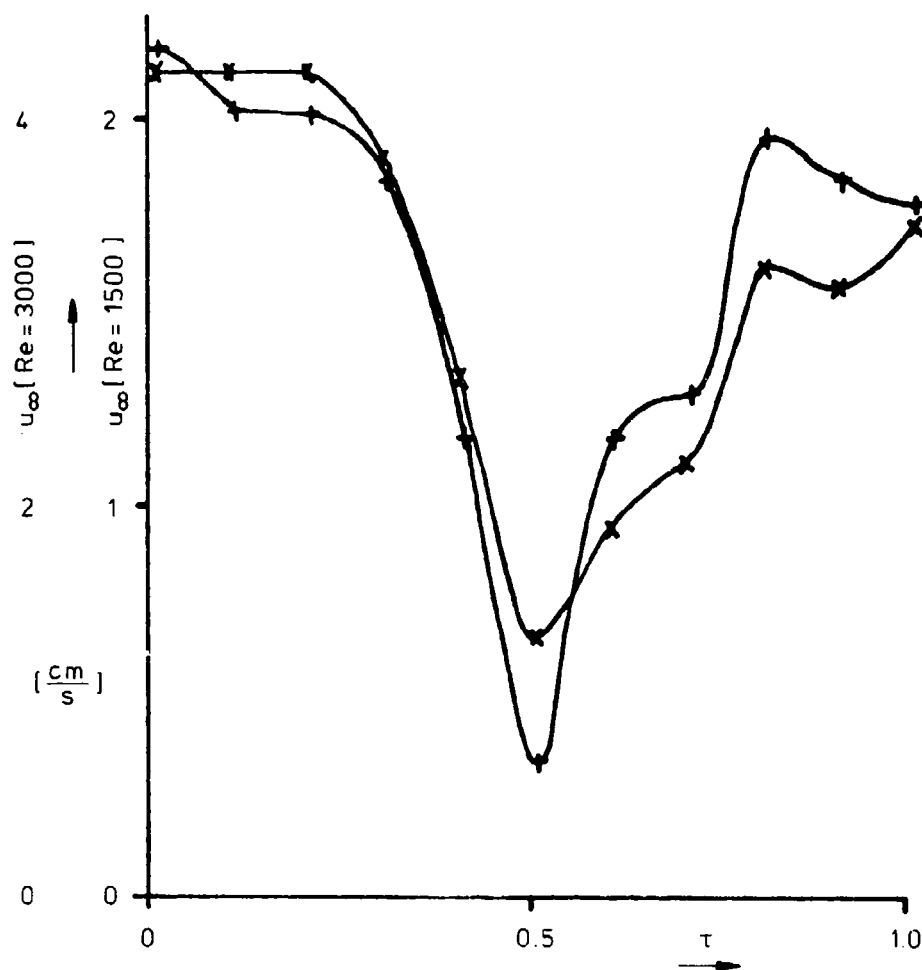


Fig. 2 Freestream velocity variation as a function of time.  $Re = 1500$  and  $Re = 3000$

velocity profiles, within the accuracy with which the velocity could be determined. The same can be said about the angle of attack. There are only small differences in the velocity distribution as a function of time, when  $\alpha$  is varied from zero to as much as six degrees. The duration of the deceleration

and acceleration phase seems to influence the shape of the freestream velocity profile, in particular for low Reynolds numbers. It was found that the oscillations caused by the wave motion exhibit larger amplitudes for shorter durations than longer ones.

The freestream velocity was determined in the following way: Aluminium powder was evenly spread over the surface of the water. Before this was done, the water was dyed with Kaliumpermanganat such that its colour became deep violet. Thereby those aluminium particles which submerge cannot be seen any more, and only the flow on the surface remains visible. In addition, the contrast between the colour of the aluminium particles and that of the fluid is enlarged. It was found that a film develops on the surface of the water within a time of about 24 hours. The film seems to hinder the motion of the aluminium particles, especially in the vicinity of the profile and of the channel walls. In order to avoid falsifications due to the varied surface tensions, all flow observations were carried out in a relatively short time after filling the table.

A camera was mounted above the water table and sequences of pictures were taken with the following exposure times:  $T_B = 0.5$  s for  $Re = 1500$ , and  $T_B = 0.25$  s for  $Re = 3000$ . The time intervals between two pictures were chosen in such a way that 10 pictures could be taken during the time in which the free-stream velocity was varied. The velocity of the surface flow was then determined in the usual way by measuring the length of the path a particle travels within one half or a quarter of a second. Fig. 2 shows the freestream velocity so obtained for the mode deceleration - acceleration for both Reynolds numbers,  $Re = 1500$ , and  $Re = 3000$ . The duration of the velocity variation was  $T = 20$  s; the profile used was NACA 4424 at an angle of attack of  $\alpha = 3^\circ$ .

Fig. 3 shows a sequence of pictures of the instantaneous flow pattern for the conditions just mentioned. (The Reynolds number is  $Re = 3000$ ) at the beginning, at  $0.4 T$ , at  $0.5 T$ , and at  $0.6 T$ . The vortex shedding can clearly be recognized during the acceleration phase. During the deceleration phase the separation point on the upper side of the profile is moved upstream. While vortex shedding occurs, the Kutta condition is no longer satisfied. It is also seen that for Reynolds numbers as low as obtained here, the diameter of the vortices leaving the profile is of the order of the maximum thickness of the profile. Further details of the flow structure could not be obtained with the technique described, because of its limited accuracy and resolution. For that reason a second set of experiments was carried out in the water tunnel of the Aerodynamisches Institut.

### Water Tunnel Experiments

The water tunnel is a Göttingen type tunnel with a propeller with four blades (Fig. 4). It is driven with a 4 KW electric motor. The velocity can be varied continuously by means of a gear. The maximum speed in the test section is  $u_\infty = 5.7$  m/s. The critical Reynolds number of the sphere, determined in the test section of the tunnel, was  $2.3 \cdot 10^5$ . The test section has a width of 25 cm, a height of 33 cm, and a length of 125 cm. The nozzle upstream of the test section has a contraction ratio of 4.

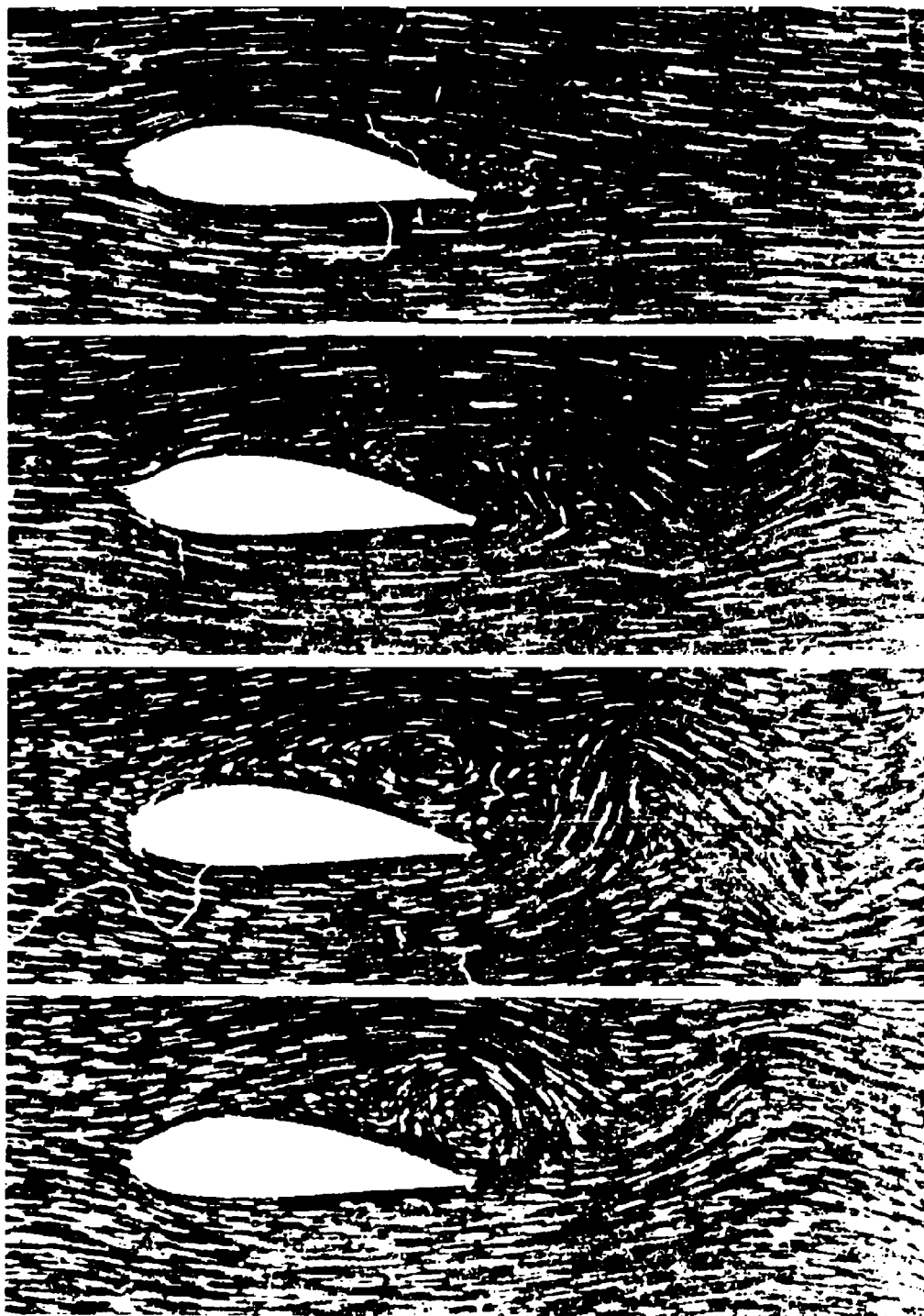


Fig. 3 Instantaneous flow pattern.  $Re = 3000$ , NACA 4424,  $\alpha = 3^\circ$

In the experiments carried out in the water tunnel two profiles were used. These were NACA 4409 and NACA 4412. The profiles were mounted in the test section, extending over the entire width of the tunnel. The flow about the profiles was made visible by injecting a fluorescent dye through small holes in the profile. The plane in which the dye was injected was lit through a slot by halogen lamps. The instantaneous freestream velocity, which was varied by varying the speed of rotation of the electric motor, was measured with a drag probe, which in turn was connected with an oscilloscope. The instantaneous flow pattern was correlated with the velocity measurements by taking photographic pictures of both, the velocity signal and the flow pattern.

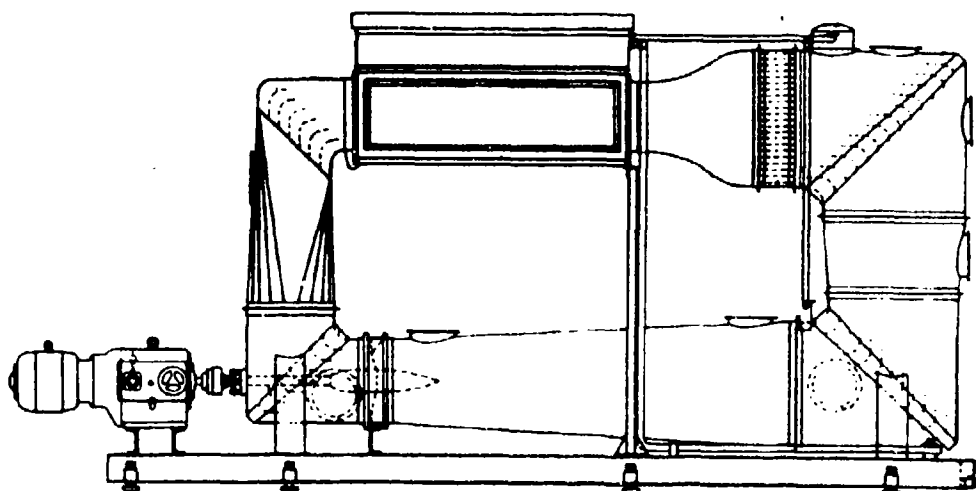


Fig. 4 Schematic of the water tunnel of the Aerodynamisches Institut

Acceleration as well as deceleration modes, and combinations thereof were employed in the experiments for several durations, velocity amplitudes, and angles of attack. The Reynolds numbers, reached in the experiments varied between  $Re = 10^4$  and  $Re = 2 \cdot 10^4$ , and the Strouhal numbers ranged from  $Sr = 0.07$  and  $Sr = 0.2$ . The corresponding freestream velocity was  $u_\infty \approx 7.5$  cm/s, and a maximum relative amplitude of 0.35.

The flow visualization studies provided sufficient information to determine the variation of the size of the separated region on the upper side of the profile as a function of the parameters just mentioned. The location of the separation point,  $x_A/l$ , and the relative maximum thickness of the separated region  $D_T/d$ , measured at the trailing edge were taken as characteristic quantities. This is schematically indicated in Fig. 5. The dimensionless time  $\tau$  was normalized by

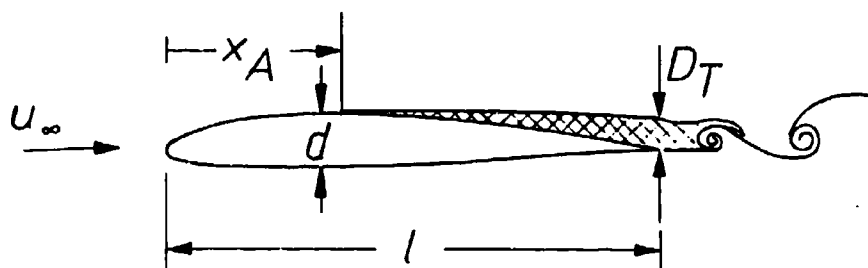


Fig. 5 Schematic of separated region of the flow

the ratio of chord length  $l$  and the initially constant freestream velocity. Some of the results obtained are shown in Figs. 6 through 10. In Fig. 6 the freestream velocity, the maximum thickness of the separated region and the location of the separation point are shown as a function of  $\tau$ , for NACA 4412 at an angle of

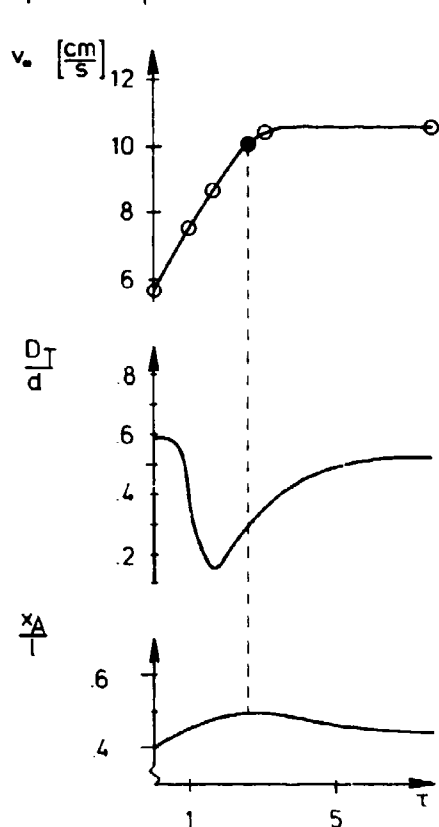


Fig. 6 Accelerated flow. Variation of freestream velocity, of maximum thickness of separated region, and of location of separation point. NACA 4412,  $\alpha = 3.8^\circ$

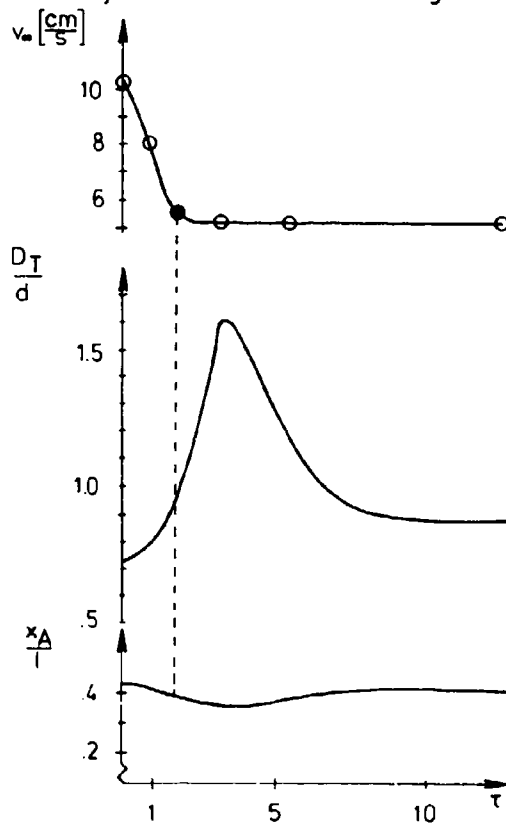


Fig. 7 Decelerated flow. Variation of freestream velocity of maximum thickness of separated region, and of location of separation point. NACA 4412,  $\alpha = 5^\circ$

attack of 3.8 degrees. The extent of the separated region on the upper side of the profile is already large at the beginning of the acceleration ( $\tau = 0$ ). The separation point is at 40 percent chord and the maximum thickness of the separated region is about 7 percent of the chord length. The flow visualization studies showed the formation of a Kármán vortex street, which did not influence the location of the separation point. The Strouhal number of the vortex street is, when based on chord length,  $Sr = 2.5$ .

During the acceleration the extent of the separated region is markedly decreased; the separation is moved downstream. Immediately downstream from the trailing edge vortex shedding is annihilated, but only a few chord lengths further downstream vortex formation can be noted again. The thickness of the separated region decreases to a minimum value of about  $D_T/d = 0.29$  for  $\tau = 0.7 \bar{\tau}$ , and the separation point is then  $x_A/l = 0.5$ . After reaching a constant freestream velocity (see Fig. 6) the size of the separated region increases again, and vortex shedding sets in in the immediate vicinity of the trailing edge. Steady state conditions are reached at roughly  $\tau = 1.5 \bar{\tau}$ .

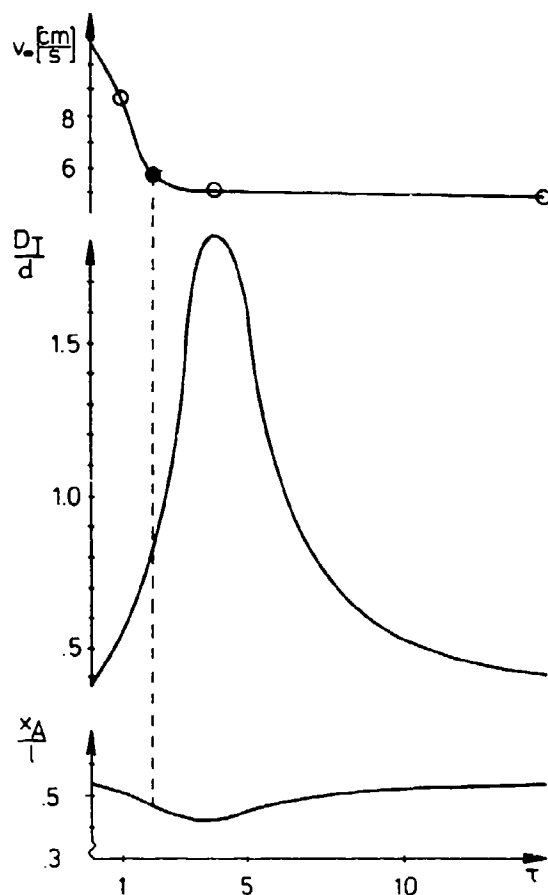


Fig. 8 Decelerated flow. Influence of thickness. NACA 4409,  $\alpha = 5^\circ$

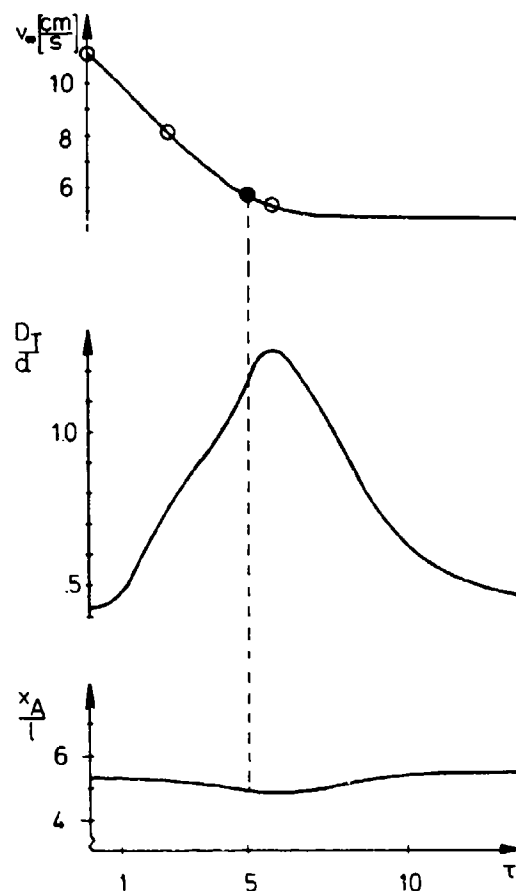


Fig. 9 Decelerated flow. Influence of duration of the transient phase. NACA 4412,  $\alpha = 5^\circ$

The results for a deceleration are shown in Fig. 7 for NACA 4409 at an angle of attack  $\alpha = 5$  degrees. It is seen that the thickness of the separated region is increased by more than a factor of two, vortex formation sets in already in the separated region, and the separation point is moved upstream as far as  $x_A/l = 0.35$ . Note that the separated region is thickest at  $\tau = 1.8 \bar{\tau}$ , that is after reaching steady freestream conditions. The flow visualization studies then show a destruction of the vortices in the separated region, its thickness decreases again; the separation point moves back to nearly the same position it had before the deceleration was started. Periodic conditions at the trailing edge are reached at about  $\tau = 3.8 \bar{\tau}$ .

In Fig. 8 it is seen that increasing the thickness of the profile enhances the process just described. The thickness of the separated region is now increased by more than a factor of three, and the return to periodic vortex formation near the trailing edge is noted as before. Since flow moves into the separated region during the deceleration phase, the Kutta condition is not satisfied, at least not at times.

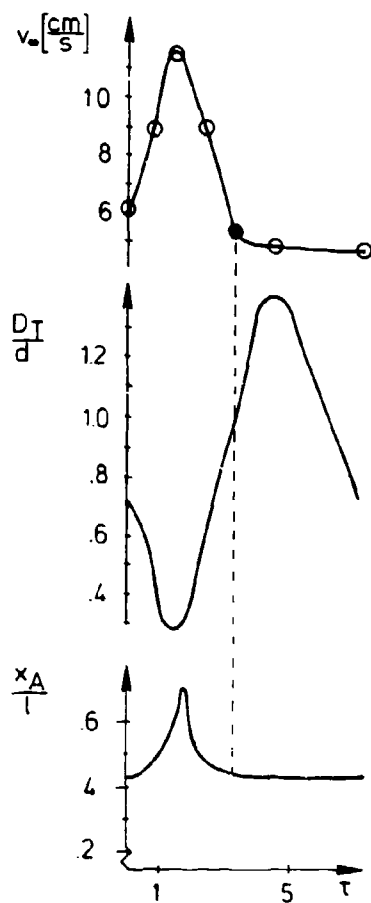


Fig. 10 Accelerated and decelerated flow.. NACA 4409,  $\alpha = 3.8^\circ$ .

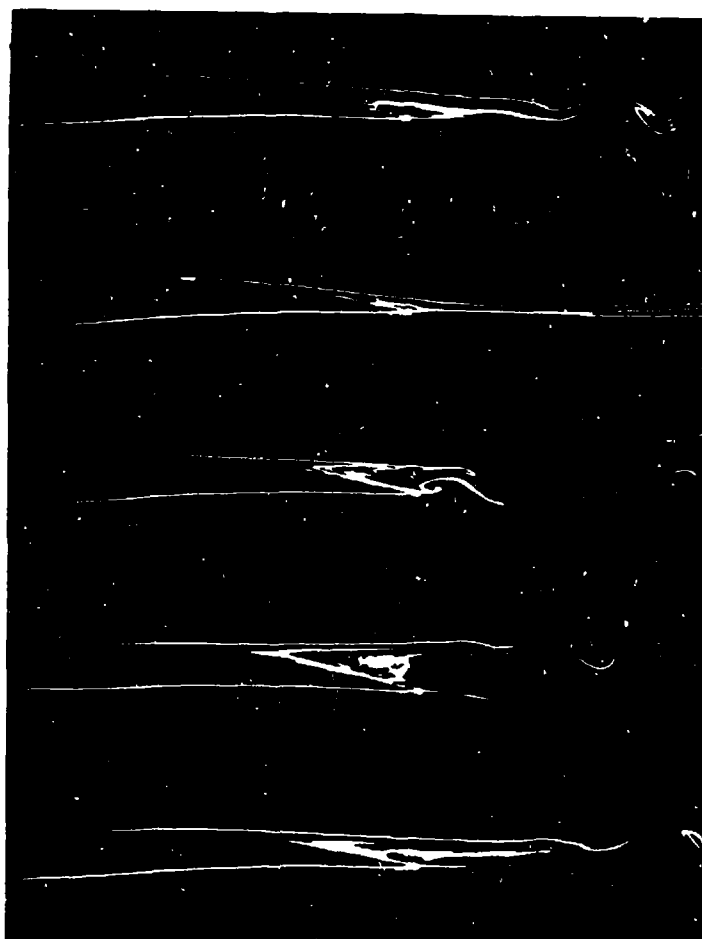


Fig. 11 Instantaneous flow pattern. Flow conditions those of Fig. 10

If the deceleration is extended over a larger time (see Fig. 9), or if the amplitude of the variation of the freestream velocity is decreased, the reaction of the flow is less pronounced. For a combination of an acceleration and a deceleration of the freestream, first a decrease and then an increase of the maximum thickness of the separated region (see Fig. 10) is noted. For the velocity variation chosen, the separation point is moved downstream, but does travel upstream of its initial position during the deceleration phase.

Fig. 11 shows a sequence of pictures of the flow pattern in the vicinity of the trailing edge for the flow conditions discussed in Fig. 10.

### PLANNED EXPERIMENTS IN AN EIFFEL TYPE WIND TUNNEL

In the third part of the investigation time-dependent pressure distributions, lift, drag and moments are to be determined for decelerated, accelerated and periodically changed freestream velocity, with profiles held at constant angles of attack. Since frequencies of the order of 5 Hz are to be obtained, an Eiffel type tunnel was chosen, in order to keep the inertia of the air in the tunnel as small as possible. The periodic variation of the freestream velocity is facilitated by a rotating flap, mounted downstream from the test section (see Fig. 12). Until now the freestream velocity in the test section was measured

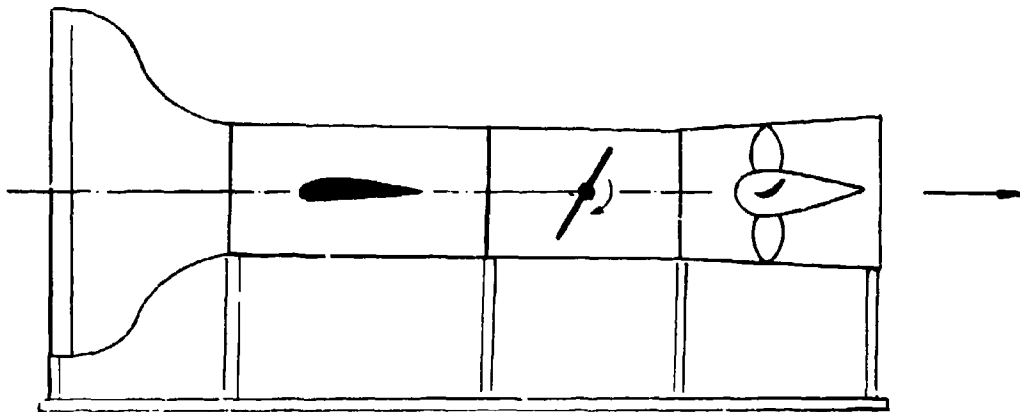


Fig. 12 Schematic of Eiffel type wind tunnel of Aerodynamisches Institut for unsteady flow analysis.

with a hot wire anemometer for frequencies up to 5 Hz. These measurements show, as indicated in Figs. 13 and 14, that the amplitudes and the frequencies exhibit a sufficient uniformity, not just at one particular station in the test section but throughout. Influences of the boundary layer on the tunnel walls could not be noted. A phase shift of about 1.5 percent was measured over the entire length of the test section. It is believed that this small variation will not impair the experiments.

The amplitudes of the variation of the freestream velocity depend on the mean freestream velocity, on the angular frequency, with which the flap can be

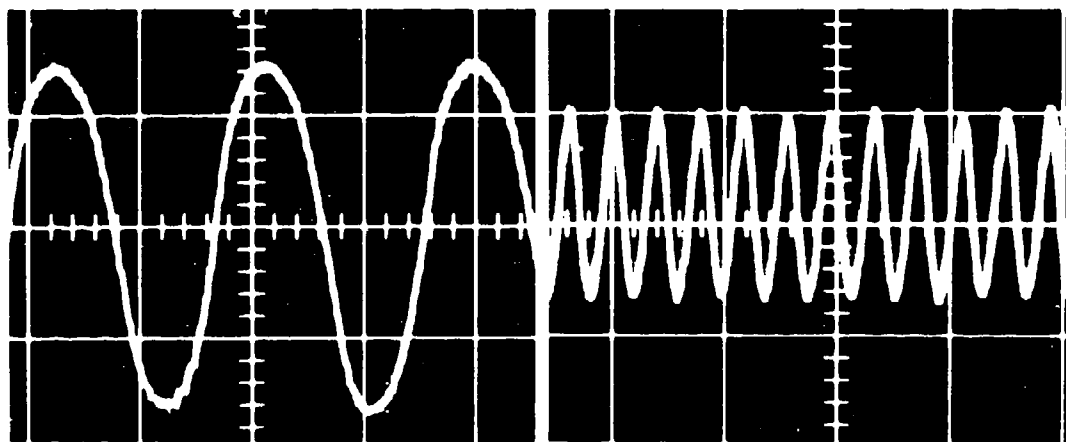


Fig. 13 Oscillograph of time-dependent freestream velocity  
 $f = 1.03 \text{ Hz}$ ,  $\Delta u_{\infty} / \bar{u}_{\infty} = 0.52$

Fig. 14 Oscillograph of time-dependent freestream velocity  
 $f = 5 \text{ Hz}$ ,  $\Delta u_{\infty} / \bar{u}_{\infty} = 0.25$

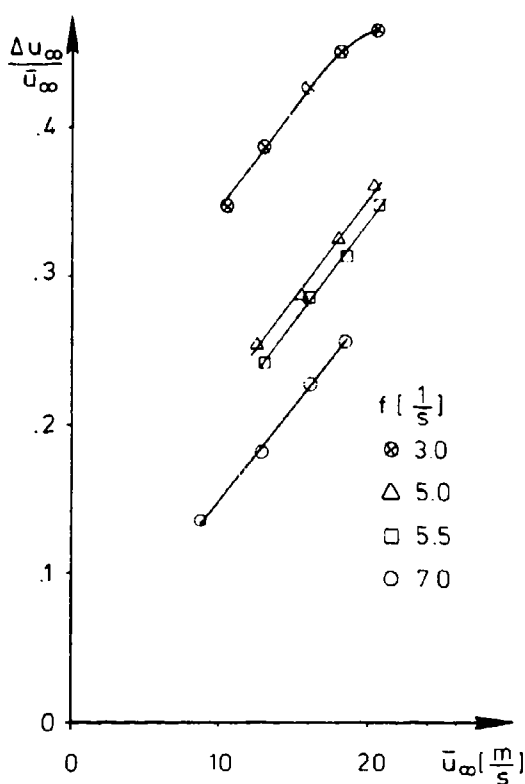


Fig. 15 Periodic variation of freestream velocity as a function of time-averaged freestream velocity

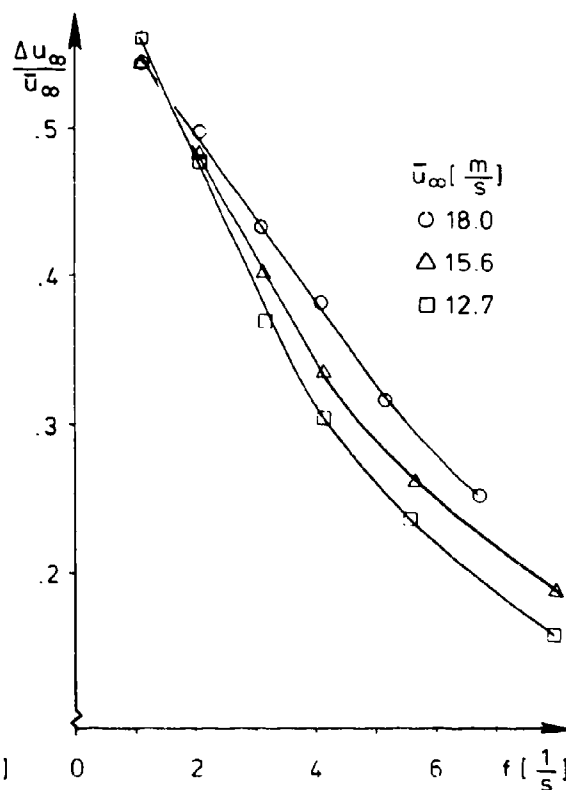


Fig. 16 Periodic variation of freestream velocity as a function of frequency

rotated, and on the size of the flap. The results obtained with a flap of the size of 80 percent of the cross section of the test section are shown in Figs. 15 and 16. It is seen that the amplitude varies linearly with the mean freestream velocity, and deviations are only noted for lower frequencies ( $f = 3$  Hz). For the maximum mean velocity of  $\bar{u}_\infty = 20$  m/s and a frequency of 5 Hz, an amplitude of about 35 percent can be obtained. A comparison with the results generated in the water tunnel is possible. The maximum Reynolds number of the flow in the Eiffel type tunnel is as large as  $Re = 2.6 \cdot 10^4$ , and the maximum Strouhal number is about 0.05.

## CONCLUSIONS

Unsteady flows about wing sections were investigated experimentally for Reynolds numbers ranging from 1500 to  $2 \cdot 10^4$  and Strouhal numbers, ranging from values of 0.05 to 0.29. For the lower Reynolds numbers,  $Re = 1500$  and  $Re = 3000$ , accelerated, decelerated, and decelerated and accelerated flows were made visible on a water table. The variation of the freestream velocity was achieved by a sluice gate. Two profiles, NACA 4412, and NACA 4424 were investigated at angles of attack of 0, 3, and 6 degrees. The flow visualization studies showed the stream upward motion of the separation point, and the thickening of the separated region, when the flow was decelerated. It was also shown that the Kutta condition was violated during the transient phases. In a second set of experiments the unsteady flow about the profiles NACA 4409 and NACA 4412 were investigated in a water tunnel at angles of attack of  $\alpha = 4$  and 5 degrees. The freestream velocity was varied from roughly 5 to 10 m/s. The corresponding Reynolds numbers were  $Re = 10^4$  and  $2 \cdot 10^4$ . The variation of the extent of the separated region, the vortex formation, and destruction in the vicinity of the trailing edge were made visible by means of a fluorescent dye. For accelerated flows, when the extent of the separated region was decreased, vortex shedding and formation of the Kármán street was delayed. Deceleration of the freestream caused substantial enlargement of the separated region and an upstream motion of the separation point. Vortex-like structures were generated immediately downstream from the separation point, resulting in the violation of the Kutta condition. The changes of the flow near the trailing edge exhibited a phase difference with respect to the changes in the freestream.

Future experiments are planned with an Eiffel type wind tunnel, in which also periodic variations of the freestream velocity can be facilitated.

## NOMENCLATURE

$A = \Delta u_\infty / \bar{u}_\infty$	dimensionless amplitude
$D_T$	thickness of separated region at trailing edge
$d$	maximum thickness of profiles
$f$	frequency
$l$	chord length

$Re = u_{\infty} L / \nu$	Reynolds number
$Sr = f L / u_{\infty}$	Strouhal number
$t$	time
$T$	duration of acceleration or deceleration
$u_{\infty}$	freestream velocity
$u_{\infty 0}$	steady freestream velocity at beginning of acceleration or deceleration
$\bar{u}_{\infty}$	time averaged freestream velocity
$x_A$	location of separation point measured from leading edge
$\alpha$	angle of attack
$\nu$	kinematic viscosity
$\tau = u_{\infty 0} t / l$	dimensionless time
$\bar{\tau} = u_{\infty 0} T / l$	dimensionless duration

#### REFERENCES

- [1] Mc.Croskey, W. J., "Some Current Research in Unsteady Fluid Dynamics", Journal of Fluids Engineering, Vol. 99, March 1977.
- [2] McAlister, K. W. and Carr, L. W., "Water-Tunnel Experiments on an Oscillating Airfoil at  $Re = 21.000$ ", NASA Technical Memorandum 78446, Ames Research Center, Moffett Field, Cal.
- [3] Satyanarayana, B. and Davis, S., "Experimental Studies of Unsteady Trailing-Edge Conditions" NASA Ames Research Center, Moffett Field, Cal.

# STREAMWISE AND SPANWISE VORTICAL PATTERNS VISUALIZED OVER AIRFOILS IN UNSTEADY FLOW

F. Finaish, P. Freymuth and W. Bank  
Department of Aerospace Engineering Sciences  
University of Colorado  
Boulder, Colorado 80309

## ABSTRACT

The relationship between the streamwise and the spanwise developments of vortical patterns over airfoils and the transition to turbulence of those patterns in unsteady flow starting from rest are the main subjects of this paper. To study the relationship between the two modes of visualization and to investigate the effect of the three-dimensional disturbances in the spanwise mode, a complementary illustration of the two modes of visualization for different Reynolds numbers and angles of attack is presented by means of selected photographic frames and sequences. Spanwise visualization of the flow field over airfoils in unsteady flow reveals the development of three-dimensional disturbances, which provide more information about the transitional stages and breakdown into turbulence.

## INTRODUCTION

Recently the development and the transition to turbulence of unsteady flow fields has received considerable attention. There is no theory explaining the variety of the flow developments and the complexity of the transitional behavior. Flow visualization is one of the keys to obtain better understanding of the physics of the flow developments and the transition to turbulence in unsteady flow fields. The work by Freymuth et al. (1,2,3) visualizes streamwise accelerating flow around airfoils after starting from rest. These visualization data have been used by Palmer et al. (4) and Finaish et al. (5) to conduct parametric analysis which further clarify the vorticity generation over airfoil surfaces in unsteady flow. Recently, the streamwise flow visualization was extended to spanwise visualization as described by Freymuth et al. (6). The modification of the experimental arrangement from streamwise to spanwise mode of visualization reveals the development of the three-dimensional transition patterns after a two-dimensional start. In the present work we conduct a complementary study which compares side by side the streamwise and spanwise visualizations at the same conditions of time, Reynolds number and angle of attack. A side by side study enhances the effectiveness of both flow visualization methods. While the streamwise method is most effective in the two-dimensional stages of vortical development, the spanwise visualizations allow more insight into the transitional stages and breaking down into turbulence.

## EXPERIMENTAL PROCEDURES

The experimental apparatus and method of our flow visualization has been described by Freymuth et al. (7). Streamwise visualization was given before (1,2,3) and the modifications to accomplish the flow visualization in spanwise mode were recently described by us (6).

Figure 1, top, shows a sketch of the experimental arrangement in which the airfoil mounted in a horizontal position to achieve the streamwise or two-dimensional flow visualization. Figure 1, bottom, shows a sketch of the spanwise or three-dimensional visualization in which the airfoil was mounted in a vertical position. All experiments were conducted in open return 0.9m by 0.9m subsonic wind tunnel at the University of Colorado. Flow was accelerated at a constant rate of  $2.4\text{m/sec}^2$  for approximately five seconds after starting from rest. Symmetric NACA 0015 airfoils were used with a range of chord length between 0.32 cm to 71 cm which allowed the variation of Reynolds number in a range between 16 to 52400 according to

$$R = a^{1/2} c^{3/2} \nu^{-1} \quad (1)$$

The angle of attack was easily adjusted in a range between  $0^\circ$  to  $90^\circ$ . Illumination of the smoke was provided by 500 watt projector lamps mounted at the top of the tunnel. After introducing the liquid titanium tetrachloride on the surface of the airfoil and accelerating the tunnel, movies were taken from the side of the tunnel through the plexiglas walls of the test section. It was possible to film 64 frames per second using a Bolex 16mm movie camera.

## METHOD OF INVESTIGATION

To investigate the relationship between the streamwise and the spanwise visualizations, movie sequences were chosen for each combination of Reynolds number and angle of attack. Three photographic sequences were selected, one visualizes the entire streamwise vortical structures (leading and trailing edge) and the others visualize the spanwise leading edge and trailing edge structures. As described previously by Palmer et al. (4) a film analyzer was used for evaluation starting with a time zero. A zero time has been defined as the time when the motion of the flow field started to be noticeable. From zero time we started to count until a certain vortex development occurred. Knowing the number of frames and the frame rate (64 frames/sec), the time until an event occurred was obtained. To nondimensionalize the time for each frame, a characteristic time  $T_c$  is defined as

$$T_c = c^{1/2} a^{-1/2} \quad (2)$$

After determining the time of each frame for the three sequences, six frames which represent the leading streamwise visualizations were selected. On the basis of the time of each frame, the corresponding frames for the spanwise visualization were obtained. The same procedures were performed for the trailing edge flow visualizations.

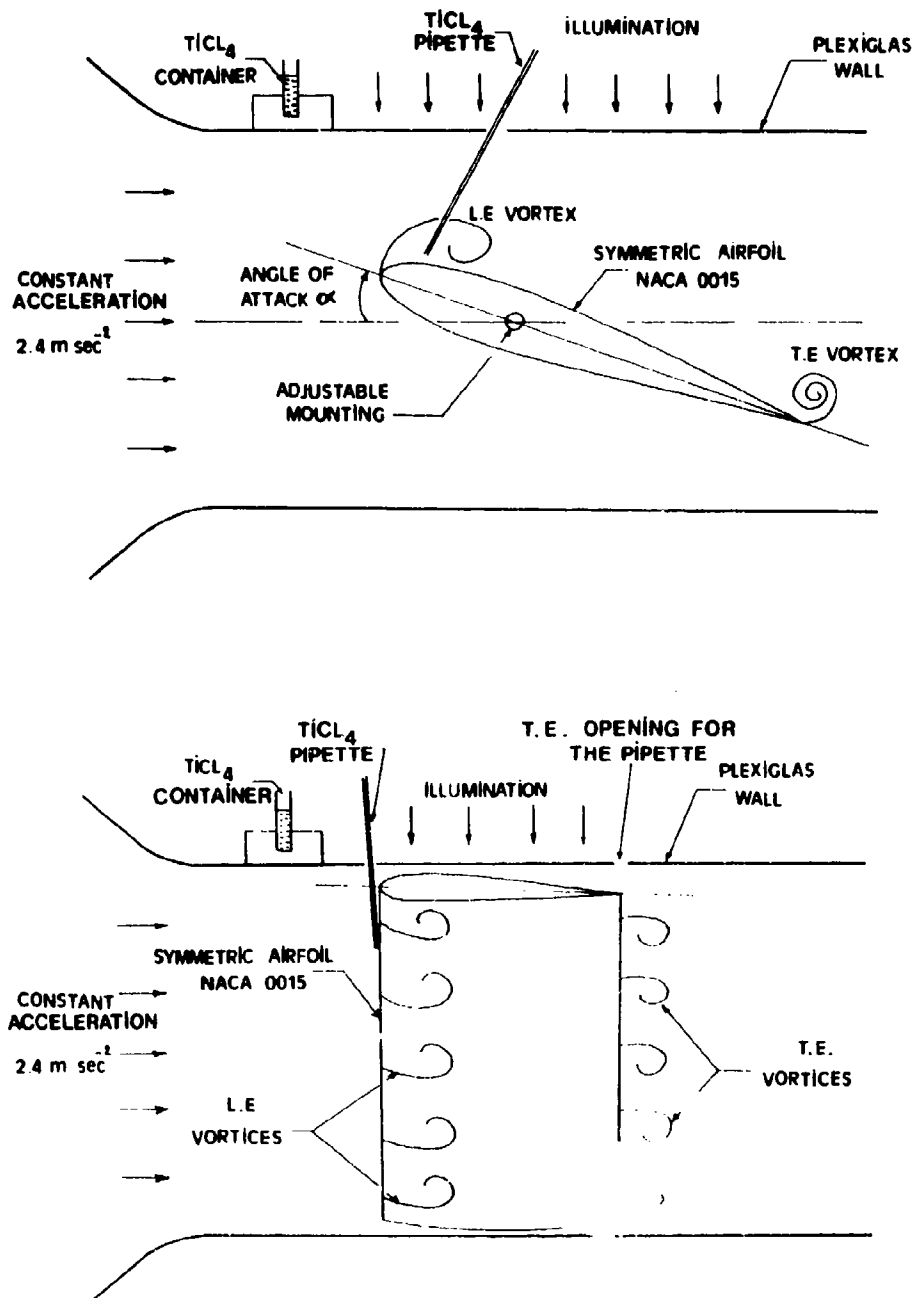


Figure 1. Sketch of the experimental arrangement; top: arrangement for streamwise visualizations; bottom: arrangement for spanwise visualizations.

The frame selection focused on the most interesting developments of the vortical patterns including the development of the three-dimensional disturbances as revealed by the spanwise mode of visualization. Hence, the time interval between the frames was not the same. (The exact frame timing can be obtained from the authors).

#### COMPLEMENTARY ILLUSTRATION OF THE STREAMWISE AND SPANWISE VISUALIZATION

To demonstrate our complementary illustration, photographic sequences for different angles of attack and Reynolds numbers were selected. Figure 2 visualizes the vortical patterns over the airfoil at different instants of time. Flow is from left to right and the relevant conditions are  $\alpha = 20^\circ$ ,  $C = 15.2$  cm and  $R = 5200$ . The first column on the left (ordered from top to bottom) illustrate the streamwise vortical developments. The second column visualizes the corresponding leading edge spanwise development. Note the two-dimensional spanwise start (column 2, frames 1,2), the transition to wavy patterns initiated with streaks in flow direction (column 2, frames 3, 4) and the onset of turbulence (column 2, frames 5,6) indicated by more chaotic patterns. Column 3 visualizes the streamwise vortical development, and the corresponding trailing edge spanwise visualization is shown in column 4. Again, we see the two-dimensional start in the spanwise mode of visualization (column 4, frames 1,2), which proceeds to a three-dimensional development starting with the horseshoe vortices (column 4, frame 3). Frames 5 and 6 in column 4 show the turbulent diffusion of the trailing edge vortex.

Figure 3 visualizes the flow over the airfoil with the same chord length (hence the same Reynolds number) at an angle of attack  $\alpha = 40^\circ$ . In this case the spanwise leading edge flow visualization (column 2) reveals the development of a wavy pattern without streaks (column 2, frame 3). Later we see a development of horseshoe array (column 2, frame 4), which diffuses quickly to turbulence as indicated in (column 2, frame 5,6). Column 3 visualizes the trailing edge flow development in streamwise mode and the corresponding trailing edge development in spanwise mode appears in column 4. The spanwise visualizations (column 4) reveal spectacular patterns of flow development. Two-dimensional vortices which develop from a vortex sheet (column 4, frame 1) twist around each other to form a three-dimensional pattern of vortex tubes. Also, the development of a horseshoe vortex in the free stream behind the trailing edge (column 4, frames 3,4) can be seen.

Figure 4 visualizes the vortical development over the airfoil with the same chord length and Reynolds number at an angle of attack  $\alpha = 60^\circ$ . The leading edge flow developments were quite similar to that when  $\alpha = 40^\circ$ . Trailing edge development shows strong interactions between the vortex tubes behind the trailing edge (column 4, frame 4). Frame 5 in column 4 shows a pattern of vortex tubes creating the trailing edge vortex. Those tubes interact with each other to diffuse to turbulence. No trailing edge horseshoe vortices were observed at this angle of attack.



Figure 2. Complementary illustration of streamwise and spanwise visualizations of accelerating flow around airfoil.  $\alpha = 20^\circ$ ,  $c = 15.2\text{cm}$ ,  $R = 5260$ . Columns 1 and 2 leading edge visualizations, columns 3 and 4 trailing edge visualizations.

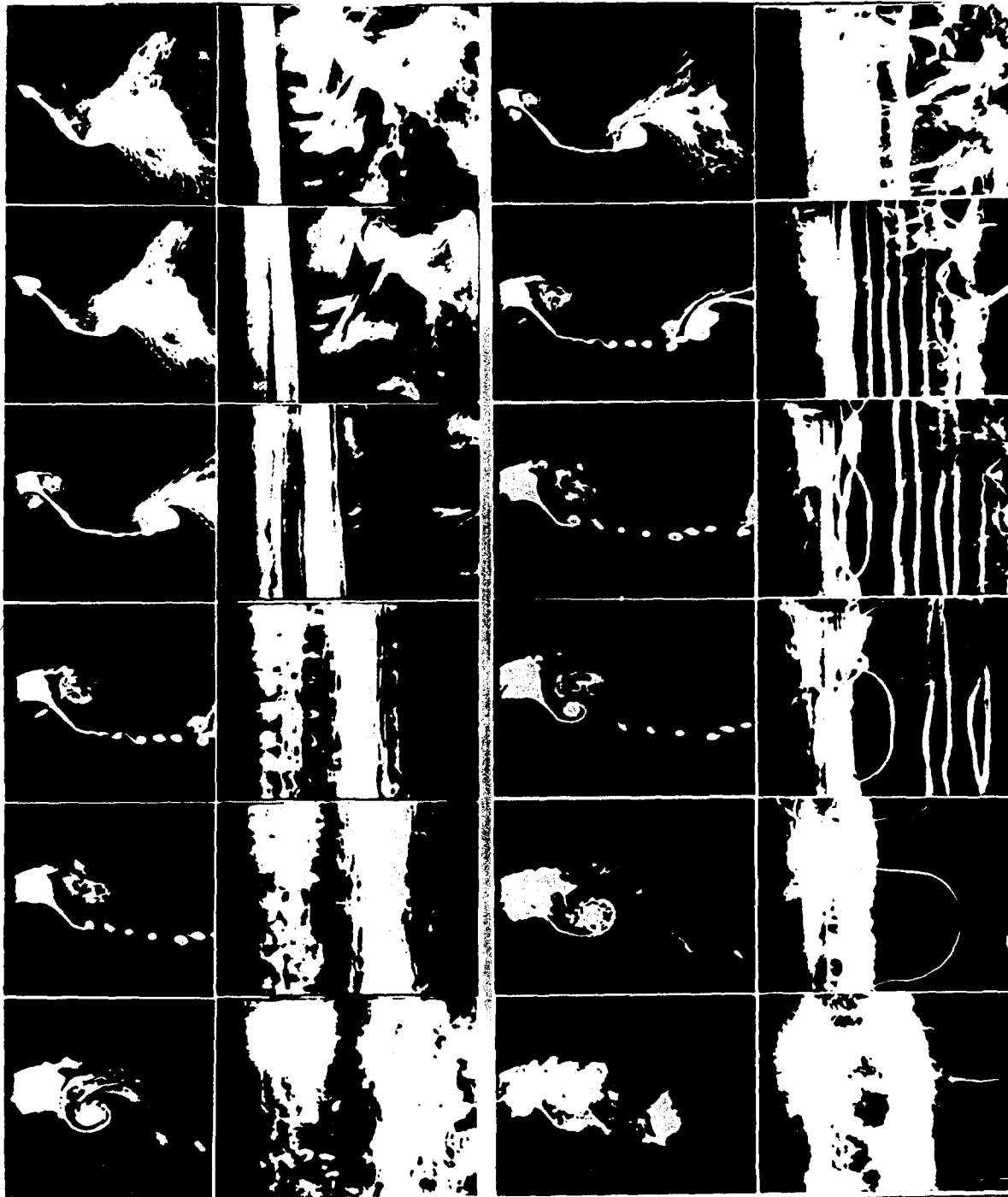


Figure 3. Complementary illustration of streamwise and spanwise visualizations of accelerating flow around airfoil.  $\alpha = 40^\circ$ ,  $c = 15.2\text{cm}$ ,  $R = 5200$ . Columns 1 and 2 leading edge visualizations, columns 3 and 4 trailing edge visualizations.

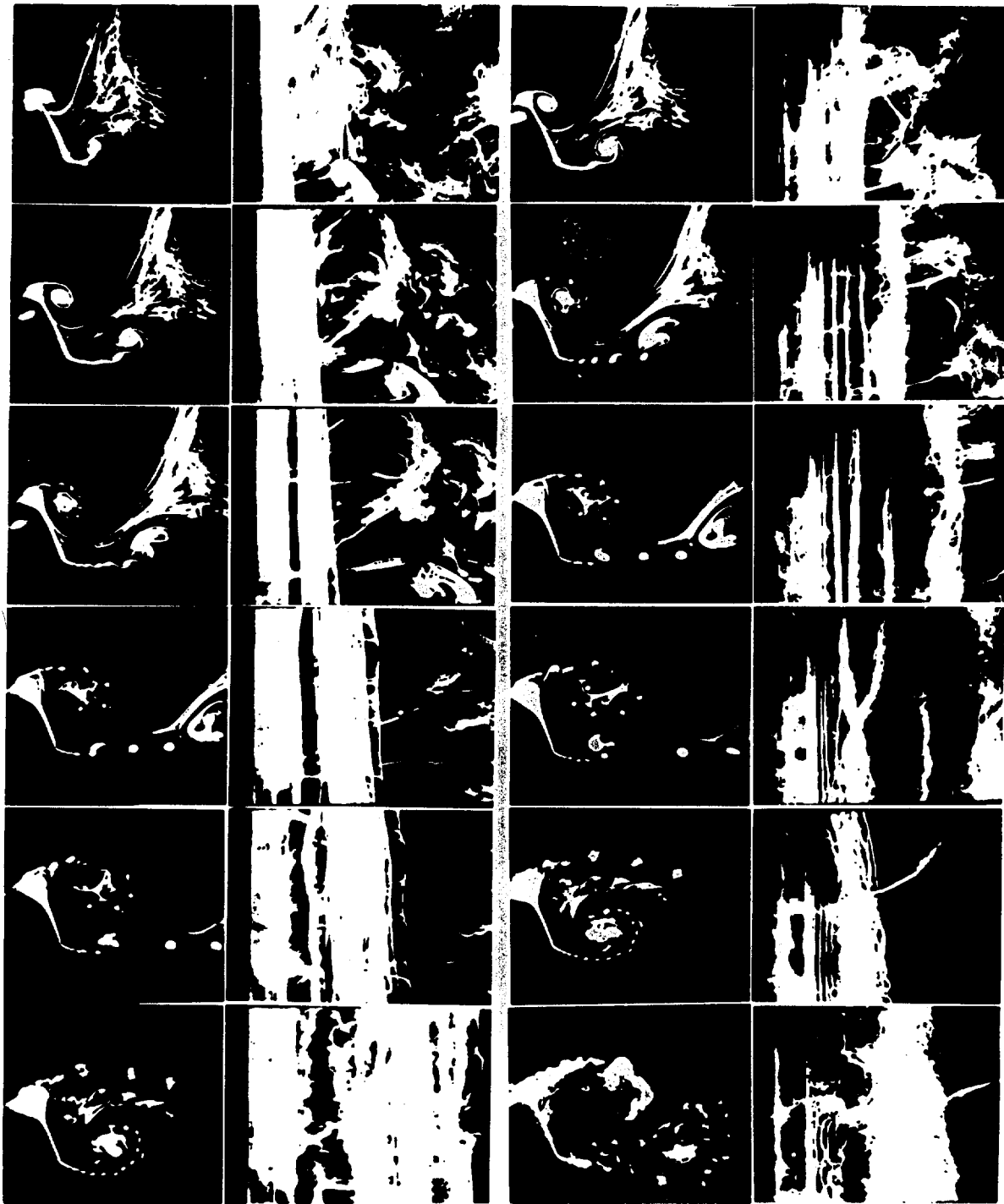


Figure 4. Complementary illustration of streamwise and spanwise visualizations of accelerating flow around airfoil.  $\alpha = 60^\circ$ ,  $c = 15.2\text{cm}$ ,  $R = 5200$ . Columns 1 and 2 leading edge visualizations, columns 3 and 4 trailing edge visualizations.

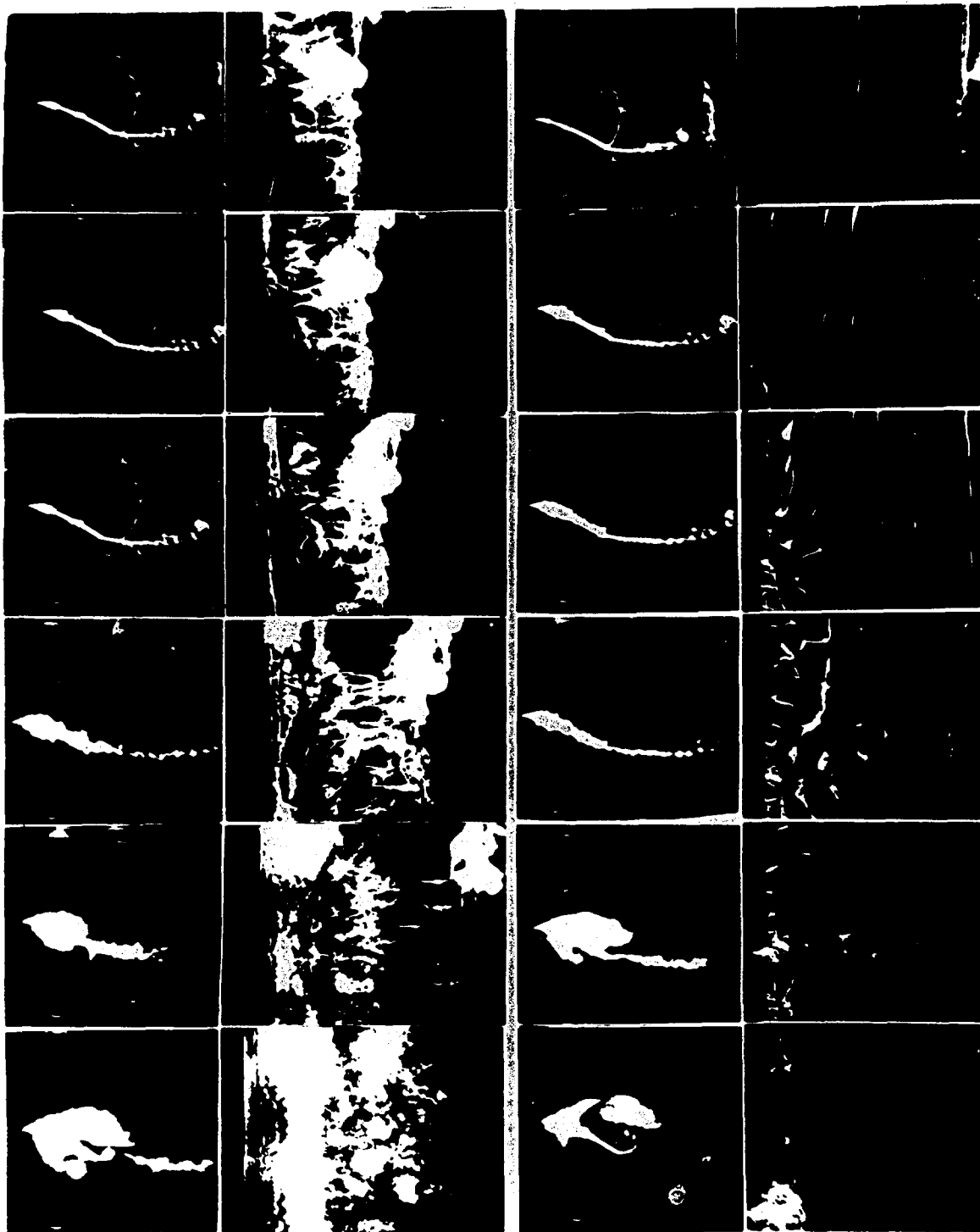


Figure 5. Complementary illustration of streamwise and spanwise visualizations of accelerating flow around airfoil.  $\alpha = 20^\circ$ ,  $c = 35.6\text{cm}$ ,  $R = 18250$ . Columns 1 and 2 leading edge visualizations, columns 3 and 4 trailing edge visualizations.

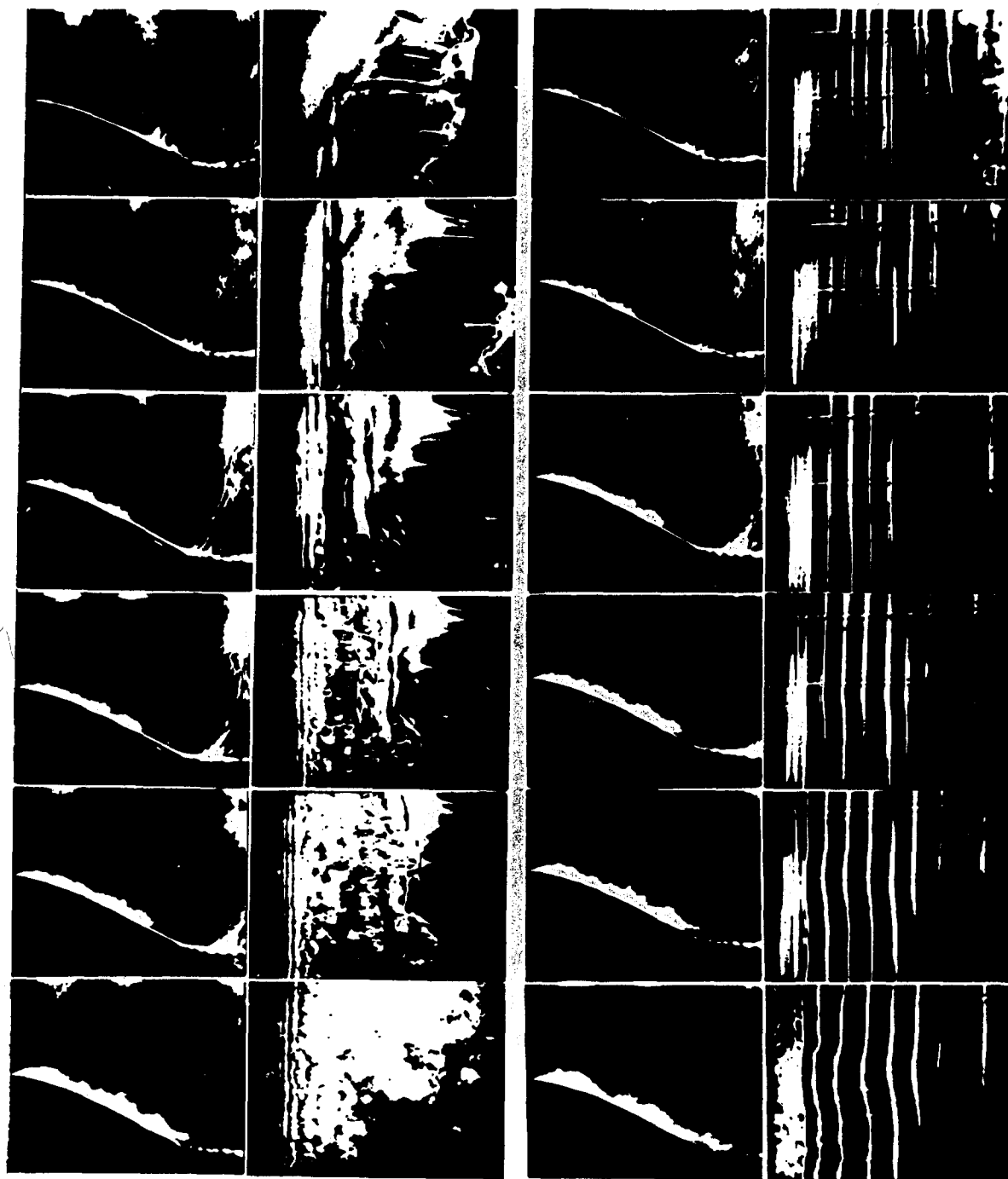


Figure 6. Complementary illustration of streamwise and spanwise visualizations of accelerating flow around airfoil.  $\alpha = 20^\circ$ ,  $c = 71\text{cm}$ ,  $R = 52400$ . Columns 1 and 2 leading edge visualizations, columns 3 and 4 trailing edge visualizations.

To investigate the effect of the Reynolds number, we performed the same experiment with different chord lengths which allow the variation of the Reynolds number according to equation 1. Figure 5 visualizes the vortical developments over an airfoil; the relevant conditions are  $\alpha = 20^\circ$ ,  $c = 35.6$  cm,  $R = 18250$ . The first column on the left illustrates the streamwise vortical developments. The second column visualizes the corresponding leading edge spanwise developments which show the three-dimensional disturbance start as spot (column 3, frame 2,3) on the surface of the airfoil which grows quickly and diffuses to turbulence (column 2, frames 5,6). Also, we see that the two-dimensional vortices become corrugated near the leading edge as indicated in frames 4, 5, and 6. Complementary illustration for the trailing edge developments is presented in columns 3 and 4. The spanwise visualization in column 4 reveals the development of the horseshoe vortices near the trailing edge (frames 2,3). The three-dimensional patterns interact very quickly near the trailing edge resembling chain link fence (column 4, frames 3,4) prior to transition to turbulence (column 4, frames 5,6).

Figure 6 visualizes the vortical developments over the airfoil with the conditions  $\alpha = 20^\circ$ ,  $c = 71$  cm, and  $R = 52400$ . Once again the spanwise leading edge visualizations show the two-dimensional start (column 2, frame 1). The developments of the horseshoe vortices (column 2, frame 2) proceeds to form  $\Lambda$  and  $\Omega$  vortices (8) (column 2, frames 3 and 4 respectively), which diffuses to turbulence as presented in (column 2, frames 5,6). The vortices developments in this case were in a form of spots over the surface of the airfoil rather than regular patterns. The spanwise trailing edge developments in column 4 show less interaction between the vortex tubes developed behind the trailing edge, compared to the trailing edge flow developments for lower Reynolds number.

## CONCLUSIONS

From our complementary illustration of the two modes of visualizations and the three-dimensional patterns observed in the spanwise mode of visualization, we obtain a reasonable insight into the transitional stages. The variety of ways of vortical developments and transitional processes depend strongly on Reynolds number and angle of attack. The visualization of flow developments for higher Reynolds numbers at  $20^\circ$  angle of attack shows random developments rather than regular patterns.

## NOMENCLATURE

$a$	Flow acceleration
$c$	Chord length of the airfoil
$T$	Time
$\alpha$	Airfoil angle of attack
$\nu$	Kinematic viscosity of the air
Subscripts:	
$c$	Characteristic time

#### ACKNOWLEDGMENTS

The authors wish to thank Mr. R. Meinzer for his technical assistance. Thanks go to Mr. A. Nowrouzi for his valuable assistance in evaluating photographic sequences. This work was supported by the AFOSR grant number 81-0027. The project was managed by Dr. M.S. Francis and currently by Dr. J. McMichael.

#### REFERENCES

1. Freymuth, P., W. Bank, and M. Palmer, "Flow Visualization and Hot Wire Anemometry," TSI Quarterly, Vol. 9, Issue 4, Oct.-Dec. 1983, pp. 11-14.
2. Freymuth, P., W. Bank, and M. Palmer, "Visualization of Accelerating Flow Around an Airfoil at High Angles of Attack," Z. Flugwiss. Weltraumforsch., Vol. 7, 1983, pp. 392-400.
3. Freymuth, P., M. Palmer, and W. Bank, "Visualization of accelerating flow around an airfoil at angles of attack 0 to 30," 8th Biennial Symposium on Turbulence, Sept. 26-28, Rolla, MO.
4. Palmer, M. and P. Freymuth, "Analysis of Vortex Development from Visualizations of Accelerated Flow around an Airfoil," starting from Rest," AIAA paper 84-1568, 1984, pp. 1-8.
5. Finaish, F., M. Palmer, and P. Freymuth, "A parametric analysis of vortex patterns visualized behind airfoils in accelerating flow," Ninth Biennial Symposium of Turbulence, Rolla, MO, October 1-3, 1984.
6. Freymuth, P., W. Bank, and F. Finaish, "Visualization of spanwise vortex structure in the starting flow behind an airfoil," Paper AIAA-85-0447, AIAA 23rd Aerospace Sciences Meeting, Reno Nevada, January 14-17, 1985.
7. Freymuth, P., W. Bank, and M. Palmer, "Use of Titanium tetrachloride for visualization of accelerating flow around airfoils," Third International Symposium on Flow Visualization, Ann Arbor, Michigan, Sept. 6-9, 1983. Proceedings to appear as "Flow Visualization," Vol. 3.
8. Hama, F.R., and J. Nutant, "Detailed flow-field observations in the transition process in a thick boundary layer," Proceedings of the 1963 Heat Transfer and Fluid Mechanics Institute, Stanford University Press, pp. 77-93, 1963.

# PRELIMINARY EXPERIMENTS IN UNSTEADY FLOW ON AIRFOILS AT LOW REYNOLDS NUMBERS

Michael Brendel  
and  
Thomas J. Mueller

Aerospace and Mechanical Engineering  
University of Notre Dame  
Notre Dame, Indiana 46556

## ABSTRACT

A program to study the aerodynamic characteristics of airfoils in unsteady flows at low Reynolds numbers has recently been initiated. An experimental facility designed to produce temporal variations in the streamwise velocity of the subsonic wind tunnel is presented. The device features a programmable input, thus allowing many variations of periodic velocity waveforms. A method to suppress higher harmonics present in sinusoidal velocity waveforms is discussed. A preliminary experiment to determine the feasibility of extending steady flow pressure measurement techniques is also presented. The data are preliminary since an independent measurement technique has not been employed to validate results. The value of unsteady pressure distributions to reveal aerodynamic parameters and boundary layer characteristics warrants further work into understanding and improving unsteady pressure measurements.

## INTRODUCTION

The aerodynamic characteristics of airfoils and wings at low Reynolds numbers has been the subject of several recent investigations. These studies have focused on steady performance properties with detailed correlation with boundary layer behavior. As a natural extension to this work, an experimental program to study low Reynolds number aerodynamics in an unsteady environment is in progress at the University of Notre Dame.

In many cases, steady or quasi-steady performance predictions are adequate in practical applications. However, situations often arise where unsteadiness is known to be important. Examples include helicopter rotors, propellers, wind turbines, turbomachinery, and many aeroelastic phenomena. Unfortunately, experiments required to model these processes rapidly become impractical due to the complex combinations of unsteadiness found, therefore, examining a single contribution to the overall unsteadiness provides a controlled means to isolate dominant effects. The present work involves streamwise unsteadiness, that is, the freestream velocity is a function of time while the airfoil remains stationary. A low frequency periodic variation in freestream velocity may represent relative velocity fluctuations in the atmospheric boundary layer while high frequency disturbances may occur due to aerodynamic interference on certain flight vehicles. Transient phenomena such as gust encounters are also considered.

A facility has been built to produce a wide variety of streamwise unsteadiness in the subsonic wind tunnel. This paper describes its construction, operation, and operating characteristics with special attention to the base flow quality. Additionally, some of the problems associated with measuring an airfoil pressure distribution in an unsteady flow will be discussed.

### EXPERIMENTAL FACILITY

Experiments are performed in the 610 x 610 mm section subsonic indraft wind tunnel. The Unsteady Flow Generator (UFG) is a self-contained apparatus which may be placed either upstream or downstream of the wind tunnel test section. In most experiments the generator will be placed downstream as shown in Figure 1. Streamwise unsteadiness is produced by the motion of four horizontal shutters which act to control the flow rate to the wind tunnel fan. Tests to date have been conducted with 152 x 610 mm (6 x 24 in) plexiglass shutters. Previous devices using this design were limited to periodic unsteadiness since the shutters could only be rotated at constant angular velocity. The quality of the periodic waveform produced by these designs was difficult to control due to the large non-linear periodic wake produced. Also, the amplitude of oscillation could only be changed by replacing the shutters in order to vary the solidity of the device. The present unsteady flow generator, with a special motor, is programmable, thus allowing periodic freestream variations to be produced by shutter oscillation rather than rotation.

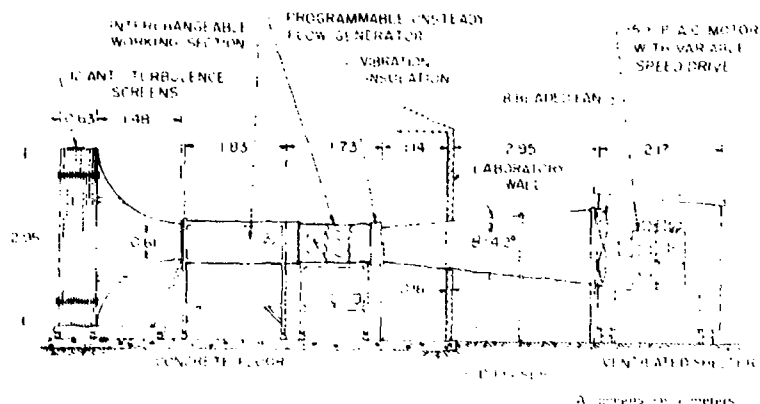


Figure 1. Subsonic Wind Tunnel with Unsteady Flow Generator

The shutters are directly coupled through a series of belts and pulleys to a printed-circuit armature DC servo motor. This type of motor has a very low armature inertia and can therefore produce rapid changes in angular velocity. The motor is connected to a DC servo amplifier which provides the rectified DC drive pulses. This configuration allows for a wide variety of unsteady base flows with non-zero mean velocity. A detail of the unsteady flow section is shown in Figure 2.

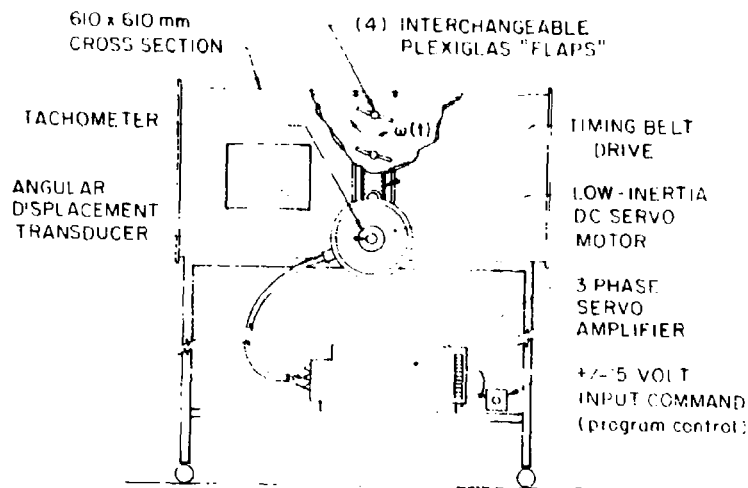


Figure 2. Unsteady Flow Generator

### Operation

Angular velocity of the motor is directly proportional to a  $\pm 15$  V input command. The servo amplifier utilizes this input and a velocity feedback loop using a tachometer to maintain desired velocity under various loading conditions. This form of command input is well suited for computer control which insures high repeatability of periodic or transient waveforms. Input commands are calculated by a 6502 microprocessor (Apple II) and output through a digital to analog converter. An angular displacement transducer, (ADT), is used in a position feedback loop that is controlled by the 6502. This prevents precession of shutters away from the mean angular position used in oscillatory waveforms. The 6502 also outputs phase-locked or event trigger pulses necessary for conditional sampling.

In periodic flows, the computer is loaded with single period velocity and displacement waveforms represented by 180 points. The frequency of the desired oscillation is determined by a time delay placed between adjacent output signals sent to the motor. The process is analogous to an endless loop tape which plays the same waveform over and over, thus a very repeatable oscillation is produced.

Transient unsteadiness is generated by rapidly rotating the shutters through a given angle, thus changing the solidity. The 6502 processor maintains the shutters at a fixed position through feedback from the ADT. An external enable, computer or manual, starts the transient sequence by first triggering any data acquisition devices and then waiting a short time before initiating shutter motion. Likewise, shutter position is held after the transient until all data acquisition has reached completion and then the process is reset. The control of the experiment by this method allows many realizations of the same phenomenon to be ensemble averaged in a reliable manner.

Although the techniques described provide very controllable shutter motions, the response of the freestream velocity is somewhat complicated. Therefore, an investigation of the base flow quality in the empty test section was undertaken to document the facility.

### Base Flow Quality

Periodic waveforms are produced by oscillating the shutters about a mean angular position. This method is limited to low frequencies ( $< 5$  Hz) due to angular acceleration restraints and shutter loading. However, control of the amplitude of the unsteadiness is afforded by this method. Higher frequencies ( $> 10$  Hz) may be obtained by rotating the flaps at a constant angular velocity plus a time dependent perturbation velocity to attenuate distortion as presented by Simpson [1]. This technique is not discussed here.

The quality of a sinusoidal base flows may be characterized by the total harmonic distortion of the streamwise velocity. As the shutter oscillates, it produces a periodic wake which interacts with the wind tunnel fan. The periodic wake requires a finite time to reach the fan; hence, the flow rate in the time responds out of phase with the driving frequency resulting in harmonic distortion. Total harmonic distortion, (THD), is determined through Fourier analysis of the test section velocity. Total harmonic distortion, in this experiment, is defined as the ratio of energy contained in the harmonics of the driving frequency to the energy contained in the driving frequency given by

$$THD = \sum_{n=2}^{\infty} \frac{\phi_{nf}}{\phi_f}$$

Additionally, the phase difference between the driving frequency and its higher harmonics can be determined. A technique to suppress the distortion has been developed whereby the shutter driving function is modified by the superposition of the driving frequency,  $f$ , with the higher harmonics,  $2f$ ,  $3f$ , ..., with appropriate phase shift determined from the frequency analysis. This method can reduce the harmonic distortion by an order of magnitude.

Base flow quality tests were conducted in an empty test section using a single-wire constant temperature anemometer. A comparison of the pure tone and harmonically suppressed driving functions with corresponding velocity variations are shown in Figures 3 and 4.

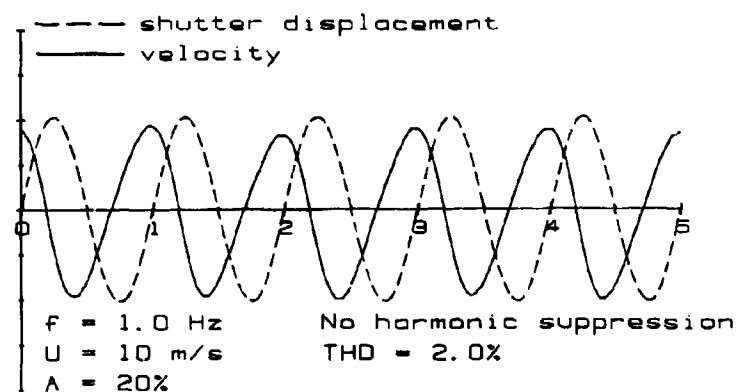


Figure 3. Shutter and Velocity Fluctuation, No Harmonic Suppression

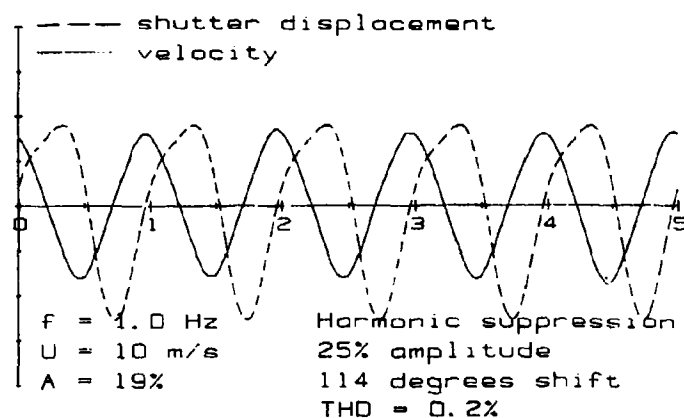


Figure 4. Shutter and Velocity Fluctuation with Harmonic Suppression

These figures show the streamwise velocity fluctuation superimposed over the fluctuating shutter displacement time history for reference. The mean flow velocity was 10 m/s with a 20% amplitude ratio,  $A$ , while the shutters oscillated  $\pm 20$  degrees with a frequency of 1 Hz about a mean angle of 20 degrees. Distortion in the pure tone case is evidenced by the skewed peaks in the velocity trace. In Figure 4, only the first harmonic,  $2f$ , was suppressed. The harmonic suppression function consisted of the first harmonic,  $2f$ , with 25% amplitude ratio relative to  $f$ , and 114 degree phase shift. This phase shift represents the unsuppressed phase difference plus 180 degrees. The resulting driving function, or shutter displacement, clearly shows the degree of modification necessary to suppress the distortion. In this example, the total harmonic distortion was reduced from 2 to 0.2 percent. This was typical of most drive frequencies and amplitudes, although lower amplitudes tended to have less initial distortion. To further illustrate, Figures 5 and 6 are the corresponding spectral density functions. One notices that the suppression of the first harmonic is at

the expense of primary and  $3f$  amplitude. However, the increase in the  $3f$  is not significant in the distortion level. Suppression of higher harmonics is possible, but has not been attempted. The phase angle used in the harmonic suppression technique is determined from the Fourier analysis, but the correction amplitude as a function of primary amplitude, 20% in this case, is determined by trial and error.

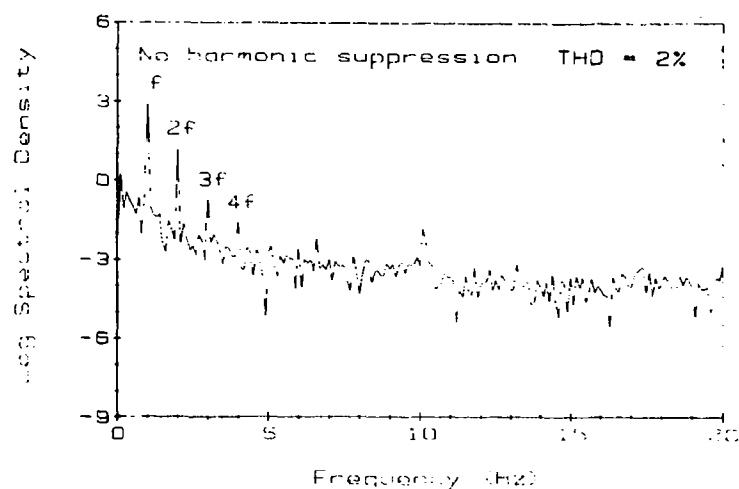


Figure 5. Velocity Spectrum

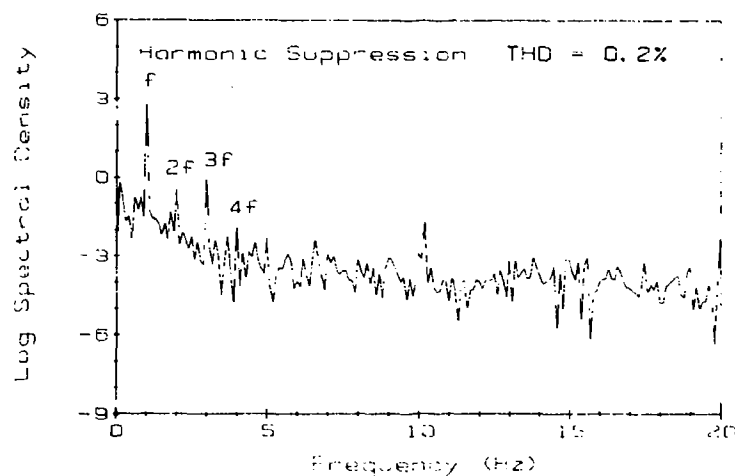


Figure 6. Velocity Spectrum

Variation of amplitude ratio,  $A$ , was dependent upon the frequency of oscillation. At very low frequencies,  $\sim 0.5$  Hz, amplitude ratios of about 40% were achieved. Near 5 Hz, the maximum amplitude ratio tested was on the order of 5%. The reduction in amplitude ratio with frequency was in part due to operating with less angular displacement since large displacements tended to excessively vibrate the wind tunnel. Also, inertia of the fluid in the tunnel would not respond as easily to the rapid pressure fluctuations.

Turbulence intensities in the test section are not significantly altered by the imposed unsteadiness. The primary increase in turbulence intensities is due to higher harmonics of the drive frequency, however levels were found to be less than 0.5% for frequencies greater than twice the drive frequency in all tested conditions.

Transient motion of the shutters can be less than 100 ms, however the dynamics of the wind tunnel may require several times this value to reach steady state. Again, the wake produced by the shutters requires time to reach the fan which modifies the tunnel flow rate due to a constant fan speed. The response time is much faster for decelerating flows than for accelerating flow since in the latter the tunnel fan must provide the energy input for the acceleration. The decelerating flow requires an impulsive exchange of momentum from the fluid in the tunnel to the shutters and support structure. Typical transient waveforms for rotation rates,  $\dot{\beta}$ , of 1 rad/s and 7 rad/s are shown in Figure 7 for a  $40^\circ$  rotation.

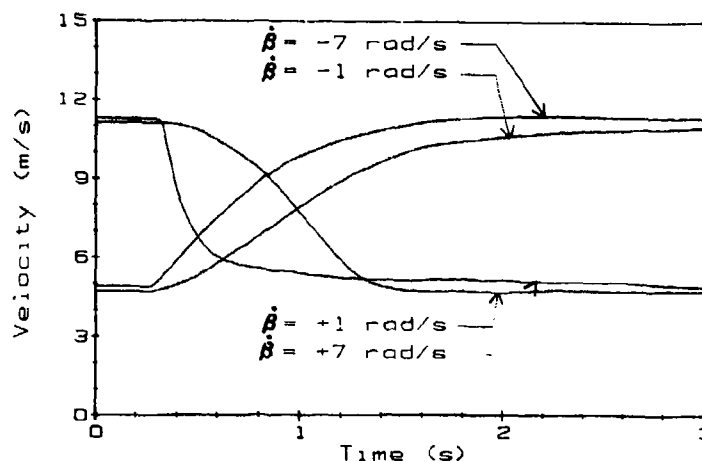


Figure 7. Typical Transient Waveforms

#### PRELIMINARY EXPERIMENTS

Use of conditional sampling, ensemble averaging, and computer controlled experiments is the key to reducing unsteady flowfield phenomena. The device described above along with support equipment provides an ideal facility for unsteady experiments. However, a thorough understanding of the instruments used to measure unsteady flowfields is necessary to insure confidence in the results. Extension of experimental techniques from steady to unsteady experiments requires careful consideration of instrument dynamics especially with mechanical devices such as force balances and pressure transducers. Ideally, the natural frequency response of a measurement system should extend several orders of magnitude above the characteristic frequency of the phenomenon to be measured.

Preliminary tests have focused on measuring unsteady pressure distributions on an airfoil since these data serve the dual purpose of

providing an estimate of aerodynamic performance parameters and general features of the boundary layer. Whereas thermal and laser anemometers have very desirable frequency characteristics, the dynamics of static pressure sensing systems has been a formidable problem particularly when tubing must connect the sensing port and the transducer. The tubing dynamics problem may be reduced by the use of miniature transducers mounted in the model, but this is an expensive alternative when detailed spacial resolution is required and may also be prohibited by model size. The present attempt is to design an experiment utilizing the existing pressure models with an external multiplexing valve and single transducer. Calculation of desired quantities such as pressure coefficient with a high degree of confidence and a minimum of correction procedures is desired. These preliminary experimental results are presented to illustrate some of the difficulties encountered.

### Apparatus

A 152 mm (6 in) chord Wortmann FX63-137 airfoil model with a total of 40 pressure taps placed along the upper and lower surfaces was used. This is the same model used by Huber [2] in the steady flow experiments. Each pressure tap was externally connected to a 48 channel Scanivalve solenoid valve through approximately 800 mm of 1.2 mm diameter tygon tubing. The positive pressure side of the transducer was connected to a pitot-tube placed 300 mm upstream and 200 mm above the airfoil quarter-chord as the reference for freestream total pressure. The output of the Scanivalve was connected to either a Setra 239 or Setra 237 differential pressure transducer. The Setra 239 is a strain gauge diaphragm transducer with a range of 0 to 1.4 kPa (0 to 0.2 psi) differential pressure and the Setra 237 is a capacitance type transducer with a range of 0 to 0.7 kPa (0 to 0.1 psi) differential. The two instruments were selected to compare transducers with different dynamic characteristics. A single hot-wire sensor coupled to a TSI 1050 anemometer bridge was placed near the pitot-tube to the monitor freestream velocity: the freestream dynamic pressure.

Data acquisition was provided by a Digital Equipment PDP 11/23 with a 12-bit ADV11-C analog to digital converter while stepping of the Scanivalve was through a 12-bit AAV11-C digital to analog converter. A schematic of this test arrangement is shown in Figure 8. For periodic freestream variations, 32 samples were taken in each period of the oscillation. Eighty oscillation periods were phase-lock averaged into 8 periods for each pressure tap and then stored on hard disk. Ultimately, 32 instantaneous pressure distributions composed of 80 single samples per tap are educted for one period of oscillation.

The pressure coefficient is defined as

$$C_p = 1 - (P_o - P_s)/Q_\infty$$

where the differential pressure,  $P_o - P_s$ , was inferred directly from the transducer voltage output and the freestream dynamic pressure was obtained from the anemometer. Frequency compensation for the periodic tests was estimated using a lumped-capacity model by Hougen [3]. This is necessary since the anemometer leads the pressure measurement.

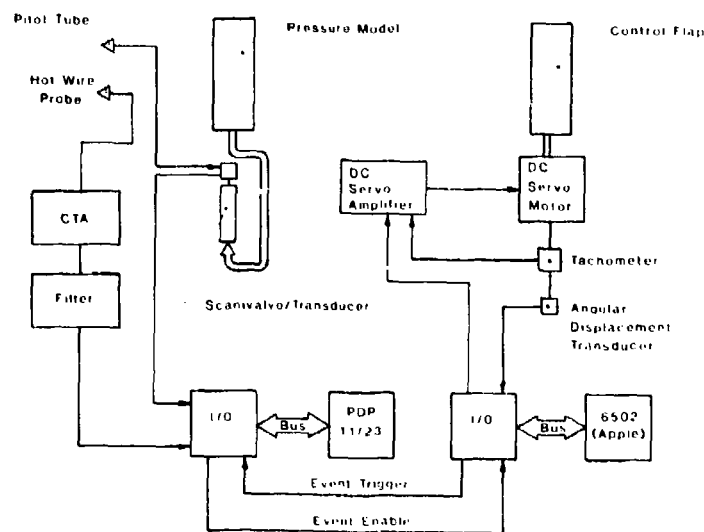


Figure 8. Test Set-Up Schematic

Another method would be to monitor freestream dynamic pressure with a Prandtl tube, however, this would require a more elaborate compensation scheme based upon the tubing geometry. The natural frequency of the pressure system using the Setra 239 was estimated to be 28 Hz with a damping ratio of one. This is a first approximation since the small tubing acts as a harmonic resonator with many natural frequencies. The Setra 239 system has an estimated natural frequency of 97 Hz and a damping ratio of 0.2. The difference between the characteristics of the two transducers is that the transducer volume in the Setra 237 is much smaller than in the Setra 239; hence, less damping capability.

#### PRESSURE MEASUREMENTS

The purpose of these preliminary experiments is to identify any unusual boundary layer phenomena that may occur in an oscillating and transient freestream. The applicability of present steady experimental techniques is also of interest. Validation of the results obtained from unsteady pressure data is very difficult without other types of measurements. At present, no attempt has been made to verify the above system dynamics. The dynamic model is an idealized second-order estimate and does not include the effect of tubing connectors or the geometry of the pressure taps themselves. In general, one may experimentally determine a transfer function for a dynamic system subjected to a known forcing function, however, the inverse problem of deducing the unknown forcing function from transducer output voltage is not straightforward.

The most disquieting observation in some preliminary data is the calculation of pressure coefficients significantly greater than unity such that they can not be attributed to experimental uncertainty. This

occurs when the transducer output voltage becomes negative, indicating airfoil static pressure exceeding the freestream total pressure. The problem is more severe in the transient cases where the freestream acceleration is on the order of  $10 \text{ m/s}^2$ . One would be tempted to explain this as an overshoot response of the Setra 237 transducer system which is underdamped, however, the overdamped Setra 239 transducer system exhibits a more severe overshoot in transient unsteadiness. This problem is being investigated.

Preliminary results tend to indicate a quasi-steady behavior for very low frequency sinusoidal variations in the freestream velocity where the dynamics of the pressure system is less suspect. Quasi-steady in this sense does not include phase parity. Figure 9 is a surface plot showing the time history of the unsteady pressure distribution over the Wortmann FX63-137 at 16 degrees angle of attack. The mean chord Reynolds number is 80,000 the velocity amplitude ratio,  $A$ , is 19%, and the Strouhal number,  $St$ , based on aerodynamic chord and mean freestream velocity is 0.01 ( $f = 0.5 \text{ Hz}$ ). The minimum pressure coefficient development is 180 degrees out of phase with the freestream velocity, that is, maxima in the freestream variation occur at the  $C_p$  minima. As expected, the laminar separation bubble indicated by the pressure plateau near the leading edge of the airfoil lengthens with decreasing freestream velocity and vice-versa. One interesting observation of these results is that the flow remains attached even when the minimum Reynolds number in the cycle is 65,000. Steady data from Huber [2] shows that the flow is separated over the upper surface for a Reynolds number of 70,000 and an angle of attack of 16 degrees. However, his tests were performed by the polar method where the angle of attack was changed in a fixed freestream velocity. The present test is essentially a "characteristic" method, as defined by Schmitz [4], where the freestream velocity varies while the angle of attack remains fixed. The observed phenomenon is not the result of the imposed unsteadiness however, but has been observed in steady flow. The aerodynamic response of this airfoil to the imposed unsteadiness is not unexpected since the time scale of the airfoil is much less than the time scale of the flow as evidenced by the low Strouhal number. Data at higher frequencies is less certain due to the pressure measurement system dynamics.

Tests are underway to better understand and optimize the measurement of pressure in these unsteady flows. The current data has provided insight to the parameters to be addressed. Although methods to compensate for transducer lag and overshoot may be found, confidence levels in unsteady pressure data will be acceptable only when independent verification of observed phenomena are completed. The use of thermal or laser anemometry and flow visualization will aid in the interpretation of unsteady pressure data.

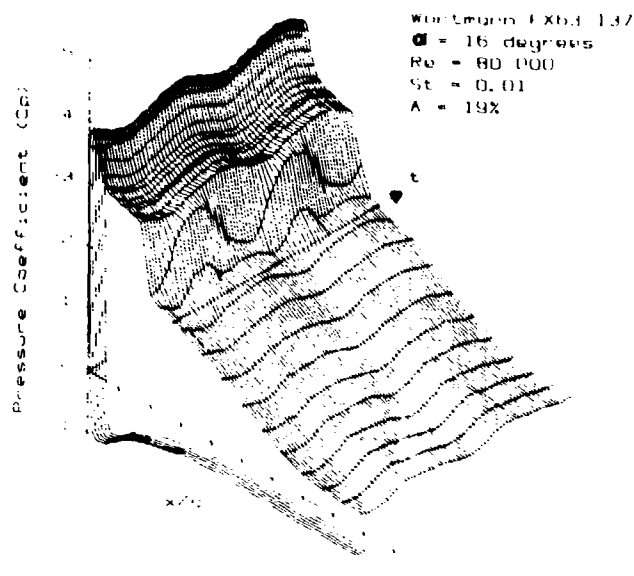


Figure 9. Pressure Distribution Variation

#### CONCLUSIONS/RECOMMENDATIONS

A device to produce streamwise velocity unsteadiness has been designed for the subsonic wind tunnel. The system and associated support hardware allows periodic and transient waveforms for the study of low Reynolds number airfoils. Periodic waveforms for frequencies less than 5 Hz can be obtained with very low harmonic distortion. The suppression of higher harmonics in sinusoidal velocity variation by modification of the shutter driving function based upon a Fourier analysis has been demonstrated. The use of the 6502 processor with 180 parts per cycle output was found to provide adequate control of the shutter mechanism. Additionally, the 6502 coupled with the PDP 11/23 data acquisition system allows the design of sophisticated conditional based experiments necessary in unsteady work.

The design of experiments for use with the unsteady flow generator require special attention to the dynamic behavior of instruments commonly used in steady situations. Pressure data will have to be supplemented by other methods such as thermal anemometry and visualization before the nature of the pressure distributions can be validated. The problems encountered here are not uncommon, but do illustrate the difficulties present when adapting steady experiments to unsteady conditions.

The usefulness of pressure distribution data in providing aerodynamic parameters and boundary layer characteristics warrants further refinement and analysis of the present system. Higher frequency oscillations or faster transients may ultimately require surface pressure transducers at the expense of spatial resolution. Future experiments must address the problems of high frequency freestream oscillations. Detailed boundary layer studies should give further

insight to the aerodynamic characteristics of low Reynolds number airfoils.

#### NOMENCLATURE

A	amplitude ratio, $\Delta u/U$
c	aerodynamic chord m
Cp	pressure coefficient, $1 - Q/Q_\infty$
f	circular frequency, driving frequency, Hz
P	pressure, Pa
Q	dynamic pressure, Pa
Re	Reynolds number based on chord
St	Strouhal number $fc/U$
t	time, s
THD	total harmonic distortion
$\Delta u$	fluctuating velocity, m/s
U	mean freestream velocity, m/s
x	distance, m
$\alpha$	angle of attack, deg
$\beta$	shutter displacement, rad
$\phi$	spectral density function, $m^2/s^2$

#### Subscripts

o	total pressure
s	static pressure
$\infty$	freestream quantity

#### ACKNOWLEDGEMENT

This work is supported by the Office of Naval Research under contract No. N00014-83-K-0239.

#### REFERENCES

1. Simpson, R.L., Sallas, J.J. and Nasburg, R.E., "Tailoring the Waveform of a Periodic Flow with a Programmable Damper," Journal of Fluids Engineering, Vol. 100, Sept. 1978, pp. 287-290.
2. Huber, A.F., "The Effects of Roughness on an Airfoil at Low Reynolds Numbers," M.S. Thesis, University of Notre Dame, May 1985.
3. Hougen, J.O., Martin, O.R., and Walsh, R.A., "Dynamics of Pneumatic Transmission Lines," Control Eng., Sept. 1963, p. 114.
4. Schmitz, F.W., "Aerodynamics of the Model Airplane, Part 1 Airfoil Measurements," Translated from German (1941) in 1967 by Redstone Scientific Information Center, Alabama.

ON EFFECTS OF THREE-DIMENSIONAL ROUGHNESS ON  
TRANSITION AND RECEPTIVITY TO DISTURBANCES

T. C. Corke and M. V. Morkovin

Fluid Dynamics Research Center  
Mechanical and Aerospace Engineering Department  
Illinois Institute of Technology  
Chicago, IL 60616

ABSTRACT

Distributed roughness with a nominal height  $k$  in a laminar boundary layer with displacement thickness  $\delta^*$  is known to lead to early non-Tollmien-Schlichting-Schubauer (TS) transition when  $k/\delta^*$  exceeds unity in non-accelerated flows. But could the commonly occurring milder roughness enhance the regular phase-conditioned TS mechanisms and also lead to early transition? The new affirmative answer rests on extensive hot-wire explorations and smoke-wire visualization of flow over smooth and rough walls. The effects appear to be three-fold. First, the low-inertia fluid in the valleys between the roughness particles evidently respond more readily to free-stream disturbances. Second, once the TS fluctuations commence, they grow at a faster rate than those over a smooth wall, and exceed substantially the theoretical rate,  $-\alpha_1$ , of normal TS modes. Here the randomness of the roughness, on the scale of 1/60th of the TS wavelength, does not impede the tuned, self-excited TS formations. Thirdly, the faster growing 2D wavefronts exhibit earlier secondary subharmonic instabilities and breakdown and hence, turbulence. The faster growth is not due to destabilization of the mean profile by the roughness, but rather it merely displaces outward the mean profile found over the smooth wall and increases somewhat its thickness. The total evidence points to the combined effect of spatial features of the rough wall boundary layer which makes it more receptive to external free-stream disturbances, especially pressure fluctuations. There is no reason

why the characteristics of the distributed roughness should not have important influence under flow conditions different from those in this experiment, for example at supersonic speeds, or with relevance to low Reynolds number airfoils, in favorable pressure gradients at TS subcritical conditions, with higher relative roughness heights. The demonstrated susceptibility to free-stream disturbances is likely to also be involved in the TS-bypass transition to turbulence observed by others.

## INTRODUCTION

Two-dimensional (2D) isolated roughness of height  $k$  (e.g. a trip wire) is known [1] to accelerate transition to turbulence by bringing about locally separated profiles over a distance of  $40k$ - $50k$ . These extra unstable profiles lead to overgrowth of the 2D Tollmien-Schlichting-Schubauer (TS) waves, secondary three-dimensional (3D) instability [2,3] and the efficient generation of turbulence. For a 3D isolated roughness the separated region is short, on the order of  $5k$ , and definitely stable for  $Re_k$  below 300. At higher  $Re_k$  the obstacle sheds high-frequency hairpin vortices [4] the connected loops of which are lifted toward the edge of the boundary layer. In a Blasius layer [5], as  $Re_k$  values approach 550-600, depending on  $x_k$ , the interaction between the stretching and the interlacing arms of the hairpin eddies with the horseshoe vortex (which trails from the upstream face of the obstacle) leads to intermittent turbulent bursts, at first rather far upstream. Here  $x_k$  is the downstream location of the roughness element relative to the boundary layer origin, which correlates with the displacement thickness,  $\delta^*$ , of a normal growing Blasius layer. The incubation distance from the offending roughness to the point of transition to turbulence,  $x_{tr}$  is initially very long, often  $x_k$  to  $4x_k$ . As  $Re_k$  increases further,  $x_{tr}$  moves rapidly toward  $x_k$ ; for an increment of only 10 in  $Re_k$ , the forward movement of  $x_{tr}$  may cover more than half the distance to  $x_k$ ; see Tani [5]. Spanwise rows of isolated 3D roughness brings about transition by this non-TS mechanism less effectively than the TS-based action of 2D trip wires with same  $k$  (except for Mach numbers in excess of about 2, where effectiveness is reversed). In both cases, the presence of locally separated regions

makes the onset of transition sensitive to free-stream disturbances, especially to pressure fluctuations [4].

Similar free-stream sensitive, long induction distances for distributed 3D roughness make judgment of cause and effect (as well as schemes of parameter correlations) very difficult. Up to the recent experiments of Corke, Bar Sever and Morkovin (CBSM) [6], the road to transition associated with distributed roughness was also thought to bypass the known (linearized) instability process like TS waves, e.g. Leventhal and Reshotko (LR) [7] and Smith and Clutter [8]. Indeed when  $k$  exceeds  $\delta^*$  at lower Reynolds numbers, low frequency broad-band fluctuations grow steadily in the BL. These fluctuation cannot be distinguished from low Re turbulence.

In this paper we will call on some of the results of CBSM to bring out the key features of transition over mild distributed roughness. In addition evidence will be presented which strongly points to an increased receptivity to stochastic free-stream disturbances of these roughened boundary layer flows.

## RESULTS

The experiments were conducted on the back wall of the IIT Two-Dimensional Flow Wind Tunnel. The test section and laboratory coordinate system are shown in the schematic in Figure 1. The false floor and ceiling in the test section were part of a special treatment to inhibit the growth of any disturbing corner flows. By that arrangement, a slightly higher pressure in the measurement section, set-up by a perforated grid at its downstream end, drew off fluid through small gaps in the corners. The use of the back wall removed any influence of freestream disturbances interacting with the thin boundary layer at a plate leading edge.

Smoke-wire flow visualization provided global information on the possibility of spanwise-preferred upstream breakdown locations and configurations and on the existence of TS wave fronts. It was used extensively for early diagnostics. As shown in Figure 1, the smoke wire was placed parallel to the measurement wall. The height of the wire away from the wall was adjusted to be close to the critical layer, where we might best mark the TS waves. The sheet of smoke

streaklines was illuminated by a two-dimensional plane of light parallel to the wall and viewed normal to the wall. It should be remarked that the wake of the thin (0.1mm diameter) smoke wire in a boundary layer modifies the profile for about  $8\delta$ - $10\delta$ . Thus the smoke registers somewhat increased disturbances compared to those in the absence of the wire. However, measurements by CBSM document no difference in the amplification rates of the TS frequencies due to the presence of the smoke wire.

To shed new light on the delicate question of the degree of contamination of the distributed-roughness effect by the quasi-two-dimensional leading edge of the abrasive paper, two configurations of the 1.04 mm particle roughness were run: protruding and recessed. In the recessed (R1) configuration the upstream smooth flat wall was lined up with the peaks of the highest roughnesses; in the protruding (R2) configuration the wall was lined up with the substrate of the same roughness sheet. The reference measurements were made on the smooth (SW) configuration of the aligned smooth wall.

All configurations were run at two tunnel speeds  $U_0 = 4.8\text{m/s}$ , designated by L for low, and  $U_0 = 6.2\text{ m/s}$ , designated by H for high. As can be seen from the comparative Table I the roughness commenced always past the critical Reynolds number of about 500, a distinct difference from the LR experiments. This choice was prompted by our requirement that there be a self-similar profile at the start so that more meaningful comparisons could ensue.

Using the same commercial sandpapers as LR, the leading edge of the recessed (R1) and the protruding (R2) graining matrix of the paper was placed at initial values of  $(k/\delta^*)$  of about 0.5, at post-TS-critical  $Re_\delta^*$  values from 700 to 875. Hot-wire and smoke-wire explorations of the boundary layers in roughness conditions 1 and 2 were compared with those over a smooth wall (3) under otherwise identical conditions. Figure 2 discloses first the primary TS wave formations typically observed in the rough cases, shown for the rough wall condition (R1) in the bottom of the figure, and at the comparable Reynolds number in the smooth wall at the top of the figure. For the rough cases, these waves are followed by early triangular breakdown patterns corresponding to secondary subharmonic instabilities [9] and by turbulent regions almost

immediately downstream. These appear in the bottom portion of the lower photograph in Figure 2 and in the enlarged view at a different instant in time over the rough wall in Figure 3.

When compared to the smooth wall layers for the same  $Re_\delta^*$  values, the fluctuations in the boundary layers over the rough walls (a) were substantially higher, (b) grew at a faster rate than those over the smooth wall and (c) exhibited early subharmonic breakdowns. Evidently the randomness of the roughness on the scale of the nominal grains  $k = 1.04$  mm (see reflecting specks in the background of Figure 3) does not impede the tuned, self excited TS formations on the order of 60 mm.

Figure 4 displays on a linear scale the spectral development in  $x$  at the maxima of  $u'$  (at which  $y \sim \delta^*$ ) for a free stream of 4.8 m/s over the recessed sandpaper which commenced at  $x = 48$  cm. The vertical distributions of the streamwise velocity fluctuations corresponding to these and other intermediate measurement stations are shown in Figure 5. The spectra represents sampling and averaging over 3 minutes, i.e. over more than 6150 net TS wavelengths and were essentially repeatable on a given day. The frequencies at branches  $B_I$  and  $B_{II}$  of the neutral curve which encloses the region of 2D TS amplification are indicated in Figure 4 for stations at 119 and 174 cm. The dashed lines represent spectra at the edge of the BL; at  $x = 119$  this spectrum represents well the free stream disturbances with  $u'/U_\infty$  of approximately 0.08%. The 30 Hz peak clearly corresponds to the most amplified 2D TS wave which past  $x = 144$  passes energy to the subharmonic. The growth of the peak at 26 Hz (especially within the approximately 1.5 wavelengths between the 136 and 146 stations) exceeds substantially the theoretical rate of normal TS modes. Nonlinearity and secondary instabilities were undoubtedly present over part of the samples beyond  $x = 144$ ; intermittent turbulence is indicated for  $x = 174$  by the broad rises below 15 Hz and above 30 Hz.

Those growths manifested in Figure 4 which are not clearly associated with secondary instability are replotted in Figure 6 for several fixed frequencies in the form of  $\log(u'(f)/u'_0(f))$  where  $u'(f)$  are the spectral fluctuation levels at  $x = 119$  where  $Re_\delta^*$  is 980. Another data set for the recessed configuration marked R1L in Figure 6 was obtained several weeks earlier over the same  $Re_\delta^*$  range from 980 to 1050. The data set marked R2L was obtained several months later over

the protruding roughness matrix for  $Re_{\delta}^*$  from 850 to 990. The non-dimensionalized frequencies associated with the instability growth for these different wall conditions is presented along with the neutral stability curve for a Blasius layer in Figure 7.

The straight broad line in Figure 6 relates the roughness-condition rates to smooth conditions; it represents growth at a constant spatial amplification rate  $-\alpha_1 \delta^*$  of 0.006 which corresponds to the maximum amplification attainable by a passively growing normal mode in a Blasius layer at  $Re_{\delta}^*$  of 1000. The overall  $u'/u'_0$  growths for the smooth wall between  $Re_{\delta}^*$  of 970 and 1110 remained below this broad line, approaching or exceeding the slope slightly at the higher  $Re$  value; furthermore, the initial  $u'_0(f)$  values over TS frequency range were approximately six times smaller in the smooth-wall runs.

#### DISCUSSION

Unquestionably, the fluctuations in the roughened BL for the same  $Re_{\delta}^*$  are substantially higher and grow at rates significantly larger than those over the smooth wall in presence of the same free-stream disturbances - and significantly larger than amplification rates of TS normal modes not subjected to additional disturbances. Neither of these two observations can be due to destabilization of the mean profile by the roughness; both LR and CBSM found that irregular roughness typical of abrasive papers in essence merely displaces the mean velocity profile found over the smooth wall outward and increases somewhat its thickness. The frequencies at which amplification occurs is within the range expected from Blasius boundary layers at these Reynolds numbers. The maximal  $Re_k$  values in the experiment, those at the leading edge of the matrix, ranged from 101 to 143, far below the critical values for isolated roughness at which unsteady motions may commence in its wake. The total evidence points to the combined effect of special features of the rough BL and free-stream disturbances, already noted for isolated 2D and 3D roughnesses in the Introduction.

Two special features of boundary layers over rough surfaces are:

- A. irregular streamwise vorticity structures trailing from the higher roughness peaks, structures which may interact (even amalgamate) when disturbed externally; and
- B. locally separated regions downstream of the peaks and generally lower-inertia fluid in the irregular valleys between peaks, which is susceptible to external disturbances, especially pressure fluctuations.

In view of these features, a higher receptivity to free-stream disturbances could be expected than over smooth wall, without local separations.

The literature on receptivity has been mostly silent concerning the expected early growth rates of stimulated TS wave relative to the theoretical rates  $-\alpha_1$  of the TS normal modes past the dominant region of excitation and seeding. When Kendall [10] reported that the rate of his turbulence-excited TS waves exceeded  $-\alpha_1$  it was a surprise. In the more orderly case of receptivity to unsteady pressure gradients, Nishioka and Morkovin [11] measured very high rates of growth of  $u'_{\max}$  in the seeding region exceeding  $\alpha_1$  by factors in excess of 10. Furthermore, the capability of harmonically heated wall strips of Liepmann et. al. [12] to counteract an existent growing TS wave depends intrinsically on the receptivity of the BL to these artificial disturbances which must generate  $180^\circ$  out of phase TS wave at rates in excess of  $-\alpha_1$ !

As a solution of the linearized Navier-Stokes equations the fluctuations in the BL must consist of superposed fields  $u' = u'_f + u'_d + u'_{TS}$  where  $u'_f$  is the external forcing field after it penetrates the BL (the non-homogeneous particular solution),  $u'_d$  the sum of the decaying continuous and discrete normal modes [13] and  $u'_{TS}$  the seeded, growing normal TS mode. The fields  $u'_d$  and  $u'_{TS}$  represent the homogeneous solutions which are needed so that the whole field  $u'$  satisfies all the boundary conditions. The growth in  $x$  of  $u'_{TS}$  in its early formation depends on the non-homogeneous forcing  $u'_f(x)$  and there is no reason why it could not exceed  $-\alpha_1$  in the region of seeding. The rate  $-\alpha_1$  of

the homogeneous solution is appropriate only when forcing has ceased. Schubauer and Skramstad [14] and others investigating TS amplification rates seeded their  $u'_{TS}$  by a vibrating ribbon so that the signal dominated the other disturbances. In the region of their measurements contributions from any additional seeding due to free-stream disturbances were dwarfed by the initially large, passively amplified normal mode. The measured growths then corresponded to  $-\alpha_1$ . However, in "natural" spectra such as those of Figure 4, without special regular excitation, the contributions from the free-stream disturbances can cause growth in excess of  $-\alpha_1$ . Incidentally, the preceding formulation show that receptivity is more a mechanism than a simple transfer function or even a simple output-input ratio occasionally mentioned in the literature. An acoustic forcing function  $u'_f$  can seed  $u'_{TS}$  waves which interfere negatively over part of the region of active receptivity. Evidently the net forcing effect of external disturbances in Figure 6 is reinforcing over the whole region.

There is no reason why the characteristics (A) and (B) of the distributed roughness should not have important influence under flow conditions different from those in the CBSM experiments, e.g., at supersonic speed, at TS subcritical conditions, with higher relative roughness, etc. Even very small roughness on walls with concave curvature should intensify substantially the Gortler centrifugal instability. The experiments of Wilkinson and Malik [15] demonstrate conclusively that small 3D roughness provides perturbation of streamwise vorticity on which cross-flow and Gortler feed. For the important case of higher  $(k/\delta)$  values. The higher susceptibility of the roughened boundary layer to free-stream disturbances, documented in Figures 2-6, should not only be present but should be strengthened. As a result of the higher levels of perturbation within the boundary layer, local and/or instantaneous formations of vorticity distributions are likely to develop which should be very unstable to the various vorticity-stretching and rotating mechanisms inherent in the nonlinear inertial 3D terms  $\vec{\omega} \cdot \text{grad}(\vec{V})$  in the vorticity equation, viscous or inviscid. These dynamic 3D vorticity interactions should lead to turbulence more directly, thus bypassing the known primary linear instabilities of orderly boundary layers such as the TS modes. In this sense, the

demonstrated susceptibility to free-stream disturbances is likely to be involved in the bypass transition of Leventhal and Reshotko [7], Smith and Clutter [8] and others, discussed earlier. The new view of the nature of distributed-roughness effects described here seems therefore relevant across the speed and roughness ranges.

#### CONCLUDING REMARK

The above interpretations underscore the difference between the simple concepts associated with the development of TS waves downstream of a vibrating ribbon and the concepts needed to understand "natural" transition (artificially unstimulated). In particular when we have excitation due to stochastic free-stream disturbances, we must account for the possibility that besides the TS self-amplification there is a continuous influx of energy spread over the the flow region and not localized as in the case of a vibrating ribbon. The efficiency of the boundary layer filter-amplifier to make use of this continuous influx in its development, which was exhibited in the presence of the distributed roughness when  $k/\delta^*$  was moderate, demonstrates this effect.

#### ACKNOWLEDGEMENTS

The work on which Figures 1-7 were based was supported by the U.S. Army Research Office under Contract SFRC No. DAAG 29-81-k-0012.

#### REFERENCES

1. Klebanoff, P. S. and Tidstrom, K. D.: Mechanism by Which a Two-Dimensional Roughness Element Induces Boundary Layer Transition. Phys. Fluids, Vol. 15, No. 7, pp. 1173-1188, 1972.
2. Hama, F. R. Long, J. D. and Hegarty, J. C.: On Transition from Laminar to Turbulent Flow, J. Appl. Phys., Vol. 18, pp. 388, 1957.
3. Perry A. E. and Chong, M. S.: On the Mechanism of Wall Turbulence, J. Fluid Mech. Vol 119, pp. 173-217, 1982.
4. Norman, R. S.: On Obstacle-Generated secondary Flows in Laminar Boundary Layers and Transition to Turbulence, PhD Thesis MMAE Department, Illinois Institute of Technology, Chicago, IL, 60616, Dec. 1972.

5. Tani, I.: "Effect of Two-Dimensional and Isolated Roughness on Laminar Flow," Boundary Layer and Flow Control, Vol. 2, pp. 637-656, Lachmann, G. V., ed., Pergamon Press, 1961.
6. Corke, T. C., Bar Sever, A. and Morkovin M. V.: Experiments on Transition Enhancement by Distributed Roughness, submitted to Phys. Fluids.
7. Leventhal, L. and Reshotko, E.: Preliminary Experimental Study of Disturbances in a Laminar Boundary Layer due to Distributed Surface Roughness. Case Western Reserve University Report FAS/TR-81-155, 1981. (Also Leventhal, L., M. S. Thesis, Case Western Reserve University, 1981)
8. Smith A.M.O. and Clutter D.W.: The Smallest Height of Roughness Capable of Affecting Boundary-Layer Transition in Low-Speed Flow, J. Aerospace Sciences, Vol. 26, p. 229, 1959.
9. Herbert, Th.: Analysis of the Subharmonic Route to Transition in Boundary Layers, AIAA Paper 84-0009, 22nd Aerospace Sciences Meeting, Jan., 1984.
10. Kendall, J. M.: Experiments on the Generation of Tollmien-Schlichting Waves in a Flat Plate Boundary Layer by Weak Free-Stream Disturbances, AIAA Paper 84-0111.
11. Nishioka, M. and Morkovin, M. V.: Boundary-Layer Receptivity to Unsteady Pressure Gradients - Experiments and 1984 Overview, submitted to J. Fluid Mech.
12. Liepmann, H. W. and Nosenchuck, D. M.: Active Control of Laminar - Turbulent Transition, J. Fluid Mech., Vol. 18, 1982, pp. 201-204.
13. Salwen, H. and Grosch, Ch.E: The Continuous Spectrum of the Orr-Sommerfeld Equation. Part 2 Eigenfunction Expansions, J. Fluid Mech. Vol. 104, 1981, pp. 445-465.
14. Schubauer G. B. and Skramstad, H. K.: Laminar-Boundary-Layer Oscillations and Transition on a Flat Plate, NACA Tech. Rept. No. 909, 1948.
15. Wilkinson, S. P. and Malik, M. R.: Stability Experiments in Rotating - Disk Flow, AIAA Paper 83-1760.

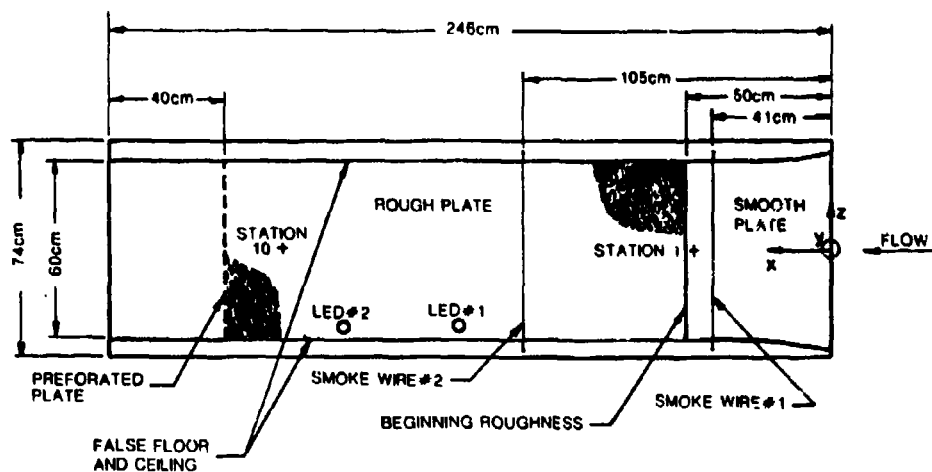


Figure 1. Side View of Test Section Showing Velocity Measurement Stations and Smoke-wire Placement.

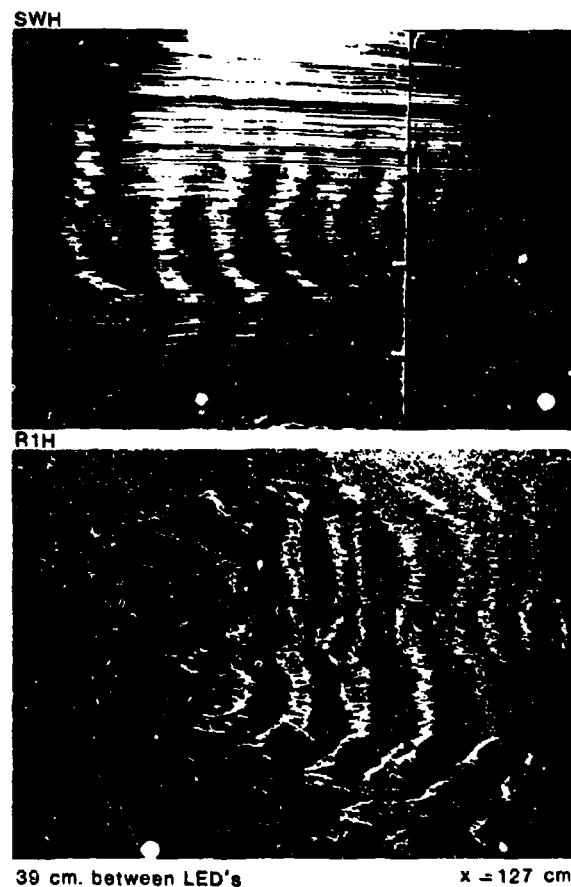
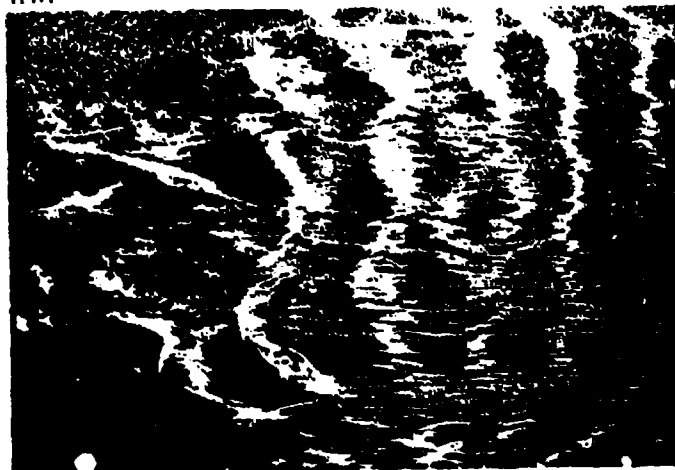


Figure 2. Visual Record of Boundary Layer Flow Over Smooth Wall (top) and Rough Wall #1 (bottom) for Higher Velocity Condition.

R1H



39 cm. between LED's

$x = 127$  cm.

Figure 3. Enlarged Visual Record of Boundary Layer Flow Over Rough Wall #1 for Higher Velocity Condition.

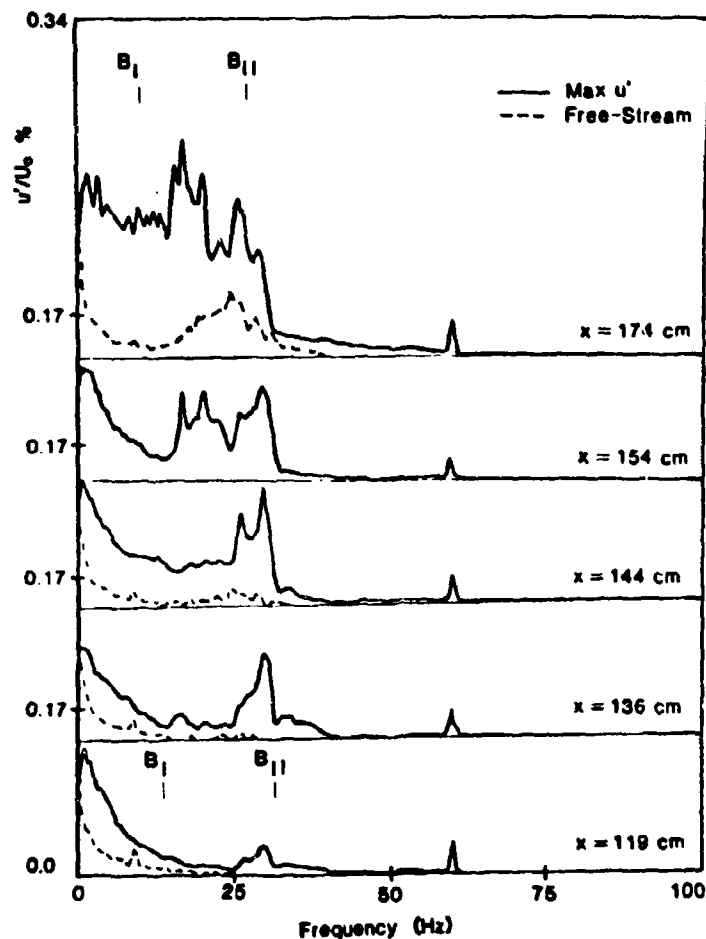


Figure 4. Streamwise Development of Spectra of Streamwise Velocity Fluctuations Along Rough Wall #1 for Lower Velocity Condition.

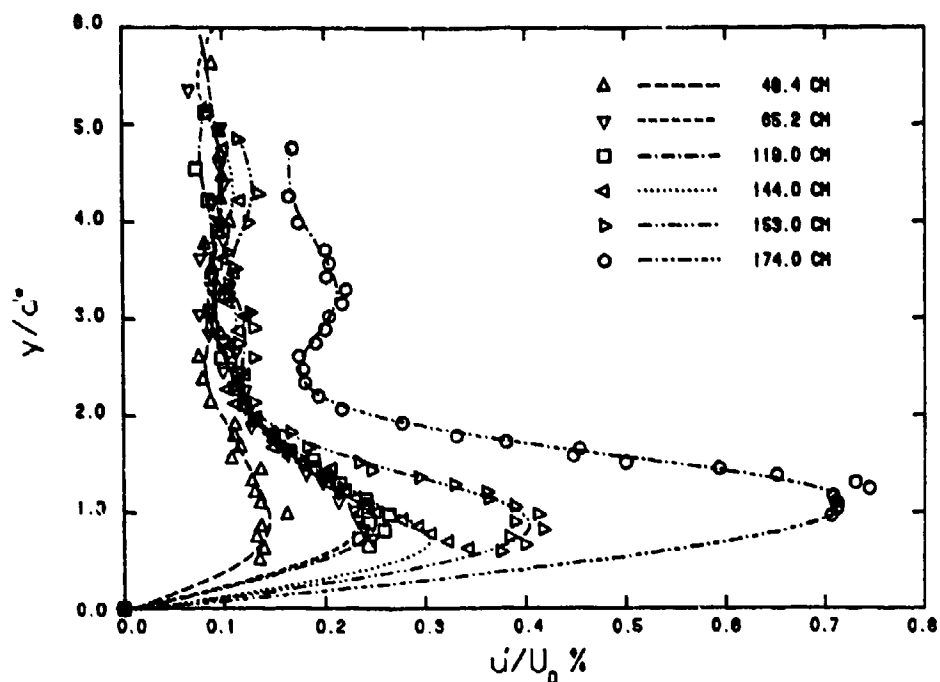


Figure 5. Vertical Distributions of Total Streamwise Velocity Fluctuation Energy at Different Stations Along Rough Wall #1 for Lower Velocity Condition.

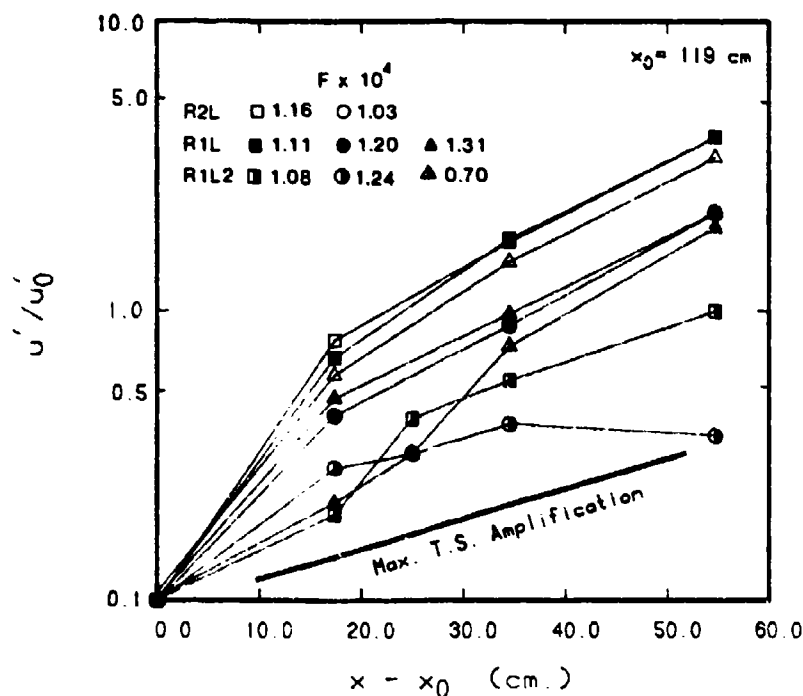


Figure 6. Disturbance Growth Characteristics of Boundary Layer Over Rough Walls and Comparison to Maximum Growth Rate in Smooth Displaced Blasius Layer.

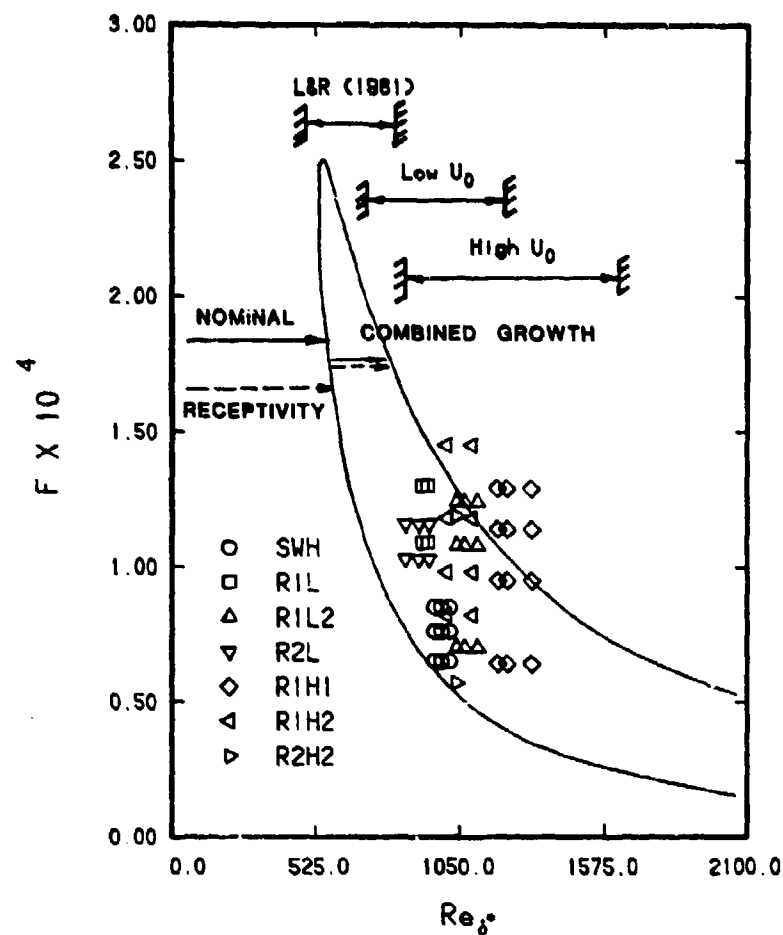


Figure 7. Distribution of Amplified Frequencies Over Rough Walls on Blasius Neutral Stability Curve.

TABLE I  
Comparison of Flow Parameters

Exp.	Rough. No.	$Re_{\delta_0}^*$	$Re_{k0}$	$k/\delta_0^*$	$(Re_{\delta}^*)_{TS}$	$(Re_{\delta}^*)_{TURB}$
Current	1	859	131	0.51	1025-1170 <sup>+</sup>	1240-1380 <sup>+</sup>
Current	2	875	143	0.50	961-1030 <sup>+</sup>	1060-1100 <sup>+</sup>
Current	1	725	101	0.48	915-990 <sup>+</sup>	-
Current	2	704	101	0.44	760-820 <sup>+</sup>	-
L & R	-	285 <sup>*</sup>	314	1.48	-	Below 490 <sup>**</sup>
L & R	-	480 <sup>*</sup>	192	0.88	-	Below 600 <sup>**</sup>

<sup>+</sup> Observed ranges.

<sup>\*</sup> Assuming  $U = 6\text{m/s}$ ,  $\nu = 1.48 \times 10^{-5}\text{m}^2/\text{s}$ .

<sup>\*\*</sup> Based on undisturbed laminar flow.

THE EFFECT OF TRIP WIRE ROUGHNESS ON THE PERFORMANCE  
OF THE WORTMANN FX 63-137 AIRFOIL AT LOW REYNOLDS NUMBERS

Arthur F. Huber II  
and  
Thomas J. Mueller

Department of Aerospace and Mechanical Engineering  
University of Notre Dame  
Notre Dame, Indiana 46556

ABSTRACT

An experimental investigation was conducted on the performance and boundary layer characteristics of the Wortmann FX 63-137 airfoil with and without trip wire roughness. Data were obtained through use of a three-component strain gage force balance and static pressure measurement equipment at a test Reynolds number of  $R_c = 100,000$ . Emphasis was placed on determining the effect of trip wire placement and size on such performance parameters as  $(C_l/C_d)_{\max}$  and  $(C_l^{3/2}/C_d)_{\max}$ . Prediction of transition location by the criterion due to Tani and Gibbings was found to have limited application. In most cases airfoil performance was degraded, but in some instances minimum drag was reduced and maximum lift to drag ratio increased.

INTRODUCTION

When the chord Reynolds number ( $R_c$ ) drops below 500,000, significant problems develop pertaining to the management of airfoil boundary layers. Lissaman states that as a general criterion there exists a critical Reynolds number of about 70,000 below which airfoil performance is quite poor and above which dramatic improvements are observed [1]. However, airfoil performance between this critical value and a Reynolds number of 500,000 still presents problems that can be directly traced to the existence of such phenomena as boundary layer separation and transition. Also, there exists the special, but not uncommon, case that separation is followed by reattachment of the flow forming what is known as a "separation bubble". The presence of such a flow structure and its behavior can have great influence on airfoil performance.

Unfortunately, a basic understanding has yet to be developed for low Reynolds number boundary layer behavior under the influence of airfoil-type pressure gradients. For this reason, design of airfoils for low Reynolds number applications remains somewhat of an imperfect science. Naturally, practical aircraft design efforts require information that is indicative of what performance levels can be expected of a particular airfoil or wing. Such information is needed not only for smooth sections in benign environments, but also for airfoils operated under conditions of wind shear, flow unsteadiness, and accumulated roughness. Unfortunately, credible data of use to the design engineer remains sorely lacking. The extreme sensitivity of the low Reynolds number flow regime to small disturbances results in

problems of an experimental nature which are not easily circumvented. However, if proper care is taken to eliminate or at least account for such phenomena, then meaningful results can be obtained [2].

It has been well known for some time that airfoil performance in the low Reynolds number regime can be greatly enhanced by the addition of devices which encourage transition. This process serves to energize the boundary layer and so prevent flow separation. Such devices include boundary layer trips (wires, tape strips, grit, etc.), surface suction or blowing, and vortex generators. However, the application of trips in particular may not always lead to performance improvement and instead can result in severe losses. The possibly detrimental effects of such surface disturbances take on added importance when one realizes that under normal operating conditions, wing sections will be contaminated with insect debris, dirt, and precipitation. Therefore, it is important that the effect of such disturbances be well documented so that realistic estimates of aircraft performance can be made in the design phase. It is the purpose of this study to investigate the performance of one airfoil operated at a low Reynolds number and under the influence of applied trip wire roughness. This work is part of a more extensive investigation dealing with the effects of a variety of surface roughness forms on airfoil performance and the interested reader is directed to Reference [3] for more information of the kind presented here.

#### ROUGHNESS CONSIDERATIONS

Investigations into roughness induced transition have in general attempted to form correlations involving the following parameters: roughness height ( $k$ ), roughness width ( $w$ ), local freestream velocity external to the boundary layer ( $U_e$ ), velocity at a height  $k$  but in the absence of roughness ( $u_k$ ), velocity gradient ( $du/dx$ ), roughness position ( $x_k$ ), location of transition ( $x_t$ ), roughness spacing, and boundary layer parameters such as the displacement thickness,  $\delta_1$ . Distinctions are often made about the type of roughness used (two or three-dimensional, geometry, etc.), the character of the movement of the location of transition, and the "efficiency" of a certain roughness type relative to others.

Of interest is whether such correlations can be used to fix the location of transition on an airfoil surface. Unfortunately, most studies in the roughness field have dealt almost exclusively with flat plates over which only the most mild, if any, pressure gradients have been applied. Hence, the applicability of such criteria for use with airfoils is questionable. Nevertheless, no other alternatives are available and so the existing criteria must be used.

A trip wire extended across a surface at a constant reference position is a two-dimensional type of surface roughness. For two-dimensional roughness heights below some critical value no effect on the natural transition location is noted. However, as the height is increased above the critical value for a given flow condition, transition will gradually move forward until it occurs at the

roughness element itself. Therefore, if the appropriate height is known, transition can be fixed at a particular position.

From their studies using flat plates, Tani and Sato [4] gave the following criterion for the Reynolds number required to cause transition at a trip wire roughness of height (i.e. diameter)  $k$ ,

$$R_{k,cr} = \frac{U_e k}{\nu} = 840. \quad (1)$$

Gibbings [5] further provided the more accurate value of 826 for this criterion and further work by these researchers [6] extended this relation to include the effects of a favorable pressure gradient.

$$R_{k,cr} = 826 \exp(-0.9 \Lambda_1). \quad (2)$$

Here,  $\Lambda_1$  is a non-dimensional pressure gradient term given as

$$\Lambda_1 = \frac{\delta_1^2}{\delta} \frac{dU}{ds}. \quad (3)$$

This expression has application for  $0 < \Lambda_1 < 0.3$ . Smith, Clutter and Darwin [7] provided a criterion similar to equation (1) for transition at a "spanwise wire", but gave it in terms of the roughness height velocity,  $u_k$ .

$$R_{k,cr} = \frac{u_k k}{\nu} = 300. \quad (4)$$

Other investigators have compiled similar criteria with the critical roughness Reynolds number varying between 200 and 400. For this study, the Tani-Gibbings criterion (equation (1)) was used since it only requires knowledge of the local freestream velocity. Thus, no determination of boundary layer velocity profiles is necessary in order to find  $u_k$ .

#### APPARATUS AND PROCEDURE

All experiments were conducted in the Notre Dame Aerodynamics Laboratory South Low Speed Wind Tunnel. (See Figure 1).

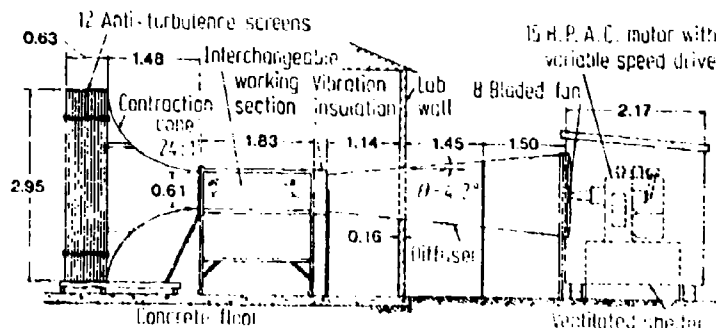


Figure 1. A Notre Dame Subsonic Indraft Wind Tunnel Arrangement (indicated lengths in meters)

This tunnel is of the in-draft, non-return type and has an operating range of between 7 and 35 m/s. The tunnel possesses a 24:1 contraction ratio and a square test section 0.61 m on a side and 1.83 m in length. An 11 kW AC induction motor is the prime mover exhausting to the atmosphere. Side plates mounted inside the test section permit airfoil measurements that approximate the two-dimensional assumption. This tunnel produces base flows whose turbulence intensities remain below 0.1% for frequencies greater than 10 Hz across its entire operating range. For more information on this facility, please consult References [8] and [9].

The airfoil section used for these experiments is the Wortmann FX 63-137 which has a design chord Reynolds number of 500,000. This airfoil is pictured in Figure 2. Two models were utilized each possessing a 15.24 cm chord, cast from a single mold, and made of epoxy which was wet sanded with No. 400 grit paper to ensure a smooth finish. The only difference between the two models is that one is fitted with forty static pressure orifices which are connected by way of tygon tubing to pressure sensitive equipment. This model permits the measurement of pressure distributions about the airfoil while the other is used for force balance and flow visualization experiments.

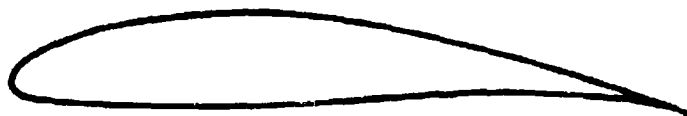


Figure 2. The Wortmann FX 63-137 Airfoil Section

The Notre Dame force balance is a three-component (lift, drag, moment) strain gage device capable of low magnitude load measurements with a high degree of accuracy and repeatability. This instrument is interfaced with an Apple microcomputer data acquisition system which, considering its voltage input resolution allows the measurement of drag forces as small as 0.0044 N.

Pressure distributions are measured through use of dual Scanivalve arrangement in which Setra System 339H electronic manometers are used to sense the static pressure at each airfoil tap. The tunnel freestream total and dynamic pressures are measured using a pitot-tube and a third electronic manometer. Data acquisition and reduction for these measurements is accomplished through use of a DEC PDP-11/23 minicomputer with 12-bit D/A and A/D conversion capabilities. The Scanivalves are switched by the computer from one orifice to the next using Scanivalve CTRL 10P/S2-S6 Solenoid Controllers.

The trip wires used in this study were K&S brand stainless steel

wires of uniform diameter. Listed sizes were checked using a digital caliper and in all cases were found to be accurate. A roughness arrangement consisted of both a trip wire and a layer of Scotch brand double-stick tape which was used to secure the wire to the airfoils' surface. This brand of tape possesses a thickness of 0.076 mm and a width of 6.35 mm. Also, being transparent, the tape can be punctured to permit pressure measurements at those taps which it covers. The roughness height to chord ratios ( $k/c$ ) of the wire-tape combinations presented herein are 0.583% and 0.300% which correspond to wire diameters of 0.81 and 0.38 mm respectively. Naturally, given the added height of the tape strips, the height to width ratios ( $h/w$ ) are greater than one.

The procedure for applying the trip wires to the airfoil surface was as follows. Airfoil chord positions were marked across the full span of a model using a "photo-blue" pencil. These lines were accurately placed by reference to airfoil templates consisting of the sectional contour and chord position lines drawn by a computer-directed plotter. A double-stick tape strip was then placed along the airfoil surface at a particular chord-wise location and a trip wire "rolled" along the surface up to the leading edge of the tape. After a test, any applied roughness was removed and the airfoil surface checked to see if any adhesive still remained on the surface. Occasionally, the surface was wiped with a towel soaked with alcohol to ensure a smooth, clean finish.

While force balance data is to be presented for the effect of trip wires placed at a variety of airfoil surface locations, two positions are the focus of attention with regard to pressure distribution measurements. Results are shown for roughness located at the respective suction peak and laminar separation points for two different angles of attack. The two trip wire heights used represent values both larger and smaller than the heights calculated (by equation (1)) as necessary to bring transition to the roughness site.

## RESULTS

The experimental data collected as part of this investigation is presented in the following manner. First, the smooth airfoil's performance is documented with reference to force balance plots which show lift, drag, and moment coefficient variation with angle of attack. Then, the effects of roughness are summarized with respect to the variation of performance parameters with roughness location and height. Additionally, pressure plots are presented which demonstrate the effects of trip wire placement and size on such boundary-layer phenomena as separation and transition.

Figure 3 provides performance curves of the smooth Wortmann airfoil at a  $R_c$  of 100,000. The most dominant feature in these curves is the hysteresis loop which is of the "clockwise" or "high  $C_{lmax}$ " type and which extends across three degrees. The maximum lift coefficient ( $C_l = 1.54$ ) occurs at  $\alpha = 16^\circ$  and is followed by a gentle decrease in lift until an angle of attack of  $19^\circ$  at which the lift coefficient abruptly decreases to 0.96. This large drop in lift

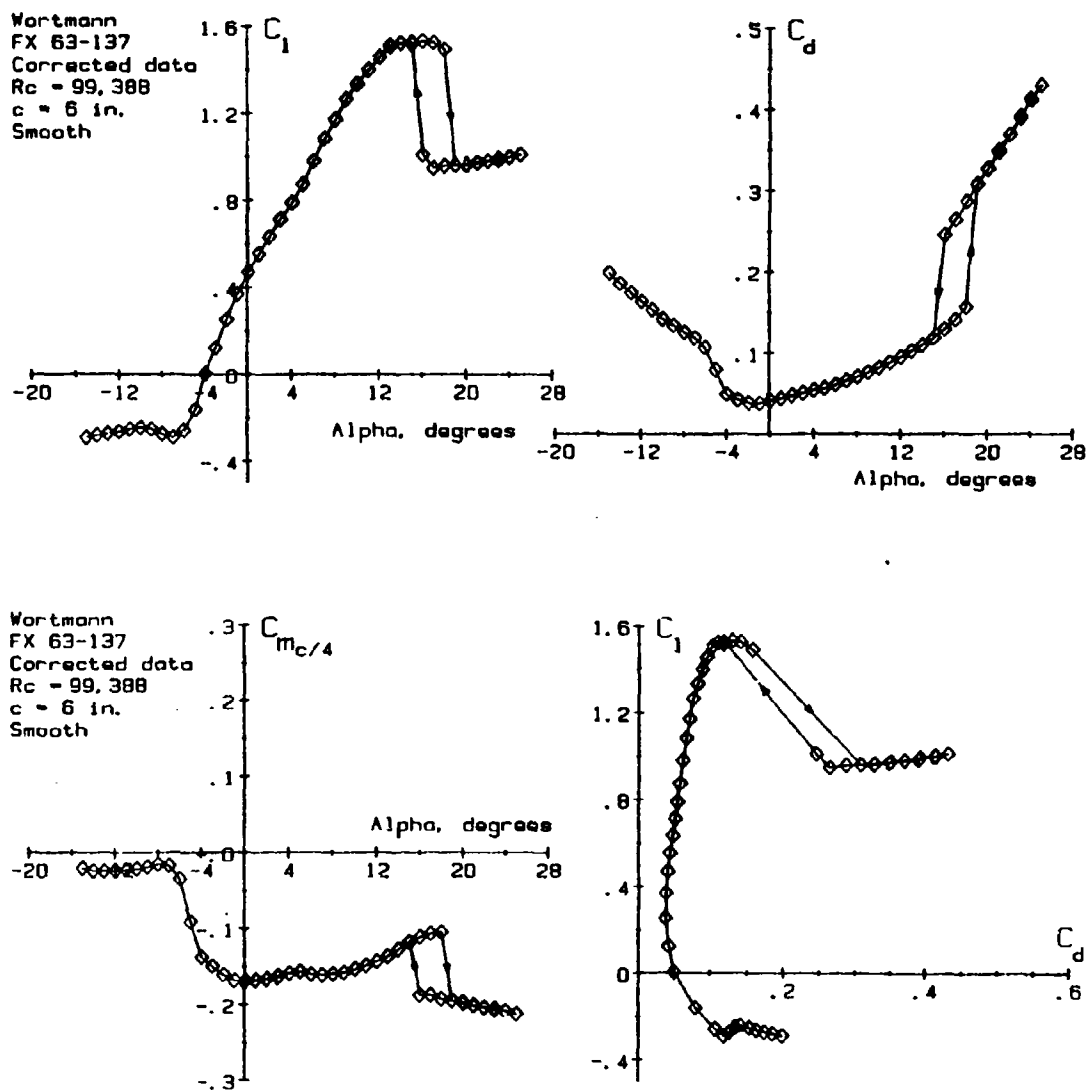


Figure 3. Performance Curves for the Smooth Wortmann FX 63-137 Airfoil at  $R_c = 100,000$  (force balance measurements)

is due to the bursting of a leading edge separation bubble which initially forms towards the rear of the airfoil at low angles of attack and moves forward with increasing incidence. Coincident with this forward movement of the bubble is its gradual decrease in length. However, the stall of this airfoil should not be characterized as one of the "leading-edge" variety since the gentle decrease in  $C_l$  past  $C_{lmax}$  indicates that turbulent separation is contributing to the drop in lift. Airfoils which possess a gentle degradation in lift are said to exhibit "tailing-edge" stall. Following the nomenclature used by Chappell [10], the stalling character of the Wortmann airfoil is known as a "combined" stall due to the occurrence of both turbulent separation and bursting of the leading edge bubble.

The abrupt drop in lift at  $\alpha = 19^\circ$  is accompanied by a large increment in drag and an increase in the magnitude of the quarter-chord moment coefficient. However, when the angle of attack is decreased again through  $19^\circ$  the lift, drag, and moment do not return to their original values until  $\alpha = 15^\circ$  at which time the lift suddenly increases while the drag and moment decrease in magnitude. This occurrence completes the hysteresis loop and is due to the reattachment of the upper surface flow as the leading edge bubble reforms.

For angles of attack between  $-5^\circ$  and  $13^\circ$ , the lift variation is seen to be non-linear with slight "kinks" at 0 and 5 degrees. These "kinks" are more pronounced at  $R_c = 80,000$  and the airfoil's performance degrades to that of a flat plate at  $R_c = 70,000$  [3]. For higher  $R_c$ 's (i.e.  $> 150,000$ ), these kinks disappear and the airfoils' performance approaches that of the design condition. At a  $R_c$  of 100,000, the minimum drag coefficient is found in the region of maximum  $C_{l\alpha}$  and is 0.038 at  $\alpha = -2^\circ$ . The quarter-chord moment coefficient reaches its magnitude at  $\alpha = 0^\circ$  where its value is -0.170. While not apparent in the drag plot, the moment curve also demonstrates a "kink" at  $\alpha = 5^\circ$ . For angles of attack lower than  $\alpha = -5^\circ$ , the lower surface flow is fully separated.

From the drag polar one could infer that  $(C_l/C_d)$  and  $(C_l^{3/2}/C_d)$  attain relatively large values as compared to most airfoils operated in the low  $R_c$  regime. This inference is entirely correct as the maximum lift to drag ratio peaks at 16.63 for  $\alpha = 9^\circ$  and  $(C_l^{3/2}/C_d)$  reaches a value of 18.85 at  $10^\circ$  angle of attack.

In contrast to the smooth airfoil's performance curves of Figure 3 are the drag polar and moment curves of Figures 4, 5, and 6. These curves present data for the airfoils' performance with the smaller ( $k/c = 0.30\%$ ) trip wire applied at the leading edge, 3.0% and 30.0% chordwise locations respectively. As is evident from these figures, trip wire placement can have significant and varied effect on the airfoil's behavior.

The most prominent feature of Figure 4 is the lack of a hysteresis loop at high angles of attack. Instead, the stall character is gentle with a large drop in lift occurring only for the highest angle of attack tested ( $25^\circ$ ). Roughness located at the leading edge prevents separation bubble formation on the upper surface by causing transition of the flow almost immediately. While this alteration of the upper surface flow has little effect at angles of attack less than  $14^\circ$ , it results in the prevention of abrupt stall. Abrupt stall is averted since no separation bubble exists which can burst and so cause leading edge stall. Accordingly, turbulent separation continues to move forward as the incidence is increased providing a gentle stall up to very large angles of attack. It is only when the point of turbulent separation moves sufficiently close to the leading edge and/or the adverse pressure gradient becomes exceedingly severe that leading edge separation finally occurs. This explanation also accounts for why the moment coefficient fails to increase in magnitude at high incidence. Since less lift is produced

on the forward part of the airfoil due to the lack of a separation bubble, the center of pressure remains aft and the moment coefficient is large and negative. For this condition,  $C_{lmax}$  is slightly lowered

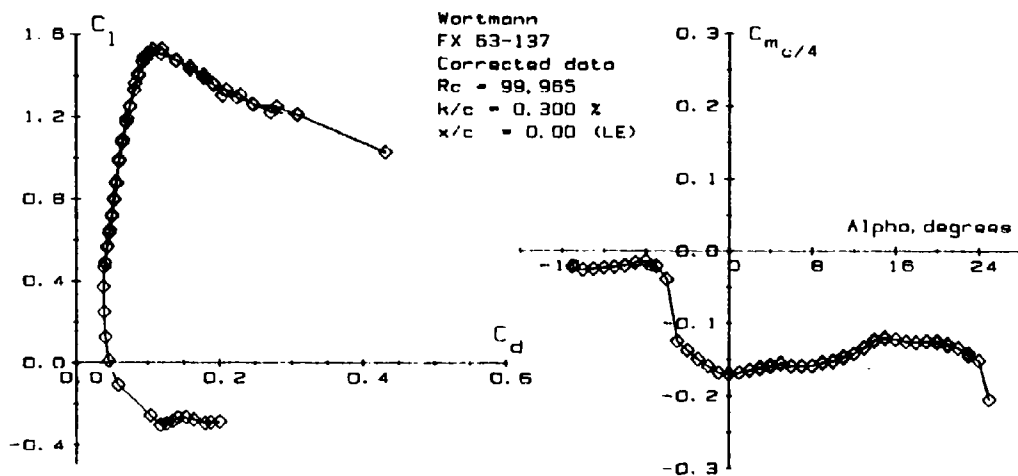


Figure 4. Performance Curves for the Wortmann Airfoil With a Trip Wire at the Leading Edge and  $k/c = 0.300\%$ .

with most other performance parameters ( $C_{dmin}$ ,  $(C_l/C_d)_{max}$ , etc.) improving slightly or remaining nearly the same. The larger trip wire reduces  $C_{lmax}$  further and increases  $C_{dmin}$ . In spite of this trend it would seem that definite benefits can be obtained with the use of leading edge roughness of the right size. Hysteresis can be eliminated, a gentle stall substituted, and little sacrifice made with regard to other performance parameters.

The case of a trip wire located at  $x/c = 3.0\%$  and with  $k/c = 0.30\%$  is shown in Figure 5. Here, the hysteresis loop reforms, but is

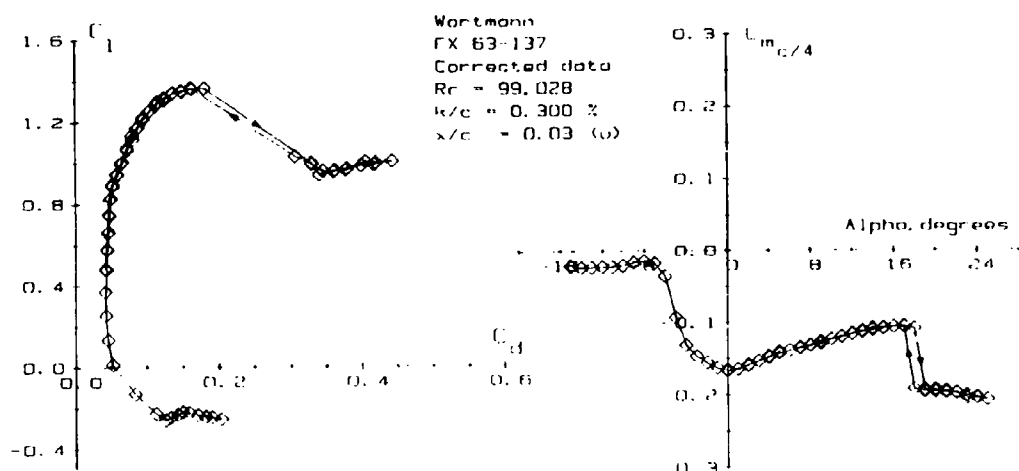


Figure 5. Performance Curves for the Wortmann Airfoil with a Trip Wire at  $x/c = 3.0\%$  (upper) and  $k/c = 0.300\%$ .

only one degree wide about  $\alpha = 18^\circ$ . Maximum lift is reduced by over 11% to 1.36 and  $(C_l^{3/2}/C_d)_{\max}$  suffers a 14% reduction to 16.12. However, maximum lift to drag ratio actually shows an increase over the smooth airfoil value reaching 17.12 (a 3% increase) at  $\alpha = 5^\circ$ . This increase is due to both a reduction in the drag and an increase in the lift as compared to the smooth airfoil's values at this incidence angle. Note the almost linear decrease in the magnitude of the moment for positive angles of attack prior to stall.

Performance curves for trip wire roughness located at the point of maximum airfoil thickness,  $x/c = 30\%$ , are presented in Figure 6. Except for the more nearly linear lift curve slope, the curves are somewhat comparable to those recorded for the smooth airfoil. The hysteresis loop is once again three degrees wide with stall and reattachment occurring at  $19^\circ$  and  $15^\circ$  respectively. The maximum lift and endurance factors are only slightly lower than the smooth airfoil values; however, minimum drag and  $(C_l/C_d)_{\max}$  both show improvement. The increase in the latter parameter is the result of reduced drag and increased lift at  $\alpha = 5^\circ$  as compared to the smooth airfoil's performance. Of interest is the steady increase in lift with incidence across all negative angles of attack. This contrasts with all other conditions in which the lift slightly increases then decreases prior to the rapid rise in lift coincident with reattachment of the lower surface flow.

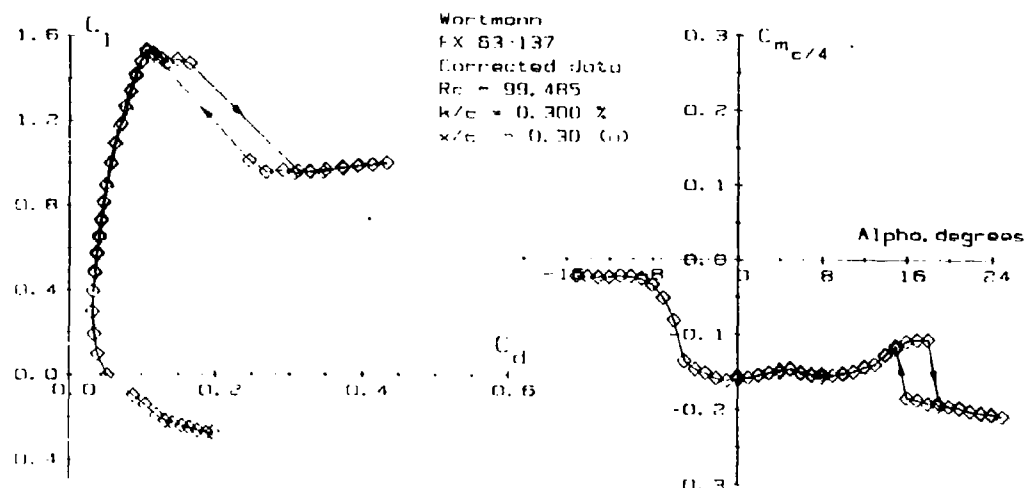


Figure 6. Performance Curves for the Wortmann Airfoil with a Trip Wire at  $x/c = 30.0\%$  (upper) and  $k/c = 0.300\%$

Figure 7 represents a summary of force balance data showing variations in certain performance parameters with trip wire height and placement. Beginning with  $C_{dmin}$ , it is apparent that this parameter is increased for virtually all trip wire heights located on the lower forward surface or leading edge. Large heights have the more undesirable effect and roughness at  $x/c = 1.0\%$  produces higher values than do trip wires further aft. Roughness on the upper surface is more complex in that various results can be obtained depending on height and location. Trip wires at  $x/c = 1.0\%$  cause higher minimum

drag values, yet as one moves aft the effect can revert to a beneficial one with larger heights actually reducing minimum drag. (One would expect, however, that some critical size exists where a further increase in  $k/c$  would reverse this favorable outcome.) Finally, when roughness is placed at the location of maximum airfoil thickness,  $C_{dmin}$  can still be reduced, but the smaller height will be the more beneficial.

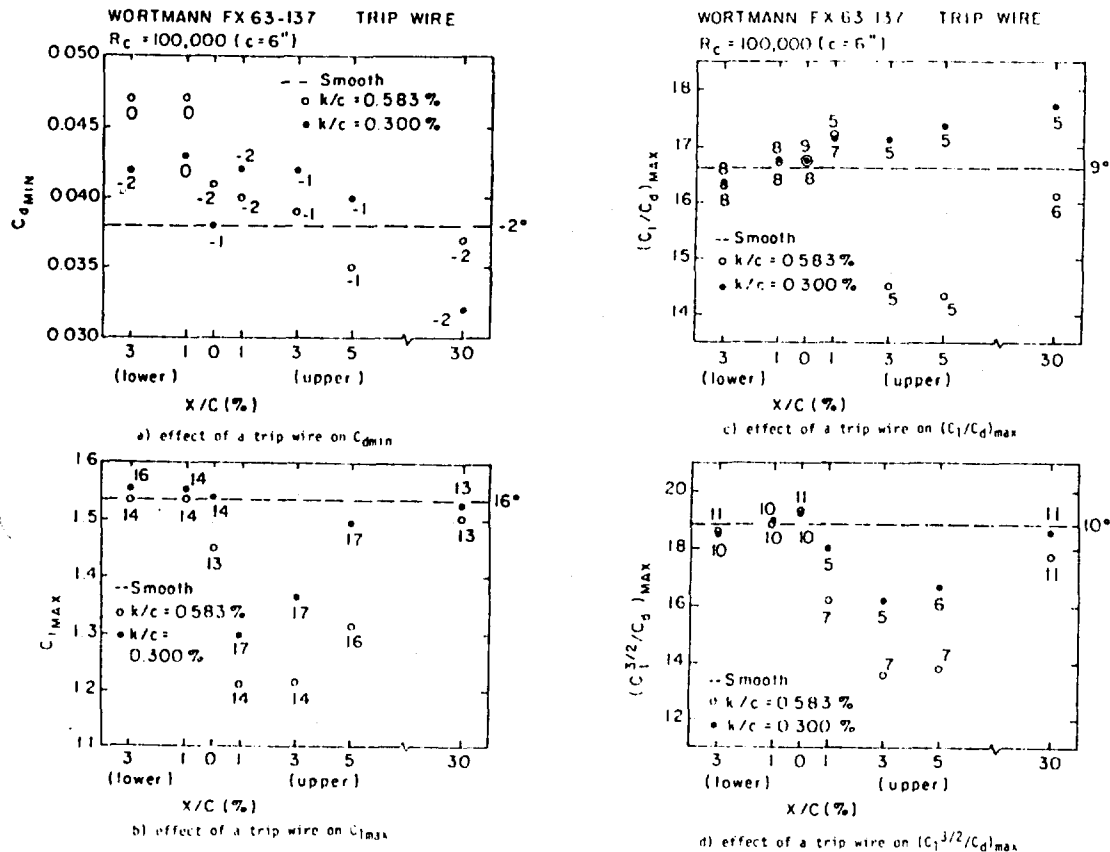


Figure 7. Performance Parameter Variation with Roughness Location and Height (angles of occurrence indicated in degrees).

As seen in Figure 7b, trip wire location and height have significant effect on maximum lift for the forward region of the upper surface. Lower surface roughness and upper surface roughness at  $x/c = 30.0\%$  have minor effect on this parameter. When situated on the leading edge, a trip wire may have a small or large effect with severe reductions occurring in  $C_{lmax}$  as  $k/c$  is increased. Roughness located at  $x/c = 1.0\%$  reduces  $C_{lmax}$  the most, the effect worsening with increasing trip wire height. As roughness is moved aft, losses in maximum lift apparently become less and less severe.

Figure 7c indicates that trip wires of varying height have little effect on  $(C_l/C_d)_{max}$  when placed on the forward lower surface or on the leading edge. However, a trip wire located on the upper surface

between 1.0 and 5.0% of chord can significantly increase or decrease this parameter depending of course on its height. A critical value for  $k/c$  (depending on position) appears to exist for which smaller values can increase  $(C_l/C_d)_{\max}$  and for which larger values decrease it. Naturally, one would suspect that another critical height exists in the lower height range at which this parameter reaches a maximal attainable level. This trend also seems to hold true for trip wires located at  $x/c = 30\%$  where the greatest values in  $(C_l/C_d)_{\max}$  were observed.

The effect on the maximum endurance factor,  $(C_l^{3/2}/C_d)_{\max}$ , of a trip wire located on the lower surface or on the leading edge is minimal with measured values very similar to those obtained for the smooth airfoil (See Figure 7d). In contrast, trip wires on the upper surface consistently lower this parameter with the decrease most significant for a large trip wire located at  $x/c = 3.0\%$ . Additionally, the angle of occurrence for this parameter can shift downward by as much as five degrees when the trip wire location corresponds to the forward position of the airfoil's upper surface.

A final set of data is presented in Figures 8 and 9 which are pressure distributions of the smooth and roughened airfoil at  $8^\circ$  and  $16^\circ$  angles of attack respectively. The points of laminar separation, transition, reattachment, and turbulent separation are marked on the smooth airfoil plots by the symbols S, T, R, and S' respectively. Along with the smooth airfoil's distributions are plots which demonstrate the effect of trip wire placement at the suction peak and laminar separation points for each angle of attack condition. For the  $8^\circ$  case, the suction peak occurs at  $x/c = 3.0\%$  while laminar separation occurs at approximately  $x/c = 37.5\%$ . Thus, trip wire placement for the latter condition is actually ahead of the true separation point and instead corresponds to the point of maximum foil thickness. At  $\alpha = 16^\circ$  the suction peak moves to  $x/c = 1.0\%$  while separation is found at the 5.0% chord location.

As shown in Figure 8, the smooth airfoil demonstrates the presence of a laminar separation bubble from about  $x/c = 37.5\%$  to  $x/c = 70.0\%$ . Transition occurs in the laminar free shear layer at approximately  $x/c = 60.0\%$  forming a turbulent free shear layer which eventually reattaches just forward of the  $x/c = 70.0\%$  location. The effect of trip wire placement at the  $x/c = 3.0\%$  position is to create a short separation region behind the roughness element which leads to rapid transition and a large pressure recovery. No laminar separation bubble forms downstream since the flow is turbulent and entrains sufficient flow energy to remain attached. The pressure plateau region just behind the trip wire represents accelerated flow that is more unstable, but not sufficiently so that transition occurs at the element itself.

Trip wires placed closer to the laminar separation point for the  $8^\circ$  incidence case demonstrate that increased  $k/c$  leads to more rapid transition and a higher pressure plateau immediately behind the roughness element. Tests involving other roughness types and a greater range of heights have substantiated this trend [3]. However,

one should again note that neither trip wire positioned at  $x/c = 30\%$  forces transition at the element site.

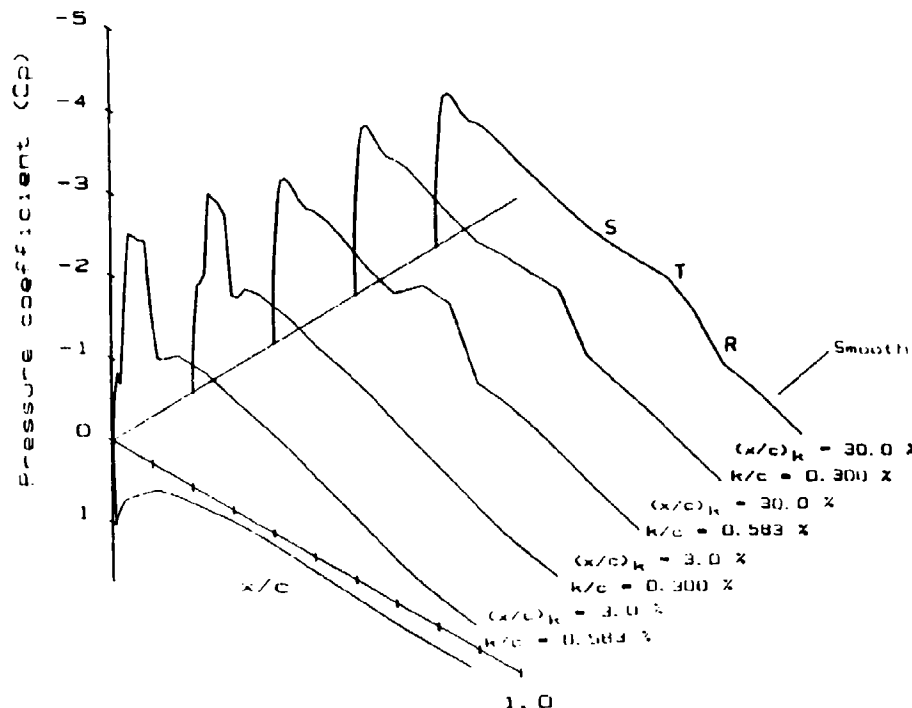


Figure 8. Pressure Distributions of the Smooth Wortmann Airfoil and the Airfoil with Trip Wire Roughness at  $x/c = 3.0\%$  and  $30.0\%$  ( $\alpha = 8^\circ$ ).

Figure 9 provides pressure distributions of the  $\alpha = 16^\circ$  condition and as one can observe in the smooth airfoil plot, a classic leading-edge bubble is present from about  $x/c = 5.0\%$  to  $x/c = 20.0\%$ . Turbulent separation is also apparent at the 75.0% chordwise location. Moving from right to left in this figure, it is observed that an increase in trip wire height significantly decreases the suction peak value when the trip wire is located at the point of laminar separation ( $x/c = 5.0\%$ ). Both wire heights produce an earlier transition although the turbulent separation point seems unaffected. As in the  $8^\circ$  case, neither trip wire brings transition to the roughness location.

When the trip wires are moved to the smooth airfoil's suction peak location, the effects on the pressure distribution become much more pronounced. With a trip wire at  $x/c = 1.0\%$  and  $k/c = 0.300\%$ , the resulting pressure plateau region is near the suction peak level, but is very short in length. Transition occurs relatively soon and leads to a sharp pressure recovery. Turbulent separation also moves forward and occurs at mid-chord. For  $k/c = 0.583\%$  at the  $x/c = 1.0\%$  location, the upper surface flow separates leading to a stalled condition. The lift is significantly reduced and the airfoil's pitch-down tendency greatly increased.

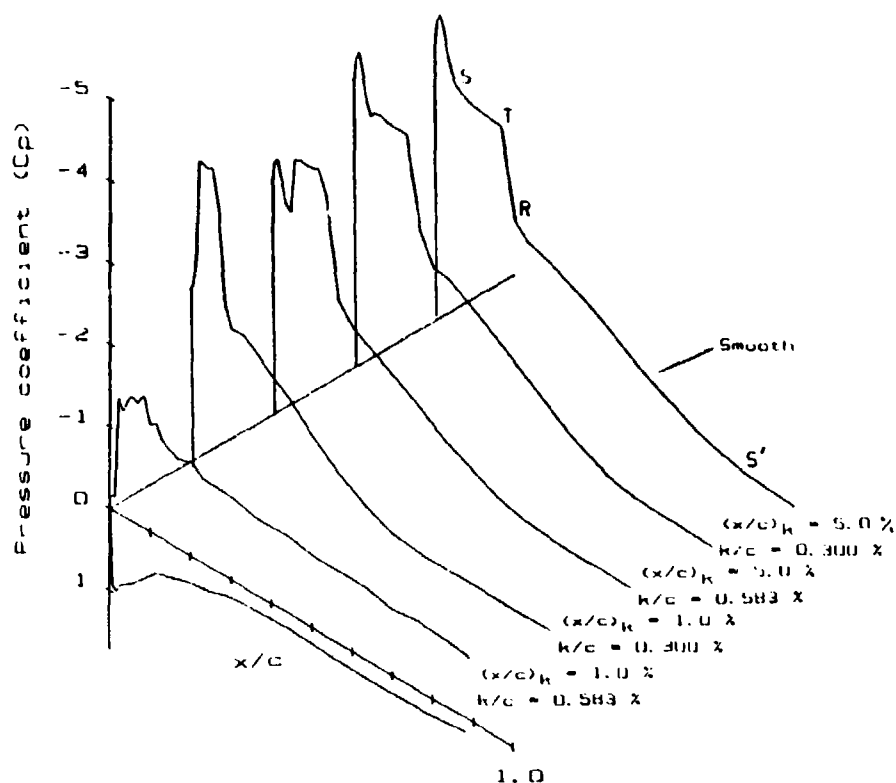


Figure 9. Pressure Distributions of the Smooth Wortmann Airfoil and the Airfoil with Trip Wire Roughness at  $x/c = 1.0\%$  and  $5.0\%$  ( $\alpha = 16^\circ$ ).

#### CONCLUSIONS

The results of this study indicate that the Wortmann FX 63-137 is a high performance low Reynolds number airfoil even when operated at off-design conditions. Experimental data show that separation phenomena, most notably the formation of laminar separation bubbles, greatly influence this airfoils' characteristics. Additionally, the occurrence of other boundary layer phenomena, such as turbulent separation, have significant effect.

The effects of the addition of trip wire roughness to the airfoils' surface are variable depending on location and height. In general, it can be stated that roughness located on the forward lower surface ( $0.01 < x/c < 0.03$ ) has little effect on the performance of the FX 63-137 except to increase the minimum drag coefficient. In contrast, trip wires located on the upper surface at or near the leading edge can significantly reduce  $C_{lmax}$  and  $(C_l^{3/2}/C_d)_{max}$  while improving or degrading  $(C_l/C_d)_{max}$  depending on the roughness height. Trip wire roughness located on the upper surface near the point of maximum airfoil thickness has limited, detrimental effect on the maximum lift and endurance factors, but can lead to reductions in

$C_{dmin}$ . Trip wires located at this position can also improve the maximum lift to drag ratio.

From the pressure distribution data, it is evident that transition can be induced to occur at positions further forward than those at which it naturally occurs. However, it is fairly difficult to bring this transition point to the roughness element itself. Typically, the flow is measurably accelerated aft of the trip wire before transition quickly occurs in the separated free shear layer. Once the flow entrains sufficient energy from the freestream, reattachment ensues while the pressure rises. Depending on the angle of attack, roughness height and position, such effects may or may not represent an improvement over the smooth airfoils' performance.

The usefulness of equation (1) to determine roughness heights appears to be questionable. Admittedly, this relationship was not developed with application to large pressure gradients in mind, but unfortunately no other criteria are available in the literature. Transition at the trip wire location is not guaranteed as was the original desire. From additional experiments [3], it is indicated that knowledge of the boundary layer thickness provides a sufficient first guess as to what range of roughness heights one may want to investigate. One should investigate a range of heights since changes in  $k/c$  can occasionally lead to a reversal of effect causing an airfoil operating above its smooth performance levels to then perform far below them.

#### NOMENCLATURE

$C_d$	airfoil sectional drag coefficient
$C_l$	airfoil sectional lift coefficient
$C_{l\alpha}$	airfoil sectional lift curve slope coefficient
$C_{mc}/4$	airfoil sectional moment coefficient measured about the quarter-chord location
$C_p$	pressure coefficient
$c$	chord length of airfoil model
$k$	roughness height
$P$	static pressure
$Q$	dynamic pressure
$R$	refers to the occurrence of reattachment
$Re_c$	Reynolds number based on chord $c$
$S$	refers to the occurrence of laminar separation
$S'$	refers to the occurrence of turbulent separation
$s$	arclength distance from stagnation point
$T$	refers to occurrence of transition
$U$	flow velocity
$x$	distance along chord line

#### Greek Symbols

$\alpha$	angle of attack
$\delta_1$	boundary layer displacement thickness
$A_1$	shape factor defined as $[\delta_1(du/ds)]/\nu$
$\nu$	kinematic viscosity

## Subscripts

cr	refers to critical value for some effect on transition
k	pertains to roughness height or location
max	refers to the maximum value of a parameter
min	refers to the minimum value of some parameter
t	as pertains to the location of transition
u	upper
u	uncorrected value

## ACKNOWLEDGEMENT

This work is supported by the Office of Naval Research under contract No. N00014-83-K-0239.

## REFERENCES

1. Lissaman, P.B.S., "Low Reynolds Number Airfoils," Annual Review of Fluid Mechanics 1983, (edited by W.S. Sears and M. VanDyke), Palo Alto, California: Annual Reviews, Inc., Vol. 15, 1983, pp. 223-239.
2. Mueller, T.J., et al, "The Influence of Free Stream Disturbances on Low Reynolds Number Airfoil Experiments," Experiments in Fluids, 1983, No. 1, pp. 3-14.
3. Huber, II, A.F., "The Effects of Roughness on an Airfoil at Low Reynolds Numbers," M.S. Thesis, University of Notre Dame, 1985.
4. Tani, I. and Sato, H., "Boundary Layer Transition by Roughness Element," Journal of the Physical Society of Japan, Vol. 11, No. 12, December 1956, pp1 1284-1291.
5. Gibbings, J.C., "On Boundary Layer Transition Wires," ARC Technical Report, C.P. No. 462, 1959.
6. Tani, I., "Low Speed Flows Involving Bubble Separations," Chapter 2, pp. 70-103 of Progress in Aeronautical Sciences, Vol. 5, MacMillan Co., 1964.
7. Smith, A.M.O. and Clutter, Darwin W., "The Smallest Height of Roughness Capable of Affecting Boundary-Layer Transition," Journal of the Aero-Space Sciences, April 1959, pp. 229-245.
8. Mueller, T.J., "Flow Visualization by Direct Injection," Chapter 7, pp. 307-375 of Fluid Mechanics Measurements, (edited by Richard J. Goldstein), Washington: Hemisphere Publishing Company, 1983.
9. Brendel, M. and Huber II, A.F., "An Experimental Investigation of Flow Quality in an Indraft Subsonic Wind Tunnel Using a Single Hot Wire Anemometer," an internal Aerodynamics Laboratory report, University of Notre Dame, November 1984.

10. Chappell, P.D., "Flow Separation and Stall Characteristics of Plane, Constant-Section Wings in Subcritical Flow," The Aeronautical Journal of the Royal Aeronautical Society , Vol. 72, January 1968, pp. 82-90.

# ACOUSTIC AND TURBULENCE INFLUENCE ON LOW-REYNOLDS NUMBER WING PRESSURE DISTRIBUTIONS

V. Sumantran, Z. Sun, J.F. Marchman III.  
Department of Aerospace and Ocean Engineering,  
Virginia Polytechnic Institute and State University,  
Blacksburg, Virginia 24060.

## ABSTRACT

Wind-tunnel tests were conducted in the Virginia Tech 6' x 6' Stability Wind-Tunnel to determine the influence of free-stream turbulence and acoustic disturbances on low Reynolds number wing aerodynamics. The wing model was based on a FX-63-137-ESM airfoil section. Strain gauge measurements, pressure distribution and flow visualization studies were conducted in the range of Reynolds numbers from 70,000 to 300,000. Starting with the very clean flow inherent in the wind-tunnel, free-stream turbulence and acoustic disturbance levels in the test-section were increased independently. A distinct alteration of the wing's performance was observed particularly with regard to the stall hysteresis loop which may even be eliminated at very low Reynolds number-high disturbance level conditions. This study also shows clearly the behavior of the laminar separation bubble which contracts and moves forward with increasing angle of attack and determines the manner in which the airfoil stalls.

## INTRODUCTION

In recent years, there has been a considerable awakening of interest in the field of Low-Reynolds number wing and airfoil aerodynamics. Much of this interest has been spurred by new areas of application that require a better understanding of the flow phenomenon in this regime. These applications include mini-RPVs, operating in a low-speed, low-altitude environment as well as fields such as gliders, inboard sections of helicopter rotor blades, jet-engine turbine and compressor blades and high-altitude RPVs.

Flow behavior at Reynolds numbers less than 500,000 is widely known to involve some significantly different characteristics compared to higher Reynolds number flows. Although airfoil behavior in this regime has been studied and catalogued since the thirties and many of these problems identified, an understanding of the detailed mechanism responsible for such behavior is not complete. What is known is that the 'laminar separation bubble' that is frequently observed on some airfoils at low Reynolds numbers determines the aerodynamic performance of the airfoil. Study of the laminar separation bubble indicates crucial dependence on factors such as the point of laminar separation, location of transition and location of turbulent boundary layer reattachment. These factors are in turn governed, to a considerable degree, by the ambient environment; more specifically, the free-stream turbulence and levels of acoustic disturbance. A study of the influence of these quantities is necessary for a better understanding of the flow phenomenon.

Force and moment data obtained from strain gauges have proven extremely useful in examining the global performance of the wing. This is true even for Reynolds numbers in the range of 70,000 to 100,000, when sufficiently sensitive strain gauges are available to yield repeatable data [1]. However, to study the details of flow behavior, it is also essential that pressure distribution and flow visualization studies also be conducted. Pressure distribution plots and flow visualization pictures can be used to define the different regions of the flow such as the laminar separation bubble, the line of reattachment and the point of turbulent separation. With proper correlation of these two procedures, it is possible to better understand the behavior and extent of the laminar separation bubble.

An interesting consequence of the laminar separation bubble for some of these airfoils is the phenomenon of hysteresis in stall. Stall hysteresis is frequently observed in flows of Reynolds numbers less than about 300,000 for many airfoils. It appears that the leading-edge geometry of the airfoil greatly influences the nature of the hysteresis loop.

Depending on airfoil geometry, two kinds of stall hysteresis loop have been observed: a) a clockwise hysteresis loop with maximum lift coefficient achieved prior to stall and b) a counter-clockwise hysteresis loop. The FX-63-137-ESM airfoil displays a clockwise hysteresis loop at Reynolds numbers where the separation bubble dominates the flow over the airfoil's upper surface. At very low Reynolds numbers, laminar separation without subsequent reattachment occurs, eliminating the hysteresis loop [1] and at higher Reynolds numbers, the location of transition may preclude laminar separation and hence the bubble. Marchman [1] has shown both of these limits to be functions of not only Reynolds number but of wing aspect ratio as well. The clockwise hysteresis loop behavior of the present airfoil can be explained as follows:

1. At low incidence, the laminar separation bubble is formed, extending over as much as 50% of the chord for these low Reynolds numbers [2].
2. Increasing the incidence causes the bubble to move forward and contract. The suction peak close to the leading edge increases and some turbulent separation may be observed close to the trailing edge. The lift coefficient increases with incidence in this range.
3. Stall corresponds to laminar separation close to the leading edge with no subsequent reattachment. The lift coefficient drops abruptly.
4. Any post-stall reduction of incidence does not immediately restore the flow. Some lower angle of attack must be reached before the laminar separation bubble can be reformed and the hysteresis loop closed.

The aerodynamics of a wing at Reynolds numbers from 70,000 to 500,000 is thus very dependent on the behavior of the laminar separation bubble. The existence and extent of the bubble are in turn, dependent on the stability of the laminar boundary layer preceding the bubble and over the bubble itself [3]. Airfoil surface roughness, ambient flow turbulence level and the acoustic environment are among the factors that have been shown to influence the laminar bubble and its subsequent effect on the airfoil aerodynamics. Any of these factors may lead to early transition from laminar to turbulent flow in the boundary layer by creating or amplifying the Tollmien-Schlichting waves in the flow. The result may be a significant alteration of the aerodynamic behavior of an airfoil at low Reynolds number flows.

It is very important that the consequences of free-stream turbulence levels and the acoustic environment on low Reynolds number aerodynamics be fully understood. Wind-tunnel turbulence level may have a large influence on the stall hysteresis loop, yet researchers continue to run tests in facilities with a very wide range of turbulence levels even though data from wind-tunnels with high free-stream turbulence must be considered of questionable utility. Unfortunately, there is no simple device such as the use of a turbulence factor to correct and compare hysteresis loop data from different tunnels. Mueller [4] has studied the influence of tunnel acoustic level on low Reynolds number flows; however, in most tunnels the acoustic environment and free-stream turbulence are coupled; i.e., they are both functions of tunnel and fan characteristics and there has been no attempt to systematically study those two influences independently in the same facility. Therefore, as a part of the work being done at Virginia Tech. a preliminary study was undertaken to better define the effects of free-stream turbulence and acoustics on the Wortmann airfoil at low Reynolds numbers.

#### EXPERIMENTAL PROCEDURE

The objective of these tests was to examine the influence of free-stream turbulence level and of the acoustic environment on both the global aerodynamics (forces and moments) and the detailed flow behavior (pressure distribution and flow visualization) of the Wortmann FX-63-137-ESM airfoil at low Reynolds numbers. A related study at Virginia Tech, [1], had already examined the 3-D aerodynamic behavior of the Wortmann airfoil at aspect ratios of 4,6,8 and 10 between Reynolds numbers of 50,000 and 500,000. This research used the same model as Reference [1].

All tests were conducted in the Virginia Tech Stability Wind-tunnel with a 6' x 6' x 28' test-section. This tunnel has two features that are of great importance for the present study : a) a set of seven fine-mesh anti-turbulence screens upstream of the test-section b) a large air-exchange tower between the fan and the test-section. This results in very low levels of free-stream turbulence with the turbulence intensity varying from 0.02% to 0.04% in the range of test velocities [5]. In addition, the air-exchange tower provides effective isolation of the test-section from the effects of fan pressure pulses and acoustics.

The wing model was based on a Wortmann FX-63-137-ESM airfoil section, originally developed for use in gliders and designed to operate at a Reynolds number of around 500,000. The model was milled from solid aluminium and could be assembled into wings of AR 4,6,8 and 10. The need to obtain clean flow at the lower end of the Reynolds number range dictated a chord of five inches. This also allowed sufficient clearance for the free development of the wing-tip vortices. All models used squared wing-tips and the surface was coated with epoxy for a uniformly smooth surface without seams. Fortyone pressure taps were built into the wing well inboard of the wing-tips, the taps being arranged diagonally to eliminate interference between pressure taps.

Measurements of the forces and moments throughout the hysteresis loop requires a remote-control arrangement to vary wing incidence with the wind-tunnel in operation. In this study, the model was mounted on a remotely controlled six-component strain-gauge strut which was operated by the tunnel's computer control and data acquisition system. This strut

is described in detail in Reference [1]. A Hewlett-Packard 9836 computer was used for experiment control as well as data acquisition. For the latter role, the computer was used in conjunction with a HP 3455A High Precision Digital Voltmeter and a HP 3495A computer controlled scanner (Fig. 1).

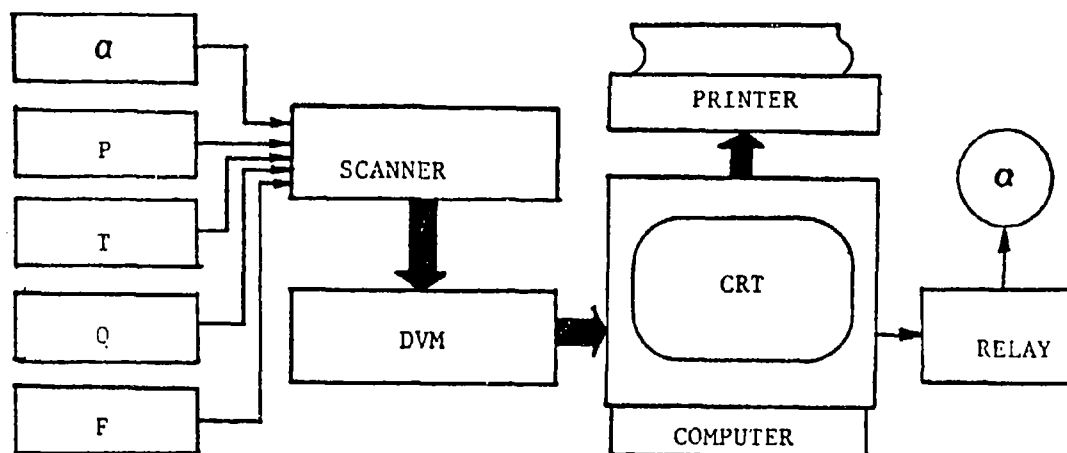


FIG 1. SCHEMATIC OF DATA ACQUISITION SYSTEM

Wing chordwise pressure distributions were obtained via a computer controlled SCANIVALVE Model J system using a SETRA SYSTEMS Model 237 pressure transducer. This system was also controlled by the tunnel's HP computer.

The flow visualization procedure used was the naphthalene/trichloroethane surface-evaporation technique. The behavior of the white naphthalene coating on the wing, upon the evaporation of the solvent, provides a view of the different regions of the flow in the boundary layer. These pictures were complemented by photographs of oil-drops on the surface to determine regions of reverse flow. These photographs, together with the pressure distribution plots, provide a correlated estimate of the flow behavior.

To investigate the influence of increased free-stream turbulence, horizontal strips were attached to the anti-turbulence screens. This procedure has been previously used in the same wind-tunnel by Saric [5] and two increased levels were obtained with the turbulence intensity of about 0.2% to 0.3% compared to the base level of about 0.02%.

The study of the influence of acoustic disturbances was conducted at a preliminary stage. The intent here was not so much to establish critical frequencies as to understand changes in the flow behavior due to the presence of these disturbances in the environment. These acoustic disturbances were created using a commercial loud-speaker installed in the ceiling of the test-section, positioned above the wing and directed at the upper surface of the wing. A signal generator and an amplifier were used to generate the desired frequency. Frequencies in the range of 100 Hz. to 5000 Hz. were used at sound levels varying from 90 dB. to 115 dB. measured at the wing.

## DATA AND RESULTS

### Comparison of Force Data and Pressure Integration.

If the results of the force measurement tests and of tests measuring pressure distributions are to be compared, a fair amount of confidence is necessary in the accuracy of both the pressure distribution plots and the force data. At low Reynolds numbers, there may be some question regarding the extent to which the flow is disturbed due to the presence of the pressure taps themselves. These matters were resolved using a comparison of the force data and the integrated pressure forces as well as flow-visualization studies.

Fig. 2 shows a sample plot comparing lift coefficient obtained from force data (for  $AR=8$ ) to that obtained from an integration of the pressure forces at  $Re = 150,000$ . The slope of the lift curve and the values of the maximum lift coefficient compare very well. The stalling angle and the extent of the hysteresis loop also show good correlation. The values of post-stall lift are lower for the case of pressure force integration because the integrated pressures cannot account for lift contributions at the unstalled wing-tips.

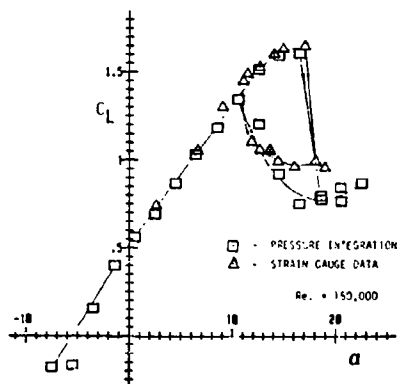


Fig.2. Comparison of Strain-Gauge Data and Pressure Integration.

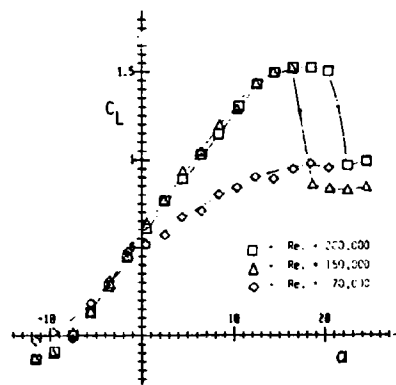


Fig.3. Types of Stall.

### Types of Stall.

Fig. 3 illustrates the three types of stall typically observed over a range of Reynolds numbers and also seen in this research. Note that for the  $Re=150,000$  and  $Re=200,000$  cases, the hysteresis loop is not shown in this figure although it is present. The stall types seen in Fig. 3 were described and classified by McCullough and Gault [6] and later by Crabtree [7] and were shown to be functions of Reynolds number.

In the  $Re=200,000$  case, the 'gentle' trailing edge type of stall is seen where turbulent separation begins at the trailing edge and moves forward as the angle of attack increases. Complete stall occurs when the turbulent separation point nears the point of laminar separation bubble reattachment resulting in the breakdown of the bubble and hence leading

edge separation. Fig. 4 shows the pressure distributions observed on the wing at three different angles of attack for this case. The upper surface distribution shows that as the angle of attack increases, the point of turbulent separation progresses from 0.5c to 0.3c where it is very close to the reattachment of the laminar bubble. The bubble is seen to exist around the 0.25c point. A further increase in incidence results in stall with separated flow over most of the upper surface.

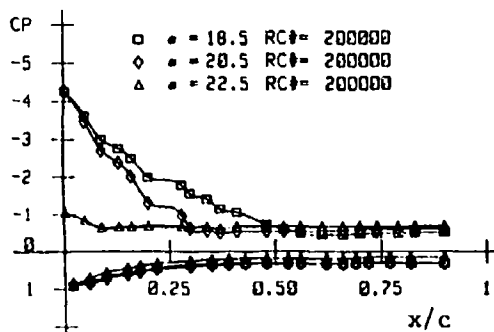


Fig.4. Trailing-Edge Stall

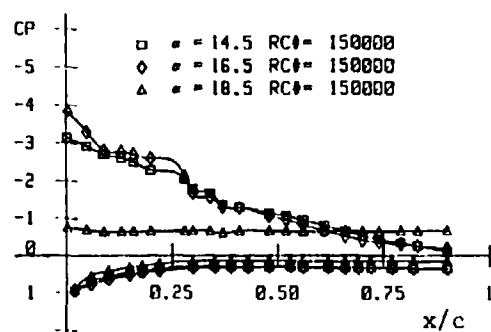


Fig.5. Leading-Edge Stall

Fig. 5 shows the pressure distributions for the  $Re=150,000$  case where the stall is more abrupt. This is more typical of the type of stall described as 'leading-edge stall' where the lift curve is linear almost all the way up to stall. Stall is primarily due to a 'bursting' of the laminar separation bubble rather than a forward motion of the turbulent separation point from the trailing edge. The pressure curves show the increase in the leading edge suction peak as  $\alpha$  increases and the resulting increase in the adverse pressure gradient near the location of bubble reattachment, followed by stall. Fig. 3 also shows the lift curve for the  $Re=70,000$  case where the stall can be characterized as 'thin-airfoil stall'. Separation occurs at or near the leading edge before a leading edge separation bubble can form : i.e., there is laminar separation with no subsequent reattachment.

#### Stall Hysteresis.

Typical stall hysteresis loops from this research are shown in Fig. 6. Reference [1] describes the effect of Reynolds number and aspect ratio on the hysteresis loops in greater detail; however, it is seen in this figure that as the Reynolds number increases, the loop moves to the right. Fig. 7 shows the upper and the lower hysteresis loop pressure distributions for an angle of attack of 16.5 degrees for  $Re=200,000$ . The laminar bubble is seen as a region of constant pressure on the upper loop curve. The flow is seen to be separated over most of the wing surface for the lower part of the loop.

## Comparison of Flow Visualization and Pressure Data.

One of the objectives of the present studies was to better define the extent of the laminar separation bubble in view of its importance in determining the overall flow behavior. It has been known for many years that at low Reynolds numbers the bubble can extend over as much as half the airfoil chord [2].

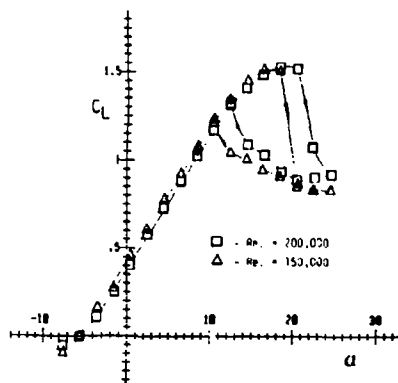


Fig. 6. Stall Hysteresis Loop

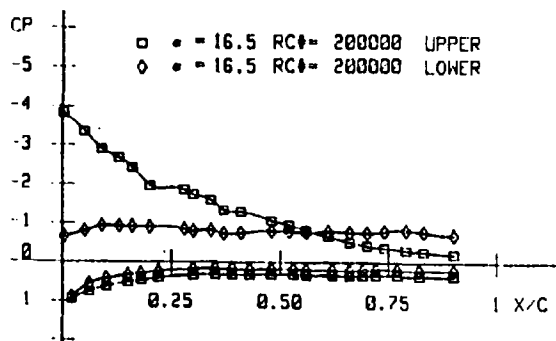


Fig. 7. Pressure Distribution on two Portions of Hysteresis Loop.

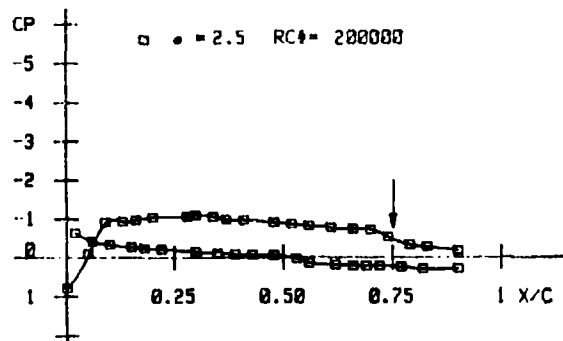


Fig. 8. Pressure Distribution and Bubble Reattachment.

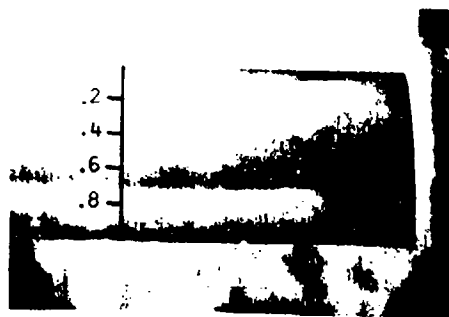


Fig. 9. Flow Visualization and Bubble Reattachment.

Fig. 8 shows the pressure distribution for the wing at  $Re=200,000$  and  $2.5$  degrees incidence. The location of flow reattachment is indicated by the kink in the curve at about  $0.75c$ . Fig. 9 shows a picture of the flow obtained using the evaporative naphthalene technique for the same case. The demarkation between the light and the dark regions denotes the spanwise line of reattachment. This was also confirmed with oil-drop surface flow studies and indicates that the bubble contracts and moves forward with increasing wing angle of attack. In many cases the oil-drop studies also indicate reverse flow within the bubble, indicating the recirculatory nature of that flow region.

## Influence of Free-Stream Turbulence.

One of the primary objectives of these tests was to examine the role of wind-tunnel free-stream turbulence in low Reynolds number aerodynamic testing. It is known that testing in facilities with different turbulence levels will give different results, especially in hysteresis loop data. Unfortunately, many past studies have been conducted in wind tunnels where free-stream turbulence levels greatly exceed those of the Virginia Tech Stability Tunnel. Hence, in order to allow better comparison of test results with those obtained in other facilities, some tests were run with excess free-stream turbulence deliberately added to the flow via a set of horizontal 'turbulence strips' attached to the anti-turbulence screens. This method, previously used by Saric [5] in studies of flat-plate boundary layer stability and transition, was effective in producing an order of magnitude increase in turbulence level, 0.02% to 0.2% at 30 fps. Turbulence levels were measured with standard hot-wire techniques.

Fig. 10 shows the influence of increased free-stream turbulence on the stall hysteresis for the AR=8 wing model at  $Re=100,000$ . It is evident that the size of the hysteresis loop is drastically reduced and, indeed, almost eliminated although the lift curve slope and the maximum lift coefficient are not significantly affected.

Fig. 11 depicts the pressure distributions for this case - at 12.5 degrees angle of attack. Curve (A), representing the upper portion of the hysteresis loop with 0.02% turbulence, shows a strong suction peak at the leading edge and attached flow all the way to the trailing edge. At the same angle of attack, on the lower portion of the hysteresis loop (B), the flow is seen to be separated over almost the entire upper surface of the airfoil; however, with free-stream turbulence increased to 0.02%, (C), the lower curve of the hysteresis loop shows an almost complete restoration of the flow.

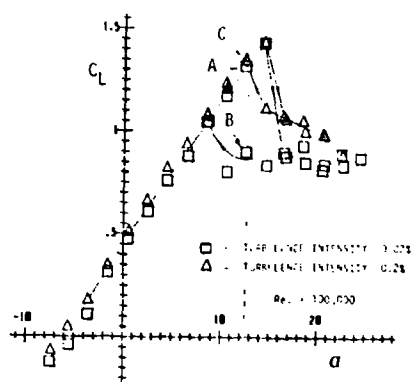


Fig.10. Turbulence Effect -  
Re.=100,000

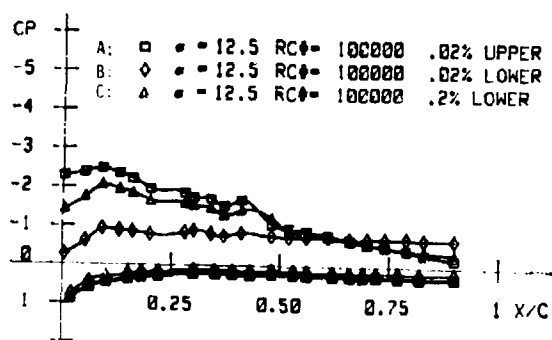


Fig.11. Turbulence Effect - Pressure  
Distribution. Re.=100,000

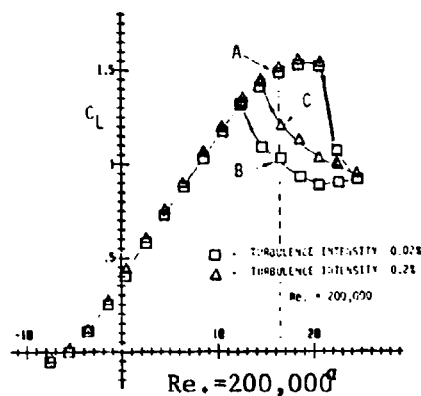


Fig.12. Turbulence Effect.

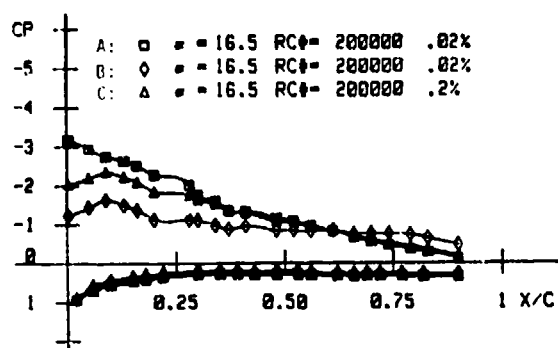


Fig.13. Turbulence Effect.

Fig. 12 shows the stall hysteresis loop for a higher Reynolds number ( $Re=200,000$ ). Here, although the hysteresis loop is reduced in size when the turbulence intensity has been increased, it is still distinctly visible. Examining Fig. 13, the pressure distributions again indicate that the increased free-stream turbulence intensity does have some effect in delaying the separation that occurs near the trailing edge even though it cannot prevent the loss of suction at the leading edge.

A further increase in free-stream turbulence to 0.3% was achieved by adding vertical turbulence strips. This change had no effect on the data for the Reynolds numbers tested.

It is therefore clearly evident that the level of free-stream turbulence in the test-section environment will strongly influence the flow behavior and thereby the performance of the airfoil. Indeed, at the lower end of the Reynolds number scale, the whole hysteresis phenomenon may be eliminated.

#### Effect of Acous. Disturbances.

No one has yet systematically studied the effect of acoustic disturbances on low Reynolds number hysteresis loops where acoustic signals are varied independent of turbulence levels. Preliminary studies conducted in the past have shown that ambient acoustics of the test-section can influence the airfoil behavior [4]. The objective of this section of the present research was to study the manner of this influence. Thus far only a preliminary attempt has been made to rigorously identify the frequencies needed to alter the flow and this will constitute part of the ongoing research.

Fig. 14 shows the hysteresis loop for  $Re=200,000$  and  $AR=4$  with and without the introduction of selected acoustic disturbances. In this case, a 5600 Hz. signal was fed into the amplifier and speaker with a noise level of about 110 dB. measured at the wing. Once again, a considerable reduction in the size of the hysteresis loop is evident when the acoustic signal is turned on. Stalling angle and the value of the maximum lift coefficient are unchanged, an effect similar to that observed when the turbulence intensity was increased. The angle at which the lower curve of the hysteresis loop rejoins the upper curve increases, indicating earlier restoration of the flow and reattachment

on the upper surface in the presence of this acoustic disturbance.

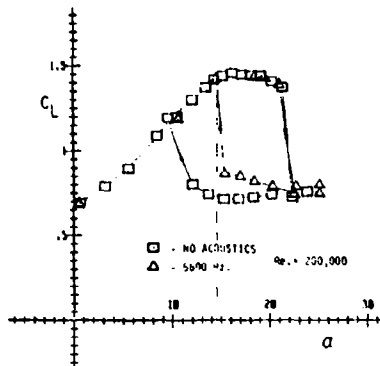


Fig. 14. Acoustic Effect - Stall Hysteresis

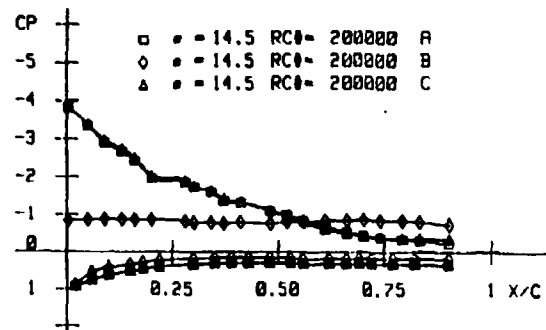


Fig. 15. Acoustic Effect - Pressure Distribution.

Fig. 15 shows the pressure distributions for three points on the hysteresis loop. Curve (A) denotes the pressure distribution on the upper curve with no acoustic disturbance at 14.5 degrees angle of attack. Curve (B) corresponds to the lower portion of the hysteresis loop at the same angle of attack with no acoustic disturbance. Curve (C) denotes the same lower loop angle of attack with the defined acoustic signal. The influence of the acoustic disturbance is thus to cause the flow to change from configuration (B) to configuration (C), resulting in a restoration of the bubble mechanism and flow reattachment on the upper surface of the airfoil. It is evident from Fig. 15 that the case (C) does represent the same flow as (A). It is interesting to note that this disturbance is merely needed to trigger the change ((B) to (C)) and once the attached upper surface flow has been established, the acoustic signal may be silenced with no further flow change resulting.

The ability of the acoustic disturbances to restore attached flow appears restricted to range of angles of attack close to the nominal angle of loop reattachment except at the lowest Reynolds number cases tested. At a Reynolds number of 100,000 it was possible to virtually eliminate the hysteresis loop with sound of sufficient magnitude and frequency. However, at the higher Reynolds numbers examined, even sound levels up to 120 dB. could not cause flow reattachment above a certain value of angle of attack in the loop. It was however seen that even when acoustic disturbances could not restore fully attached flow, they could alter the pressure distribution and give a temporary increase in lift as is seen in the increased lift values for the lower loop with acoustic disturbance. Depending on the test conditions, these cases yielded pressure data that did not achieve the high suction peak or the extent of the attached turbulent flow on the upper surface.

Fig. 16 illustrates the effect of noise that is not of sufficient power or frequency to fully restore the boundary layer over the upper surface but is successful in increasing the lift. Even though these curves are for the 15 degree case rather than the 14.5 degree case shown in Fig. 15, the two cases are close enough in angle of attack to permit comparison. Both the 4830 Hz. and the 5200 Hz. cases are able to give an upper surface pressure distribution which appears similar to that for an

attached flow; however, they exhibit much lower suction near the leading edge than the attached flow cases of Fig. 15 and this flow is maintained only as long as the acoustic signal is 'on'. In Fig. 15, the 5600 Hz. acoustic signal causes the pressure distribution to 'jump' from curve (B) to curve (C) and the flow will remain in the curve (C) form even after the sound is turned off. The two curves seen in Fig. 16 will, however, only exist as long as the acoustic signal is present. These signals are not sufficient to cause a full, stable reattachment of the flow.

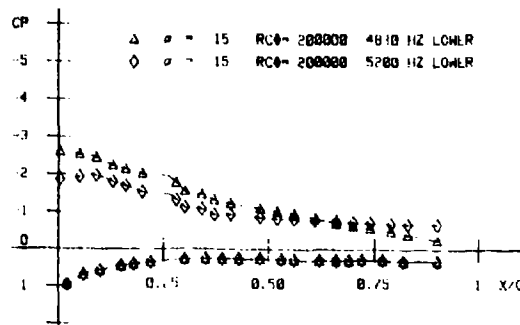


Fig.16. Acoustic Effect - Incomplete Flow Restoration.

These data combined with those of the previous section, show that although the acoustic environment and the turbulence level in the flow can both cause similar effects, they work quite independently. It is clear that studies of these effects need to be made in facility where free-stream turbulence and the acoustic environment are not both dependent on the same variable. The effects of the two types of disturbances may or may not be cumulative and the degree to which they are cumulative may be strong function of the Reynolds number.

#### CONCLUSIONS

1. Pressure and Flow visualization data show that the laminar separation bubble may be quite large, extending over almost half of chord. Increases in the Reynolds number cause a contraction of the extent of the bubble.
2. At higher Reynolds numbers, stall depends on the turbulent separation that is observed close to the trailing edge downstream of reattachment of the bubble and this point of separation moves upstream along the airfoil surface with increasing angle of attack.
3. Tunnel free-stream turbulence can greatly alter the test data and even eliminate the hysteresis behavior at lower Reynolds numbers. It appears that the range of turbulence levels between 0.02% and 0.2% is quite important while further increases above 0.2% may have negligible effect. While turbulence levels do not appear to greatly affect maximum lift coefficient for the Wortmann airfoil, it does have a pronounced influence on the hysteresis loop. On other airfoils such as the Miley

airfoil with a 'reverse' hysteresis loop, maximum lift coefficient could be greatly altered by variations in tunnel turbulence levels.

4. The acoustic environment influences low Re flow behavior in much the same way as free-stream turbulence. At low Reynolds numbers, noise can eliminate the hysteresis loop while at high Reynolds numbers, the hysteresis loop can be considerably altered. As is the effect of free-stream turbulence, there seems to be a limit beyond which increases in the magnitude of the disturbance produces no further changes in aerodynamic behavior.

5. Flow visualization studies such as the evaporative naphthalene technique together with pressure distribution plots can provide excellent estimates of the behavior of the laminar separation bubble and the boundary layer.

#### ACKNOWLEDGEMENTS

The authors would like to acknowledge the financial support of the Office of Naval Research under contract number N00014-84-0093 as well as that of the Virginia Tech Department of Aerospace and Ocean Engineering, without which this research would have been impossible.

#### REFERENCES

1. Marchman, J.F., Abtahi, A.A., Sumantran, V., "Aspect Ratio Effect on the Aerodynamics of a Wortmann Airfoil at Low Reynolds Numbers", Proceedings of the conference on Low Reynolds Number Airfoil Aerodynamics, University of Notre Dame, June 1985.
2. Tani, I., "Low Speed Flows Involving Bubble Separations", Progress in Aerospace Sciences, Vol. 5., pp. 70-103.
3. Gault, D.E., "An Experimental Investigation of Regions of Separated Laminar Flow", NACA. TN, 3505, 1955.
4. Pohlen, L.J., Mueller, T.J., "Boundary Layer characteristics of the Miley Airfoil at Low Reynolds Numbers, AIAA-83-1795, July 1983.
5. Saric, W.S., Yeates, L.G., "Generation of Crossflow Vortices in a 3-D Flat Plate Flow", VPI-E-84.35 Report, Nov. 1984.
6. McCullough, G.B., Gault, D.E., "Examples of 3 Representative Types of Airfoil Section Stall at Low Speed", NACA 2502, 1951.
7. Crabtree, L.F., "The Formation of Regions of Separated Flow on Wing Surfaces", Part I, RAE Rep. Aero., 2528, Nov. 1954.

PROPELLER SLIPSTREAM/WING BOUNDARY LAYER  
EFFECTS AT LOW REYNOLDS NUMBERS

Stan J. Miley and Richard M. Howard  
Department of Aerospace Engineering  
Texas A&M University  
College Station, Texas 77843

Bruce J. Holmes  
NASA Langley Research Center  
Hampton, Virginia 23665

ABSTRACT

The effects of a propeller slipstream on the wing laminar boundary are being investigated. Hot-wire velocity sensor measurements have been performed in flight and in a wind tunnel. It is shown that the boundary layer cycles between a laminar state and a turbulent state at the propeller blade passage rate. The cyclic length of the turbulent state increases with decreasing laminar stability. Analyses of the time varying velocity profiles show the turbulent state to lie in a transition region between fully laminar and fully turbulent. The observed cyclic boundary layer has characteristics similar to relaminarizing flow and laminar flow with external turbulence.

INTRODUCTION

A research program is in progress to investigate the behavior of the laminar boundary layer as affected by a propeller slipstream. Although the investigation is directed towards manned propeller driven aircraft, much of the experimental work to date has been performed at Reynolds numbers less than  $1 \times 10^5$ . These results are therefore also applicable to low Reynolds number aircraft.

Early observations of the effect of the propeller slipstream on boundary layer transition have not resulted in consistent conclusions. Young and Morris [1,2], and Hood and Gaydos [3] concluded from their investigations that the propeller slipstream caused the point of transition to move forward to a location near the leading edge. Reports by Zalovecik [4], and Zalovecik and Skoog [5] describe wing boundary layer measurements in propeller slipstreams performed on P-47 aircraft utilizing an NACA 230 series wing section and an NACA 66 series laminar flow wing section. Their results show little effect of the slipstream on transition for the NACA 230 section; however, the test with the NACA 66 series section resulted in the transition point location moving forward from 50 to 20 percent chord. The general consensus from this early work is that the propeller slipstream reduced the extent of laminar flow by forcing transition to occur earlier.

Recent work by Holmes, Obara and Yip [6] and Holmes, et al. [7] brings into question the validity of the ability of the early

measurement methods to accurately determine transition. Time-dependent behavior, particularly at frequencies associated with propeller blade passage rate, was not measurable by techniques commonly employed at that time. Measurements by Holmes, et al. [7] using surface hot-wire sensors indicate the existence of a cyclic turbulent behavior resulting in convected regions of turbulent packets between which the boundary layer appears to remain laminar (Figure 1).

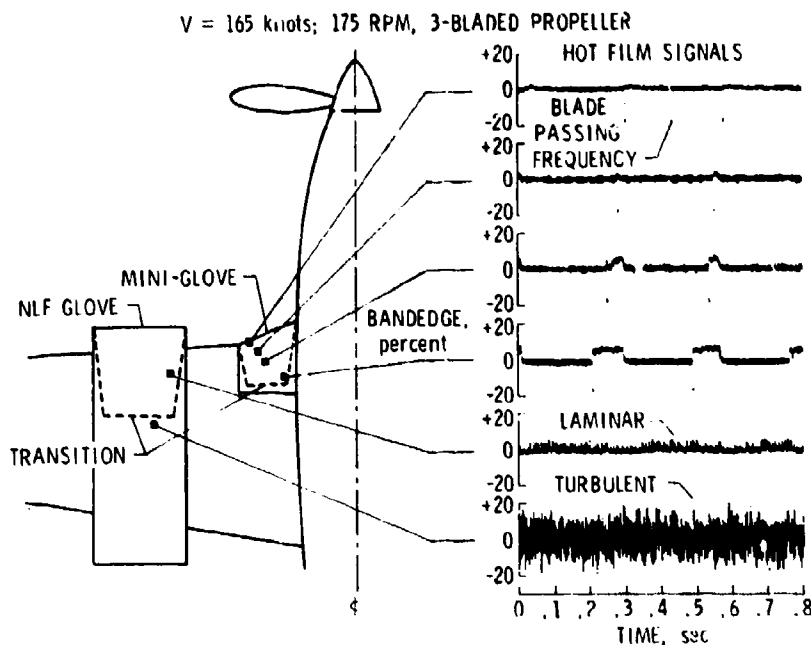


Figure 1. Surface hot-film measurements by Holmes et al. [7] showing cyclic laminar/turbulence behavior of boundary layer within propeller slipstream.

## EXPERIMENTAL INVESTIGATIONS

### Flight Experiments

At Texas A&M University, flight measurements of the wing boundary layer in the slipstream have been made on a Gulfstream Aerospace GA-7 Cougar at two chord locations using a dual-probe hot-wire velocity sensing system. One probe was located adjacent to the surface well within the boundary layer and the other was located directly above in the external flow. The results of the flight test are shown in Figures 2-4.

The signal traces are time histories of the local flow velocities in the boundary layer near the surface and in the external flow. The boundary layer velocity signal shows a periodic laminar/turbulent behavior. The change to turbulent flow results in an increase in the velocity seen by the probe because of the fuller turbulent profile. This change in profile results from periodic disturbances in the external flow due to the viscous wake shed from the propeller blade.

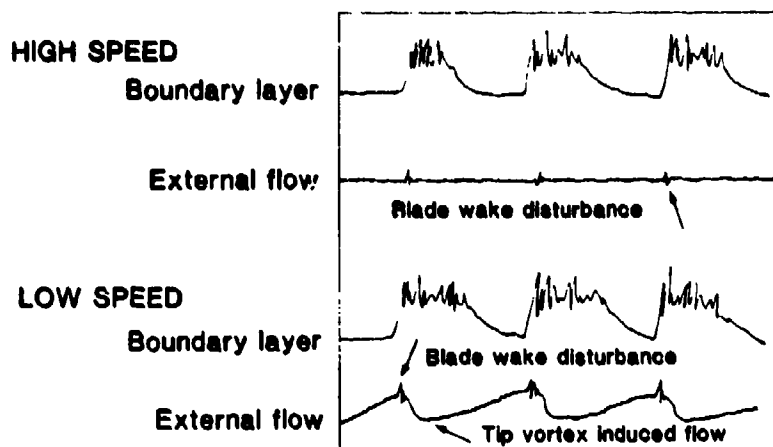


Figure 2. Identification of hot-wire velocity sensor signals in Figures 3-4.

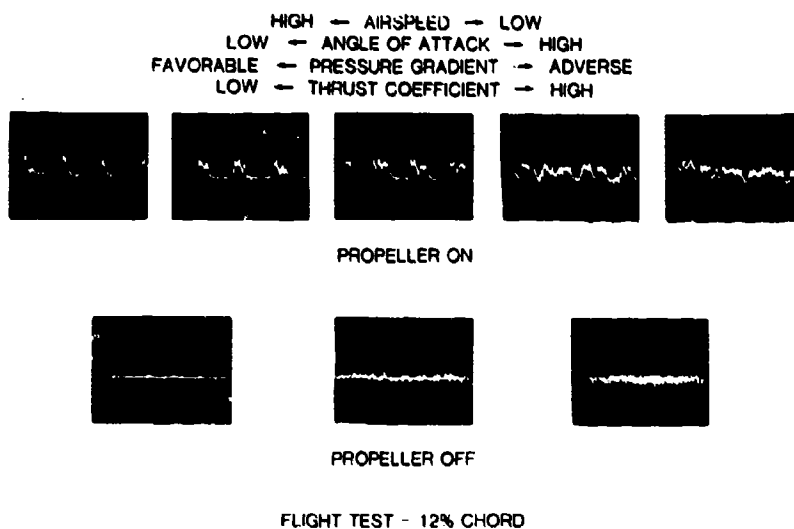
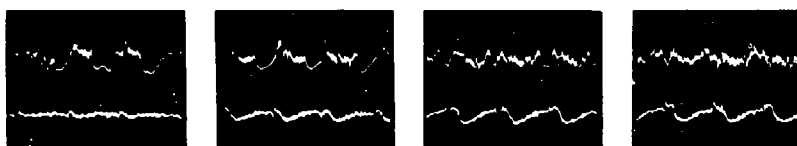


Figure 3. Velocity signal in boundary layer near surface, showing cyclic laminar/turbulent flow (propeller on) and laminar-transition-turbulence (propeller off).

The length of time which the cyclic turbulence remains in the boundary layer is dependent upon the laminar stability in the differing pressure gradients from the high-speed to the low-speed end. At the high-speed end, the pressure gradient is strongly favorable, and laminar stability is correspondingly high. Here, the boundary layer reverts almost immediately back to laminar flow after the passage of the external disturbance. At the low-speed end, the pressure gradient is no longer strongly favorable, laminar stability is greatly decreased, and the turbulence remains for almost the total cycle.

HIGH ← AIRSPEED → LOW  
 LOW ← ANGLE OF ATTACK → HIGH  
 FAVORABLE ← PRESSURE GRADIENT → ADVERSE  
 LOW ← THRUST COEFFICIENT → HIGH



PROPELLER ON

FLIGHT TEST - 30% CHORD

Figure 4. Velocity signals in boundary layer near surface and in external flow.

The effect of reduced laminar stability at the 30 percent chord location is evident in Figure 4. Here also is seen the character of the external flow disturbance due to the propeller slipstream. The viscous blade wake appears as a short wave impulse barely discernible at the high-speed end. As the speed is reduced, the propeller blade operates at an increasingly higher angle of attack and the viscous wake grows, leading to a more pronounced impulse disturbance signal. This is noted in the figures in terms of the propeller thrust coefficient. The low frequency wave pattern which develops in the external slipstream flow is due to the propeller tip vortex. As demonstrated by Sparks and Miley [8], the helical tip vortex induces an axial component in the slipstream velocity which increases with vortex strength (propeller thrust coefficient), and as the edge of the slipstream boundary is approached. While the tip vortex induced flow dominates the slipstream velocity signal, it will be shown that it is the relatively smaller blade viscous wake disturbance which is affecting the laminar boundary layer.

A slipstream disturbance flow model (Figure 5) was constructed from an analysis of the flight data. The viscous wake from the propeller blade forms a helical sheet which is split by the wing. The turbulence in the helical wake is seen by a stationary point in the boundary layer as a periodic change in external flow turbulence. The laminar boundary layer responds by transitioning to the turbulent state and then returning to the laminar state through a reverse-transitional process based upon the degree of local laminar stability.

#### Wind Tunnel Investigation

A small-scale wind tunnel test program was begun to study the boundary layer response in more detail. The test model was a 30-inch chord NACA 0012 composite wing section with an 18-inch diameter single-bladed propeller and electric motor mounted at wing level at

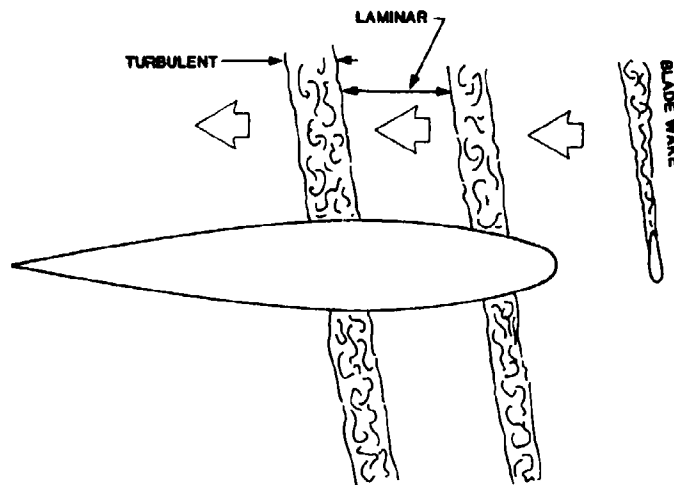


Figure 5. Slipstream disturbance flow model.

one-fifth chord distance upstream. Measurements were made at various angles of attack with a constant temperature hot-wire anemometer system and dual-probe configuration similar to that used in flight. The probes were traversed in a chordwise direction along the airfoil with the probe support free to pivot allowing the sensors to follow the airfoil contour. The probe heights above the surface were maintained at approximately 0.01 and 1.0 inches.

Two runs are shown in Figures 6-8. Figure 6 describes the signals seen in the photographs in the following figures. In each photograph the upper trace is the velocity in the boundary layer near the surface; the middle trace is the velocity for the external flow probe; and the lower trace is the trigger signal for the oscilloscope obtained from a magnetic proximity transducer sensing propeller blade passage. Figure 7 shows a series of measurements at  $-3$  degrees angle of attack resulting in a favorable pressure gradient along the upper surface. The upper row of photographs shows time histories of velocities at chord locations indicated with the propeller off. Transition takes place at approximately 70 percent chord at a chord Reynolds number of  $6 \times 10^5$ . Low frequency Tollmien-Schlichting waves appear with intermittent bursts of turbulence.

The lower row of photographs shows the velocities measured with the propeller running. The growth of the turbulent part of the cycle increases with decreasing laminar stability in the chordwise direction. Evident also is cyclic relaminarization of the previously turbulent region on the aft portion of the airfoil. Note this effect in the photograph for the 80 percent chord location. This behavior was seen in the flight data, but is more pronounced here, possibly due to the low Reynolds number. The waveform of the cyclic velocity variation can be noted, with the immediate jump to a turbulent velocity level with the arrival of the external disturbance. After the disturbance passes, the velocity returns to the laminar level as an exponential decay.

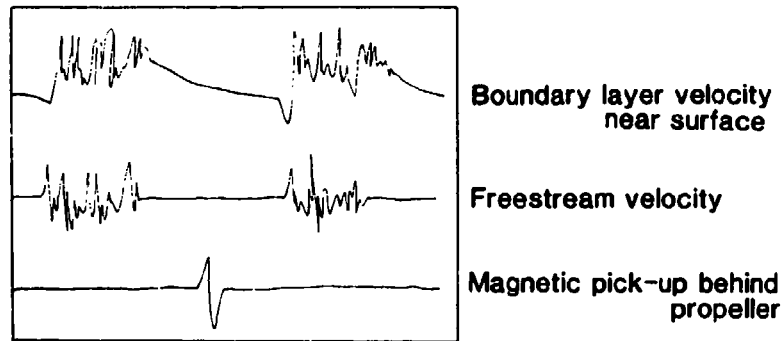


Figure 6. Identification of hot-wire velocity sensor signals in Figures 7-8.

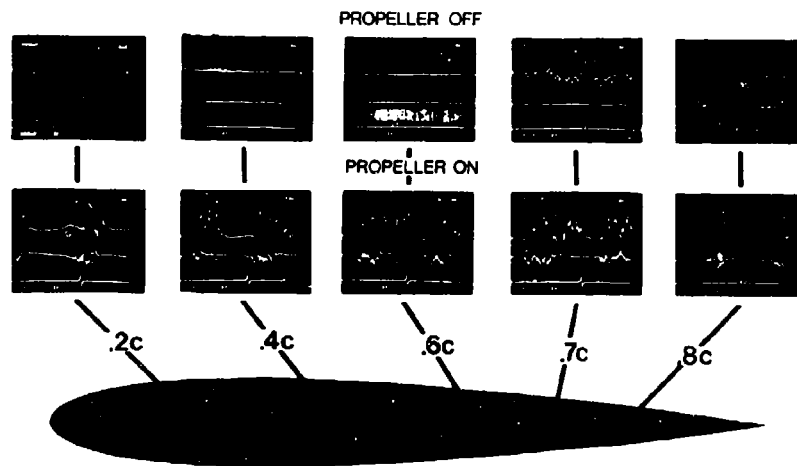


Figure 7. Velocity signals in boundary layer near surface and in external flow, showing cyclic laminar/turbulent flow (propeller on) and laminar-transition-turbulence (propeller off).  $-3^\circ$  angle of attack.

Figure 8 shows the results for 1 degree angle of attack. The pressure gradient is less favorable over the upper surface; the laminar boundary layer responds by transitioning now at 40 percent chord. More evident here is the cyclic relaminarization of the previously turbulent boundary layer. For the low test Reynolds number, the propeller slipstream appears to have a beneficial effect in the turbulent flow region of the airfoil. The mechanism behind the relaminarization is not understood at present. Possibilities include a reaction to the cyclic external flow turbulence and/or three-dimensional effects from the swirl component in the helical wake sheet.

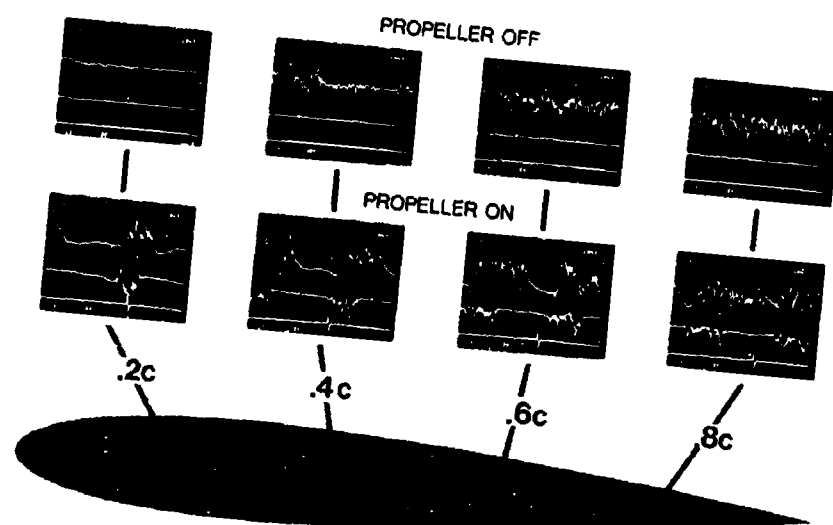


Figure 8. Velocity signals in boundary layer near surface and in external flow, showing cyclic laminar/turbulent flow (propeller on) and laminar-transition-turbulence (propeller off).  $+1^\circ$  angle of attack.

A second series of experiments was conducted utilizing a single hot-wire probe to traverse the boundary layer normal to the surface. Runs were made at three angles of attack. The velocity time histories were digitized through a microcomputer and stored on floppy disk for analysis. Sufficient data were taken to construct time histories of the mean velocity profile, and of the turbulence intensity at each corresponding point within the profile. A representative plot of these data is given in Figure 9. The mean streamwise velocity across a blade wake passage cycle is plotted with the turbulence intensity superimposed as a "turbulence intensity envelope". Three positions across the boundary layer are displayed. The upper trace shows the external flow turbulent disturbance. There is a velocity defect, characteristic of momentum-loss wake profiles. The lower trace shows the response near the surface to be an increase to a turbulent velocity followed by a decay back to the laminar state, as has been seen previously. The turbulence intensity decreases with the reversion to laminar flow.

#### ANALYSIS AND RESULTS

Figure 10 shows three sets of velocity profiles, each set including three profiles at different points in the wake passage cycle. Each set represents a different angle of attack, giving pressure gradient effects ranging from favorable to adverse. The profiles were not normalized with respect to their individual thicknesses. Note that the bottom line does not represent the surface of the airfoil but the lowest point in the boundary layer at which measurements could be taken. The profiles within each set are identified according to their position in the wake passage cycle, i.e. "laminar," "reverse-transitional," and "turbulent". Each of these positions also

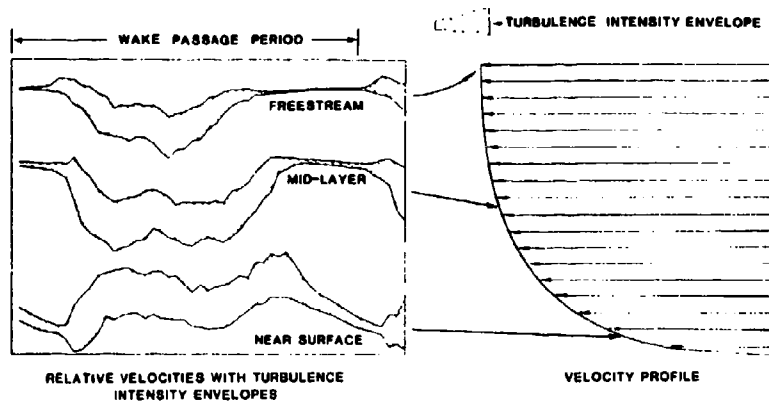


Figure 9. Time histories of the mean velocity and turbulence intensity at three vertical positions in the boundary layer. Data for one wake passage cycle.

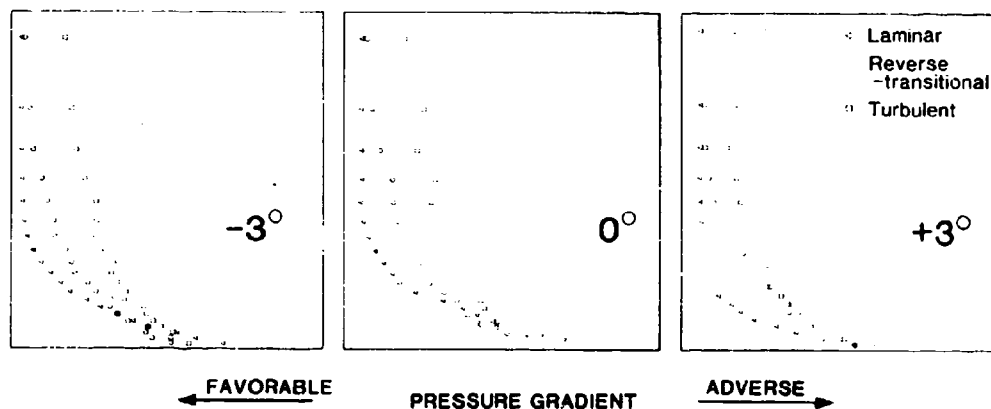


Figure 10. Boundary layer velocity profiles for three different angles of attack and for three different positions in the wake passage cycle.

corresponds to a level of external flow turbulence intensity. The turbulence intensity distribution (profile) through the boundary layer for the 0 degree angle of attack case is shown in Figure 11. Due to limitations of the digitizer, the upper cut-off frequency of the data is approximately 100 hertz. Also, the wind tunnel has a low frequency unsteadiness which was not removed from the data. It is seen that there is a correspondence between the external flow turbulence intensity, the boundary layer velocity profile, and the boundary layer turbulence intensity profile.

The effect of external flow turbulence on laminar and turbulent boundary layers has been investigated to a limited extent, primarily with concern to heat transfer. The work of Dyban, Epik and Surpun [9] is summarized in Figure 12. The laminar boundary layer over a flat

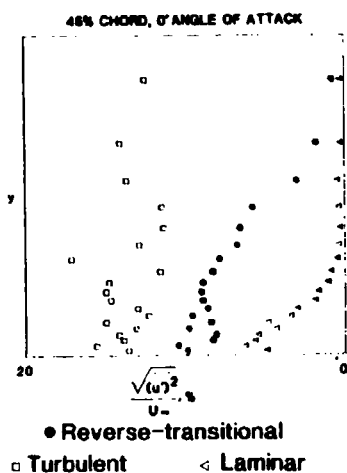
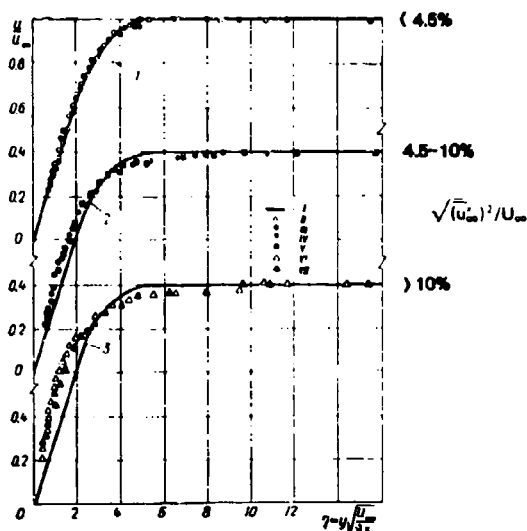
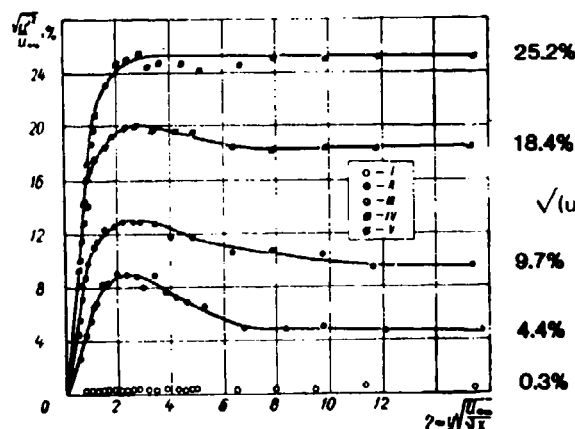


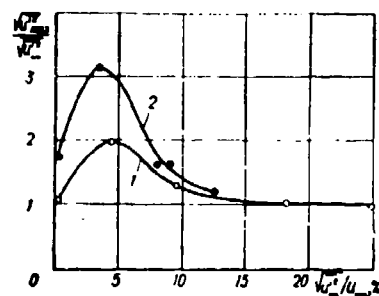
Figure 11. Turbulence intensity profiles for three different positions in the wake passage cycle.  $0^\circ$  angle of attack.



a) Boundary layer velocity profiles for three ranges of external flow turbulence. Blasius (flat plate) profile shown for reference.



b) Boundary layer turbulence intensity profiles for different external flow turbulence intensity levels.



c) Ratio of boundary layer peak turbulence intensity to external flow turbulence intensity for two different Reynolds numbers.

Figure 12. Results from Dyban et al. [9].

plate is subjected to different levels of external flow turbulence intensity. The resulting boundary layer velocity and turbulence intensity profiles are shown in the figure. As the external flow turbulence intensity is increased, the velocity profile becomes fuller. Three distinct ranges of external turbulence intensity have been identified according to the respective generation of turbulence within the boundary layer. As shown in Figure 12c, these ranges are: for an external turbulence intensity less than 4.5 percent, the generated turbulence intensity in the boundary layer increases at a faster rate

than the external flow turbulence intensity, the generated intensity reaching peak levels 2 to 3 times as large depending on the Reynolds number; for 4.5 to 10 percent external flow turbulence intensity, the generated turbulence intensity in the boundary layer increases at a slower rate than the external flow turbulence intensity, reversing the trend in the first range; and for an external flow turbulence intensity greater than 10 percent, the rate of increase of generated turbulence intensity in the boundary layer monotonically approaches that of the external flow. The boundary layer velocity and turbulence intensity profiles in Figure 12 are identified respectively according to these ranges.

Comparison of the wind tunnel measurements with the the work of Dyban et al. [9] supports the view that the laminar boundary layer within the slipstream can be characterized as a boundary layer with a cyclic variation of external flow turbulence. As indicated in Figure 5, the source of the external flow turbulence is the viscous wake from the propeller blade. The passage of the wake over a point on the wing alters the laminar boundary layer according to the behavior shown in Figures 10-12. The increase in mean velocity shown in Figures 2-4 is the result of the change in the velocity profile. The length of the turbulence signal in Figures 2-4 is in part due to the change in the turbulence intensity profile. The available data show that near the surface, the turbulence will persist some time after the passage of the external turbulence. It is expected that the local pressure gradient will affect the rate of decay of the generated turbulence. This is presently being investigated. It is also important to note that with a definite turbulence profile within the boundary layer, a single point measurement by a hot-wire sensor can give misleading information. A thinner boundary layer would register a shorter turbulence time length than a thicker one because of the relative position of the sensor. With the present understanding, the model of Figure 5 has been updated, and the current model is shown in Figure 13. In this figure the relative thickness of the boundary layer and the persistence of the turbulence is emphasized.

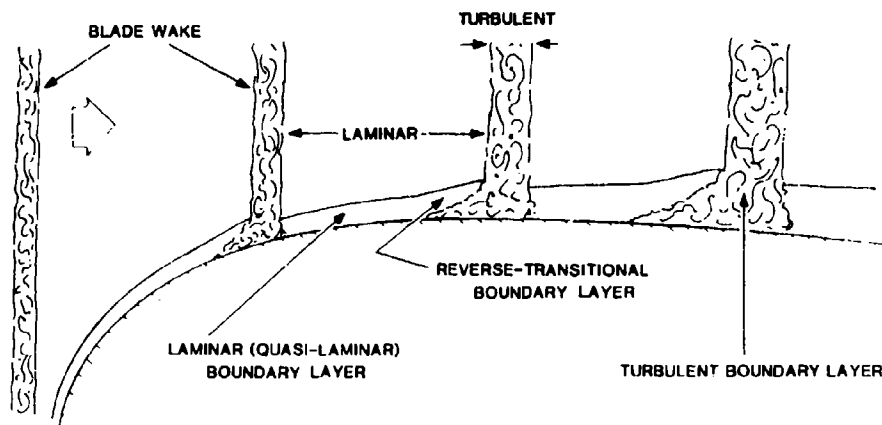


Figure 13. Current slipstream flow disturbance model, showing effect on laminar boundary layer.

An analysis was performed to determine where these external turbulence boundary layers lie in relation to conventional laminar and turbulent flows. Shape factor correlations between  $H_{12}$  and  $H_{32}$  were calculated from the wind tunnel data. Data for each time step in the wake passage cycle were averaged over fifty cycles, smoothed, fit with a cubic spline and integrated for values of  $H_{12}$  and  $H_{32}$ . Figure 14 shows the correlation across a wake passage cycle for an angle of attack of 0 degrees at chord locations of 15 and 45 percent, and for an angle of attack of 3 degrees at a chord location of 30 percent. Also included in the figure are the wake passage cycle time histories of the freestream mean velocity and turbulence intensity at the three chord positions. The curves plotted in the figure are the correlations utilized by Eppler [11] for laminar and turbulent flow as determined from similar solutions and empirical data.

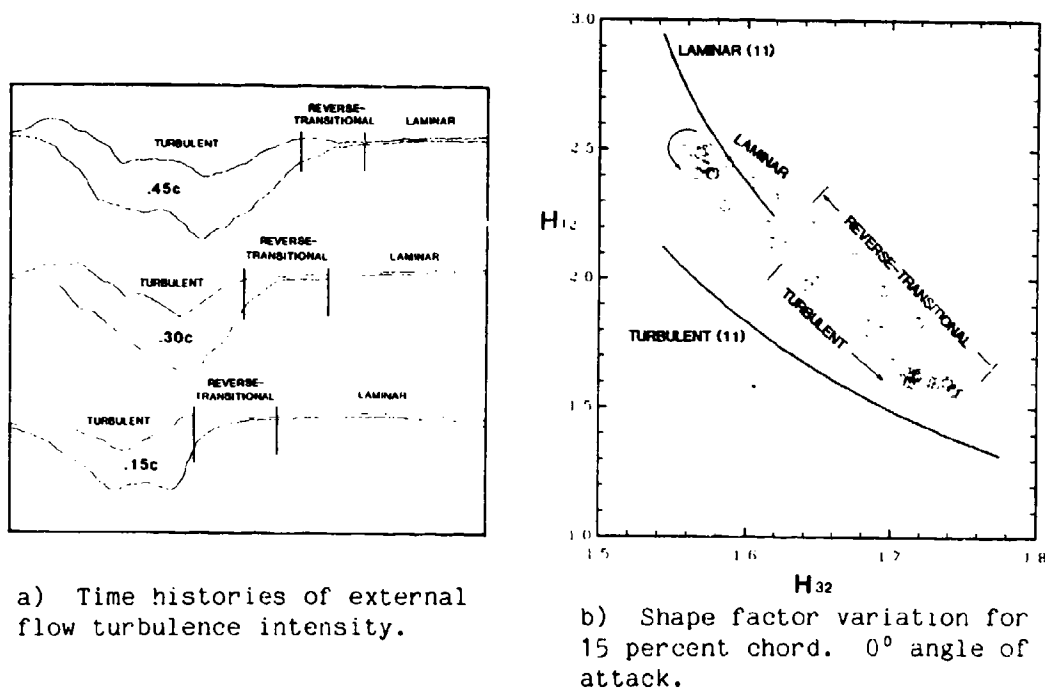
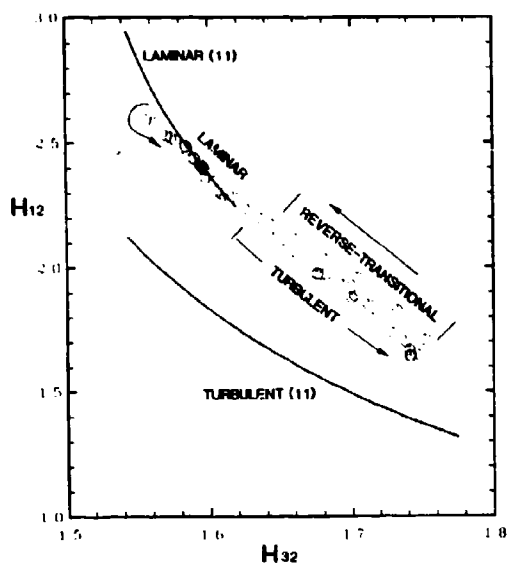
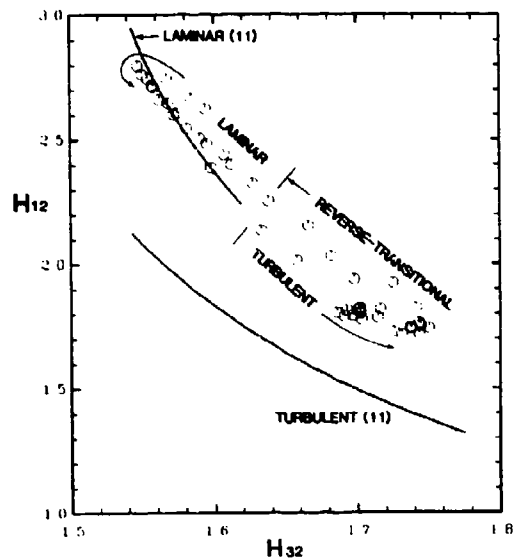


Figure 14. Variation of boundary layer shape factors through wake passage cycle.

In Figure 14 the time step data points corresponding to conditions where the boundary layer is indicated to be laminar lie on the laminar shape factor curve. The effect of the more adverse pressure gradient at 3 degrees angle of attack is seen by noting that the respective data points are shifted to lower values of  $H_{32}$ . As the cycle is progressed, the velocity profile shifts to a highly stable form under the influence of the external turbulence, then reverts back to the conventional laminar range. In each case the shape factor correlation indicates that the boundary layer based on velocity profile behavior never attains the predicted turbulent relationship. In Figure 15, shape factors determined from the external turbulence flow boundary layer velocity profiles of Dyban et al. [9] and from relaminarization flow boundary layer velocity profiles of reference [10] are plotted with the laminar and turbulent correlation curves. The external



c) Shape factor variation for 45 percent chord.  $0^\circ$  angle of attack.



d) Shape factor variation for 30 percent chord.  $+3^\circ$  angle of attack.

Figure 14. Concluded.

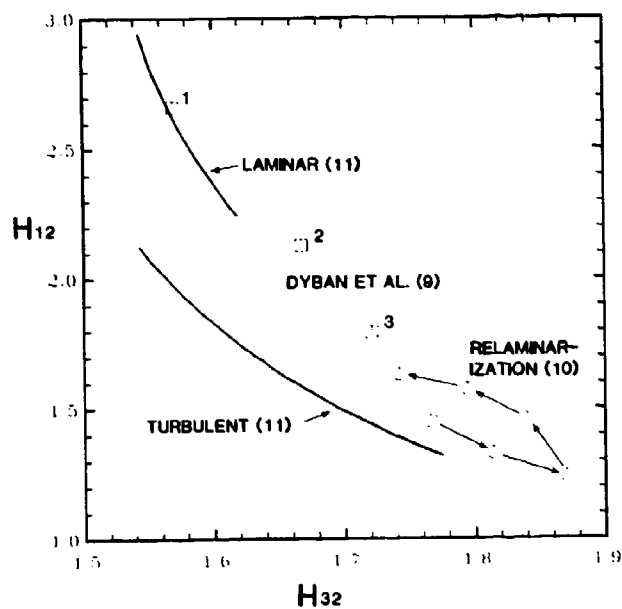


Figure 15. Boundary layer shape factor variation for external flow turbulence of Dyban et al. [9] and for relaminarizing flow [10].

turbulence shape parameter values follow that same path as the slipstream results. The relaminarizing flow shape parameter values initially move in the direction of a newer (younger) turbulent boundary layer, then loop back and proceed in the direction of the laminar curve. The relaminarizing boundary layer is initially turbulent. Under the action of a strongly favorable pressure gradient, a reversion to a laminar-like state takes place. The progress of the relaminarization in relation to the laminar and turbulent curves is noted in the figure. The turbulence intensity profiles of the relaminarizing flow from reference [10] are given in Figure 16. The profiles are similar to those of the external flow turbulence boundary layers.

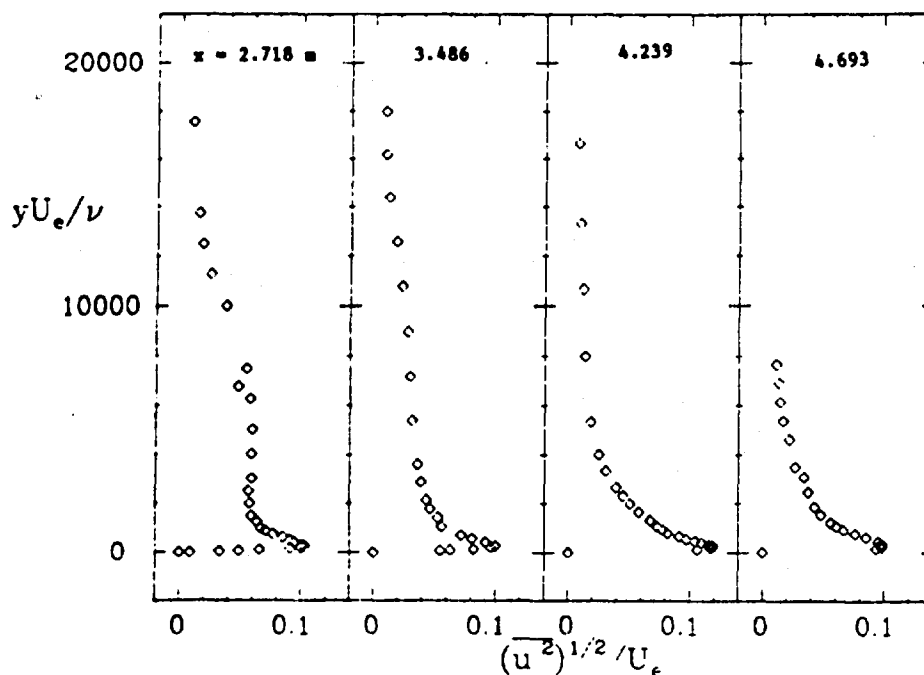


Figure 16. Boundary layer turbulence intensity profiles for relaminarizing flow [10]. Increasing values of  $x$  denote downstream progress towards relaminarization.

The results in Figures 14 and 15 raise the question of a class of boundary layers which lie between the fully laminar and fully turbulent states. In the case of the external turbulence flows, the terms "pseudo-laminar" and "pseudo-turbulent" have been used. In consideration of where they lie in terms of shape parameter values, the term "transitional" may be more appropriate. The implication of the data in the figures is that a "transitional" shape factor correlation curve may exist which connects laminar and turbulent flows. This concept will be investigated in the effort to develop a practical boundary layer prediction method for the slipstream case.

#### SUMMARY

The laminar boundary layer within a propeller slipstream is affected by the viscous wake from the propeller blade. The wake forms

a helical sheet which is split by the wing and passes over the upper and lower surfaces. Across a propeller blade wake passage cycle, the boundary layer at a point on the airfoil surface goes through the distinct phases of turbulent, reverse-transitional and laminar behavior consistent with a cyclic variation in external flow turbulence. The turbulent phase is characteristic of boundary layer flow with external turbulence, and exhibits velocity profiles which lie in a transitional region between fully laminar and fully turbulent flow. The cyclic external turbulence may also influence the turbulent boundary layer in such a way as to cause periodic relaminarization as has been observed in flight and in the wind tunnel.

#### ACKNOWLEDGEMENT

This work is supported by NASA Langley Research Center  
Grant No. NAG 1-344.

#### REFERENCES

1. Young, A.D. and Morris, D.E., "Note on Flight Tests on the Effect of Slipstream on Boundary Layer Flow," R&M No. 1957, Brit. A.R.C., 1939.
2. Young, A.D. and Morris, D.E., "Further Note on Flight Tests on the Effect of Slipstream on Boundary-Layer Flow," RAE Rep. No. B.A. 1404b, 1939.
3. Hood, M.J. and Gaydos, M.E., "Effects of Propellers and Vibration on the Extent of Laminar Flow on the NACA 27-212 Airfoil," NACA ACR (WR L-784), 1939.
4. Zalovecik, J.A., "Flight Investigation of the Boundary Layer and Profile Drag Characteristics of Smooth Wing Sections on a P-47D Airplane," NACA WR L-86, 1945.
5. Zalovecik, J.A., and Skoog, R.B., "Flight Investigation of Boundary Layer Transition and Profile Drag of an Experimental Low-Drag Wing Installed on a Fighter-Type Airplane," NACA WR L-94, 1945.
6. Holmes, B.J., Obara, C.J., and Yip, L.P., "Natural Laminar Flow Experiments on Modern Airplane Surfaces," NASA TP 2256, 1984.
7. Holmes, B.J., Obara, C.J., Gregorek, G.M., Hoffman, M.J., and Freuhler, R.J., "Flight Investigation of Natural Laminar Flow on the Bellanca Skyrocket II," SAE Paper 830717, 1983.
8. Sparks, S.P. and Miley, S.J., "Development of a Propeller Afterbody Analysis with Contracting Slipstream," SAE Technical Paper Series 830743, April 1983.
9. Dyban, Ye.P., Epik, E.Ya., and Surpun, T.T., "Characteristics of the Laminar Boundary Layer in the Presence of Elevated Free-Stream Turbulence," Fluid Mechanics - Soviet Research, Vol. 5, No. 4, July-August 1976, pp. 30-36.

10. Kline, S.J., Cantwell, B.J. and Lilley, G.M., ed. "The 1980-81 AFSOR-HTTM-Stanford Conference on Complex Turbulent Flows: Comparison of Computation and Experiment," Thermosciences Division, Mechanical Engineering Department, Stanford University, 1981.
11. Eppler, R. and Somers, D.M., "A Computer Program for the Design and Analysis of Low-Speed Airfoils," NASA TM 80210, 1980.